CODING FOR SPATIAL ORIENTATION IN HUMANS AND ANIMALS: BEHAVIOR, CIRCUITS AND NEURONS,

2nd Edition

EDITED BY: Desdemona Fricker, Mathieu Beraneck, Michele Tagliabue and K. J. Jeffery

PUBLISHED IN: Frontiers in Neural Circuits and Frontiers in Neurology

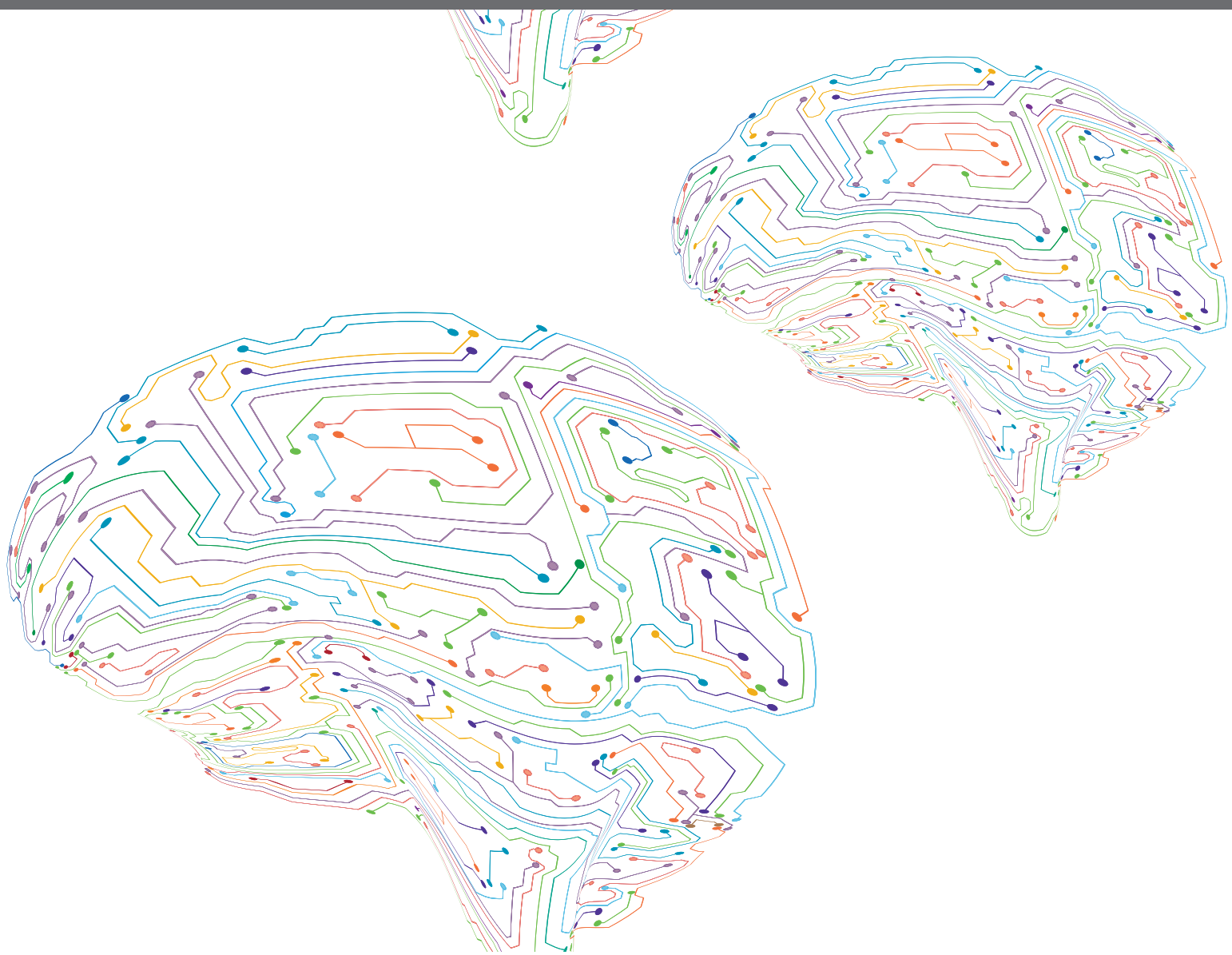

frontiers Research Topics

ISSN 1664-8714
ISBN 978-2-88966-430-6
DOI 10.3389/978-2-88966-430-6

About Frontiers

Frontiers is more than just an open-access publisher of scholarly articles: it is a pioneering approach to the world of academia, radically improving the way scholarly research is managed. The grand vision of Frontiers is a world where all people have an equal opportunity to seek, share and generate knowledge. Frontiers provides immediate and permanent online open access to all its publications, but this alone is not enough to realize our grand goals.

Frontiers Journal Series

The Frontiers Journal Series is a multi-tier and interdisciplinary set of open-access, online journals, promising a paradigm shift from the current review, selection and dissemination processes in academic publishing. All Frontiers journals are driven by researchers for researchers; therefore, they constitute a service to the scholarly community. At the same time, the Frontiers Journal Series operates on a revolutionary invention, the tiered publishing system, initially addressing specific communities of scholars, and gradually climbing up to broader public understanding, thus serving the interests of the lay society, too.

Dedication to Quality

Each Frontiers article is a landmark of the highest quality, thanks to genuinely collaborative interactions between authors and review editors, who include some of the world's best academicians. Research must be certified by peers before entering a stream of knowledge that may eventually reach the public - and shape society; therefore, Frontiers only applies the most rigorous and unbiased reviews.
Frontiers revolutionizes research publishing by freely delivering the most outstanding research, evaluated with no bias from both the academic and social point of view. By applying the most advanced information technologies, Frontiers is catapulting scholarly publishing into a new generation.

What are Frontiers Research Topics?

Frontiers Research Topics are very popular trademarks of the Frontiers Journals Series: they are collections of at least ten articles, all centered on a particular subject. With their unique mix of varied contributions from Original Research to Review Articles, Frontiers Research Topics unify the most influential researchers, the latest key findings and historical advances in a hot research area! Find out more on how to host your own Frontiers Research Topic or contribute to one as an author by contacting the Frontiers Editorial Office: researchtopics@frontiersin.org

CODING FOR SPATIAL ORIENTATION IN HUMANS AND ANIMALS: BEHAVIOR, CIRCUITS AND NEURONS,
2nd Edition

Topic Editors:
Desdemona Fricker, UMR8002 Centre de neuroscience et de cognition intégrative (INCC), France
Mathieu Beraneck, Université Paris Descartes, France
Michele Tagliabue, Université Paris Descartes, France
K. J. Jeffery, University College London, United Kingdom

Publisher's note: In this 2nd edition, the following article has been added: Fricker D, Beraneck M, Tagliabue M and Jeffery KJ (2020) Editorial: Coding for Spatial Orientation in Humans and Animals: Behavior, Circuits and Neurons. *Front. Neural Circuits* 14:619073. doi: 10.3389/fncir.2020.619073

Citation: Fricker, D., Beraneck, M., Tagliabue, M., Jeffery, K. J., eds. (2021). Coding for Spatial Orientation in Humans and Animals: Behavior, Circuits and Neurons, 2nd Edition. Lausanne: Frontiers Media SA. doi: 10.3389/978-2-88966-430-6

Table of Contents

frontiers in Neural Circuits

EDITORIAL
published: 25 November 2020
doi: 10.3389/fncir.2020.619073

Editorial: Coding for Spatial Orientation in Humans and Animals: Behavior, Circuits and Neurons

Desdemona Fricker[1], Mathieu Beraneck[1]*, Michele Tagliabue[1]* and Kate J. Jeffery[2]**

[1] Integrative Neuroscience & Cognition Center, CNRS UMR 8002, Université de Paris, Paris, France, [2] Department of Experimental Psychology, Institute of Behavioural Neuroscience, University College London, London, United Kingdom

Keywords: anatomy, physiology, model, head direction, grid cell, self-motion, vestibular, visual

Editorial on the Research Topic

Coding for Spatial Orientation in Humans and Animals: Behavior, Circuits and Neurons

The goal of this Research Topic was to bring together articles on spatial orientation, from behavior and brain wide circuits to single cell anatomy and the function of neuronal networks. This research is aimed at understanding how the brain integrates multisensory spatial information, using diverse experimental approaches in humans and in rodents, as well as *in silico* computational tools.

Articles in this collection address a broad range of aspects of spatial orientation. Human studies are especially challenging when it comes to understanding the transformation of sensory information into motor commands. Blouin et al. analyzed cortical activation during movement planning and suggest that a cognitive representation for planning arm movements after body motion is necessary to store spatial information before triggering movement.

Maintaining spatial orientation requires monitoring self-motion cues and it depends on the integration of visual, proprioceptive, kinesthetic, and vestibular information. Stahn et al. investigated spatial updating during parabolic flight maneuvers, showing that updating performance critically depends on gravity.

Spatial disorientation is a major risk for pilots and a frequent cause of aircraft accidents. Tamura et al. examine electrodermal activity as a biomarker to evaluate spatial disorientation in pilot candidates, and they suggest that it may give a useful correlate for the severity of motion sickness.

Spatial navigation abilities change throughout life. To help to elucidate the cerebral bases of spatial navigation deficits as we get older, the study by Ramanoël et al. evaluated the effect of aging, showing age-related differences in the functional and structural connectivity of the spatial navigation brain network, and in particular between low-level visual areas and high-level spatial areas.

To investigate the physiology and pathology of spatial navigation, healthy human subjects and patients with neurological disorders can be examined either in real space or in virtual reality (VR). Schöberl et al. reviewed the advantages and limitations of real space navigation testing and different VR-based navigation paradigms, and discussed their potential future applications in clinical neurology.

The perception of optic flow is a fundamental part of the spatial toolkit. Solari et al. experimentally tested speed perception for conditions in which only portions of the visual field were visible, and captured the features of the human perceptual data in a biologically-inspired computational model.

This Research Topic puts special emphasis on the understanding the neural basis of spatial orientation across different species. The vestibular system is particularly important as a highly

Edited and reviewed by:
Jérôme Epsztein, Institut National de la Santé et de la Recherche Médicale (INSERM), France

****Correspondence:***
Desdemona Fricker
desdemona.fricker@parisdescartes.fr
Mathieu Beraneck
mathieu.beraneck@parisdescartes.fr
Michele Tagliabue
michele.tagliabue@parisdescartes.fr
Kate J. Jeffery
k.jeffery@ucl.ac.uk

Received: *19 October 2020*
Accepted: *03 November 2020*
Published: *25 November 2020*

Citation:
Fricker D, Beraneck M, Tagliabue M and Jeffery KJ (2020) Editorial: Coding for Spatial Orientation in Humans and Animals: Behavior, Circuits and Neurons. Front. Neural Circuits 14:619073. doi: 10.3389/fncir.2020.619073

preserved sensory detector of orientation. Smith offers a comprehensive review of the growing evidence for the role of the otoliths in spatial memory, in both rodents and humans. He points out that loss of otolithic function impairs normal spatial memory and also impairs the normal function of head direction cells in the thalamus and place cells in the hippocampus.

The Review article by O'Mara and Aggleton addresses spatial and memory research that has long been focused on the hippocampus and entorhinal cortex, in rodents and in humans. The authors present evidence suggesting that spatial signals originally identified in the hippocampus are also observed in subcortical regions and they argue that subcortical circuitry should be better addressed in contemporary theories of spatial processing.

Dillingham and Vann summarize the mixed evidence regarding the contribution of the head direction system to behavior. Their Perspective discusses the observation that lesions of the mammillary nuclei, which lead to a disrupted head direction signal in downstream brain areas, do not lead to impaired performance on spatial tasks.

The rodent model system is particularly useful for detailed circuit analysis with modern tools such as virus-mediated trans-synaptic tracing. A tracing study in mice by Bohne et al. revealed a polysynaptic circuit from the deep cerebellar nuclei to the hippocampus via the thalamus. This result strengthens the notion of the cerebellum's involvement in spatial navigation.

Honda and Furuta employed sparse viral labeling techniques in rats to examine projections of presubicular neurons. Their highly detailed anatomical reconstructions offer novel insights into the anatomical organization of how head-direction information reaches the medial entorhinal cortex.

Decoding of neural population activity is a popular approach to assess the dynamics of spatial signals. Xu et al. provided an overview of different approaches, comparing machine learning and statistical model-based decoding methods, for head direction signals in thalamo-cortical brain areas.

Jayakumar et al. applied computational modeling to investigate grid cells in medial entorhinal cortex. Their model of grid cell generation was based on a combination of directionally tuned oscillators and Hebbian learning, and showed that grid cells encode invariant properties of an environment.

Laptev and Burgess presented a model of parallel place and grid cell attractor systems that provides a better account of classic place cell experiments than a model with only one attractor. Their study supports the hypothesis that grid cells are responsible for performing path integration while place cells are receiving information about environmental cues and external landmarks. Importantly the model makes predictions that can be tested in future experiments.

We are impressed with the broad range of contributions included in this Topic, and pleased that scientists from all walks of spatial orientation research chose to publish in this volume. We thank the authors for their contributions, and are grateful to the reviewers for their efforts.

AUTHOR CONTRIBUTIONS

All authors listed have made a substantial, direct and intellectual contribution to the work, and approved it for publication.

Conflict of Interest: The authors declare that the research was conducted in the absence of any commercial or financial relationships that could be construed as a potential conflict of interest.

frontiers in Neurology

ORIGINAL RESEARCH
published: 04 December 2018
doi: 10.3389/fneur.2018.01056

Wrist-Worn Electrodermal Activity as a Novel Neurophysiological Biomarker of Autonomic Symptoms in Spatial Disorientation

Atsushi Tamura[1], Tetsuya Iwamoto[2], Hirokazu Ozaki[2], Mikihiko Kimura[2], Yukiko Tsujimoto[2] and Yoshiro Wada[3]*

[1] Department of Otolaryngology-Head and Neck Surgery, National Defense Medical College, Tokorozawa, Japan, [2] Aeromedical Laboratory, Japan Air Self-Defense Force, Sayama, Japan, [3] Department of Otolaryngology-Head and Neck Surgery, Nara Medical University, Kashihara, Japan

Background: Spatial disorientation is one of the most frequent causes of aircraft accidents, and is thus a major problem affecting air safety. Although a number of studies have examined spatial disorientation, the precise physiological changes occurring as a direct result of spatial disorientation and motion sickness remain unclear. The present study sought to investigate electrodermal activity (EDA) and subjective autonomic symptoms during spatial disorientation training, and to develop an indicator of physiological changes for pilot candidates.

Methods: In the current study, we investigated changes in EDA measured using a wrist-worn device, and subjective autonomic nervous system symptoms during spatial disorientation training for pilot candidates. We then used the Graybiel diagnostic criteria to develop a novel physiological biomarker.

Results: We found that maximum EDA change and peak amplitude were significantly increased in participants with a Graybiel score of $\geq$3 points compared with those who scored $<$2 points. Furthermore, for symptoms of cold sweating and saliva secretion (from the seven Graybiel diagnostic criteria), the maximum EDA change in participants with scores $\geq$1 point was significantly higher than that of participants scoring 0 points.

Conclusion: Our results indicate that EDA data measured with a wrist-worn device could provide a useful method for objective evaluation of the severity of spatial disorientation and motion sickness.

Keywords: electrodermal activity, spatial disorientation, motion sickness, autonomic nervous system symptoms, pilot

OPEN ACCESS

Edited by:
Michele Tagliabue, Université Paris Descartes, France

Reviewed by:
Hideo Shojaku, University of Toyama, Japan
Seong-Hae Jeong, Chungnam National University, South Korea

****Correspondence:***
Atsushi Tamura
morningconference@r8.dion.ne.jp

Specialty section:
This article was submitted to Neuro-Otology, a section of the journal Frontiers in Neurology

Received: *29 July 2018*
Accepted: *20 November 2018*
Published: *04 December 2018*

Citation:
Tamura A, Iwamoto T, Ozaki H, Kimura M, Tsujimoto Y and Wada Y (2018) Wrist-Worn Electrodermal Activity as a Novel Neurophysiological Biomarker of Autonomic Symptoms in Spatial Disorientation. Front. Neurol. 9:1056. doi: 10.3389/fneur.2018.01056

INTRODUCTION

In daily life, our brain subconsciously generates a mental image of our physical body in relation to the surrounding space. This image involves inner spatial axes corresponding to direction, position, size, shape, distance, and motion, and this function occurs both at rest and during motion in relation to space (1, 2). This ability of the brain to reproduce the physical space around us is called spatial orientation. Spatial orientation results from the integration of multiple sensory inputs from the visual, vestibular, and somatosensory systems in the brain (3, 4).

Spatial orientation in flight is sometimes difficult to achieve because the various types of sensory stimuli (visual, vestibular, and somatosensory inputs) vary in magnitude, direction, and frequency. Any differences or discrepancies between visual, vestibular, and somatosensory inputs result in a "sensory mismatch" that can produce illusions and lead to spatial disorientation (1, 2). In addition, when deprived of vision (e.g., because of clouds, fog, or low-light conditions at night), even experienced aircraft pilots may be unable to maintain spatial orientation, and commonly experience spatial disorientation. Spatial disorientation can lead to several autonomic symptoms that are commonly referred to collectively as motion sickness, including nausea, salivation, and cold sweating (5, 6).

Numerous studies have evaluated spatial disorientation and motion sickness over many years. Objective evaluations of motion sickness using physiological indices have utilized various measures, including electroencephalographic responses (7), changes in heart rate, blood pressure, and body temperature (8), altered breathing and maximum oxygen intake (9), and characteristic eye movements (10). However, evaluating the onset mechanisms and physiological changes that occur during spatial disorientation remains difficult (8) because spatial disorientation affects the visual and vestibular systems, making it difficult to simultaneously evaluate all *in vivo* changes. In addition, even if various physiological or biochemical markers are used, individual differences exist in the degree of spatial disorientation, making it difficult to develop a method for objective evaluation. Furthermore, devices for measuring spatial disorientation must be sufficiently portable for measuring physiological markers during movement.

In recent years, various devices have been tested for spatial disorientation training in pilots (11–14). However, despite intensive efforts in the development of spatial disorientation training programs (11–14), advanced hardware (10–14), and research (7–10, 14), the operational impact of spatial disorientation in terms of crew and aircraft losses remains significant. Conventional spatial orientation training is primarily composed of lectures on the anatomy and physiology of the sensory systems. Significant efforts have also been made to reproduce various types of visual and vestibular spatial disorientation that pilots might encounter in flight, with limited and variable success.

Electrodermal activity (EDA) refers to the electrical changes measured at the surface of the skin that arise when the skin receives innervating signals from the brain, and can be used to evaluate sympathetic activity (15–17). For most people, emotional arousal, increased cognitive workload, and/or physical exertion cause the brain to send signals to the skin, thus increasing the level of sweating. Although this increase in sweat on the surface of the skin may not be noticeable, electrical conductance increases significantly as the pores of the skin begin to fill below the surface (18–20).

Past studies have investigated changes in autonomic nervous system symptoms using EDA as an indicator of spatial disorientation and motion sickness (14, 21, 22). Some previous studies have reported that EDA exhibits marked changes with the degree of spatial disorientation and motion sickness, and that EDA levels are sensitive to simulator sickness (14, 21). However, other studies have reported that EDA does not change significantly with these variables (22). Therefore, it remains unclear whether EDA changes during spatial disorientation and motion sickness.

In previous studies, EDA measurements were carried out by attaching electrodes to the palm, fingers, and ankle (18, 22). However, in addition to requiring several electrodes, these electrodes typically detach easily, making EDA difficult to measure accurately (18, 22).

Recently, a number of researchers have measured EDA using wrist-worn devices to specifically evaluate autonomic nerve function in patients with various diseases, and to monitor activity during sleep (16, 23–25). However, to the best of our knowledge, no previous studies have measured EDA using a wrist-worn device during spatial disorientation training. Thus, we hypothesized that EDA levels measured using a wrist-worn device may provide a novel neurophysiological biomarker that could be used to objectively evaluate the degree of spatial disorientation.

Using a different approach, Gordon et al. examined the components of saliva as an objective assessment of motion sickness, reporting that the amount of amylase in saliva was significantly higher in people who are prone to motion sickness compared with those who are not (26). In addition, the researchers suggested that the amount of amylase in saliva could provide an indicator of a person's susceptibility to motion sickness. They interpreted their results as indicating that the sympathetic nervous system tended to work more actively for people who were prone to motion sickness because amylase secretion in saliva is regulated by the sympathetic nervous system. Therefore, in the current study, we hypothesized that alterations in autonomic function would also be reflected in EDA changes, alongside salivary secretion and various autonomic neurological symptoms.

The present study sought to investigate EDA using a wrist-worn device while measuring subjective autonomic symptoms during spatial disorientation training, as well as examining the correlation between these variables. Overall, we sought to develop an indicator of physiological changes during spatial disorientation training for pilot candidates.

MATERIALS AND METHODS

Participants

A group of 177 healthy pilot candidates aged 22–25 years old (mean age: 22.7 years; male/female: 170/7) participated in this study. All participants belonged to the Japan Air Self-Defense Force. Participants had no previous medical history of eye, ear, or equilibrium disorders. We carried out an interview with each participant about their physical and emotional condition before the experiment, and confirmed that no participants had abnormal health conditions, and none were sleepy, hungry, or thirsty before commencing spatial disorientation training. The protocol was approved by the Ethics Committee of the Aeromedical Laboratory (Notification No. 25-2-1). Written informed consent was obtained from each participant, and the

investigations were conducted in accord with the principles of the Declaration of Helsinki.

Device for Spatial Disorientation Training

We used a spatial disorientation training device GYROLAB GL-4000 (Environmental Tectonics Corporation, Southampton, PA, USA) located at the Aeromedical Laboratory of the Japan Air-Self Defense Force to produce a variety of spatial disorientation environments (10). The cockpit of this training device had degrees of freedom on four axes: planetary (3.05-m radius), pitch, roll, and yaw (**Figure 1A**). In the cockpit, animated images and still images were presented on a screen (120 × 70° field of view) located 0.9 m in front of the participants using a projector (**Figure 1B**). We monitored participants' head position in real time through a charge-coupled device (CCD) camera mounted in the cockpit. During training, we communicated with participants using headsets. Participants were securely fastened into their seats via five-point seatbelts. Participants' heads were aligned with the headrest of the seat and were not fixed in place, enabling them to sit in a way that approximated the posture of an active pilot (10).

Spatial Disorientation Training for Pilot Candidates

We used a spatial orientation training device to present visual and vestibular stimuli to participants as spatial disorientation training. In the daytime simulation (i.e., daytime takeoff, turning operation during daytime), we used the projector to present animated images consisting of a runway, towns, forests, mountains, clouds, and a blue sky. Nighttime simulation included the same images, but with poor visual information, and contained runway approach lights, town lights, and stars. In the nighttime simulation (i.e., nighttime takeoff, turning operation at night), we reduced brightness so that outlines (such as those of mountains or buildings) disappeared and spatial information was poor.

The content of the spatial disorientation training is shown in **Table 1**. False visual reference illusions may cause pilots to orient their aircraft in relation to a false horizon; these illusions can be caused by flying over a banked cloud, night flying over a featureless terrain with ground lights that are indistinguishable from a dark sky with stars, or night flying over a featureless terrain with a clearly defined pattern of ground lights and a dark, starless sky. The somatogravic illusion involves a sudden forward linear acceleration during level flight, in which the pilot experiences the illusory perception that the nose of the aircraft is pitching up. This illusion is caused by a sudden return to level flight following a gradual and prolonged turn that went unnoticed by the pilot. Similarly, the Coriolis illusion involves the simultaneous stimulation of two semi-circular canals, and is associated with a sudden tilting (forward or backwards) of the pilot's head while the aircraft is turning. This illusion can occur when a pilot tilts their head down (to look at an approach chart or to write a note on their knee board), up (to look at an overhead instrument or switch), or sideways. The graveyard spin is an illusion that pilots may experience when they intentionally or unintentionally enter a spin (**Table 1**).

We exposed participants to a visual illusion, vestibular illusion, or a combination of the two for 30 min using the spatial disorientation training device (**Figure 2**). Spatial disorientation training was conducted according to the protocols defined by the Japan Air Self-Defense Force, and the training time and EDA measurement time were the same for all participants.

Evaluation of Electrodermal Activity

To investigate the changes in EDA obtained using a wrist-worn device during spatial disorientation training, we used a device called the Q sensor 2.0 (Affectiva, Waltham, MA, USA) (**Figure 3**). The Q sensor measures electrical conductance (the

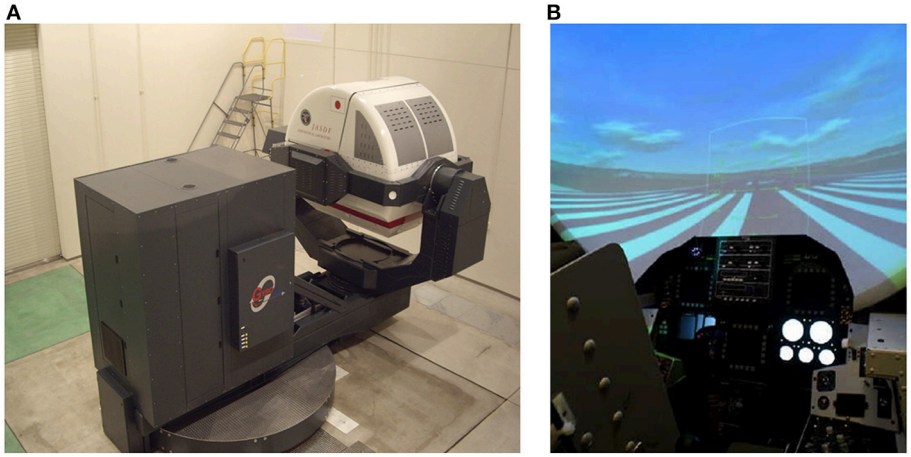

FIGURE 1 | Device used to produce a variety of tilt environments with visual stimulation. Publication of these images has been approved by the Aeromedical Laboratory, Japan Air Self-Defense Force. **(A)** Spatial orientation training device, GYROLAB GL-4000. **(B)** Inside the cockpit. Images were projected onto a screen in front of the participants.

TABLE 1 | Spatial disorientation training for candidate pilots.

1	Daytime take off	Take off at daytime
2	Nighttime take off	Take off with poor visual information at nighttime
3	Turning operation at daytime	Daytime flight
4	False visual reference illusions	A false visual reference illusion can be caused by city lights, clouds, stars, and darkness.
5	Turning operation in clouds	Flight in environments with poor visual information in clouds
6	False visual reference illusions	A false visual reference illusion can be caused by city lights, clouds, stars, and darkness.
7	Turning operation at nighttime	Flight in environments with poor visual information at nighttime
8	False visual reference illusions at nighttime	A false visual reference illusion can be caused by city lights, clouds, stars, and darkness.
9	Somatogravic illusion	The rapid acceleration pushes the pilot back in their seat, giving them the sensation of a nose up attitude. To correct this, the pilot noses the plane over toward the earth.
10	The Leans	The leans occur when a quick correction of a banked attitude happens too slowly. The sensory membrane in the inner ear sends the brain information inducing the sensation of banking in the opposite direction. However, the disoriented pilot tends to over-bank in the wrong direction, potentially rolling the aircraft.
11	Loop	Loop inside and outside clouds in the daytime.
12	Coriolis illusion	The Coriolis illusion is caused by making a quick head movement during a constant rate turn that has ceased stimulating the inner ear.
13	Graveyard spin	When a pilot is recovering from a spin that has stopped, the fluid in the inner ear can create the illusion that they have entered a spin in the other direction.

Participants were exposed to the visual illusion, vestibular illusion, and a combination of the two using a spatial disorientation training device.

inverse of resistance) across the skin, by passing a minuscule amount of direct current between two electrodes that are in contact with the skin. The units of measurement in this system are microsiemens (μS). Participants were asked to wear the Q sensor during spatial disorientation training. In this experiment, all participants wore the Q sensor on their left wrists because they were required to operate switches in the spatial orientation training device with their right hands, causing movement that could affect the skin conductance data. To avoid this problem, we fixed the left hand of each participant in position beside the seat. The position was confirmed via a CCD camera in the training device.

After training, we reviewed and annotated the EDA data recorded by the Q sensor. Two 12-mm disposable silver-coated electrodes were applied to the volar surface of the wrist on the side without arterial line access. The raw EDA signals were downloaded daily and the data were analyzed off-line using company-provided software (Affectiva Q version 2.01.56) (**Figure 2**). We then calculated the maximum change in EDA, the number of EDA peaks, the mean and median amplitude, and the area under the curve (AUC) values for the EDA data in all participants. We defined the maximum change as the difference between the minimum EDA value before spatial disorientation training and the maximum EDA value during training. Peak EDA measurements were visually evaluated using every short-term phasic increase in EDA >0.01 μS (27). We used ImageJ software version 1.44p (http://rsbweb.nih.gov/ij/download.html) to measure the AUC (28). The units of measurement were pixels.

Evaluation of Subjective Autonomic Symptoms

To evaluate subjective autonomic symptoms, we used the Graybiel diagnostic score and quantified the severity of autonomic symptoms during spatial disorientation training (29) (**Table 2**). Two examiners observed and evaluated the complexion and sweating state of the participants, and scored the data after training, according to the diagnostic categorization (29) (**Table 2**).

We divided participants into three groups according to their total Graybiel scores: (1) 0 points ($n = 59$), (2) 1–2 points ($n = 64$), and (3) ≥3 points groups ($n = 54$). In addition, we compared the maximum EDA change between these three groups.

We also divided the participants into two groups according to Graybiel scores, for each autonomic symptom: (1) 0 points group and (2) ≥1 points group for the seven autonomic symptoms. For the nausea syndrome, we divided participants into: (1) 0 points group ($n = 104$) and (2) ≥1 points group ($n = 73$). For skin color, we divided participants into: (1) 0 points group ($n = 122$) and (2) ≥1 points group ($n = 55$). For cold sweating, we divided participants into: (1) 0 points group ($n = 153$) and (2) ≥1 points group ($n = 24$). For increased salivation, we divided participants into: (1) 0 points group ($n = 151$) and (2) ≥1 points group ($n = 26$). For drowsiness, we divided participants into: (1) 0 points group ($n = 162$) and (2) ≥1 points group ($n = 15$). For pain, we divided participants into: (1) 0 points group ($n = 168$) and (2) ≥1 points group ($n = 9$). For central nervous system function, we divided participants into: (1) 0 points group ($n = 160$) and (2) ≥1 points group ($n = 17$).

In addition, we compared the maximum EDA change between the two groups for each autonomic symptom.

Statistical Analysis

We assessed the maximum EDA change, the number of EDA peaks, the mean EDA amplitude, and the AUC values for the EDA data among the three groups using one-way analysis of variance (ANOVA) with Tukey-Kramer multiple comparison tests. The relationship between the maximum EDA change and the total EDA score in the ≥3 points group was investigated using Pearson's correlation coefficients after detecting outliers using the Smirnov-Grubbs test. The maximum EDA change between the two groups for each autonomic symptom was assessed using Welch's *t*-tests, and Cohen's *d* was used to calculate effect sizes. A value of $p < 0.05$ was considered statistically significant.

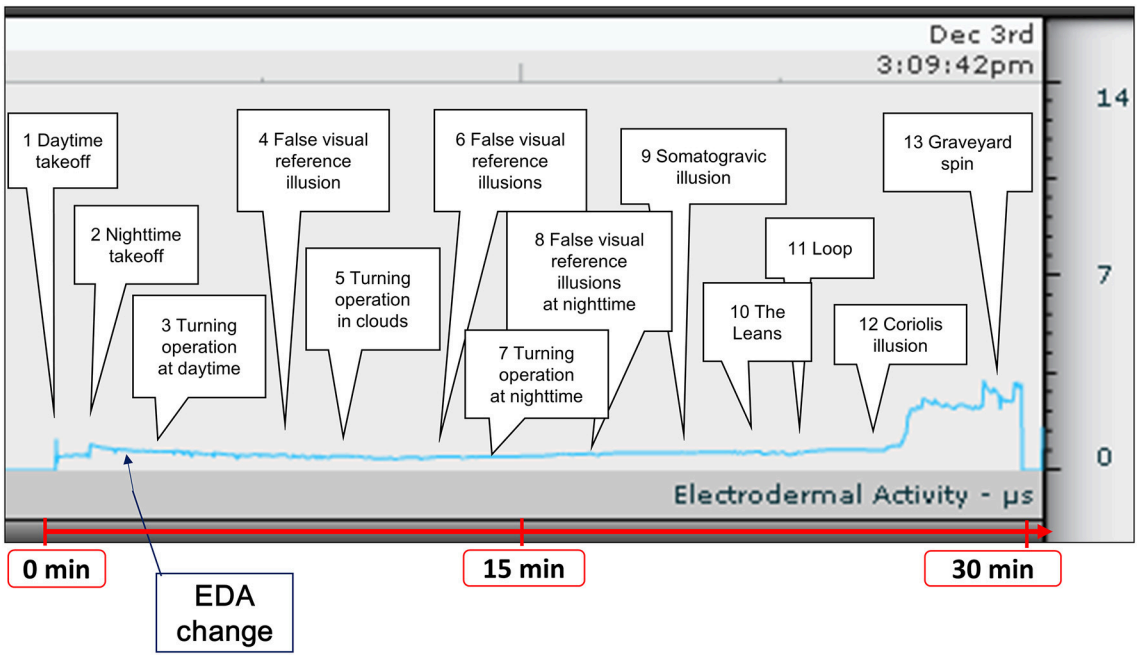

FIGURE 2 | Time course of spatial disorientation training and a representative example of EDA measurement. Participants were exposed to spatial disorientation training, including a visual illusion, vestibular illusion, and a combination of the two for ∼30 min. We recorded EDA changes during training. EDA, electrodermal activity.

FIGURE 3 | Device used to evaluate EDA. The wrist-worn EDA evaluation device, Q sensor. EDA, electrodermal activity.

RESULTS

Evaluation of EDA and Subjective Autonomic Symptoms

We conducted EDA analysis during and immediately after spatial disorientation training (**Table 1**), and administered a questionnaire about autonomic symptoms experienced during training. To measure autonomic symptoms, we used Graybiel's diagnostic criteria and scored participants accordingly (29) (**Table 2**). We were able to measure EDA in all participants during training (**Figure 2** and **Supplementary Table 1**). The maximum amount of change in EDA was significantly higher in the ≥3 points group compared with the 0 points group ($p < 0.01$) and the 1–2 points group ($p < 0.05$) (**Figure 4**). We observed no significant differences between the 0 points and 1–2 points groups (**Figure 4**).

Correlation Between Maximum EDA Change and Total Graybiel Score in the ≥3 Points Group

We investigated the relationship between the maximum EDA change and the total Graybiel score in the ≥3 points group (**Figure 5**). We identified and excluded two outliers (with scores of 18 points and 36 points) with respect to Graybiel scores using the Smirnov-Grubbs test. No significant ($p > 0.05$) correlation ($r = -0.059$) was observed between the maximum change in EDA and the total Graybiel score.

Evaluation of the Number of EDA Peaks, the Mean EDA Amplitude and Subjective Autonomic Symptoms

We investigated the number of EDA peaks, as well as the median and mean EDA amplitude in the 0 points, 1–2 points, and ≥3 points groups (Graybiel score). We found no significant changes in the number of EDA peaks during spatial disorientation training between the 0 points group, 1–2 points group, or ≥3 points group (**Figure 6**). The median EDA amplitudes were as follows: 0.80 µS (0 points group), 0.09 µS (1–2 points group), and 1.52 µS (≥3 points group). The mean EDA amplitude was significantly higher in the ≥3 points group compared with the

TABLE 2 | Evaluation of subjective autonomic symptoms.

Category	Pathognomonic 16 points	Major 8 points	Minor 4 points	Minimal 2 points	AQS 1 point
Nausea syndrome	Vomiting	Nausea 2, 3	Nausea 1	Epigastric discomfort	Epigastric awareness
Skin color		Pallor 3	Pallor 2	Pallor 1	Flushing
Cold sweating		3	2	1	
Increased salivation		3	2	1	
Drowsiness		3	2	1	
Pain					Headache
Central nervous system					Dizziness

We used the Graybiel diagnostic criteria and quantified the severity of autonomic symptoms. AQS, additional qualifying symptoms.

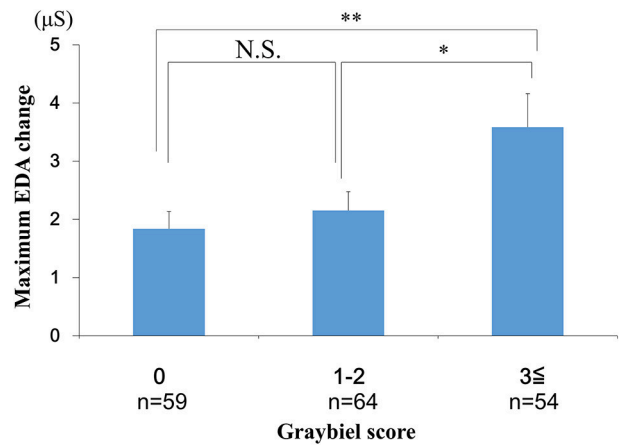

FIGURE 4 | Evaluation of EDA and subjective autonomic symptoms during spatial disorientation training using the Q sensor and Graybiel criteria, respectively. The maximum amount of change was significantly greater in the ≥3 points group compared with the 0 points group ($p < 0.01$) and the 1–2 points group ($p < 0.05$). EDA, electrodermal activity. The error bars represent the mean (S.E.) in all graphs. *$p < 0.05$, **$p < 0.01$.

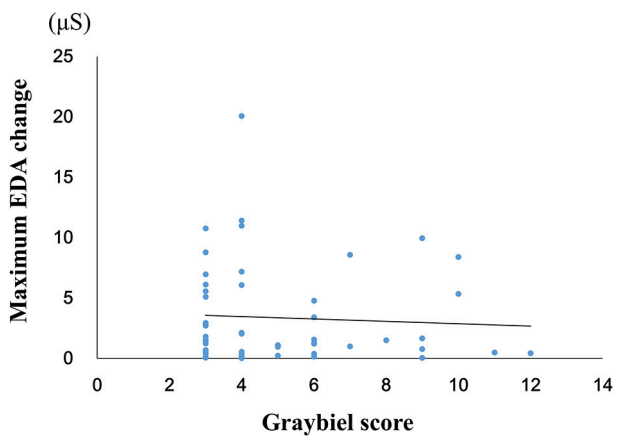

FIGURE 5 | Relationship between the maximum amount of EDA change and the total Graybiel score in the ≥3 points group. No significant ($p > 0.05$) correlation ($r = -0.059$) was observed between the maximum EDA change and the total Graybiel score.

0 points group ($p < 0.01$) and the 1–2 points group ($p < 0.05$) (**Figure 7**). However, we observed no significant differences between the 0 points and 1–2 points groups (**Figure 7**).

Evaluation of the Area Under the Curve for the EDA Data and Subjective Autonomic Symptoms

We examined the AUC values for the EDA data. We divided the AUC data into three groups according to the Graybiel score (0, 1–2, and ≥3 points groups) and performed statistical analyses. The analyses revealed no significant differences between the 0 points group, 1–2 points group, and the ≥3 points group (**Figure 8**).

Evaluation of EDA Data and Subjective Autonomic Symptoms for Each of the Seven Graybiel Diagnostic Categorizations

Finally, we divided the participants into groups based on whether they had Graybiel scores of 0 or ≥1 for all seven Graybiel diagnostic criteria (nausea, skin color, cold sweating, increased salivation, drowsiness, pain, central nervous system) and evaluated changes in EDA. For cold sweating, the maximum EDA change was significantly higher in the ≥1 points group compared with the 0 points group ($p < 0.05$, Cohen's $d = 1.70$) (**Figure 9A**). For salivation, the maximum EDA change was also significantly higher in the ≥1 points group compared with the 0 points group ($p < 0.05$, Cohen's $d = 1.02$) (**Figure 9B**). Eight participants scored ≥1 point for both salivation and cold sweating symptoms.

However, we observed no significant differences between the 0 points and ≥1 points groups for the other five autonomic symptoms (**Figures 9C–G**). For nausea, the maximum EDA change was not significantly higher in the ≥1 points group compared with the 0 points group ($p > 0.05$, Cohen's $d = 0.09$) (**Figure 9C**). For skin color, the maximum EDA change was not significantly higher in the ≥1 points group compared with the 0 points group ($p > 0.05$, Cohen's $d = 0.29$) (**Figure 9D**). For drowsiness, the maximum EDA change was not significantly higher in the ≥1 points group compared with the 0 points group ($p > 0.05$, Cohen's $d = 0.88$) (**Figure 9E**). For pain, the maximum EDA change was not significantly higher in the ≥1 points

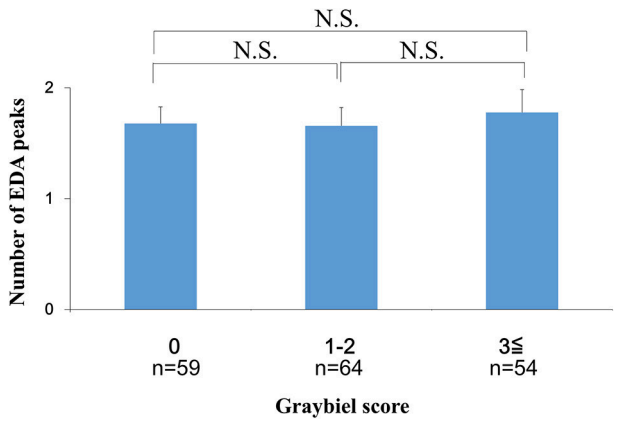

FIGURE 6 | Evaluation of the number of EDA peaks and subjective autonomic symptoms during spatial disorientation training using the Q sensor and Graybiel criteria, respectively. We found no significant differences ($p > 0.05$) in the number of EDA peaks between the 0, 1–2, and ≥3 points groups. EDA, electrodermal activity. The error bars represent the mean (S.E.) in all graphs.

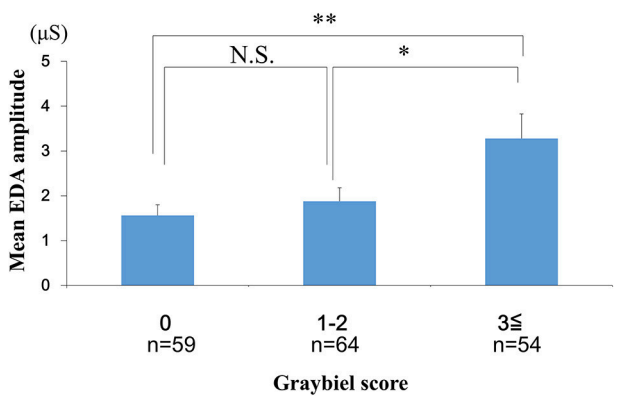

FIGURE 7 | Evaluation of the mean EDA amplitude and subjective autonomic symptoms during spatial disorientation training using the Q sensor and Graybiel criteria, respectively. The mean amplitude was significantly increased in the ≥3 points group compared with the 0 points ($p < 0.01$) and the 1–2 points groups ($p < 0.05$). EDA, electrodermal activity. The error bars represent the mean (S.E.) in all graphs. *$p < 0.05$, **$p < 0.01$.

group compared with the 0 points group ($p > 0.05$, Cohen's $d = 0.82$) (**Figure 9F**). For central nervous system symptoms, the maximum EDA change was not significantly higher in the ≥1 points group compared with the 0 points group ($p > 0.05$, Cohen's $d = 1.14$) (**Figure 9G**).

DISCUSSION

Spatial disorientation is a major risk for pilots (30, 31), and spatial disorientation-related accidents have been reported in many fighter aircraft and rotorcrafts (2, 32, 33). Therefore, in the interests of aviation safety, spatial disorientation training is considered to be important for pilots and pilot candidates (11–14). However, spatial disorientation affects the vestibular and visual systems independently and simultaneously. Thus, objective assessments of spatial disorientation and motion sickness can be difficult to conduct, as are scientific evaluations of the efficacy of spatial disorientation training. In addition, to the best of our knowledge, no previous studies have examined which types of spatial disorientation training are most effective for reducing spatial disorientation.

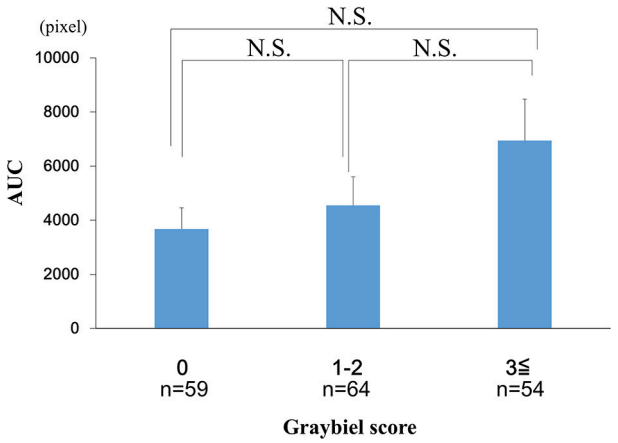

FIGURE 8 | Evaluation of the AUC of the EDA data and subjective autonomic symptoms during spatial disorientation training using Q sensor and Graybiel criteria, respectively. We found no significant differences ($p > 0.05$) in the AUC between the 0, 1–2, and ≥3 points groups. AUC, area under the curve. EDA, electrodermal activity. The error bars represent the mean (S.E.) in all graphs.

EDA reflects electrical changes measured at the skin surface that arise when the skin receives innervating signals from the brain. Previous experiments on spatial disorientation and motion sickness have used EDA as an indicator of changes in autonomic nervous system symptoms, revealing that EDA levels are sensitive to simulator sickness (14, 21).

One recent study reported that various physiological changes occurred during boarding in a flight simulator, and proposed that measuring EDA changes could provide a useful indicator (34). Although this previous study was similar to the current study, the details of the device used for measurement were not described, and it is possible that multiple electrodes were attached in the same way as in earlier studies.

With the recent development of wrist-worn EDA measuring devices, problems associated with attaching multiple electrodes and unexpected electrode detachment have been effectively resolved (18, 22). Accordingly, in the present study, we investigated the relationship between EDA changes and subjective autonomic symptoms using a novel wrist-worn EDA measurement device.

To evaluate subjective autonomic symptoms, we used the Graybiel diagnostic score (29) and quantified the severity of autonomic symptoms in our research. Graybiel diagnostic score has been established as a method for evaluating the severity of autonomic symptoms (29), and there have been many reports using this diagnostic score in the past (35–39). Recently, the Simulator Sickness Questionnaire (SSQ) has been used

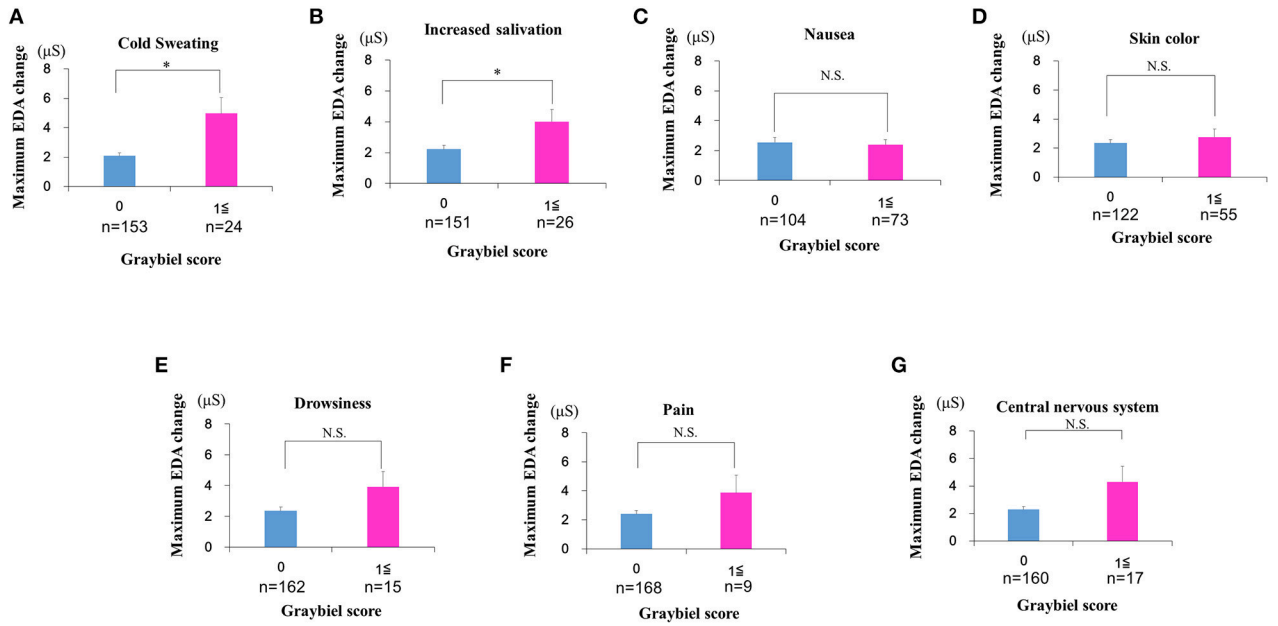

FIGURE 9 | Evaluation of EDA using the Q sensor and subjective autonomic symptoms during spatial disorientation training for each of the seven Graybiel diagnostic categorizations. **(A–G)** The maximum amount of EDA change was significantly higher in the ≥1 points group compared with the 0 points group for "cold sweating" and "salivation" ($p < 0.05$, each) **(A,B)**. However, we observed no significant changes between the 0 points group and the ≥1 points group for the other five autonomic symptoms **(C–G)**. The error bars represent the mean (S.E.) in all graphs. *$p < 0.05$.

as a subjective evaluation method (40). The items regarding autonomic symptoms examined by the SSQ are relatively similar to Graybiel diagnosis. However, the SSQ is literally an evaluation of autonomic symptoms focusing on simulator sickness, which is different from the purpose of the current study. In addition, the calculation method for scaling in the SSQ is relatively complex. For these reasons, we used Graybiel diagnosis in the current study, which has been widely used for subjective evaluation in motion sickness research (29).

In the current study, few participants exhibited high Graybiel scores. Therefore, as shown in **Figures 4**, **6–8**, we re-grouped participants so that the number was approximately equal between groups ($n = 59, 64, 54$). These groups corresponded to Graybiel cut-off values of 0, 1–2, and ≥3 (**Figures 4**, **6–8**). In **Figure 9**, we further simplified the groupings, as there were seven items to consider. We separated participants into those who had no symptoms (0) and those who had some symptoms (≥1). Based on this classification, we examined the relationship between EDA and autonomic nervous system symptoms.

To date, the relationship between the severity of spatial disorientation and changes in EDA remains unclear. In one previous study, spatial disorientation training was performed using a simulator similar to that used in the present study, measuring several physiological markers and reporting that the change in EDA was not significantly different compared with that before training (22). However, it was reported that the EDA amplitude was higher during experimental conditions, although this increase did not reach statistical significance (22). However, it is possible that a significant difference was not found because the sample size used in the final analysis was reduced from 16 to 12 due to erroneous electrode placement in four of the participants (22).

In contrast to the previous study described above, in the current study we were able to measure EDA in a large number of participants. In addition, unlike past reports, we demonstrated a simple method for measuring EDA during spatial disorientation training with a limited timeframe using a compact wrist-worn device (18, 22). To our knowledge, this is the first study to report EDA measurement with a wrist-worn device, and to evaluate the correlation between autonomic symptoms and EDA during spatial disorientation training. Although the results revealed a relationship between autonomic symptoms and the degree of EDA change and mean amplitude, this was limited to instances in which the participants experienced strong symptoms, and two kinds of autonomic symptoms.

In the case of spatial disorientation and motion sickness, the role of sympathetic and parasympathetic nervous function has not yet been clarified. Furthermore, it remains unclear whether dysfunction of the autonomic nervous system causes spatial disorientation and motion sickness, or whether spatial disorientation and motion sickness cause dysfunction of the autonomic nervous system. Gordon et al. examined the components of saliva as an objective assessment of motion sickness, reporting that the amount of amylase in saliva was significantly higher in people who were prone to motion sickness compared with that in people who were not, suggesting that salivary amylase levels could provide an indicator of susceptibility to motion sickness (26). Because amylase secretion

in saliva is regulated by the sympathetic nervous system, the authors concluded that the sympathetic nervous system may work more actively in people who are prone to motion sickness.

In addition, one previous study measured heart rate variability (HRV) to evaluate the state of spatial disorientation and motion sickness by capturing changes in the autonomic nervous system (41). The power spectra of HRV contain high frequency (HF) components indicating parasympathetic nervous activity, low frequency (LF) components reflecting both sympathetic and parasympathetic activity and relating to the average heart rate of the subject, and LF/HF components reflecting the balance between sympathetic nervous system activity and parasympathetic nervous system activity (41, 42). The study mentioned above indicated that sympathetic nervous function (such as decreased HF and increased LF/HF) became active as symptoms of motion sickness appeared and the condition became severe (41).

A previous experiment, in which motion sickness was caused by loading a visual stimulus stepwise, reported that HF decreased first, followed by an increase in LF/HF (43). Thus, the autonomic nervous system activity at the onset of motion sickness was thought to be caused by suppression of parasympathetic nervous function rather than promotion of sympathetic nervous function.

Despite the different indicator items, these reports indicate that hyperactivity of the sympathetic nervous system could provide an indicator of susceptibility of spatial disorientation and motion sickness. This finding suggests that spatial disorientation and motion sickness may cause suppression of parasympathetic nervous function and activation of sympathetic nervous function, indicating autonomic nervous system dysfunction. Based on these reports, we considered that inter-individual autonomic symptom variability was caused by differences in the susceptibility of participants to spatial disorientation. In the current experiments, all participants were healthy pilot candidates of the Japan Air Self-Defense Force who did not have any abnormal physical conditions. The results revealed that the symptoms of cold sweating and salivation increased with increasing EDA. However, depending on physical conditions and daily fluctuations of autonomic nervous activity, small inter-individual differences may exist, even if the same experiment is performed. Further verification will be necessary to confirm whether autonomic nervous dysfunction is the cause or the result of spatial disorientation and motion sickness, and to investigate how much EDA and autonomic symptoms are affected by physical condition.

When we examined participants with total Graybiel scores of $\geq$3 points, we observed no significant ($p > 0.05$) correlation ($r = -0.059$) between the maximum EDA change and total Graybiel score (**Figure 3**). In addition, we found no significant ($p > 0.05$) differences between the AUC of the EDA data and the total Graybiel score (**Figure 6**). We speculate that this finding was due to a combination of individual differences between participants and several important experimental limitations, as described below.

In this study, EDA measurements were carried out during 30 min of spatial disorientation training. For example, although there was no significant difference between each group in the AUC of the EDA results, significant differences were observed among some groups in maximum EDA change and mean amplitude. We speculate that the correlation between maximum EDA change, mean amplitude and Graybiel scores could be explained by the maximum EDA change representing temporary extreme motion sickness, with mean amplitude representing a sustained level in the measurement period of motion sickness. Thus, we consider that maximum EDA change and mean amplitude are appropriate parameters for examining EDA changes.

EDA increased in all subjects immediately after the Coriolis illusion was started. The Coriolis illusion has been used to investigate various physiological changes in motion sickness and spatial disorientation (44). Although the current study only examined changes in EDA, the Coriolis illusion is also considered to be a suitable method for investigating physiological changes in spatial disorientation.

The present findings should be interpreted within the context of the following limitations. First, we analyzed the EDA data without considering individual differences in EDA values under normal circumstances. Importantly, we investigated the maximum change in EDA values from immediately before the start of the spatial disorientation training to the end of training in all participants. The skin conductance level (SCL) is a numerical value reflecting tonic EDA (43). However, the Q sensor used in this study was unable to easily measure SCL. Although participants' original tonic EDA appeared to be slightly larger than 0 microsiemens (μS), a value of 0 μS was considered to indicate tonic EDA because of the limitations of the device. We considered the value of EDA just before spatial disorientation training as the tonic state, and considered the change from the tonic state to be the phasic state. However, when we reviewed the measured EDA data, there were no participants with high EDA values related to excitement and anxiety before training, and the EDA value immediately before the start of the training in all subjects was 0 μS. Therefore, we assumed 0 μS as the reference value in all cases, and calculated the EDA change amount subsequently.

Second, we did not consider the impact of filtering during EDA measurement. The Q sensor we used initially had no filter. However, using a filter introduces the possibility of distorting the EDA signal without artifacts. Importantly, no artifacts were detected in the current study. Thus, we consider that filtering was unlikely to have substantially influenced our results. Nevertheless, the potential impact of filters on EDA measurement should be considered in future studies.

Third, when participants flexed their necks to experience the Coriolis illusion, there may have been a difference in neck bending speed (21). Therefore, the strength of the Coriolis illusion may have differed between participants, potentially affecting the subsequent changes in autonomic nervous system symptoms and EDA.

Fourth, participants may have under-declared or over-reported subjective symptoms. This is a common limitation of subjective evaluation methods (24, 25), and highlights the

importance of objective evaluation methods, such as the wrist-worn EDA device.

Fifth, all participants were pilot candidates in the Japan Air Self-Defense Force, which is predominantly male. The gender imbalance in our sample may have affected the results.

Sixth, all participants wore the Q sensor on their left wrists. The left hand of each participant was in a fixed position beside the seat in the spatial disorientation device. Interestingly, a previous study reported that human EDA exhibits left-right asymmetry (45). Because of the tight training schedule of the candidate pilots, we were not able to verify EDA asymmetry in the participants by measuring it on both sides. We hope to address this issue in future studies. With respect to the issue of movement-based changes in EDA, participants in our study were unable to move their left hands during the training session. Although we did not find evidence of pronounced movement-based noise, low-amplitude noise accompanying the movement of the spatial disorientation training device was present. However, this low-amplitude noise did not appear to affect the EDA data. Therefore, we believe that the results of this experiment accurately reflected the severity of spatial disorientation and motion sickness.

Seventh, we evaluated the sympathetic component of the autonomic nervous system, but were unable to evaluate the parasympathetic nervous system in this experiment. Previous studies indicated that sympathetic activity was increased as symptoms of motion sickness appeared and as its severity increased (41, 46). However, the precise roles of the sympathetic and parasympathetic nervous systems at the time of onset of spatial disorientation and motion sickness are not well-understood. In the current experiment, we evaluated the autonomic nervous system and focused on EDA. However, we only evaluated the sympathetic nervous system, and were unable to evaluate the parasympathetic system because the interior of the spatial disorientation training device we used in this experiment was narrow, making it difficult to use a large biological monitoring system to measure both the sympathetic and parasympathetic nervous systems. In the future, we plan to evaluate the parasympathetic nervous system in addition to the sympathetic nervous system.

CONCLUSION

Despite the limitations described above, the current results, taken together with the findings of previous studies, indicate that EDA can be easily measured using a compact device, and that autonomic nervous system activity can be functionally evaluated during spatial disorientation training. Our findings also indicate that the severity of spatial disorientation and motion sickness can be evaluated using this method. Future research will extend our understanding of EDA and autonomic symptoms with respect to spatial disorientation and motion sickness.

AUTHOR CONTRIBUTIONS

AT organized the whole study. AT, TI, HO, YT, and YW were involved in the study concept and design. AT, TI, HO, and YW performed the research and analyzed the data. MK and YT provided laboratory facility support. AT wrote the manuscript. All authors reviewed the manuscript.

ACKNOWLEDGMENTS

We are grateful to the Jupitor Corporation for their help with the operation of the GYROLAB GL-4000. We also thank Dr. Risa Tamura (Department of Rehabilitation, Self-Defense Forces Central Hospital, Tokyo, Japan) for her advice regarding the discussion section. We thank Sydney Koke, MFA, and Peter Mittwede, MD, PhD, from Edanz Group (www.edanzediting.com/ac) for editing a draft of this manuscript.

SUPPLEMENTARY MATERIAL

The Supplementary Material for this article can be found online at: https://www.frontiersin.org/articles/10.3389/fneur.2018.01056/full#supplementary-material

REFERENCES

1. Benson AJ. Spatial disorientation-general aspects. In: Dehnin G, Sharp GR, Ernsting J, editors. *Aviation Medicine*. London: Tri-Med Books Ltd (1978). p. 405–33.
2. Gillingham KK. The spatial disorientation problem in the United States Air Force. *J Vestib Res*. (1992) 2:297–306.
3. Howard IP. *Human Visual Orientation*. New York, NY: John Wiley and Sons (1982).
4. Luxon AV, Raglan E. Neurological examination of the hearing impaired dizzy patients. In: House JW, O'Conner AF, editors. *Handbook of Neuro-Otological Diagnosis*. New York, NY; Basel: Marcel Dekker Inc (1987). p. 15.
5. Krueger WW. Controlling motion sickness and spatial disorientation and enhancing vestibular rehabilitation with a user-worn see-through display. *Laryngoscope* (2011) 121 Suppl. 2:S17–35. doi: 10.1002/lary.21373
6. Takahashi M, Toriyabe I, Takei Y, Kanzaki J. Study on experimental motion sickness in children. *Acta Otolaryngol.* (1994) 114:231–7. doi: 10.3109/00016489409126049
7. Chelen WE, Kabrisky M, Rogers S. Spectral analysis of the electroencephalographic response to motion sickness. *Aviat Space Environ Med*. (1993) 64:24–9.
8. Graybiel A, Lackner JR. Evaluation of the relationship between motion sickness symptomatology and blood pressure, heart rate, and body temperature. *Aviat Space Environ Med*. (1980) 51:211–4.
9. Jennings RT, Davis JR, Santy PA. Comparison of aerobic fitness and space motion sickness during the shuttle program. *Aviat Space Environ Med*. (1988) 58:448–51.
10. Tamura A, Wada Y, Shimizu N, Inui T, Shiotani A. Correlation of climbing perception and eye movements during daytime and nighttime takeoffs using a flight simulator. *Acta Otolaryngol.* (2016) 136:433–8. doi: 10.3109/00016489.2015.1132844
11. Nooij SA, Groen EL. Rolling into spatial disorientation: simulator demonstration of the post-roll (Gillingham) illusion. *Aviat Space Environ Med*. (2011) 82:505–12. doi: 10.3357/ASEM.2946.2011
12. Cheung B, McKinley RA, Steels B, Sceviour R, Cosman V, Holst P. Simulator study of helmet-mounted symbology system concepts in

degraded visual environments. *Aerosp Med Hum Perform*. (2015) 86:588–98. doi: 10.3357/AMHP.4232.2015
13. Chen W, Chao JG, Chen XW, Wang JK, Tan C. Quantitative orientation preference and susceptibility to space motion sickness simulated in a virtual reality environment. *Brain Res Bull*. (2015) 113:17–26. doi: 10.1016/j.brainresbull.2015.01.007
14. Miller JC, Sharkey TJ, Graham GA, McCauley ME. Autonomic physiological data associated with simulator discomfort. *Aviat Space Environ Med*. (1993) 64:813–9.
15. Kekecs Z, Szekely A, Varga K. Alterations in electrodermal activity and cardiac parasympathetic tone during hypnosis. *Psychophysiology* (2016) 53:268–77. doi: 10.1111/psyp.12570
16. Alvarez V, Reinsberger C, Scirica B, O'Brien MH, Avery KR, Henderson G, et al. Continuous electrodermal activity as a potential novel neurophysiological biomarker of prognosis after cardiac arrest: a pilot study. *Resuscitation* (2015) 93:128–35. doi: 10.1016/j.resuscitation.2015.06.006
17. McCormick C, Hessl D, Macari SL, Ozonoff S, Green C, Rogers SJ. Electrodermal and behavioral responses of children with autism spectrum disorders to sensory and repetitive stimuli. *Autism Res*. (2014) 7:468–80. doi: 10.1002/aur.1382
18. Fowles DC, Christie MJ, Edelberg R, Grings WW, Lykken DT, Venables PH. Publication recommendations for electrodermal measurements. *Psychophysiology* (1981) 18:232–9. doi: 10.1111/j.1469-8986.1981.tb03024.x
19. Ledowski T, Bromilow J, Wu J, Paech MJ, Storm H, Schug SA. The assessment of postoperative pain by monitoring skin conductance: results of a prospective study. *Anaesthesia* (2007) 62:989–93. doi: 10.1111/j.1365-2044.2007.05191.x
20. Yamamoto K, Hornykiewicz O. Proposal for a noradrenaline hypothesis of schizophrenia. *Prog Neuro Psychoph*. (2004) 28:913–22. doi: 10.1016/j.pnpbp.2004.05.033
21. Westmoreland D, Krell RW, Self BP. Physiological responses to the Coriolis illusion: effects of head position and vision. *Aviat Space Environ Med*. (2007) 78:985–9. doi: 10.3357/ASEM.2010.2007
22. Cheung B, Hofer K, Heskin R, Smith A. Physiological and behavioral responses to an exposure of pitch illusion in the simulator. *Aviat Space Environ Med*. (2004) 75:657–65.
23. Picard RW. Future affective technology for autism and emotion communication. *Philos Trans R Soc Lond B Biol Sci*. (2009) 364:3575–84. doi: 10.1098/rstb.2009.0143
24. Poh MZ, Loddenkemper T, Reinsberger C, Swenson NC, Goyal S, Sabtala MC, et al. Convulsive seizure detection using a wrist-worn electrodermal activity and accelerometry biosensor. *Epilepsia* (2012) 53:93–7. doi: 10.1111/j.1528-1167.2012.03444.x
25. Sano A, Picard RW, Stickgold R. Quantitative analysis of wrist electrodermal activity during sleep. *Int J Psychophysiol*. (2014) 94:382–9. doi: 10.1016/j.ijpsycho.2014.09.011
26. Gordon CR, Jackman Y, Ben-Aryeh H, Doweck I, Spitzer O, Szargel R, et al. Salivary secretion and seasickness susceptibility. *Aviat Space Environ Med*. (1992) 63:356–9.
27. Boucsein W, Fowles DC, Grimnes S, Ben-Shakhar G, Roth WT, Dawson ME, et al. Publication recommendations for electrodermal measurements. *Psychophysiology* (2012) 49:1017–34. doi: 10.1111/j.1469-8986.2012.01384.x
28. Mizokami D, Araki K, Tanaka N, Suzuki H, Tomifuji M, Yamashita T, et al. Gene therapy of c-myc suppressor FUSE-binding protein-interacting repressor by Sendai virus delivery prevents tracheal stenosis. *PLoS ONE* (2015) 10:e0116279. doi: 10.1371/journal.pone.0116279
29. Graybiel A, Wood CD, Miller EF, Cramer DB. Diagnostic criteria for grading the severity of acute motion sickness. *Aerosp Med*. (1968) 39:453–5.
30. Holmes SR, Bunting A, Brown DL, Hiatt KL, Braithwaite MG, Harrigan MJ. Survey of spatial disorientation in military pilots and navigators. *Aviat Space Environ Med*. (2003) 74:957–65.
31. Takada Y, Hisada T, Kuwada N, Sakai M, Akamatsu T. Survey of severe spatial disorientation episodes in Japan Air Self-Defense Force fighter pilots showing increased severity in night flight. *Mil Med*. (2009) 174:626–30. doi: 10.7205/MILMED-D-01-6308
32. Lyons TJ, Ercoline W, O'Toole K, Grayson K. Aircraft and related factors in crashes involving spatial disorientation: 15 years of U.S. Air Force data. *Aviat Space Environ Med*. (2006) 77:720–3.
33. Poisson RJ, Miller ME. Spatial disorientation mishap trends in the U.S. Air force 1993–2013. *Aviat Space Environ Med*. (2014) 85:919–24. doi: 10.3357/ASEM.3971.2014
34. Feng C, Wanyan X, Yang K, Zhuang D, Wu X. A comprehensive prediction and evaluation method of pilot workload. *Technol Health Care* (2018) 26:65–78. doi: 10.3233/THC-174201
35. Miller EF, Graybiel A. Altered susceptibility to motion sickness as a function of subgravity level. *Space Life Sci*. (1973) 4:295–306. doi: 10.1007/BF00924477
36. Graybiel A, Miller EF, Homick JL. Individual differences in susceptibility to motion sickness among six Skylab astronauts. *Acta Astronaut*. (1975) 2:155–74. doi: 10.1016/0094-5765(75)90051-X
37. Cheung BS, Money KE. The influence of age on susceptibility to motion sickness in monkeys. *J Vestib Res*. (1992) 2:247–55.
38. Cheung B, Heskin R, Hofer K, Gagnon M. The menstrual cycle and susceptibility to coriolis-induced sickness. *J Vestib Res*. (2001) 11:129–36.
39. Cheung B, Hofer K. Desensitization to strong vestibular stimuli improves tolerance to simulated aircraft motion. *Aviat Space Environ Med*. (2005) 76:1099–104.
40. Kennedy RS, Fowlkes JE, Berbaum KS, Lilienthal MG. Use of a motion sickness history questionnaire for prediction of simulator sickness. *Aviat Space Environ Med*. (1992) 63:588–93.
41. Harm DL, Schlegel TT. Predicting motion sickness during parabolic flight. *Auton Neurosci*. (2002) 97:116–21. doi: 10.1016/S1566-0702(02)00043-7
42. Billman GE. The effect of heart rate on the heart rate variability response to autonomic interventions. *Front Physiol*. (2013) 4:222. doi: 10.3389/fphys.2013.00222
43. Oinuma M, Hirayanagi K, Yajima K, Igarashi M, Arakawa Y. Changes in cardio-respiratory function, heart rate variabilities, and electrogastrogram preceding motion sickness-like symptoms induced by visual reality stimulus. *J Aerosp Environ Med*. (2004) 43:99–109.
44. Watanuki K, Takahashi M, Ikeda T. Perception of surrounding space controls posture, gaze, and sensation during Coriolis stimulation. *Aviat Space Environ Med*. (2000) 71:381–7.
45. Hugdahl K. Hemispheric asymmetry and bilateral electrodermal recordings: a review of the evidence. *Psychophysiology* (1984) 21:371–93. doi: 10.1111/j.1469-8986.1984.tb00215.x
46. Doweck I, Gordon CR, Shlitner A, Spitzer O, Gonen A, Binah O, et al. Alterations in R-R variability associated with experimental motion sickness. *J Auton Nerv Syst*. (1997) 67:31–7. doi: 10.1016/S0165-1838(97)00090-8

Conflict of Interest Statement: The authors declare that the research was conducted in the absence of any commercial or financial relationships that could be construed as a potential conflict of interest.

frontiers in Neural Circuits

ORIGINAL RESEARCH
published: 14 January 2019
doi: 10.3389/fncir.2018.00120

Modeling the Effect of Environmental Geometries on Grid Cell Representations

Samyukta Jayakumar[1], *Rukhmani Narayanamurthy*[1], *Reshma Ramesh*[2], *Karthik Soman*[3], *Vignesh Muralidharan*[4] *and V. Srinivasa Chakravarthy*[1]*

[1] Department of Biotechnology, Bhupat and Jyoti Mehta School of Biosciences, Indian Institute of Technology Madras, Chennai, India, [2] Department of Biotechnology, Rajalakshmi Engineering College, Chennai, India, [3] Department of Bioengineering, University of California, Berkeley, Berkeley, CA, United States, [4] Department of Psychology, University of California, San Diego, San Diego, CA, United States

Grid cells are a special class of spatial cells found in the medial entorhinal cortex (MEC) characterized by their strikingly regular hexagonal firing fields. This spatially periodic firing pattern is originally considered to be independent of the geometric properties of the environment. However, this notion was contested by examining the grid cell periodicity in environments with different polarity (Krupic et al., 2015) and in connected environments (Carpenter et al., 2015). Aforementioned experimental results demonstrated the dependence of grid cell activity on environmental geometry. Analysis of grid cell periodicity on practically infinite variations of environmental geometry imposes a limitation on the experimental study. Hence we analyze the dependence of grid cell periodicity on the environmental geometry purely from a computational point of view. We use a hierarchical oscillatory network model where velocity inputs are presented to a layer of Head Direction cells, outputs of which are projected to a Path Integration layer. The Lateral Anti-Hebbian Network (LAHN) is used to perform feature extraction from the Path Integration neurons thereby producing a spectrum of spatial cell responses. We simulated the model in five types of environmental geometries such as: (1) connected environments, (2) convex shapes, (3) concave shapes, (4) regular polygons with varying number of sides, and (5) transforming environment. Simulation results point to a greater function for grid cells than what was believed hitherto. Grid cells in the model encode not just the local position but also more global information like the shape of the environment. Furthermore, the model is able to capture the invariant attributes of the physical space ingrained in its LAHN layer, thereby revealing its ability to classify an environment using this information. The proposed model is interesting not only because it is able to capture the experimental results but, more importantly, it is able to make many important predictions on the effect of the environmental geometry on the grid cell periodicity and suggesting the possibility of grid cells encoding the invariant properties of an environment.

Keywords: grid cells, spatial cells, oscillatory path integration, Lateral Anti-Hebbian Network, connected environment, concave environment, convex environment

OPEN ACCESS

Edited by:
K. J. Jeffery,
University College London,
United Kingdom

Reviewed by:
Federico Stella,
Institute of Science and Technology Austria (IST Austria), Austria
Ya-tang Li,
California Institute of Technology, United States

***Correspondence:**
V. Srinivasa Chakravarthy
schakra@iitm.ac.in

Received: *09 August 2018*
Accepted: *20 December 2018*
Published: *14 January 2019*

Citation:
Jayakumar S, Narayanamurthy R, Ramesh R, Soman K, Muralidharan V and Chakravarthy VS (2019) Modeling the Effect of Environmental Geometries on Grid Cell Representations. Front. Neural Circuits 12:120. doi: 10.3389/fncir.2018.00120

INTRODUCTION

Spatial navigation is essential for the survival of a mobile organism. Entorhinal cortex (EC), an important cortical area that forms input to the hippocampus, was reported to have neurons known as grid cells which fire when the animal is at points that have a spatially periodic structure (Hafting et al., 2005). Since the periodicity encountered is often hexagonal, these cells are further known as hexagonal grid cells (Hafting et al., 2005). Albeit grid cells were initially discovered in rats (Hafting et al., 2005), these cells have also been reported in mice (Fyhn et al., 2008), bats (Ulanovsky and Moss, 2007; Yartsev et al., 2011), monkeys (Killian et al., 2012), and humans (Jacobs et al., 2013; Moser et al., 2014). Experimental studies in human adults who are at genetic risk for Alzheimer's disease have reported that the neural degeneration originates in the EC, with the loss of grid cell representations causing further impairment of spatial navigation performance of the patient (Kunz et al., 2015).

Preliminary studies on the effects of environmental geometry on spatial cells such as place cells (Barry et al., 2006) and grid cells have been conducted. Place cells are critical for coding the animal's position in space. They fire when the animal is situated in a particular space of the environment known as its firing field (O'Keefe and Dostrovsky, 1971). Remapping of place cells occurred when sufficient changes to the geometry (Lever et al., 2002), color (Bostock et al., 1991), or odor (Anderson and Jeffery, 2003) of the environment were made. Grid cells are equally crucial for spatial navigation by path integration i.e., tracking position by integrating self-motion even without the presence of external sensory landmarks (Hafting et al., 2005; Fuhs and Touretzky, 2006; McNaughton et al., 2006; Burgess et al., 2007; Hasselmo et al., 2007; Fiete et al., 2008; Hasselmo, 2008; Moser et al., 2014; Bush et al., 2015). Grid cells have been proposed to have a role in computing directional vector between the start and goal location (which was termed as vector navigation) that further aids the animal in reaching its goal location (Bush et al., 2015). The variation of the grid scale across the dorsal to ventral medial entorhinal cortex (MEC) axis (Brun et al., 2008; Stensola et al., 2012), acts like a ruler with different resolutions to measure the distance traversed by the animal from its starting location. The features of the grid cells that are stated above help the animal to navigate the environment efficiently.

MEC conveys spatial information from the higher sensory cortical areas to the hippocampus (Barnes et al., 1990; Quirk et al., 1992; Fyhn et al., 2004). It is believed that the dynamic representation of the spatial location of an animal is created and updated by the MEC and the grid cells are a proof of it (Savelli et al., 2008). Hargreaves et al. (2005) initially recorded MEC grid cells from an environment (Hargreaves et al., 2005). Since the size of the environment was relatively small, the neurons did not show obvious grid like firing patterns. It was ambiguous in prior studies whether all spatially modulated cells in the MEC were variants of the grid cells or whether a subset resembled the place cells of the hippocampus (Savelli et al., 2008). Savelli et al. (2008) conducted an experiment where the rats were allowed to forage a small box which was placed inside a larger box. After sometime, the small box was removed from the large box without removing the rats and now the rats foraged the larger box for the rest of the experiment. It was observed that some cells that showed place cell like response in the small box, showed grid cell like response in the larger box and the cells showing boundary cell like response showed no change upon the removal of the small box. From the aforementioned experiments it is possible to draw two inferences: firstly, it suggests that there were two major classes of spatial neurons, the grid cells and the boundary cells. The boundary cells may therefore be binding the grid cell firing to the boundaries of the environment. Secondly, the experiment strongly demonstrated that the spatial firing of the MEC cells was strongly influenced by the boundaries of the environment, in the sense that representation of the MEC cells changed predominantly when the local cues of the environment were altered. In this paper, we are addressing the second inference from a purely computational point of view.

Grid cells were initially considered to be the universal metric for navigation due to their minimal remapping property across the environment (Hafting et al., 2005; Fyhn et al., 2007). But this feature of grid field invariance across the environment was contested by the experiment conducted by O'Keefe (Krupic et al., 2015) wherein rats were allowed to forage inside differently shaped environments such as circle, square, hexagon, and trapezoid. Analysis of grid cell activity in each environment revealed that the hexagonal grid field symmetry was affected by the symmetries of the environmental shape. Circle, the most symmetric environment, had a regular hexagonal firing field. As the number of axes of symmetry dropped, the regular hexagonal firing field started to transform into a skewed hexagonal field. This experimental study pointed out that grid cell firing fields were not invariant with respect to the environment but exhibit a definite dependence on the geometry of the environment.

Another interesting experimental study (Carpenter et al., 2015) considered how grid cells responded when the animal foraged inside similar environments connected by a corridor. A key result of the study was that initially the grid fields in each room had a high spatial correlation between them; as the time progressed, this correlation decreased and the grid fields in the two environments became a continuum, forming a global representation of the connected pair of environments. This study revealed a new face of the grid cell coding, whereby the periodic firing fields of the grid cell could rearrange among themselves to reflect the global shape of connectivity of the environment.

Most of the experimental studies on grid cells were performed on either square or circular environments, and have not explored the rich possibilities of varying environmental geometries. Another study by Stensola et al. (2015) focused on analyzing the shear induced asymmetry on entorhinal grid cells (Stensola et al., 2015). Here, the animal was allowed to explore different square enclosures with a rotational offset which elliptically distorts the grid patterns. This distortion is then analytically reversed by a shearing transformation on the grid patterns

Abbreviations: EC, Entorhinal Cortex; HD, Head Direction; HGS, Hexagonal Gridness Score; LAHN, Lateral Anti-hebbian Network; MEC, Medial Entorhinal Cortex; PCA, Principal Component Analysis; PI, Path Integration; SOM, Self Organizing Map; MLP, Multi-Layer Perceptron.

explaining the phenomenon of anchoring of grid patterns to specific reference points in the enclosure. Although this study involves exploring the change in grid representation, it does not involve analyzing the representations in different environmental geometries, thereby placing it outside the scope of our current study. Apart from the study of Barry et al. (2007) and Krupic et al. (2015), to the best of our knowledge, no experimental studies have been conducted on grid cells under varying environmental geometries.

Krupic et al. (2014) also studied the changes in grid representations in varying environmental geometries from a computational point of view. The proposed model is not biologically plausible as the firing patterns of grid cells are generated based on the assumption that each of the N-number of fields on an abstract semi-infinite 2-D plane interact with each other via attractive and repulsive forces. These fields are not intrinsically generated by neural dynamics, but are distributed a priori over the space and controlled by the dynamics of the abstract force equation. Theoretical studies have been made on grid cell coding in non-Euclidean space (Urdapilleta et al., 2015) which predicted the transformation of the hexagonal pattern of firing field to heptagonal pattern with the change from Euclidean to non-Euclidean space. But the problem of studying grid cell coding as a function of practically infinite variations of the environmental geometry poses a Himalayan challenge to spatial cell researchers. Hence, we propose to classify environmental geometries into the following five broad categories and study the emergent grid fields using computational modeling.

i. Connected environments
ii. Convex shaped environments
iii. Concave shaped environments
iv. Regular polygon environments with varying number of sides
v. Transforming the environment

The previously mentioned studies, from a pure computational point of view, would result in a better understanding of the spatial encoding inside the brain generated by the grid cells. We show that our simulations not only explain and confirm earlier studies, but also make a number of testable predictions verifiable by experiments.

METHODS

To achieve the goal of studying the effect of environmental geometry on grid cell coding, we used the model as explained below. In this model, the virtual animal is represented as a point in two–dimensional space and is made to forage inside the aforementioned range of environments. **Figure 1** shows the model architecture. Values of the parameters used in the equations are given in **Table 1**.

In essence, the model has three stages as described below.

Direction Encoding Stage

The Head Direction (HD) stage is modeled using a two-dimensional layer of neurons whose afferent weight connections are trainable using Hebbian rule. In addition to this, the neuronal layer ensures topography in its representation by training it using

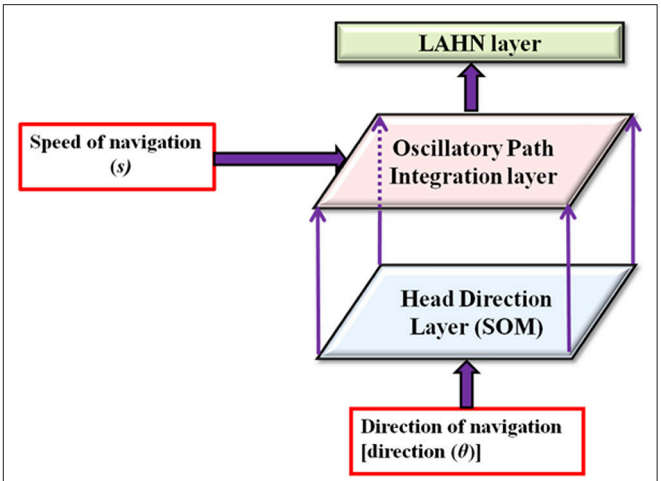

FIGURE 1 | Model architecture. Model receives the velocity information as input and passes through a hierarchy of processing stages such as head direction layer, path integration layer and lateral anti hebbian network (LAHN). Arrows show the direction of flow of information from one hierarchy to the next.

TABLE 1 | Parameter values.

Parameter	Values
Ω_{PI}	12π rad/s
μ	1
η_F	0.01
η_L	0.01
β	50
dt	0.01 s
n	20 (number of neurons in lahn)

Kohonen's Self-Organizing Map (SOM) algorithm (Kohonen, 1982). The network is trained using unit vectors that span the complete 360° angular space. Projection of the animal's current direction on the HD layer forms a neural representation of it and hence forms the directional map (Kohonen, 1982). The response equation of the SOM neuron is given as:

$$\theta_{HD} = \psi^T W \tag{1}$$

ψ is the two dimensional input given to the SOM such that

$\psi = [\cos(\theta)\ \sin(\theta)]$ where θ is the actual direction of navigation

W is the afferent weight matrix of the SOM, where the weight vectors are normalized.

Oscillatory Path Integration (PI) Stage

This stage consists of a two dimensional array of phase oscillators, which has one-to-one connections with the HD layer. The directional input from Equation (1) is fed to the phase dynamics of the oscillator so that each oscillator corresponding to a specific direction codes for that component of the positional information as the phase of the oscillator. The dynamics of phase oscillator is

given as

$$\frac{d(\chi_u(i,j))}{dt} = -\chi_v(i,j)[\Omega_{PI} + \beta s\theta_{HD}(i,j)] + \chi_u(i,j)[\mu - (\chi_u(i,j)^2 + \chi_u(i,j)^2)] \quad (2)$$

$$\frac{d(\chi_v(i,j))}{dt} = \chi_u(i,j)[\Omega_{PI} + \beta s\theta_{HD}(i,j)] + \chi_v(i,j)[\mu - (\chi_u(i,j)^2 + \chi_v(i,j)^2)] \quad (3)$$

χ_u and χ_v are the u and v state variables of the PI oscillator.

β *is* the spatial scale parameter.

s is the speed of the navigation such that $s = ||X(t)–X(t−1)||$ where X is the position vector of the animal.

μ is the parameter that controls the limit cycle behavior of the oscillator. Here μ is taken as 1.

Lateral Anti-hebbian Network (LAHN) Stage

LAHN is an unsupervised neural network (Földiák, 1989) that extracts optimal features from the input. The network has 1D array of neurons with lateral inhibitory and afferent excitatory connections. These weight connections are trainable using biologically plausible neural learning rules such as Hebbian (for afferent weights) and Anti-Hebbian (for lateral weights). The lateral inhibitory connections induce competition among the neurons and the afferent Hebbian connections extract principal components from the input (Oja, 1982). This network connectivity hence ensures optimal feature extraction from the input data. It has also been observed that neurons that give rise to grid representations are connected via GABAergic interneurons (Pastoll et al., 2013), thereby establishing inhibitory lateral connections between them as seen in the LAHN layer of the model.

The response of the network is given by the following equation.

$$\xi_i(t) = \sum_{j=1}^{m} q_{ij}\chi_j(t) + \sum_{k=1}^{n} w_{ik}\xi_k(t-1) \quad (4)$$

q is the afferent weight connections and w is the lateral weight connections.

ξ is the response of the network.

n is the total number of neurons in the LAHN layer.

m is the dimension of the input.

The afferent connections are updated by a variation of the Hebbian rule and the lateral connections are updated by Anti-Hebbian rule as given below.

$$\Delta q_{ij} = \eta_F[\chi_j(t)\xi_i(t) - q_{ij}\xi_i{}^2(t)] \quad (5)$$

$$\Delta w_{ik} = -\eta_L\xi_i(t)\xi_k(t-1) \quad (6)$$

$\eta_F$and η_L are the forward and lateral learning rates, respectively.

It has been proved that training the weights of LAHN using Equations (5) and (6) makes the network weights to converge to the subspace spanned by the principle components (PC) of the input data (Földiák, 1989). We have previously showed that training of LAHN on oscillatory path integration values can potentially give rise to a wide variety of spatial cells (Soman et al., 2018b). Although the LAHN layer in the model exhibits a variety of spatial cells, we primarily focused on the hexagonal grid cells to compare with the experimental results.

Trajectory Generation

The trajectory is designed using dynamics of curvature constrained motion (Soman et al., 2018b) which is governed by the following equations:

$$\dot{x}(t) = \sigma(t)\cos\Theta(t) \quad (7)$$

$$\dot{y}(t) = \sigma(t)\sin\Theta(t) \quad (8)$$

$$\sigma(t) = ||X_{pos} - X_{wall}|| \quad (9)$$

$$\left|\dot{\Theta}(t)\right| \leq \frac{\gamma(t)}{\rho} \quad (10)$$

x and y determine the position of the virtual animal in 2d space, while its speed is controlled by σ. To ensure that there is high degree of randomness (Equation 10) when it is far off from the boundary and low randomness when it is close by and to prevent it from crossing the boundary, the speed of the virtual agent is reduced when the virtual animal is close to the border (Equation 9).

The model comprises of a pure Path Integration system (i.e., it integrates velocity information at each point in the trajectory), therefore information given to the system can be treated as a sequence problem where continuous integration of the input takes place. The spatial patterns (output of the system) thus depend highly on the way path integration is performed in the model. In such a system, the pattern of the trajectory matters and also changes when there is a change in the shape of the environment, thereby influencing the activity of the spatial cells. In conclusion, behavioral anisotropy has a profound influence on the spatial representation in the model.

Quantification of Gridness

The neuronal firing activity is represented in the form of three maps namely, the firing field map of the neuron, firing rate map and the autocorrelation map. Red dots are marked on the positions of the animal's trajectory where the SC layer neuron activity crosses a certain threshold value (ε_{sc}). The activity (firing rate) of the neuron in its firing field is determined by the firing rate map. In the firing rate map, high activity is indicated by red and no activity by blue.

Hexagonal gridness is quantified by a gridness score value (Hafting et al., 2005) computed from the autocorrelation map which is obtained from the firing rate map using the following equation.

$$r(\tau_x,\tau_y) = \frac{M\sum_{x,y}\lambda(x,y)\lambda(x-\tau_x,y-\tau_y) - \sum_{x,y}\lambda(x,y)\sum_{x,y}\lambda(x-\tau_x,y-\tau_y)}{\sqrt{[M\sum_{x,y}\lambda(x,y)^2 - [\sum_{x,y}\lambda(x,y)]^2][M\sum_{x,y}\lambda(x-\tau_x,y-\tau_y)^2 - [\lambda(x-\tau_x,y-\tau_y)]^2}} \quad (11)$$

r is the autocorrelation map.
$\lambda(x,y)$ is the firing rate at (x,y) location of the rate map.
M is the total number of pixels in the rate map.
τ_x and τ_y corresponds to x and y coordinate spatial lags.
Hexagonal Gridness Score (HGS) is computed as given below.

$$HGS = \min[cor(r, r^{60^0}), cor(r, r^{120^0})] - \max[cor(r, r^{30^0}), cor(r, r^{90^0}), cor(r, r^{150^0})] \quad (12)$$

Designing the Environments

Generation of Regular Polygons With Varying Number of Sides

The polygons are constructed using a unit circle with center at (0, 0). The circle is then sectored into equal angular separation based on the number of sides given as the input.

The positional coordinates of the points on the unit circle that form the polygon are given by

$$[X_k \;\; Y_k] = \left[\cos(\frac{2\pi k}{n}) \;\; \sin(\frac{2\pi k}{n})\right]$$

Angle separation $= 2\pi/n$; $n =$ number of sides.

The X_k and Y_k coordinates are then connected to generate the regular polygon (**Figure 9**).

Generation of Connected Environments

The connected environment used for our study has the same boundary conditions used in the experiment (Carpenter et al., 2015). The two compartments (e.g., square-square) connected via a rectangular corridor are constructed by joining the corner coordinates of the two environments (**Figures 2A**, **3A,G**). For connected environments with varying distances between the two compartments, we introduce a distance parameter "*d*". The displacement between the two squares is parallel to one side of each of the two square environments (**Figures 3M–O**).

Generation of Concave Boundaries

In this category, we consider the annulus, horseshoe and S-shape as instances of concave shapes. To construct an annulus shape, two circles are generated separately (of different radius) and then combined to form two concentric circles (**Figure 5A**). In the case of a horseshoe (**Figure 5B**), two semicircles are concatenated to obtain the shape. The coordinates of both these shapes are

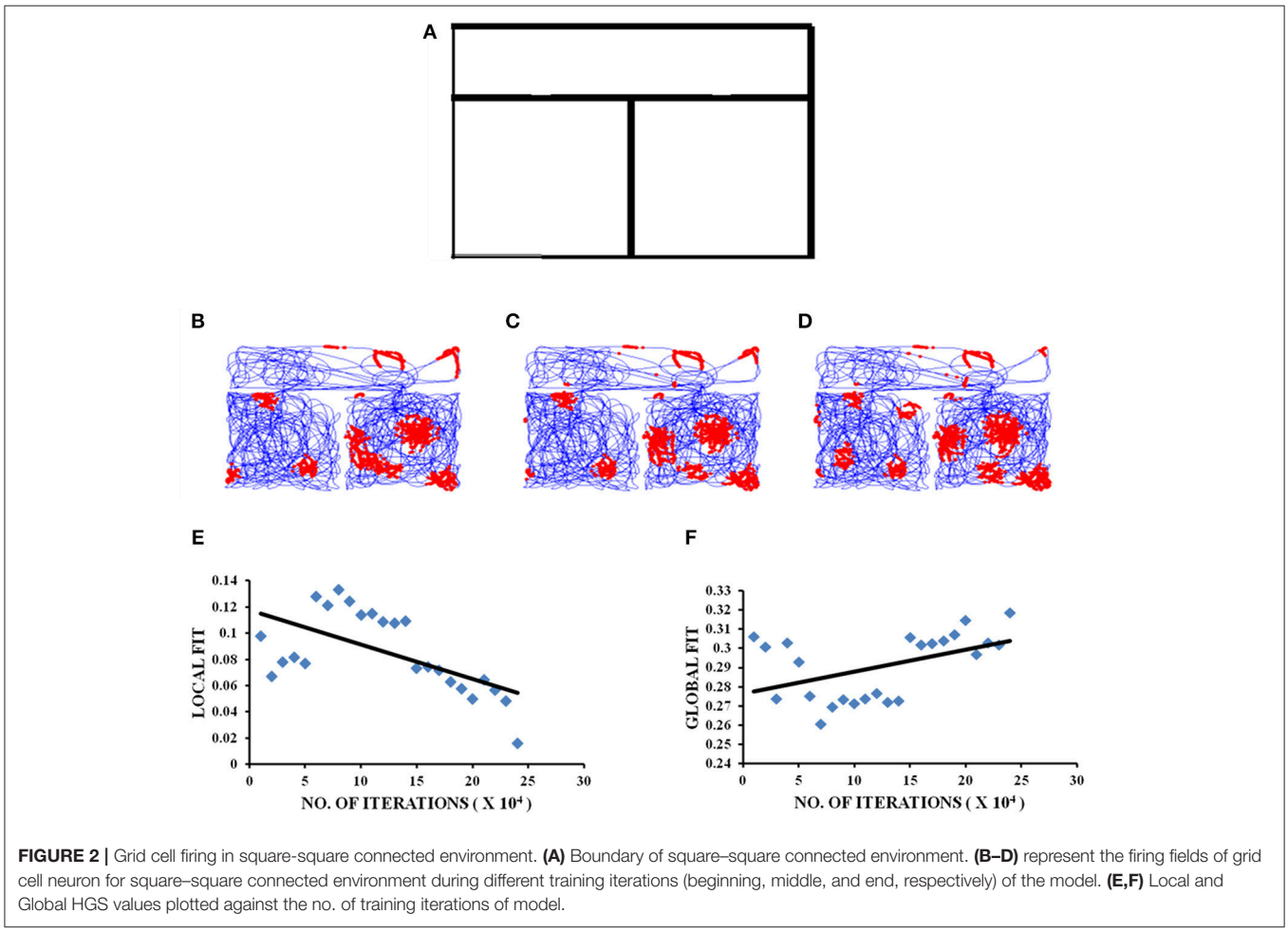

FIGURE 2 | Grid cell firing in square-square connected environment. **(A)** Boundary of square–square connected environment. **(B–D)** represent the firing fields of grid cell neuron for square–square connected environment during different training iterations (beginning, middle, and end, respectively) of the model. **(E,F)** Local and Global HGS values plotted against the no. of training iterations of model.

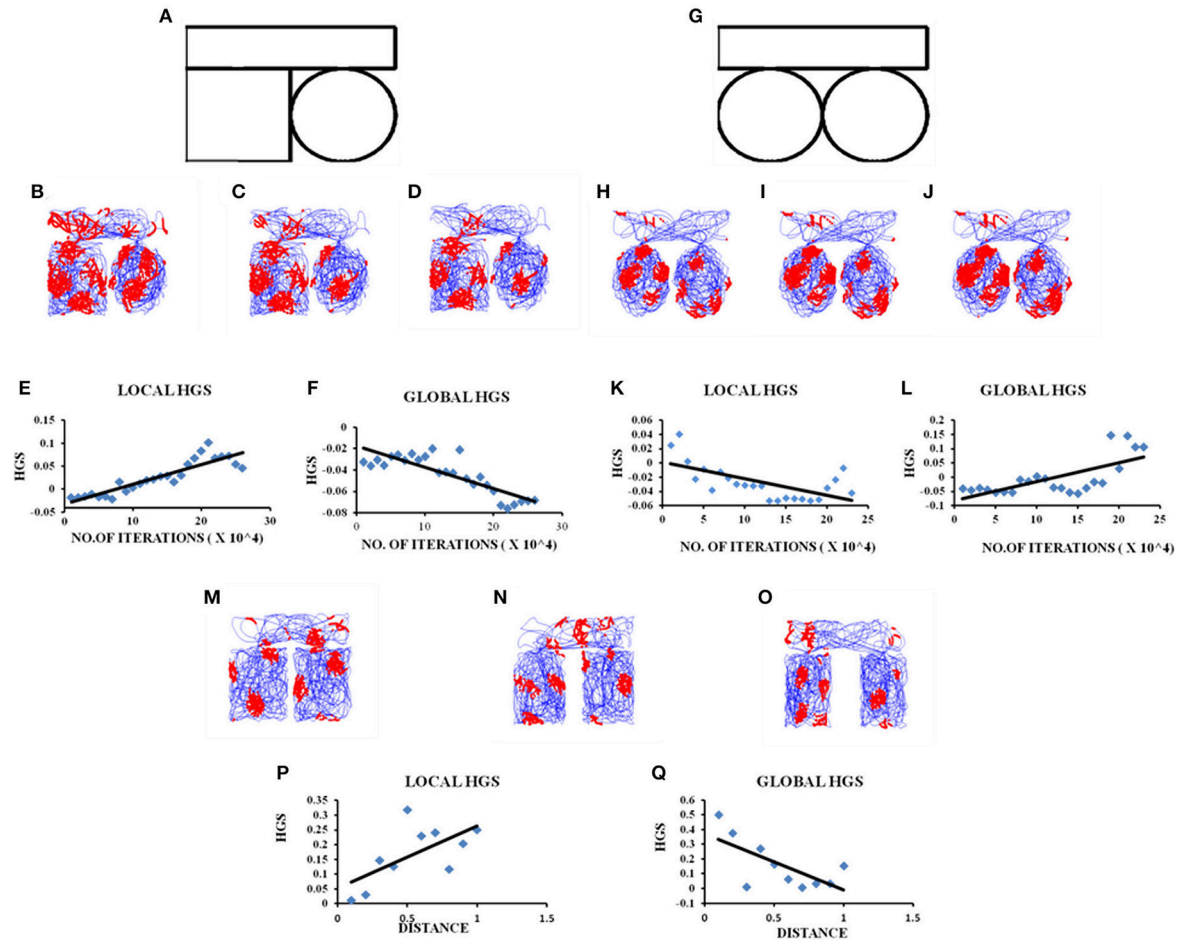

FIGURE 3 | Grid cell firing in circle-circle, square-circle environments and in square–square Connected Environment with increasing distances. **(A)** Boundary of square–circle connected environment. **(B–D)** represent the firing fields of the grid cell in the LAHN for square–circle connected environment at different training iterations (beginning, middle, and end, respectively) of the model. **(E,F)** Local and Global HGS values plotted against the no. of training iterations of model. **(G)** Boundary of circle–circle connected environment. **(H–J)** represent the firing fields of the grid cell in the LAHN for circle–circle connected environment at different training iterations (beginning, middle, and end, respectively) of the model. **(K,L)** Local and Global HGS values plotted against the no. of training iterations of model. **(M–O)** firing field maps (corresponding to end iteration of LAHN training) of the grid cell with respect to distances (d) = 0.1, 0.5, and 1 unit, respectively. **(P,Q)** Local and Global HGS $_{final}$ with respect to the distance between the compartments.

determined using the following equations

$$[X_1 \;\; Y_1] = \left[r_1\cos(\theta) \;\; r_1\sin(\theta)\right]\text{; corresponds to the outer arc}$$
$$[X_2 \;\; Y_2] = \left[r_2\cos(\theta) \;\; r_2\sin(\theta)\right]\text{; corresponds to the inner arc}$$

r_1 and r_2 = radii of the outer and inner arcs, respectively, with $r_1 > r_2$. For the annulus, θ varied from 0 to 360° and in the case of horseshoe it varied from 0 to 180°. The S-shaped boundary is generated by concatenating two horseshoe boundaries, with one of the horseshoes inverted to form the S- shape (**Figure 5C**).

Generation of Transforming Environment

The objective of studying a transforming environment is to see if the network output codes not just the position, but also the global property of the output environment. In the transforming environment, the boundary comprises of a 5 × 2 rectangular boundary (configuration 1) (**Figure 11A**) that evolves over time to a square (configuration 2) of 5 × 5 dimensions (**Figure 11B**). The exploration of the environment by the virtual agent is concurrent with this transformation.

RESULTS

Visual Input Is Not Imperative for the Prescribed Model

The model is capable of simulating spatial cell responses even in the absence of any visual cues (Soman et al., 2018b). Furthermore, since it is a velocity driven model, information about the geometry of the environment is implicitly coded in the velocity itself. This is due to the fact that the trajectory of the virtual animal is constrained by the shape of the external environment (Equations (7–10).

Grid Cell Response to the Shape of Connected Environments

We perform two different studies to understand the grid cell coding that emerges when the animal forages the environments connected by a narrow corridor. In the first study we manipulate the shapes of the connected environments and analyze the grid fields. In the second study we fix the shape but vary the distance between the connected environments.

Manipulating the Shapes of the Connected Environments

We simulate connected environments with boundaries and corridor in the same dimensions (the dimension of the square room is 1.8 × 1.8 units and that of the corridor is 0.8 unit)as used in the experimental study (Carpenter et al., 2015). We verify grid cell coding under three schemes such as square–square, square-circle and circle–circle as shown in **Figures 2A**, **3A,G**). The virtual animal is allowed to forage the environment in these three cases. For each case, the model is trained and the resulting grid fields are analyzed as shown in **Figures 2**, **3**.

The local and global fits for the square–square connected environment are calculated in the same manner as mentioned in the experimental paper (Carpenter et al., 2015). As for the other two connected environments (square–circle and circle–circle), the global HGS is computed by calculating the HGS values over the entire connected environment and the local HGS is obtained by calculating the HGS values for the two environments separately and averaging them. In the square–square connected environment, the global fit shows an increasing trend (**Figure 2F**) with respect to the LAHN training time (Regression analysis: Global fit $R^2 = 0.3826$, $p < 0.05$). Local fit shows a decreasing trend (**Figure 2E**; Regression analysis: Local fit $R^2 = 0.771$, $p < 0.001$).

A similar analysis is performed for connected environments with different shapes such as square–circle. These boundaries are connected in the exact same manner as in the square–square case. In this case, the global HGS shows a reverse trend (**Figure 3F**) compared to the square–square case (Regression analysis: Global fit $R^2 = 0.7042$, $p < 0.001$) and the local HGS shows an increasing trend (**Figure 3E**). (Regression analysis: Local fit $R^2 = 0.8152$, $p < 0.001$).

We then connect two circles exactly in the same manner as the ones before. Similar analysis is carried out where the global HGS shows an increasing trend (**Figure 3L**) (Regression analysis: Global fit $R^2 = 0.4833$, $p < 0.001$) and the local HGS shows a decreasing trend (**Figure 3K**) (Regression analysis: Local fit $R^2 = 0.4071$, $p < 0.001$). These trends are similar to the square-square case.

The realignment of the grid fields from a local to global continuum is available for viewing in the **Supplementary Material (Videos 1–3)**.

Manipulating the Distance Between the Connected Environments

Experimental studies showed that grid cells were capable of forming coherent global representations in a connected environment (Carpenter et al., 2015). Our next objective is to examine whether this globally representative property of grid firing is retained with increasing distance between the connected environments. To examine this property we connect two square compartments and vary the distance between them (distance (d) ranging from 0.1 to 1 unit, in increments of 0.1). The boundary conditions of the compartments and the corridor are set in the same ratio as in the experiment (Carpenter et al., 2015). The agent is allowed to forage the environment for a period of 10 sessions. Each session consists of five trips and for each session the distance between the two compartments is increased by a value of 0.1.

HGS values (HGS_{final}) are computed at the time of convergence of LAHN and the global and local fits are calculated. These scores are taken into account owing to the fact that convergence corresponds to the completion of the training session of the weights. The global HGS values over the distances show a decreasing trend (**Figure 3Q**; Regression analysis: Global fit $R^2 = 0.4585$, $p < 0.05$) while the values of the local HGS show an increasing trend (**Figure 3P**; Regression analysis: Local fit $R^2 = 0.4142$, $p < 0.05$).

Grid Cell Response in Convex Shaped Environment

The influence of environmental geometry on grid cell symmetry was contested by Krupic et al. (2015), and the notion that grid cells can serve as a universal metric for navigation was challenged. We conduct a similar study using our computational model where we generate square and trapezoidal boundaries in the same dimensions as used in the experiment (Krupic et al., 2015). The HGS values are calculated from the autocorrelation map. Both the square and trapezoid boundaries are divided into two halves of equal areas and analysis is performed to check the similarity in the gridness between the two halves for both the boundaries. The HGS analyses are carried out independently for each side and then for the complete shape in case of both trapezoid and square. The average HGS for the left side of the trapezoid is less compared to its right (left = 0.050763, right = 0.14143; **Figure 4B**) and is more or less equal for both sides of the square (left = 0.201337, right = 0.20981, **Figure 4A**). Another study on the similarity between the grid patterns of both the halves in the square and trapezoid enclosures was conducted. It is seen from the **Figure 4C** that the similarity in grid patterns is high in the square than in the trapezium. Additionally, an analysis to determine the ellipticity of the grid field in the autocorrelogram is conducted. It can be observed that the trapezoid boundary has a higher ellipticity in grid fields than that of a square boundary (**Figure 4D**).

Grid Cell Response in Concave Shaped Environment

A similar study of grid cell spatial coding is conducted using concave shaped environments like horseshoe, annulus and S shape (**Figure 5**).

Horseshoe Shaped Environment

The inner radius (r) of the horseshoe is varied from 0 to 2 units with a step size of 0.2. The horseshoe boundary with $r = 0$ approximates a semicircle. The virtual agent is made to

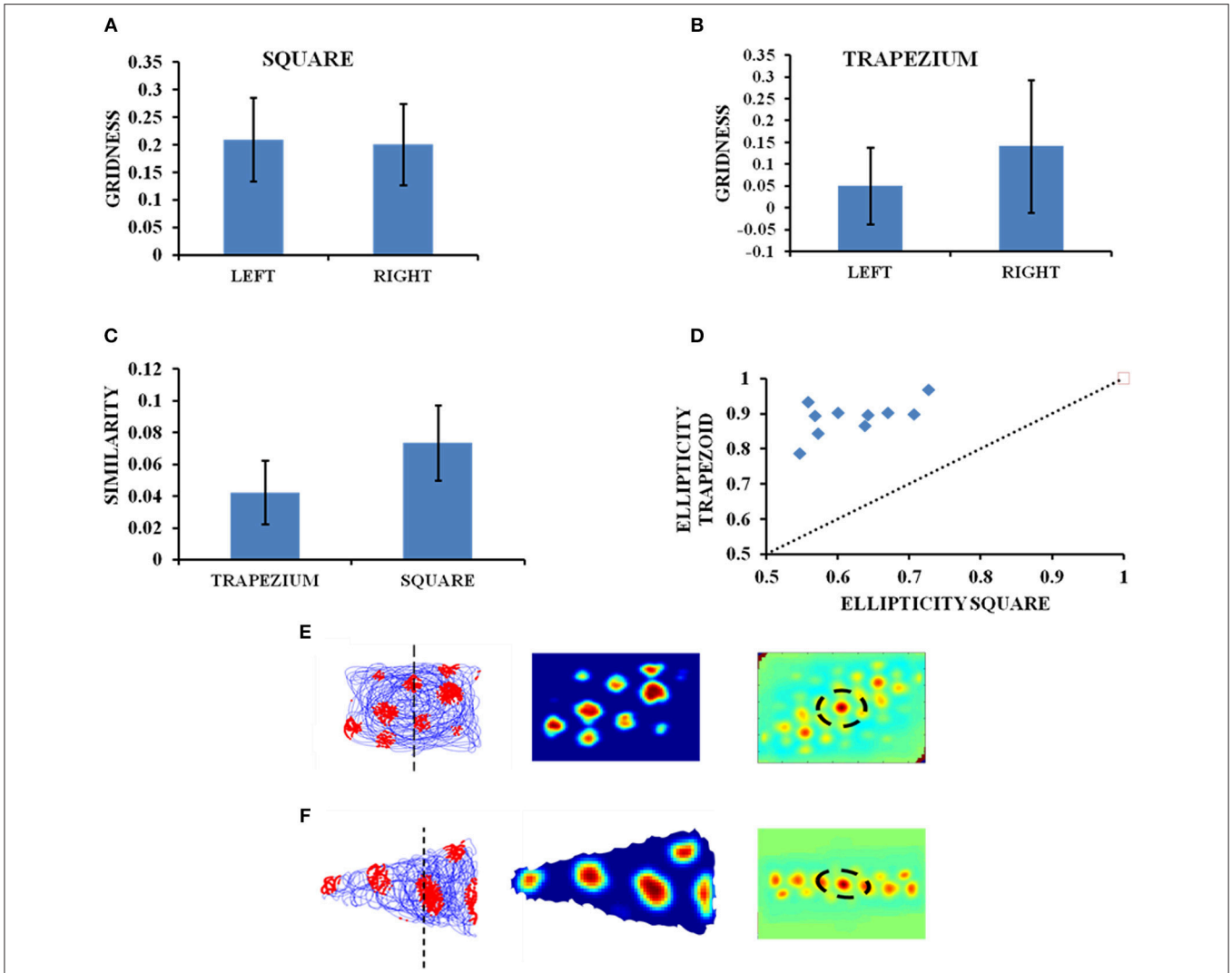

FIGURE 4 | Grid cell firing in square and trapezoid enclosures. **(A,B)** Average HGS values plotted for the left and right orientation of the square and trapezium boundaries. **(C)** Model results—Right and left sides of square are more similar than that of a trapezium. **(D)** Model results—Ellipticity between a square and a trapezoid. **(E,F)** Firing field, firing rate, and autocorrelation maps of the square and trapezoid boundaries, respectively.

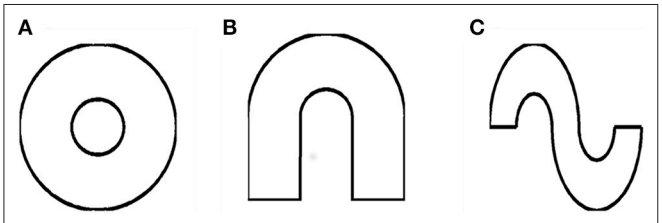

FIGURE 5 | Simulated concave shaped environments **(A)** Annulus, **(B)** Horseshoe, and **(C)** S-Shape, respectively.

traverse the environment. Firing activity of the grid cells under various r values is shown in **Figures 6A–C**. HGS values show a decreasing trend (**Figure 6D**) as the inner radius of the horseshoe is increased (Single factor ANOVA, $p < 0.001$).

Annulus Shaped Environment

A similar analysis is performed with the second type of concave boundary i.e., annulus shaped environment. Annulus with inner radius 0 approximates to a circular boundary. Firing activity of the grid cells under various r values is shown in **Figures 7A–C**. The HGS values are found to have the same decreasing trend as that of horseshoe, as the inner radii of the annulus is increased (Single factor ANOVA, $p < 0.001$) (**Figure 7D**).

S Shaped Environment

In case of an environment like the S shape, where two similar horseshoes are concatenated at a common end, it is found that as the inner radius of the S shape increased from 0 to 1 unit with a step size of 0.2, the HGS values show a decreasing trend (Single factor ANOVA, $p < 0.001$) (**Figure 8D**).

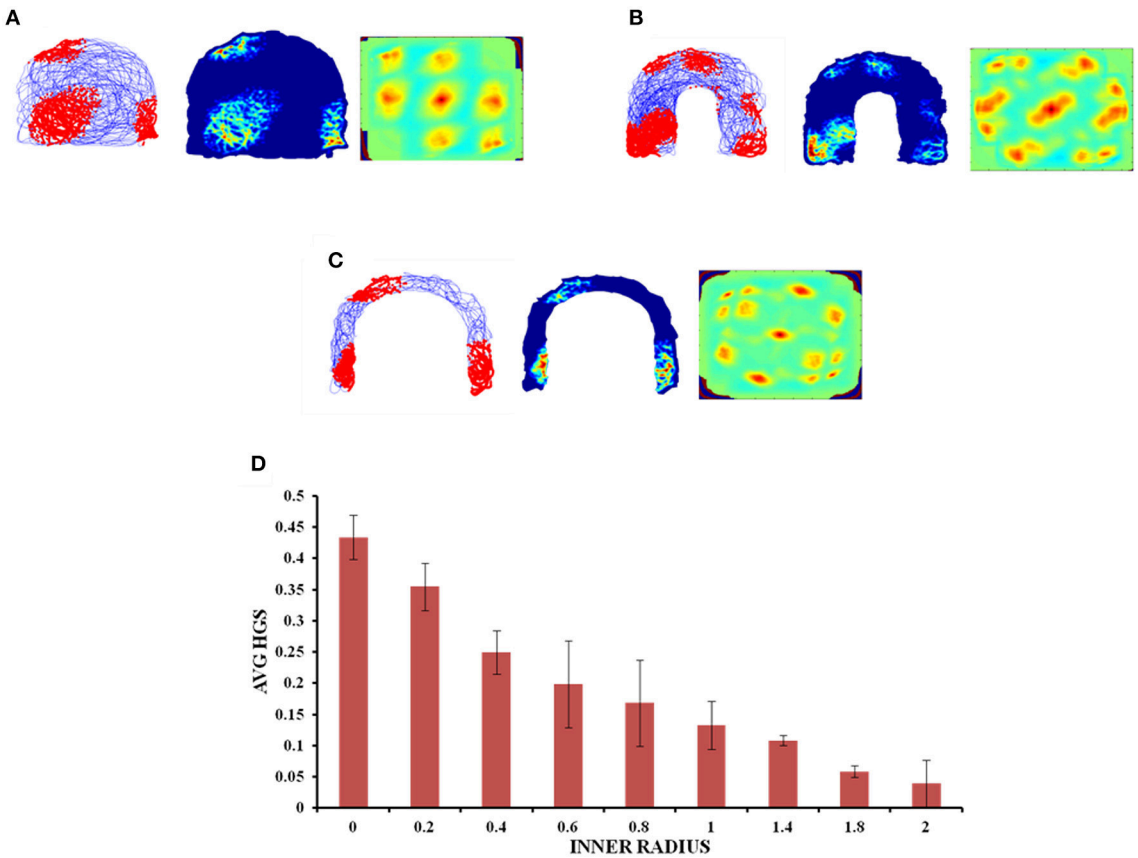

FIGURE 6 | Grid cell responses in horseshoe shaped environment. **(A–C)** Firing field, firing rate, and auto correlation maps of horseshoe boundary with varying inner radii of 0, 0.8, and 2, respectively. **(D)** Average HGS values vs. inner radii of horseshoe shaped environment.

Grid Cell Response to Increasing Lines of Symmetry in the Environment

Most of the grid cell experimental recordings were carried out either in square or circular shaped environments (Krupic et al., 2015). Here we address the problem of grid cell coding for environments in the shape of n-sided regular polygons. Specifically we consider the range of n from 3 to 10. This study would give an understanding on how the grid cell code will vary if the number of sides increases and the polygon approximates a circle (a regular polygon with infinite sides). In other words, it is analogous to the study of the influence of environmental symmetry on the grid cell code. **Figure 9** shows the simulated environments used for this study.

The virtual animal is then allowed to forage inside these shapes and the resultant trajectory is given as input to the model. **Figures 10A–H** show the resultant firing field, firing rate and autocorrelation maps of the respective polygons. We compute the HGS values from the spatial autocorrelograms. It is observed that the HGS values shows an increasing trend with respect to the number of sides of the polygon (Single factor ANOVA, $p < 0.001$) (**Figure 10I**).

Deciphering the Global Feature of the Environment From LAHN Activity

The results described so far point to the fact that the simulated grid neuron is sensitive to a global feature of an environment such as its shape. To make a more general statement, we need to show that the LAHN neurons code for a more invariant and global feature of an environment, in addition to just the local features such as position or displacement. To numerically prove this qualitative statement, the virtual animal is allowed to forage in a rectangular configuration. Over the course of time, where a rat was made to forage inside multi the environment is transformed into a square. To prove the above hypothesis, we show that the LAHN neural responses have information to classify the environment—Rectangle vs. Square. We implement this classifier using a Multi-Layer Perceptron (MLP).

The MLP is used here to classify the configuration (either rectangle or square) based on the activity of the LAHN. The MLP is trained using the standard back propagation algorithm (LeCun, 1988) with a single hidden layer of neurons [see **Supplementary Material** for MLP training (B)]. The classification accuracy after training comes to 74.74%. To confirm for the global invariant feature in the LAHN, we

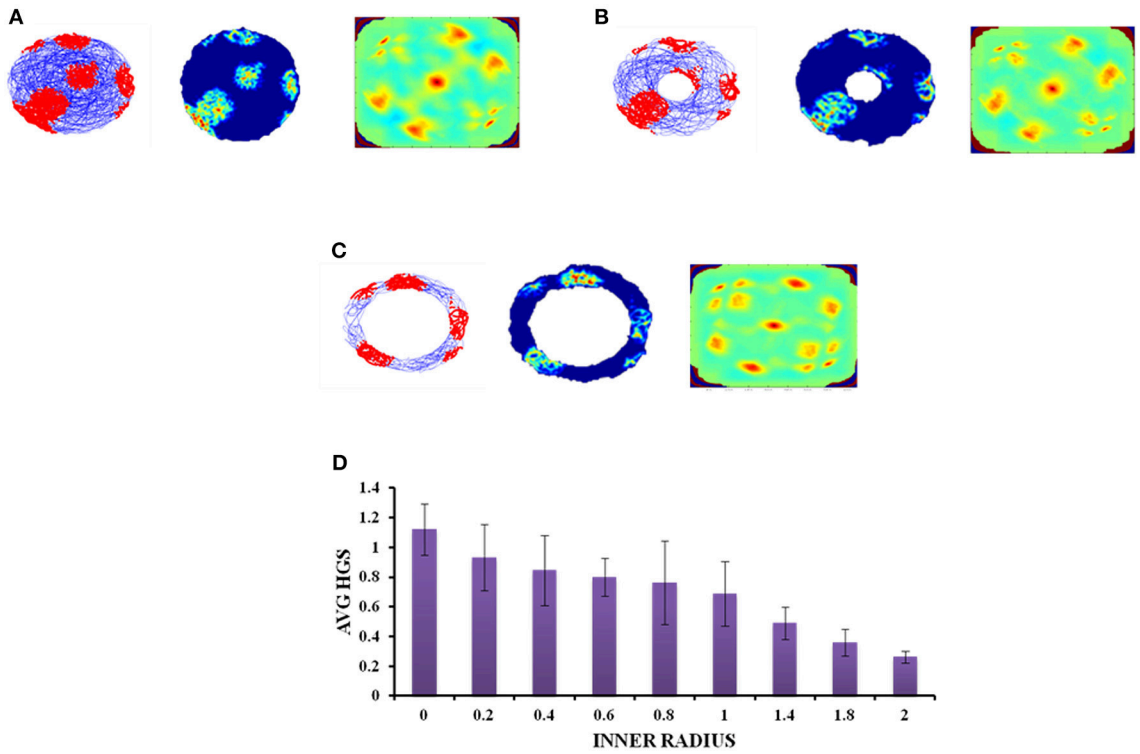

FIGURE 7 | Grid cell response in annulus shaped environment. **(A–C)** Firing field, firing rate, and auto correlation maps of grid activity in the annulus environment with varying inner radii of 0, 0.8, and 2, respectively. **(D)** Average HGS values vs. varying inner radii of annulus.

trained another MLP with partially learned LAHN and its classification accuracy comes to 52.33%. Furthermore, it can be observed from **Figure 12C** that the Mean Square Error of the network output with respect to the untrained LAHN input is 0.5307 (configuration 1) and 0.2854 (configuration 2); while for a trained LAHN input it is 0.1503 (configuration 1) and 0.1359 (configuration 2). This proves that as the LAHN learns the representations of the animal's navigating space, it encodes both local (like displacement, position) and global (like the environmental configuration) spatial features. For efficient navigation, both of these features are pertinent and the animal must be performing Simultaneous Localization And Mapping (SLAM) (Milford and Wyeth, 2010).

DISCUSSION

Grid cell firing fields, characterized by their hexagonal spatial periodicities, are considered to serve as a universal metric for spatial navigation. This notion was contested by some experimental studies (Krupic et al., 2015) showing the dependence of grid cell coding on the environmental shape. However, the experimental studies have limitations with regard to the grid cell recording under different environmental shapes. This forms the motivation of the present paper which seeks to study, using computational modeling, grid cell activity under different environmental geometries without any limitations that plague experimental efforts. Since we chose to study the grid cell activity under various environmental conditions, we systematically divided the simulations into five categories such as connected environments, convex shaped environments, concave shaped environments, regular polygonal environments (with varying number of sides), and transforming environment. Finally, through the numerical analysis and MLP classifier we show the potentiality of the spatial cells to encode the global and invariant feature of the environment rather than local features like position, displacement etc.

The experimental study conducted by Carpenter et al. (2015) where the rat foraged between two similar square boxes connected via a corridor, forms the special case of the formerly stated modeling study where the shape is square-square and distance is zero. The modeling results concur with the experimental results (**Figure 2**). In the experimental case it was observed that initially the grid cell firing was controlled by the local cues, in the sense that the firing replicated between the two compartments. However, with further exploration, the similarities between the grid firing fields of the compartments decreased, suggesting that with increasing trials, global cues controlled the firing of grid cells. This trend is captured in the model (**Figure 2**). Hence, the aforementioned simulation and further analysis of the grid cell activity in the connected environments form a viable empirical study.

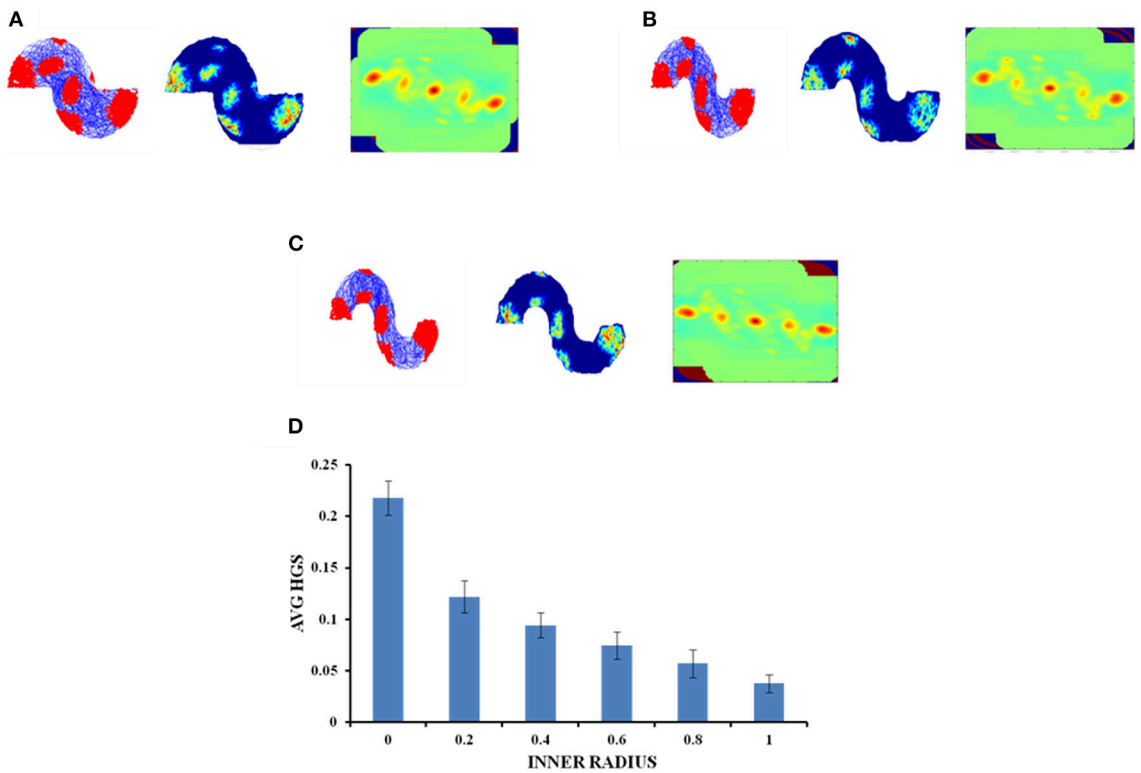

FIGURE 8 | Grid cell response in S-Shape Boundary. **(A–C)** Firing field, firing rate, and auto correlation maps of S shape boundary with varying inner radii of 0, 0.8, and 2, respectively. **(D)** Average HGS values vs. varying inner radii of S- Shape.

In the connected environment study, we manipulated the shapes of the connected regions from a square-square to a square-circle and circle-circle boundary. HGS values are computed while the model is undergoing training. The interesting result is that in the case of identical connected environments, such as square-square and circle-circle, the global HGS values (HGS value computed from the connected environment as a whole) show an increasing trend and the local HGS values (average of the HGS values computed from each connected region separately) show a decreasing trend with respect to the training time of the model. This means that as the animal gets more and more familiar with the environment (with increasing training sessions in the model), the grid fields start to realign themselves and form a continuum in the case of similar shaped connected environments. In order to determine whether the global representation of the connected environments depend on the similarity between the two connected boundaries, we performed a similar analysis in a square-circle environment. On the contrary, in this case it showed a negative trend in the global HGS and a positive trend in the local HGS value. Thus, it is possible to infer from the grid cell HGS variation whether the animal is exploring in a similar or dissimilar connected environment. This is a novel insight into the grid cell code purely from the computational point of view, and an easily testable prediction for future experiments.

After studying the grid cell coding scheme with respect to the shapes of the connected environments, we delved into the dependence of grid cell coding scheme on the distance between the connected environments. This study, along with the formerly stated one, is pertinent especially with regard to large scale navigation where the animal is not restricted to just one environment but shuttles between multiple environments of different shapes at different locations. Hence to get an insight on the grid cell coding with respect to the distance between the connected environments, we simulated a connected environment (square-square) and varied the distance between the two compartments of the environment. Our hypothesis was that since

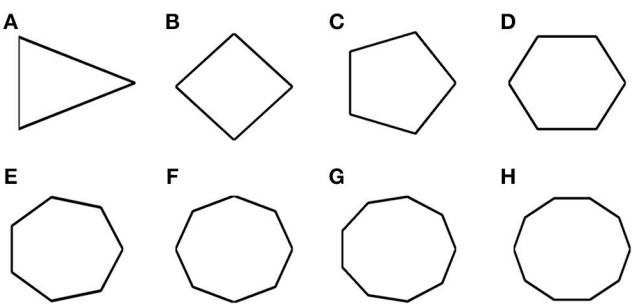

FIGURE 9 | Boundaries of n- sided polygons. **(A–H)** Environmental shapes used for the analysis of grid cell coding with respect to the number of sides of the polygon; arranged in the order of triangle, square, pentagon, hexagon, heptagon, octagon, nonagon, and decagon (from left to right).

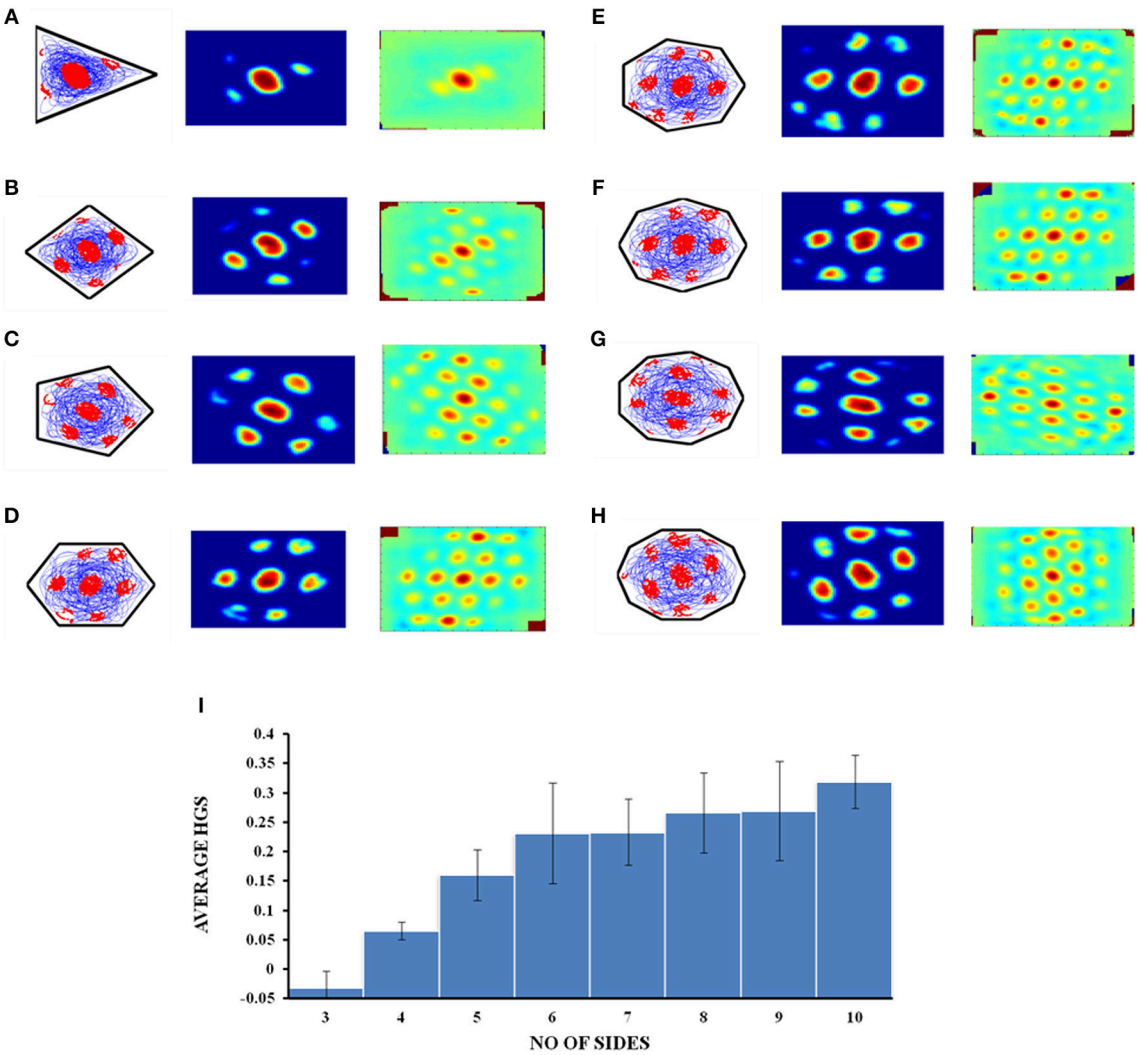

FIGURE 10 | Grid cell firing in regular polygons. **(A–H)** Firing field, firing rate map and autocorrelogram (from left to right) of triangle, square, pentagon, hexagon, heptagon, octagon, nonagon, and decagon shapes, respectively. **(I)** The average HGS value of the grid field obtained for each polygon vs. the number of sides of the polygon. The plot shows an increasing trend as the polarity of the environment decreases.

grid cells code for the distance traveled by the animal (O'Keefe and Burgess, 2005) (due to its regularly periodic hexagonal firing field), the distance between the connected environments should also be reflected in its activity. On performing the analysis, the variation in the global HGS values show a decreasing trend and local HGS values show an increasing trend with increasing distance between environments. This variation in the gridness score points out the possibility that grid cells encode for the global distance between the environments and this information is pertinent to large scale navigation. It is observed from the grid cell representations that the two compartments, even though connected, are treated as independent at larger distances.

Hence at the outset, when the distance between the compartments is minimal, the representation is more global as opposed to local. As the distance between the two compartments increases, the grid cells seem to lose their ability to form global representations and the firing becomes localized to their respective compartments. From the above simulations, the inference is that grid cells may not code just for distance but also for the entire structure of the environment. The methods defined previously can be easily extended to the case of connected environments with more than two components. We can consider a network of environments with complex spatial arrangements and connectivity. It would be interesting to study the evolution of local vs. global organization of the grid fields in such systems. In addition to the spatial arrangements of the environments in such complex systems, the frequency of visitation of that agent to individual components may also determine the overall grid field organization. Such studies might pave way to the formulation of deep laws that govern the spatial encoding of brain in compound environments with complex navigational patterns followed by the agent.

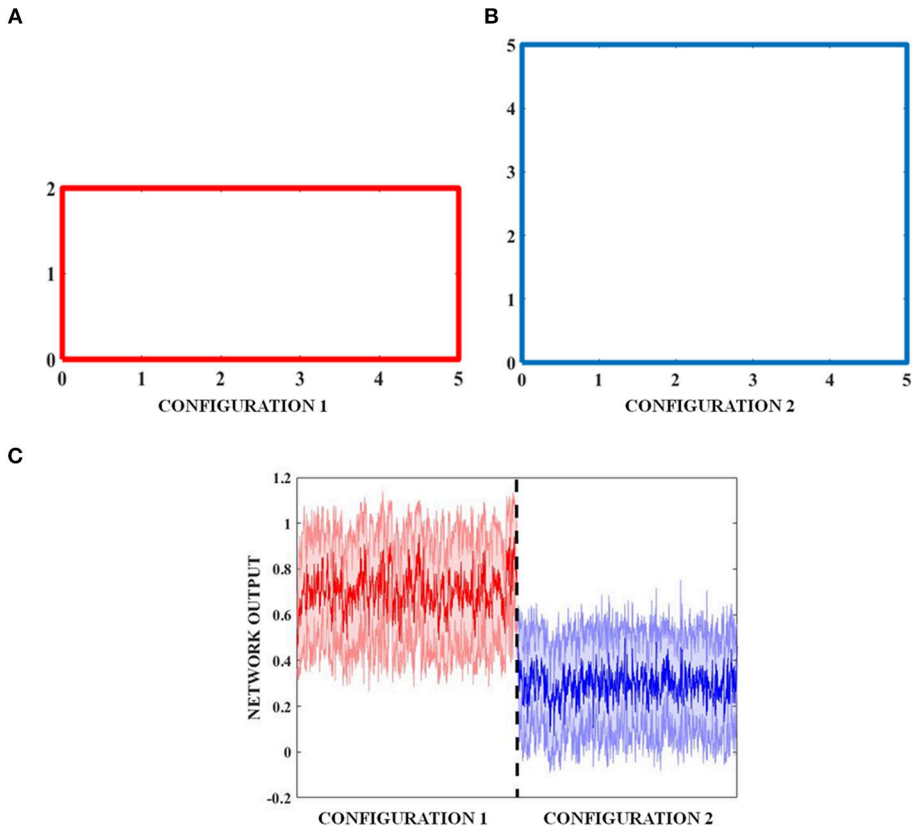

FIGURE 11 | Transforming environment. **(A)** Rectangle **(B)** Temporal transformation of the rectangle to a square by increasing its breadth, and **(C)** shaded plot of the classification of the two boundaries by MLP.

Oscillatory path integration stage of the model is vital to capture the results that are indicated above. Here, the position is encoded as the phase of the oscillator (Equations 2, 3). If a grid cell is activated at one point in space in one case (for instance, in connected environments separated by distance d_1) and not activated at the same point in the second case (distance d_2), the reason must be that the afferent input to the grid cell from the oscillators is different (Equation 4) in both the cases. Different configurations of the environment make the oscillator code for the same position at different phases of the oscillator. Also, since position is encoded as a periodic quantity at this oscillatory stage [as it does in oscillatory interference model (Burgess et al., 2007)], this periodicity is reflected in the spatial firing fields of the grid cell in the LAHN.

The objective of the next simulation study is to essentially capture the results of the experimental work by Krupic et al. (2015), where a rat was made to forage inside multiple boundaries of different shapes such as circle, square, trapezium and hexagon. This study explained the permanent effect exerted by the environmental geometry on grid cell firing and grid field symmetry. To determine the impact of environmental characteristics on homogeneity and symmetry of grid patterns, the grid firing in two shapes such as square and trapezium was analyzed. It was found that in a highly polar environment like a trapezium there was a decrease in the regularity of the hexagon (reflected in the HGS score) and the pattern becomes highly elliptical across the entire enclosure. To estimate the regularity of grid patterns, the trapezoid and square were divided into two parts of equal area and the firing fields on both the sides were compared. The autocorrelation maps showed that there was a strong difference in local spatial structures between the two sides of a trapezoid unlike a square wherein they were highly similar. The gridness of left (narrower) side of the trapezoid was found to be low when compared to its right (broader) side. Also when the square and trapezoid boundaries were compared as a whole, the latter had a lower gridness. This was because when a trapezoid is divided into two, the left side resembled a triangle and the right side, a square.

The simulation results are consistent with the experimental data (**Figure 4**). We performed the comparative study as mentioned above using our model i.e., between both sides of the trapezoid and square and between both the shapes as whole and obtained congruent results (**Figure 4**). From the firing rate map (**Figures 4E,F**) and autocorrelation map (**Figures 4E,F**) we are able to see that the left side of the trapezoid has less local spatial structure compared to its right side. In the case of a square, little difference is observed between its two halves. A study on the similarity of the grid patterns between the two halves of both

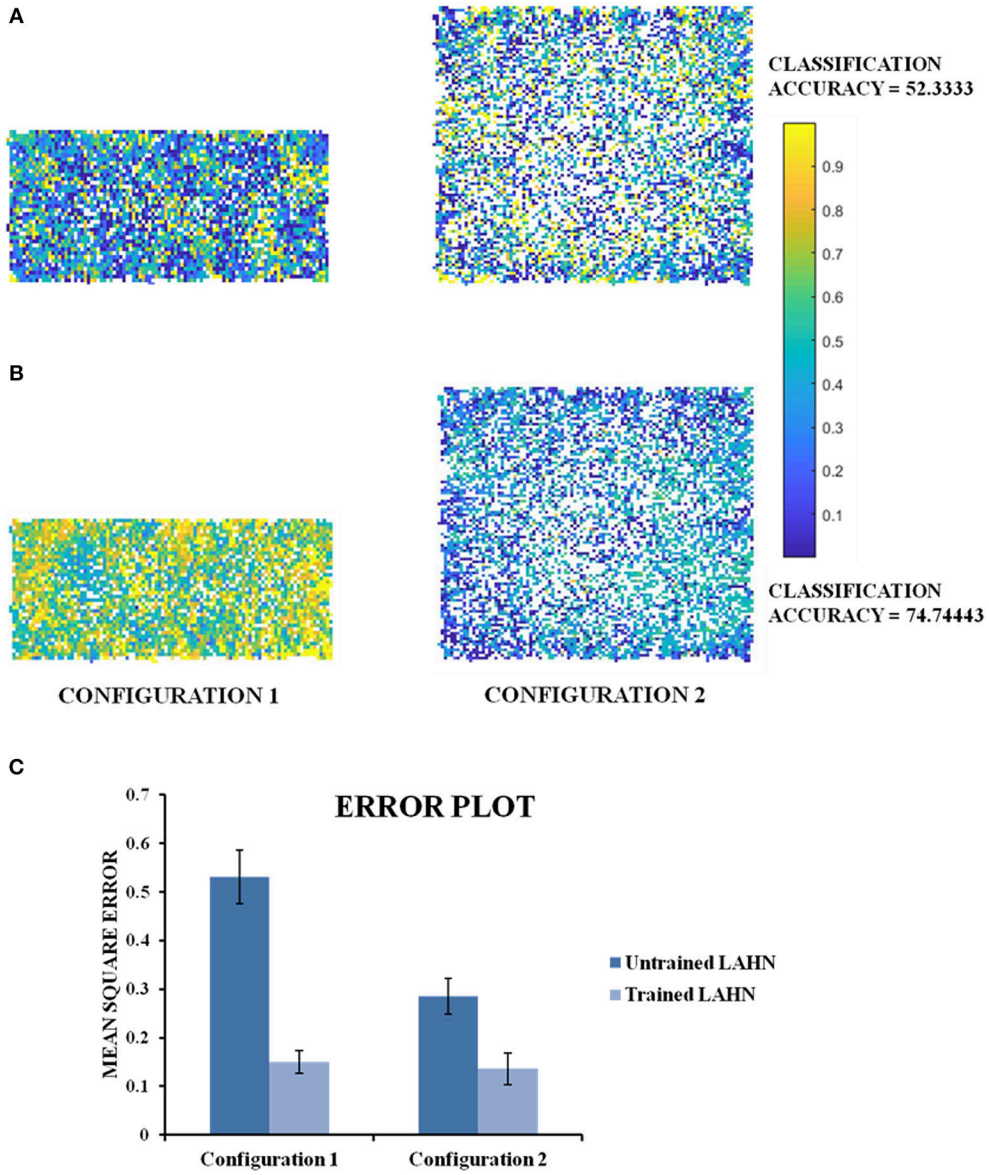

FIGURE 12 | Classification maps of the MLP output. **(A)** MLP classification maps using initial training periods of LAHN as input. It gives a classification accuracy of 52.33% **(B)** MLP classification maps using fully trained LAHN as input. It gives a classification accuracy of 74.74%.Yellow and dark blue denote configuration 1 and configuration 2, respectively. The intermediate color gradient represents output of the network activity between 0 and 1. **(C)** Mean Square Error of the MLP network output.

the trapezoid and square enclosures, respectively, revealed that the patterns are more similar in the square enclosure than in the trapezoid enclosure. In addition to this the ellipticity of the grid fields from the autocorrelation maps of the trapezoid and square boundaries were obtained and plotted as observed in the **Figure 4D**. It can be inferred that the grid fields in the trapezoid boundary are more elliptical than the grid fields in the square boundary and this as well is in congruence with the experimental results (Krupic et al., 2015).

Since the model successfully captured the experimental results (Krupic et al., 2015) in the convex shaped environments such as square and trapezoid, we extended our study by varying the number of sides of a regular polygon. The aim of this study is to understand the effect of the number of lines of symmetry in the environment on the grid fields. We found that the HGS values show an increasing trend with respect to the number of sides of the regular polygon (**Figure 10I**). In other words, higher symmetry in the environment leads to higher HGS values. Hence we predict that the HGS score should be maximum for a circular environment (where the number of lines of symmetry is infinite). It was also observed from the experiment (Krupic et al., 2015), that the circular boundary is considered to be highly unpolarized

when compared to all the other boundaries and hence showed high gridness scores.

The above experimental study focuses on explaining the influence of the polarity of the environment on grid representations. But this study takes into account only discreet environments such as square, hexagon, circle and trapezium. The N-Sided Polygon study that we have conducted is a generalization of this experimental study where we dynamically analyse the polarity induced asymmetry in grid representations by gradually increasing the number of sides of the environment (maintaining a continuum) until the outline approximates a circle (considered to be highly non-polar).

Since the real world navigation occurs in environments with arbitrary shapes, we conducted the simulation on concave shapes too. We considered concave shapes such as horseshoe, annulus and S-shaped environments (**Figure 5**). As the inner radius of the horseshoe increased, the hexagonal grid representation in the auto correlation map appeared to lose its regularity. This is captured by the decreasing HGS values as shown in the graph (**Figure 6D**). The same trend is observed for the other two concave boundaries as well, i.e., annulus and S-Shape (**Figures 7D**, **8D**). It can be observed that, since the annulus with inner radius 0 approximates a circular boundary, its HGS value tends to be the highest. It can be noted that as the inner radii of the aforementioned concave environments increase, the space available for the virtual animal to traverse shrinks. This reduced availability of space may be the reason behind the deviation from the hexagonal spatial coding of the grid cell, as reflected in the reduced HGS values across all the three concave shapes. This can be experimentally tested in many ways by implementing environments similar to the ones that we have simulated in this study (**Figures 6**–**8**) with less space given to the animal for exploration. There is also a need to develop a strong mathematical framework that explains the relationship between the observed spatial coding and the geometry of the environment. Hence the proposed modeling study gives a new dimension to the grid cell coding with a good number of testable predictions.

In all the studies stated above, we looked for grid fields only for the sake of comparison with empirical evidence. However, we hypothesize that it is not just the grid cells but the entire LAHN that implicitly codes for the global structure of the environment rather than just local structure of the space in which the animal navigates. To underpin this, we decoded the LAHN neural information using MLP whose precision was measured in terms of classification accuracy. We constructed a transforming environment (rectangle to square) and collected the spatial cell responses which were fed as input to the MLP network to check if the LAHN was able to account for this transformation. At any given time, for a given position (x, y) of the virtual animal, the MLP is able to decipher the information about the configuration it had traversed in **Figure 11C**. This is denoted by the classification accuracy obtained from MLP. A high classification accuracy of 74.74% (**Figure 12B**) is observed on using trained LAHN input. Conversely when partially trained LAHN is used, the classification accuracy decreased to 52.33% (**Figure 12A**). This serves as a proof-of-principle that global information is encoded in the population activity of LAHN.

MODEL PREDICTIONS

In our connected environment study, the model was able to show that the locally and globally representing properties of the grid cells are sensitive to the shape of the environments that are connected with each other. We believe that this could be verified by connecting environments of different shapes in a similar fashion as in Carpenter et al.'s experiment (Carpenter et al., 2015) and analyzing how the representations emerge as the animal forages in this context. This would in turn elucidate the underpinnings of the global pattern of the grid cell that allows it to be a spatial metric (McNaughton et al., 2006; Fiete et al., 2008; Buzsáki and Moser, 2013). Moreover, testing the global and local representing properties of grid cells in connected environments by varying the distance between the compartments, will offer a holistic idea of the factors that these properties of grid cells are sensitive to.

We hypothesize that the LAHN layer in our model approximates a population of cells present in the Hippocampus and the medial Entorhinal Cortex thus focussing on population activity instead of single cell activity. This ensemble of neurons in the LAHN thus holds global information regarding the environmental geometry. The above prediction can be proved empirically by conducting experiments in which the rat is allowed to forage in a square boundary, one side of which is gradually extended until it approximates a rectangle without any interruption to the animal's navigation during the transformation (similar to the transforming environment study). As the rat is navigating in this environment, the collective activity of a population of cells from the hippocampus and medial entorhinal cortex can then be recorded instead of single cell recording. These neural signals can then be decoded using algorithms such as Bayesian decoders (Kloosterman, 2011; Kloosterman et al., 2013) to decipher the shape of the environment rather than just the position information.

FUTURE DIRECTIONS

In the model, we give direct velocity inputs to the path integration layer which is further fed to the LAHN layer where spatial cells emerge. A more biologically plausible approach would be to account for the representation of motion-related inputs driven by the locomotion of the animal instead of providing explicit position coordinates or velocity inputs. The motion-related information is conferred to the nervous system by the sensory streams that include vision and proprioception. Although the model accounts for spatial cell responses even in the absence of visual cues, the presence of visual input has been proved to offer more stability to the responses of the spatial cells (Soman et al., 2018a). In the light of this view, it would be more interesting to study the extent of stability that the sensory inputs (particularly vision) offer to the spatial cells when the global characteristics of the environment changes. Furthermore, we would also like to decode the complete boundary information of complex environments (contours, mazes etc.,) using the collective response of the LAHN layer in the model.

DATA ACCESSIBITLITY

The simulation code is available at the ModelDB database (http://senselab.med.yale.edu/ModelDB/showModel.cshtml?model=240118) Access code: Env_Grid_Model.

AUTHOR CONTRIBUTIONS

All authors contributed equally to the work. RN and SJ performed coding, trajectory generation, analysis of the model, and manuscript preparation. RR performed trajectory generation and analysis of the model. KS and VM performed designing the model, coding, analysis of the model, and manuscript preparation. VC performed designing the model and manuscript preparation.

SUPPLEMENTARY MATERIAL

The Supplementary Material for this article can be found online at: https://www.frontiersin.org/articles/10.3389/fncir.2018.00120/full#supplementary-material

REFERENCES

Anderson, M. I., and Jeffery, K. J. (2003). Heterogeneous modulation of place cell firing by changes in context. *J. Neurosci.* 23, 8827–8835. doi: 10.1523/JNEUROSCI.23-26-08827.2003

Barnes, C. A., McNaughton, B. L., Mizumori, S. J., Leonard, B. W., and Lin, L. H. (1990). Chapter Comparison of spatial and temporal characteristics of neuronal activity in sequential stages of hippocampal processing. *Prog. Brain Res.* 83, 287–300. doi: 10.1016/S0079-6123(08)61257-1

Barry, C., Hayman, R., Burgess, N., and Jeffery, K. J. (2007). Experience-dependent rescaling of entorhinal grids. *Nat. Neurosci.* 10, 682–684. doi: 10.1038/nn1905

Barry, C., Lever, C., Hayman, R., Hartley, T., Burton, S., O'Keefe, J., et al. (2006). The boundary vector cell model of place cell firing and spatial memory. *Rev. Neurosci.* 17, 71–97. doi: 10.1515/REVNEURO.2006.17.1-2.71

Bostock, E., Muller, R. U., and Kubie, J. L. (1991). Experience-dependent modifications of hippocampal place cell firing. *Hippocampus* 1, 193–205. doi: 10.1002/hipo.450010207

Brun, V. H., Solstad, T., Kjelstrup, K. B., Fyhn, M., Witter, M. P., Moser, E. I., et al. (2008). Progressive increase in grid scale from dorsal to ventral medial entorhinal cortex. *Hippocampus* 18, 1200–1212. doi: 10.1002/hipo.20504

Burgess, N., Barry, C., and O'Keefe, J. (2007). An oscillatory interference model of grid cell firing. *Hippocampus* 17, 801–812. doi: 10.1002/hipo.20327

Bush, D., Barry, C., Manson, D., and Burgess, N. (2015). Using grid cells for navigation. *Neuron* 87, 507–520. doi: 10.1016/j.neuron.2015.07.006

Buzsáki, G., and Moser, E. I. (2013). Memory, navigation and theta rhythm in the hippocampal-entorhinal system. *Nat. Neurosci.* 16, 130–138. doi: 10.1038/nn.3304

Carpenter, F., Manson, D., Jeffery, K., Burgess, N., and Barry, C. (2015). Grid cells form a global representation of connected environments. *Curr. Biol.* 25, 1176–1182. doi: 10.1016/j.cub.2015.02.037

Fiete, I. R., Burak, Y., and Brookings, T. (2008). What grid cells convey about rat location. *J. Neurosci.* 28, 6858–6871. doi: 10.1523/JNEUROSCI.5684-07.2008

Földiák, P. (1989). "Adaptive network for optimal linear feature extraction," in *Proceedings of the IEEE/INNS International Joint Conference on Neural Networks, Vol. 1* (Washington, DC; New York, NY: IEEE Press), 401–405.

Fuhs, M. C., and Touretzky, D. S. (2006). A spin glass model of path integration in rat medial entorhinal cortex. *J. Neurosci.* 26, 4266–4276. doi: 10.1523/JNEUROSCI.4353-05.2006

Fyhn, M., Hafting, T., Treves, A., Moser, M. B., and Moser, E. I. (2007). Hippocampal remapping and grid realignment in entorhinal cortex. *Nature* 446, 190–194. doi: 10.1038/nature05601

Fyhn, M., Hafting, T., Witter, M. P., Moser, E. I., and Moser, M. B. (2008). Grid cells in mice. *Hippocampus* 18, 1230–1238. doi: 10.1002/hipo.20472

Fyhn, M., Molden, S., Witter, M. P., Moser, E. I., and Moser, M. B. (2004). Spatial representation in the entorhinal cortex. *Science* 305, 1258–1264. doi: 10.1126/science.1099901

Hafting, T., Fyhn, M., Molden, S., Moser, M. B., and Moser, E. I. (2005). Microstructure of a spatial map in the entorhinal cortex. *Nature* 436, 801–806. doi: 10.1038/nature03721

Hargreaves, E. L., Rao, G., Lee, I., and Knierim, J. J. (2005). Major dissociation between medial and lateral entorhinal input to dorsal hippocampus. *Science* 308, 1792–1794. doi: 10.1126/science.1110449

Hasselmo, M. E. (2008). Grid cell mechanisms and function: contributions of entorhinal persistent spiking and phase resetting. *Hippocampus* 18, 1213–1229. doi: 10.1002/hipo.20512

Hasselmo, M. E., Giocomo, L. M., and Zilli, E. A. (2007). Grid cell firing may arise from interference of theta frequency membrane potential oscillations in single neurons. *Hippocampus* 17, 1252–1271. doi: 10.1002/hipo.20374

Jacobs, J., Weidemann, C. T., Miller, J. F., Solway, A., Burke, J. F., Wei, X. X., et al. (2013). Direct recordings of grid-like neuronal activity in human spatial navigation. *Nat. Neurosci.* 16, 1188–1190. doi: 10.1038/nn.3466

Killian, N. J., Jutras, M. J., and Buffalo, E. A. (2012). A map of visual space in the primate entorhinal cortex. *Nature* 491, 761–764. doi: 10.1038/nature11587

Kloosterman, F. (2011). Analysis of hippocampal memory replay using neural population decoding. *Neuronal Network Anal.* 67, 259–282. doi: 10.1007/7657_2011_8

Kloosterman, F., Layton, S. P., Chen, Z., and Wilson, M. A. (2013). Bayesian decoding using unsorted spikes in the rat hippocampus. *J. Neurophysiol.* 111, 217–227. doi: 10.1152/jn.01046.2012

Kohonen, T. (1982). Self-organized formation of topologically correct feature maps. *Biol. Cybernet.* 43, 59–69. doi: 10.1007/BF00337288

Krupic, J., Bauza, M., Burton, S., Barry, C., and O'Keefe, J. (2015). Grid cell symmetry is shaped by environmental geometry. *Nature* 518, 232–235. doi: 10.1038/nature14153

Krupic, J., Bauza, M., Burton, S., Lever, C., and O'Keefe, J. (2014). How environment geometry affects grid cell symmetry and what we can learn from it. *Phil. Trans. R. Soc. B* 369:20130188. doi: 10.1098/rstb.2013.0188

Kunz, L., Schröder, T. N., Lee, H., Montag, C., Lachmann, B., Sariyska, R., et al. (2015). Reduced grid-cell-like representations in adults at genetic risk for Alzheimer's disease. *Science* 350, 430–433. doi: 10.1126/science.aac8128

LeCun, Y. (1988). "A theoretical framework for back-propagation," in *Proceedings of the 1988 Connectionist Models Summer School, CMU*, eds D. Touretzky, G. Hinton, and T. Sejnowski (Pittsburgh, PA: Morgan Kaufmann), 21–28.

Lever, C., Wills, T., Cacucci, F., Burgess, N., and O'Keefe, J. (2002). Long-term plasticity in hippocampal place-cell representation of environmental geometry. *Nature* 416, 90–94. doi: 10.1038/416090a

McNaughton, B. L., Battaglia, F. P., Jensen, O., Moser, E. I., and Moser, M. B. (2006). Path integration and the neural basis of the 'cognitive map'. *Nat. Rev. Neurosci.* 7, 663–678. doi: 10.1038/nrn1932

Milford, M., and Wyeth, G. (2010). Persistent navigation and mapping using a biologically inspired SLAM system. *Int. J. Robot. Res.* 29, 1131–1153. doi: 10.1177/0278364909340592

Moser, E. I., Roudi, Y., Witter, M. P., Kentros, C., Bonhoeffer, T., and Moser, M. B. (2014). Grid cells and cortical representation. *Nat. Rev. Neurosci.* 15, 466–481. doi: 10.1038/nrn3766

Oja, E. (1982). Simplified neuron model as a principal component analyzer. *J. Math. Biol.* 15, 267–273. doi: 10.1007/BF00275687

O'Keefe, J., and Burgess, N. (2005). Dual phase and rate coding in hippocampal place cells: theoretical significance and relationship to entorhinal grid cells. *Hippocampus* 15, 853–866. doi: 10.1002/hipo.20115

O'Keefe, J., and Dostrovsky, J. (1971). The hippocampus as a spatial map. Preliminary evidence from unit activity in the freely-moving rat. *Brain Res.* 34, 171–175. doi: 10.1016/0006-8993(71)90358-1

Pastoll, H., Solanka, L., van Rossum, M. C., and Nolan, M. F. (2013). Feedback inhibition enables theta-nested gamma oscillations and grid firing fields. *Neuron* 77, 141–154. doi: 10.1016/j.neuron.2012.11.032

Quirk, G. J., Muller, R. U., Kubie, J. L., and Ranck, J. B. (1992). The positional firing properties of medial entorhinal neurons: description and comparison with hippocampal place cells. *J. Neurosci.* 12, 1945–1963. doi: 10.1523/JNEUROSCI.12-05-01945.1992

Savelli, F., Yoganarasimha, D., and Knierim, J. J. (2008). Influence of boundary removal on the spatial representations of the medial entorhinal cortex. *Hippocampus* 18, 1270–1282. doi: 10.1002/hipo.20511

Soman, K., Muralidharan, V., and Chakravarthy, V. S. (2018a). A model of multisensory integration and its influence on hippocampal spatial cell responses. *IEEE Transac. Cogn. Dev. Syst.* 10, 637–646. doi: 10.1109/TCDS.2017.2752369

Soman, K., Muralidharan, V., and Chakravarthy, V. S. (2018b). A unified hierarchical oscillatory network model of head direction cells, spatially periodic cells and place cells. *Eur. J. Neurosci.* 47, 1266–1281. doi: 10.1111/ejn.13918

Stensola, H., Stensola, T., Solstad, T., Frøland, K., Moser, M. B., and Moser, E. I. (2012). The entorhinal grid map is discretized. *Nature* 492, 72–78. doi: 10.1038/nature11649

Stensola, T., Stensola, H., Moser, M. B., and Moser, E. I. (2015). Shearing-induced asymmetry in entorhinal grid cells. *Nature* 518, 207–212. doi: 10.1038/nature14151

Ulanovsky, N., and Moss, C. F. (2007). Hippocampal cellular and network activity in freely moving echolocating bats. *Nat. Neurosci.* 10, 224–233. doi: 10.1038/nn1829

Urdapilleta, E., Troiani, F., Stella, F., and Treves, A. (2015). Can rodents conceive hyperbolic spaces? *J. Roy. Soc. Interface* 12:20141214. doi: 10.1098/rsif.2014.1214

Yartsev, M. M., Witter, M. P., and Ulanovsky, N. (2011). Grid cells without theta oscillations in the entorhinal cortex of bats. *Nature* 479, 103–107. doi: 10.1038/nature10583

Conflict of Interest Statement: The authors declare that the research was conducted in the absence of any commercial or financial relationships that could be construed as a potential conflict of interest.

frontiers in Neural Circuits

ORIGINAL RESEARCH
published: 12 July 2019
doi: 10.3389/fncir.2019.00045

Multiple Patterns of Axonal Collateralization of Single Layer III Neurons of the Rat Presubiculum

Yoshiko Honda[1]* *and Takahiro Furuta*[2]

[1]Department of Anatomy, School of Medicine, Tokyo Women's Medical University, Tokyo, Japan, [2]Department of Oral Anatomy and Neurobiology, Graduate School of Dentistry, Osaka University, Osaka, Japan

The presubiculum plays a key role in processing and integrating spatial and head-directional information. Layer III neurons of the presubiculum provide strong projections to the superficial layers of the medial entorhinal cortex (MEC) in the rat. Our previous study revealed that the terminal distribution of efferents from layer III cells of the presubiculum was organized in a band-like fashion within the MEC, and the transverse axis of these zones ran parallel to the rhinal fissure. Identifying axonal branching patterns of layer III neurons of the presubiculum is important to further elucidate the functional roles of the presubiculum. In the present study, we visualized all axonal processes and terminal distributions of single presubicular layer III neurons in the rat, using *in vivo* injection of a viral vector expressing membrane-targeted palmitoylation site-attached green fluorescent protein (GFP). We found that layer III of the rat presubiculum comprised multiple types of neurons (n = 12) with characteristic patterns of axonal collateralization, including cortical projection neurons (n = 6) and several types of intrinsic connectional neurons (n = 6). Two of six cortical projection neurons provided two or three major axonal branches to the MEC and formed elaborate terminal arbors within the superficial layers of the MEC. The width and axis of the area of their terminal distribution resembled that of the band-like terminal field seen in our massive-scale observation. Two of the other four cortical projection neurons gave off axonal branches to the MEC and also to the subiculum, and each of the other two neurons sent axons to the subiculum or parasubiculum. Patterns of axonal arborization of six intrinsic connectional neurons were distinct from each other, with four neurons sending many axonal branches to both superficial and deep layers of the presubiculum and the other two neurons showing sparse axonal branches with terminations confined to layers III–V of the presubiculum. These data demonstrate that layer III of the rat presubiculum consists of multiple types of cortical projection neurons and interneurons, and also suggest that inputs from a single presubicular layer III neuron can directly affect a band-like zone of the MEC.

Keywords: single neuronal tracing, Sindbis viral vector, axonal arborization, morphology, postsubiculum, medial entorhinal cortex

OPEN ACCESS

Edited by:
Desdemona Fricker, UMR8119 Centre de Neurophysique, Physiologie, Pathologie, France

Reviewed by:
Yoshiyuki Kubota, National Institute for Physiological Sciences (NIPS), Japan
Andrea Burgalossi, University of Tübingen, Germany
Patricia Preston-Ferrer, University of Tübingen, in collaboration with reviewer AB

***Correspondence:**
Yoshiko Honda
honday@twmu.ac.jp

Received: *10 April 2019*
Accepted: *27 June 2019*
Published: *12 July 2019*

Citation:
Honda Y and Furuta T (2019) Multiple Patterns of Axonal Collateralization of Single Layer III Neurons of the Rat Presubiculum. Front. Neural Circuits 13:45. doi: 10.3389/fncir.2019.00045

Abbreviations: AB, angular bundle; CA, cornu ammonis; cc, corpus callosum; dhc, dorsal hippocampal commissure; dist, distal; EC, entorhinal cortex; GFP, green fluorescent protein; hf, hippocampal fissure; ld, lamina dissecans; LEC, lateral entorhinal cortex; MEC, medial entorhinal cortex; mol, molecular layer; ParS, parasubiculum; pcl, pyramidal cell layer; PreS, presubiculum; prox, proximal; pyr, pyramidal; rf, rhinal fissure; RS, retrosplenial cortex; sept, septal; Sub, subiculum; temp, temporal.

INTRODUCTION

Connectivity among the hippocampal formation [dentate gyrus, cornu ammonis (CA), and subiculum], presubiculum (PreS) and entorhinal cortex (EC) are crucial for memory formation. Sensory information converges on EC and is transmitted to the hippocampal formation. Signals are processed in the internal circuit, propagated to the cortical and subcortical structures, then return to EC. Back projections from the hippocampal formation to EC include two pathways: one a direct back pathway (i.e., from CA1 and the subiculum to the deep layers of EC; Tamamaki and Nojyo, 1995); and the other an indirect pathway. This indirect back pathway mainly originates in the subiculum (Sub) and reaches EC *via* PreS or parasubiculum (ParS; Caballero-Bleda and Witter, 1994). We have studied the major projections from layer III of PreS to the superficial layers of the medial entorhinal cortex (MEC) and found that the presubicular projections terminated in a band-like zonal area of MEC (Honda and Ishizuka, 2004). The transverse axes of these zones were disposed parallel to the rhinal fissure and their longitudinal axes were perpendicular to the boundary between MEC and the lateral entorhinal cortex (LEC). This finding raises the question of whether the terminal arborizations of each single entorhinal projection neuron in layer III of PreS constitutes such a band-like zone. However, little is known about the axonal branching patterns of each presubicular neuron (Honda et al., 2011). To address this, we visualized all axonal processes of single presubicular neurons in layer III, using *in vivo* injection of a virally expressed membrane-targeted palmitoylation site-attached green fluorescent protein (palGFP; Furuta et al., 2001). This vector is useful as a highly sensitive anterograde tracer for tracing long, finely arborized axonal branches (Kuramoto et al., 2009; Matsuda et al., 2009). Axonal tracing through many serial sections enabled identification of multiple types of single layer III neurons in rat PreS based on axonal morphology.

MATERIALS AND METHODS

The present experiments were approved by the Animal Care and Use Committee of Tokyo Women's Medical University, and all conformed to the Guidelines for the Care and Use of Laboratory Animals (National Institutes of Health, USA). We used eight adult male Wistar rats (280–305 g body weight; Clea Japan, Tokyo, Japan), with every effort made to minimize the number of animals used and the pain and distress of animals.

Constitution of Recombinant Sindbis Virus

The DNA construct containing the sequences for GFP tagged with a membrane-targeting palmitoylation site was inserted into the PmaCI site of pSinRep5 (Invitrogen, Carlsbad, CA, USA) as fully described by Furuta et al. (2001). The recombinant Sindbis virus, which was produced with the pSinRep5 containing the construct, was replication deficient and designed so that infected cells would express palGFP under the control of a powerful sub-genomic promoter of the virus.

Injection of Viral Vector

Rats were initially sedated with 5% isoflurane and a surgical level of anesthesia was maintained by intramuscular injection of a mixture of ketamine (60 mg/kg body weight) and xylazine (20 mg/kg body weight). Each animal was placed in a stereotaxic frame, and a hole was drilled in the skull at coordinates derived from the atlas of (Paxinos and Watson, 1998; **Table 1**). Between 2,000 and 4,000 infectious units (IU) of palGFP-expressing Sindbis virus vector (Furuta et al., 2001) in 0.5–1.0 μl of 5 mM phosphate-buffered saline (PBS; pH 7.4) containing 0.5%–2.0% bovine serum albumin was pressure-injected stereotactically into part of PreS through a glass micropipette attached to a Picospritzer II (General Valve, Fairfield, NJ, USA). All injections were performed unilaterally (left side).

Fixation and Cutting

After a survival period of 72 h, rats were re-anesthetized by intraperitoneal injection of sodium pentobarbital (80 mg/kg body weight) and perfused transcardially with physiological saline followed by 4% formaldehyde in 0.1 M phosphate buffer (PB; pH 7.4), and the brains were removed. Brains were cut into several blocks and post-fixed with the same fixative for 4–5 h at 4°C. We created an "extended" hippocampal formation (Ishizuka, 2001; Honda and Ishizuka, 2004; Honda et al., 2008) to facilitate analysis of the laminar and topographical distributions of labeled axonal arbors and terminal boutons. In brief, cerebral hemispheres were dissected free from the diencephalon and gently flattened in fixative to reduce the natural concavity of the hippocampal formation and parahippocampal areas (**Figure 1A**). After cryoprotection with 20% sucrose in PB, transverse sections of the flattened hemisphere, perpendicular to the "extended" septotemporal (longitudinal) axis of the hippocampal formation, were cut at a thickness of 50 μm using a freezing microtome.

Immunostaining for GFP

After confirming the presence of several GFP-expressing cells in sections containing PreS under a fluorescent microscope, all sections were immunostained with antibody against purified GFP. Sections were first incubated in PBS containing 0.1% hydrogen peroxide for 1 h at room temperature and washed in PBS. Sections were then incubated overnight at 4°C with anti-GFP antibody solution (1:500, A11120; Molecular Probes, Eugene, OR, USA; **Table 2**) containing 0.3% Triton X-100 and 1% normal donkey serum (NDS) in PBS. After rinses with PBS, sections were incubated in biotinylated anti-mouse IgG solution (1:100, AP192B; Millipore, Temecula, CA, USA; **Table 2**) containing 0.3% Triton X-100 and 1% NDS in PBS for 1 h at room temperature. Following a series of rinses with PBS, sections were incubated in avidin-biotin complex solution (Vectastain ABC Elite kit; Vector Laboratories, Burlingame, CA, USA). Sections were rinsed in PBS and placed in a solution of 0.05% 3,3′-diamininobenzidine-4HCl (DAB), 0.4% nickel (II) acetate, and 0.005% H_2O_2 in 50 mM Tris-HCl buffer (pH 7.6) for 30 min at room temperature. After several washes in Tris-buffered saline (TBS), all sections were serially mounted on gelatin-coated slides and counterstained with neutral red.

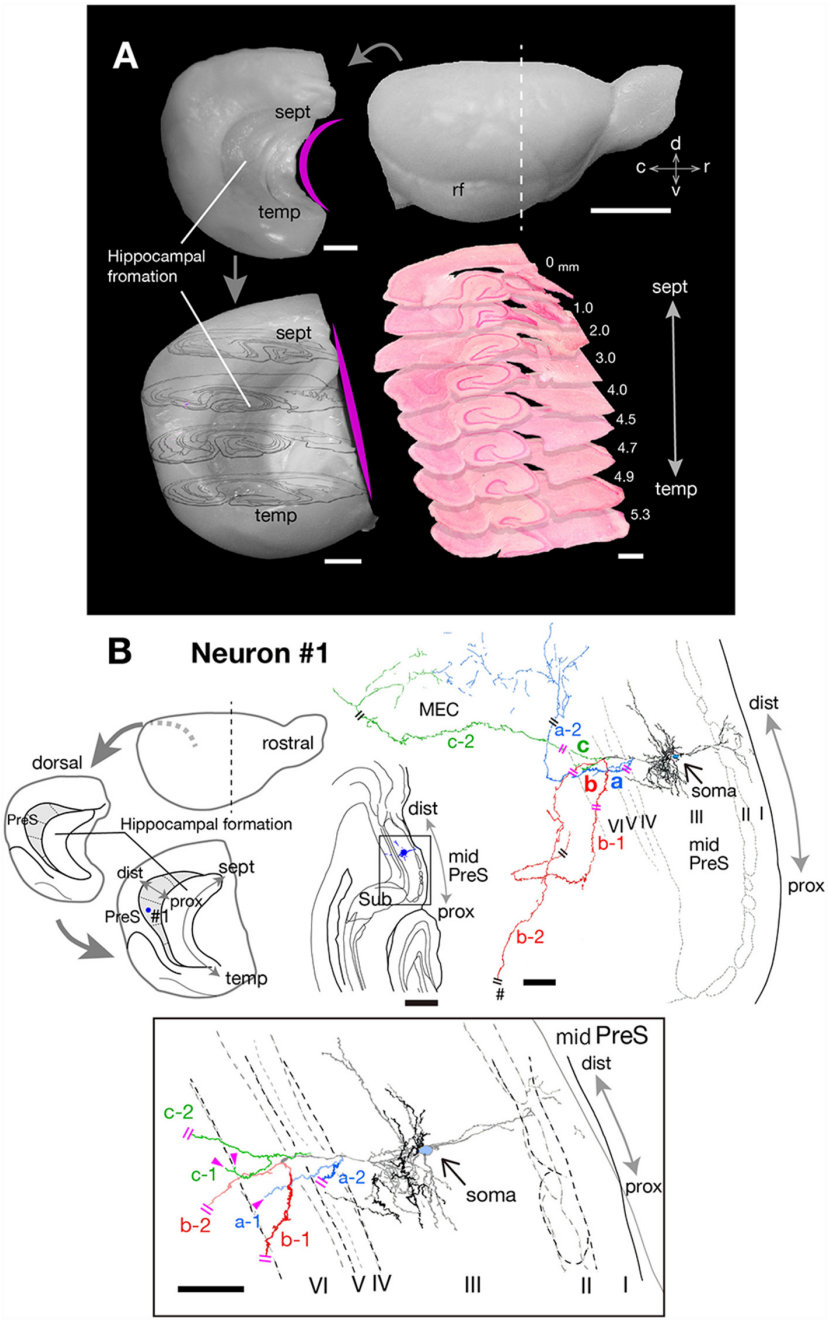

FIGURE 1 | (A) Explanatory diagrams of the preparation of extended hippocampus and the cutting plane perpendicular to the longitudinal (septotemporal) axis of the hippocampus. Upper right is the right-side view of a rat brain. The white dotted line indicates the first cutting-plane line, which cut-off the frontal brain block. Upper left is a curved left hemisphere, which is removed from the diencephalon. Lower left is a flattened left hemisphere, in which the longitudinal axis of the hippocampal formation is approximately linear and the drawings of four cutting planes are superimposed on it. Lower right is the superposition of nine transverse sections of the flattened left hemisphere, perpendicular to the longitudinal axis of the hippocampus. **(B)** Schematic diagrams of the extended hippocampus as shown in **(A)**. Shaded regions represent PreS and the septotemporal parcellation (see also **Figure 6**) is indicated by small dotted lines. The localization of cell body of neuron #1 is represented as a blue-colored circle. A drawing of the section which includes the cell body and several dendrites (upper middle) and camera lucida reconstruction of the axonal morphology (upper right) of neuron #1. The cell body is painted over in blue. Three main axonal branches a, b and c and their collaterals are represented by blue, red and green, respectively. Dendrites and the main axon that comes directly out of the cell body are colored in black. The lower enclosed figure is a superposition of a drawing of five sections around the cell body of neuron #1 and arrowheads filled in magenta indicate the points of axonal endings of branches a-1 and c-1 in layer VI of PreS near the level of the cell body. Short double lines (magenta) indicate that the axon continues further, and a pound sign indicates an axonal branch entering the dorsal hippocampal commissure. Short double lines (magenta) on the axonal arbors of the whole drawing of neuron #1 indicate the same position as that of the enclosed figure. Scale bars = 5 mm in the upper right and 1 mm in the other photomicrographs of **(A)**, and 500 μm in the upper-middle and 100 μm in the upper-right and lower enclosed diagrams in **(B)**.

TABLE 1 | The location of cell bodies and number of main axon collaterals to the termination areas or layers from each layer III neuron of PreS.

Cell No. (Rat No.)	†	Location of cell body			Neuron Type	Number of labeled axonal arbors											
		sept-temp	prox-dist	depth		PreS (layer)						Sub	MEC		ParS (sup/ deep)	cc, dhc	fim
						II	III			V	VI		I–III	V–VI			
							sup	m	deep								
#5 (41)	a	sept	m	sup	np	2	6	4	0	1	2	1	0	0	0	0	0
#8 (81)	a	m-sept	m	m	p	0	4	12	4	0	1	0	0	0	0	0	0
#4 (41)	a	m-sept	prox	m	p	0	0	2	0	0	4	8	0	1	0	1	0
#11 (72)	a	m-sept	dist	m	p	0	0	6	2	0	0	0	0	0	0	0	0
#9 (36)	c	m	prox	sup	np	2	6	5	5	1	0	0	0	0	0	0	0
#1 (18)	a	m	m	m	p	0	0	0	0	0	2	0	*	0	0	2	0
#3 (41)	a	m	m	deep	p	7	1	1	4	0	21	3	5	1	0	2	1
#10 (27)	b	m	dist	sup	np	3	12	0	4	0	0	0	0	0	0	0	0
#7 (19)	a	m	dist	m	np	3	2	3	19	6	4	0	0	0	0	0	0
#6 (19)	a	m	dist	m	p	0	0	1	1	*	1	0	0	0	17 (9/8)	0	0
#12 (81)	b	m	dist	deep	np	0	0	0	3	2	0	0	0	0	0	0	0
#2 (28)	c	m-temp	m	sup	p	0	3	2	0	0	1	0	*	0	0	0	0

**Making terminal plexus, m, middle; np, non-pyramidal; p, pyramidal; sup, superficial. †Coordination of the injection site: a = AP-7.3, ML-3.2, D+3.4, b = AP-7.2, ML-4.1, D+4.8, c = AP-7.32, ML-4.1, D+4.8. The density patterns of shading indicate the approximate quantity of axonal arbors*

TABLE 2 | Antibodies used in this study.

Name	Host species	Clonality (Clone ID)	Source, Cat. #, RRID	Concentration used
Mouse anti-green fluorescent protein (GFP)	mouse	Monoclonal antibody (3E6)	Molecular Probes, A-11120, RRID:AB_221568	1:500
Donkey anti-mouse IgG, biotin-conjugated	donkey	Polyclonal antibody	Millipore, AP192B, RRID:AB_92624	1:100

Sections were then dehydrated in an ethanol series, cleared with xylene, and coverslipped.

Reconstruction and Imaging of Labeled Neurons

Axons and dendrites of labeled neurons were first traced under an Eclipse 80i microscope (Nikon, Tokyo, Japan) attached with a camera lucida apparatus (at ×40 magnification). In the process of neuronal tracing, we labeled the axonal arbor by painting with several colors to identify each axonal branch originating from a single cell body. When there were any inexact points of joining and tracing fragments of axonal fibers, such as in cases where the target axonal branch was indistinguishable from other overlapping processes, we excluded these fibers from our dataset. Some neurons were also mapped and reconstructed using a computer-assisted microscope system and data analysis program (Neurolucida™; MicroBrightField, Colchester, VT, USA; at ×100 magnification). Shrinkage of section thicknesses was corrected along the z (depth) axis by Neurolucida™. In addition, two-dimensional unfolded maps were prepared as previously described (Honda and Ishizuka, 2004). Digital photomicrographs were taken using a LINCE™ (Claro, Aomori, Japan) with the extended focus application. The number of focus levels was 25, and the focus step size was 5 μm. Captured digital images were trimmed and adjusted to obtain optimal resolution, brightness, and contrast in Adobe Photoshop™ software (Adobe Systems, San Jose, CA, USA).

NOMENCLATURE

We have used the terms "septal-temporal" and "dorsal-ventral" interchangeably to represent the longitudinal direction of PreS (for details, see Ishizuka, 2001). We have also used the term "proximal-distal" to represent the transverse direction of PreS and EC instead of "anterior-posterior" and/or "medial-lateral." In PreS, the term "proximal" means near Sub, whereas "distal" means distant from Sub. In EC, the term "proximal" means near ParS, whereas "distal" means near the rhinal fissure. The cutting plane and XY-direction of all traced images and photomicrographs in our figures were substantially the same. The so-called "postsubiculum" is treated as the septal part of PreS, on the basis of the strong similarities in connectivity and cytoarchitecture between the septal and temporal parts of PreS (Honda and Ishizuka, 2004; Honda et al., 2008). For purposes of description, we divided PreS into five portions along the septotemporal axis (septal, mid-septal, middle, mid-temporal, temporal), each about 1 mm long. According to this compartmentalization, PreS, septal PreS, mid-septal PreS, and the septal part of mid-PreS seem to correspond to the postsubiculum.

RESULTS

The cell bodies of infected neurons were diffusely distributed with sufficient distance between each other within a radius of about 1 mm from the center of injection. Consequently, we could reconstruct the whole shape of axonal processes originated from multiple virus-infected neurons within the same hemisphere of the same animal. In the present study, 54 presubicular neurons (including layers II–VI of PreS) were visualized in all animals of **Table 1**, of which 37 neurons (68.5%) were successfully reconstructed. In detail, 100% in layer II (4 neurons reconstructed/4 neurons visualized), 70.5% in layer III (12/17), 47.6% in layer V (10/21), and 100% in layer VI (8/8). The shortest distance between nearby virus-infected neurons was approximately 50 μm and the longest distance was 900 μm along the proximodistal or septotemporal axes of PreS. Twelve single layer-III presubicular neurons with labeled axons were successfully reconstructed in eight hemispheres ipsilateral to the injection site (**Table 1**). Six of the 12 neurons (including both pyramidal and non-pyramidal neurons) were cortical projection neurons that sent axons to MEC and/or Sub, or to ParS. The other six neurons were intrinsic projection-type neurons that sent many recurrent fibers to several layers of PreS but did not send efferents to other cortical areas.

Cortical Projection Neurons

Within the six cortical projection neurons, two sent fibers only to MEC (neurons #1 and #2; **Figures 1–6**) and another two sent axon collaterals to both MEC and Sub (neurons #3 and #4; **Figures 7**, **8**). One of the remaining two neurons projected only to Sub (neuron #5; **Figure 9**), and the other provided numerous branches only to ParS (neuron #6; **Figure 10**). All neurons had two or more recurrent collaterals, which terminated in one or more layers of PreS (**Table 1**).

MEC Projection Neurons

Neuron #1 was a pyramidal neuron with the cell body located at the middle depth of layer III of the mid-proximodistal part of mid-PreS (**Figures 1B**, **6A**). This neuron gave off three major axonal branches (a, b and c in **Figure 1B**), with their three collaterals (a-2, b-1 and c-2 in **Figures 1B**, **2**, **3**) reaching layers II and III of MEC. As seen in **Figure 2**, different patterns of termination were seen in MEC, i.e., branches a-2 and c-2 provided complex terminal arborizations with many en passant boutons, while branch b-1 showed no terminal arborizations in layer III of MEC. While ascending in layer III of MEC, branch b-1 formed several en passant boutons (not shown). Both branches a-2 and c-2 formed elaborate terminal arbors that seemed to face each other, while their terminal distributions rarely overlapped within layer III of MEC (**Figures 3B,D**). To clarify the positional relationship between the soma and axon terminals, we created representations of these structures on an unfolded map of the entire PreS and EC. The area of termination of neuron #1 showed a band-like pattern, with the transverse axis disposed parallel to the rhinal fissure and the longitudinal axis perpendicular to the boundary between MEC and LEC (**Figure 6A**). This band-like field was about 0.5 mm in width and located in the distalmost region of MEC. A small cluster of terminals was seen at the more proximal part of MEC, corresponding to terminals derived from branch b-1. From branch b, an additional axonal branch entered the dorsal hippocampal commissure (b-2 in **Figures 1B**, **3**). Both branches a and c showed a short recurrent collateral, which reached layer

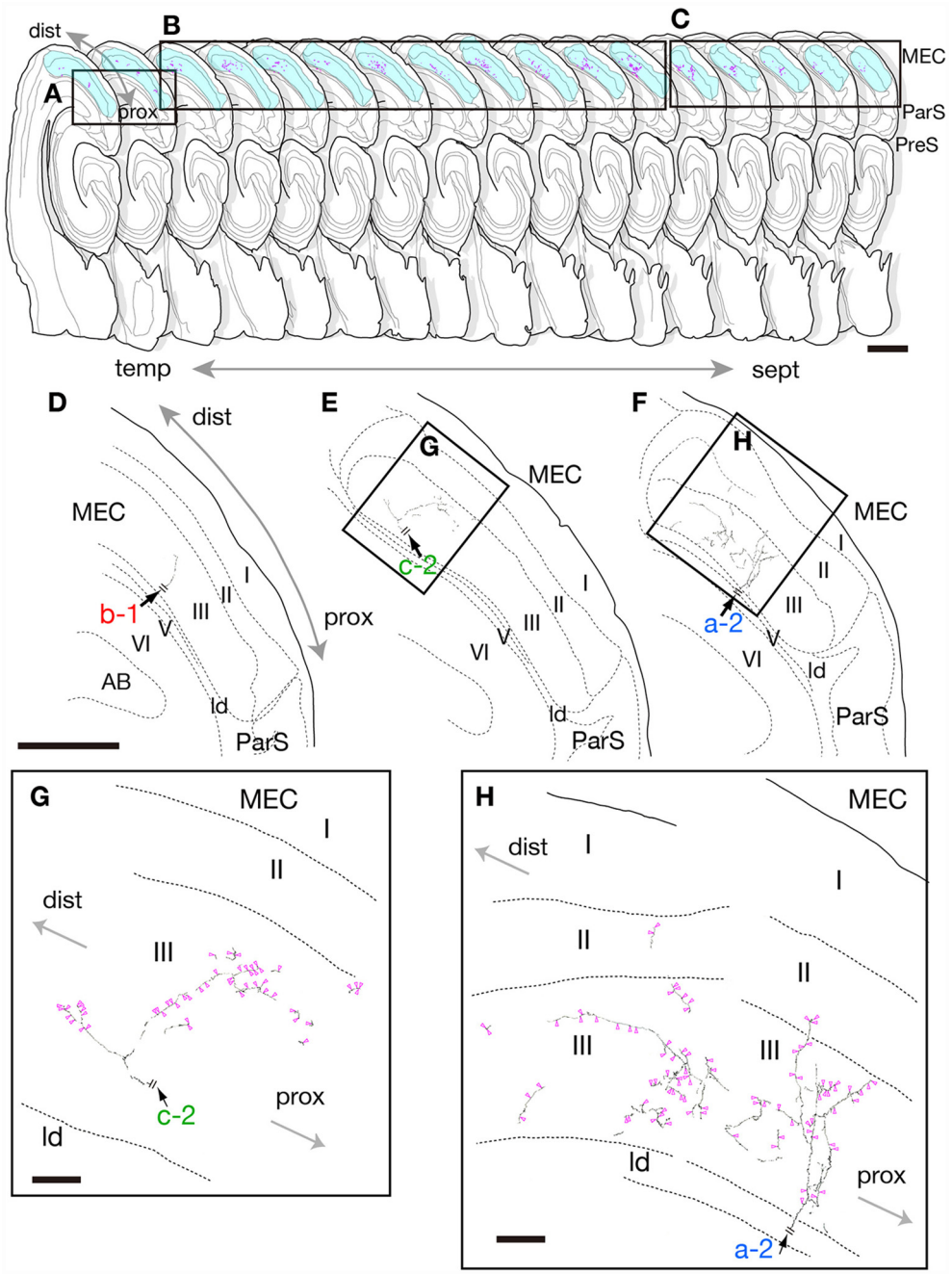

FIGURE 2 | Drawing of 17 serial sections of the same hemisphere as neuron #1 are aligned in septotemporal order (upper) and camera lucida reconstruction of the terminal domain of each of axonal branches a-2, b-1 and c-2 in medial entorhinal cortex (MEC; middle and lower). Each axon is a continuation of the branches in **Figure 1B**. Short double lines (black) indicate the same position as in the whole drawing of neuron #1 in **Figure 1B**. Panels **(D–F)** are superpositions of drawings from two, 10 and five sections, i.e., **(A–C)**, respectively, as area arranged from temporal **(D)** to septal **(F)** levels. Higher-powered magnification of the rectangles in **(E,F)** are indicated as **(G,H)**, respectively. Panels **(G,H)** are superpositions of the drawing of five or seven sections using a ×100 objective lens. Magenta-open arrowheads indicate the position of identifiable axonal boutons. Scale bars = 1 mm in the upper row, 500 μm in the middle row **(D–F)** and 50 μm in **(G,H)**.

VI of PreS near the cell body (a-1 and c-1 in **Figures 1B**, **3A**) and they formed small terminal boutons on branch endings (not shown).

Neuron #2 was an atypical pyramidal neuron (**Figure 4A**), with an apical dendrite (arrow in **Figure 5D**) directed more temporally to the cell body and giving off branches approximately parallel to the plane perpendicular to the septotemporal axis of PreS. The soma was located at the superficial part of layer III in the mid-proximodistal portion of the mid-temporal PreS (**Figures 4A**, **6B**). An axon emanating

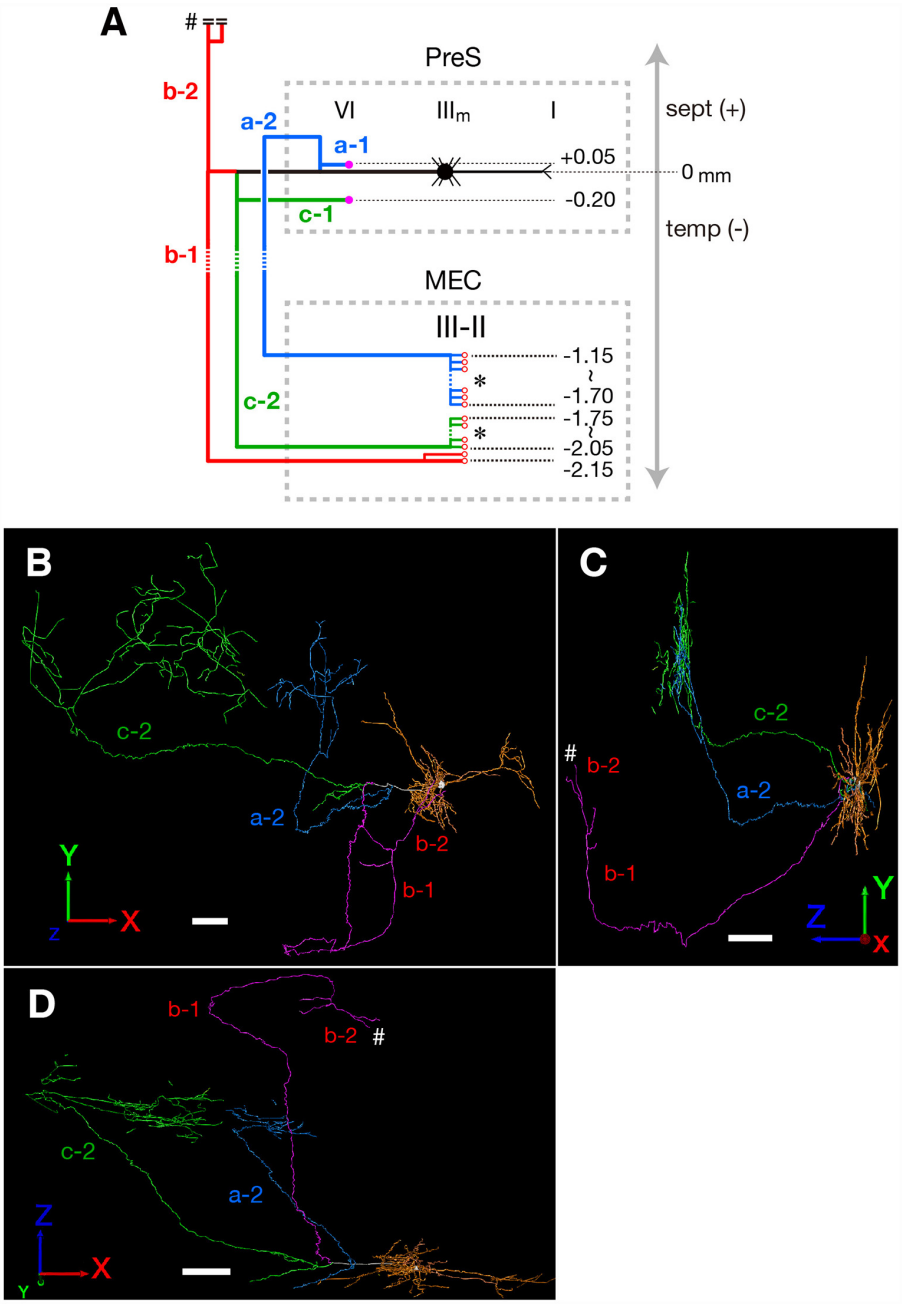

FIGURE 3 | (A) Schematic diagram of the axonal branching pattern for neuron #1. The main axon that comes directly out of the cell body is colored in black, and the other axonal branches are represented using the same colors as in **Figure 1B**. The dendrites and cell body are represented schematically as thin black lines and a black filled circle. Small red-open circles indicate terminal levels of axonal branches within layers II–III of MEC and asterisks near those terminals indicate the existence of complex terminal arborizations that form the plexus. Numbers indicate the septotemporal levels of terminations for each axon collateral when the level of cell body is set as the zero-point. Short double lines and a pound sign at the upper end of branch b-2 indicate that the nerve continues farther through the dorsal hippocampal commissure. Dotted rectangles indicate areas of PreS and MEC. IIIm in PreS represents the middle depth of layer III of PreS. The level of each axonal branching point is not necessarily accurate. **(B–D)** Images of 3D-reconstructed neuron #1 are indicated; a frontal view from the z-axial direction **(B)**, a view of the right side from the x-axial direction **(C)** and a view of the bottom from the y axial direction **(D)**. The z-axis corresponds to septal and temporal (longitudinal axis of the hippocampal formation). In PreS, the x-axis corresponds to superficial and deep, and the y-axis to proximal (near Sub) and distal. In EC, the x axis corresponds to proximal (near ParS) and distal (near rhinal fissure), and the y-axis to superficial and deep. The cell body is represented as a white circle and the dendrites are colored as orange. The main axon that comes directly out of the cell body is colored in white, and the other axonal branches are represented using the same colors as in **Figure 1B**. White pound signs at the end of branch b-2 in **(C,D)** indicate that the branch enters into the dorsal hippocampal commissure and continues farther. In comparison with **Figure 1B**, higher magnification is used in the 3D-reconstruction and the number and volume of terminal arbors appear to be increasing in (**B–D**; see "Materials and Methods" section). Scale bars = 100 μm in **(B–D)**.

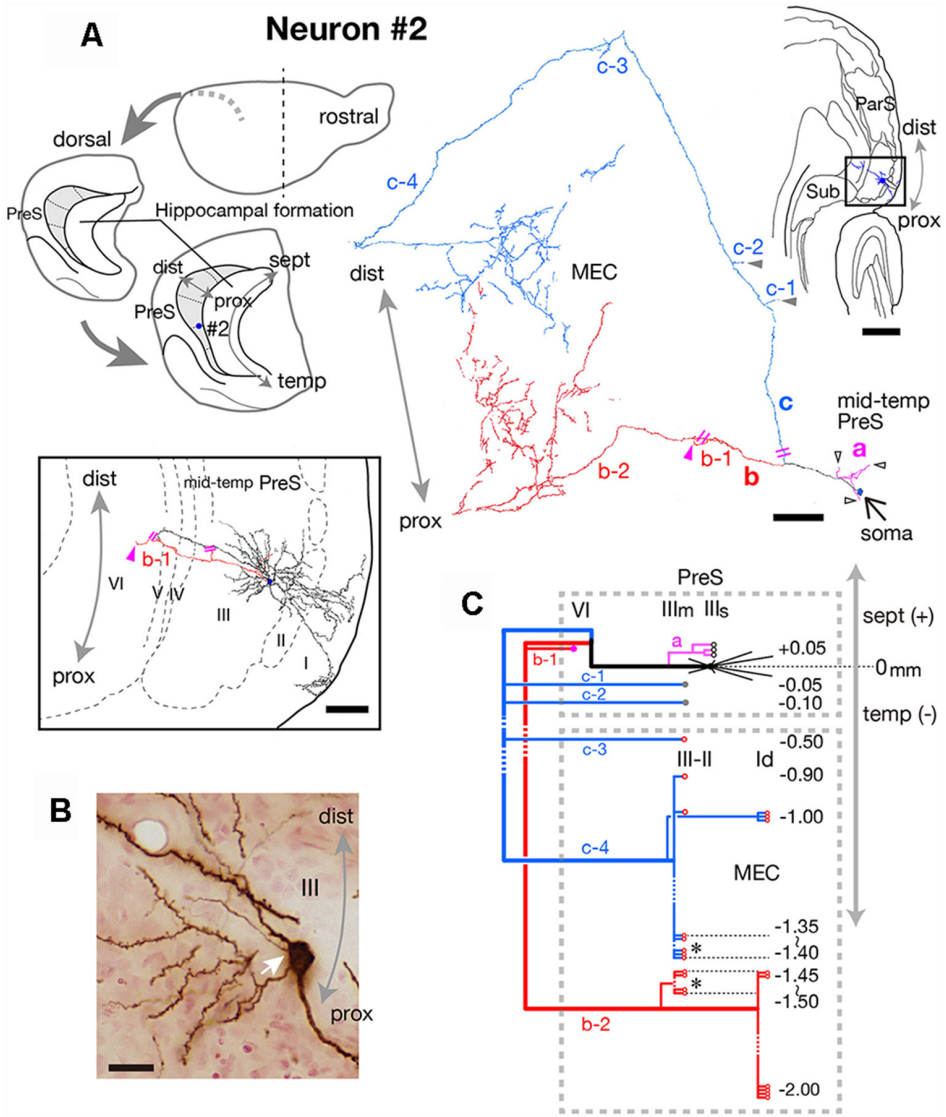

FIGURE 4 | (A) Schematic diagrams of the extended hippocampus as shown in **Figure 1A** (upper left). The localization of cell body of neuron #2 is represented as a blue-colored circle. A drawing of the section that includes the cell body and several dendrites (upper right) and camera lucida reconstruction of axonal morphology (upper middle) of neuron #2. The cell body is painted over in blue. The three main axonal branches a, b and c and their collaterals are represented by magenta, red and blue, respectively. The main axons that come directly out of the cell body are colored in black. The black-open, gray and magenta arrowheads indicate points of axonal endings in the superficial part of layer III, middle part of layer III, and layer VI of PreS, respectively. Indications of axonal ending points in MEC are omitted from this drawing. The lower enclosed figure is a superposition of a drawing of sections around the cell body of neuron #2 and arrowheads filled in magenta indicate the points of axonal endings of branch b-1 in layer VI of PreS near the level of the cell body. Short double lines (magenta) indicate that the axon continues further. Short double lines (magenta) on the axonal arbors of the whole drawing of neuron #2 indicate the same position as that of the enclosed figure. **(B)** Composite photomicrograph of the cell body and proximal parts of its processes taken by stacking different focal planes. White arrow indicates the point of origin of the main axon, which comes directly out of the cell body. **(C)** Schematic diagram of the axonal branching pattern of neuron #2. The axonal branches are represented using the same colors as in **(A)**. Black-open, gray and magenta circles indicate terminal levels of axonal branches within the superficial part of layer III, middle part of layer III and layer VI of PreS, respectively. Red-open circles indicate terminal levels of axonal branches within the superficial layers of MEC. Asterisks near those terminals indicate the existence of complex terminal arborizations that form a plexus. Numbers indicate septotemporal levels of terminations for each axon collateral when the level of the cell body is set as the zero-point. IIIs and IIIm in PreS represent the superficial and middle depths of layer III of PreS. The level of each axonal branching point is not necessarily accurate. Scale bars = 500 μm in the upper-right and 100 μm in the middle and lower enclosed diagrams in **(A)**, and 20 μm in **(B)**.

directly from the cell body (white arrow in **Figure 4B**) sent a short recurrent collateral to the superficial part of PreS near the cell body (branch a in **Figures 4A,C**), then bifurcated into two major axonal branches b and c toward the superficial layers of MEC (**Figures 4A,C**). After providing a recurrent collateral b-1 to layer VI of PreS, which formed several en passant boutons within layer VI (not shown), branch b-2 ran into layer VI of MEC, then vertically ascended to the superficial

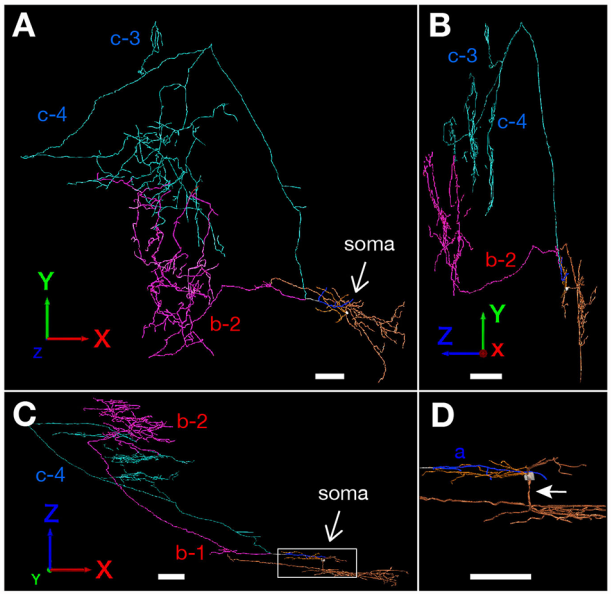

FIGURE 5 | The 3D-reconstructed images of neuron #2 are indicated: a frontal view from the z-axial direction **(A)**; a view of the right side from the x-axial direction **(B)**; and a view of the bottom from the y-axial direction **(C)**. The cell body and main axon that comes directly out of the cell body are colored in white, and the three main axonal branches a, b and c and their collaterals are represented by blue, magenta and pale blue, respectively. Dendrites are colored as orange. **(D)** High magnification of the rectangle in **(C)**. White arrow indicates a shaft of apical dendrite. Scale bars = 100 μm in **(A–D)**.

layers to form a complex terminal arborization within layer III (**Figures 4A,C**, **5**). Branch c had two recurrent collaterals, c-1 and c-2, both terminating in the middle part of layer III of PreS. One collateral (c-3) ran through the lamina dissecans of MEC and terminated in layer III of MEC without any complex terminal arborizations (**Figures 4A,C**, **5**). On the other hand, branch c-4 arborized extensively within the superficial layers through almost 0.5 mm along the septotemporal axis of MEC (**Figure 4C**) and formed a complex terminal arborization at the level adjoining the b-2 axon terminal ramification (asterisks in **Figure 4C**). Similar to neuron #1, plexuses of the b-2 and c-4 terminal arborizations expanded along the proximodistal axis and seemed to face each other within the superficial layers of MEC, while the terminal distributions rarely overlapped (**Figures 4A**, **5**). Both branches b-2 and c-4 sent one axon collateral to the deep part of layer I of MEC that reached levels separate from the terminal arborizations in layers II–III (**Figure 4C**). As seen in the unfolded map (**Figure 6B**), axon terminals in layer III of MEC distributed in a band-like fashion similar to the terminal distribution pattern of neuron #1 (**Figure 6A**). Compared with neuron #1, the band-like terminal region of neuron #2 was located more proximally in MEC (**Figures 6A,B**), probably because the cell body of neuron #2 was situated at a more temporal level of PreS than the cell body of neuron #1 (**Figure 6C**). No commissural axonal branches ascending in the white matter could be found for neuron #2.

In conclusion, neuron #1 was a pyramidal neuron, and neuron #2 was an atypical pyramidal neuron, both had two axonal branches which formed a complex terminal arborization within the superficial layers of MEC.

MEC/Sub Projection Neurons

Neuron #3 was a spiny pyramidal neuron, and the locus of the cell body was in the deep part of layer III in the mid-proximodistal portion of mid-PreS (**Figure 7A**). This neuron provided four types of axonal branches, classified by the terminal regions. The first group comprised branches that had several short recurrent collaterals terminating in layers III or VI of PreS (magenta branches in **Figures 7A,B**), and the second consisted of axonal branches reaching layer III of MEC and also supplying several recurrent collaterals to layer VI of PreS (green branches in **Figures 7A,B**). The third group represented branches bifurcating into collaterals projecting to layer VI of MEC and to the contralateral hemisphere through the corpus callosum (red branches in **Figures 7A,B**), and also showing two short recurrent collaterals terminating in layer VI of PreS. The last group comprised branches reaching the pyramidal cell layer of Sub (blue, pale blue and purple branches in **Figures 7A,B**), which provided many recurrent collaterals to layers II, III and VI of PreS. The complex terminal arborizations within the superficial layers of the proximal (near Sub) part of PreS derived from a single axonal branch that also provided collaterals to layer VI of PreS and to Sub (pale blue branches in **Figures 7A,B**). Interestingly, terminations of the three axonal branches within Sub distributed at similar intervals of 0.25–0.3 mm along the septotemporal axis (**Figure 7B**). Moreover, one such branch bifurcated into collaterals to the contralateral hemisphere through the corpus callosum and to subcortical areas *via* the fimbria-fornix (pound sign and double pound sign on pale blue branches in **Figures 7A,B**). All axonal arbors which terminated in layer VI of PreS and MEC formed small terminal boutons in their target layer. As seen in the unfolded map (**Figure 7C**), the proximodistal range of the terminal distribution was about 500 μm, similar to the band-like terminal regions of neurons #1 and #2 (as shown in **Figure 6**), but the septotemporal length was significantly shorter than those of neurons #1 and #2.

Neuron #4 was an atypical pyramidal cell with a curved apical dendrite that ran obliquely across layer I and reached the pial surface (**Figure 8A**). Dendritic spines were relatively sparse (**Figure 8B**). The cell body was located at the middle depth of layer III of the proximal portion of the mid-septal PreS (**Figures 7A,C**), and provided many axonal arbors to Sub (**Figure 8C**). Four major branches (magenta, green, blue and pale blue branches in **Figures 8A,C**) were sent out from the main axonal shaft (white arrow in **Figure 8B**), each showing collaterals that terminated in the pyramidal cell layer of Sub. One of the major branches (pale blue branch in **Figure 8C**) ascended to the septal levels and bifurcated into recurrent collaterals to layers III and VI of PreS and a commissural axonal branch, which entered the dorsal hippocampal commissure (pound signs in **Figures 8A,C**). A descending axonal arbor (green branch in **Figures 8A,C**) was also present, sending collaterals to both

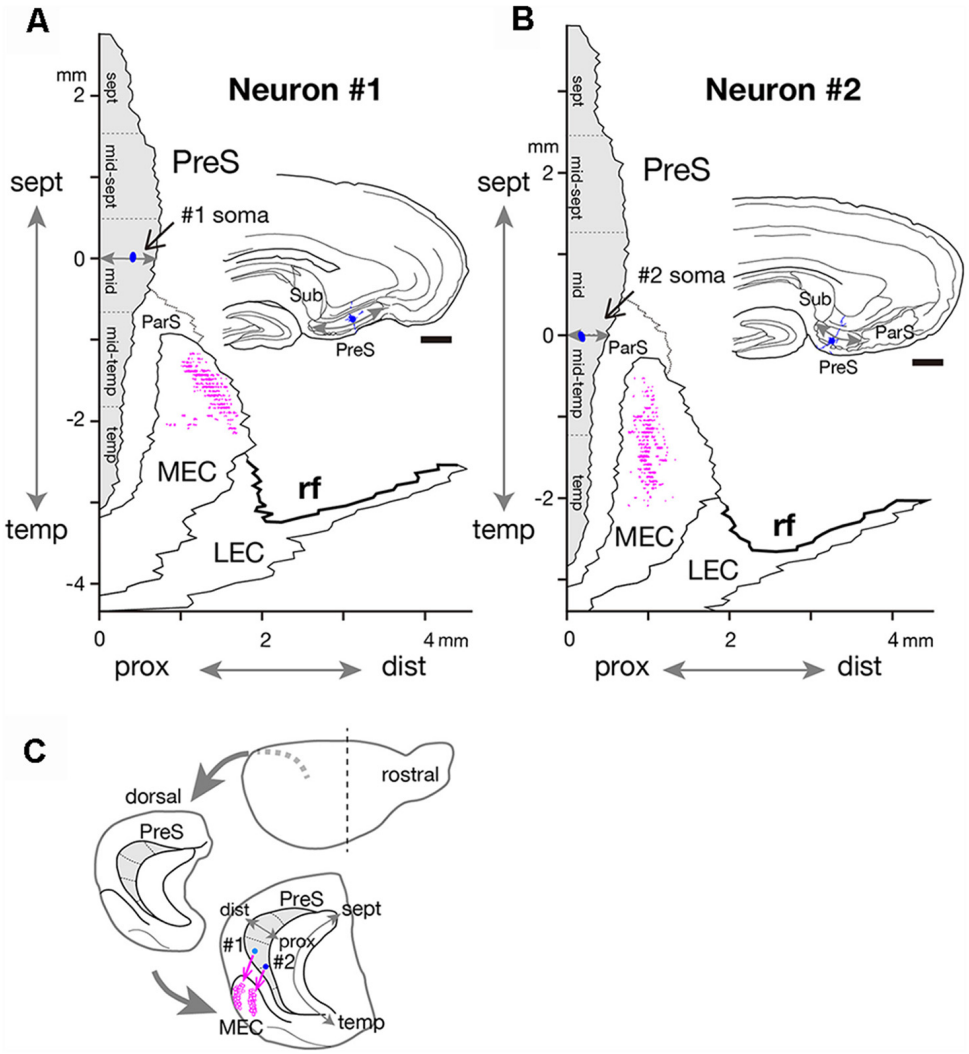

FIGURE 6 | Two-dimensional unfolded maps of layer III of PreS and MEC with surrounding areas, showing the locations of the cell body (blue filled circles) and axon terminals (magenta dots) of neurons #1 **(A)** and #2 **(B)**. The vertical axis of the map indicates the distance from the septotemporal level of the cell body, and the horizontal axis indicates the distance from the proximal end of PreS. For details, see Honda and Ishizuka (2004) and Honda et al. (2008). Drawings of the sections for neurons #1 and #2, which include the cell body (blue circle) and several dendrites (blue short lines) are inserted in each unfolded map. A gray double arrow in each drawing indicates the proximodistal length of PreS. **(C)** Schematic diagrams of the extended hippocampus as shown in **Figure 1A**. The location of cell body in PreS is represented as light blue- (neuron #1) and blue- (neuron #2) colored circles and the terminal distribution in layers II–III of MEC are schematically shown by magenta-open circles. Scale bars = 500 μm in **(A,B)**.

layer V of MEC and the pyramidal cell layer of Sub (red and purple branches in **Figures 8A,C**), in addition to three recurrent collaterals to layer VI of PreS. All axonal arbors which terminated in the deep layers of PreS and MEC formed small terminal boutons in their target layers.

Taken together, two distinct types of MEC/Sub projection neurons were observed; neuron #3 was a spiny pyramidal neuron, which had both commissural and subcortical projection fibers and also provided many recurrent collaterals to various layers of PreS, while neuron #4 was an atypical pyramidal neuron, which had relatively sparse recurrent collaterals and provided more axonal arbors to Sub than to MEC.

Subicular Projection Neuron

As seen in **Figure 9**, neuron #5 was a subicular projection neuron, which had only one axonal arbor to Sub. The spindle-shaped cell body (white arrow in **Figure 9B**) was located in the superficial part of layer III of the mid-proximodistal portion of the septal PreS (**Figures 7A,C**). The form of dendritic arborization extended widely to the more temporal levels for about 0.5 mm along the septotemporal axis (not shown) within layers I–III of PreS (**Figure 9A**). Many of the axonal collaterals projected to levels more septal than the cell body. One of the main branches showed a collateral that terminated in layer V of PreS at a level 0.35 mm more septal than the cell body,

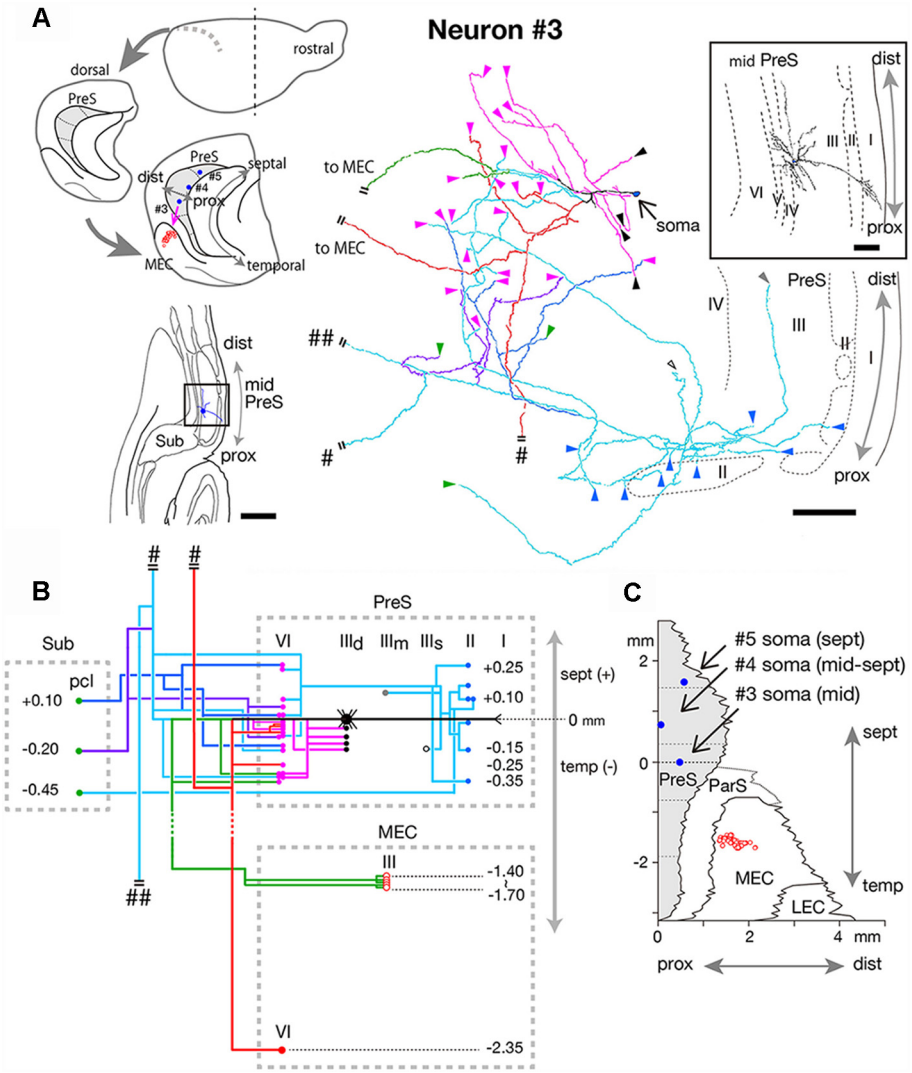

FIGURE 7 | (A) Schematic diagrams of the extended hippocampus as shown in **Figure 1A** (upper left). The locations of cell body of neurons #3, #4, and #5 in PreS are schematically represented as blue-colored circles. The terminal distribution in layers II–III of MEC originated from neuron #3 is schematically shown by red-open circles. Lower left is a drawing of the section of neuron #3, which includes the cell body and several dendrites. Camera lucida reconstruction of axonal morphology of neuron #3 (middle). The enclosed figure is a superposition of drawings of the soma and dendrites. The cell body is painted over in blue. The main axonal branches and their collaterals are represented by magenta, red, green and pale blue. One of the collaterals from the pale blue branch is colored in blue and the other in purple. Short double lines indicate that the axon continues farther. The points of axonal endings in layer II of PreS are indicated as blue arrowheads. Axonal endings in the superficial, middle and deep depths of layer III of PreS are indicated as open, gray and black arrowheads, respectively. Magenta arrowheads indicate points of endings in layer VI of PreS. **(B)** Schematic diagram of the axonal branching pattern of neuron #3. The axonal branches are represented using the same colors as in **(A)**. Blue, black-open, gray, black and magenta circles indicate terminal levels of axonal branches within the superficial, middle, and deep parts of layer III and layer VI of PreS, respectively. Red-open and red-colored circles indicate terminal levels of axonal branches within layers III and VI of MEC, respectively. IIId in PreS represents the deep part of layer III of PreS. The level of each axonal branching point is not necessarily accurate. Short double lines indicate that the axon continues farther. Single and double pound signs in **(A,B)** indicate that the axonal branches run into the corpus callosum and fimbria/fornix, respectively. **(C)** Two-dimensional unfolded map of layer III of PreS (shaded region), ParS and EC, showing the locations of the cell body (blue filled circles) of neurons #3, #4, and #5 and axon terminals (red-open circles) of the green branch of neuron #3 in layer III of MEC. Scale bars = 500 μm in the lower-left and 100 μm in the right and enclosed diagrams in **(A)**.

while many shorter recurrent collaterals terminated within the superficial part of layer III (magenta branches in **Figures 9A,C**). Branches were seen specifically projecting to layer II (yellow branch in **Figures 9A,C**) or layer VI (pale blue branch in **Figures 9A,C**) of PreS, and the latter bifurcated into an axonal arbor reaching to Sub at a level 0.55 mm more septal than the cell body (green branch in **Figures 9A,C**). All remaining branches innervated the middle depth of layer III of PreS (blue branches in **Figures 9A,C**).

In summary, neuron #5 was a fusiform cell, which provided one axon collateral to Sub in addition to many recurrent collaterals to PreS itself.

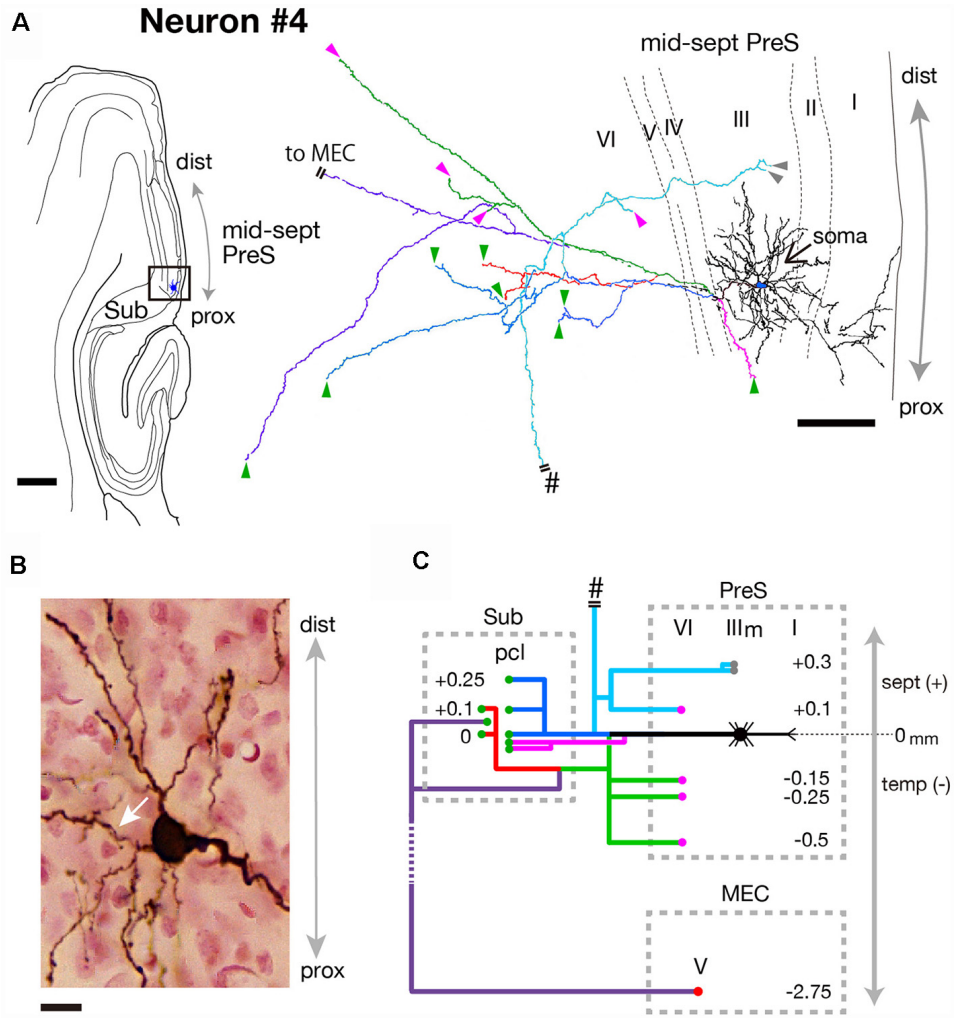

FIGURE 8 | (A) A drawing of the section which includes the cell body and several dendrites (left) and camera lucida reconstruction of the axonal morphology of neuron #4 (right). The cell body is painted over in blue. The main axonal branches and their collaterals are represented by blue, magenta and green. One of the collaterals from the blue branch is colored in pale blue and two branches from green are colored in red and purple. Short double lines indicate that the axon continues farther. The points of axonal endings at the middle depth of layer III of PreS and in layer VI of PreS are indicated as gray and magenta arrowheads, respectively. Axonal endings in the pyramidal cell layer of Sub are indicated as green arrowheads. **(B)** Composite photomicrograph of the cell body and proximal parts of its processes taken by stacking different focal planes. A white arrow indicates the main axon. **(C)** Schematic diagram of the axonal branching pattern for neuron #4. The main axon is colored in black, and the other axonal branches are represented using the same colors as in **(A)**. Gray- and magenta-colored circles indicate terminal levels of axonal branches within the middle part of layer III and layer VI of PreS, respectively. Green- and red-colored circles indicate terminal levels of axonal branches within the pyramidal cell layer of Sub and layer V of MEC, respectively. The level of each axonal branching point is not necessarily accurate. Short double lines indicate that the axon continues farther. Pound signs in **(A,C)** indicate that the axonal branches run into the corpus callosum. Scale bars = 500 μm in the left and 100 μm in the right in **(A)** and 10 μm in **(B)**.

Parasubicular Projection Neuron

At the level of mid-PreS, an elongated region was seen that seemed to be the septal-most part of ParS. Our previous study also confirmed that this region was not included in the intrinsic connectivity of PreS (Honda et al., 2008). The fusiform-shaped cell body of neuron #6 was located at the middle depth of layer III of the distal portion of mid-PreS and provided many axonal collaterals specifically to the septal-most part of ParS (**Figure 10A**). Ascending dendritic arbors were spiny and reached to layers I and II/III of ParS, and the descending dendrites reached to layer III of the distal part of PreS. This neuron seemed to be a bitufted type, as defined by the form of dendritic arborization, while the axonal arbors extended horizontally from the distal edge of PreS to several layers of the proximal part of ParS. We plotted precise localizations of soma and the axon terminals (purple-open arrowheads in **Figure 10A** and purple-open circles in **Figure 10C**) of neuron #6 on the unfolded map as shown in **Figure 10B**. The termination of the blue, pale blue and green axons of neuron #6 (**Figures 10A,C**) was localized in the proximal region of the septal-most part of ParS (**Figure 10B**). The main axonal shaft branched into two major collaterals (blue and green branches in

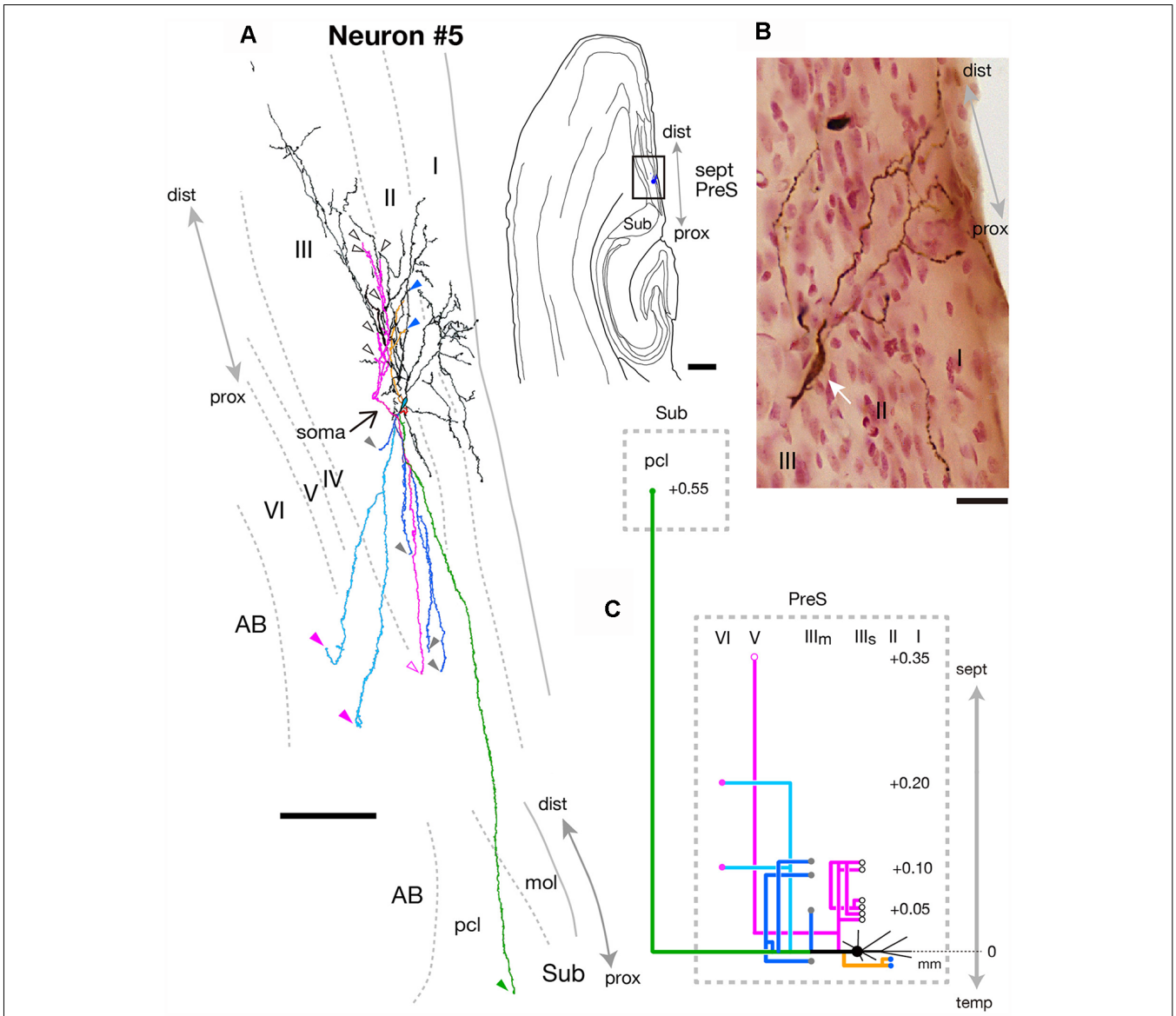

FIGURE 9 | (A) A drawing of the section which includes the cell body and several dendrites (right) and camera lucida reconstruction of axonal morphology of neuron #5 (left). Dendrites and the main axon are colored in black. The main axonal branches and their collaterals are represented by orange, magenta and green. One of the collaterals from the green branch is colored in pale blue and three branches from the green branch are colored in blue. Points of axonal endings in layer II, the superficial and middle depths of layer III, layer V and layer VI of PreS are indicated as blue, white-open, gray, magenta-open and magenta arrowheads, respectively. The point of axonal ending in the pyramidal cell layer of Sub is indicated as a green arrowhead. **(B)** Composite photomicrograph of the cell body and proximal parts of its processes taken by stacking different focal planes. White arrow indicates the spindle-shaped cell body. **(C)** Schematic diagram of the axonal branching pattern for neuron #5. The axonal branches are represented using the same colors as in **(A)**. Blue, white-open, gray, magenta-open and magenta circles indicate terminal levels of axonal branches within layer II, the superficial and middle parts of layer III, layer V and layer VI of PreS, respectively. A green circle indicates the terminal level of axonal branches within the pyramidal cell layer of Sub. The level of each axonal branching point is not necessarily accurate. Scale bars = 500 μm in the right and 100 μm in the left in **(A)** and 20 μm in **(B)**.

Figures 10A,C), which mostly innervated ParS and also provided one major collateral for intrinsic projection (magenta branch in **Figures 10A,C**). From one of the two major collaterals to ParS (blue branch in **Figures 10A,C**), two branches bifurcated, each specifically terminating in the superficial layers (layers II/III) or deep layers (mostly layers IV–V, including lamina dissecans) of ParS. This major branch also displayed several short recurrents to layers III and V near the level of the cell body (pale blue branches in **Figures 10A,C**). A major axonal branch for intrinsic connection (magenta branch in **Figures 10A,C**) bifurcated into two collaterals, one of which terminated in the deep part of layer III while the other descended for about 0.2 mm temporal from the cell body, then formed an intricate terminal arborization within layers IV–V of PreS (asterisk in **Figure 10C**).

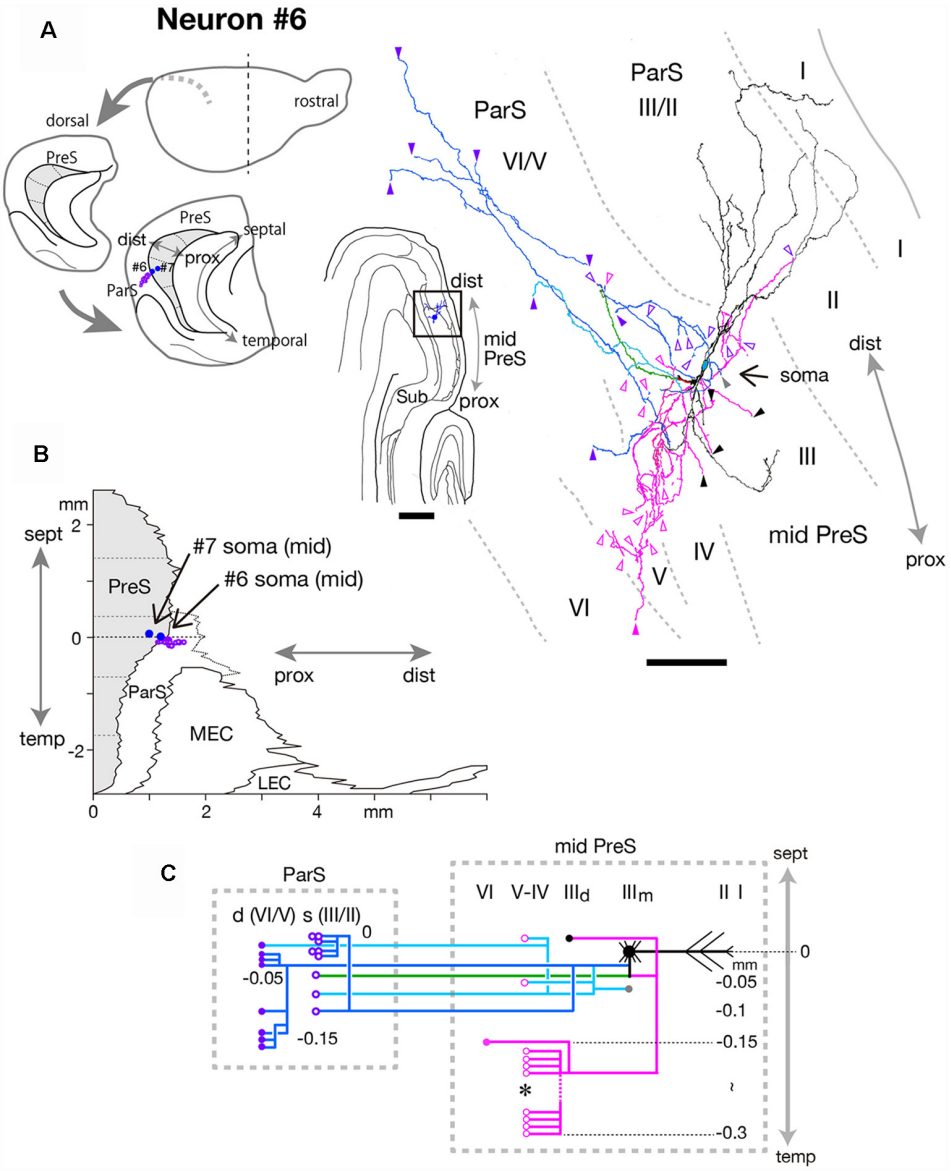

FIGURE 10 | (A) Schematic diagrams of the extended hippocampus as shown in **Figure 1A** (left). The locations of cell body of neurons #6 and #7 in PreS are schematically represented as blue-colored circles. The terminal distribution in the superficial layers of ParS originated from neuron #6 is schematically shown by purple-open circles. Middle is a drawing of the section of neuron #6, which includes the cell body and several dendrites. Camera lucida reconstruction of axonal morphology of neuron #6 (right). Dendrites and the main axon are colored in black, and the main axonal branches and their collaterals are represented by blue, magenta and green. One of the collaterals from the blue branch is colored in pale blue. Gray, black, magenta-open and magenta arrowheads indicate the points of ending of axonal branches in the middle and deep parts of layer III, layer V and layer VI of PreS, respectively. Purple-open and purple arrowheads indicate points of endings of axon collaterals in the superficial (layers II/III) and deep (layers V/VI) layers of ParS, respectively. **(B)** Two-dimensional unfolded map of layer III of PreS, ParS and EC, showing the locations of the cell body (blue-colored circles) of neurons #6 and #7 and axon terminals (purple-open circles) of neuron #6 in the superficial layers of ParS. **(C)** Schematic of axonal branching pattern for neuron #6. The axonal branches are represented using the same colors as in **(A)**. Gray, black, magenta-open and magenta circles indicate terminal levels of axonal branches within the middle and deep parts of layer III, layer V and layer VI of PreS, respectively. Purple-open and purple circles indicate terminal levels of axonal branches within the superficial (layers II/III) and deep (layers V/VI) layers of ParS, respectively. An asterisk indicates the presence of complex terminal arborization forming a plexus. The level of each axonal branching point is not necessarily accurate. Scale bar = 500 μm in the middle and 100 μm in the right in **(A)**.

Taken together, these findings indicate neuron #6 was a fusiform cell, which sent many axonal arbors to ParS and also had recurrent axon collaterals for dense intrinsic connections within PreS.

Intrinsic Connectional Neurons

Within six intrinsic projection neurons, four gave off many axonal branches reaching to both superficial and deep layers of PreS (**Figure 11**), while the other two displayed

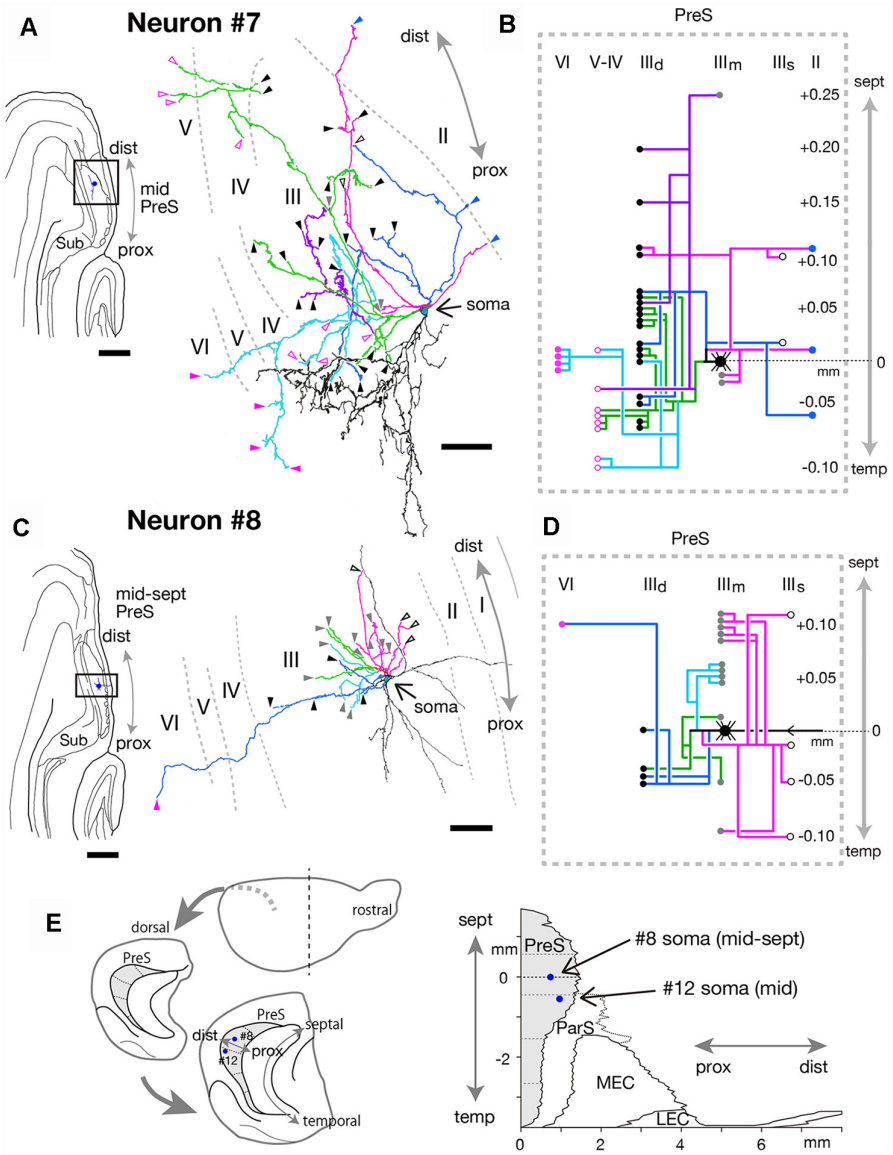

FIGURE 11 | (A,C) A drawing of the section which includes the cell body and several dendrites (left) and camera lucida reconstruction of axonal morphology (right) of neurons #7 **(A)** and #8 **(C)**. Dendrites are colored in black. The main axonal branches and their collaterals are represented by magenta, blue, green (in **A**) and pale blue (in **C**). In **(A)**, one of the collaterals from the green branch is colored in purple and the other in pale blue. Blue arrowheads indicate points of endings of axonal branches in layer II of PreS. White-open, gray, black, magenta-open and magenta arrowheads indicate the points of endings of axonal branches in the superficial, middle and deep parts of layer III, layer V and layer VI of PreS, respectively. **(B,D)** Schematic diagrams of each axonal branching pattern for neurons #7 **(B)** and #8 **(D)**. The axonal branches are represented using the same colors as in **(A,C)**. Blue, white-open, gray, black, magenta-open and magenta circles indicate terminal levels of axonal branches within layer II, the superficial, middle and deep parts of layer III, layer V and layer VI of PreS, respectively. **(E)** Schematic diagrams of the extended hippocampus as shown in **Figure 1A** (left). The locations of cell body of neurons #8 and #12 in PreS are represented as blue-colored circles. Two-dimensional unfolded map of layer III of PreS, ParS and EC, showing the locations of the cell body (blue-colored circles) of neurons #8 and #12 are inserted in (**E**, right). Scale bars = 500 μm in the left and 50 μm in the right in **(A,C)**.

sparse axonal branches, for which terminations were confined to layers III–V or restricted within layer III of PreS (**Figure 12**).

Neurons With Numerous Axonal Collaterals

The cell body of neuron #7 was located at the middle depth of layer III of the distal portion of mid-PreS, which was at a distance of 50 μm from the cell body of neuron #6 (in the same animal; **Figures 10A,B**, **11A,B**). The dendrites were spiny and showed a unique arborization pattern, arborizing extensively in a direction deep to the cell body (**Figure 11A**). A main axonal shaft provided three major branches (magenta, green and blue branches in **Figures 11A,B**), one of which formed complex terminal arborizations within the deep part of layer III near

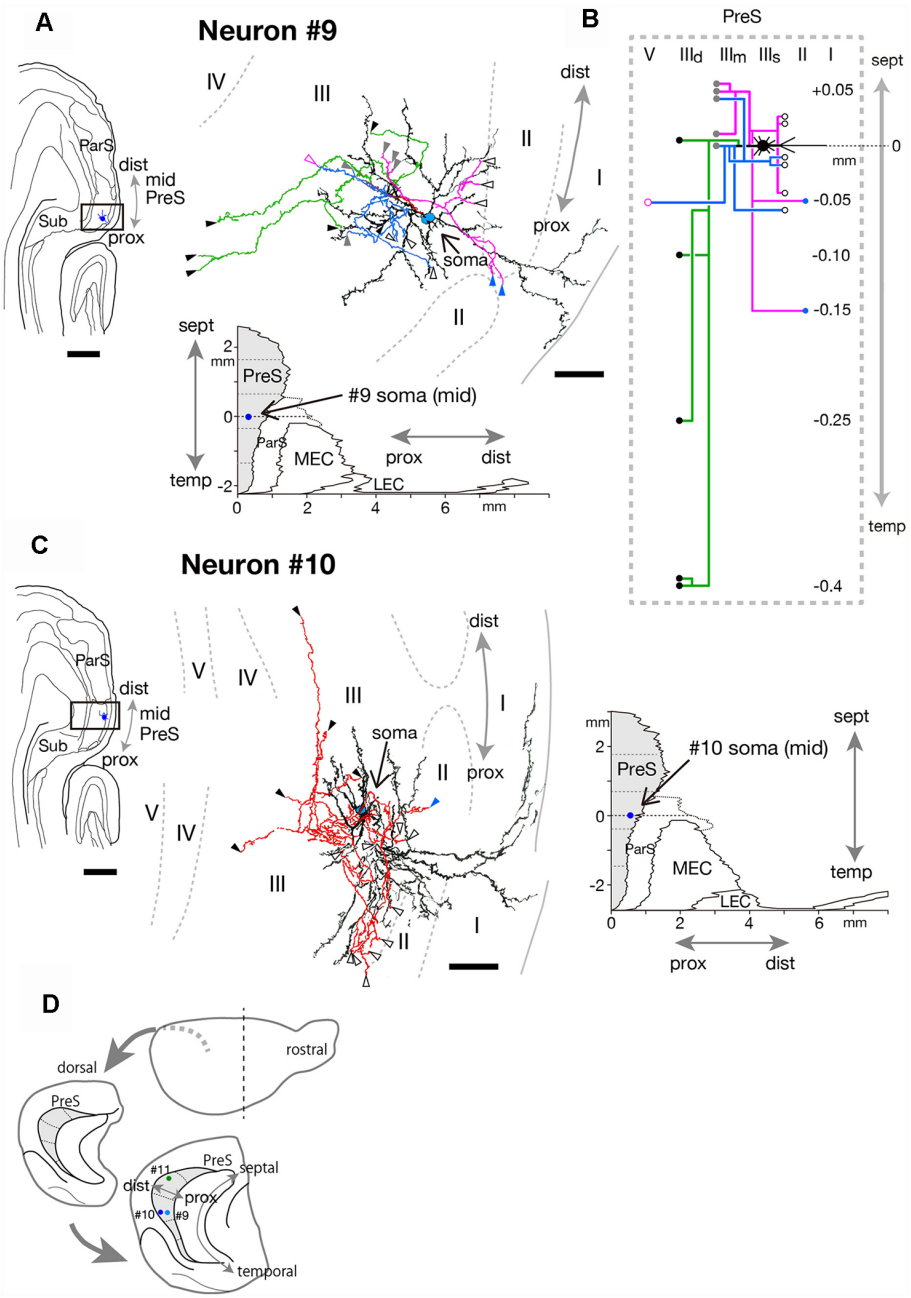

FIGURE 12 | (A,C) A drawing of the section which includes the cell body and several dendrites (left) and camera lucida reconstruction of axonal morphology (right) of neurons #9 **(A)** and #10 **(C)**. Dendrites are colored in black. The main axonal branches and their collaterals are represented by magenta, blue and green in **(A)**. In **(C)**, all axons are colored in red. Blue, white-open, gray, black, magenta-open and magenta arrowheads indicate the points of endings of axonal branches in layer II, the superficial, middle and deep parts of layer III, layer V and layer VI of PreS, respectively. In **(C)**, some axon terminals are not denoted because of overlapping arbors. **(B)** Schematic diagrams of each axonal branching pattern for neuron #9. The axonal branches and the terminal levels are represented using the same colors as in **(A)**. The level of each axonal branching point is not necessarily accurate. **(D)** Schematic diagrams of the extended hippocampus as shown in **Figure 1A**. The locations of cell body of neurons #9, #10, and #11 in PreS are schematically represented as pale blue-, blue-, and green-colored circles, respectively. Scale bars = 500 μm in the left and 50 μm in the right in **(A,C)**.

the level of the cell body (green branches in **Figures 11A,B**), with a collateral sending many branches to layers V and VI (pale blue branches in **Figures 11A,B**) and another collateral providing several axonal branches to the middle and deep parts of layer III from 0.05 mm temporal to 0.25 mm septal to the cell body (purple branch in **Figures 11A,B**). The other two major branches (magenta and blue branches in **Figures 11A,B**) gave off ascending collaterals to layer II and the superficial part of

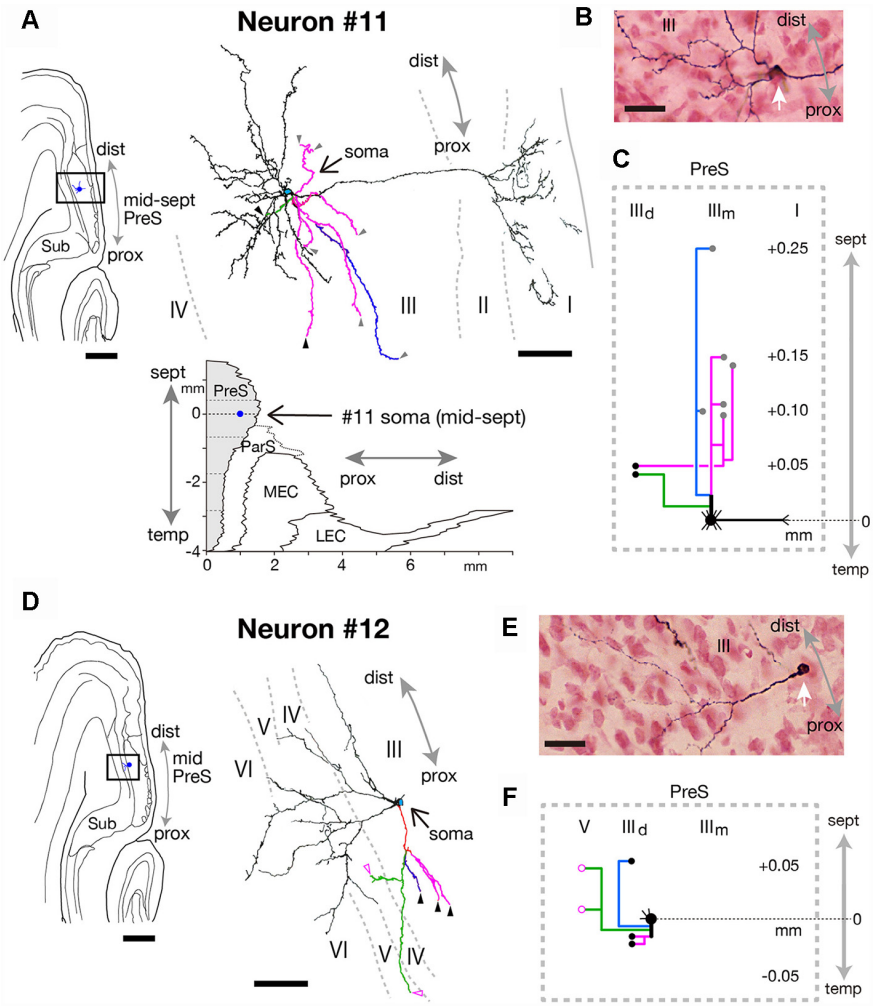

FIGURE 13 | (A,D) A drawing of the section which includes the cell body and several dendrites (left) and camera lucida reconstruction of axonal morphology (right) of neurons #11 **(A)** and #12 **(D)**. A two-dimensional unfolded map of layer III of PreS (shaded region), ParS and EC, showing the locations of the cell body (blue filled circles) of neuron #11 is inserted in **(A)**. In the camera lucida reconstruction, dendrites are colored in black. The main axonal branches and their collaterals are represented by magenta, blue, and green. Gray, black and magenta-open arrowheads indicate points of endings of axonal branches in the middle and deep parts of layer III and layer V of PreS, respectively. **(B,E)** Composite photomicrographs of each cell body and proximal parts of the processes of neurons #11 **(B)** and #12 **(E)** taken by stacking different focal planes. White arrows indicate cell bodies. **(C,F)** Schematic diagrams of each axonal branching pattern of neurons #11 **(C)** and #12 **(F)**. The axonal branches and the terminal levels are represented using the same colors as in **(A,D)**. The level of each axonal branching point is not necessarily accurate. Scale bars = 500 μm in the left and 50 μm in the right in **(A,D)**, and 20 μm in **(B,E)**.

layer III, and also bifurcated several branches to the deep part of layer III.

Neuron #8 also showed characteristic dendritic arborization, i.e., one dendritic arbor spread in distal and superficial directions and the other mostly extending in a proximal direction from the cell body (**Figure 11C**). Dendrites of this neuron were relatively thin and smooth. The soma was located at the middle depth of layer III of the mid-proximodistal part of the mid-septal PreS (**Figures 11C,E**) and gave off four major axonal branches (magenta, blue, pale blue and green branches in **Figures 11C,D**), with all terminating within about 0.2 mm of the septotemporal range. One major branch sent many collaterals to a level 0.1 mm septal to the cell body and fewer to more temporal levels, and all collaterals terminated in the superficial or middle depth of layer III (magenta branches in **Figures 11C,D**). One of the other major branches specifically projected to the middle depth of layer III at a more septal level (pale blue branches in **Figures 11C,D**), while the other two provided collaterals mostly to the middle and deep parts of layer III at the level of the cell body or more temporal levels (blue and green branches in **Figures 11C,D**). One descending axonal arbor bifurcated from the major branch (blue branches in **Figures 11C,D**) and terminated at the deep part of layer VI.

Cell bodies of neurons #9 and #10 were located at the superficial part of layer III in the proximal and distal portions of mid-PreS, respectively (**Figures 12A,C,D**; in different animal).

The axonal branches formed a local plexus at levels near the cell body and terminated in layers II, III and V. In addition, neuron #9 had long descending axonal branches (green branches in **Figures 12A,B**) that reached to a level about 0.4 mm temporal to the cell body.

In conclusion, neurons #7, #8, #9 and #10 had many recurrent axon collaterals, which mainly terminated in the deep and/or superficial part of layer III of PreS. Neurons #7 and #8 had asymmetric axonal domains, which was offset in the more distal part and deeper layers in neuron #7, while in the more distal and superficial part of layer III in neuron #8.

Neurons With Sparse Axonal Branches

The cell bodies of neurons #11 and #12 were both located at the middle depth of layer III of the distal part of PreS, but with slightly different septotemporal distributions. The cell body of neuron #12 was located in mid-PreS, while that of neuron #11 was located in mid-septal PreS (**Figures 11E**, **12D**, **13A**). Both neurons provided a small number of axonal branches, for which the terminal distributions were confined to layer III (in neuron #11) or layers III and V (in neuron #12; **Figure 13**). Neuron #11 was a pyramidal neuron with spiny dendritic arbors (**Figures 13A,B**) and axonal branches mostly innervating the middle depth of layer III only at levels more septal to the cell body (**Figure 13C**). On the other hand, neuron #12 sent axons to more proximal and deeper parts than the cell body (**Figures 13D,F**). The dendrites were thin and displayed many small spines, particularly at the part distant from the cell body (**Figure 13E**). The dendritic morphology of neuron #12 showed a unique pattern, with dendritic arbors proximodistally expanding to the deeper layers (**Figure 13D**), resembling the shape of dendritic arbors in neuron #7 but with fewer ramifications (**Figure 11A**).

In summary, we identified a type of interneurons with sparse axonal branches; neuron #11 was a pyramidal neuron and neuron #12 had characteristic morphology, i.e., both dendrites and axons mostly spread over the deep layers of PreS. In both neurons, the dendritic and axonal domains directed toward distinct regions.

DISCUSSION

Methodological Considerations

The present study used a single neuron-tracing method to demonstrate that each presubicular layer III neuron has various patterns of axonal collateralization. Our results indicate that layer III of PreS comprises several subtypes of intrinsic connection neurons and cortical connection neurons, including MEC- and/or Sub-projecting cells. The Sindbis virus vector used in the present study has already been demonstrated to infect neurons without preference with regard to specific neuronal type (Kuramoto et al., 2009), so our results appear useful for anatomical classification of neurons in layer III of PreS. This virus vector has been reported to not cause degenerative changes in neuronal processes over survival periods between 18 and 72 h (Furuta et al., 2001). In the present study, no obvious degenerative changes such as beading or disconnection in the axons were detected. We, therefore, speculate that our results demonstrate characteristics of the normal, not pathological, morphology of the axonal branches of presubicular layer III neurons. We have performed trials for determining the optimum conditions for virus infection and GFP expression; in particular, we have varied the volume, dilution and BSA concentration of injected virus solution, and also varied the survival time of infected animals. Accordingly, we could conceivably estimate optimal experimental conditions, which enabled us to visualize and reconstruct the previously unreported structures of single neurons, such as the intricate terminal arborization of single MEC projection neurons and axonal collateralization of single subicular and parasubicular projection neurons in layer III of PreS. In some cases, the distance between infected neurons was as short as 50 μm (such as neurons #6 and #7), but we could successfully trace axonal structures by identifying the cell of origin. In our results, several long, commissural and/or subcortical projection fibers could be found in some layer III neurons. One possibility is that other types and/or subtypes of layer III neurons may be identified by investigating commissural and subcortical projection patterns at a single neuronal level, for future studies.

Band-Like Terminal Zones of MEC Projection Neurons

Our previous tracer study indicated that the presubicular projections terminated in the zone or band-like area in layer III of MEC perpendicular to MEC/LEC boundary and almost parallel with the rhinal fissure (Honda and Ishizuka, 2004). Here, we elucidated that the width (about 500 μm) and axis of these zones closely matched the terminal fields of the single neuronal projection shown in the present results (**Figure 6**). Using two-dimensional unfolded maps, we have previously demonstrated the topographic nature of presubiculo-entorhinal projections in that the septotemporal or longitudinal axis of PreS corresponds to the axis on MEC/LEC boundary. That is, the septal PreS projects to the band-like zone near the rhinal fissure and the temporal PreS projects to the band-like zone away from the rhinal fissure (Honda and Ishizuka, 2004). As seen in **Figure 6**, the patterns of entorhinal projection of both neurons #1 and #2 are consistent with a topographic manner in which the band-like terminal field of neuron #2 is located closer to ParS/MEC boundary than that of neuron #1, because the cell body of neuron #2 is located at a more temporal level than that of neuron #1. We speculate that both two presubicular layer III neurons are considered major types of entorhinal projection cells as previously reported for PreS HD cells (Preston-Ferrer et al., 2016). Multiple modules of grid cell clustering have recently been reported in rat MEC, with a band-like appearance dorsoventrally, but not mediolaterally (Stensola et al., 2012). Our findings suggest that single presubicular HD cells can simultaneously activate one or more band-like grid cell modules in the superficial layers of MEC and affect a wide range of grid-cell activities (Ray et al., 2017; Naumann et al., 2018).

We have elucidated that the distribution pattern of cells with origins of CA1 and subicular projections was also arranged as band-like zones in layer III of EC in the rat and rabbit (Honda et al., 2012; Honda and Shibata, 2017). We, therefore, propose that such a band-like pattern in EC be inferred to be fundamental for memory function and highly conserved across animal species.

MEC/Sub Projection Neurons

Similar to neurons #1 and #2, neuron #3 was a spiny pyramidal cell that projected to cortical areas other than PreS itself; all three, therefore, seem to represent excitatory neurons. Considering the long distance of axonal projection, neuron #4 is likely also excitatory, although the possibility that it represents a kind of long-range projection-type γ-aminobutyric acid (GABA)ergic neuron cannot be denied (van Haeften et al., 1997; Tomioka et al., 2005), given the relatively smooth dendritic arbors. Neurons #3 and #4 can also transmit signals to subcortical areas concurrently with the ipsilateral PreS, Sub and MEC, through axonal branches that enter into the fimbria/fornix, dorsal hippocampal commissure, or corpus callosum. The target areas remain uncertain because we cut-off both the corpus callosum and fimbria/fornix in the process of separating the hemispheres from the diencephalon in order to make serial sections perpendicular to the long axis of the hippocampal formation. Nonetheless, the commissural axonal branches from these neurons can presumably terminate in the contralateral MEC, as a major commissural projection of layer III in rat PreS (Honda and Ishizuka, 2004). As for the subcortical efferents, we propose the existence of several minor projections originating from layer III of PreS to the anterior thalamic nuclei and/or lateral mammillary nucleus, in addition to the major projections originating from deep layers of PreS (Huang et al., 2017; Simonnet and Fricker, 2018). In our results, all four MEC and MEC/Sub projection neurons gave off recurrent collaterals to layer VI of PreS. Accordingly, the targeted layer VI cells could receive the same excitatory signals as the other cortical or subcortical areas. Although the postsynaptic targets of these recurrent collaterals remain uncertain, several kinds of inhibitory neurons in layer VI of PreS could conceivably receive inputs and affect the microcircuit within PreS (Nassar et al., 2018). Moreover, synaptic connectivity among excitatory neurons reportedly increases in probability toward the deep layers of PreS in the rat (Peng et al., 2017). This suggests that excitatory signals from recurrent collaterals of MEC and/or MEC/Sub projection neurons can directly activate the subcortical projection neurons in layer VI.

Subicular Projection Neurons

We have previously confirmed that in cases with wheat germ agglutinin-horseradish peroxidase injection into various parts of PreS, many cells labeled in a retrograde manner, but without any distinct deposits of anterograde labels could be detected in the pyramidal cell layer of Sub (Honda and Ishizuka, 2015). Accordingly, the subiculo-presubicular projection was mostly unidirectional, with few, if any, projections from PreS to Sub in the rat. Funahashi et al. (1999) elucidated presubicular inputs to Sub by slice electrophysiology, but the cells of origins were in the deep layers of PreS. The present results of a single neuron study revealed that layer III of PreS involved several kinds of subicular projection neurons, including neurons that innervate only Sub (such as neuron #5), unlike Sub/MEC projection neurons (neurons #3 and #4). Minor connections such as the presubiculo-subicular projection can be successfully detected by our labeling method. Axonal branches of all Sub and Sub/MEC projection neurons terminated in the pyramidal cell layer of Sub, but not in the molecular layer, suggesting that the proximal (near the cell body) position of dendritic or axonal arbors of the pyramidal neurons of Sub are more likely to receive inputs from layer III neurons of PreS.

Parasubicular Projection Neurons

According to Nassar et al. (2015), some cluster 2 cells in mice that contained quasi-fast-spiking, basket-cell-like interneurons and were confirmed to be located at the distal part of PreS projecting into the nearby ParS and extensively ramifying within the superficial or deep layers of ParS. Our neuron #7 seemed to be a similar type because some of the axonal branches extended more distally toward ParS. Our results demonstrated that layer III of the distal PreS comprised several subtypes of neurons including parasubicular projection neurons such as neuron #6 and also interneurons such as neurons #7 and #12. Both interneurons tended to ramify more densely in the deeper layers and occupied regions distinct from the zones of dendrites. This suggests that presubiculo-parasubicular projection and its regulation by some kinds of intra- or interlaminar interactions can exist at least within the distal portion of PreS.

Classification of Interneurons

From the perspective of morphological characteristics (regarded as interneurons with axons ramifying locally), five of our six intrinsic connection neurons in our results seem to be classifiable as inhibitory interneurons, while only neuron #11, a small, spiny pyramidal-type neuron, can be excitatory. Within the five presumable inhibitory interneurons, three (neurons #7, #9 and #10) showed densely spiny dendritic arbors. Some kinds of GABAergic interneurons in the rat neocortex are spiny (Kubota et al., 2011) and glutamatergic spiny pyramidal cells with locally confined axons that do not leave the cortical gray matter have also been reported (regarded as "intrinsic glutamatergic spiny cells" in DeFelipe et al., 2013). Rat GABAergic cortical interneurons have already been classified into many subtypes by their electrophysiological and morphological properties (Karube et al., 2004; Uematsu et al., 2008). We will need to evaluate the degree of axosomatic contacts, axon branching patterns, and bouton distribution quantitatively to collate reported data and our results. According to the classification of GABAergic interneurons by DeFelipe et al. (2013), most of our interneurons seem to be translaminar type, with axons not confined to a single layer. As shown in **Figures 12**, **13**, our neurons #7 and #12 are both identified as displaced and descending types, because relative localizations of the dendritic and axonal

arbors are shifted and not colocalized, and are depicted as mostly descending, radial arborizations. Neuron #8 seems to be identified as an intracolumnar type because the axonal arbors are confined to a single cortical column size at a diameter of 300 μm. On the other hand, neuron #9 can be defined as a transcolumnar type, because the axonal branches distributed for a distance >400 μm along the septotemporal axis. In the present study, our first priority was to visualize and completely trace the whole axonal morphology. We thus did not detect the expression of neuron markers such as parvalbumin and somatostatin. In mouse PreS, Simonnet et al. (2017) reported the existence of a pyramidal-Martinotti-cell feedback loop within layer III, which works as an inhibitory microcircuit for tuning and maintaining head direction signals in PreS. In the present study, we did not find Martinotti cells in layer III of rat PreS, but layer III pyramidal neurons in our results were also likely to participate in such feedback regulatory mechanisms. In another study using *in vitro* brain slices, Simonnet et al. (2013) classified the small regular spiking cells in layers II/III of rat PreS as "Cluster 1," and also described that most cells in Cluster 1 are small, pyramid-shaped neurons. Some neurons in our results (including neurons #8 and #11) were similar to their Cluster 1 cells when only considering the dendritic morphology.

Superficial layers of rat MEC reportedly receive cell-type-specific intralaminar and ascending interlaminar feedback inputs, with those inputs attributed to the striking asymmetry of the deep to superficial microcircuitry within MEC (Beed et al., 2010). Moreover, Nilssen et al. (2018) reported that layer II of rat LEC contains "fan cells," in which dendrites fan toward the direction of the pial surface with the axon descending to the deep layers, and that such fan cells were specifically connected to two types of inhibitory interneurons (fast spiking and non-fast spiking cells) in the vicinity of the cell body. Fan cells were suggested to be an important component of local circuits within the superficial layers of LEC. In the present study, neurons #11 and #12 could be considered as a kind of interneuron with a distinctive polarity in the dendritic and axonal domains and seem to participate in focal microcircuits, which straddle the neighboring cortical columns in rat PreS.

Patterns of Distribution of Cortical and Intrinsic Projection Neurons

We divided layer III of PreS into multiple regions along the septotemporal, proximodistal and also superficial-to-deep axes, and demonstrated the locations of soma and terminations of axonal branches. In our study, as seen in **Table 1**, the majority of cortical (MEC/Sub, Sub, and ParS) projection neurons were distributed in regions from the septal to mid-PreS. Previously, the septal half of PreS (also called the postsubiculum) has been featured for its functional importance (Boccara et al., 2010; Bett et al., 2013) and our results raise the possibility that the septal half of PreS is much more divergent in neuronal subtypes, especially for cortical projections. On the other hand, no distinct distribution patterns that correlated with cell-type specificity could be found along proximodistal or superficial-to-deep axes. This may be partially due to an insufficient number of samples. We should collect more data for future studies, but it can be assumed that the larger the number of certain subtypes of neurons, the higher the infection probability, and if so, there is also a possibility that the proportion of each neuronal subtype in our study may reflect an actual quantitative statement to a certain extent, even with such a small total number ($n = 12$).

In conclusion, we have demonstrated the morphological features of the 12 layer III neurons of PreS, including cortical and intrinsic projection neurons, and have indicated the existence of multiple types of MEC projection neurons with distinct patterns of axonal collateralization. Layer III of PreS also comprises a wide variety of intrinsic projection neurons, which may play a critical role in mechanisms underlying head-directional signaling.

DATA AVAILABILITY

The raw data supporting the conclusions of this manuscript will be made available by the authors, without undue reservation, to any qualified researcher.

ETHICS STATEMENT

The present experiments were approved by the Animal Care and Use Committee of Tokyo Women's Medical University, and all conformed to the Guidelines for the Care and Use of Laboratory Animals (National Institutes of Health, Bethesda, MD, USA). We used eight adult male Wistar rats (280–305 g body weight; Clea Japan, Tokyo, Japan), and every effort was made to minimize the number of animals used and the pain and distress of animals.

AUTHOR CONTRIBUTIONS

All authors had full access to all the data in the study and take responsibility for the integrity of the data and the accuracy of the data analysis. YH and TF: study concept, design, drafting of the manuscript, analysis and interpretation of data. YH: acquisition of data and obtained funding. TF: critical revision of the manuscript for important intellectual content.

FUNDING

This work was supported by Japan Society for the Promotion of Science (JSPS) KAKENHI Grant number JP15K09363 to YH.

ACKNOWLEDGMENTS

We wish to thank Dr. Takeshi Kaneko (Kyoto University) and Dr. Hideshi Shibata (Tokyo University of Agriculture and Technology) for the helpful discussions.

REFERENCES

Beed, P., Bendels, M. H. K., Wiegand, H. F., Leibold, C., Johenning, F. W., and Schmitz, D. (2010). Analysis of excitatory microcircuitry in the medial entorhinal cortex reveals cell-type-specific differences. *Neuron* 68, 1059–1066. doi: 10.1016/j.neuron.2010.12.009

Bett, D., Stevenson, C. H., Shires, K. L., Smith, M. T., Martin, S. J., Dudchenko, P. A., et al. (2013). The postsubiculum and spatial learning: the role of postsubicular synaptic activity and synaptic plasticity in hippocampal place cell, object, and object-location memory. *J. Neurosci.* 33, 6928–6943. doi: 10.1523/jneurosci.5476-12.2013

Boccara, C. N., Sargolini, F., Thoresen, V. H., Solstad, T., Witter, M. P., Moser, E. I., et al. (2010). Grid cells in pre- and parasubiculum. *Nat. Neurosci.* 13, 987–994. doi: 10.1038/nn.2602

Caballero-Bleda, M., and Witter, M. P. (1994). Projections from the presubiculum and the parasubiculum to morphologically characterized entorhinal-hippocampal projection neurons in the rat. *Exp. Brain Res.* 101, 93–108. doi: 10.1007/bf00243220

DeFelipe, J., López-Cruz, P. L., Benavides-Piccione, R., Bielza, C., Larrañaga, P., Anderson, S., et al. (2013). New insights into the classification and nomenclature of cortical GABAergic interneurons. *Nat. Rev. Neurosci.* 14, 202–216. doi: 10.1038/nrn3444

Funahashi, M., Harris, E., and Stewart, M. (1999). Re-entrant activity in a presubiculum-subiculum circuit generates epileptiform activity *in vitro*. *Brain Res.* 849, 139–146. doi: 10.1016/s0006-8993(99)02045-4

Furuta, T., Tomioka, R., Taki, K., Nakamura, K., Tamamaki, N., and Kaneko, T. (2001). *In vitro* transduction of central neurons using recombinant sindbis virus: golgi-like labeling of dendrites and axons with membrane-targeted fluorescent proteins. *J. Histochem. Cytochem.* 49, 1497–1507. doi: 10.1177/002215540104901203

Honda, Y., Furuta, T., Kaneko, T., Shibata, H., and Sasaki, H. (2011). Patterns of axonal collateralization of single layer V cortical projection neurons in the rat presubiculum. *J. Comp. Neurol.* 519, 1395–1412. doi: 10.1002/cne.22578

Honda, Y., and Ishizuka, N. (2004). Organization of connectivity of the rat presubiculum: I. Efferent projections to the medial entorhinal cortex. *J. Comp. Neurol.* 473, 463–484. doi: 10.1002/cne.20093

Honda, Y., and Ishizuka, N. (2015). Topographic distribution of cortical projection cells in the rat subiculum. *Neurosci. Res.* 92, 1–20. doi: 10.1016/j.neures.2014.11.011

Honda, Y., Sasaki, H., Umitsu, Y., and Ishizuka, N. (2012). Zonal distribution of perforant path cells in layer III of the entorhinal area projecting to CA1 and subiculum in the rat. *Neurosci. Res.* 74, 200–209. doi: 10.1016/j.neures.2012.10.005

Honda, Y., and Shibata, H. (2017). Organizational connectivity among the CA1, subiculum, presubiculum, and entorhinal cortex in the rabbit. *J. Comp. Neurol.* 525, 3705–3741. doi: 10.1002/cne.24297

Honda, Y., Umitsu, Y., and Ishizuka, N. (2008). Organization of connectivity of the rat presubiculum: II. Associational and commissural connections. *J. Comp. Neurol.* 506, 640–658. doi: 10.1002/cne.21572

Huang, L. W., Simonnet, J., Nassar, M., Richevaux, L., Lofredi, R., and Fricker, D. (2017). Laminar localization and projection-specific properties of presubicular neurons targeting the lateral mammillary nucleus, thalamus, or medial entorhinal cortex. *eNeuro* 4:ENEURO.0370-16.2017. doi: 10.1523/eneuro.0370-16.2017

Ishizuka, N. (2001). Laminar organization of pyramidal cell layer of the subiculum in the rat. *J. Comp. Neurol.* 435, 89–110. doi: 10.1002/cne.1195

Karube, F., Kubota, Y., and Kawaguchi, Y. (2004). Axon branching and synaptic bouton phenotypes in GABAergic nonpyramidal cell subtypes. *J. Neurosci.* 24, 2853–2865. doi: 10.1523/jneurosci.4814-03.2004

Kubota, Y., Shigematsu, N., Karube, F., Sekigawa, A., Kato, S., Yamaguchi, N., et al. (2011). Selective coexpression of multiple chemical markers defines discrete populations of neocortical GABAergic neurons. *Cereb. Cortex* 21, 1803–1817. doi: 10.1093/cercor/bhq252

Kuramoto, E., Furuta, T., Nakamura, K. C., Unzai, T., Hioki, H., and Kaneko, T. (2009). Two types of thalamocortical projections from the motor thalamic nuclei of the rat: a single neuron-tracing study using viral vectors. *Cereb. Cortex* 19, 2065–2077. doi: 10.1093/cercor/bhn231

Matsuda, W., Furuta, T., Nakamura, K. C., Hioki, H., Fujiyama, F., Arai, R., et al. (2009). Single nigrostriatal dopaminergic neurons form widely spread and highly dense axonal arborizations in the neostriatum. *J. Neurosci.* 29, 444–453. doi: 10.1523/JNEUROSCI.4029-08.2009

Nassar, M., Simonnet, J., Huang, L. W., Mathon, B., Cohen, I., Bendels, M. H. K., et al. (2018). Anterior thalamic excitation and feedforward inhibition of presubicular neurons projecting to medial entorhinal cortex. *J. Neurosci.* 38, 6411–6425. doi: 10.1523/jneurosci.0014-18.2018

Nassar, M., Simonnet, J., Lofredi, R., Cohen, I., Savary, E., Yanagawa, Y., et al. (2015). Diversity and overlap of parvalbumin and somatostatin expressing interneurons in mouse presubiculum. *Front. Neural Circuits* 9:20. doi: 10.3389/fncir.2015.00020

Naumann, R. K., Preston-Ferrer, P., Brecht, M., and Burgalossi, A. (2018). Structural modularity and grid activity in the medial entorhinal cortex. *J. Neurophysiol.* 119, 2129–2144. doi: 10.1152/jn.00574.2017

Nilssen, E. S., Jacobsen, B., Fjeld, G., Nair, R. R., Blankvoort, S., Kentros, C., et al. (2018). Inhibitory connectivity dominates the fan cell network in layer II of lateral entorhinal cortex. *J. Neurosci.* 38, 9712–9727. doi: 10.1523/jneurosci.1290-18.2018

Paxinos, G., and Watson, C. (1998). *The Rat Brain in Stereotaxic Coordinates*. 4th Edn. San Diego, CA: Academic Press.

Peng, Y., Barreda Tomás, F. J., Klisch, C., Vida, I., and Geiger, J. R. P. (2017). Layer-specific organization of local excitatory and inhibitory synaptic connectivity in the rat presubiculum. *Cereb. Cortex* 27, 2435–2452. doi: 10.1093/cercor/bhx049

Preston-Ferrer, P., Coletta, S., Frey, M., and Burgalossi, A. (2016). Anatomical organization of presubicular head-direction circuits. *Elife* 5:e14592. doi: 10.7554/elife.14592

Ray, S., Burgalossi, A., Brecht, M., and Naumann, R. K. (2017). Complementary modular microcircuits of the rat medial entorhinal cortex. *Front. Syst. Neurosci.* 11:20. doi: 10.3389/fnsys.2017.00020

Simonnet, J., Eugène, E., Cohen, I., Miles, R., and Fricker, D. (2013). Cellular neuroanatomy of rat presubiculum. *Eur. J. Neurosci.* 37, 583–597. doi: 10.1111/ejn.1206

Simonnet, J., and Fricker, D. (2018). Cellular components and circuitry of the presubiculum and its functional role in the head direction system. *Cell Tissue Res.* 373, 541–556. doi: 10.1007/s00441-018-2841-y

Simonnet, J., Nassar, M., Stella, F., Cohen, I., Mathon, B., Boccara, C. N., et al. (2017). Activity dependent feedback inhibition may maintain head direction signals in mouse presubiculum. *Nat. Commun.* 8:16032. doi: 10.1101/106005

Stensola, H., Stensola, T., Solstad, T., Frøland, K., Moser, M. B., and Moser, E. I. (2012). The entorhinal grid map is discretized. *Nature* 492, 72–78. doi: 10.1038/nature11649

Tamamaki, N., and Nojyo, Y. (1995). Preservation of topography in the connections between the subiculum, field CA1, and the entorhinal cortex in rats. *J. Comp. Neurol.* 353, 379–390. doi: 10.1002/cne.903530306

Tomioka, R., Okamoto, K., Furuta, T., Fujiyama, F., Iwasato, T., Yanagawa, Y., et al. (2005). Demonstration of long-range GABAergic connections distributed throughout the mouse neocortex. *Eur. J. Neurosci.* 21, 1587–1600. doi: 10.1111/j.1460-9568.2005.03989.x

Uematsu, M., Hirai, Y., Karube, F., Ebihara, S., Kato, M., Abe, K., et al. (2008). Quantitative chemical composition of cortical GABAergic neurons revealed in transgenic venus-expressing rats. *Cereb. Cortex* 18, 315–330. doi: 10.1093/cercor/bhm056

van Haeften, T., Wouterlood, F. G., Jorritsma-Byham, B., and Witter, M. P. (1997). GABAergic presubicular projections to the medial entorhinal cortex of the rat. *J. Neurosci.* 17, 862–874. doi: 10.1523/jneurosci.17-02-00862.1997

Conflict of Interest Statement: The authors declare that the research was conducted in the absence of any commercial or financial relationships that could be construed as a potential conflict of interest.

frontiers in Neural Circuits

REVIEW
published: 07 August 2019
doi: 10.3389/fncir.2019.00052

Space and Memory (Far) Beyond the Hippocampus: Many Subcortical Structures Also Support Cognitive Mapping and Mnemonic Processing

Shane M. O'Mara[1]* *and John P. Aggleton*[2]

[1]School of Psychology and Institute of Neuroscience, Trinity College, Dublin, Ireland, [2]School of Psychology, Cardiff University, Cardiff, United Kingdom

Memory research remains focused on just a few brain structures—in particular, the hippocampal formation (the hippocampus and entorhinal cortex). Three key discoveries promote this continued focus: the striking demonstrations of enduring anterograde amnesia after bilateral hippocampal damage; the realization that synapses in the hippocampal formation are plastic e.g., when responding to short bursts of patterned stimulation ("long-term potentiation" or LTP); and the discovery of a panoply of spatially-tuned cells, principally surveyed in the hippocampal formation (place cells coding for position; head-direction cells, providing compass-like information; and grid cells, providing a metric for 3D space). Recent anatomical, behavioral, and electrophysiological work extends this picture to a growing network of subcortical brain structures, including the anterior thalamic nuclei, rostral midline thalamic nuclei, and the claustrum. There are, for example, spatially-tuned cells in all of these regions, including cells with properties similar to place cells of the hippocampus proper. These findings add new perspectives to what had been originally been proposed—but often overlooked—half a century ago: that damage to an extended network of structures connected to the hippocampal formation results in diencephalic amnesia. We suggest these new findings extend spatial signaling in the brain far beyond the hippocampal formation, with profound implications for theories of the neural bases of spatial and mnemonic functions.

Keywords: memory, hippocampal formation, space, anterior thalamus, claustrum, diencephalic amnesia

OPEN ACCESS

Edited by:
KJ Jeffery,
University College London,
United Kingdom

Reviewed by:
Benjamin J. Clark,
University of New Mexico,
United States
John C. Dalrymple-Alford,
University of Canterbury,
New Zealand
Rebecca D. Burwell,
Brown University, United States

***Correspondence:**
Shane M. O'Mara
shane.omara@tcd.ie

Received: *16 May 2019*
Accepted: *22 July 2019*
Published: *07 August 2019*

Citation:
O'Mara SM and Aggleton JP (2019) Space and Memory (Far) Beyond the Hippocampus: Many Subcortical Structures Also Support Cognitive Mapping and Mnemonic Processing. Front. Neural Circuits 13:52. doi: 10.3389/fncir.2019.00052

INTRODUCTION

An intensive research effort over the past four decades has revealed that discrete populations of cells, present in widely distributed networks in the brain, code for differing aspects of three-dimensional space (for comprehensive reviews, see Grieves and Jeffery, 2017; Hunsaker and Kesner, 2018). There has been a sustained research emphasis on the precise roles played by two connected structures (the entorhinal cortex and the hippocampus;

collectively, the hippocampal formation) because these structures have been identified as having vital importance for certain types of memory (and, particularly, for spatial memory). Less attention has been given to the contributions from other structures connected to the hippocampal formation, although these structures seemingly play similarly vital roles in memory.

Here, we will focus on spatial mapping functions subserved by particular brain regions and networks, similar to those performed by the hippocampal formation: namely, the rostral midline and anterior nuclei of the thalamus, as well as the claustrum. These regions are less investigated and less well-understood than the hippocampal formation; they are not as frequently incorporated into theoretical accounts of spatial coding in the brain and are less well-recognized as spatial processing nodes (The one possible exception concerns the appreciation that the anterodorsal thalamic nucleus contains head-direction cells; Taube, 1995, 2007). Unexpectedly, there are cells in all of these subcortical sites that code for aspects of three-dimensional space, including positional information, boundary or perimeter information, as well as head directional and object information (Jankowski et al., 2014, 2015, 2017; Jankowski and O'Mara, 2015; Matulewicz et al., 2019). Moreover, it is now clear that lesions of the rostral and anterior thalamic nuclei can result in deficits in the performance of spatial and non-spatial mnemonic tasks that appear comparable to those resulting from lesions within the entorhinal-hippocampal axis. The few lesion investigations of the claustrum indicate that claustral lesions also disrupt certain aspects of spatial processing.

For clarity, we should note that the term "hippocampus" refers to the CA fields, dentate gyrus, and subiculum. Meanwhile the "hippocampal formation," additionally includes the entorhinal cortex, presubiculum, and parasubiculum, which are also parts of the parahippocampal region (Witter, 2002). Some authorities treat the postsubiculum as distinct from the presubiculum (e.g., van Groen and Wyss, 1990b), and we shall follow this practice. Finally, the term "hippocampus proper" refers to the CA fields but not the subiculum.

MEMORY RESEARCH HAS FOCUSED ESPECIALLY ON THE HIPPOCAMPAL FORMATION

The effort to understand how the brain encodes and supports memory functions has been underway for well over a century (Squire, 1987; Aggleton and Morris, 2018). Over that time, substantial progress has been made in elucidating the brain structures that support memory (including spatial memory), with one particular region remaining in the spotlight, namely, the hippocampal formation (Buzsáki and Moser, 2013). Memory research has focused particularly on the hippocampal formation for at least three interrelated reasons. The early description of the amnestic Patient HM demonstrated a clear and striking case of amnesia that has often been attributed to bilateral loss of the hippocampal formation (Scoville and Milner, 1957). Despite the fact that the surgery clearly involved additional gray and white matter (Annese et al., 2014), HM's amnesia case-study continues to exercise a powerful hold on theoretical and experimental analyses in the memory literature. His near life-long, enduring and non-resolving amnesia, has provided, and continues to provide, a source of fertile hypotheses regarding the neural bases of learning and memory. A second reason for focusing on the hippocampal formation was the important and influential demonstration that synapses in the hippocampus are plastic, e.g., they display "long-term potentiation" (LTP), which results from a brief period (∼1 s) of high-frequency electrical stimulation. While LTP was initially demonstrated by Bliss and Lømo (1973), it followed an original prediction by Hebb (1949). Subsequent demonstrations that pharmacological inhibitors of hippocampal LTP effectively inhibited learning and memory in spatial memory tasks, have also provided a rich source of theory and experiment focused on the role of the hippocampal formation in learning and memory (e.g., Bliss and Collingridge, 1993; van Praag et al., 1999; Lynch, 2004; Malenka and Bear, 2004; Larkin et al., 2008; Tsokas et al., 2016; Grewe et al., 2017). Added information has come from recent "engram" studies, which appear to show that the stimulation of specific hippocampal cell ensembles can reactivate a representation, e.g., a particular context (Tonegawa et al., 2015; Park et al., 2016).

The third powerful impetus derives from the work of John O'Keefe and his collaborators over the past four decades (e.g., O'Keefe and Dostrovsky, 1971; O'Keefe and Nadel, 1978, 1979; O'Keefe and Burgess, 1996; Krupic et al., 2015). In particular, O'Keefe's work reanimated earlier suggestions by Tolman (1948) that there must be a "cognitive map" within the brain. Tolman's experiments showed that rats were capable of engaging in "latent" learning—learning "on the fly" whilst exploring mazes, and subsequently using this information to solve route-finding problems in these self-same mazes when usual routes to reward were blocked (see also O'Mara, 2017). Tolman speculated that, contrary to the motor movement reinforcement theories of Clark Hull and others (e.g., Hull, 1943; Spence, 1956), rats were inducing or inferring something like a "survey map" of their environment, which allowed them to flexibly navigate that environment. O'Keefe's demonstration of the existence of place cells in the hippocampus (O'Keefe and Dostrovsky, 1971) and his subsequent elaboration of the cognitive mapping theory with O'Keefe and Nadel (1978) in their book "*The Hippocampus as a Cognitive Map*" ensured that the hippocampus would remain a focus for investigations of spatial processing by the brain.

In the decades after O'Keefe's initial demonstration of the existence of place cells, further discoveries indicated that the brain coded for differing aspects of three-dimensional space. In particular, the head-direction cells described by Taube et al. (1990a,b) suggested that, in addition to representations of place, the brain also maintains a representation of a compass-like heading in relation to the external three-dimensional world. However, missing from this picture was a sense of how the brain might code a metric for space—a sense of relative distance, and how a metric for space might play a role in spatial processing. The discovery of "grid cells" within the entorhinal cortex by Hafting et al. (2005) provided this missing link, powerfully reinforcing

the idea that the entorhinal-hippocampal axis plays the central role in how the brain codes for space.

Current theories (e.g., Buzsáki and Moser, 2013) of the means by which the brain represents space (and memory) rely on an anatomical model revolving around the existence of cells representing position (place cells), heading (head-direction cells) and relative distance (grid cells). The key structures implicated are the hippocampus (principally concerned with representing spatial position), the postsubiculum and presubiculum, along with related anterior thalamic areas (principally concerned with representing heading information), and the entorhinal cortex (principally concerned with representing metric information). This tripartite anatomical-structural model now dominates theoretical views of spatial navigation and spatial representation. Biologically-inspired models of spatial navigation rely similarly on core ideas revolving around the dissociation of place information from heading information and their subsequent integration in other downstream areas to facilitate goal-directed navigation (e.g., Barrera and Weitzenfeld, 2008). We suggest that there are important components of this overall theoretical picture missing, in particular relating to evolutionarily-conserved brain regions that remain under-explored to this point. We further suggest that significant revisions of current models of how the brain controls behavioral choices in a spatial context are warranted.

Here, we briefly review evidence suggesting that this dominant picture needs a considerable degree of extension. The hippocampal formation has vital interconnections with a wide variety of brain regions, so much so, in fact, that Aggleton and Brown (1999) suggested we should more properly think of an "extended hippocampal formation" when considering memory (see also Delay and Brion, 1969; Ranganath and Ritchey, 2012). Key elements within the extended hippocampal formation include the fornix, the mammillary bodies, the anterior thalamic nuclei, and retrosplenial cortex (Bubb et al., 2017). What are now archaic neuroanatomical constructions (such as "the trisynaptic loop") are giving way to recent neuroanatomical and neurophysiological investigations, suggesting that interactions between the hippocampal formation, as a key spatial hub, in association with a distributed network of other key locations is a more appropriate functional neuroanatomical conception of the structures that support cognitive mapping (**Figure 1**).

EVIDENCE FROM NEODECORTICATE ANIMAL PREPARATIONS

In the 1970s and 1980s a number of investigators investigated what functions could continue to be performed in the absence of a cerebral cortex and hippocampal formation. These preparations usually involved a bilateral removal of the developing cerebral cortex and hippocampus (decortication) at various time points postnatally. Such studies are rarely performed now. However, these early studies indicated that in the absence of a cortex and hippocampus, decorticate rats were capable of learning a variety of spatial and non-spatial tasks, suggesting that subcortical circuitry could, under some conditions, support processes such as nesting, food retrieval and foraging, and successfully returning to a point of origin, and the learning of complex spatial tasks where errors were prevented (for reviews, see Kolb and Whishaw, 1989; Whishaw, 1990). Furthermore, decorticate animals were also capable of successfully learning stimulus relations and responses in a variety of classical conditioning tasks, suggesting that the learning of classically-conditioned avoidance responses dependent on temporal relations remains intact in these animals. Subsequent investigations, particularly those using the rabbit classically-conditioned nictitating membrane preparation, have suggested that such learning requires intact cerebellar and brainstem nuclei (McCormick and Thompson, 1984; Thompson, 1986). In an interesting convergence, Rochefort et al. (2011) found that genetically-modified L7PKCI mice with deficits in PKC-dependent plasticity at parallel fiber–Purkinje cell synapses in the cerebellum have defective place cell processing in tasks requiring vestibular self-motion cues. Recent evidence (Watson et al., 2019) suggests there is a topographically-organized and direct anatomical cerebellar-hippocampal CA1 pathway; moreover, simultaneous local-field potential recordings conducted in the freely-moving animal disclosed synchronization of activity between area CA1 and cerebellum over behaviorally-relevant, subsecond, timescales during home-cage exploration and pellet retrieval on a linear track.

The key message from the early decortication studies is that there are subcortical circuits present capable of supporting complex chains of learned behavior in the absences of a cerebral cortex and hippocampus. The remaining subcortical structures include thalamic, brainstem, cerebellar and spinal structures, thus providing useful clues regarding the structures that might interact with hippocampal and cortical structures to support spatial and other forms of memory. Subsequent electrophysiological, anatomical and transgenic data suggest that there is a profound modulation of hippocampal processing by motor state. It will be of great interest in future experiments to focus on the interactions between the hippocampal formation and subcortical structures to understand the crucial contributions of these structures during spatial and mnemonic processing.

EVENT MEMORY AND THE ANTERIOR THALAMIC NUCLEI

More than 80 years ago, Papez (1937) proposed that "the hypothalamus, the anterior thalamic nuclei, the gyrus cinguli, and the hippocampus, and their interconnections, constitute a harmonious mechanism which may elaborate the functions of central emotion as well as participating in emotional expression." Although sometimes overlooked by certain theorists, the notion of a "*Papez circuit*" was and continues to be a highly influential concept, in particular because Papez, first, correctly highlighted a major circuit critical for overall hippocampal function; and second, Papez placed the hippocampus clearly within a network connected to a wide variety of anatomically-connected and functionally-conserved structures (Bubb et al., 2017). Papez' emphasis on emotion was, in certain respects, somewhat

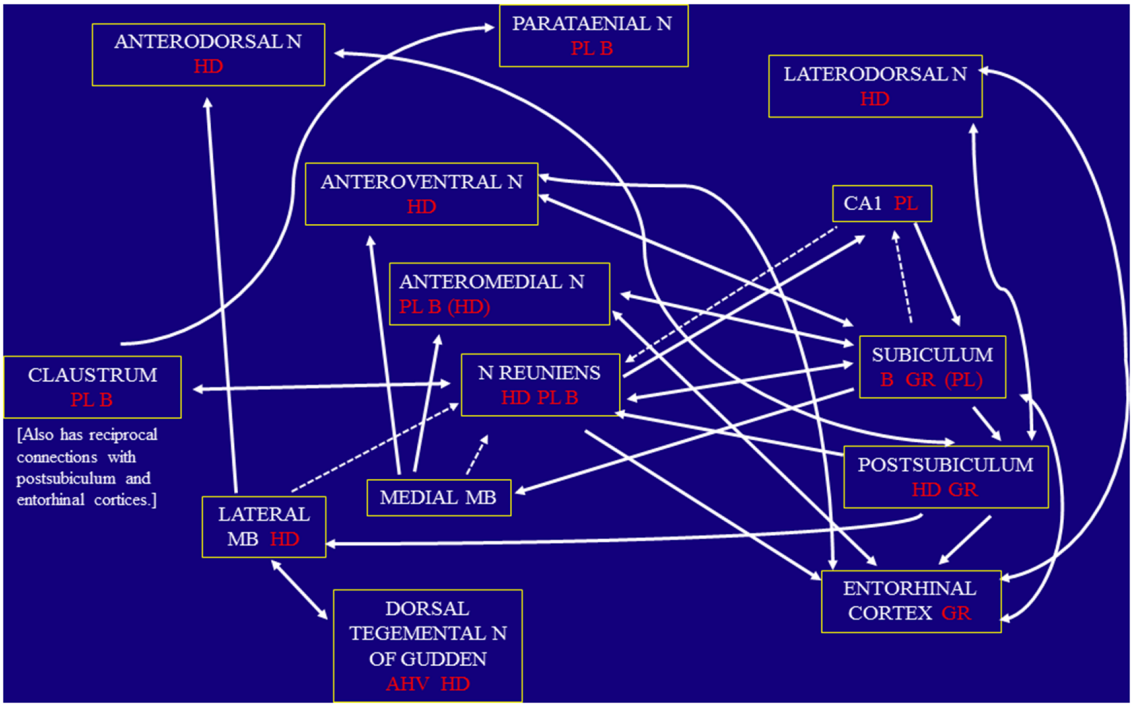

FIGURE 1 | Schematic diagram showing the pattern of direct connections between the three key regions under consideration, namely the rostral thalamus, claustrum, and hippocampal formation. The dashed arrows indicate those connections that are especially light. The diagram also indicates the location of angular head velocity (AHV), border/perimeter (B), grid (GR), head-direction (HD), and place (PL) cells, based on current evidence. Parentheses indicate when the frequency of these spatial cells is low. Other abbreviations: MB, mammillary bodies; N, nucleus.

misplaced, although ventral hippocampal structures certainly play a role in regulating the HPA axis and, therefore, the stress response (Lowry, 2002; Herman and Mueller, 2006; Ulrich-Lai and Herman, 2009; Myers et al., 2017).

A considerable volume of data from diverse sources supports the idea that the anterior thalamus also plays a critical and central role in explicit, event memory. The phenomenon of diencephalic amnesia (the best known example of which is Korsakoff's amnesia or syndrome; Albert et al., 1979) strongly suggests that the core mnemonic deficits seen in these patients principally derive from degeneration of the anterior thalamic nuclei, with possible contributions from adjacent midline thalamic nuclei, including the parataenial nucleus (Mair et al., 1979; Mayes et al., 1988; Harding et al., 2000; Segobin et al., 2019). Additionally, studies of patients with rostral thalamic strokes that disrupt the projections from the mammillary bodies to the anterior thalamic nuclei (Carlesimo et al., 2011) add further support for the importance of the anterior thalamic nuclei, along with their mammillary inputs, for episodic memory (Vann and Aggleton, 2004; Vann and Nelson, 2015). Moreover, patients with bilateral fornix damage show deficits in memory on verbal and non-verbal tasks that tax supraspan item memory, while short-term memory tasks are spared (Hodges and Carpenter, 1991; McMackin et al., 1995). Significant correlations between recollective memory and mammillary body volume in such cases further reinforce the notion that hippocampal–medial diencephalic interactions have a vital role in aspects of episodic memory (Tsivilis et al., 2008). Complementary observations have been made in both fornix-transected monkeys (e.g., Gaffan, 1994) and fornix-transected rats (e.g., Ennaceur and Aggleton, 1997; Easton et al., 2009). The key finding across differing patient groups is that the pattern of memory deficits in diencephalic amnesia appears both qualitatively and quantitatively similar to that in amnesics with relatively selective hippocampal pathology (Aggleton, 2008).

SPATIAL CODING BY NEURONS IN THE MAIN HIPPOCAMPAL OUTPUT: THE SUBICULUM

The subiculum is the main, yet largely underexplored, output target for hippocampal area CA1 (and, thus, for the hippocampus proper). There have been relatively few investigations of the firing properties of subiculum cells, compared to area CA1 place cells; we briefly survey some here. Unlike area CA1, the subiculum displays a remarkable heterogeneity of spatial responding.

Sharp and Green (1994) found that there were indeed subiculum neurons showing location-specific activity; their firing fields tended to be somewhat larger and more variable than those of area CA1. Subicular cells also displayed ectopic spiking—that is, they showed much higher rates of "out-of-field" firing compared to hippocampal CA1 place cells. They also found

that subiculum neurons could be classified as bursting and non-bursting types, based on their spiking, similar to previous observations *in vitro* (see also Stewart and Wong, 1993; Staff et al., 2000; Jung et al., 2001; Anderson and O'Mara, 2003). Recent studies now indicate that sparsely bursting subiculum cells potentially carry more spatial information than other subiculum cell types (Simonnet and Brecht, 2019).

Additionally, Anderson and O'Mara (2004) reported that subiculum cells do not respond to the presence or movement of objects within an arena. Instead, their activity is best predicted by the position and movement of the rat within the arena (behaviorally, the animal did respond to the movement of the objects, suggesting such spatial-object manipulations are subserved by a network independent of the subiculum). Subsequently, Brotons-Mas et al. (2010) reported that about 45% of subiculum place cells show remarkable stability in across multiple light and dark transitions: these cells displayed no evidence for remapping during multiple transitions across light and dark explorations of an open field. The remaining cells showed some degree of remapping, with some units replicating their locational firing across specific light-to-dark conditions, whereas others were strongly affected by light–dark transitions. Brotons-Mas et al. (2010) suggested that because a plurality of units was stable across light–dark transitions, the subiculum participates in or supports the neurocognitive processing underlying path integration because subiculum units appear relatively unresponsive to visual inputs and are perhaps more responsive to cues arising from whole-body movement. Subsequently, Brotons-Mas et al. (2017) conducted extensive spatial phenotyping of subiculum spatial responses using a foraging task in two experimental paradigms—a variably-sized recording arena (small, medium, large), and an arena with systematically inserted barriers in differing locations. Subiculum units showed strongly heterogeneous spatial coding, with place cells, barrier- or perimeter-related cells, as well as boundary-vector cells (Lever et al., 2009), and certain units that showed grid-like patterns of activity in larger arenas.

Adding to this remarkable heterogeneity of cell types, Olson et al. (2017) have described another population of subicular units that code for the axis of travel the animal is currently undertaking. In these experiments, rats foraged in environments with multiple, interconnected paths, of which many had branch-points enabling movement trajectories in opposite directions. Olson et al. (2017) found that about 10% of recorded neurons fired preferentially at head directions approximately 180° apart. Moreover, these firing preferences were preserved during maze rotations, indicating these cells responded to the larger spatial allocentric context, rather than the track itself. These firing preferences were absent during recordings in a trajectory-unconstrained, open-field, circular arena (Olson et al., 2017).

There have been relatively few studies of the subiculum during brain imaging in humans, partly because it is a difficult structure localize using conventional functional magnetic resonance imaging (fMRI) techniques. Two recent studies point to roles for the human subiculum in scene discrimination and head direction processing. Hodgetts et al. (2017), using ultra-high field 7 T high-resolution fMRI, suggest that the subiculum has a particular role during scene, but not face or object, discriminations of previously learned scenes. Kim and Maguire (2018), again using fMRI, had subjects navigate in a 3D space, using a virtual "spaceship." They found activations in the anterior thalamus and subiculum reflecting the horizontal component of 3D head direction (or "azimuth"), whereas retrosplenial cortex responded to the vertical component of 3D head direction ("pitch"). These data suggest a role for the subiculum in both mnemonic and spatial processing in humans. Meanwhile, a very early study in humans (Vitte et al., 1996), using low-field imaging (1.5 T) suggests that vestibular stimulation (cold irrigation of the external auditory meatus) induced strong activations in the hippocampal formation, subiculum, and retrosplenial cortex (Suzuki et al., 2001, using a similar methodology, also found activations in the human intraparietal sulcus). In addition, a study of whole-body motion in nonhuman primates (O'Mara et al., 1994; Figure 9) reported units responsive to axial and translational movement in the hippocampus proper, as well as in the subiculum. It will be particularly interesting to analyze the nature extent of subicular and thalamic activation in humans with ultrahigh field fMRI resulting from caloric stimulation of the vestibular system.

Tentatively, we can conclude that the subiculum appears to code space in a flexible manner, being involved in the processing of allocentric information, external cues, and path integration, thus broadly supporting spatial navigation. It almost certainly has roles in other forms of memory, given its close connectivity to both the hippocampus proper and the anterior thalamic nuclei, although these roles have not yet been fully explored. An example has been suggested by Deadwyler and Hampson (2004), who found that CA1 and subiculum acted in a complementary fashion to bridge temporal gaps during the performance of a spatial delayed nonmatch-to-sample task.

SPATIAL CODING BY NEURONS IN THE ANTERIOR THALAMIC NUCLEI

It has been known for some time that the anterodorsal nucleus of the thalamus contains a substantial population of head-direction cells (Blair and Sharp, 1995; Taube, 1995; Goodridge and Taube, 1997). These cells are thought to contribute to path integration (Frohardt et al., 2006), as well as mapping and navigation in 3D space (Laurens et al., 2016; Page et al., 2018; Angelaki et al., 2019; but see Taube et al., 2013; Shinder and Taube, 2019), the latter function potentially in association with retrosplenial cortex (Kim and Maguire, 2018). Meanwhile, head-direction cells have also been recorded in the anteroventral thalamic nucleus (Tsanov et al., 2011).

Along with the anterodorsal nucleus, the adjacent laterodorsal thalamic nucleus also contains a significant concentration of head-direction cells (Mizumori and Williams, 1993). Again, like the anterodorsal thalamic nucleus, it is reciprocally linked with the retrosplenial cortex, postsubiculum, and presubiculum (van Groen and Wyss, 1992; Clark and Harvey, 2016). Unlike the anterior thalamic nuclei, the laterodorsal nucleus appears to lack inputs from the mammillary bodies, while potentially

being more dependent on its visual inputs (Mizumori and Williams, 1993; Clark and Harvey, 2016). Lesions of the rat laterodorsal nucleus cause mild deficits in location learning in the water maze (van Groen et al., 2002) that are exacerbated when the cell loss extends into the adjacent anterodorsal and anteroventral nuclei (Wilton et al., 2001; van Groen et al., 2002). Transient laterodorsal lesions can disrupt hippocampal place cells and impair spatial learning (Mizumori et al., 1994) while neuropathology in this area has been associated with impairments in conscious recollection (Edelstyn et al., 2006). For these reasons, this nucleus appears to parallel the anterodorsal thalamic nucleus, being distinguished by its greater visual inputs.

Returning to the rostral thalamus, much less is known regarding spatial coding in the other anterior thalamic nuclei and other rostral thalamic nuclei, i.e., excluding the anterodorsal nucleus. These additional thalamic sites are, however, of particular interest as the subiculum provides dense, direct inputs to the anteromedial and anteroventral nuclei, contrasting with the projections from the postsubiculum and presubiculum to the anterodorsal thalamic nuclei (Meibach and Siegel, 1977; van Groen and Wyss, 1990a,b; Bubb et al., 2017; **Figure 1**). Of the various midline nuclei, nucleus reuniens stands out because of its inputs from the subiculum and CA1, as well as its dense, direct projections to the hippocampus, especially to CA1 (Herkenham, 1978; Vertes et al., 2007). Based on their respective connectivity, it had previously been predicted that the anterior thalamic nuclei process information with high spatial and temporal resolution (Aggleton et al., 2010), whereas rostral midline thalamic nuclei have more diffuse roles in attention, control, and arousal (Van der Werf et al., 2002; Vertes et al., 2007). Our current findings strongly support the first prediction but appear to substantially moderate the second prediction, because they show the widespread presence of a diverse population of spatially-responsive neurons in these midline nuclei.

In nucleus reuniens, for example, there is an (unexpected) population of cells coding for head direction (Jankowski et al., 2014), extending the numbers of brain regions coding for head direction to at least 10 (Grieves and Jeffery, 2017). The head-direction cells found in nucleus reuniens are similar in a great many respects to those found in other regions that show head-direction coding: they are not affected by changing visual conditions from light to dark and back to light, or by changing arena shape; they do not remap across days, maintaining a constant orientation. They are also present from the first exposure to the recording environment. Interestingly, theta-cycle skipping cells are also present in nucleus reuniens, similar to the theta-skipping cells found in entorhinal cortex (e.g., Brandon et al., 2013); theta-skipping cells in nucleus reuniens do not code either for head-direction or for place and may instead perform a clock-like or timing function. Finally, nucleus reuniens head-direction cells are not place cells: they are not spatially-modulated in the sense of having a place-related signal (Jankowski et al., 2014).

Nucleus reuniens also provides a substantial anatomical output to hippocampal area CA1, offering a means by which it can modulate spatial coding in the hippocampus proper. For example, combined lesions of the rhomboid nucleus and nucleus reuniens (ReRh) seemingly spare CA1 place cell spatial characteristics in familiar environments, but affect firing in unfamiliar environments (Cholvin et al., 2018). In that experiment, after ReRh lesions, spatial coherence decreased for the first exploration session in a novel environment. Recordings conducted over a 5-day period then showed that ReRh lesions result in a marked and enduring decrease in place field stability and lower firing variability (Cholvin et al., 2018). These data suggest that inputs from ReRh modulate spatial remapping in the hippocampus; it may be that the head directional signal provides a stabilizing directional signal while exploring unfamiliar environments.

Jankowski et al. (2015) recorded in the parataenial nucleus, anteromedial nucleus, and nucleus reuniens, finding place cells and other spatial cells in each of these nuclei. In the parataenial nucleus 29.2% of cells recorded were place cells, whereas 6.2% of cells recorded in the anteromedial nucleus were place cells, with head-direction cells a further 9.7% of recorded cells, with a small number of perimeter/border cells (0.5%). The percentages of place cells recorded in nucleus reuniens was 2.0%, and 2.0% perimeter/border cells; head-direction cells were described separately and quantified at 8.7% (Jankowski et al., 2014). The variation in the percentage of place cells present across these nuclei suggests that the spatial code is more or less sparse for the differing nuclei. More than this, the phenotypic characteristics of the place cells vary in these differing nuclei, with the place fields of cells in nucleus reuniens being the largest and, thereby, carrying the lowest spatial information. Meanwhile, the place fields in the parataenial nucleus occupy the smallest percentage of the recording arena, carrying the highest spatial information. The anteromedial nucleus occupies an intermediate position. In other words, across these anatomically-closely-related nuclei, there appears to be a spatial information content gradient.

In addition to place cells, there is also a population of neurons that respond to the presence of impassable perimeters in the recording arena. These neurons are found in nucleus reuniens and the anteromedial thalamic nucleus (Jankowski et al., 2015). Temporal evolution analyses suggest that the perimeter cells and place cells in these nuclei appear on the first exposure of the animal to the arena. Finally, as noted above, recordings in the anteromedial nucleus of the thalamus also disclose a population of head-direction cells in a hitherto unsuspected and untheorized-about location. These head-direction cells are active also from the first exposure of the animal to the arena, suggesting that early pre-processing of spatial information occurs rapidly in subcortical brain structures.

Perimeters are an important part of the environment, as they formally shape the geometry of the perceptible environment, as well as constraining behavioral trajectories. Perimeters can comprise vertical walls, vertical drops, watercourses, etc.; they can be impassable, or can be passed through at crossings of various types (some perimeters may be perceptual, as in light-to-dark perimeters, perhaps signaling danger or safety). Matulewicz et al. (2019) have surveyed perimeter-related discharge of units in the anteromedial and parataenial

nuclei. Matulewicz et al. (2019) found neurons whose firing patterns reflected the presence of walls and drops, irrespective of arena shape (circular or square). Moreover, the firing patterns of these perimeter-responsive units were stable across multiple sleep-wake cycles, and were independent of either light or dark conditions, suggesting that these units are not directly modulated by visual input. Furthermore, these neurons respond in similar ways to both opaque and clear barriers; this latter feature is remarkable because "see-through" or clear barriers (such as Plexiglas) are not part of the natural environment. These neurons respond to perimeter modifications by remapping their firing when two walls of the four present in a rectangular recording arena are removed from recording session to recording session. Further experiments will be required to further explore potential coding differences induced by distal landmarks and proximal tactile cues, under conditions where these information types are explicitly opposed to each other.

SUMMARY OF SPATIAL CODING BY ANTERIOR THALAMIC NUCLEI

Overall, recordings within the various rostral thalamic nuclei reveal the presence of spatially-responsive cells. The origin of their spatial signals is not yet known, leaving us with (at least) three hypotheses to entertain. The first is that the hippocampal and rostral thalamic spatial systems operate in parallel (in a fashion similar to the accessory optic system); the second is that one is subordinate to the other, for example, the hippocampal formation provides information necessary for the spatial activity observed in the rostral thalamus, or *vice versa*; and third, that there are reciprocal and interdependent relationships between these spatial nodes.

Current findings only provide an incomplete data-set with regard to these three hypotheses. Most of the focus has been on the consequences of anterior thalamic lesions upon hippocampal and parahippocampal activity, stemming from the significance of the anterodorsal nucleus for head-direction signals (Taube, 1995). Consequently, it is known that anterior thalamic lesions cause an absence of postsubiculum head-direction signals (Goodridge and Taube, 1997). While postsubiculum lesions change the properties of anterodorsal head-direction cells, these spatial cells are still present (Goodridge and Taube, 1997), reflecting an asymmetric relationship. Likewise, medial entorhinal cortex lesions leave anterior thalamic head direction activity largely unaffected (Clark and Taube, 2011). In contrast, a disruption of the head-direction network following anterior thalamic lesions impairs parahippocampal "grid cell" activity (Winter et al., 2015). Meanwhile, CA1 place cells appear largely unaffected after anterior thalamic lesions (Calton et al., 2003), although there are alterations to firing patterns in unfamiliar environments after nucleus reuniens lesions (Cholvin et al., 2018). Consequently, with the exception of the head-direction network, little is known about the interdependencies of the various spatial cell types found in the hippocampal formation and anterior thalamus.

SPATIAL SIGNALING AND OTHER POSSIBLE FUNCTIONS PERFORMED BY THE CLAUSTRUM

The claustrum is an underexplored and enigmatic paracortical structure. The claustrum of the rat is a bilateral subcortical sheet of gray matter, spanning approximately the rostral half of the telencephalon, almost to the frontal poles, and caudally to the motor strip. It is bordered by the orbitofrontal cortex, rostrally, both caudally and medially by the caudoputamen, and by the insular cortex laterally (Buchanan and Johnson, 2011; Dillingham et al., 2017, 2019). Anatomically, the claustrum receives projections from the entire cortical mantle. These projections are organized in a topographic fashion, with association cortex projecting to the anterior claustrum and sensory cortices projecting to the posterior portion of the claustrum. In addition, there are also claustrum connections to and from the hippocampal formation, retrosplenial cortex, entorhinal cortex, and a wide variety of subcortical structures, although the existence of projections from the anterior thalamus to the claustrum continues to be a matter of debate (Dillingham et al., 2017, 2019). Comprehensive lesion investigations of the claustrum have yet to be undertaken for technical reasons: the claustrum is a difficult target for the injection-targeting used in lesion analyses, although chemogenetic approaches (such as DREADDs) may prove more tractable.

There have been many hypotheses regarding the functions of the claustrum over the years, most notably that it orchestrates consciousness in the mammalian brain (Crick and Koch, 2005). There have been intermittent anatomical explorations of the claustrum that conclude it does not comprise striatal tissue, but rather can be thought best of as a paracortical tissue. Functional investigations of the claustrum are relatively few in number; we briefly survey some relevant studies here. There have been very few lesion studies of the claustrum. Aclaustral humans are rarely reported: one study of a patient with striking, transient, but symmetric, bilateral, claustral lesions arising from mumps encephalitis (Ishii et al., 2011) reported that during the acute phase of infection the patient experienced visual and auditory hallucinations that resolved with treatment for concurrent epilepsy. With the infection resolved, subsequent imaging showed no persisting lesions of the bilateral claustrum. Intriguingly, Cascella et al. (2011) reported that schizophrenic patients with delusions may have an atrophic left claustrum.

The possible relationship between the claustrum and consciousness continues to receive interest. In an early report, Gabor and Peele (1964) found that electrical stimulation of the claustrum in the awake behaving cat resulted in a state of behavioral relaxation and subsequent induction of sleep.

Koubeissi et al. (2014) investigated a human epilepsy patient implanted with deep-brain electrodes in the claustrum, reporting loss of consciousness on stimulation onset and return of consciousness on stimulus offset. The patient had previously undergone a left hippocampal resection for epilepsy; she was seizure-free for 4 years, after which her seizures returned. Depth electrodes were implanted for seizure sampling. The results of

stimulation of the claustral electrode were dramatic: stimulation "resulted in immediate impairment of consciousness, in 10 out of 10 times, with arrest of reading, onset of blank staring, unresponsiveness to auditory or visual commands, and slowing of spontaneous respiratory movements. The patient returned to baseline as soon as the stimulation stopped with no recollection of the events during the stimulation period." However, a more recent report of bilateral claustral stimulation in five patients (Bickel and Parvizi, 2019) reported that no "changes in subject's awareness were elicited with unilateral or bilateral electrical perturbation of the claustrum." It is unclear why the earlier report was not replicated. Perhaps minor differences in electrode placement in the claustrum result in major differences for awareness, or perhaps there is an idiopathic (and perhaps unique) neurological circumstance in the earlier report. Or it might be the case that the claustrum plays a role in orchestrating some of the cortical changes occurring during the wake-sleep transition (Renouard et al., 2015).

Olson and Graybiel (1980) suggested that there is a somatosensory map of the complete surface of the body, arranged longitudinally in the claustrum (in the anesthetized cat preparation). Remedios et al. (2010) have recorded claustral neurons in the conscious, behaving, head-fixed non-human primate, finding neurons responsive to a variety of naturalistic sensory stimuli, especially auditory and visual stimuli. They concluded that the claustrum overall is a multisensory structure, but that individual claustral neurons are unimodal, and that these unimodal neurons are the prevalent neurons present in this preparation. Remedios et al. (2012) also reported in conference proceedings that when aclaustral rats were placed in the center of an eight-arm radial arm maze, they would freeze, apparently unable or unwilling to explore any of the arms. These data await a full report, however.

Jankowski and O'Mara (2015) conducted what appears to be the first freely moving recordings in the rat claustrum. These recordings, remarkably, disclose the existence of a population of spatially-responsive neurons in the claustrum, including place cells, perimeter cells, and object responsive cells. Claustral place cells do not remap during light-dark-light transitions, although their spatial information content falls a little in the dark and is restored in the light. Visual input, therefore, does not seem to affect claustral place cell position, although it does have some effect on claustral place cell spatial information content. Analyses of the temporal evolution of claustral place cells show that they appear to be present from the earliest exposure to the environment. Object responsive cells in the claustrum react to the initial presentation of an object (for example, a glass bottle) with increased firing activity around the object, and near-zero firing activity away from the object. These cells track the repositioning of the object (Jankowski and O'Mara, 2015). Moreover, claustral place cells do not respond to the presence of an object. By contrast, the firing fields of claustral object-responsive cells track the positioning and repositioning of the object in the environment. Claustral units also respond to the perimeter of the environment, showing a penumbra of activity associated with an impassable perimeter. This firing field is very tightly bound to the perimeter, and such cells exhibit near-zero firing rates away from the perimeter itself. Finally, Jankowski and O'Mara (2015) also noted the presence of both theta-modulated and fast-firing bursting cells in the claustrum. The fast-firing cells fired up to 30 Hz or more. These fast-firing cells are not spatially-modulated or spatially-responsive.

One hypothesis that accounts for this unexpected pattern of activity is that the claustrum dynamically represents extended space (in a similar fashion to hippocampal area CA1) but that the claustrum also incorporates landmark (or object) information. We have not, however, observed the presence of head-direction cells in the claustrum. The existence of claustral spatial cells is remarkable, as they are currently unpredicted by any current theory of claustral function, or indeed, any more general theory of the representation of space within the mammalian brain. It may be that the claustrum provides dynamic information about body position and landmark information to the cortex in order to enable moment-to-moment control of behavior.

SPATIAL PROCESSING ACROSS DIFFERING STRUCTURES

A remarkably diverse, but anatomically interconnected, set of neural structures support similar aspects of spatial coding within the brain. **Figure 1** illustrates this contention in respect of anterior thalamic nuclei and related structures. Neurons coding for head-direction are found distributed across eight of these structures; neurons coding for place are found in six of these structures; neurons coding for borders or perimeters are found in four structures; and grid cells are found in at least three of these structures. Notably, several structures code for diverse aspects of space, simultaneously. The subiculum possesses border, grid and place cells, as does nucleus reuniens, for example. The head-direction signal is very widely distributed; in their review, Grieves and Jeffery (2017) find head-directional coding is present in at least eleven distinct but interconnected brain regions (across cortical and subcortical structures). This very widespread distribution of head direction signals suggests head direction coding may play a greater, but more subtle role, in cognition than is generally recognized (O'Mara, 2017). Head direction information may reflect in some structures the continuous recalibration of orienting or attentional responses (e.g., during social interaction; Nummenmaa and Calder, 2009), whereas in other structures it might play a fundamental role in the stable coding of place (see Cholvin et al., 2018). A richer panoply of tasks will be required to test such ideas. The same may be true of the other signals; for many years there was an apparent absence of place cells outside the hippocampus proper. This absences of evidence may simply reflect the conservatism of neural cartographers, rather than a conservatism of the representation of space within diverse brain structures. It is apparent, however, that there is a rich and diverse representation of space far beyond the confines of the entorhinal-hippocampal neuraxis. Moreover, such considerations lend weight to the view that the brain is especially concerned with action-oriented cognitive processing (Gentsch et al., 2016).

SOME SPECULATIONS AND CONCLUSIONS

The hippocampal formation, anterior thalamus, and claustrum show a remarkable rapidity and speed of spatial coding. Maps of space emerge very rapidly and are representationally rich. At present, we do not have a good theoretical account for why there is such redundancy in spatial representations in the brain, nor do we have a good theory to predict across differing neural systems the rapid emergence of such representationally rich coding. One hypothesis worth considering is that of Barsalou (2010) who suggests that "The cognitive system utilizes the environment and the body as external informational structures that complement internal representations….internal representations of a situated character, implemented *via* simulations in the brain's modal systems, making them well suited for interfacing with external structures". There has been comparatively little consideration given in contemporary neuroscience to the idea that the brain uses the external environment as a kind of "cognitive surface," or that it supports the structure of cognition. This might reflect the bias in sensory neuroscience, which has followed the stimulus from the receptor surface into the brain. However, behavioral responses are not aligned along sensory axes; rather, intrinsic activity within the brain determines, in large part, the nature of the processing of sensory stimuli are subjected to (Raichle, 2015; Yamins and DiCarlo, 2016; Dadarlat and Stryker, 2017; Stringer et al., 2019).

The hypothesis that the anterior thalamus engages in extensive pre-processing of stimuli, and generates the elements, or at least some elements of a cognitive map, is an attractive one, for it allows an exploration of the idea that differing types of maps are important at differing temporal scales. Such maps might be adaptively significant, depending on the behavioral and environmental context of the organism. Invoking action maps to escape a predator requires instantaneous action selection and route selection, whereas latent learning during safe periods of exploration might instead operate on an entirely different temporal scale. It may be that the claustrum, given its cortical anatomical position and connectivity allows the rapid selection of action responses in 3D space, when there are temporal constraints requiring the rapid co-ordination of adaptive behavioral responses. The extended hippocampal formation (entorhinal cortex-hippocampus-anterior thalamus) might, by contrast, be more specifically engaged in richer representational action over longer time scales (an idea that finds merit in the possible role of the extended hippocampal formation in imagination and prospection: Buckner, 2010; Maguire and Hassabis, 2011; Zeidman and Maguire, 2016). In turn, it may be that the evolved and adaptive function of memory is to serve present and possible future biological needs, rather than recalling the past in any veridical sense. Hence, the loss of detail over time often observed for many autobiographical experiences; supporting such a view, Conway (2005) suggests, for example, that "for many experiences simply recalling the meaning or the 'gist' may be sufficient".

Finally, we note that biologically-inspired models of spatial navigation rely on core ideas revolving around the dissociation of place information from heading information and their subsequent integration in other downstream areas to facilitate goal-directed navigation (e.g., Barrera and Weitzenfeld, 2008). Here, we suggest that there are important components of this overall theoretical picture missing, in particular relating to an extended and extensive variety of evolutionarily-conserved brain regions (notably the thalamic nuclei, but also the claustrum), which support a wide range of spatial functions. These brain regions continue to be under-explored to this point. We further suggest that significant revision of current models of how the brain controls behavioral choices in a spatial context may be warranted.

AUTHOR CONTRIBUTIONS

SO and JA jointly conceived and jointly wrote the manuscript.

FUNDING

The work described here was supported in part by a Wellcome Trust Senior Investigator Award to JA and SO, and a Science Foundation Ireland Principal Investigator Award #103722/Z14/Z to SO.

REFERENCES

Aggleton, J. P. (2008). Understanding anterograde amnesia: disconnections and hidden lesions. *Q. J. Exp. Psychol.* 61, 1441–1471. doi: 10.1080/17470210802215335

Aggleton, J. P., and Brown, M. W. (1999). Episodic memory, amnesia and the hippocampal-anterior thalamic axis. *Behav. Brain Sci.* 22, 425–444. doi: 10.1017/s0140525x99002034

Aggleton, J. P., and Morris, R. G. (2018). Memory: looking back and looking forward. *Brain Neurosci. Adv.* 2:2398212818794830. doi: 10.1177/2398212818794830

Aggleton, J. P., O'Mara, S. M., Vann, S. D., Wright, N. F., Tsanov, M., and Erichsen, J. T. (2010). Hippocampal-anterior thalamic pathways for memory: uncovering a network of direct and indirect actions. *Eur. J. Neurosci.* 31, 2292–2307. doi: 10.1111/j.1460-9568.2010.07251.x

Albert, M. S., Butters, N., and Levin, J. (1979). Temporal gradients in the retrograde amnesia of patients with alcoholic Korsakoff's disease. *Arch. Neurol.* 36, 211–216. doi: 10.1001/archneur.1979.00500400065010

Anderson, M. I., and O'Mara, S. M. (2003). Analysis of recordings of single-unit firing and population activity in the dorsal subiculum of unrestrained, freely moving rats. *J. Neurophysiol.* 90, 655–665. doi: 10.1152/jn.00723.2002

Anderson, M. I., and O'Mara, S. M. (2004). Responses of dorsal subicular neurons of rats during object exploration in an extended environment. *Exp. Brain Res.* 159, 519–529. doi: 10.1007/s00221-004-1977-z

Angelaki, D. E., Ng, J., Abrego, A. M., Cham, H. X., Dickman, J. D., and Laurens, J. (2019). A gravity-based three-dimensional compass in the mouse brain. *BioRxiv* [Preprint]. doi: 10.1101/570382

Annese, J., Schenker-Ahmed, N. M., Bartsch, H., Maechler, P., Sheh, C., Thomas, N., et al. (2014). Postmortem examination of patient HM's brain based on histological sectioning and digital 3D reconstruction. *Nat. Commun.* 5:3122. doi: 10.1038/ncomms4122

Barrera, A., and Weitzenfeld, A. (2008). Biologically-inspired robot spatial cognition based on rat neurophysiological studies. *Auton. Robot.* 25, 147–169. doi: 10.1007/s10514-007-9074-3

Barsalou, L. W. (2010). Grounded cognition: past, present and future. *Top. Cogn. Sci.* 2, 716–724. doi: 10.1111/j.1756-8765.2010.01115.x

Bickel, S., and Parvizi, J. (2019). Electrical stimulation of the human claustrum. *Epil. Behav.* doi: 10.1016/j.yebeh.2019.03.051 [Epub ahead of print].

Blair, H. T., and Sharp, P. E. (1995). Anticipatory head direction signals in anterior thalamus: evidence for a thalamocortical circuit that integrates angular head motion to compute head direction. *J. Neurosci.* 15, 6260–6270. doi: 10.1523/jneurosci.15-09-06260.1995

Bliss, T. V., and Collingridge, G. L. (1993). A synaptic model of memory: long-term potentiation in the hippocampus. *Nature* 361, 31–39. doi: 10.1038/361031a0

Bliss, T. V., and Lømo, T. (1973). Long-lasting potentiation of synaptic transmission in the dentate area of the anaesthetized rabbit following stimulation of the perforant path. *J. Physiol.* 232, 331–356. doi: 10.1113/jphysiol.1973.sp010273

Brandon, M. P., Bogaard, A. R., Schultheiss, N. W., and Hasselmo, M. E. (2013). Segregation of cortical head direction cell assemblies on alternating θ cycles. *Nat. Neurosci.* 16, 739–748. doi: 10.1038/nn.3383

Brotons-Mas, J. R., Montejo, N., O'Mara, S. M., and Sanchez-Vives, M. V. (2010). Stability of subicular place fields across multiple light and dark transitions. *Eur. J. Neurosci.* 32, 648–658. doi: 10.1111/j.1460-9568.2010.07308.x

Brotons-Mas, J. R., Schaffelhofer, S., Guger, C., O'Mara, S. M., and Sanchez-Vives, M. V. (2017). Heterogeneous spatial representation by different subpopulations of neurons in the subiculum. *Neuroscience* 343, 174–189. doi: 10.1016/j.neuroscience.2016.11.042

Bubb, E. J., Kinnavane, L., and Aggleton, J. P. (2017). Hippocampal-diencephalic-cingulate networks for memory and emotion: an anatomical guide. *Brain Neurosci. Adv.* 1:2398212817723443. doi: 10.1177/23982128177 23443

Buchanan, K. J., and Johnson, J. I. (2011). Diversity of spatial relationships of the claustrum and insula in branches of the mammalian radiation. *Ann. N Y Acad. Sci.* 1225, E30–E63. doi: 10.1111/j.1749-6632.2011.06022.x

Buckner, R. L. (2010). The role of the hippocampus in prediction and imagination. *Annu. Rev. Psychol.* 61, 27–48. doi: 10.1146/annurev.psych.60. 110707.163508

Buzsáki, G., and Moser, E. I. (2013). Memory, navigation and theta rhythm in the hippocampal-entorhinal system. *Nat. Neurosci.* 16, 130–138. doi: 10.1038/nn. 3304

Calton, J. L., Stackman, R. W., Goodridge, J. P., Archey, W. B., Dudchenko, P. A., and Taube, J. S. (2003). Hippocampal place cell instability after lesions of the head direction cell network. *J. Neurosci.* 23, 9719–9731. doi: 10.1523/jneurosci. 23-30-09719.2003

Carlesimo, G. A., Lombardi, M. G., and Caltagirone, C. (2011). Vascular thalamic amnesia: a reappraisal. *Neuropsychologia* 49, 777–789. doi: 10.1016/j. neuropsychologia.2011.01.026

Cascella, N. G., Gerner, G. J., Fieldstone, S. C., Sawa, A., and Schretlen, D. J. (2011). The insula-claustrum region and delusions in schizophrenia. *Schizophr. Res.* 133, 77–81. doi: 10.1016/j.schres.2011.08.004

Cholvin, T., Hok, V., Giorgi, L., Chaillan, F. A., and Poucet, B. (2018). Ventral midline thalamus is necessary for hippocampal place field stability and cell firing modulation. *J. Neurosci.* 38, 158–172. doi: 10.1523/JNEUROSCI.2039-17. 2017

Clark, B. J., and Harvey, R. E. (2016). Do the anterior and lateral thalamic nuclei make distinct contributions to spatial representation and memory? *Neurobiol. Learn. Mem.* 133, 69–78. doi: 10.1016/j.nlm.2016.06.002

Clark, B. J., and Taube, J. S. (2011). Intact landmark control and angular path integration by head direction cells in the anterodorsal thalamus after lesions of the medial entorhinal cortex. *Hippocampus* 21, 767–782. doi: 10.1002/hipo. 20874

Conway, M. A. (2005). Memory and the self. *J. Mem. Lang.* 53, 594–628. doi: 10.1016/j.jml.2005.08.005

Crick, F. C., and Koch, C. (2005). What is the function of the claustrum? *Philos. Trans. R. Soc. Lond. B Biol. Sci.* 360, 1271–1279. doi: 10.1098/rstb.2005.1661

Dadarlat, M. C., and Stryker, M. P. (2017). Locomotion enhances neural encoding of visual stimuli in mouse V1. *J. Neurosci.* 37, 3764–3775. doi: 10.1523/JNEUROSCI.2728-16.2017

Deadwyler, S. A., and Hampson, R. E. (2004). Differential but complementary mnemonic functions of the hippocampus and subiculum. *Neuron* 42, 465–476. doi: 10.1016/S0896-6273(04)00195-3

Delay, J., and Brion, S. (1969). *Le Syndrome de Korsakoff*. Paris: Masson.

Dillingham, C. M., Jankowski, M. M., Chandra, R., Frost, B. E., and O'Mara, S. M. (2017). The claustrum: considerations regarding its anatomy, functions and a programme for research. *Brain Neurosci. Adv.* 1:2398212817718962. doi: 10.1177/2398212817718962

Dillingham, C. M., Mathiasen, M. L., Frost, B. E., Lambert, M. A., Bubb, E. J., Jankowski, M. M., et al. (2019). The anatomical boundary of the rat claustrum. *Front. Neuroanat.* 13:53. doi: 10.3389/fnana.2019.00053

Easton, A., Zinkivskay, A., and Eacott, M. J. (2009). Recollection is impaired, but familiarity remains intact in rats with lesions of the fornix. *Hippocampus* 19, 837–843. doi: 10.1002/hipo.20567

Edelstyn, N. M., Hunter, B., and Ellis, S. J. (2006). Bilateral dorsolateral thalamic lesions disrupts conscious recollection. *Neuropsychologia* 44, 931–938. doi: 10.1016/j.neuropsychologia.2005.08.012

Ennaceur, A., and Aggleton, J. P. (1997). The effects of neurotoxic lesions of the perirhinal cortex combined to fornix transection on object recognition memory in the rat. *Behav. Brain Res.* 88, 181–193. doi: 10.1016/s0166-4328(97)02297-3

Frohardt, R. J., Bassett, J. P., and Taube, J. S. (2006). Path integration and lesions within the head direction cell circuit: comparison between the roles of the anterodorsal thalamus and dorsal tegmental nucleus. *Behav. Neurosci.* 120, 135–149. doi: 10.1037/0735-7044.120.1.135

Gabor, A. J., and Peele, T. L. (1964). Alterations of behavior following stimulation of the claustrum of the cat. *Electroencephalogr. Clin. Neurophysiol.* 17, 513–519. doi: 10.1016/0013-4694(64)90181-6

Gaffan, D. (1994). Scene-specific memory for objects: a model of episodic memory impairment in monkeys with fornix transection. *J. Cogn. Neurosci.* 6, 305–320. doi: 10.1162/jocn.1994.6.4.305

Gentsch, A., Weber, A., Synofzik, M., Vosgerau, G., and Schütz-Bosbach, S. (2016). Towards a common framework of grounded action cognition: relating motor control, perception and cognition. *Cognition* 146, 81–89. doi: 10.1016/j. cognition.2015.09.010

Goodridge, J. P., and Taube, J. S. (1997). Interaction between the postsubiculum and anterior thalamus in the generation of head direction cell activity. *J. Neurosci.* 17, 9315–9330. doi: 10.1523/jneurosci.17-23-09315.1997

Grewe, B. F., Gründemann, J., Kitch, L. J., Lecoq, J. A., Parker, J. G., Marshall, J. D., et al. (2017). Neural ensemble dynamics underlying a long-term associative memory. *Nature* 543, 670–675. doi: 10.1038/nature21682

Grieves, R. M., and Jeffery, K. J. (2017). The representation of space in the brain. *Behav. Processes* 135, 113–131. doi: 10.1016/j.beproc.2016.12.012

Hafting, T., Fyhn, M., Molden, S., Moser, M. B., and Moser, E. I. (2005). Microstructure of a spatial map in the entorhinal cortex. *Nature* 436, 801–806. doi: 10.1038/nature03721

Harding, A., Halliday, G., Caine, D., and Kril, J. (2000). Degeneration of anterior thalamic nuclei differentiates alcoholics with amnesia. *Brain* 123, 141–154. doi: 10.1093/brain/123.1.141

Hebb, D. O. (1949). *The Organization of Behavior: A Neuropsychological Theory*. New York, NY: Wiley.

Herkenham, M. (1978). The connections of the nucleus reuniens thalami: evidence for a direct thalamo-hippocampal pathway in the rat. *J. Comp. Neurol.* 177, 589–609. doi: 10.1002/cne.901770405

Herman, J. P., and Mueller, N. K. (2006). Role of the ventral subiculum in stress integration. *Behav. Brain Res.* 174, 215–224. doi: 10.1016/j.bbr.2006.05.035

Hodges, J. R., and Carpenter, K. (1991). Anterograde amnesia with fornix damage following removal of IIIrd ventricle colloid cyst. *J. Neurol. Neurosurg. Psychiatry* 54, 633–638. doi: 10.1136/jnnp.54.7.633

Hodgetts, C. J., Voets, N. L., Thomas, A. G., Clare, S., Lawrence, A. D., and Graham, K. S. (2017). Ultra-high-field fMRI reveals a role for the subiculum in scene perceptual discrimination. *J. Neurosci.* 37, 3150–3159. doi: 10.1523/JNEUROSCI.3225-16.2017

Hull, C. L. (1943). *Principles of Behavior: An Introduction to Behavior Theory*. New York, NY: Appleton-Century-Crofts.

Hunsaker, M. R., and Kesner, R. P. (2018). Unfolding the cognitive map: the role of hippocampal and extra-hippocampal substrates based on a systems analysis of spatial processing. *Neurobiol. Learn. Mem.* 147, 90–119. doi: 10.1016/j.nlm. 2017.11.012

Ishii, K., Tsuji, H., and Tamaoka, A. (2011). Mumps virus encephalitis with symmetric claustrum lesions. *AJNR Am. J. Neuroradiol.* 32:E139. doi: 10.3174/ajnr.A2603

Jankowski, M. M., Islam, M. N., and O'Mara, S. M. (2017). Dynamics of spontaneous local field potentials in the anterior claustrum of freely moving rats. *Brain Res.* 1677, 101–117. doi: 10.1016/j.brainres.2017.09.021

Jankowski, M. M., Islam, M. N., Wright, N. F., Vann, S. D., Erichsen, J. T., Aggleton, J. P., et al. (2014). Nucleus reuniens of the thalamus contains head direction cells. *Elife* 3:e03075. doi: 10.7554/eLife.03075

Jankowski, M. M., and O'Mara, S. M. (2015). Dynamics of place, boundary and object encoding in rat anterior claustrum. *Front. Behav. Neurosci.* 9:250. doi: 10.3389/fnbeh.2015.00250

Jankowski, M. M., Passecker, J., Islam, M. N., Vann, S., Erichsen, J. T., Aggleton, J. P., et al. (2015). Evidence for spatially-responsive neurons in the rostral thalamus. *Front. Behav. Neurosci.* 9:256. doi: 10.3389/fnbeh.2015.00256

Jung, H. Y., Staff, N. P., and Spruston, N. (2001). Action potential bursting in subicular pyramidal neurons is driven by a calcium tail current. *J. Neurosci.* 21, 3312–3321. doi: 10.1523/jneurosci.21-10-03312.2001

Kim, M., and Maguire, E. A. (2018). Encoding of 3D head direction information in the human brain. *Hippocampus* 29, 619–629. doi: 10.1002/hipo.23060

Kolb, B., and Whishaw, I. Q. (1989). Plasticity in the neocortex: mechanisms underlying recovery from early brain damage. *Prog. Neurobiol.* 32, 235–276. doi: 10.1016/0301-0082(89)90023-3

Koubeissi, M. Z., Bartolomei, F., Beltagy, A., and Picard, F. (2014). Electrical stimulation of a small brain area reversibly disrupts consciousness. *Epilepsy Behav.* 37, 32–35. doi: 10.1016/j.yebeh.2014.05.027

Krupic, J., Bauza, M., Burton, S., Barry, C., and O'Keefe, J. (2015). Grid cell symmetry is shaped by environmental geometry. *Nature* 518, 232–235. doi: 10.1038/nature14153

Larkin, A. E., Fahey, B., Gobbo, O., Callaghan, C. K., Cahill, E., O'Mara, S. M., et al. (2008). Blockade of NMDA receptors pre-training, but not post-training, impairs object displacement learning in the rat. *Brain Res.* 1199, 126–132. doi: 10.1016/j.brainres.2008.01.019

Laurens, J., Kim, B., Dickman, J. D., and Angelaki, D. E. (2016). Gravity orientation tuning in macaque anterior thalamus. *Nat. Neurosci.* 19, 1566–1568. doi: 10.1038/nn.4423

Lever, C., Burton, S., Jeewajee, A., O'Keefe, J., and Burgess, N. (2009). Boundary vector cells in the subiculum of the hippocampal formation. *J. Neurosci.* 29, 9771–9777. doi: 10.1523/JNEUROSCI.1319-09.2009

Lowry, C. A. (2002). Functional subsets of serotonergic neurones: implications for control of the hypothalamic-pituitary-adrenal axis. *J. Neuroendocrinol.* 14, 911–923. doi: 10.1046/j.1365-2826.2002.00861.x

Lynch, M. A. (2004). Long-term potentiation and memory. *Physiol. Rev.* 84, 87–136. doi: 10.1152/physrev.00014.2003

Maguire, E. A., and Hassabis, D. (2011). Role of the hippocampus in imagination and future thinking. *Proc. Natl. Acad. Sci. U S A* 108:E39. doi: 10.1073/pnas.1018876108

Mair, W. G., Warrington, E. K., and Weiskrantz, L. (1979). Memory disorder in Korsakoff's psychosis: a neuropathological and neuropsychological investigation of two cases. *Brain* 102, 749–783. doi: 10.1093/brain/102.4.749

Malenka, R. C., and Bear, M. F. (2004). LTP and LTD: an embarrassment of riches. *Neuron* 44, 5–21. doi: 10.1016/j.neuron.2004.09.012

Matulewicz, P., Ulrich, K., Islam, M. N., Mathiasen, M. L., Aggleton, J. P., and O'Mara, S. M. (2019). Proximal perimeter encoding in the rat rostral thalamus. *Sci. Rep.* 9:2865. doi: 10.1038/s41598-019-39396-8

Mayes, A. R., Meudell, P. R., Mann, D., and Pickering, A. (1988). Location of lesions in Korsakoff's syndrome: neuropsychological and neuropathological data on two patients. *Cortex* 24, 367–388. doi: 10.1016/s0010-9452(88)80001-7

McCormick, D. A., and Thompson, R. F. (1984). Cerebellum: essential involvement in the classically conditioned eyelid response. *Science* 223, 296–299. doi: 10.1126/science.6701513

McMackin, D., Cockburn, J., Anslow, P., and Gaffan, D. (1995). Correlation of fornix damage with memory impairment in six cases of colloid cyst removal. *Acta Neurochir.* 135, 12–18. doi: 10.1007/bf02307408

Meibach, R. C., and Siegel, A. (1977). Thalamic projections of the hippocampal formation: evidence for an alternate pathway involving the internal capsule. *Brain Res.* 134, 1–12. doi: 10.1016/0006-8993(77)90921-0

Mizumori, S. J. Y., Miya, D. Y., and Ward, K. E. (1994). Reversible inactivation of the lateral dorsal thalamus disrupts hippocampal place representation and impairs spatial learning. *Brain Res.* 644, 168–174. doi: 10.1016/0006-8993(94)90361-1

Mizumori, S. J., and Williams, J. D. (1993). Directionally selective mnemonic properties of neurons in the lateral dorsal nucleus of the thalamus of rats. *J. Neurosci.* 13, 4015–4028. doi: 10.1523/jneurosci.13-09-04015.1993

Myers, B., Scheimann, J. R., Franco-Villanueva, A., and Herman, J. P. (2017). Ascending mechanisms of stress integration: implications for brainstem regulation of neuroendocrine and behavioral stress responses. *Neurosci. Biobehav. Rev.* 74, 366–375. doi: 10.1016/j.neubiorev.2016.05.011

Nummenmaa, L., and Calder, A. J. (2009). Neural mechanisms of social attention. *Trends Cogn. Sci.* 13, 135–143. doi: 10.1016/j.tics.2008.12.006

O'Keefe, J., and Burgess, N. (1996). Geometric determinants of the place fields of hippocampal neurons. *Nature* 381, 425–428. doi: 10.1038/381425a0

O'Keefe, J., and Dostrovsky, J. (1971). The hippocampus as a spatial map: preliminary evidence from unit activity in the freely-moving rat. *Brain Res.* 34, 171–175. doi: 10.1016/0006-8993(71)90358-1

O'Keefe, J., and Nadel, L. (1978). *The Hippocampus as a Cognitive Map*. Oxford: Clarendon Press.

O'Keefe, J., and Nadel, L. (1979). Précis of O'Keefe and Nadel's 'The hippocampus as a cognitive map'. *Behav. Brain Sci.* 2, 487–494. doi: 10.1017/S0140525X00063949

Olson, C. R., and Graybiel, A. M. (1980). Sensory maps in the claustrum of the cat. *Nature* 288, 479–481. doi: 10.1038/288479a0

Olson, J. M., Tongprasearth, K., and Nitz, D. A. (2017). Subiculum neurons map the current axis of travel. *Nat. Neurosci.* 20, 170–172. doi: 10.1038/nn.4464

O'Mara, S. M. (2017). Place cells: knowing where you are depends on knowing where you're heading. *Curr. Biol.* 27, R834–R836. doi: 10.1016/j.cub.2017.06.081

O'Mara, S. M., Rolls, E. T., Berthoz, A., and Kesner, R. P. (1994). Neurons responding to whole-body motion in the primate hippocampus. *J. Neurosci.* 14, 6511–6523. doi: 10.1523/jneurosci.14-11-06511.1994

Page, H. J., Wilson, J. J., and Jeffery, K. J. (2018). A dual-axis rotation rule for updating the head direction cell reference frame during movement in three dimensions. *J. Neurophysiol.* 119, 192–208. doi: 10.1152/jn.00501.2017

Papez, J. W. (1937). A proposed mechanism of emotion. *Arch. Neurol. Psychiatry* 38, 725–743. doi: 10.1001/archneurpsyc.1937.02260220069003

Park, S., Kramer, E. E., Mercaldo, V., Rashid, A. J., Insel, N., Frankland, P. W., et al. (2016). Neuronal allocation to a hippocampal engram. *Neuropsychopharmacology* 41, 2987–2993. doi: 10.1038/npp.2016.73

Raichle, M. E. (2015). The restless brain: how intrinsic activity organizes brain function. *Philos. Trans. R. Soc. Lond. B Biol. Sci.* 370:20140172. doi: 10.1098/rstb.2014.0172

Ranganath, C., and Ritchey, M. (2012). Two cortical systems for memory-guided behaviour. *Nat. Rev. Neurosci.* 13, 713–726. doi: 10.1038/nrn3338

Remedios, R., Logothetis, N. K., and Kayser, C. (2010). Unimodal responses prevail within the multisensory claustrum. *J. Neurosci.* 30, 12902–12907. doi: 10.1523/JNEUROSCI.2937-10.2010

Remedios, R., Logothetis, N., and Kayser, C. (2012). "The claustrum and the orchestra of cognitive control," in *Talk Presented at Francis Crick Memorial Conference: Consciousness in Human and Non-Human Animals* (Cambridge, UK), 2012-07-07. Available online at: http://fcmconference.org/#program

Renouard, L., Billwiller, F., Ogawa, K., Clément, O., Camargo, N., Abdelkarim, M., et al. (2015). The supramammillary nucleus and the claustrum activate the cortex during REM sleep. *Sci. Adv.* 1:e1400177. doi: 10.1126/sciadv.1400177

Rochefort, C., Arabo, A., André, M., Poucet, B., Save, E., and Rondi-Reig, L. (2011). Cerebellum shapes hippocampal spatial code. *Science* 334, 385–389. doi: 10.1126/science.1207403

Scoville, W. B., and Milner, B. (1957). Loss of recent memory after bilateral hippocampal lesions. *J. Neurol. Neurosurg. Psychiatry* 20, 11–21. doi: 10.1136/jnnp.20.1.11

Segobin, S., Laniepce, A., Ritz, L., Lannuzel, C., Boudehent, C., Cabé, N., et al. (2019). Dissociating thalamic alterations in alcohol use disorder defines specificity of Korsakoff's syndrome. *Brain* 142, 1458–1470. doi: 10.1093/brain/awz056

Sharp, P. E., and Green, C. (1994). Spatial correlates of firing patterns of single cells in the subiculum of the freely moving rat. *J. Neurosci.* 14, 2339–2356. doi: 10.1523/jneurosci.14-04-02339.1994

Shinder, M. E., and Taube, J. S. (2019). Three-dimensional tuning of head direction cells in rats. *J. Neurophysiol.* 121, 4–37. doi: 10.1152/jn.00880.2017

Simonnet, J., and Brecht, M. (2019). Burst firing and spatial coding in subicular principal cells. *J. Neurosci.* 39, 3651–3662. doi: 10.1523/JNEUROSCI.1656-18.2019

Spence, K. W. (1956). *Behavior Theory and Conditioning (Vol. 35).* New Haven: Yale University Press.

Squire, L. R. (1987). *Memory and Brain.* New York: Oxford University Press.

Staff, N. P., Jung, H. Y., Thiagarajan, T., Yao, M., and Spruston, N. (2000). Resting and active properties of pyramidal neurons in subiculum and CA1 of rat hippocampus. *J. Neurophysiol.* 84, 2398–2408. doi: 10.1152/jn.2000.84.5.2398

Stewart, M., and Wong, R. K. (1993). Intrinsic properties and evoked responses of guinea pig subicular neurons *in vitro*. *J. Neurophysiol.* 70, 232–245. doi: 10.1152/jn.1993.70.1.232

Stringer, C., Pachitariu, M., Steinmetz, N., Reddy, C. B., Carandini, M., and Harris, K. D. (2019). Spontaneous behaviors drive multidimensional, brain-wide activity. *Cell* 1:100. doi: 10.1126/science.aav7893

Suzuki, M., Kitano, H., Ito, R., Kitanishi, T., Yazawa, Y., Ogawa, T., et al. (2001). Cortical and subcortical vestibular response to caloric stimulation detected by functional magnetic resonance imaging. *Cogn. Brain Res.* 12, 441–449. doi: 10.1016/s0926-6410(01)00080-5

Taube, J. S. (1995). Head direction cells recorded in the anterior thalamic nuclei of freely moving rats. *J. Neurosci.* 15, 70–86. doi: 10.1523/jneurosci.15-01-00070.1995

Taube, J. S. (2007). The head direction signal: origins and sensory-motor integration. *Annu. Rev. Neurosci.* 30, 181–207. doi: 10.1146/annurev.neuro.29.051605.112854

Taube, J. S., Muller, R. U., and Ranck, J. B. (1990a). Head-direction cells recorded from the postsubiculum in freely moving rats. I. Description and quantitative analysis. *J. Neurosci.* 10, 420–435. doi: 10.1523/jneurosci.10-02-00420.1990

Taube, J. S., Muller, R. U., and Ranck, J. B. (1990b). Head-direction cells recorded from the postsubiculum in freely moving rats. II. Effects of environmental manipulations. *J. Neurosci.* 10, 436–447. doi: 10.1523/jneurosci.10-02-00436.1990

Taube, J. S., Wang, S. S., Kim, S. Y., and Frohardt, R. J. (2013). Updating of the spatial reference frame of head direction cells in response to locomotion in the vertical plane. *J. Neurophysiol.* 109, 873–888. doi: 10.1152/jn.00239.2012

Thompson, R. F. (1986). The neurobiology of learning and memory. *Science* 233, 941–947. doi: 10.1126/science.3738519

Tolman, E. C. (1948). Cognitive maps in rats and men. *Psychol. Rev.* 55, 189–208. doi: 10.1037/h0061626

Tonegawa, S., Liu, X., Ramirez, S., and Redondo, R. (2015). Memory engram cells have come of age. *Neuron* 87, 918–931. doi: 10.1016/j.neuron.2015.08.002

Tsanov, M., Chah, E., Vann, S. D., Reilly, R. B., Erichsen, J. T., Aggleton, J. P., et al. (2011). Theta-modulated head direction cells in the rat anterior thalamus. *J. Neurosci.* 31, 9489–9502. doi: 10.1523/JNEUROSCI.0353-11.2011

Tsivilis, D., Vann, S. D., Denby, C., Roberts, N., Mayes, A. R., Montaldi, D., et al. (2008). A disproportionate role for the fornix and mammillary bodies in recall versus recognition memory. *Nat. Neurosci.* 11, 834–842. doi: 10.1038/nn.2149

Tsokas, P., Hsieh, C., Yao, Y., Lesburgueres, E., Wallace, E. J. C., Tcherepanov, A., et al. (2016). Compensation for PKMζ in long-term potentiation and spatial long-term memory in mutant mice. *Elife* 5:e14846. doi: 10.7554/eLife.14846

Ulrich-Lai, Y. M., and Herman, J. P. (2009). Neural regulation of endocrine and autonomic stress responses. *Nat. Rev. Neurosci.* 10, 397–409. doi: 10.1038/nrn2647

Van der Werf, T. D., Witter, M. P., and Groenewegen, H. J. (2002). The intralaminar and midline nuclei of the thalamus. Anatomical and functional evidence for participation in processes of arousal and awareness. *Brain Res. Rev.* 39, 107–140. doi: 10.1016/s0165-0173(02)00181-9

van Groen, T., Kadish, I., and Wyss, J. M. (2002). The role of the laterodorsal nucleus of the thalamus in spatial learning and memory in the rat. *Behav. Brain Res.* 136, 329–337. doi: 10.1016/s0166-4328(02)00199-7

van Groen, T., and Wyss, J. M. (1990a). The connections of presubiculum and parasubiculum in the rat. *Brain Res.* 518, 227–243. doi: 10.1016/0006-8993(90)90976-i

van Groen, T., and Wyss, J. M. (1990b). The postsubicular cortex in the rat: characterization of the fourth region of the subicular cortex and its connections. *Brain Res.* 529, 165–177. doi: 10.1016/0006-8993(90)90824-u

van Groen, T., and Wyss, J. M. (1992). Projections from the laterodorsal nucleus of the thalamus to the limbic and visual cortices in the rat. *J. Comp. Neurol.* 324, 427–448. doi: 10.1002/cne.903240310

van Praag, H., Christie, B. R., Sejnowski, T. J., and Gage, F. H. (1999). Running enhances neurogenesis, learning, and long-term potentiation in mice. *Proc. Natl. Acad. Sci. U S A* 96, 13427–13431. doi: 10.1073/pnas.96.23.13427

Vann, S. D., and Aggleton, J. P. (2004). The mammillary bodies: two memory systems in one? *Nat. Rev. Neurosci.* 5, 35–44. doi: 10.1038/nrn1299

Vann, S. D., and Nelson, A. J. (2015). The mammillary bodies and memory: more than a hippocampal relay. *Prog. Brain Res.* 219, 163–185. doi: 10.1016/bs.pbr.2015.03.006

Vertes, R. P., Hoover, W. B., Szigeti-Buck, K., and Leranth, C. (2007). Nucleus reuniens of the midline thalamus: link between the medial prefrontal cortex and the hippocampus. *Brain Res. Bull.* 71, 601–609. doi: 10.1016/j.brainresbull.2006.12.002

Vitte, E., Derosier, C., Caritu, Y., Berthoz, A., Hasboun, D., and Soulie, D. (1996). Activation of the hippocampal formation by vestibular stimulation: a functional magnetic resonance imaging study. *Exp. Brain Res.* 112, 523–526. doi: 10.1007/bf00227958

Watson, T. C., Obiang, P., Torres-Herraez, A., Watilliaux, A., Coulon, P., Rochefort, C., et al. (2019). Anatomical and physiological foundations of cerebello-hippocampal interactions. *Elife* 8:e41896. doi: 10.7554/eLife.41896

Whishaw, I. Q. (1990). "The decorticate rat," in *The Cerebral Cortex of the Rat*, eds B. Kolb and R. C. Tees (Cambridge, MA: The MIT Press), 239–267.

Wilton, L. A. K., Baird, A. L., Muir, J. L., Honey, R. C., and Aggleton, J. P. (2001). Loss of the thalamic nuclei for "head direction" impairs performance on spatial memory tasks in rats. *Behav. Neurosci.* 115, 861–869. doi: 10.1037/0735-7044.115.4.861

Winter, S. S., Clark, B. J., and Taube, J. S. (2015). Disruption of the head direction cell network impairs the parahippocampal grid cell signal. *Science* 347, 870–874. doi: 10.1126/science.1259591

Witter, M. P. (2002). "The parahippocampal region: past, present and future," in *The Parahippocampal Region*, eds M. Witter and F. Wouterlood (Oxford: Oxford University press), 3–19.

Yamins, D. L., and DiCarlo, J. J. (2016). Using goal-driven deep learning models to understand sensory cortex. *Nat. Neurosci.* 19, 356–365. doi: 10.1038/nn.4244

Zeidman, P., and Maguire, E. A. (2016). Anterior hippocampus: the anatomy of perception, imagination and episodic memory. *Nat. Rev. Neurosci.* 17, 173–182. doi: 10.1038/nrn.2015.24

Conflict of Interest Statement: The authors declare that the research was conducted in the absence of any commercial or financial relationships that could be construed as a potential conflict of interest.

frontiers in Neural Circuits

ORIGINAL RESEARCH
published: 09 August 2019
doi: 10.3389/fncir.2019.00051

A New Projection From the Deep Cerebellar Nuclei to the Hippocampus *via* the Ventrolateral and Laterodorsal Thalamus in Mice

Pauline Bohne[1], *Martin K. Schwarz*[2], *Stefan Herlitze*[1] *and Melanie D. Mark*[1]*

[1]*Department of General Zoology and Neurobiology, Ruhr-University Bochum, Bochum, Germany,* [2]*Institute of Experimental Epileptology and Cognition Research (EECR), University of Bonn Medical School, Bonn, Germany*

The cerebellar involvement in cognitive functions such as attention, language, working memory, emotion, goal-directed behavior and spatial navigation is constantly growing. However, an exact connectivity map between the hippocampus and cerebellum in mice is still unknown. Here, we conducted a tracing study to identify the sequence of transsynaptic, cerebellar-hippocampal connections in the mouse brain using combinations of Recombinant adeno-associated virus (rAAV) and pseudotyped deletion-mutant rabies (RABV) viruses. Stereotaxic injection of a primarily anterograde rAAV-WGA (wheat germ agglutinin)-Cre tracer virus in the deep cerebellar nuclei (DCN) of a Cre-dependent tdTomato reporter mouse resulted in strong tdTomato labeling in hippocampal CA1 neurons, retrosplenial cortex (RSC), rhinal cortex (RC) as well as thalamic and cerebellar areas. Whereas hippocampal injections with the retrograde tracer virus rAAV-TTC (tetanus toxin C fragment)-eGFP, displayed eGFP positive cells in the rhinal cortex and subiculum. To determine the sequence of mono-transsynaptic connections between the cerebellum and hippocampus, we used the retrograde tracer RABVΔG-eGFP(EnvA). The tracing revealed a direct connection from the dentate gyrus (DG) in the hippocampus to the RSC, RC and subiculum (S), which are monosynaptically connected to thalamic laterodorsal and ventrolateral areas. These thalamic nuclei are directly connected to cerebellar fastigial (FN), interposed (IntP) and lateral (Lat) nuclei, discovering a new projection route from the fastigial to the laterodorsal thalamic nucleus in the mouse brain. Collectively, our findings suggest a new cerebellar-hippocampal connection *via* the laterodorsal and ventrolateral thalamus to RSC, RC and S. These results strengthen the notion of the cerebellum's involvement in cognitive functions such as spatial navigation *via* a polysynaptic circuitry.

Keywords: cerebellar-hippocampal projection, cerebellum, hippocampus, thalamus, circuitry, rabies, rAAV

OPEN ACCESS

Edited by:
Mathieu Beraneck,
Université Paris Descartes, France

Reviewed by:
Paul Smith,
University of Otago, New Zealand
Guillaume P. Dugue,
École Normale Supérieure, France

***Correspondence:**
Melanie D. Mark
melanie.mark@rub.de

Received: *21 January 2019*
Accepted: *22 July 2019*
Published: *09 August 2019*

Citation:
Bohne P, Schwarz MK, Herlitze S and Mark MD (2019) A New Projection From the Deep Cerebellar Nuclei to the Hippocampus via the Ventrolateral and Laterodorsal Thalamus in Mice. Front. Neural Circuits 13:51. doi: 10.3389/fncir.2019.00051

INTRODUCTION

The cerebellum was exclusively associated with motor coordination related tasks such as balance, precise timing of movements or motor learning. However, recent functional brain imaging studies with cerebellar degenerative disease and cerebellar lesioned patients support the cerebellar contribution in cognitive functions such as attention, language, working memory, emotion,

and in visuospatial navigation (Schmahmann and Pandya, 1991; Timmann and Daum, 2007; Baillieux et al., 2008a,b; Molinari et al., 2008; Timmann et al., 2010). In support of these human studies, rodents with impairments in their cerebellum demonstrated a reduction in hippocampal based behavioral tasks such as goal-directed and spatial navigation tests (Colombel et al., 2004; Burguière et al., 2010; Rochefort et al., 2011). An anatomical cerebellar-hippocampal connection in the mouse brain supporting its participation in spatial navigation has not been investigated. It is not yet clear whether this is through a direct monosynaptic projection from the cerebellum to the hippocampus, or by polysynaptic transmission involving e.g., the thalamus (Rochefort et al., 2013). Moreover, the exact sequence and the identity of connected neuronal populations are not known.

Evidence for a direct, monosynaptic connection between the cerebellum and hippocampus is weak. In the 1980s transient direct projection from the cerebral cortex to the deep cerebellar nuclei (DCN) and cortex in young kittens, rabbit fetuses and in pouch young North American opossum have been reported (Tolbert and Panneton, 1983, 1984; Cabana and Martin, 1986; Tolbert, 1989a,b). Additionally, a sparse projection from the cerebellum to the neocortex in adult rats was demonstrated (Wild and Williams, 2000). Direct cerebrocerebellar projections have also been reported in chicken and zebra finches, however, they are sparse and temporary (Wild and Williams, 2000; Liu et al., 2012). Since most of these studies used polysynaptic radiolabeled amino acids or wheat germ agglutinin conjugated to horseradish peroxidase (WGA-HRP) as tracers, the interpretation of these results is difficult.

To explore the neuronal connectivity between structures in the mammalian brain, recombinant viruses including AAV and/or modified rabies viruses have presently become the tool of choice. Recombinant adeno-associated viruses (rAAVs) offer great advantages in cell-specific labeling due to deletion of almost all coding sequences resulting in non-pathogenicity, loss of self-reproduction (Xiao et al., 1997; Büning et al., 2008; Kwon and Schaffer, 2008) and long-term expression of introduced proteins combined with little to no mammalian immune reaction (Kaplitt et al., 1994; Xiao et al., 1996, 1997; Chamberlin et al., 1998). The main disadvantage of rAAVs in tracing studies is their incapability to cross synaptic junctions, although certain rAAV serotypes have been reported to support anterograde transsynaptic transport at high titers (Ohta et al., 2011; Deneris and Wyler, 2012). Yet, they can express proteins that cross synapses (WGA), however, this strategy can not distinguish between strong polysynaptic from potential weak direct connections (Wickersham et al., 2007a). The sequence of traversed synapses can only be roughly estimated. Thus, only an additional monosynaptically restricted tracing approach can unequivocally determine the sequence of synaptic connections. Therefore, we confirmed our rAAV tracing results with tracings utilizing a deletion-mutant rabies virus RABVΔG-eGFP (EnVA). This modified rabies virus (RABV) expresses eGFP at the expense of the rabies virus glycoprotein, limiting its potential for retrograde transsynaptic transport. To reveal monosynaptic connectivity maps the glycoprotein has to be transcomplemented in the initially infected cell population (Ugolini, 1995; Kelly and Strick, 2000; Wickersham et al., 2007a,b). This transcomplementation can be accomplished upon rAAV targeted glycoprotein expression in the source cell population (Niedworok et al., 2012). Therefore this tracing method can determine the hierarchy of anatomical connectivity in the brain and a potential cerebellar-hippocampal monosynaptic connection.

Here, we report a tracing study, identifying a sequential connectivity map between the cerebellum and the hippocampus in the mouse brain. Stereotaxic injections with the tracer virus rAAV CMV-WGA-Cre in the DCN of tdTomato-reporter mice resulted in stained neurons in the rhinal cortex, subiculum, hippocampal CA1 region and also to some extent in the thalamus. In contrast, injections of the same virus in the hippocampus resulted in fluorescently stained Purkinje cells and molecular layer interneurons, in addition to stainings in the pons, thalamus and hippocampus, including CA1 pyramidal neurons, neurons of the dentate gyrus (DG), pre- and parasubiculum and lateral entorhinal cortex. However, after injection of the retrograde tracers rAAV TTC-eGFP in the DG and rAAV CMV-WGA-Cre in a tdTomatoJ reporter mouse in cerebellar CrusI/CrusII region, we detected overlapping fluorescence in rhinal cortex (RhC), DG and subiculum (S), indicating that at least the same areas are involved in forming a cerebellar-hippocampal connection. To finally determine the hierarchy of monosynaptic connections between the cerebellum and hippocampus, we applied a modified retrograde RABV, SADΔG-eGFP (EnVA) in the rhinal cortex (RhC), subiculum (S), DG and retrosplenial cortex (RSC). We found monosynaptic projections from the laterodorsal and ventrolateral thalamus to the S and retrosplenial agranular cortex (RSA), of which both are reported to be involved in spatial navigation (Rochefort et al., 2013). eGFP positive neurons were detected in mainly the contralateral interpositus and fastigial, but not dentate nucleus of cerebellar DCN. Taken together, our findings suggest a new projection from the fastigial nucleus to the laterodorsal thalamic nuclei to S and RSC, which are connected to the hippocampus. In addition, our results show a potential sequence of polysynaptic cerebellar-hippocampal connections *via* the thalamus to various cortical areas.

MATERIALS AND METHODS

Plasmid Construction

pAAV constructs (pAAV-CMV-WGA-CRE and pAAV-CMV-TTC-GFP) were amplified by PCR from the original vectors and cloned into the pAAV-MCS (Stratagene). WGA-Cre was amplified from pAAV-EF1a-mCherry-IRES-WGA-Cre (University of North Carolina Vector Core, Chapel Hill, NC, USA). TTC was amplified from psK1-TTC, which was kindly provided as a gift by Dr. Neil F. Fairweather (Imperial College London, UK).

Virus Production

rAAV8 production of virus from pAAV-CMV-WGA-Cre and pAAV-CMV-TTC-eGFP constructs were performed by a

modified method (Grieger et al., 2006). Briefly, low passage 293T cells were cotransfected with pAAV-CMV-WGA-Cre or pAAV-CMV-TTC-eGFP, pAAV-RC, and pHelper using the Polyethylenimine (PEI) based protocol. Three days after transfection cells were removed from the dishes, pelleted (3,700 g, 20 min, 4°C), resuspended in 10 ml lysis buffer (150 mN NaCl, 50 mM Tris-HCl, pH 8.5) and lysed *via* six freeze/thaw cycles in dry ice/ethanol and 37°C water bath (each 15 min). To get rid of free DNA, cell suspension was treated with DNase I (Roche) for 30 min at 37°C. The cell debris was spun down at 3,700 g for 20 min at 4°C. The supernatant was collected in a syringe and filtered into a 15 ml falcon tube through a 0.2 μm filter to obtain the crude lysate. Then the supernatant was resuspended in a polyethylene glycol (PEG) solution overnight at 4°C and pelleted at 3,700 g for 20 min at 4°C. The pellet was resuspended in PBS, 0.001% pluronic and aliquots were stored at −80°C until further use.

SADΔG-eGFP (EnVA) and helper plasmids pAAV8-CBA-mRFP-IRES-TvA and pAAV8-CBA-RG-mCherry were produced as previously described (Niedworok et al., 2012). Briefly, BHK cells were plated at a density of 1.5×10^7. The following day, cells were transfected with 15 mg plasmid pCAGG/SAD-G by CaP transfection. Twenty-four hours later rabies virus SADΔG-eGFP was added at a multiplicity of infection (MOI) of 3. Forty-eight hours later the SADΔG-eGFP containing supernatant was equally distributed into four 15 cm plates containing pCAGGs/SAD-G (15 mg/plate) transfected BHK cells (1.5×10^7 cells/plate). Two days later the virus-containing supernatant was applied onto four 15 cm plates containing BHK-EnvARGCD cells ($\sim 1.5 \times 10^7$ cells/plate) at a MOI of 1.5 for pseudotyping. Twelve hours later cells were trypsinized and replated onto eight 15 cm dishes. Pseudotyped rabies virus-containing supernatant was harvested 2 days later. The supernatant was spun at 2,000 rpm at 4°C for 10 min. and subsequently filtered through a 0.45 mm filter (Nalgene SFCA Bottletop Filter, Thermo Fisher Scientific, Waltham, MA, USA). The filtered virus suspension was centrifuged for 90 min at 25,000 rpm (SW28, 4°C) in a Beckmann 80 K ultracentrifuge (Beckman Coulter, Brea, CA, USA). After centrifugation the supernatant was discarded and the pellet was aspirated in ice-cold PBS (pH 7.4). Pseudotyped rabies virus-containing solution was aliquoted in 6 μl aliquots and frozen at −80°C.

Mice

For the tracing study adult male and female mice obtained from JAX labs, C57Bl6/J (JAX 000664) and Gt(ROSA)26Sor$^{tm9(CAG\text{-}tdTomato)Hze}$/J (abbreviated as tdTomato$^{+/+}$; JAX 007909, Madisen et al., 2010), were used. Mice were housed in a 12 h light/dark cycle with food and water *ad libitum*. The present study was carried out in accordance with the European Communities Council Directive of 2010 (2010/63/EU) for care of laboratory animals and approved by a local ethics committee (Bezirksamt Arnsberg) and the animal care committee of North Rhine-Westphalia, Germany, based at the LANUV (Landesamt für Umweltschutz, Naturschutz und Verbraucherschutz, Nordrhein-Westfalen, D-45659 Recklinghausen, Germany). The study was supervised by the animal welfare commission of the Ruhr-University Bochum. All efforts were made to minimize the number of mice used for this study.

Intracranial Injections

Viruses were injected in adult mouse brains for each specified region tested. Mice were deeply anesthetized with 1.5%–2.0% isoflurane and placed into a stereotactic frame (Narishige, Japan). The skin was opened with a sagittal incision along the midline. A small craniotomy was performed for virus injections. 0.2–1 μl of viruses were applied in 100 μm steps using pressure injection in 2 min intervals (see **Table 1**). A customized glass pipette attached to a 5 ml syringe was used for virus delivery. At the end of injection the skin was sutured (Surgicryl Monofilament, Belgium). After the surgery, animals received subcutaneous injection of carprofen (2 mg/kg) for analgesia. Animals were placed individually into their home cages to recover.

rAAV8-CMV-WGA-CRE was injected into the fastigial nucleus of the DCN, CrusI/CrusII of the cerebellar cortex and DG, AAV8-CMV-TTC-eGFP in the hippocampus proper (CA1/CA3) and DG of Gt(ROSA)$^{26Sortm9(CAG\text{-}tdTomato)Hze}$/J mice. Coordinates and volumes of injected viruses are listed in **Table 1**. Expression times varied between 3 and 8 months.

The helper viruses for rabies infection (rAAV8-CBA-mRFP-IRES-TvA and rAAV8-CBA-RG-mCherry, ratio 1:2) were injected 1 week before the deletion mutant rabies virus RABVΔG-eGFP to allow stable infection and expression of TVA and RG. Rabies virus was injected into the hippocampus, RSC, rhinal cortex, laterodorsal and ventrolateral thalamus of C57BL6/J mice. For injected volumes and injection sites, see **Table 2**. Mice were perfused and analyzed 7 days after RABV application.

Histology

Mice were anesthetized with ketamine and xylazine (100 mg/kg and 10 mg/kg, respectively) and perfused transcardially with ice-cold 4% PFA (paraformaldehyde, Sigma-Aldrich) in PBS (pH 7.4). Brains were dissected and post-fixed for 1 h in 4% PFA in PBS, then cryoprotected in 30% sucrose in PBS at 4°C overnight. Brains were sliced in 35 μm thick sections using a Leica microtome. The sections were mounted with Roti-Mount FluorCare (Carl Roth) before analysis for fluorescence.

Imaging

All images were acquired using a Leica TCS SP5 confocal laser scanning microscope (Leica DMI6000 B, Wetzlar, Germany) interfaced to a personal computer, running Leica Application Suite Advanced Fluorescence software (LAS AF 2.6). eGFP was excited with an Argon laser at 488 nm, while mCherry, tdTomato or mRFP were excited with a DPSS laser at 561 nm. Double-fluorescent images were obtained using the alternating acquisition mode. Sequential z-stacks were made for each section and crosstalk of the fluorophores was eliminated automatically with LAS AF software. Images were further analyzed using ImageJ. Schematic images show a quantitative localization from a combination of slices from ≥3 mice analyzed. Representative confocal images may be presented from different animals.

TABLE 1 | Injection site coordinates, number of animals and injected volumes of rAAV8-CMV-WGA-Cre and rAAV8-CMV-TTC-eGFP tracers.

	Structure	AP* (mm)	ML* (mm)	DV* (mm)	*n*	Volume rAAV (μl)
Hippocampus	Dentate gyrus	−2.54	± 1.5	1.8–1.6	3	1
	CA1/CA3	−2.18	± 2.1	1.9–1.5	2	1
Cingulate cortex	Agranular and granular RSC	−2.54	± 0.3	0.75–0.25	3	1
Cerebellum	Medial (fastigial) nucleus	−6.25	± 0.7	2.4–2.2	3	1
	Crus I/II	−6.4	−2.7	1.7–1.07	2	1

AP, anterior-posterior; ML, mediolateral; DV, dorsoventral (all relative to Bregma).

TABLE 2 | Injection site coordinates and number of animals and injected volumes of rAAV8-CBA-RG-mCherry/rAAV8-CBA- mRFP-IRES-TvA helpers and RABVΔG-eGFP tracers.

	Structure	AP* (mm)	ML* (mm)	DV* (mm)	*n*	Volume rAAV/RABV (μl)
Hippocampus	CA1/CA3	−2.18	± 2.1	1.9–1.5	3	1/1
	Dentate gyrus	−1.94	± 0.75	2.1–1.8	3	0.2/0.2
	Subiculum	−3.52	± 2.2	1.5–1.3	5	0.2/0.1
Rhinal Cortex	Lateral-, ento-, perirhinal	−4.84	−4.2	1.65–0.55	4	0.6/0.3
Retrosplenial cortex	Agranular and granular RSC	−1.46	± 0.25	0.25–0.1	3	0.5/0.5
Thalamus	Laterodorsal nuclei	−1.46	−1.5	2.25–1.9	4	0.2/0.2
	Ventrolateral nuclei	−1.58	−1	3.25–2.9	3	0.2/0.2

AP, anterior-posterior; ML, mediolateral; DV, dorsoventral (all relative to Bregma).

Statistics

All statistical analyses were calculated with SigmaPlot software. Data were initially analyzed for normality by the Shapiro–Wilk test ($p \geq 0.05$), then tested for equal variance with the Equal Variance Test ($p \geq 0.05$). If data sets passed both tests, a *t*-test for comparison of tow groups or a One-Way analysis of variance (ANOVA; *post hoc t*-test) for comparison of more than two groups was used. If the normality tests failed, data sets were analyzed using the Mann-Whitney-*U* test for comparison of two groups. Significance for comparisons: $^{*}p \leq 0.05$, $^{**}p \leq 0.01$; $^{***}p \leq 0.001$. Cell counts from specific areas of $n \geq 3$ mice are presented as mean ± standard error of the mean (SEM) from all rabies injected mice. For counting, every second slice was imaged for eGFP^{+} cells followed by manual cell count using ImageJ.

RESULTS

AAV-Mediated Polysynaptic Circuit Tracing of the Mouse Cerebellar-Hippocampal Connections

To visualize cerebellar-hippocampal connections, we first performed polysynaptic circuit tracing utilizing a Cre-recombinase encoding rAAV injected into the cerebellum or hippocampus of Cre-dependent tdTomato reporter mice (Madisen et al., 2010). In this virus, the transsynaptic transporter protein WGA was fused to the Cre recombinase (**Figure 1A**) and expressed under the control of the CMV promoter (Chamberlin et al., 1998). Since the expression efficiency of WGA-Cre may be region-specific, rAAV serotype 8 was used due to its higher efficacy to infect hippocampal and cerebellar neurons (Heinemann et al., 1991; Broekman et al., 2006). Initially, rAAV8-CMV-WGA-Cre was injected into the DCN bilaterally (1 μl, AP: −6.25 mm, MT: −0.7 mm, DV: 2.4–2.2 mm) from four tdTomato mice to induce tdTomato expression in WGA-Cre positive cells (**Figure 1B**). After 5 months of expression, single tdTomato^{+} neurons were detected in the lateral entorhinal cortex (Lent; **Figures 1DI,I'**), parasubiculum (PaS, **Figures 1DII,II'**), RSC (**Figures 1DIII,III'**) and also in parts of the hippocampus, including CA1 pyramidal neurons and in the stratum oriens layer (**Figures 1CI'–III'**) as represented by red dots and lines in the brain schemes. Fluorescent fibers and a few cells were detected in thalamic regions, including bilaterally in the medial geniculate nucleus (MGV, **Figure 1DIII**) and the magnocellular red nucleus (RMC; **Supplementary Figure S1B**). We also found fluorescent structures in the periaqueductal gray (DLPAG), the ventral secondary auditory cortex, frontal association cortex, olfactory bulb or the C3 posteromedial cortical amygdaloid nucleus (**Supplementary Figure S1**).

To trace from the hippocampus to the cerebellum we injected rAAV8-CMV-WGA-Cre unilaterally in the right dentate gyrus (DG, AP: −2.54 mm, ML: −1.5 mm, DV: 1.8 −1.6 mm, 1 μl) from three tdTomatoJ mice (**Figure 2**). After 4 months of expression tdTomato^{+} neurons in the cerebellum distributed equally over the ipsi-, and contralateral sides. We found cerebellar Purkinje cells classified by their typical morphology and location (**Figure 2CI'**). tdTomato^{+} neurons were additionally detected in the bilateral simple lobules and lobules 4 and 5 (**Figures 2CII,II',III,III'**). Additionally, fluorescently labeled axons in the ipsilateral inferior olive (IO) and paramedian reticular nucleus (PMn; **Figures 2CI,DI,I'**), but not somata were observed. Numerous neurons were bilaterally expressing tdTomato in the visual and RSC, close to the cerebellum at −4.96 mm from Bregma (**Figures 2DII–II'**). However, the rhinal cortex was only stained on the ipsilateral and not the contralateral side (**Figures 2DI,III–III'**). In contrast, the contralateral central nucleus of the inferior colliculus (CIC), but not the ipsilateral side showed tdTomato^{+} neurons (**Figure 2DII**). Overall, we found differences in tdTomato

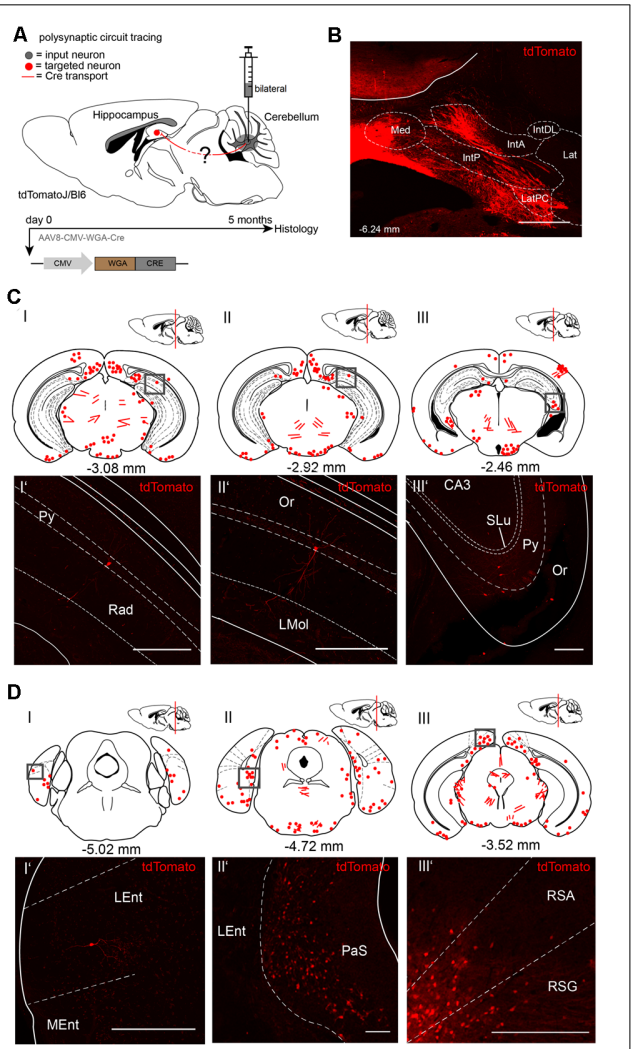

FIGURE 1 | Mapping recombinant adeno-associated viruse (rAAV) mediated polysynaptic targets from the deep cerebellar nuclei (DCN) to the hippocampus using the tracer rAAV8-CMV-WGA-Cre in tdTomatoJ$^{+/+}$ mice. **(A)** Schematic of sagittal section from an adult tdTomatoJ$^{+/+}$ mouse brain (n = 4) injected bilaterally with 1 μl rAAV8-CMV-WGA-Cre in the DCN, (gray dot) for 5 months to trace the polysynaptic circuit (red line) to the hippocampus (red dot). **(B)** Confocal image depicting the injection site from an adult tdTomatoJ$^{+/+}$ mouse brain in the DCN. Scale bar: 250 μm. **(CI–III)** Schematic of coronal sections showing quantitative localization of tdTomato^{+} neuron cell bodies (red dots) or neurites (red lines) at different distances from Bregma (−3.08 mm, −2.92 mm, −2.46 mm) after rAAV8-CMV-WAG-Cre injection in the DCN. Squared boxes represent confocal images presented in **(CI'–III')**. **(CI'–III')** Single tdTomato^{+} neurons were observed in the hippocampal pyramidal layer (Py, **CI'–III'**) or stratum oriens (Or, **CIII'**). Scale bars: 250 μm. **(D)** Schematic of coronal sections showing quantitative localization of tdTomato^{+} neuron cell bodies (red dots) or neurites (red lines) at different distances from Bregma (−5.02 mm, −4.72 mm, −3.52 mm) after rAAV8-CMV-WAG-Cre injection in the DCN **(DI–III)**. Squared boxes represent confocal images presented in **(DI'–III')**. **(DI'–III')** tdTomato^{+} neurons were found in the parasubiculum (PaS, **DII'**) and in both retrosplenial granular (RSG, **DIII'**) and agranular (RSA, **DIII'**) cortex. Scale bars: 250 μm. IntA, anterior interposed cerebellar nucleus; IntP, posterior interposed cerebellar nucleus; Lat, lateral (dentate) cerebellar nucleus; LatPC, parvicellular Lat; Med, medial (fastigial) cerebellar nucleus. The mouse brains in this figure has been reproduced from Franklin and Paxinos (2001).

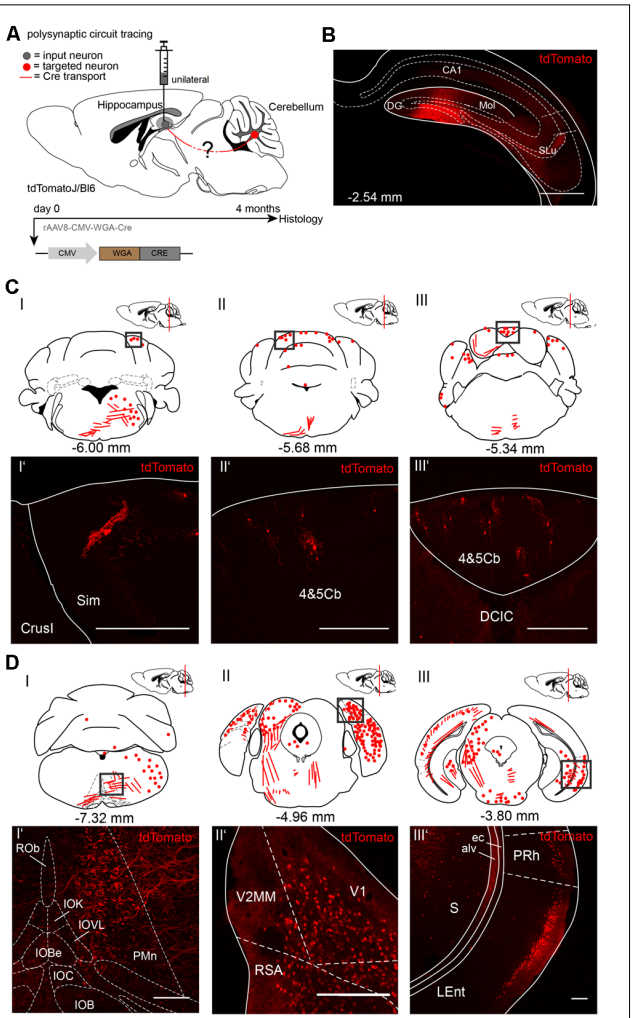

FIGURE 2 | Mapping rAAV mediated polysynaptic targets from the dentate gyrus to cerebellum using the tracer rAAV8-CMV-WGA-Cre in tdTomatoJ$^{+/+}$ mice. **(A)** Schematic of sagittal section from an adult tdTomatoJ$^{+/+}$ mouse brain injected unilaterally with 1 μl rAAV8-CMV-WGA-Cre in the dentate gyrus (gray dot) for 4 months to trace the polysynaptic circuit (red line) to the cerebellum (red dot). **(B)** Confocal image of a coronal section from an adult tdTomatoJ$^{+/+}$ mouse brain injected with rAAV8-CMV-WGA-Cre showing the injection site in the DG and hippocampus proper. Scale bar: 250 μm. **(CI–III)** Schematic of coronal sections showing quantitative localization of tdTomato^{+} neuron cell bodies (red dots) or neurites (red lines) at different distances from Bregma (−6.00 mm, −5.68 mm, −5.34 mm) after rAAV8-CMV-WGA-Cre injection in the dentate gyrus. Squared boxes represent confocal images presented in **(CI'–III')**. **(CI'–III')** Example single tdTomato^{+} neurons were imaged from the cerebellar lobulus simplex (Sim, **CI'**) and lobes 4 and 5, (4&5Cb, **CII'–III'**). Scale bars: 250 μm. **(DI–III)** Schematic of coronal sections showing quantitative localization of tdTomato^{+} neuron cell bodies (red dots) or neurites (red lines) at different distances from Bregma (−7.32 mm, −4.96 mm, −3.80 mm) after rAAV8-CMV-WGA-Cre injection in the dentate gyrus. Squared boxes represent confocal images presented in **(DI'–III')**. **(DI'–III')** Representative tdTomato^{+} axons were imaged from the ipsilateral side of injection from the paramedian reticular nucleus (PMn) and parts of the inferior olive (IO, **DI'**), while tdTomato^{+} cells were seen in primary visual cortex (V1) and retrosplenial agranular cortex (RSA, **DII'**), lateral entorhinal (LEnt) and perirhinal cortices (PRh, **DIII'**) and subiculum (S, **DIII'**). Scale bars: 150 μm. The mouse brains in this figure has been reproduced from Franklin and Paxinos (2001).

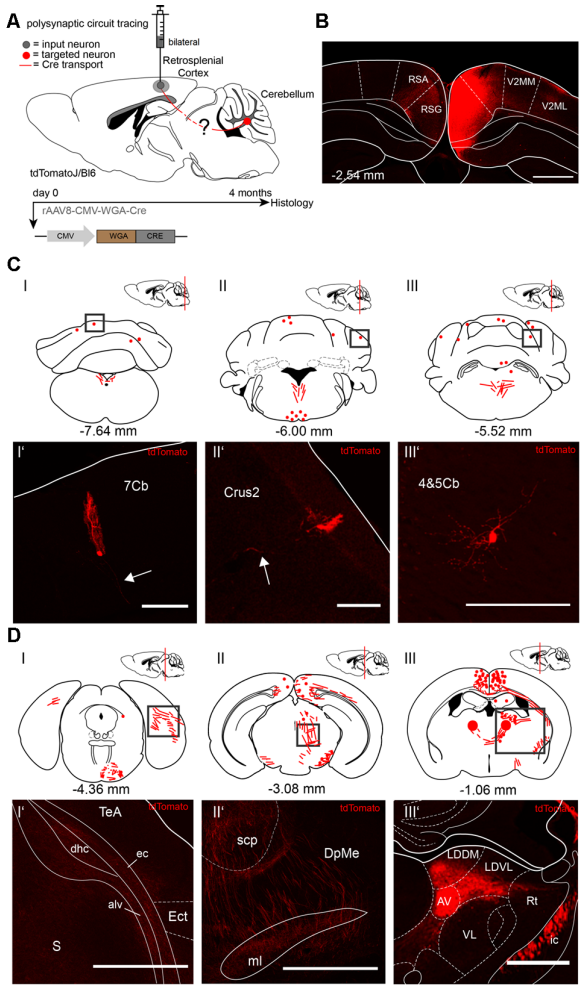

FIGURE 3 | Mapping rAAV mediated polysynaptic targets from the retrosplenial cortex (RSC) to cerebellum using the tracer rAAV8-CMV-WGA-Cre in tdTomatoJ$^{+/+}$ mice. **(A)** Schematic of sagittal section from an adult tdTomatoJ$^{+/+}$ mouse brain injected bilaterally with each 1 μl rAAV8-CMV-WGA-Cre in the RSC, granular (RSG) and agranular (RSA) parts (gray dot) for 4 months to trace the polysynaptic circuit (red line) to the cerebellum (red dot). **(B)** Confocal image of a coronal section from an adult tdTomatoJ$^{+/+}$ mouse brain injected with rAAV8-CMV-WGA-Cre showing the injection sites in the retrosplenial cortices (RSC). Scale bar: 250 μm. **(CI–III)** Schematic of coronal sections showing quantitative localization of tdTomato^{+} neuron cell bodies (red dots) or neurites (red lines) at different distances from Bregma (−7.64 mm, −6.00 mm, −5.52 mm) after rAAV8-CMV-WGA-Cre injection in the RSC. Squared boxes represent confocal images presented in **(CI'–III')**. **(CI'–III')** Example single tdTomato^{+} neurons were imaged from the cerebellar lobule 7 (7Cb, **CI'**), cerebellar Crus2 **(CII')** and lobes 4 and 5, (4&5Cb, **CIII'**). Arrows pointing to tdTomato^{+} axons. Scale bars: 250 μm **(I',II')**, 100 μm (**I''**). **(DI–III)** Schematic of coronal sections showing quantitative localization of tdTomato^{+} neuron cell bodies (red dots) or neurites (red lines) at different distances from Bregma (−4.36 mm, −3.08 mm, −1.06 mm) after rAAV8-CMV-WGA-Cre injection in the RSC. Squared boxes represent confocal images presented in **(DI'–III')**. **(DI'–III')** Example single tdTomato^{+} neurites were imaged from the left dorsal hippocampal commissure (dhc), alveus of the hippocampus (alv) and external capsule (ec, **DI'**), thalamic deep mesencephalic nucleus (DpME), superior cerebellar peduncle (scp) and medial lemniscus (ml, **DII'**), laterodorsal thalamic nuclei, dorsomedial (LDDM) and ventrolateral (LDVL), anteroventral thalamic nucleus

(*Continued*)

FIGURE 3 | Continued
(AV) and internal capsule (ic, **DIII'**) that are expressing tdTomato^{+} neurites. Scale bars: 150 μm. The mouse brains in this figure has been reproduced from Franklin and Paxinos (2001).

expression in the thalamus following injection of WGA-Cre in the hippocampus vs. the cerebellar DCN. Injection in the cerebellar DCN showed more labeling in the thalamus, except for in the lateral posterior thalamus (**Supplementary Figure S2C**), suggesting the existence of different pathways connecting the cerebellum with the hippocampus in a loop, as was reported for motor-related areas (Dum and Strick, 2003; Kelly and Strick, 2003). We also found tdTomato+ neurites crossing the MGD/MGV (medial geniculate nucleus, dorsal and ventral parts; **Supplementary Figure S2B**) and dorsal raphe nucleus (DRN, **Supplementary Figure S2B'**). Some tdTomato+ expressing cells were seen in the medial septal nucleus (MS, **Supplementary Figure S2D**) and neurites in the lateral septal nucleus (LSI, **Supplementary Figure S2D'**).

Since both injections of rAAV8-CMV-WGA-Cre virus in the cerebellar DCN (**Figure 1**) and hippocampus (**Figure 2**) demonstrated tdTomato^{+} neurons in the RSC, we injected the RSC, granular (RSG) and agranular (RSA) parts of two tdTomatoJ mice bilaterally (**Figure 3**) to further dissect the synaptic connections between the cerebellum and hippocampus (AP: −2.54 mm, ML: ± 0.3 mm, DV: 0.75–0.25 mm; 1 μl per site). Four months of expression and tracing time, we observed tdTomato^{+} cerebellar Purkinje cells (**Figures 3CI',II'**) with their positive axons (arrows) and molecular layer interneurons (**Figure 3CIII'**) equally distributed over the cerebellar lobules (**Figure 3C**). We also detected tdTomato^{+} neurites in the right dorsal hippocampal commissure (dhc), alveus of the hippocampus (alv) and external capsule (ec) but not in the ectorhinal cortex (Ect) at −4.36 mm from Bregma, close to the cerebellum (**Figures 3DI–I'**). tdTomatoJ^{+} neurites crossed the superior cerebellar peduncle (scp), thalamic deep mesencephalic nucleus (DpMe) and medial lemniscus (ml) in the thalamus at −3.08 mm from Bregma (**Figures 3DII–II'**), while tdTomato^{+} cell somata were also seen in the right laterodorsal thalamic nuclei, dorsomedial (LDDM) and ventrolateral (LDVL) and bilateral anteroventral thalamic nuclei (AV; **Figures 3DIII–III'**).

To further explore the cerebellar-hippocampal circuitry as reported previously for motor-related areas, we injected the anterograde tracer rAAV8-CMV-WGA-Cre in left cerebellar Crus1/Crus2 (**Figures 4A,BII**; AP: −6.4 mm, ML: −2.7 mm, DV: 1.7–1.07), which may be involved in sequence-based navigation, and the retrograde tracer rAAV8-CMV-TTC-eGFP in the left DG of tdTomatoJ mice (**Figures 4A,BI**; Burguière et al., 2010; Iglói et al., 2015). Since rAAV8-CMV-TTC-eGFP requires a longer expression time in the hippocampus compared to WGA-Cre, it was initially injected 3 months prior to rAAV8-CMV-WGA-Cre (**Figure 4A**). Unilateral injection of rAAV8-CMV-TTC-eGFP in the DG resulted in eGFP^{+} neurons in the DG (**Figure 4CI"**), perirhinal (PRh) and LEnt (**Figures 4CI,CI'**), the subiculum (S) and

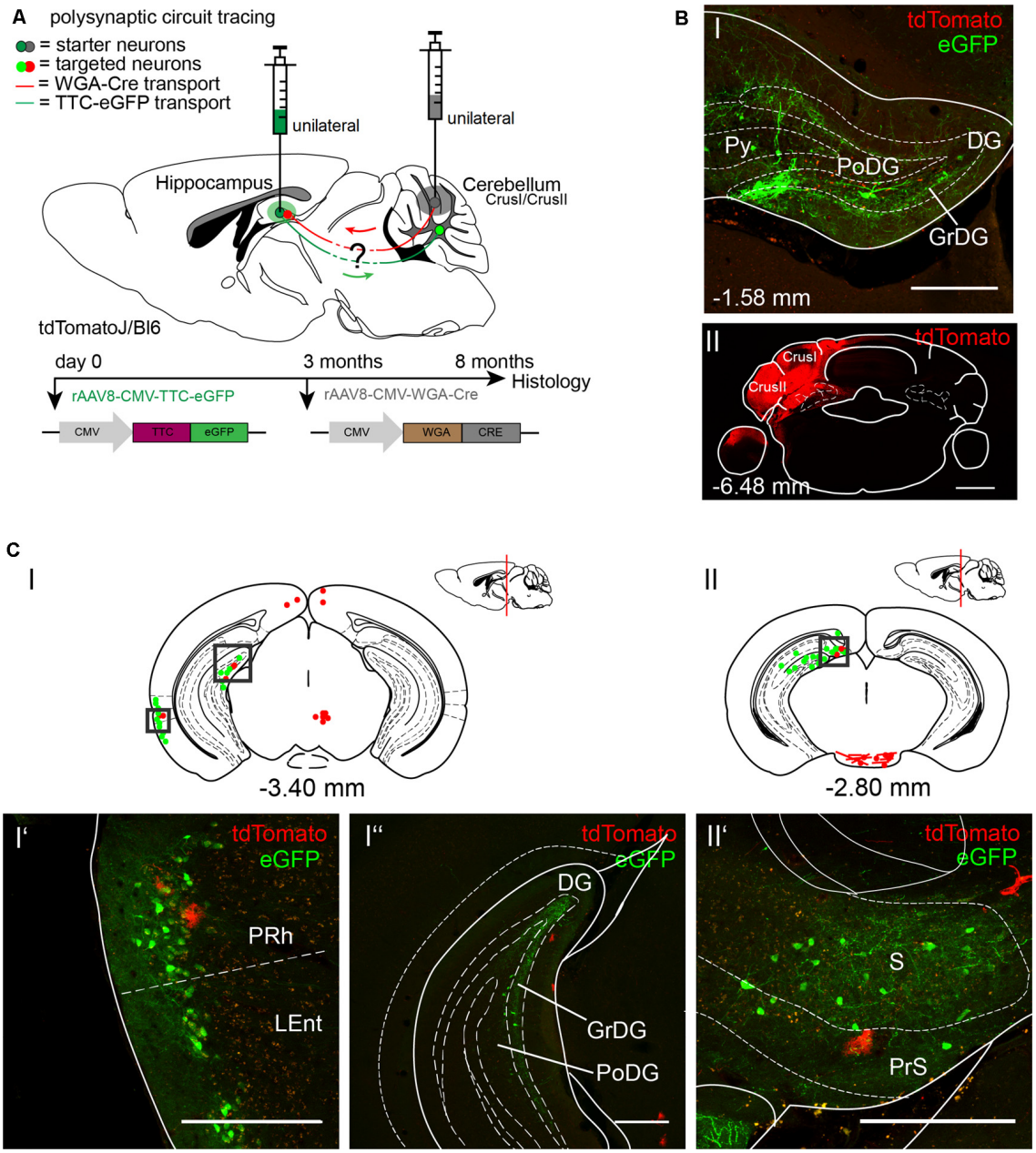

FIGURE 4 | Mapping the shared circuit between the dentate gyrus and cerebellar cortex with an rAAV retrograde and anterograde tracer. **(A)** Schematic of sagittal section from an adult tdTomatoJ$^{+/+}$ mouse brain injected with 1 μl of the retrograde specific rAAV8-CMV-TTC-eGFP (green dot) in the dentate gyrus for 8 months and rAAV8-CMV-WGA-Cre (1 μl) in the cerebellar CrusI/CrusII (gray dot) for 5 months to determine the common polysynaptic circuits (red and green lines). The viruses were injected at different time points to allow better expression of rAAV8-CMV-TTC-eGFP. **(B)** Confocal image of a coronal section from an adult tdTomatoJ$^{+/+}$ mouse brain injected unilaterally with rAAV8-CMV-TTC-eGFP in the dentate gyrus [DG, green, upper **(I)**] and rAAV8-CMV-WGA-Cre in cerebellar CrusI/CrusII [red, lower **(II)**]. Cell bodies stained with tdTomato are evident in the dentate gyrus. Scale bars: 250 μm. **(CI,II)** Schematic of coronal sections showing quantitative localization of tdTomato^{+} (red dots) and eGFP^{+} (green dots) neuronal cell bodies or neurites (red lines) at different distances from Bregma (−3.40 mm, −2.80 mm). Squared boxes represent images in **(CI'–CII')**. **(CI'–II')** Example images from squared boxes in **(CI'–II')** of tdTomato^{+} and eGFP^{+} positive cell bodies in perirhinal cortex (PRh, **I'**), dentate gyrus (DG, **I''**) and presubiculum (PrS, **II'**) where circuits are shared. Scale bars: 250 μm. The mouse brains in this figure has been reproduced from Franklin and Paxinos (2001).

presubiculum (PrS; **Figures 4CII,CII'**), but failed to label structures beyond these areas. The injection of WGA-Cre in cerebellar Crus1/Crus2 resulted in tdTomato^{+} cells, likely astrocytes, in similar areas such as the PRh (**Figure 4CI'**) and PrS (**Figure 4CII'**), but no neurons were identified expressing both fluorescent proteins.

Retrograde Monosynaptic Tracing of the Mouse Hippocampal-Thalamic-Cerebellar Circuitry Using Deletion Mutant Rabies Virus

To determine the sequence of connections between the cerebellum and hippocampus in more detail, we used the retrograde mono-transsynaptic tracer RABVΔG-eGFP (EnvA), allowing a retrograde step-by-step tracings to the cerebellum, starting from the hippocampus (Wickersham et al., 2007a,b). To allow efficient infection, as well as transsynaptic traversal of neurons by our modified RABV we first infected the hippocampus proper and DG of 6 C57/Bl6 mice (three mice/area) with two rAAV expressing the rabies virus glycoprotein and the TVA receptor (Niedworok et al., 2012). One week later we injected into the same site RABVΔG-EGFP (EnvA). We injected both the hippocampus proper and DG for two reasons (**Figure 5**). First, the connectivity of this structure is well described and serves as a valuable control for obtained tracings results. Second, we wanted to test a possible existence of a weak but monosynaptic cerebellar projection to the hippocampus. After 1 week of RABV expression in the hippocampus (DG and CA1/CA3, see **Table 2** in the "Materials and Methods" section for coordinates), eGFP$^+$ neurons appeared in the rhinal cortex (RC), including entorhinal (Ent), PRh, LEnt and parts of the medial entorhinal (MEnt) cortex, PrS and S (**Figure 5C**), lateral and medial supramammillary nuclei, mammillary tract and medial septal nucleus, as well as nuclei in the dorsal raphe and horizontal limb of the diagonal band (HDB; **Supplementary Figure S3**). We found significantly more eGFP$^+$ neurons in the RC (5,517 cells) compared to RSC, S and PrS/PaS ($p = 0.001$; $p = 0.002$; $p = 0.016$, each t-test $n = 3$; **Figures 5DI,EI**). Graphical illustration of the distribution of eGFP$^+$ neurons depending to their distance to Bregma of the RC showed that the LEnt provides strongest synaptic input to the hippocampus (2,261 cells), followed by Ect (1,476), PRh (1,452) and MEnt (328; **Figures 5DIII,DIV**; analyzed with One-way ANOVA). Notably, we did not detect fluorescence in the cerebellum or in the thalamus.

Since the hippocampus receives inputs predominantly *via* the dentate gyrus, we next bilaterally injected only the DG with the above-mentioned viruses (each 0.2 µl) to differentiate the synaptic inputs to the hippocampus proper and DG (**Figure 6**). Similarly, eGFP$^+$ neurons were found in the same areas as after rAAV8-CMV-WGA-Cre injections into the CA1/CA3 region, including PRh and LEnt (**Figures 6CI',II'**) but also ectorhinal cortex (Repapi et al., 2009), PaS (**Figure 6CI'**), S and CA1 (**Figures 6CIII',III"**), suggesting a monosynaptic input from these regions to the DG. We also found eGFP$^+$ cells in the lateral and medial supramammillary nuclei medial raphe nucleus and nuclei in the horizontal limb of the diagonal band (**Supplementary Figure S4**). We confirmed that neurons of the PRh synapse onto DG and the CA1 neurons, as previously reported by Agster and Burwell (2013). Projections from Ect, LEnt and MEnt to the DG have already been described in mice, as well as the input from the supramammillary nuclei but a monosynaptic projection from the PaS to the DG as observed

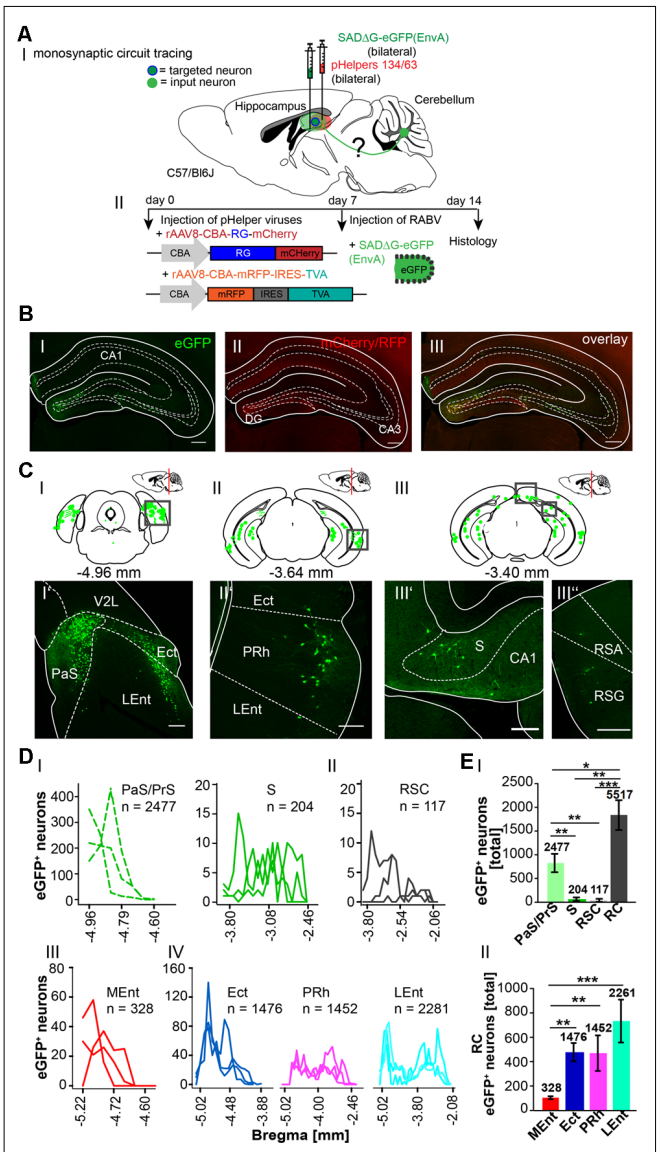

FIGURE 5 | Inputs into the hippocampus using a monosynaptic, retrograde modified RABV tracer. **(AI)** Schematic of sagittal section from an adult mouse brain injected with the retrograde specific modified RABV tracer (green dots) and pH in the hippocampus (1 µl). The pHelper viruses rAAV8-CBA-RG-mCherry and rAAV8-CBA-mRFP-IRES-TVA were injected 7 days prior to the SADΔG-eGFP (EnvA) rabies virus (1:2 ratio, 1 µl/site). Animals were sacrificed 7 days after RABV injection. **(AII)** Overview of the bilaterally injected hippocampus. The framed area represents the hippocampus shown in **(B)**. Scale bar: 1 mm. **(B)** Higher magnification of the right injection site (Bregma −1.94 mm) showing hippocampal neurons infected with the Helper virus (RFP$^+$; **BI**) or rabies virus (eGFP$^+$; **BII**). Scale bar: 250 µm. Merge **(BIII)** of images in **(B')** and **(B")** showing double-fluorescent neurons in the dentate gyrus. Scale bar: 250 µm. **(CI–III)** Schematic of coronal sections showing quantitative localization of eGFP$^+$ (green dots) neuronal cell bodies at different distances from Bregma (−4.96 mm, −3.64 mm, −3.40 mm) in all analyzed mice ($n = 3$). Squared boxes represent images in **(CI'–III")**. **(CI'–III")** Example images from squared boxes in **(CI–III)** demonstrate that eGFP$^+$ cell bodies represent inputs into the dentate gyrus from the parasubiculum (PaS, **I'**), ectorhinal cortex (Ect, **I'**), lateral entorhinal cortex (LEnt, **I'**), perirhinal cortex (PRh, **II'**), subiculum (S, **III'**)

(*Continued*)

FIGURE 5 | Continued
and RSC, agranular and granular parts (RSA, RSG, **III"**). **(D)** Graphical illustration showing the representative number of eGFP$^+$ neurons found at different mm from Bregma in Para-, and Pre-subiculum, S (PaS, Pre; **DI**) and the RSC **(DII)**, with each line representing the count in one mouse. **(DI,II)** A total of 2,477 eGFP expressing cells were count in PaS/Pre of $n = 3$ mice (dotted lines), while only 204 eGFP$^+$ cells were detected in the S **(DI)** and 117 cells in the RSC **(DII)**. A total of 2281 eGFP+ cells were found in the Ent, followed by 1476 eGFP+ cells in the Ect and 1452 cells in the PRh (DIV). **(EI)** Statistical analysis comparing all input areas to the Hippocampus. With a total of 5,517 eGFP$^+$ cells, the rhinal cortex (RC) provides significantly more input to the murine Hippocampus compared to RSC ($p = 0.001$, *t*-test), S ($p = 0.002$, *t*-test) and Pre/PaS ($p = 0.016$, *t*-test). Pre/PaS significantly increased projections compared to S ($p = 0.003$, *t*-test) and RSC ($p = 0.002$, *t*-test). **(DIII)** Graphical illustration showing the representative number of eGFP$^+$ neurons found at different mm from Bregma in Ect (1,476 neurons), PRh (1,452), LEnt (2,261) and medial entorhinal cortex (MEnt, 328). All areas that provide monosynaptic input to the hippocampus as revealed by eGFP+ cells. The RC provides strongest synaptic input to the hippocampus compared to RSC ($p = 0.001$, *t*-test), S ($p = 0.002$, *t*-test) and PaS/PrS ($p = 0.016$, *t*-test). A total of 2477 eGFP+ cells were found in the PaS/PrS, which is significantly more compared to S ($p = 0.003$, *t*-test) and RSC ($p = 0.002$, *t*-test). **(EII)** Total number of eGFP$^+$ neurons in the rhinal cortex of $n = 3$ mice showing significantly more projections (One-way analysis of variance, ANOVA), *post hoc* Tukey ($p < 0.05$) from the Ect (1,476 cells) PRh (1,422) and LEnt (2,261) compared to the MEnt (328). Significance for comparisons: $^*p \leq 0.05$; $^{**}p \leq 0.01$; $^{***}p \leq 0.001$. DG, dentate gyrus; Ect, ectorhinal cortex; LEnt, lateral entorhinal cortex; MEnt, medial entorhinal cortex; PaS, parasubiculum; PRh, perirhinal cortex; PrS, presubiculum; Py, pyramidal cell layer of the hippocampus; RSA, agranular retrosplenial cortex; RSC, retrosplenial cortex; RSG, granular retrosplenial cortex; RC, rhinal cortex; S, subiculum; V2L, secondary visual cortex, lateral area. The mouse brains in this figure has been reproduced from Franklin and Paxinos (2001).

here has not been reported (**Figure 6CI'**; Vertes and McKenna, 2000; van Groen et al., 2002b,c; Hartley et al., 2013). Thus, injections of modified RABV in the hippocampus and DG both confirmed already known projections, but also revealed a new projection from the PaS to the DG. Analysis revealed that the DG receives most input from the RC (4,889 cells in ≥3 mice, **Figure 6F**), when compared to CA1 and S ($p < 0.001$, *t*-test), which is in accordance with our results presented in **Figure 5D**. With these findings, we show that RC input to the hippocampus is delivered *via* the DG. Within the RC, the LEnt contributed the most synaptic input to the DG ($n = 3{,}122$ cells) compared to the PRh ($n = 1{,}141$ cells), Ect ($n = 440$ cells) and MEnt ($n = 186$ cells, One-Way-ANOVA, **Figures 6D,FII**).

To further explore whether the cerebellum synapses directly on other hippocampal input regions including the S (**Figure 7**), RSC (**Figure 8**) and Ent (**Figure 9**), the modified RABV was injected in these areas of C57/Bl6 mice. Bilateral injection of RABVΔG-eGFP virus in the S (AP: −3.52 mm, ML: ± 2.2 mm; DV: 1.5–1.3 mm, $n = 5$) resulted in double-fluorescent neurons in the subiculum resulting from infection from both rAAV helper viruses (mCherry/RFP, 0.2 µl) and rabies virus (eGFP, 0.1 µl; **Figure 7AII**). The laterodorsal thalamic nucleus, dorsomedial (LDDM) and ventrolateral parts (LDVL) showed eGFP$^+$ neurons, representing direct monosynaptic input to the S (**Figure 7BII'**). Only 2–5 eGFP$^+$ cells were observed in the PRh of each S injected mouse, thus confirming sparse input from the RC to the S. Additionally, we found a total of 28,093 CA1 pyramidal

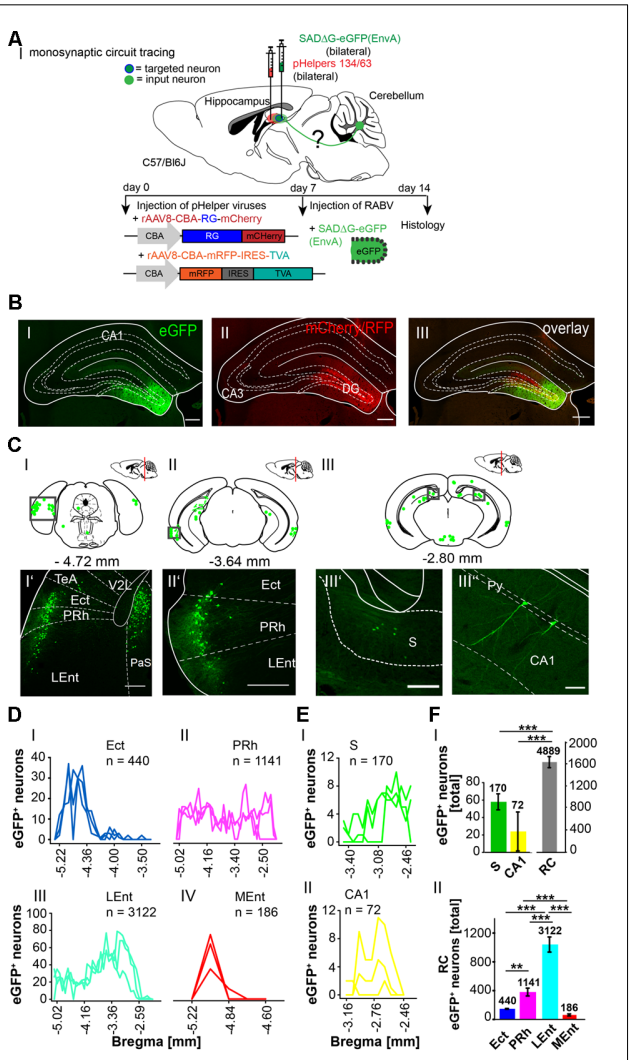

FIGURE 6 | Mapping monosynaptic input areas to the dentate gyrus in C57/Bl6 mice using the retrograde SADΔG-eGFP tracer. **(AI)** Scheme of a sagittal section from an adult mouse brain injected with the retrograde specific RABV tracer (green circle) in the dentate gyrus of C57/Bl6 mice ($n = 3$). The pHelper viruses rAAV8-CBA-RG-mCherry and rAAV8-CBA-mRFP-IRES-TVA (1:2 ratio, 0.2 µl) were injected 7 days prior to the SADΔG-eGFP (EnvA) rabies virus (0.2 µl). **(B)** Confocal image showing one exemplary injection site in the left DG with rabies virus (eGFP, **BI**) and pHelpers (mcherry, **BII**) in the DG. Overlay reveals coinfected starter neurons for monosynaptic retrograde tracing **(BIII)**. Scale bars: 250 µm. **(CI–III)** Coronal brain sections at −4.72 mm, −3.64 mm and −2.80 mm from Bregma depicting eGFP$^+$ neurons (green dots) by retrograde monosynaptic transport from the DG. **(CI–III")** Confocal image from boxed area presented in CI representing several eGFP$^+$ neurons in the outer layers of the RC, including Ect, PRh and LEnt **(CI'–II')**, the S **(CIII')** and pyramidal CA1 cells of the hippocampus **(CIII")**, representing input to the DG. Scale bars: 250 µm. **(D)** Line plots mapping the individual distribution of eGFP$^+$ neurons by retrograde monosynaptic transport from the DG to the Ect **(DI)**, PRh **(DII)**, LEnt **(DIII)** and MEnt **(DIV)** in all mice. Each line represents the count of eGFP$^+$ cell bodies in one mouse. **(E)** Line plots mapping the individual distribution of eGFP$^+$ neurons by retrograde monosynaptic transport from the DG to the S **(EI)** and CA1 **(EII)**. **(FI)** Compared to S and CA1, the RC provides the most input to the DG revealed by monosynaptic retrograde transport (*t*-test, for S: $p \leq 0.001$; for CA1 $p \leq 0.001$). **(FII)** Within the RC,
(*Continued*)

FIGURE 6 | Continued
the LEnt forms significantly more synapses with the DG with a total of 3,122 eGFP$^+$ cells compared to PRh ($p \leq 0.001$), Ect ($p \leq 0.001$) and MEnt ($p \leq 0.001$, all One-Way-ANOVA). In the PRh a total of 1,141 cells was counted and is the second strongest input source to the DG compared to Ect ($p = 0.006$) and MEnt ($p = 0.001$, One-Way-ANOVA). Significance for comparisons: $^{**}p \leq 0.01$; $^{***}p \leq 0.001$. DG, dentate gyrus; Ect, ectorhinal cortex; LEnt, lateral entorhinal cortex; MEnt, medial entorhinal cortex; PRh, perirhinal cortex; Py, pyramidal cell layer of the hippocampus; RC, rhinal cortex; S, subiculum; TeA, temporal association cortex; V2L, secondary visual cortex, lateral area. The mouse brains in this figure has been reproduced from Franklin and Paxinos (2001).

cells at various distances from Bregma (**Figures 7BI",DI**) and 1,034 cells in the RSC (**Figures 7BI',DIII**). To our knowledge, the LDDM has not been reported before to synapse on the subiculum directly and a total of 639 cells were counted in all mice in the laterodorsal thalamus. These are significantly more compared to the LPMR ($p \leq 0.001$) and LPLR ($p = 0.006$) or VL ($p = 0.024$, One-Way-ANOVA, **Figure 7CIV**).

The RSC has been previously proposed to connect the cerebellum with the hippocampus *via* a polysynaptic circuitry (Rochefort et al., 2013). To identify these circuits, we bilaterally injected the monosynaptic RABVΔG-eGFP (0.5 µl each rAAV helpers and RABV) in the retrosplenial cortex, granular (RSG) and agranular (RSA) areas (**Figure 8A**) at −1.46 mm from Bregma (ML: ± 0.25 mm; DV: 0.25–0.1 mm; $n = 3$). An average of nine neurons in both regions were co-expressing both helper (mCh/RFP) and RABV (eGFP, **Figure 8AII**). Although there was no tracer observed in the cerebellum, staining in the left LDDM and LDVL, as well as in the ventrolateral thalamic nucleus (VL) at −1.22 mm from Bregma (**Figure 8BIII'**) was evident, indicating a direct monosynaptic input from the thalamus to the RSA as reported for the LDDM in rats (Sripanidkulchai and Wyss, 1986). In all mice analyzed, the thalamic nuclei equally project to the RSC, except the AV, which has significantly less eGFP$^+$ cells than the LDDM ($p = 0.027$, One-Way-ANOVA, **Figure 8EII**). We also found eGFP$^+$ cells in the S and hippocampal CA1 (**Figures 8BI',II'**), with the S forming more synapses on the RSC than the CA1 cells ($p = 0.011$, t-test). Additionally, few eGFP$^+$ neurons in the medial and median raphe nuclei, lateral supramammillary nucleus, dorsal secondary auditory cortex and the pontine reticular nucleus (**Supplementary Figure S5**) were detected.

Since the RC provides strong monosynaptic input to the dentate gyrus in mice (Hartley et al., 2013), we wanted to test the possibility of a monosynaptic connection between the RC and the cerebellum. Injection of the modified RABV (0.3 µl) in the left rhinal cortex at −4.84 mm from Bregma (ML: −4.2 mm, DV: 1.65–0.55, $n = 4$) revealed co-expressing neurons distributed in the LEnt (**Figure 9AII**). Many eGFP+ neurons were observed at the ipsilateral side, predominantly in hippocampal CA1, CA2 and CA3 region (**Figures 9BI,II,II'**) and S (**Figure 9BI'**) and RSC (**Figure 9BII**), indicating direct monosynaptic input from these areas to the RC. eGFP$^+$ expressing neurons were also detected in the DG bilaterally and in the ipsilateral LPMR and medial geniculate nucleus, dorsal (MGD) and ventral

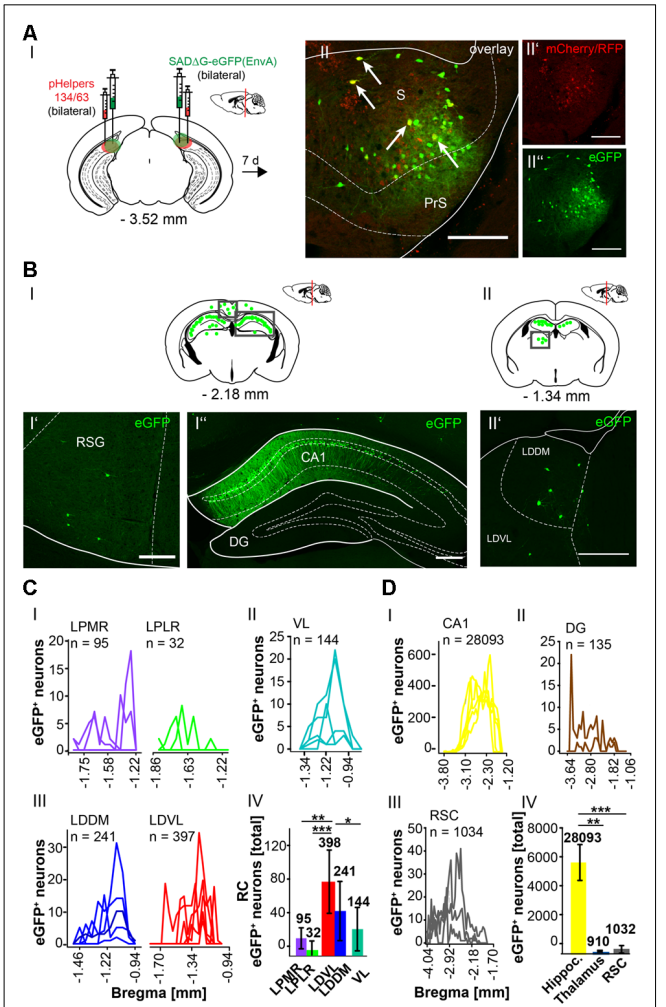

FIGURE 7 | Identifying a monosynaptic circuit to the subiculum from the thalamus using the retrograde, modified RABV tracer. **(A)** Schematic of a coronal section at Bregma −3.52 mm **(AI)** from an adult mouse brain injected bilaterally with the retrograde specific, modified RABV tracer (green circle, 0.1 µl, **AII"**) and pHelper mixture (red circle, **AII'**) in the subiculum (S) and presubiculum (PrS) of $n = 5$ mice. The pHelper viruses rAAV8-CBA-RG-mCherry and rAAV8-CBA-mRFP-IRES-TVA (1:2 ratio, 0.2 µl) were injected 7 days prior to the SADΔG-eGFP (EnvA) rabies virus. Animals were sacrificed 7 days after modified RABV injection. **(AII)** Confocal image showing co-expression of both pHelper and rabies viruses. Scale bars: 250 µm. **(BI)** Coronal brain scheme at −2.18 mm from Bregma showing eGFP$^+$ neurons (green dots) by monosynaptic retrograde transport from the S and PrS to the (RSG, **BI'**) and hippocampal CA1 **(BI")**. **(BII)** Coronal brain section at Bregma −1.34 mm depicting eGFP$^+$ neurons by monosynaptic retrograde transport from the S and PrS to hippocampal CA1 and laterodorsal and ventrolateral thalamus (LDDM/LDVL, **BII'**). Scale bar: 250 µm. **(CI–III)** Line plots mapping the individual distribution of eGFP$^+$ neurons by retrograde monosynaptic transport from the S and PrS to the lateral posterior thalamic nucleus, mediorostral and laterorostral parts (LPMR/LPLR, **CI**), ventrolateral thalamus (VL, **CII**) and LDDM and LDVL **(CIII)**. **(CIV)** With total 398 eGFP$^+$ cells, the LDVL provides strongest synaptic input to the S and PrS compared to LPMR ($p \leq 0.001$), LPLR ($p = 0.006$) and VL ($p = 0.024$, analyzed with One-Way-ANOVA; **DI**) Line plots mapping the individual distribution of eGFP$^+$ neurons by retrograde monosynaptic transport from the S and PrS to the CA1 **(DI)** and DG **(DII)** region of the hippocampus and to the RSC **(DIII)**. eGFP$^+$ cells in the DG were found in two of the five analyzed mice.

(*Continued*)

FIGURE 7 | Continued
(DIV) Compared to the thalamic nuclei **(CI–III)** and RSC **(DIII)**, the hippocampus exhibited a total of 28,228 eGFP$^+$ cells, which is significantly more than in the thalamus (p = 0.008, Mann-Whitney U) and RSC ($p \leq 0.001$, t-test). Significance for comparisons: *$p \leq 0.05$; **$p \leq 0.01$; ***$p \leq 0.001$. DG, dentate gyrus; LDDM, dorsomedial laterodorsal thalamic nucleus; LDVL, ventrolateral laterodorsal thalamic nucleus; LPLR, laterorostral lateral posterior thalamic nucleus; LPMR, mediorostral lateral posterior thalamic nucleus; PrS, Presubiculum; RSC, retrosplenial cortex; RSG, granular retrosplenial cortex; S, Subiculum; VL, ventrolateral thalamus. The mouse brains in this figure has been reproduced from Franklin and Paxinos (2001).

parts (MGV; **Supplementary Figure S6**). Furthermore, the RC receives less synaptic input from the Barrington's nucleus and the gigantocellular reticular nucleus in the pons, the ipsilateral motor cortex M2, the medial septal nucleus, the lambdoid zone and the ipsilateral nucleus of the horizontal limb of the diagonal band (**Supplementary Figure S6**). eGFP$^+$ cells were also detected and analyzed in the thalamus, including LDDM/LDVL and VL (**Figures 9BIII',CIII**). Within the thalamus, the VL forms more synapses with the RC compared to LDVL ($p \leq 0.001$), LPMR (p = 0.002) and LPLR (p = 0.002, One-Way-ANOVA; **Figure 9D**). However, the hippocampus innervates the RC to a greater extent than the S (p = < 0.001, t-test), RSC (p = 0.029, Mann-Whitney-U-test) and thalamus (p = 0.029, Mann-Whitney-U-test; **Figure 9EIII**). Since we injected the RC unilaterally, we are able to differentiate between inputs from ipsi-, and/or contralateral sites (**Supplementary Figure S7**). We observed a tendency of ipsilateral rather than contralateral cells projecting to the RC from the RSC and DG (**Supplementary Figures S7A,B**). Interestingly, significantly more ipsilateral cells from the CA3 hippocampus proper (p = 0.002, t-test) and S (p = 0.029, Mann-Whitney-U-test) synapse on the RC compared to contralateral cells. However, no eGFP$^+$ neurons were seen in the cerebellum.

In this article, we show that LDDM/LDVL and VL in the thalamus is involved in the polysynaptic connections between the cerebellum and hippocampus *via* the S, RSC and RC utilizing both polysynaptic tracers, rAAV8-CMV-WGA-Cre and rAAV8-CMV-TTC-eGFP (**Figure 3**) and a modified RABV (**Figures 7–9**). It has been reported that the LDDM participates in spatial learning and memory, while the VL is known to receive fastigial nucleus input in non-human primates (van Groen et al., 2002b; Kelly and Strick, 2003). Based on these data we injected the modified RABV in these thalamic nuclei to identify a potential three-synapse projection pathway from the cerebellum to the hippocampus *via* relay in the thalamus, RSC and/or S and RC. Unilateral injection in the LDDM and LDVL regions of C57/Bl6 mice ($n \geq 4$) at −1.46 mm from Bregma (**Figure 10**) revealed co-expression of both helper (mCh/RFP, 0.2 µl) and RABV (eGFP, 0.2 µl) in neurons from both regions (**Figure 10AII**). We were able to identify a new projection pathway to the LDDM/LDVL from only contralateral areas of the DCN, the medial (fastigial, Med) nucleus (**Figures 10BI–IV,C**). Neurons of the interpositus nucleus (IntP) and lateral (dentate, Lat) nucleus of the DCN also provide strong monosynaptic input to the LDDM/LDVL

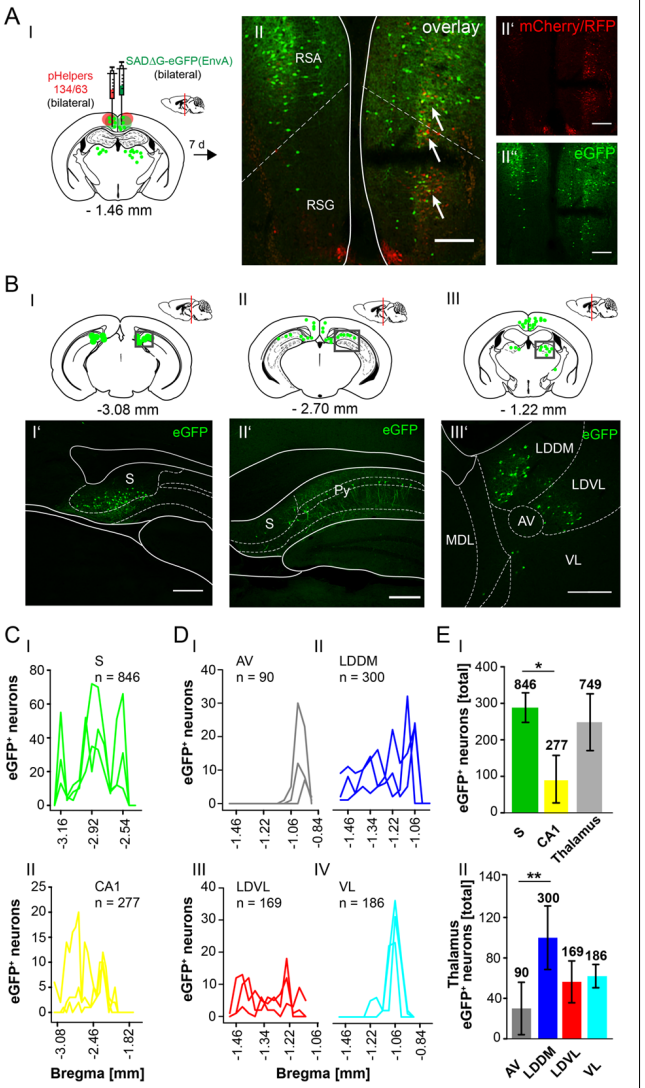

FIGURE 8 | Mapping the circuit between the RSC and thalamus. **(AI)** Schematic of coronal section at Bregma −1.46 mm and confocal images of rabies infection site **(AII")** and pHelpers **(AII')** depicting virus spread to the RSA and RSG areas **(AII)**. Green dots represent the retrograde specific, modified RABV tracer expression. The pHelper viruses rAAV8-CBA-RG-mCherry and rAAV8-CBA-mRFP-IRES-TVA (1:2 ratio, 0.5 µl) were injected 7 days prior to the SADΔG-eGFP (EnvA) rabies virus (0.5 µl). Mice (n = 3) were sacrificed 7 days after modified RABV injection. Double infected neurons represent starter neurons for retrograde transport in RSA and RSG (arrows, **AII**). Scale bars: 150 µm**. (BI–III)** Coronal brain sections at Bregma −3.08 mm **(BI)**, −2.70 mm **(BII)** and −1.22 mm **(BIII)** depicting eGFP$^+$ neurons (green dots) undergoing monosynaptic retrograde transport from the RSC. **(BI'–III')** Images from boxed areas in **(BI–BIII)**. eGFP$^+$ neurons outside the injection site were detected in the S **(BI')**, CA1 pyramidal cells **(BII')** and in the LDDM and LDVL **(BIII')**. Scale bars: 250 µm. **(C)** Line plots mapping the distribution of eGFP$^+$ neurons per mouse by retrograde monosynaptic transport from the RSC to the S **(CI)** and CA1 **(CII)** and their distance to Bregma. **(D)** Line plots mapping the distribution of eGFP$^+$ neurons per mouse by retrograde monosynaptic transport from the RSC to AV **(DI)**, LDDM **(DII)**, LDVL **(DIII)** and VL **(DIV)**. **(EI)** A total of 846 eGFP$^+$ cells was found in all mice in the S, showing significantly more input from the S to the RSC compared to the CA1 region (p = 0.011, t-test), but not the

(*Continued*)

FIGURE 8 | Continued
thalamus ($p = 0.473$, *t*-test). **(EII)** Within the thalamus, the LDDM showed significantly more eGFP$^+$ cells then the AV ($p = 0.027$, One-Way-ANOVA), but no other significance was found between the nuclei (LDVL $p = 0.185$; VL $p = 0.273$). Significance for comparisons: $^*p \leq 0.05$; $^{**}p \leq 0.01$. AV, anteroventral thalamic nucleus; DLG, dorsal lateral geniculate nucleus; LDDM, dorsomedial laterodorsal thalamic nucleus; LDVL, ventrolateral laterodorsal thalamic nucleus; LPLR, laterorostral lateral posterior thalamic nucleus; LPMR, mediorostral lateral posterior thalamic nucleus; MDL, lateral mediodorsal thalamic nucleus; Po, posterior thalamic nuclear group; Py, pyramidal cell layer of the hippocampus; RSA, agranular retrosplenial cortex; RSG, granular retrosplenial cortex; S, Subiculum; VL, ventrolateral thalamic nucleus. The mouse brains in this figure has been reproduced from Franklin and Paxinos (2001).

(**Figures 10B,C**). A total of 732 cells were seen in the DCN in all mice (**Figure 10D**), however, the Med forms less synapses with the LDDM/LDVL than IntP and Lat ($p \leq 0.001$, One-Way-ANOVA; **Figure 10D**). Injection of 0.2 µl RABV in the VL at −1.58 mm from Bregma (**Figure 11A**) revealed co-expressing starter neurons only in the desired area (**Figure 11AII**). We found both ipsi- and contralateral staining in the DCN (**Figure 11BI**) that was present through all slices analyzed. The contralateral Lat and IntP of the DCN were identified as a strong synaptic input source to the VL (**Figures 11BI",BII'**), but significantly fewer cells were seen in the Med ($p \leq 0.001$ compared to IntP, One-Way-ANOVA; **Figure 11D**). In general, the contralateral DCN had more eGFP$^+$ neurons than the ipsilateral sites (**Figure 11D**, each *t*-test). We also found several eGFP$^+$ neurons in the pons, equally distributed (**Figure 11BI**).

Taken together, we were able to identify a polysynaptic cerebellar-hippocampal connection by use of monosynaptic retrograde and polysynaptic anterograde and retrograde virus-based tracing. We found a new projection pathway from the medial cerebellar nucleus to the laterodorsal thalamic nuclei, which has not been reported. We also found that the Med projects to the ventrolateral thalamic nuclei in mice, as well as the interpositus cerebellar nuclei synapse on laterodorsal and ventrolateral thalamic nuclei which has been described partially in other species. Both thalamic nuclei synapse on either the subiculum, rhinal cortex and RSC may communicate *via* direct monosynaptic connections, as well as projecting to the hippocampus (**Figure 12**).

DISCUSSION

The cerebellum assists in spatial navigation by participating in building the hippocampal spatial map (Rochefort et al., 2011). The vestibular system plays a vital role in stabilizing gaze during head movements in addition to controlling posture and spontaneous reflexes. Impairments in vestibular inputs diminish learning and memory in particular spatial learning by affecting the proper function of head direction, place and grid cells. Moreover, loss of the vestibular system leads to degeneration of the hippocampus and its dendritic branches and impaired spatial memory in humans (Brandt et al., 2005; Smith et al., 2005; Cronin et al., 2017). Consequently, the cerebellum must

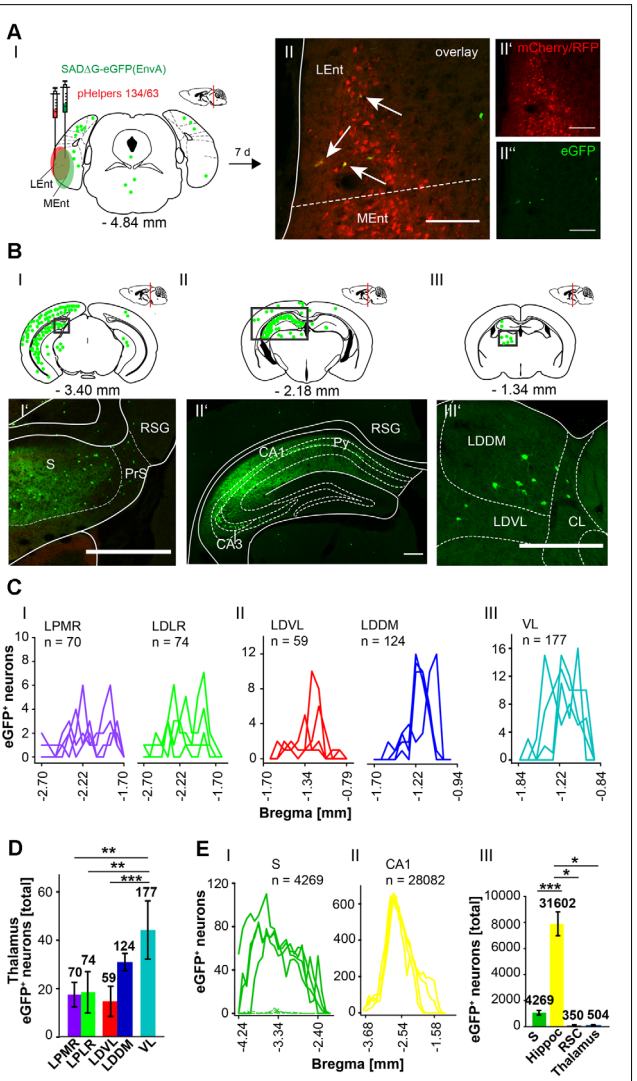

FIGURE 9 | Identifying inputs into the rhinal cortex from the subiculum, hippocampal CA1 region and thalamus using the retrograde, modified RABV tracer. **(AI)** Schematic of coronal section at Bregma −4.84 mm depicting the injection site in $n = 4$ mice. Confocal images show exemplary infection of pHelpers **(AII')** and rabies virus **(AII")** depicting virus spread in the rhinal cortex including lateral (Lent) and medial (MEnt) entorhinal cortices (RC). Overlay reveals coinfected starter cells (arrows in **AII**) of retrograde monosynaptic transport. Green dots represent the retrograde specific, modified RABV tracer expression (0.3 µl). The pHelper viruses rAAV8-CBA-RG-mCherry and rAAV8-CBA-mRFP-IRES-TVA (1:2 ratio, 0.6 µl) were injected 7 days prior to the SADΔG-eGFP (EnvA) rabies virus. Mice were sacrificed 7 days after RABV injection. Scale bar: 150 µm. **(BI–III)** Coronal brain section at Bregma −3.40 mm **(BI)** and −2.18 mm **(BII)** and **(BIII)** −1.34 mm depicting eGFP$^+$ neurons (green dots) by monosynaptic retrograde transport from the rhinal cortex. Rabies infected cells were present in the S **(BI')**, CA1 region of ipsilateral hippocampus and RSC **(BII')**. **(BIII')** Single eGFP$^+$ neurons were found in ipsilateral LDDM and LDVL, but also centrolateral thalamic nucleus (CL) Scale bars: 250 µm. **(C)** Line plots mapping the distribution of eGFP$^+$ neurons per mouse by retrograde monosynaptic transport from the RC to different thalamic nuclei. eGFP$^+$ cells were found in the mediorostral and laterorostral lateral posterior (LPMR/LPLR, **CI**), ventrolateral and dorsomedial laterodorsal (LDVL/LDDM, **CII**) and ventrolateral (VL, **CIII**) thalamic nuclei. **(D)** Compared to all thalamic nuclei,

(*Continued*)

FIGURE 9 | Continued
the VL had a total of 177 eGFP$^+$ cells and thus provides strongest monosynaptic input to the RC compared to LDVL ($p \leq 0.001$), LPLR ($p = 0.002$) and LPMR ($p = 0.002$; One-Way-ANOVA). **(E)** Line plots mapping the distribution of eGFP$^+$ neurons per mouse by retrograde monosynaptic transport from the RC to S **(EI)** and CA1 **(EII)**. **(EIII)** Compared to all areas where eGFP$^+$ cells were found, the hippocampus (including CA1, DG and CA3 (shown in **Supplementary Figures S6**, **S7**) provides strong synaptic input to the RC revealed by monosynaptic retrograde transport compared to S ($p \leq 0.001$, *t*-test), RSC ($p = 0.029$, Mann-Whitney-*U*-test) and thalamus ($p = 0.029$, Mann-Whitney-*U*-test). Significance for comparisons: $^*p \leq 0.05$; $^{**}p \leq 0.01$; $^{***}p \leq 0.001$. CL, centrolateral thalamic nucleus; LDDM, dorsomedial laterodorsal thalamic nucleus; LEnt, lateral entorhinal cortex; LDVL, ventrolateral laterodorsal thalamic nucleus; LPLR, laterorostral lateral posterior thalamic nucleus; LPMR, mediorostral lateral posterior thalamic nucleus; MEnt, mendial entorhinal cortex; PrS, Presubiculum; Py, pyramidal cell layer of the hippocampus; RSC, Retrosplenial cortex; RSG, granular retrosplenial cortex; S, Subiculum; VL, ventrolateral thalamic nucleus. The mouse brains in this figure has been reproduced from Franklin and Paxinos (2001).

synaptically communicate with the hippocampus, either directly or indirectly through other brain regions, possibly involved in navigation such as the subiculum (S) or RSC. Previous studies already showed a functional connectivity between cerebellum and hippocampus in both human and mice (Fischer et al., 2008; O'Reilly et al., 2010; Iglói et al., 2015; Onuki et al., 2015; Watson et al., 2019), but the identification of a neuronal pathway remains to be determined. To improve our understanding of how the cerebellum synaptically communicates with the hippocampus, we used both polysynaptic anterograde and retrograde and monosynaptic retrograde virus-based approaches. Based on our tracing results, we here propose a polysynaptic circuitry from cerebellar fastigial nucleus (Med) with a relay in the LDDM/LDVL and VL, which in turn synapses on S, RC and RSC, which all project to the hippocampus (**Figure 12**). We, however, failed to identify a monosynaptic projection between cerebellum and hippocampus. This seems reasonable since the cerebellum has been shown to connect with the cerebral cortex *via* only polysynaptic circuits in primates (Evarts and Thach, 1969; Middleton and Strick, 1994, 2001; Kelly and Strick, 2003). Moreover, the involvement of the laterodorsal and ventrolateral thalamic nuclei has been confirmed in other studies, as each known cerebellar projection synapses onto the thalamus, that functions as a relay (Buckner et al., 2011).

Both tracer viruses, modified RABV and rAAV8-CMV-WGA-Cre/rAAV8-CMV-TTC-eGFP failed to identify a monosynaptic projection from the cerebellum to the hippocampus. However, we cannot exclude the possibility that a weak monosynaptic transneuronal connection between both structures exist, which is not detectable with our tracing methods. In agreement with our findings, tracing studies using rabies virus as a retrograde, polysynaptic, transneuronal tracer in the dentate gyrus of the hippocampus, found a multisynaptic pathway to restricted regions of the cerebellum which include lobules VI/VII, Crus I, lobule IX and paraflocculus (Watson et al., 2019). Additionally, they performed cerebello-hippocampal LFP coherence recordings in combination with spatial navigation tests in mice to confirm the synchronization

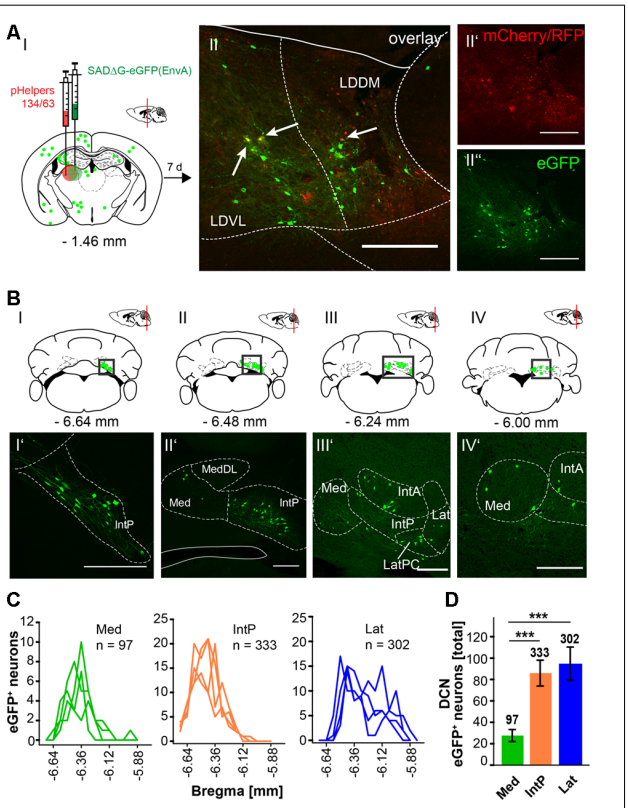

FIGURE 10 | Retrograde modified RABV expression in the laterodorsal thalamus revealed monosynaptic input from the contralateral DCN. **(AI)** Schematic of coronal section at Bregma −1.46 mm and confocal images from an exemplary adult mouse brain injected unilaterally with pHelpers **(AII')** and rabies virus **(AII")** in the laterodorsal (dorsomedial and ventrolateral) thalamus (LDDM/LDVL $n = 4$). Green dots represent the retrograde specific, modified RABV tracer expression. The pHelper viruses rAAV8-CBA-RG-mCherry and rAAV8-CBA-mRFP-IRES-TVA (0.2 µl) were injected 7 days prior to the SADΔG-eGFP (EnvA) rabies virus (0.2 µl). Animals were sacrificed 7 days after RABV injection. **(AII)** Double stained neurons were only seen in the desired area as indicated by arrows and indicate starter neurons of retrograde monosynaptic transport. Scale bars: 250 µm. **(BI–IV)** Schematic of coronal brain sections at Bregma −6.64 mm **(BI)**, −6.48 mm **(BII)**, −6.24 mm **(BIII)** and −6.00 mm **(BIV)** depicting eGFP$^+$ neurons (green dots) by monosynaptic retrograde transport from the laterodorsal thalamus. Confocal images showing rabies-infected cells in the contralateral cerebellar interpositus (IntP, **BI'–BIV'**), medial (Med, fastigial, **BII'–IV'**) and lateral (Lat, **BIII',BIV'**) nuclei. Scale bars: 250 µm. **(C)** Line plots mapping the distribution of total eGFP$^+$ neurons per mouse by retrograde monosynaptic transport from the LDDM/LDVL to the DCN, medial (green lines), interposed (orange lines) and lateral (blue lines) and their distance to Bregma. **(D)** A total of 333 eGFP$^+$ cells were counted for the IntP/IntA and 302 cells were detected in the Lat of all animals, thus showing significantly more input from these two nuclei compared to the Med (97 cells, each $p \leq 0.001$, One-Way-ANOVA). Significance for comparisons: $^{***}p \leq 0.001$. IntA, anterior interposed cerebellar nucleus; IntP, posterior interposed cerebellar nucleus; Lat, lateral (dentate) cerebellar nucleus; LatPC, parvicellular Lat; LDDM, dorsomedial laterodorsal thalamic nucleus; LDVL, ventrolateral laterodorsal thalamic nucleus; Med, medial (fastigial) cerebellar nucleus; MedDL, dorsolateral protuberance of the Med. The mouse brains in this figure has been reproduced from Franklin and Paxinos (2001).

of LFP activity between CrusI and the dorsal hippocampus (DG) during these tasks. In the 80s tracing studies using polysynaptic

radiolabeled amino acids or wheat germ agglutinin conjugated to horseradish peroxidase (WGA-HRP) reported a transient direct projection from the cerebral cortex to the DCN and/or cerebellar cortex in young kittens, rabbit fetuses and in pouch young North American opossum (Tolbert and Panneton, 1983, 1984; Panneton and Tolbert, 1984; Cabana and Martin, 1986; Tolbert, 1989a,b). In addition transient hippocampal projections to the cerebellum in chicken, from areas of the hippocampal formation project to lobules VI–VIII in young but not adult animals were observed (Liu et al., 2012). Direct cerebrocerebellar projections have also been reported in zebra finches and rats (Wild and Williams, 2000), however, they were sparse and temporary. Note that most of these studies used radiolabeled amino acids or WGA-HRP tracers, which cannot distinguish between mono- and polysynaptic connections thus, the interpretation of these results are error-prone.

In the last decade, more advanced WGA tracing tools have been developed combining the CRE and rAAV systems to optimize the specificity and expression of the WGA tracer in the brain (Jarvik et al., 1981). Despite these advances, the interpretation of the data is limited. For example the transduction of rAAV tagged with a fluorescent protein show conflicting reports in the literature, depending on the serotype, region of interest or titer used (Ohta et al., 2011; Espallergues et al., 2012). Moreover the serotype AAV8 used in this study was previously demonstrated to have a higher efficacy to infect hippocampal and cerebellar neurons (Heinemann et al., 1991; Broekman et al., 2006), but in addition has been observed to transport minimally in the retrograde direction *via* axonal terminals (Hastings et al., 1981; Carlson et al., 2016). Similarly, WGA has also been reported to be bidirectional depending on the serotype and brain region, although it has a preference for anterograde transport (Whitney et al., 2016). In this study, we used a rAAV-WGA-Cre vector, which transduced in the cerebellar and hippocampal regions. However, due to the high expression levels needed of WGA-Cre in transduced cells for transneuronal labeling over multiple synapses, long incubation times were required (Hendricks et al., 2003). In order to circumvent these bidirectional, polysynaptic pitfalls using the rAAV-WGA-Cre system, we implemented and confirmed the initial connections using the AAV system with the deletion-mutant rabies virus system. The advantages of this system are that one can track not only the injection site and spread of the virus but also monosynaptic, retrograde connections. However, we are limited to the interpretation of our results with trisynaptic connections (A to B to C). For example, we can determine a projection from A to B but not with certainty A to B to C because, we cannot assume that A is connected to C *via* B. The cells traced in B may be connected with other local cells in B expressing the rabies virus, which receive input from cells in C. Moreover, the rAAV helper viruses could be presynaptically transferred from axons projecting into the injection site. To control for this, we screened for mCherry/RFP fluorescence outside the injection site and found that only in one case (**Supplementary Figure S6B**), red fluorescence was seen in a synaptically connected area. However, no eGFP$^+$ cells were observed due to the high expression of glycoprotein and TVA

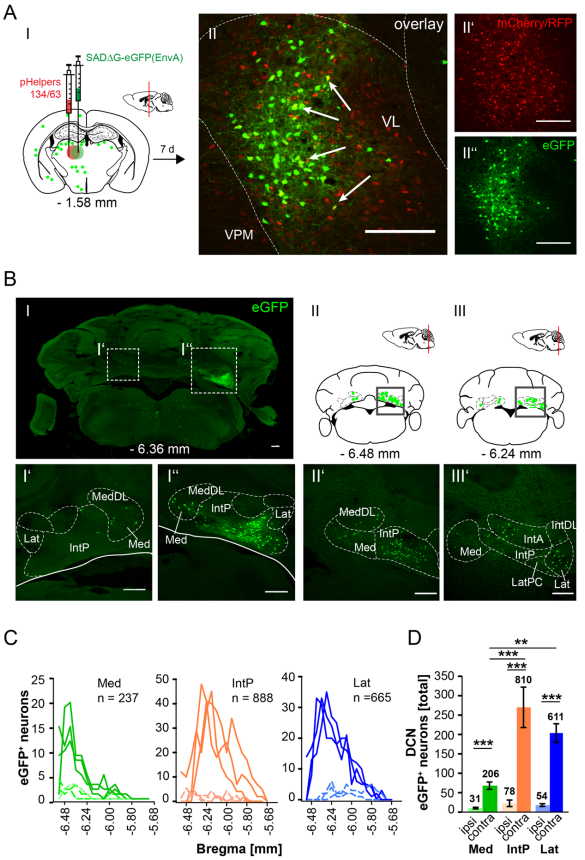

FIGURE 11 | Retrograde, modified RABV expression in the ventrolateral thalamus revealed monosynaptic input from the contralateral and ipsilateral cerebellar nuclei. **(AI)** Schematic of coronal section at Bregma −1.58 mm and confocal image **(AII)** from an exemplary adult mouse brain injected unilaterally with pHelpers **(AII')** and rabies virus **(AII")** in the ventrolateral thalamus (VL, $n = 3$). Green dots represent the retrograde specific, modified RABV tracer expression. The pHelper viruses rAAV8-CBA-RG-mCherry and rAAV8-CBA-mRFP-IRES-TVA (1:2 ratio, 0.2 μl) were injected 7 days prior to the SADΔG-eGFP (EnvA) rabies virus (0.2 μl). Mice were sacrificed 7 days after modified RABV injection. **(AII)** Double stained neurons indicate coexpression were only seen in the desired area as indicated by arrows and indicate starter neurons of retrograde monosynaptic transport. Scale bars: 250 μm. **(B)** Confocal image of a coronal brain section at Bregma −6.36 mm **(BI)** showing eGFP$^+$ neurons in the DCN. Boxed regions indicate magnified images in **(BI')** and **(BI")**. The contralateral cerebellar nucleus interpositus strongly projects to the VL **(BI")**, supported by weaker input from the ipsi-, and contralateral fastigial nucleus **(BI'–I")**. The monosynaptic projection from the IntP to the VL resembles a new projection pathway of the cerebellum to the contralateral thalamus, which has not been reported yet. Scale bar: 250 μm. **(BII,BIII)** Schematic of coronal brain sections at Bregma −6.48 mm **(BII)** and −6.24 mm **(BIII)** showing monosynaptic projections from the ipsi-, and contralateral Med **(BII,BIII,BII')** and contralateral Lat **(BIII')**. **(C)** Line plots mapping the distribution of total eGFP$^+$ neurons per mouse by retrograde monosynaptic transport from the VL to the Med, IntP and Lat, ipsi-, (dashed lines) and contralateral (thick lines) sites. **(D)** Contralateral nuclei generally provide more synaptic input to the VL than ipsilateral nuclei ($p \leq 0.001$, all t-test). However, contralateral IntP and Lat provide more synaptic input to the VL than the Med (for IntP $p \leq 0.001$; for Lat $p = 0.006$, One-Way-ANOVA). Significance for comparisons: $^{**}p \leq 0.01$; $^{***}p \leq 0.001$. IntA, anterior interposed cerebellar nucleus; IntP, posterior interposed cerebellar nucleus; IntDL, dorsolateral hump of IntP; Lat, lateral

(*Continued*)

FIGURE 11 | Continued
(dentate) cerebellar nucleus; LatPC, parvicellular Lat; Med, medial (fastigial) cerebellar nucleus; MedDL, dorsolateral protuberance of the medial cerebellar nucleus; VL, ventrolateral thalamic nucleus; VPM, ventral posteromedial thalamic nucleus. The mouse brains in this figure has been reproduced from Franklin and Paxinos (2001).

receptor required for RABV transcomplementation (Ugolini, 1995; Kelly and Strick, 2000; Wickersham et al., 2007a,b).

We describe here the first tracing study between the cerebellum and hippocampus in mice using a mono-transsynaptic, retrograde tracer system based on a modified rabies virus and well-established polysynaptic tracers rAAV8-CMV-WGA-Cre and rAAV8-CMV-TTC-eGFP (summarized in **Figure 12**). Our observations strengthen the notion of a polysynaptic circuitry between the cerebellum and hippocampus, that utilizes the thalamus as a relay center to cortical areas as first described in monkeys by the Strick lab (Middleton and Strick, 1994). This and work from others suggests that the RSC connects to the cerebellum with the hippocampus *via* polysynaptic circuits as it receives projections from the vestibular nuclei in the pons *via* the lateral thalamic nuclei which have been shown to receive cerebellar input (Sripanidkulchai and Wyss, 1986; Middleton and Strick, 1994, 2001; Rochefort et al., 2013). The injection of rAAV8-CMV-WGA-Cre in the RSC resulted in a strong staining, predominately in the thalamus, including the dorsomedial laterodorsal thalamus (LDDM), anteroventral thalamic nucleus and other areas (**Figure 3**). This is not surprising, since these two nuclei have been reported to project to RSA and RSG in rats and receive projections from

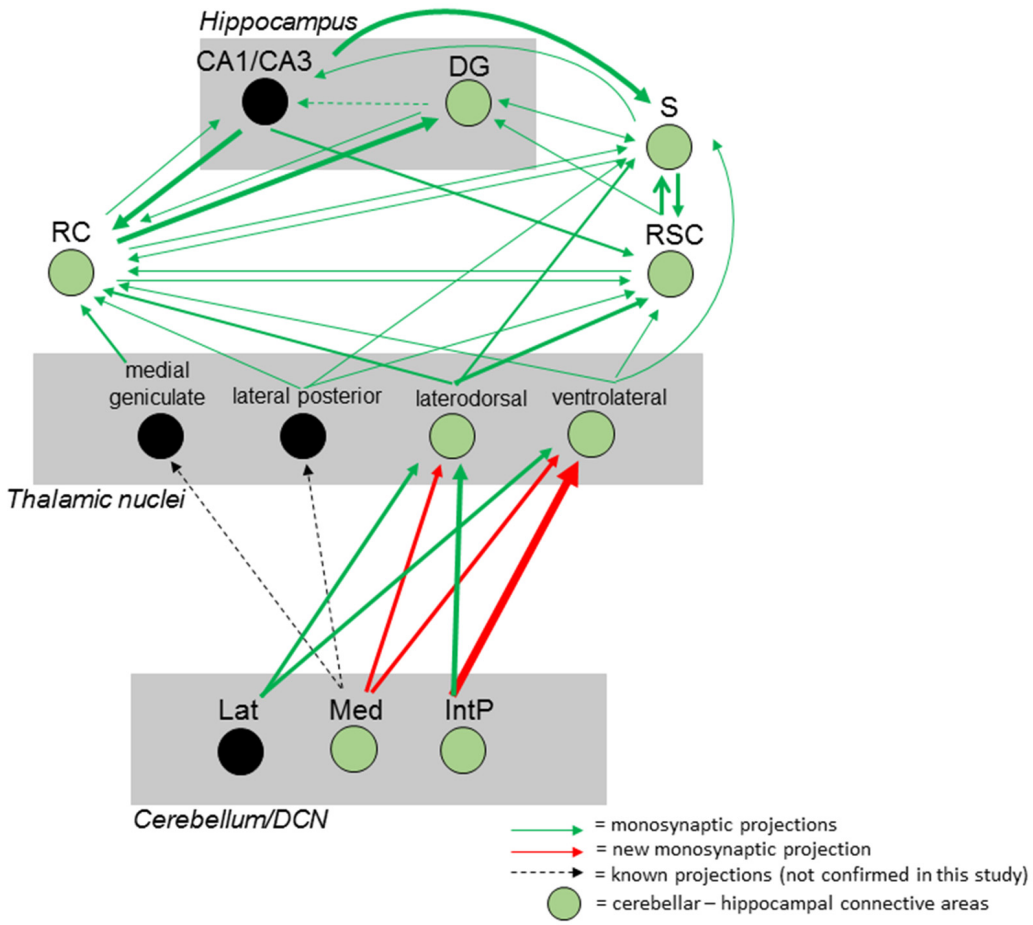

FIGURE 12 | Summary of the mouse cerebellar-hippocampal circuit. Known (black arrows) and observed (green) monosynaptic projections between the cerebellum and hippocampus *via* the thalamus, retrosplenial (RSC) and rhinal (RC) cortices and/or subiculum (S). A step by step injection of rabies virus started in the DG confirmed monosynaptic input from S, RC and RSC. While the S projects to and receives input from CA1/CA3 and DG, RSC, and RC, monosynaptic input was confirmed from the laterodorsal, ventrolateral and lateral posterior thalamic nuclei. Injections in the RSC confirmed monosynaptic input from these thalamic nuclei, too. By injecting these thalamic nuclei, new monosynaptic projections (red arrows) from the medial cerebellar nucleus to the laterodorsal and ventrolateral thalamus, as well as a new monosynaptic projection from the posterior interpositus cerebellar nucleus to the ventrolateral thalamus were identified in this study. Injecting the RC confirmed additional monosynaptic input from the medial geniculate thalamic nucleus which was not injected with rabies and can only be hypothesized to connect the cerebellum with the hippocampus (black circles). Thickness of arrows indicate strength of observed projections. IntP, posterior interposed cerebellar nucleus; Lat, lateral (dentate) cerebellar nucleus; Med, medial (fastigial) cerebellar nucleus; DG, dentate gyrus; S, subiculum; RC, rhinal cortex; RSC, retrosplenial cortex.

the RSC (Sripanidkulchai and Wyss, 1986; Vann et al., 2009). Injections of the WGA-Cre tracer in the DCN (**Figure 1**) and DG (**Figure 2**) only resulted in little to no cells expressing tdTomato in the thalamus, instead more neurites were seen crossing these thalamic nuclei. Both the LDDM and ventrolateral (LDVL) thalamic nuclei participate in spatial learning and memory but there is no projection from the cerebellum reported (van Groen et al., 2002a). rAAV8-CMV-WGA-Cre injections in the RSA stained the LDDM and cerebellar lobules IV, V, VI, VIII and X, as well as right PFl, CrusI, CrusII and left simple lobule, suggesting a cerebellar connection to the LDDM. Since the LDDM and LDVL are known to project to the RSC, which in turn projects to the subiculum and dentate gyrus, the RSA might serve as relay between the cerebellum and the hippocampus (van Groen and Wyss, 1990, 2003; Wyss and Van Groen, 1992; Aggleton et al., 2014). The same principle may be applied to the subiculum, which was shown in this study, but also by other scientists to project to the DG and RSC (Hartley et al., 2013; Sun et al., 2014) and receives input from the LDDM/LDVL. Thus, the subiculum might also serve as a linker between cerebellum and hippocampus *via* the laterodorsal thalamic nucleus.

Additional injections with our mono-transsynaptic RABV in the RSC (**Figure 8**), rhinal cortex (**Figure 9**) and subiculum (**Figure 7**) demonstrated projections from the laterodorsal medial and ventral (LDDM, LDVL) thalamic nuclei. These lateral posterior regions of the thalamus are known to connect with the fastigial nucleus. Furthermore recently published work by Rondi-Reig's lab confirmed a polysynaptic cerebello-hippocampal pathway both anatomically and functionally, implementing a CrusI/fastigial nucleus/dentate gyrus pathway important for spatial navigation in mice (Pearlstein et al., 2011; Watson et al., 2019). Thus, injecting the laterodorsal (**Figure 10**) thalamic nuclei, which are involved in spatial learning and memory (van Groen et al., 2002b) revealed innervation of the contralateral cerebellar interpositus and fastigial nucleus (**Figure 10**), which has not been reported before (van Groen et al., 2002a). The ventrolateral thalamic nucleus (VL) was stained after modified RABV injection in the RSC (**Figure 8**), S (**Figure 7**) and RC (**Figure 9**) and although there were only a few neurons expressing eGFP, they verify monosynaptic projections from the VL to these areas, which is involved in spatial navigation (Alexander and Nitz, 2015; Chrastil et al., 2015). The VL was shown to receive projections from the fastigial nucleus in non-human primates and shown to serve as a relay of these axons to the primary motor cortex (Kelly and Strick, 2003). Moreover lesion of the FN resulted in degenerated hippocampal fibers in different species suggesting a FN projection to the hippocampus of unknown relay (Harper and Heath, 1973; Heath and Harper, 1974). Injection of modified rabies virus in the VL (**Figure 11**) revealed contralateral innervation from all DCN, but also ipsilateral input from the fastigial nucleus. Thus, we were able to confirm fastigial nucleus input to the hippocampus with a relay in the ventrolateral thalamus.

Surprisingly, we did not observe tdTomato$^+$ cells in the LDDM/LDVL or the VL following rAAV-WGA-Cre injections in the DCN. Instead, we found a few cells in the lateral posterior thalamic nuclei. Moreover, rAAV-WGA-Cre injections in the DCN revealed the most tdTomato expression in the medial cerebellar nucleus. However RABV injections in the LDDM/LDLV (**Figure 10**) and VL (**Figure 11**) showed that the medial cerebellar nucleus provides significantly less input to these regions than interposed or lateral cerebellar nucleus. This may explain why we did not see tdTomato expression after rAAV-WGA-Cre injection in the DCN. The projection from the cerebellum to the hippocampus proposed by our data is mostly based on step-by-step retrograde monosynaptic transport, which may differ from an anterograde hippocampal-cerebellar pathway.

Several studies suggested cerebellar participation in spatial navigation (Rochefort et al., 2011; Iglói et al., 2015; Onuki et al., 2015). Although these studies support cerebellar involvement in spatial navigation, a direct neuronal projection pathway is still elusive. We here present a tracing study in mice that shows a cerebellar-hippocampal polysynaptic projection pathway *via* the laterodorsal and ventrolateral thalamus to RSC, subiculum and rhinal cortex. We were able to show new projections from the cerebellar interpositus and fastigial nucleus to contralateral LDDM/LDVL and VL, but also ipsilateral projections from the cerebellar fastigial nucleus to the VL. In contrast to Watson et al. (2019), who found retrogradely-labeled rabies-infected cells mostly in the dentate and fastigial nuclei, we here report monosynaptic input from mostly interpositus and dentate nuclei to LDDM/LDVL and VL, with 3–4 times fewer cells in the fastigial nucleus. However, our results further strengthen the notion of a cerebellar participation in hippocampal-based spatial navigation processing, however functional studies to confirm this polysynaptic connection needs to be investigated.

ETHICS STATEMENT

The present study was carried out in accordance with the European Communities Council Directive of 2010 (2010/63/EU) for care of laboratory animals and approved by a local ethics committee (Bezirksamt Arnsberg) and the animal care committee of North Rhine-Westphalia, Germany, based at the LANUV (Landesamt für Umweltschutz, Naturschutz und Verbraucherschutz, Nordrhein-Westfalen, D-45659 Recklinghausen, Germany). The study was supervised by the animal welfare commission of the Ruhr-University Bochum. All efforts were made to minimize the number of mice used for this study.

AUTHOR CONTRIBUTIONS

MM and SH conceived and designed the experiments. PB and MM performed tracing studies, rAAV virus production and tracing vector design performed by PB and MM. Modified rabies virus provided by MS. MM, PB, SH and MS wrote the manuscript.

FUNDING

This work was supported by the Deutsche Forschungsgemeinschaft (DFG) Grants, MA 5806/1-2 and MA 5806/2-1 (to MM), SFB project P03 (to MS) and He2471/

23-1, He2471/21-1, He2471/19-1 Priority Program (SPP1926), SFB874 project B10 (Project number 122679504) and SFB1280 project A07 (to SH).

ACKNOWLEDGMENTS

We would like to thank Stephanie Krämer, Margareta Möllmann, Petra Knipschild, Gina Hillgruber and Manuela Schmidt for their excellent technical assistance.

SUPPLEMENTARY MATERIAL

The Supplementary Material for this article can be found online at: https://www.frontiersin.org/articles/10.3389/fncir.2019.00051/full#supplementary-material

FIGURE S1 | Additional polysynaptic targets observed after injection of the polysynaptic anterograde tracer AAV8-CMV-WGA-Cre in the DCN of tdTomato$^+$ mice. **(A)** Example single tdTomato$^+$ cell bodies were imaged from the dorsal raphe nuclei [dorsal part (DRD), ventral (DRV), ventrolateral (DRVL), the raphe cap (RC) and ventrolateral periaqueducal gray (VLPAG)] and the lateral lemniscus, dorsal (DLL) and intermediate nucleus (ILL; **A'**) at −4.60 mm from Bregma. Scale bars: 250 μm. **(B)** Example single tdTomato$^+$ cell bodies were imaged from the magnocellular red nucleus (RMC) and superior cerebellar peduncle (scp) and right dorsal and ventral medial geniculate nucleus (MGD, MGV; **B'**) at −3.80 mm from Bregma. tdTomato$^+$ neurites were additionally seen in the posterior intralaminar thalamic nucleus (PIL), suprageniculate thalamic nucleus (SG) and the medial part of the medial geniculate nucleus (MGM). Scale bars: 250 μm **(C)** Example single tdTomato$^+$ cell bodies imaged from the prerubral field (PRI; **C**) and lateral secondary visual cortex (V2L; **C'**) at −2.54 mm from Bregma. Scale bars: 250 μm. **(D)** Polysynaptically tdTomato$^+$ cells at 2.58 mm from Bregma seen in the granular cell layer of the olfactory bulb (GrO) and internal plexiform layer of the olfactory bulb (IPl) and frontal association cortex (FrA; **D'**) Scale bars: 250 μm. The mouse brains in this figure has been reproduced from Franklin and Paxinos (2001).

FIGURE S2 | Additional polysynaptic targets observed after injection of the polysynaptic anterograde tracer AAV8-CMV-WGA-Cre in the dentate gyrus of tdTomato$^+$ mice. **(A)** Polysynaptic tdTomato$^+$ cells at −4.36 mm from Bregma in the external cortex of the inferior colliculus (ECIC), nucleus of the brachium of the inferior colliculus (BIC) and the brachium colliculus (bic). **(A')** tdTomato$^+$ neurites in the lateral lemniscus, intermediate (ILL) and ventral nuclei (VLL). Scale bar: 100 μm. **(A")** tdTomato$^+$ cell bodies and neurites in the tectospinal tract (ts), median raphe nucleus (MnR) and paramedian raphe nucleus (PMnR) and the reticulotegmental nucleus of the pons (RtTg). Scale bars: 100 μm. **(B)** Exemplary tdTomato$^+$ neurites in the medial geniculate nucleus, dorsal (MGD), ventral (MGV) and medial (MGM) parts and the suprageniculate thalamic nucleus (SG) at −3.28 mm from Bregma. Scale bar: 100 μm **(C)** Exemplary tdTomato$^+$ neurites in the lateral posterior thalamic nucleus, mediorostral (LPMR) and laterorostral parts (LPLR). **(C')** tdTomato$^+$ cell bodies in the secondary visual cortex, mediolateral area (V2ML). Scale bars 100 μm. **(D)** At 0.74 mm from Bregma, tdTomato$^+$ cell bodies were seen in the medial septal nucleus (MS) and in the nucleus of the vertical limb of the diagonal band (VDB). Scale bar: 250 μm. **(D')** Intense tdTomato$^+$ neurites in the lambdoid septal zone (Ld) and dorsal (LSD) and intermediate nuclei of the lateral septal nucleus (LSI). Scale bars: 250 μm. The mouse brains in this figure has been reproduced from Franklin and Paxinos (2001).

FIGURE S3 | Additional monosynaptic connected areas observed after injection of the retrograde tracer SADΔG-eGFP in the Hippocampus of C57/Bl6 mice. **(A)** Coronal brain section at −3.88 mm from Bregma depicting an eGFP$^+$ neuron (green dots) in the rostral linear nucleus of the raphe (RLi) and interpeduncular nucleus, rostral subnucleus (IPR, **A'**) by retrograde monosynaptic transport from the hippocampus. Scale bar: 100 μm. **(B)** Confocal image from boxed area depicting eGFP$^+$ cell bodies in the medial and lateral supramammillary nucleus (SuML, SuMM) at −2.70 mm from Bregma. Scale bar: 500 μm. **(C)** Confocal image of eGFP$^+$ neurons in the nucleus of the horizontal limb of the diagonal band (HDB) at – 0.34 mm from Bregma. Scale bar: 200 μm. **(D)** Confocal image of a multiple eGFP$^+$ cell bodies in the medial septal nucleus (MS) and medial preoptic area (MPA). Scale bar: 250 μm. The mouse brains in this figure has been reproduced from Franklin and Paxinos (2001).

FIGURE S4 | Additional monosynaptic connected areas observed after injection of the retrograde tracer SADΔG-eGFP in the Dentate Gyrus of C57/Bl6 mice. **(A)** Coronal brain section at −6.12 mm from Bregma depicting a eGFP$^+$ neuron (green dots) in the alpha part of the gigantocellular reticular nucleus (GiA) by retrograde monosynaptic transport from the dentate gyrus (DG). Scale bar: 250 μm. **(B)** Confocal image from boxed area depicting a single eGFP$^+$ cell body in the ventrolateral periaqueductal gray (VLPAG) at −4.72 mm from Bregma. Scale bar: 250 μm. **(C)** Confocal image of eGFP$^+$ neurons in the lateral supramammillary nucleus (SuML) at −2.80 mm from Bregma. Scale bar: 250 μm. **(D)** Confocal image of a multiple eGFP$^+$ cell bodies in the nucleus of the ventral limb of the diagonal band (VDB). Scale bar: 250 μm. The mouse brains in this figure has been reproduced from Franklin and Paxinos (2001).

FIGURE S5 | Additional monosynaptic connected areas observed after injection of the retrograde tracer SADΔG-eGFP in the retrosplenial cortex of C57/Bl6 mice. **(A)** Coronal brain section at −5.68 mm from Bregma depicting a eGFP$^+$ neuron (green dots) in the pontine reticular nucleus (PnC) by retrograde monosynaptic transport from the retrosplenial cortex (RC). Scale bar: 100 μm. **(B,B')** Confocal images from boxed areas depicting eGFP$^+$ cell bodies in the medial raphe nucleus (MnR; **B**, Scale bar: 250 μm) and B9 serotonergic cells **(B'**, Scale bar: 100 μm) at −4.48 mm from Bregma**. (C)** Confocal image of eGFP$^+$ neurons in the lateral supramammillary nucleus (SuML) at −3.16 mm from Bregma. Scale bar: 250 μm. **(D)** Confocal image of a single rabies-infected cell in the secondary auditory cortex (AuD). Scale bar: 100 μm. The mouse brains in this figure has been reproduced from Franklin and Paxinos (2001).

FIGURE S6 | Additional monosynaptic connected areas observed after injection of the retrograde tracer SADΔG-eGFP in the rhinal cortex of C57/Bl6 mice. **(A)** Confocal image showing higher magnification of a eGFP$^+$ neuron in the Barrington's nucleus (Bar) in the pons at −5.52 mm from Bregma. Scale bar: 250 μm **(A')** Single eGFP$^+$ cell in the alpha part of the gigantocellular reticular nucleus (GiA) in the pons at −5.52 mm from Bregma. Scale bar: 250 μm. **(B)** Several pyramidal cell-like neurons in the CA1 region and pyramidal cell layer (Py) at −3.80 mm from Bregma on the ipsilateral side. Scale bar: 250 μm. **(B')** Only one cell in the Py was seen on the contralateral side. Scale bar: 250 μm. **(B")** Confocal image showing several eGFP$^+$ cells in the dorsal (MGD) and ventral (MGV) parts of medial geniculate nucleus at −3.40 mm from Bregma. Scale bar: scale bar: 250 μm. **(C)** Brain scheme at −1.82 mm. Green dots represent eGFP$^+$ cells in all analyzed mice in the RSC, ipsilateral CA1 and CA2. High magnification image showing one representative single eGFP$^+$ neuron found in the ipsilateral mediorostral lateral posterior (LPMR) of the thalamus. Scale bar: 250 μm **(D)** Brain scheme at 0.86 mm from Bregma showing representative summarized eGFP$^+$ cells. Squared boxes represent areas of confocal images of the ipsilateral secondary motor cortex (M2, **D'**), ipsilateral nucleus of the horizontal limb (HDB, **D"**) and medial septal nucleus (MS) and lambdoid zone (Ld; **D"'**). Scale bars: 250 μm. The mouse brains in this figure has been reproduced from Franklin and Paxinos (2001).

FIGURE S7 | Additional statistical analysis of all eGFP$^+$ neurons observed in different regions on the murine brain after injection of the retrograde tracer SADΔG-eGFP in the rhinal cortex of C57/Bl6 mice. **(A)** eGFP$^+$ cells that were found in the RSC at different mm from Bregma. The four traces represent the analyzed $n = 4$ mice. **(AI)** A total of 275 eGFP$^+$ cells were found in the ipsilateral RSC, while only 76 cells were found in the contralateral RSC **(AII)**. **(AIII)** No statistical difference was found between ipsi., and contralateral sites. *T*-test, $p = 0.069$. **(B)** Summary of eGFP$^+$ cells that were found in the DG and CA3 at different mm from Bregma. The four traces represent the analyzed $n = 4$ mice. **(BI)** A total of 207 eGFP$^+$ cells were found in the ipsilateral DG, while 145 cells were found in the contralateral DG. No statistical difference was found between sites. *T*-test, $p = 0.249$ **(BIII)**. **(BII)** Traces of all eGFP$^+$ cells observed in the ipsilateral (orange thick lines, 2,472 cells) and contralateral (dashed lines, 698) CA3 region of the hippocampus. Three-thousand one-hundred and seventy cells were found in all analyzed mice, with significantly more input on the RC from the

ipsilateral CA3 cells (*t*-test, $p = 0.002$; **BIII)**. **(BIII)** A total of 28,082 eGFP$^+$ cells were found in the CA1, with only eight cells found on the contralateral site (data not shown). Significantly more cells from the CA1 region are connected to the RC when compared to all CA3 cells (*t*-test, $p = \leq 0.001$) and all cells from the DG (*t*-test, $p = 0.029$). **(C)** Total eGFP$^+$ neurons observed in the subiculum. Significantly more cells from the ipsilateral S (4,233) compared to the contralateral S (36) provide input to the RC (*t*-test, $p = 0.029$). Significance for comparisons: ns not significant; $^*p \leq 0.05$; $^{**}p \leq 0.01$; $^{***}p \leq 0.001$.

REFERENCES

Aggleton, J. P., Saunders, R. C., Wright, N. F., and Vann, S. D. (2014). The origin of projections from the posterior cingulate and retrosplenial cortices to the anterior, medial dorsal and laterodorsal thalamic nuclei of macaque monkeys. *Eur. J. Neurosci.* 39, 107–123. doi: 10.1111/ejn.12389

Agster, K. L., and Burwell, R. D. (2013). Hippocampal and subicular efferents and afferents of the perirhinal, postrhinal, and entorhinal cortices of the rat. *Behav. Brain Res.* 254, 50–64. doi: 10.1016/j.bbr.2013.07.005

Alexander, A. S., and Nitz, D. A. (2015). Retrosplenial cortex maps the conjunction of internal and external spaces. *Nat. Neurosci.* 18, 1143–1151. doi: 10.1038/nn.4058

Baillieux, H., De Smet, H. J., Paquier, P. F., De Deyn, P. P., and Marien, P. (2008a). Cerebellar neurocognition: insights into the bottom of the brain. *Clin. Neurol. Neurosurg.* 110, 763–773. doi: 10.1016/j.clineuro.2008.05.013

Baillieux, H., Verslegers, W., Paquier, P., De Deyn, P. P., and Marien, P. (2008b). Cerebellar cognitive affective syndrome associated with topiramate. *Clin. Neurol. Neurosurg.* 110, 496–499. doi: 10.1016/j.clineuro.2008.01.003

Brandt, T., Schautzer, F., Hamilton, D. A., Bruning, R., Markowitsch, H. J., Kalla, R., et al. (2005). Vestibular loss causes hippocampal atrophy and impaired spatial memory in humans. *Brain* 128, 2732–2741. doi: 10.1093/brain/awh617

Broekman, M. L., Comer, L. A., Hyman, B. T., and Sena-Esteves, M. (2006). Adeno-associated virus vectors serotyped with AAV8 capsid are more efficient than AAV-1 or -2 serotypes for widespread gene delivery to the neonatal mouse brain. *Neuroscience* 138, 501–510. doi: 10.1016/j.neuroscience.2005.11.057

Buckner, R. L., Krienen, F. M., Castellanos, A., Diaz, J. C., and Yeo, B. T. (2011). The organization of the human cerebellum estimated by intrinsic functional connectivity. *J. Neurophysiol.* 106, 2322–2345. doi: 10.1152/jn.00339.2011

Büning, H., Perabo, L., Coutelle, O., Quadt-Humme, S., and Hallek, M. (2008). Recent developments in adeno-associated virus vector technology. *J. Gene Med.* 10, 717–733. doi: 10.1002/jgm.1205

Burguière, E., Arabo, A., Jarlier, F., De Zeeuw, C. I., and Rondi-Reig, L. (2010). Role of the cerebellar cortex in conditioned goal-directed behavior. *J. Neurosci.* 30, 13265–13271. doi: 10.1523/jneurosci.2190-10.2010

Cabana, T., and Martin, G. F. (1986). Development of projections from somatic motor-sensory areas of neocortex to the diencephalon and brainstem in the North American opossum. *J. Comp. Neurol.* 251, 506–516. doi: 10.1002/cne.902510406

Carlson, K. S., Whitney, M. S., Gadziola, M. A., Deneris, E. S., and Wesson, D. W. (2016). Preservation of essential odor-guided behaviors and odor-based reversal learning after targeting adult brain serotonin synthesis. *eNeuro* 3:ENEURO.0257-16.2016. doi: 10.1523/eneuro.0257-16.2016

Chamberlin, N. L., Du, B., de Lacalle, S., and Saper, C. B. (1998). Recombinant adeno-associated virus vector: use for transgene expression and anterograde tract tracing in the CNS. *Brain Res.* 793, 169–175. doi: 10.1016/s0006-8993(98)00169-3

Chrastil, E. R., Sherrill, K. R., Hasselmo, M. E., and Stern, C. E. (2015). There and back again: hippocampus and retrosplenial cortex track homing distance during human path integration. *J. Neurosci.* 35, 15442–15452. doi: 10.1523/jneurosci.1209-15.2015

Colombel, C., Lalonde, R., and Caston, J. (2004). The effects of unilateral removal of the cerebellar hemispheres on spatial learning and memory in rats. *Brain Res.* 1004, 108–115. doi: 10.1016/j.brainres.2003.10.075

Cronin, T., Arshad, Q., and Seemungal, B. M. (2017). Vestibular deficits in neurodegenerative disorders: balance, dizziness, and spatial disorientation. *Front. Neurol.* 8:538. doi: 10.3389/fneur.2017.00538

Deneris, E. S., and Wyler, S. C. (2012). Serotonergic transcriptional networks and potential importance to mental health. *Nat. Neurosci.* 15, 519–527. doi: 10.1038/nn.3039

Dum, R. P., and Strick, P. L. (2003). An unfolded map of the cerebellar dentate nucleus and its projections to the cerebral cortex. *J. Neurophysiol.* 89, 634–639. doi: 10.1152/jn.00626.2002

Espallergues, J., Teegarden, S. L., Veerakumar, A., Boulden, J., Challis, C., Jochems, J., et al. (2012). HDAC6 regulates glucocorticoid receptor signaling in serotonin pathways with critical impact on stress resilience. *J. Neurosci.* 32, 4400–4416. doi: 10.1523/jneurosci.5634-11.2012

Evarts, E. V., and Thach, W. T. (1969). Motor mechanisms of the CNS: cerebrocerebellar interrelations. *Annu. Rev. Physiol.* 31, 451–498. doi: 10.1146/annurev.ph.31.030169.002315

Fischer, A. H., van der Loo, B., Shär, M. G., Zbinden, R., Duru, F., Brunckhorst, C., et al. (2008). Serological evidence for the association of Bartonella henselae infection with arrhythmogenic right ventricular cardiomyopathy. *Clin. Cardiol.* 31, 469–471. doi: 10.1002/clc.20269

Franklin, K. B. J., and Paxinos, G. (2001). *The Mouse Brain in Stereotaxic Coordinates*. 2nd Edn. San Diego: Academic Press.

Grieger, J. C., Choi, V. M., and Samulski, R. J. (2006). Production and characterization of adeno-associated viral vectors. *Nat. Protoc.* 1, 1412–1428. doi: 10.1038/nprot.2006.207

Harper, J. W., and Heath, R. G. (1973). Anatomic connections of the fastigial nucleus to the rostral forebrain in the cat. *Exp. Neurol.* 39, 285–292. doi: 10.1016/0014-4886(73)90231-8

Hartley, T., Lever, C., Burgess, N., and O'Keefe, J. (2013). Space in the brain: how the hippocampal formation supports spatial cognition. *Philos. Trans. R. Soc. Lond. B Biol. Sci.* 369:20120510. doi: 10.1098/rstb.2012.0510

Hastings, W. L., Aaron, J. L., Deneris, J., Kessler, T. R., Pons, A. B., Razzeca, K. J., et al. (1981). A retrospective study of nine calves surviving five months on the pneumatic total artificial heart. *Trans. Am. Soc. Artif. Intern. Organs* 27, 71–76.

Heath, R. G., and Harper, J. W. (1974). Ascending projections of the cerebellar fastigial nucleus to the hippocampus, amygdala and other temporal lobe sites: evoked potential and histological studies in monkeys and cats. *Exp. Neurol.* 45, 268–287. doi: 10.1016/0014-4886(74)90118-6

Heinemann, S. F., Boulter, J., Connolly, J., Deneris, E., Duvoisin, R., Hartley, M., et al. (1991). Brain nicotinic receptor genes. *NIDA Res. Monogr.* 111, 3–23.

Hendricks, T. J., Fyodorov, D. V., Wegman, L. J., Lelutiu, N. B., Pehek, E. A., Yamamoto, B., et al. (2003). Pet-1 ETS gene plays a critical role in 5-HT neuron development and is required for normal anxiety-like and aggressive behavior. *Neuron* 37, 233–247. doi: 10.1016/s0896-6273(02)01167-4

Iglói, K., Doeller, C. F., Paradis, A. L., Benchenane, K., Berthoz, A., Burgess, N., et al. (2015). Interaction between hippocampus and cerebellum crus I in sequence-based but not place-based navigation. *Cereb. Cortex* 25, 4146–4154. doi: 10.1093/cercor/bhu132

Jarvik, R. K., Kessler, T. R., McGill, L. D., Olsen, D. B., DeVries, W. C., Deneris, J., et al. (1981). Determinants of pannus formation in long-surviving artificial heart calves, and its prevention. *Trans. Am. Soc. Artif. Intern. Organs* 27, 90–96.

Kaplitt, M. G., Leone, P., Samulski, R. J., Xiao, X., Pfaff, D. W., O'Malley, K. L., et al. (1994). Long-term gene expression and phenotypic correction using adeno-associated virus vectors in the mammalian brain. *Nat. Genet.* 8, 148–154. doi: 10.1038/ng1094-148

Kelly, R. M., and Strick, P. L. (2000). Rabies as a transneuronal tracer of circuits in the central nervous system. *J. Neurosci. Methods* 103, 63–71. doi: 10.1016/s0165-0270(00)00296-x

Kelly, R. M., and Strick, P. L. (2003). Cerebellar loops with motor cortex and prefrontal cortex of a nonhuman primate. *J. Neurosci.* 23, 8432–8444. doi: 10.1523/JNEUROSCI.23-23-08432.2003

Kwon, I., and Schaffer, D. V. (2008). Designer gene delivery vectors: molecular engineering and evolution of adeno-associated viral vectors for enhanced gene transfer. *Pharm. Res.* 25, 489–499. doi: 10.1007/s11095-007-9431-0

Liu, W., Zhang, Y., Yuan, W., Wang, J., and Li, S. (2012). A direct hippocampo-cerebellar projection in chicken. *Anat. Rec.* 295, 1311–1320. doi: 10.1002/ar.22515

Madisen, L., Zwingman, T. A., Sunkin, S. M., Oh, S. W., Zariwala, H. A., Gu, H., et al. (2010). A robust and high-throughput Cre reporting and characterization system for the whole mouse brain. *Nat. Neurosci.* 13, 133–140. doi: 10.1038/nn.2467

Middleton, F. A., and Strick, P. L. (1994). Anatomical evidence for cerebellar and basal ganglia involvement in higher cognitive function. *Science* 266, 458–461. doi: 10.1126/science.7939688

Middleton, F. A., and Strick, P. L. (2001). Cerebellar projections to the prefrontal cortex of the primate. *J. Neurosci.* 21, 700–712. doi: 10.1523/JNEUROSCI.21-02-00700.2001

Molinari, M., Chiricozzi, F. R., Clausi, S., Tedesco, A. M., De Lisa, M., and Leggio, M. G. (2008). Cerebellum and detection of sequences, from perception to cognition. *Cerebellum* 7, 611–615. doi: 10.1007/s12311-008-0060-x

Niedworok, C. J., Schwarz, I., Ledderose, J., Giese, G., Conzelmann, K. K., and Schwarz, M. K. (2012). Charting monosynaptic connectivity maps by two-color light-sheet fluorescence microscopy. *Cell Rep.* 2, 1375–1386. doi: 10.1016/j.celrep.2012.10.008

Ohta, Y., Kosaka, Y., Kishimoto, N., Wang, J., Smith, S. B., Honig, G., et al. (2011). Convergence of the insulin and serotonin programs in the pancreatic β-cell. *Diabetes* 60, 3208–3216. doi: 10.2337/db10-1192

Onuki, Y., Van Someren, E. J., De Zeeuw, C. I., and Van der Werf, Y. D. (2015). Hippocampal-cerebellar interaction during spatio-temporal prediction. *Cereb. Cortex* 25, 313–321. doi: 10.1093/cercor/bht221

O'Reilly, J. X., Beckmann, C. F., Tomassini, V., Ramnani, N., and Johansen-Berg, H. (2010). Distinct and overlapping functional zones in the cerebellum defined by resting state functional connectivity. *Cereb. Cortex* 20, 953–965. doi: 10.1093/cercor/bhp157

Panneton, W. M., and Tolbert, D. L. (1984). The collateral origin of a transient cerebrocerebellar pathway in kittens. *Brain Res.* 316, 247–254. doi: 10.1016/0165-3806(84)90309-2

Pearlstein, E., Bras, H., Deneris, E. S., and Vinay, L. (2011). Contribution of 5-HT to locomotion—the paradox of *Pet-1*$^{-/-}$ mice. *Eur. J. Neurosci.* 33, 1812–1822. doi: 10.1111/j.1460-9568.2011.07679.x

Repapi, E., Sayers, I., Wain, L. V., Burton, P. R., Johnson, T., Obeidat, M., et al. (2009). Genome-wide association study identifies five loci associated with lung function. *Nat. Genet.* 42, 36–44. doi: 10.1038/ng.501

Rochefort, C., Arabo, A., Andre, M., Poucet, B., Save, E., and Rondi-Reig, L. (2011). Cerebellum shapes hippocampal spatial code. *Science* 334, 385–389. doi: 10.1126/science.1207403

Rochefort, C., Lefort, J. M., and Rondi-Reig, L. (2013). The cerebellum: a new key structure in the navigation system. *Front. Neural Circuits* 7:35. doi: 10.3389/fncir.2013.00035

Schmahmann, J. D., and Pandya, D. N. (1991). Projections to the basis pontis from the superior temporal sulcus and superior temporal region in the rhesus monkey. *J. Comp. Neurol.* 308, 224–248. doi: 10.1002/cne.903080209

Smith, P. F., Zheng, Y., Horii, A., and Darlington, C. L. (2005). Does vestibular damage cause cognitive dysfunction in humans? *J. Vestib. Res.* 15, 1–9. doi: 10.3233/VES-190672

Sripanidkulchai, K., and Wyss, J. M. (1986). Thalamic projections to retrosplenial cortex in the rat. *J. Comp. Neurol.* 254, 143–165. doi: 10.1002/cne.902540202

Sun, Y., Nguyen, A. Q., Nguyen, J. P., Le, L., Saur, D., Choi, J., et al. (2014). Cell-type-specific circuit connectivity of hippocampal CA1 revealed through Cre-dependent rabies tracing. *Cell Rep.* 7, 269–280. doi: 10.1016/j.celrep.2014.02.030

Timmann, D., and Daum, I. (2007). Cerebellar contributions to cognitive functions: a progress report after two decades of research. *Cerebellum* 6, 159–162. doi: 10.1080/14734220701496448

Timmann, D., Drepper, J., Frings, M., Maschke, M., Richter, S., Gerwig, M., et al. (2010). The human cerebellum contributes to motor, emotional, and cognitive associative learning. A review. *Cortex* 46, 845–857. doi: 10.1016/j.cortex.2009.06.009

Tolbert, D. L. (1989a). Absence of impulse activity in cortical neurons with transient projections to the cerebellum. *Dev. Brain Res.* 50, 241–249. doi: 10.1016/0165-3806(89)90200-9

Tolbert, D. L. (1989b). Somatotopically organized transient projections from the primary somatosensory cortex to the cerebellar cortex. *Dev. Brain Res.* 45, 113–127. doi: 10.1016/0165-3806(89)90013-8

Tolbert, D. L., and Panneton, W. M. (1983). Transient cerebrocerebellar projections in kittens: postnatal development and topography. *J. Comp. Neurol.* 221, 216–228. doi: 10.1002/cne.902210209

Tolbert, D. L., and Panneton, W. M. (1984). The transience of cerebrocerebellar projections is due to selective elimination of axon collaterals and not neuronal death. *Brain Res.* 318, 301–306. doi: 10.1016/0165-3806(84)90034-8

Ugolini, G. (1995). Specificity of rabies virus as a transneuronal tracer of motor networks: transfer from hypoglossal motoneurons to connected second-order and higher order central nervous system cell groups. *J. Comp. Neurol.* 356, 457–480. doi: 10.1002/cne.903560312

van Groen, T., and Wyss, J. M. (1990). Connections of the retrosplenial granular a cortex in the rat. *J. Comp. Neurol.* 300, 593–606. doi: 10.1002/cne.903000412

van Groen, T., and Wyss, J. M. (2003). Connections of the retrosplenial granular b cortex in the rat. *J. Comp. Neurol.* 463, 249–263. doi: 10.1002/cne.10757

van Groen, T., Kadish, I., and Wyss, J. M. (2002a). Old rats remember old tricks; memories of the water maze persist for 12 months. *Behav. Brain Res.* 136, 247–255. doi: 10.1016/s0166-4328(02)00137-7

van Groen, T., Kadish, I., and Wyss, J. M. (2002b). The role of the laterodorsal nucleus of the thalamus in spatial learning and memory in the rat. *Behav. Brain Res.* 136, 329–337. doi: 10.1016/s0166-4328(02)00199-7

van Groen, T., Kadish, I., and Wyss, J. M. (2002c). Species differences in the projections from the entorhinal cortex to the hippocampus. *Brain Res. Bull.* 57, 553–556. doi: 10.1016/s0361-9230(01)00683-9

Vann, S. D., Aggleton, J. P., and Maguire, E. A. (2009). What does the retrosplenial cortex do? *Nat. Rev. Neurosci.* 10, 792–802. doi: 10.1038/nrn2733

Vertes, R. P., and McKenna, J. T. (2000). Collateral projections from the supramammillary nucleus to the medial septum and hippocampus. *Synapse* 38, 281–293. doi: 10.1002/1098-2396(20001201)38:3<281::aid-syn7>3.0.co;2-6

Watson, T. C., Obiang, P., Torres-Herraez, A., Watilliaux, A., Coulon, P., Rochefort, C., et al. (2019). Anatomical and physiological foundations of cerebello-hippocampal interaction. *eLife* 8:e41896. doi: 10.7554/eLife.41896

Whitney, M. S., Shemery, A. M., Yaw, A. M., Donovan, L. J., Glass, J. D., and Deneris, E. S. (2016). Adult brain serotonin deficiency causes hyperactivity, circadian disruption, and elimination of siestas. *J. Neurosci.* 36, 9828–9842. doi: 10.1523/JNEUROSCI.1469-16.2016

Wickersham, I. R., Finke, S., Conzelmann, K. K., and Callaway, E. M. (2007a). Retrograde neuronal tracing with a deletion-mutant rabies virus. *Nat. Methods* 4, 47–49. doi: 10.1038/nmeth999

Wickersham, I. R., Lyon, D. C., Barnard, R. J., Mori, T., Finke, S., Conzelmann, K. K., et al. (2007b). Monosynaptic restriction of transsynaptic tracing from single, genetically targeted neurons. *Neuron* 53, 639–647. doi: 10.1016/j.neuron.2007.01.033

Wild, J. M., and Williams, M. N. (2000). A direct cerebrocerebellar projection in adult birds and rats. *Neuroscience* 96, 333–339. doi: 10.1016/s0306-4522(99)00546-1

Wyss, J. M., and Van Groen, T. (1992). Connections between the retrosplenial cortex and the hippocampal formation in the rat: a review. *Hippocampus* 2, 1–11. doi: 10.1002/hipo.450020102

Xiao, X., Li, J., McCown, T. J., and Samulski, R. J. (1997). Gene transfer by adeno-associated virus vectors into the central nervous system. *Exp. Neurol.* 144, 113–124. doi: 10.1006/exnr.1996.6396

Xiao, X., Li, J., and Samulski, R. J. (1996). Efficient long-term gene transfer into muscle tissue of immunocompetent mice by adeno-associated virus vector. *J. Virol.* 70, 8098–8108.

Conflict of Interest Statement: The authors declare that the research was conducted in the absence of any commercial or financial relationships that could be construed as a potential conflict of interest.

frontiers in Neural Circuits

PERSPECTIVE
published: 13 September 2019
doi: 10.3389/fncir.2019.00060

Why Isn't the Head Direction System Necessary for Direction? Lessons From the Lateral Mammillary Nuclei

Christopher M. Dillingham and Seralynne D. Vann*

School of Psychology, Cardiff University, Cardiff, United Kingdom

Complex spatial representations in the hippocampal formation and related cortical areas require input from the head direction system. However, a recurrent finding is that behavior apparently supported by these spatial representations does not appear to require input from generative head direction regions, i.e., lateral mammillary nuclei (LMN). Spatial tasks that tax direction discrimination should be particularly sensitive to the loss of head direction information, however, this has been repeatedly shown not to be the case. A further dissociation between electrophysiological properties of the head direction system and behavior comes in the form of geometric-based navigation which is impaired following lesions to the head direction system, yet head direction cells are not normally guided by geometric cues. We explore this apparent mismatch between behavioral and electrophysiological studies and highlight future experiments that are needed to generate models that encompass both neurophysiological and behavioral findings.

Keywords: spatial memory, rodent, head-direction cells, dosral tegmental nucleus of Gudden, anterodorsal thalamic nucleus

OPEN ACCESS

Edited by:
Kate J. Jeffery,
University College London,
United Kingdom

Reviewed by:
Paul A. Dudchenko,
University of Stirling,
United Kingdom
Benjamin J. Clark,
University of New Mexico,
United States
Jeffrey S. Taube,
Dartmouth College,
United States

****Correspondence:***
Christopher M. Dillingham
dillinghamc@cardiff.ac.uk

Received: *30 May 2019*
Accepted: *26 August 2019*
Published: *13 September 2019*

Citation:
Dillingham CM and Vann SD (2019) Why Isn't the Head Direction System Necessary for Direction? Lessons From the Lateral Mammillary Nuclei. Front. Neural Circuits 13:60. doi: 10.3389/fncir.2019.00060

INTRODUCTION

The ability to navigate through environments, and remember locations within those environments, is key to survival. Navigation requires a cognitive representation of both the environment and current position within the environment. Several positional correlates have been identified in the rodent brain, including hippocampal place cells (O'Keefe and Dostrovsky, 1971), which fire as a function of the animal's position in two-dimensional space, while entorhinal grid cells constitute a boundary-defined representation of multiple, hexagonally arranged place fields (Hafting et al., 2005). Information relating to environmental features is represented by a number of classes of neurons including border cells, which fire in proximity to the boundaries of the environment (Hartley et al., 2000), and head direction cells (Taube et al., 1990), a class of cell that fires preferentially in reference to an animals' directional heading in space.

Since their initial discovery in the postsubiculum (PoSub), head direction cells have been recorded in numerous other cortical and subcortical brain regions, including the retrosplenial (Chen et al., 1994; Cho and Sharp, 2001; Jacob et al., 2017), posterior parietal (PPC; Chen et al., 1994), medial entorhinal (MEC; Sargolini et al., 2006), and precentral cortices (Mehlman et al., 2019), the anterodorsal (ADN; Blair and Sharp, 1995; Taube, 1995), laterodorsal (Mizumori and Williams, 1993), anteroventral thalamic nuclei

(Tsanov et al., 2011), nucleus reuniens (Jankowski et al., 2014), the dorsal striatum (Wiener, 1993; Mizumori et al., 2000, 2005; Ragozzino et al., 2001; Mehlman et al., 2019), the dorsal tegmental nucleus of Gudden (DTg; Sharp et al., 2001), and the lateral mammillary nuclei (LMN; Blair et al., 1998; Stackman and Taube, 1998). The traditional hierarchical model of the head direction system (for a more detailed recent review see Weiss and Derdikman, 2018) involves a vestibular/vestibulomotor-derived head direction signal which ascends to the LMN and is then updated through the integration of external sensory inputs, e.g., visual information from PoSub (Yoder et al., 2015), through to ADN, PoSub and MEC. At each ascending stage, cells receive updated, more complex input, which is reflected in the spatial information content of the neurons within the respective regions. For instance, a higher proportion of head direction cells exhibit a conjunctive head-direction/boundary signal in the PoSub than in ADN, which is thought to represent the integration of head direction with positional sensory input, e.g., whisking/optic flow, resulting from self-motion (Peyrache et al., 2017). An additional example of this hierarchical increase in complexity comes from bidirectional cells in the retrosplenial cortex (RSC; Jacob et al., 2017), which can represent two sensory modalities, i.e., olfaction and vision within a given environment (within compartment), or can represent a single sensory modality differently across contexts (between compartment).

While we know that the head direction system is necessary for accurate positional representation surprisingly little is understood about how this system contributes at a behavioral level. Manipulations of the LMN are particularly informative for studying the head direction system as these nuclei lie at the base of this highly interconnected hierarchy that integrates external cues, e.g., visual (Yoder et al., 2015), with those derived from self-motion (i.e., proprioceptive). Moreover, the high proportion of head direction cells in the LMN (Stackman and Taube, 1998; Taube and Bassett, 2003) allow for perturbation of the system while limiting confounding damage to additional pathways. In this review, we will consider what is currently known about the LMN's contribution at an electrophysiological level, and at a behavioral level, and how this combined knowledge helps us understand the role of the head direction system in spatial cognition.

HOW DOES THE HEAD DIRECTION SIGNAL CONTRIBUTE TO SPATIAL SIGNALS REPRESENTING THE ENVIRONMENT?

Unlike hippocampal place cells whose spatial representations are context-dependent (e.g., Alme et al., 2014), the representation of head direction, border and grid cells maintain their intrinsic firing pattern across contexts (Hafting et al., 2005; Fyhn et al., 2007). Together these cells enable animals to encode features of an enclosed environment (Krupic et al., 2015) as well as positional information within that environment (Lever et al., 2009; Hinman et al., 2019). The head direction signal is seemingly important for both grid cell and place cell systems. Entorhinal grid cell periodicity is significantly disrupted following inactivation of the anterior thalamus, which includes ADN (Winter et al., 2015), although this could also reflect associated damage to the anteroventral and anteromedial thalamic nuclei e.g., through attenuation of MEC theta power (see Brandon et al., 2012). Grieves et al. (2016) showed that in multi-compartment environments, place cell repetition is more frequent if the compartments are in a parallel compared to radial configuration, suggesting direction information helps distinguish compartments. Consistent with this, LMN lesions increase place field repetition in radial compartments, likely reflecting the loss of directional information in these animals (Harland et al., 2017). While lesions of LMN do not degrade the spatial content of hippocampal place fields (Sharp and Koester, 2008), ADN lesions and, to a greater extent, PoSub lesions reduce the information content of place fields (Calton et al., 2003), albeit leaving the place fields intact. The increase in magnitude of impairment with each step along the ascending head direction pathway appears to co-occur with greater influence of descending visual inputs (V1-PoSub-RSC-ADN; **Figure 1**). Together these results suggest a hierarchical dependence of spatial systems that is borne out both by the sequence of anatomical inputs as well as the sequence of developmental emergence of spatial representations, i.e., directional tuning is fully developed earlier than place or grid cells (Langston et al., 2010; Wills et al., 2010). Grid cells appear to be the most complex of the spatial correlates so far identified, combining head direction, border and place signals. Consistent with this, inactivation of the hippocampus dramatically reduces the spatial information content of grid cells but interestingly leads to an increase in their directionality (Hafting et al., 2008; Bonnevie et al., 2013). While inactivation of the MEC does not degrade the spatial information content of hippocampal place fields it does induce place field remapping (Miao et al., 2015). However, large permanent lesions of the entorhinal cortex reduce place cell firing rate and spatial information content (Van Cauter et al., 2008) suggesting functional interdependence between grid cell and place cell networks.

DO LMN LESIONS DISRUPT THE USE OF DIRECTIONAL CUES?

Surprisingly, given the strong physiological influence of the head direction system on more spatially complex downstream systems, LMN lesions often have little to no effect on spatial tasks that would be presumed to involve a heading component. The reinforced T-maze task requires animals to alternate direction in a T-shaped maze in order to retrieve a reward (**Figure 2A**). In intact animals, head direction cells are landmark-locked to features of the maze (Dudchenko and Zinyuk, 2005) so it would be expected that disrupting the head direction system would disrupt T-maze performance. This is not the case as rats with neurotoxic LMN lesions show no impairment on standard T-maze alternation (**Figure 2B**; Vann, 2005, 2011). When performing the T-maze task, animals are able to use a number of different strategies, including relying on the use of allocentric, directional or intramaze cues. As a result, impairments in LMN lesion rats may be masked by animals using

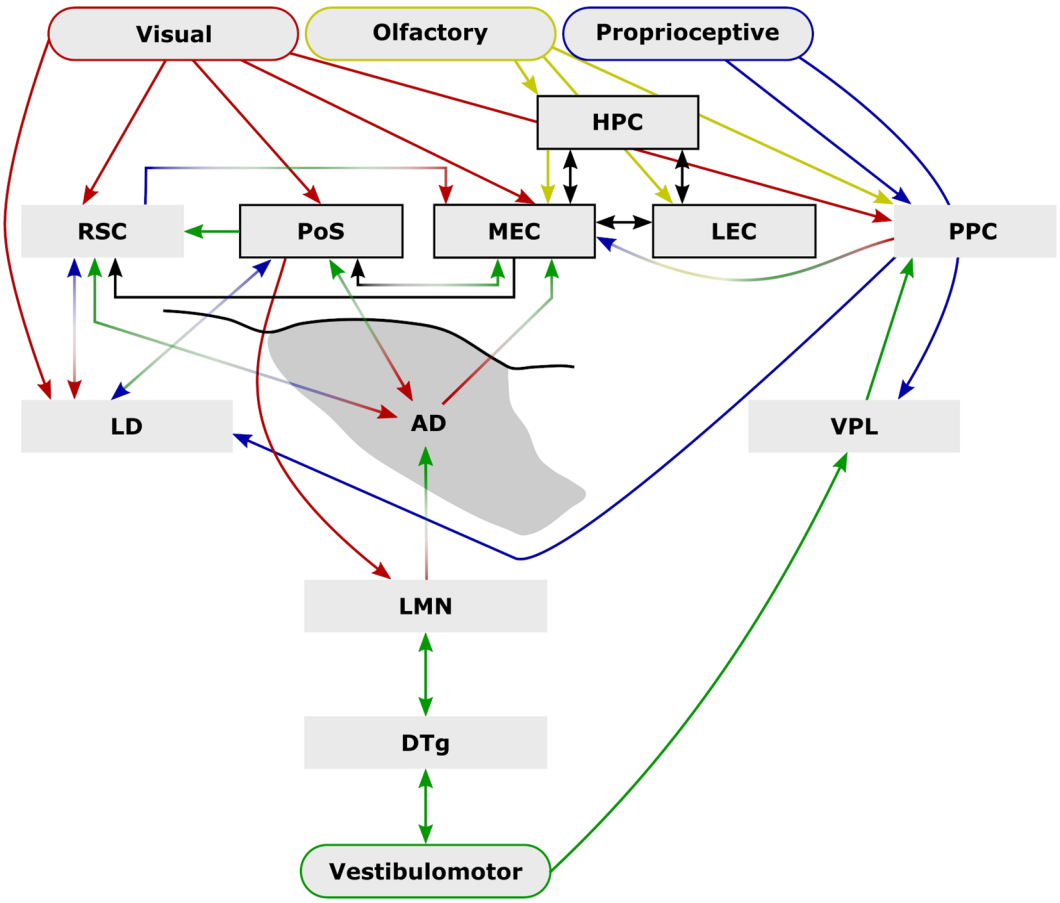

FIGURE 1 | External sensory input is critical to spatial navigation. Ascending vestibulomotor (green) projections elicit directional tuning in many subcortical and cortical regions while descending visual (red), olfactory (yellow), and proprioceptive (blue) inputs are integrated to form complex physiological representations of space. Some of the extensive inter-communication between brain areas that encode space shown here demonstrate the capacity for compensation following disruption (e.g., lesion, or conflict between senses) while parallel pathways may provide additional compensatory mechanisms [e.g., vestibulomotor-ventral posterolateral thalamic nucleus (VPL)–posterior parietal cortex (PPC)] that may explain the mild behavioral impairment following lateral mammillary nucleus (LMN) or anterodorsal thalamic nucleus (ADN) lesions. Arrows indicate anatomical connections while their colors represent their possible sensory contributions. Structures and connections within the hippocampal formation that are not principally directional are shown black (arrows and boxes). Abbreviations: DTg, dorsal tegmental nucleus of Gudden; LD, laterodorsal thalamic nucleus; LEC, lateral entorhinal cortex; HPC, CA1–3 and dentate gyrus subfields of the hippocampal formation; MEC, medial entorhinal cortex; PoSub, postsubiculum; RSC, retrosplenial cortex.

non-directional cues to perform the task. Modifying the task to restrict the cue-types that are available makes it possible to determine which cues animals are able to use. By carrying out sample and test runs in two separate adjacent mazes, animals are prevented from using intramaze or odor cues to perform the task. However, this manipulation also puts allocentric and directional cues into conflict for a subset of trials as alternating on the basis of direction requires animals to return to the same allocentric location (**Figure 2A**). Rats with neurotoxic lesions of the LMN show a mild impairment on this two-maze manipulation (**Figure 2B**; Vann, 2011). This impairment could reflect a greater reliance on intramaze cues or a greater sensitivity to the mismatch between direction and allocentric cues. This was examined by subsequently removing the mismatch between visual allocentric and direction cues by testing the animals in the dark (**Figure 2A**). This resulted in the lesion animals performing equivalently to the controls (**Figure 2B**). Together, these data suggest that animals with LMN lesions are less likely to use directional information when it is put in conflict with another spatial cue i.e., in this case visual allocentric information. However, when this conflict is removed, and direction cues become the most salient (Futter and Aggleton, 2006), animals with a disrupted head direction system are unimpaired (Vann, 2011).

In the T-maze task, animals have to choose between reward locations that are separated by 180°. This quite crude direction discrimination appears to be possible with an impaired head direction system. In contrast, the radial-arm maze task typically requires animals to discriminate between eight radially-oriented arms that are separated by 45°. This task would, therefore, be expected to require a more accurate directional representation. Additionally, LMN lesions increase place cell repetition in

radially-oriented arms (Harland et al., 2017), which should also reduce animals' ability to discriminate between the arms in a radial-arm maze. Nevertheless, lesions of the LMN failed to affect performance on this task (Vann, 2018). Furthermore, when manipulations were carried out to either reduce the reliance on intramaze cues or remove visual allocentric cues, LMN lesion rats were still unimpaired. Both of these manipulations would presumably increase reliance on internal direction systems, yet no lesion-induced impairment was found (Vann, 2018). It was not the case that the lesions in this experiment were ineffective, as the same animals were impaired on other spatial tasks and had reduced c-Fos expression in the RSC (Vann, 2011).

Watermaze tasks can be particularly useful for assessing spatial memory as they remove possible confounds of odor trails, the use of which can mask impairments in using allocentric spatial cues. Furthermore, watermaze tasks do not typically confine animals' choices to specific "arms," potentially enabling more subtle impairments in heading judgments to be detected. To date, two studies have looked at the contribution of the LMN to watermaze tasks carried out in a circular pool. The first study used a working memory procedure where animals were required to learn a new platform location within each session (Vann, 2005). LMN lesion animals showed an initial impairment on this task but with continued training their performance matched that of controls. This impairment is comparable to rats with discrete combined lesions of ADN/anteroventral thalamic nuclei where performance on a similar working memory task in the watermaze was only mildly impaired (van Groen et al., 2002). The second study looking at LMN contribution (Harland et al., 2015) tested animals on a reference memory task where the platform remained in the same spatial location across sessions. On this task, the LMN lesion rats performed equivalently to controls. However, when the platform was subsequently moved to the opposite spatial location (reversal) a lesion-induced deficit emerged. These findings suggest there is a dependence on the head direction system in situations that require rapid encoding of spatial information.

THE EFFECT OF HEAD DIRECTION SYSTEM LESIONS ON FOOD-CARRYING TASKS

Food-carrying tasks are typically run on open dry mazes with equally positioned entrances/exits around the edge, one of which contains a home refuge. The task requires animals to search for food on the maze and once animals have located the food, they carry it back to their refuge. As such, this task requires animals to keep track of their location within the environment, locate themselves with respect to their refuge, and then orient themselves to return to the refuge. It would, therefore, be expected that accurate performance on this task would depend on an intact head direction system. Consistent with this, lesions of a number of head direction areas have been found to impair animals' accuracy of performance on this task (e.g., Frohardt et al., 2006; Clark and Taube, 2009; Dwyer et al., 2013; Peckford et al., 2014; Yoder et al., 2019).

To date, no study has successfully assessed the impact of selective LMN lesions on food-carrying tasks. However, comparisons with the findings from ADN lesions on this task could be particularly informative because LMN and ADN lesion effects appear to be quantitatively and qualitatively similar on other tasks (e.g., van Groen et al., 2002; Peckford et al., 2014). As with lesions to other head direction areas, ADN lesions impair performance on food-carrying tasks with animals more likely to return to a location adjacent to the refuge (Frohardt et al., 2006; Peckford et al., 2014). ADN lesions, therefore, result in a slightly less accurate angle of return indicating a role for the head direction system in fine-tuned direction discrimination. The assumption, therefore, is that LMN lesions would also result in a less accurate return trajectory on this task, consistent with previous LMN-lesion impairments observed on tasks that require rapid, flexible spatial learning.

A study which assessed the effects of large electrolytic DTg lesions on food-carrying tasks found impairments that were considerably greater than the impairments observed following ADN lesions (Frohardt et al., 2006). This could suggest that the DTg lesions reflect more than just the loss of the DTg-LMN-ADN head direction signal, i.e., the DTg could be influencing an additional pathway. The DTg is reciprocally connected with the supragenual nucleus (Biazoli et al., 2006; Clark et al., 2012a), and nucleus prepositus hypoglossi (Butler and Taube, 2015, 2017), both of which contain a significant proportion of angular head velocity cells and, in turn, are interconnected with the vestibular nuclei. However, lesions of the vestibular nuclei appear to increase animals' reliance on the use of visual spatial cues to navigate while reducing their ability to use idiothetic cues (Stackman and Herbert, 2002), which seems very different from lesions of LMN where the use of visual spatial cues is impaired. Alternatively, given the location of the DTg, large electrolytic lesion may have substantial non-selective effects due to involvement of adjacent regions, e.g., dorsal raphe nuclei, and fibers of passage; this may explain DTg lesions appearing far more disruptive than lesions of LMN or ADN in some studies (Frohardt et al., 2006; Dwyer et al., 2013). Consistent with this interpretation, more discrete electrolytic DTg lesions impair rats' ability to use visual-spatial cues while leaving intact their ability to use directional cues (Clark et al., 2013), a pattern of findings comparable to those found following LMN lesions (Vann, 2005, 2011).

IS THE HEAD DIRECTION SYSTEM A GEOMETRIC SYSTEM?

Given the importance of geometrical cues for orientation and navigation, it is possible that the head direction system has a role in geometry-based navigation. To test this, rats with LMN lesions were required to learn the location of a platform in a rectangular watermaze on the basis of geometric features (Vann, 2011). The configuration of long and short walls results in the two diagonally-opposed corners of the rectangle being geometrically identical (**Figure 2C**). Consequently, there are two "correct" corners, which could contain a platform whereas the remaining two corners are incorrect (with no

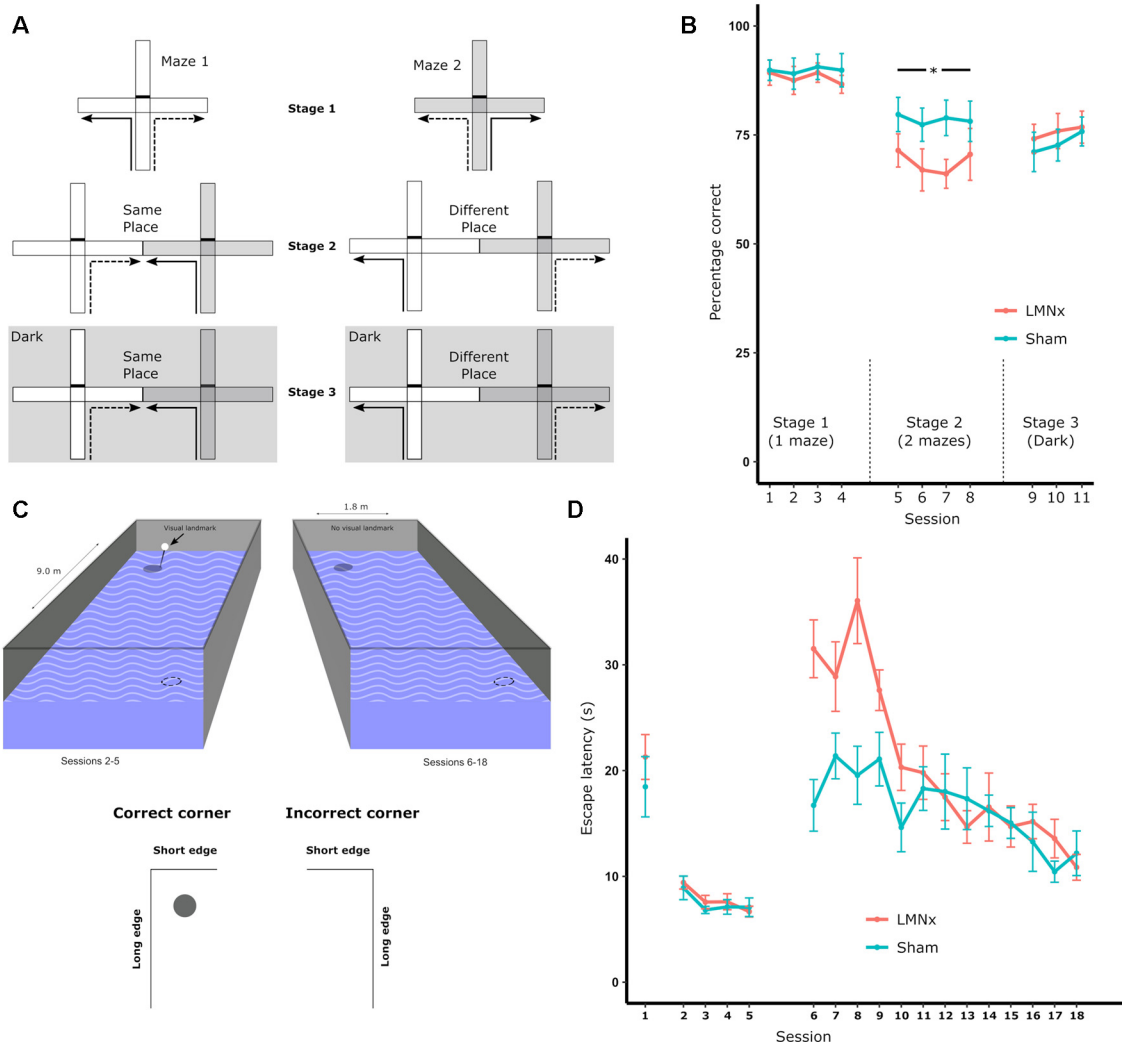

FIGURE 2 | (A) Schematic of the T-maze alternation task: solid lines indicate the forced sample phase while dashed lines indicate the correct response in the choice phase. Arm access could be blocked by placing a barrier at the entrance of the arm (effectively turning the cross-maze into a T-maze configuration). Initial training on the task (Stage 1) permitted the use of multiple strategies supporting alternation, i.e., allocentric, intramaze, idiothetic, direction alternation (with reference to a known bearing). The task was then systematically modified in order to prevent the use of intramaze cues (Stage 2) or the use of intramaze and visual allocentric cues (Stage 3). These manipulations included using two mazes instead of one (Stage 2 and 3) or running in the dark, as illustrated with the dark gray hatched background (Stage 3); **(B)** percentage of correct choices for all three stages; **(C)** schematic of the geometric cue task. Rats were tested in a rectangular insert within a circular maze. A curtain was drawn around the maze throughout to encourage the use of intramaze cues for learning. The solid circles depict the submerged platform and the dotted circles indicate the geometrically identical platform location (on each trial there was only one platform). The visible landmark (black bar) was attached to the platform for Sessions 2–5 of the experiment; **(D)** the mean escape latencies for the two groups during training when they were required to find a platform beneath a landmark in a circular pool (Session 1), beneath a landmark in a rectangular pool (Session 2–5), and without a landmark in a rectangular pool (Session 5–18). The vertical lines depict the standard error of the mean. Abbreviations: LMNx, lateral mammillary nuclei lesion group; Sham, surgical control; *$p < 0.05$. Data are taken from Vann (2011).

escape platform); rats had to learn to swim to the correct corners to escape. Rats with LMN lesions showed a striking impairment at the beginning of training, despite performing normally on pre-training procedures used to familiarize them with non-spatial aspects of the task (**Figure 2D**). Once again, however, the impairment was transient and, by the end of training, the lesion animals were performing at a level equivalent to the controls (**Figure 2D**; Vann, 2011). This geometric watermaze task appears particularly sensitive to disruption of the head direction system as lesions focused on the ADN also impair performance on this task whereas animals with lesions of the medial mammillary body system (Vann, 2013) or lesions of the fornix (Aggleton et al., 2009) appear unimpaired.

Stable, stimulus-locked sensory cues are critical to minimizing errors in cognitive representations of space, e.g., due to internally-generated drift in directional tuning in the absence of visual input (Taube et al., 1990; Goodridge et al., 1998). It would, therefore, be expected that salient geometric features of

enclosed environments would be used preferentially by spatially-responsive cells and in subsequent navigational strategies (Gallistel, 1990). However, experimental evidence seems to suggest otherwise. For example, rotation of highly geometrically polarized enclosures is insufficient to drive rotations in the preferred firing direction of head direction cells throughout the LMN-ADN-PoSub-RSC axis (Knight et al., 2011). However, geometric cues do control head direction cell firing in animals that are disorientated (Knight et al., 2011; Clark et al., 2012b) suggesting that while geometric cues can control head direction cell activity, they are not used preferentially. One explanation is that while geometric features are stable, they are not necessarily visually salient, and their recognition is reliant on the detection of how light is differentially reflected off surfaces. In low or dim light the contrast in luminance would be lower such that updating positional information from these features would be more reliant on sensory inputs that require proximity to the feature, e.g., somatosensory/haptic flow (particularly so given the relatively poor resolution of vision in rodents). When behavioral studies specifically require the use of geometric cues, these cues appear less salient to animals with an impaired head direction system, i.e., lesion animals are less readily able to use these cues to navigate. However, this initial impairment can be overcome with repeated training suggesting the head direction contribution may be important for directing initial attention to the geometric cues (Vann, 2011), particularly so in aversive conditions when rapid learning is required.

WHAT COMPENSATORY MECHANISMS SUPPORT FUNCTION FOLLOWING LMN LESIONS?

As described, behavioral deficits observed following LMN lesions tend to be very mild and/or transient, so it is likely that compensatory mechanisms are able to support function when this directional pathway is lost. These mechanisms include behavioral compensation whereby animals adopt different behavioral strategies to perform the tasks or functional compensation where different brain regions are able to support similar functions to mitigate the effects of the lesion. For instance, while Yoder et al. (2019) found that PoSub lesions in naïve animals caused impairments in path integration (food-carrying task), Bett et al. (2012) found no impairment in PoSub lesion animals that had been pre-trained prior to surgery. Pre-training likely acts as a compensatory mechanism by enabling animals to use previously learned strategies (Yoder et al., 2019) and/or form neurally-distributed representations of the environment which could better support navigation when directional information is limited.

First, we will consider behavioral compensation. Animals can often use a number of different cues and strategies to perform spatial tasks. In particular, tasks where animals have limited options, such as T-maze alternation, can often be supported by more habitual striatal-based behavior (Valerio et al., 2010; Gibson et al., 2013). The idea that animals use different strategies when head direction information is limited is additionally supported by work using an inverted navigation approach. The head direction signal is severely degraded when rats navigate upside-down (Taube et al., 2004; Calton and Taube, 2005; Gibson et al., 2013) making it possible to assess the head direction system's contribution to navigation without using surgical intervention. Rats tasked with navigating towards a goal location (i.e., an escape hole), while inverted, were impaired when there were four possible release locations but performance was intact when only two release locations were used as long as salient visual landmarks were available (Valerio et al., 2010). It appears that the head direction signal is needed when flexible navigation is required but the use of a habit-like strategy could support performance in some conditions. This is a similar to findings from LMN-lesion studies. Impairments are often most pronounced when animals have to adapt behavior or respond flexibly, as is the case during both the reversal and working memory tasks in the watermaze. Both the radial-arm maze task and water maze task are unlikely to be supported by habit-like strategies from the outset but it appears that when learning is slow and incremental, again the head direction system is not so critical. Together these highlight the importance of probing behavioral impairments to determine exactly how animals are performing the task and what cues are being used. A consistent finding, however, is that rapid, flexible learning appears most sensitive to lesions within the head direction systems.

An additional explanation for the mild lesion effects following LMN lesions is that there is redundancy within the head direction system. Initially there just appeared to be a single head direction pathway, however, now it is apparent that there is a distributed head direction system across numerous brain regions. At present, it is not clear how these additional areas relate to the LMN-based system. For example, lesions of the LMN result in a small reduction in RSC activity, as measured by the immediate early gene c-Fos (Vann, 2018), but it is not known whether the retrosplenial head direction signal is dependent on indirect inputs from LMN. From current anatomical knowledge, it would not be expected that the head direction signal in the anteroventral nucleus, nucleus reuniens, laterodorsal thalamus or the striatum would depend on direct inputs from the LMN (Dillingham et al., 2015). So it is possible that even with the loss of LMN there is sufficient directional information to support task performance. Consistent with this idea, there is anatomical evidence for parallel streams of ascending vestibular projections that may also provide functional compensation (**Figure 1**). One such possibility involves projections from the vestibular nuclei which ascend to the ventral posterolateral thalamus (VPL), contributing to a proprioceptive representation in the PPC (McNaughton et al., 1989; Mimica et al., 2018). Vestibulomotor, i.e., idiothetic, information is sufficient to generate a head direction signal (Goodridge and Taube, 1997; Calton and Taube, 2009; Clark et al., 2010; Clark and Taube, 2011; Yoder et al., 2015; Mehlman et al., 2019) and it is possible that parallel ascending vestibular-VPL-PPC projections subserve a parallel directional pathway. The PPC, in turn, projects strongly to the parahippocampal region, including direct projections to the MEC as well as reciprocal connections with the RSC.

Lesions of the DTg (Bassett et al., 2007), LMN (Blair et al., 1999), or ADN abolish the head direction signal in the PoSub (Goodridge and Taube, 1997) and the MEC (Winter et al., 2015). It would, therefore, be expected that if the vestibular-VPL-PPC axis does provide a parallel source of heading information, lesions within the LMN-ADN pathway would spare the PPC head direction signal, however, to our knowledge, this has not yet been tested.

Unlike medial mammillary projections to the anterior thalamic nuclei, projections from the LMN to the ADN are bilateral, which provides a degree of anatomical compensation. Blair et al. (1999) compared the effects of unilateral and bilateral LMN lesions on head direction firing in ADN and found that while unilateral lesions induced some impairments in ADN directional tuning immediately following the lesion, they were transient, and recovery of function was evident within a few days. Consistent with other studies (Blair et al., 1998; Bassett et al., 2007), however, bilateral LMN lesions abolished directional firing permanently. Head direction cell firing in LMN that results from head movements towards the hemisphere in which the cell is located, i.e., ipsiversive turns, result in narrower tuning curves than contraversive turns (Blair et al., 1998). Following the transient effects of unilateral LMN lesions, head direction tuning curves in ADN were found to be narrower in response to head turns in the direction of the intact hemisphere, suggesting that compensation to the lesion was, at least in part, due to an increase in the influence of intact contralateral projections (Blair et al., 1999). In addition to the loss of ADN head direction cell tuning following bilateral LMN lesions, there was an emergence of increased theta band-entrained firing activity along with velocity-dependent firing. These changes again may point towards a level of plasticity through either an increased responsiveness to non-directional inputs or through an increased reliance on non-vestibular directional sense, e.g., *via* somatosensory-laterodorsal thalamic nucleus connections (Bezdudnaya and Keller, 2008).

DISCUSSION

At a neurophysiological level, the generative network of the head direction system (**Figure 1**) is critical for complex spatial processing in downstream structures. However, this neurophysiological importance is not mirrored by the scale of the behavioral impairments observed following lesions to this network, particularly with respect to the LMN. It is perhaps unsurprising that given the evolutionary importance of effective navigational strategies, there is considerable scope for compensation, e.g., through dependence on multiple external cues (**Figure 1**). Compared to other neural correlates of space (e.g., place cells, grid cells, object cell, boundary-vector cells), subcortical head direction cells are relatively rudimentary in the information they encode, i.e., a representation of the position of the head in a single plane (yaw) with respect to a salient visual landmark, without providing other metrics, e.g., distance from landmarks (but see Peyrache et al., 2017). In that sense, they may be seen as both the product of combined representations, e.g., vestibular and motor (i.e., angular velocity), as well as the building blocks to more informative representations of space, i.e., attractor network models. An effective cognitive spatial representation must also be rapidly updated both with respect to changes that result from self-motion as well as in response to external changes and in that sense, subcortical head direction cells have their limitations, e.g., in the absence of visual cues, drift in directional tuning represents a less stable substrate for path integration than the relative stability of the hippocampal place signal (Save et al., 2000).

We have known of the existence of head direction cells for 30 years (Taube et al., 1990) yet our understanding of their behavioral contributions is surprisingly lacking. There are remarkably few studies that have studied behavioral contributions of these structures. Lesions of these regions are technically difficult as they are typically small structures that are adjacent to other key spatial memory regions. When lesions encroach into adjacent regions the results can be very difficult to interpret. A further issue is interpreting lesions of head direction regions in terms of head direction. Head direction cells typically make up the minority of cells within these structures (proportions of head direction cells in regions within the DTg-LMN-ADN-PoSub axis range from 12.5% to 60%; Taube and Bassett, 2003); it is likely that non-head direction cells also contribute to these tasks, making the behavioral contribution of the head direction system less than assumed. In light of compensatory mechanisms that might mask behavioral effects of LMN/DTg lesions, chronic lesion paradigms, which are typically employed within the head direction-system literature, may not be sufficiently sensitive. Approaches that use reversible inactivation with high temporal precision, e.g., optogenetics, may be more informative in this sense (e.g., Butler et al., 2017). Combining such techniques with approaches that permit the targeting of distinct neuronal populations that share common anatomical connectivity and/or neurochemical properties could enable temporary inactivation of head direction cells while leaving other cells intact. It is essential to combine these techniques with well-designed behavioral studies if we are to solve the puzzle of how the head direction system contributes to spatial navigation.

AUTHOR CONTRIBUTIONS

CD and SV both conceived and wrote the article.

FUNDING

The authors are supported by the Wellcome Trust (212273/Z/18/Z).

ACKNOWLEDGMENTS

We thank the reviewers for their helpful and constructive feedback on the manuscript.

REFERENCES

Aggleton, J. P., Poirier, G. L., Aggleton, H. S., Vann, S. D., and Pearce, J. M. (2009). Lesions of the fornix and anterior thalamic nuclei dissociate different aspects of hippocampal-dependent spatial learning: implications for the neural basis of scene learning. *Behav. Neurosci.* 123, 504–519. doi: 10.1037/a0015404

Alme, C. B., Miao, C., Jezek, K., Treves, A., Moser, E. I., and Moser, M. B. (2014). Place cells in the hippocampus: eleven maps for eleven rooms. *Proc. Natl. Acad. Sci. U S A* 111, 18428–18435. doi: 10.1073/pnas.1421056111

Bassett, J. P., Tullman, M. L., and Taube, J. S. (2007). Lesions of the tegmentomammillary circuit in the head direction system disrupt the head direction signal in the anterior thalamus. *J. Neurosci.* 27, 7564–7577. doi: 10.1523/JNEUROSCI.0268-07.2007

Bett, D., Wood, E. R., and Dudchenko, P. A. (2012). The postsubiculum is necessary for spatial alternation but not for homing by path integration. *Behav. Neurosci.* 126, 237–248. doi: 10.1037/a0027163

Bezdudnaya, T., and Keller, A. (2008). Laterodorsal nucleus of the thalamus: a processor of somatosensory inputs. *J. Comp. Neurol.* 507, 1979–1989. doi: 10.1002/cne.21664

Biazoli, C. E. Jr., Goto, M., Campos, A. M., and Canteras, N. S. (2006). The supragenual nucleus: a putative relay station for ascending vestibular signs to head direction cells. *Brain Res.* 1094, 138–148. doi: 10.1016/j.brainres.2006.03.101

Blair, H. T., Cho, J. W., and Sharp, P. E. (1998). Role of the lateral mammillary nucleus in the rat head direction circuit: a combined single unit recording and lesion study. *Neuron* 21, 1387–1397. doi: 10.1016/s0896-6273(00)80657-1

Blair, H. T., Cho, J. W., and Sharp, P. E. (1999). The anterior thalamic head-direction signal is abolished by bilateral but not unilateral lesions of the lateral mammillary nucleus. *J. Neurosci.* 19, 6673–6683. doi: 10.1523/JNEUROSCI.19-15-06673.1999

Blair, H. T., and Sharp, P. E. (1995). Anticipatory head direction signals in anterior thalamus: evidence for a thalamocortical circuit that integrates angular head motion to compute head direction. *J. Neurosci.* 15, 6260–6270. doi: 10.1523/JNEUROSCI.15-09-06260.1995

Bonnevie, T., Dunn, B., Fyhn, M., Hafting, T., Derdikman, D., Kubie, J. L., et al. (2013). Grid cells require excitatory drive from the hippocampus. *Nat. Neurosci.* 16, 309–317. doi: 10.1038/nn.3311

Brandon, M. P., Bogaard, A. R., Andrews, C. M., and Hasselmo, M. E. (2012). Head direction cells in the postsubiculum do not show replay of prior waking sequences during sleep. *Hippocampus* 22, 604–618. doi: 10.1002/hipo.20924

Butler, W. N., and Taube, J. S. (2015). The nucleus prepositus hypoglossi contributes to head direction cell stability in rats. *J. Neurosci.* 35, 2547–2558. doi: 10.1523/JNEUROSCI.3254-14.2015

Butler, W. N., Smith, K. S., van der Meer, M. A. A., and Taube, J. S. (2017). The head-direction signal plays a functional role as a neural compass during navigation. *Curr. Biol.* 27, 1259–1267. doi: 10.1016/j.cub.2017.03.033

Butler, W. N., and Taube, J. S. (2017). Oscillatory synchrony between head direction cells recorded bilaterally in the anterodorsal thalamic nuclei. *J. Neurophysiol.* 117, 1847–1852. doi: 10.1152/jn.00881.2016

Calton, J. L., Stackman, R. W., Goodridge, J. P., Archey, W. B., Dudchenko, P. A., and Taube, J. S. (2003). Hippocampal place cell instability after lesions of the head direction cell network. *J. Neurosci.* 23, 9719–9731. doi: 10.1523/JNEUROSCI.23-30-09719.2003

Calton, J. L., and Taube, J. S. (2005). Degradation of head direction cell activity during inverted locomotion. *J. Neurosci.* 25, 2420–2428. doi: 10.1523/JNEUROSCI.3511-04.2005

Calton, J. L., and Taube, J. S. (2009). Where am I and how will I get there from here? A role for posterior parietal cortex in the integration of spatial information and route planning. *Neurobiol. Learn. Mem.* 91, 186–196. doi: 10.1016/j.nlm.2008.09.015

Chen, L. L., Lin, L. H., Green, E. J., Barnes, C. A., and McNaughton, B. L. (1994). Head-direction cells in the rat posterior cortex. I. Anatomical distribution and behavioral modulation. *Exp. Brain Res.* 101, 8–23. doi: 10.1007/bf00243212

Cho, J., and Sharp, P. E. (2001). Head direction, place, and movement correlates for cells in the rat retrosplenial cortex. *Behav. Neurosci.* 115, 3–25. doi: 10.1037/0735-7044.115.1.3

Clark, B. J., Bassett, J. P., Wang, S. S., and Taube, J. S. (2010). Impaired head direction cell representation in the anterodorsal thalamus after lesions of the retrosplenial cortex. *J. Neurosci.* 30, 5289–5302. doi: 10.1523/JNEUROSCI.3380-09.2010

Clark, B. J., Brown, J. E., and Taube, J. S. (2012a). Head direction cell activity in the anterodorsal thalamus requires intact supragenual nuclei. *J. Neurophysiol.* 108, 2767–2784. doi: 10.1152/jn.00295.2012

Clark, B. J., Harris, M. J., and Taube, J. S. (2012b). Control of anterodorsal thalamic head direction cells by environmental boundaries: comparison with conflicting distal landmarks. *Hippocampus* 22, 172–187. doi: 10.1002/hipo.20880

Clark, B. J., Rice, J. P., Akers, K. G., Candelaria-Cook, F. T., Taube, J. S., and Hamilton, D. A. (2013). Lesions of the dorsal tegmental nuclei disrupt control of navigation by distal landmarks in cued, directional, and place variants of the Morris water task. *Behav. Neurosci.* 127, 566–581. doi: 10.1037/a0033087

Clark, B. J., and Taube, J. S. (2009). Deficits in landmark navigation and path integration after lesions of the interpeduncular nucleus. *Behav. Neurosci.* 123, 490–503. doi: 10.1037/a0015477

Clark, B. J., and Taube, J. S. (2011). Intact landmark control and angular path integration by head direction cells in the anterodorsal thalamus after lesions of the medial entorhinal cortex. *Hippocampus* 21, 767–782. doi: 10.1002/hipo.20874

Dillingham, C. M., Frizzati, A., Nelson, A. J., and Vann, S. D. (2015). How do mammillary body inputs contribute to anterior thalamic function? *Neurosci. Biobehav. Rev.* 54, 108–119. doi: 10.1016/j.neubiorev.2014.07.025

Dudchenko, P. A., and Zinyuk, L. E. (2005). The formation of cognitive maps of adjacent environments: evidence from the head direction cell system. *Behav. Neurosci.* 119, 1511–1523. doi: 10.1037/0735-7044.119.6.1511

Dwyer, J. A., Ingram, M. L., Snow, A. C., Thorpe, C. M., Martin, G. M., and Skinner, D. M. (2013). The effects of bilateral lesions to the dorsal tegmental nucleus on spatial learning in rats. *Behav. Neurosci.* 127, 867–877. doi: 10.1037/a0034931

Frohardt, R. J., Bassett, J. P., and Taube, J. S. (2006). Path integration and lesions within the head direction cell circuit: comparison between the roles of the anterodorsal thalamus and dorsal tegmental nucleus. *Behav. Neurosci.* 120, 135–149. doi: 10.1037/0735-7044.120.1.135

Futter, J. E., and Aggleton, J. P. (2006). How rats perform spatial working memory tasks: limitations in the use of egocentric and idiothetic working memory. *Q. J. Exp. Psychol.* 59, 77–99. doi: 10.1080/02724990544000068

Fyhn, M., Hafting, T., Treves, A., Moser, M. B., and Moser, E. I. (2007). Hippocampal remapping and grid realignment in entorhinal cortex. *Nature* 446, 190–194. doi: 10.1038/nature05601

Gallistel, C. R. (1990). Representations in animal cognition: an introduction. *Cognition* 37, 1–22. doi: 10.1016/0010-0277(90)90016-d

Gibson, B., Butler, W. N., and Taube, J. S. (2013). The head-direction signal is critical for navigation requiring a cognitive map but not for learning a spatial habit. *Curr. Biol.* 23, 1536–1540. doi: 10.1016/j.cub.2013.06.030

Goodridge, J. P., and Taube, J. S. (1997). Interaction between the postsubiculum and anterior thalamus in the generation of head direction cell activity. *J. Neurosci.* 17, 9315–9330. doi: 10.1523/JNEUROSCI.17-23-09315.1997

Goodridge, J. P., Dudchenko, P. A., Worboys, K. A., Golob, E. J., and Taube, J. S. (1998). Cue control and head direction cells. *Behav. Neurosci.* 112, 749–761. doi: 10.1037/0735-7044.112.4.749

Grieves, R. M., Jenkins, B. W., Harland, B. C., Wood, E. R., and Dudchenko, P. A. (2016). Place field repetition and spatial learning in a multicompartment environment. *Hippocampus* 26, 118–134. doi: 10.1002/hipo.22496

Hafting, T., Fyhn, M., Bonnevie, T., Moser, M. B., and Moser, E. I. (2008). Hippocampus-independent phase precession in entorhinal grid cells. *Nature* 453, 1248–1252. doi: 10.1038/nature06957

Hafting, T., Fyhn, M., Molden, S., Moser, M. B., and Moser, E. I. (2005). Microstructure of a spatial map in the entorhinal cortex. *Nature* 436, 801–806. doi: 10.1038/nature03721

Harland, B., Grieves, R. M., Bett, D., Stentiford, R., Wood, E. R., and Dudchenko, P. A. (2017). Lesions of the head direction cell system increase hippocampal place field repetition. *Curr. Biol.* 27, 2706.e2–2712.e2. doi: 10.1016/j.cub.2017.07.071

Harland, B., Wood, E. R., and Dudchenko, P. A. (2015). The head direction cell system and behavior: the effects of lesions to the lateral mammillary bodies

on spatial memory in a novel landmark task and in the water maze. *Behav. Neurosci.* 129, 709–719. doi: 10.1037/bne0000106

Hartley, T., Burgess, N., Lever, C., Cacucci, F., and O'Keefe, J. (2000). Modeling place fields in terms of the cortical inputs to the hippocampus. *Hippocampus* 10, 369–379. doi: 10.1002/1098-1063(2000)10:4<369::aid-hipo3>3.0.co;2-0

Hinman, J. R., Chapman, G. W., and Hasselmo, M. E. (2019). Neuronal representation of environmental boundaries in egocentric coordinates. *Nat. Commun.* 10:2772. doi: 10.1038/s41467-019-10722-y

Jacob, P. Y., Casali, G., Spieser, L., Page, H., Overington, D., and Jeffery, K. (2017). An independent, landmark-dominated head-direction signal in dysgranular retrosplenial cortex. *Nat. Neurosci.* 20, 173–175. doi: 10.1038/nn.4465

Jankowski, M. M., Islam, M. N., Wright, N. F., Vann, S. D., Erichsen, J. T., Aggleton, J. P., et al. (2014). Nucleus reuniens of the thalamus contains head direction cells. *Elife* 3:e03075. doi: 10.7554/elife.03075

Knight, R., Hayman, R., Lin Ginzberg, L., and Jeffery, K. (2011). Geometric cues influence head direction cells only weakly in nondisoriented rats. *J. Neurosci.* 31, 15681–15692. doi: 10.1523/JNEUROSCI.2257-11.2011

Krupic, J., Bauza, M., Burton, S., Barry, C., and O'Keefe, J. (2015). Grid cell symmetry is shaped by environmental geometry. *Nature* 518, 232–235. doi: 10.1038/nature14153

Langston, R. F., Ainge, J. A., Couey, J. J., Canto, C. B., Bjerknes, T. L., Witter, M. P., et al. (2010). Development of the spatial representation system in the rat. *Science* 328, 1576–1580. doi: 10.1126/science.1188210

Lever, C., Burton, S., Jeewajee, A., O'Keefe, J., and Burgess, N. (2009). Boundary vector cells in the subiculum of the hippocampal formation. *J. Neurosci.* 29, 9771–9777. doi: 10.1523/JNEUROSCI.1319-09.2009

McNaughton, B. L., Leonard, B., and Chen, L. (1989). Cortical-hippocampal interactions and cognitive mapping: a hypothesis based on reintegration of the parietal and inferotemporal pathways for visual processing. *Psychobiology* 17, 230–235. doi: 10.1007/bf03337774

Mehlman, M. L., Winter, S. S., Valerio, S., and Taube, J. S. (2019). Functional and anatomical relationships between the medial precentral cortex, dorsal striatum and head direction cell circuitry. I. Recording studies. *J. Neurophysiol.* 121, 350–370. doi: 10.1152/jn.00143.2018

Miao, C., Cao, Q., Ito, H. T., Yamahachi, H., Witter, M. P., Moser, M. B., et al. (2015). Hippocampal remapping after partial inactivation of the medial entorhinal cortex. *Neuron* 88, 590–603. doi: 10.1016/j.neuron.2015.09.051

Mimica, B., Dunn, B. A., Tombaz, T., Bojja, V., and Whitlock, J. R. (2018). Efficient cortical coding of 3D posture in freely behaving rats. *Science* 362, 584–589. doi: 10.1126/science.aau2013

Mizumori, S. J., and Williams, J. D. (1993). Directionally selective mnemonic properties of neurons in the lateral dorsal nucleus of the thalamus of rats. *J. Neurosci.* 13, 4015–4028. doi: 10.1523/JNEUROSCI.13-09-04015.1993

Mizumori, S. J., Canfield, J. G., and Yeshenko, O. (2005). Parallel and interrelated neural systems underlying adaptive navigation. *Integr. Comp. Biol.* 45, 547–554. doi: 10.1093/icb/45.3.547

Mizumori, S. J., Cooper, B. G., Leutgeb, S., and Pratt, W. E. (2000). A neural systems analysis of adaptive navigation. *Mol. Neurobiol.* 21, 57–82. doi: 10.1385/mn:21:1-2:057

O'Keefe, J., and Dostrovsky, J. (1971). The hippocampus as a spatial map. Preliminary evidence from unit activity in the freely-moving rat. *Brain Res.* 34, 171–175. doi: 10.1016/0006-8993(71)90358-1

Peckford, G., Dwyer, J. A., Snow, A. C., Thorpe, C. M., Martin, G. M., and Skinner, D. M. (2014). The effects of lesions to the postsubiculum or the anterior dorsal nucleus of the thalamus on spatial learning in rats. *Hippocampus* 128, 654–665. doi: 10.1037/bne0000019

Peyrache, A., Schieferstein, N., and Buzsaki, G. (2017). Transformation of the head-direction signal into a spatial code. *Nat. Commun.* 8:1752. doi: 10.1038/s41467-017-01908-3

Ragozzino, K. E., Leutgeb, S., and Mizumori, S. J. (2001). Dorsal striatal head direction and hippocampal place representations during spatial navigation. *Exp. Brain Res.* 139, 372–376. doi: 10.1007/s002210100795

Sargolini, F., Fyhn, M., Hafting, T., McNaughton, B. L., Witter, M. P., Moser, M. B., et al. (2006). Conjunctive representation of position, direction and velocity in entorhinal cortex. *Science* 312, 758–762. doi: 10.1126/science.1125572

Save, E., Nerad, L., and Poucet, B. (2000). Contribution of multiple sensory information to place field stability in hippocampal place cells. *Hippocampus* 10, 64–76. doi: 10.1002/(SICI)1098-1063(2000)10:1<64::AID-HIPO7>3.0.CO;2-Y

Sharp, P. E., and Koester, K. (2008). Lesions of the mammillary body region severely disrupt the cortical head direction, but not place cell signal. *Hippocampus* 18, 766–784. doi: 10.1002/hipo.20436

Sharp, P. E., Tinkelman, A., and Cho, J. (2001). Angular velocity and head direction signals recorded from the dorsal tegmental nucleus of gudden in the rat: implications for path integration in the head direction cell circuit. *Behav. Neurosci.* 115, 571–588. doi: 10.1037/0735-7044.115.3.571

Stackman, R. W., and Herbert, A. M. (2002). Rats with lesions of the vestibular system require a visual landmark for spatial navigation. *Behav. Brain Res.* 128, 27–40. doi: 10.1016/s0166-4328(01)00270-4

Stackman, R. W., and Taube, J. S. (1998). Firing properties of rat lateral mammillary single units: head direction, head pitch and angular head velocity. *J. Neurosci.* 18, 9020–9037. doi: 10.1523/JNEUROSCI.18-21-09020.1998

Taube, J. S. (1995). Head direction cells recorded in the anterior thalamic nuclei of freely moving rats. *J. Neurosci.* 15, 70–86. doi: 10.1523/JNEUROSCI.15-01-00070.1995

Taube, J. S., and Bassett, J. P. (2003). Persistent neural activity in head direction cells. *Cereb. Cortex* 13, 1162–1172. doi: 10.1093/cercor/bhg102

Taube, J. S., Muller, R. U., and Ranck, J. B. Jr. (1990). Head-direction cells recorded from the postsubiculum in freely moving rats. II. Effects of environmental manipulations. *J. Neurosci.* 10, 436–447. doi: 10.1523/JNEUROSCI.10-02-00436.1990

Taube, J. S., Stackman, R. W., Calton, J. L., and Oman, C. M. (2004). Rat head direction cell responses in zero-gravity parabolic flight. *J. Neurophysiol.* 92, 2887–2997. doi: 10.1152/jn.00887.2003

Tsanov, M., Chah, E., Vann, S. D., Reilly, R. B., Erichsen, J. T., Aggleton, J. P., et al. (2011). Theta-modulated head direction cells in the rat anterior thalamus. *J. Neurosci.* 31, 9489–9502. doi: 10.1523/JNEUROSCI.0353-11.2011

Valerio, S., Clark, B. J., Chan, J. H., Frost, C. P., Harris, M. J., and Taube, J. S. (2010). Directional learning, but no spatial mapping by rats performing a navigational task in an inverted orientation. *Neurobiol. Learn. Mem.* 93, 495–505. doi: 10.1016/j.nlm.2010.01.007

Van Cauter, T., Poucet, B., and Save, E. (2008). Unstable CA1 place cell representation in rats with entorhinal cortex lesions. *Eur. J. Neurosci.* 27, 1933–1946. doi: 10.1111/j.1460-9568.2008.06158.x

van Groen, T., Kadish, I., and Michael Wyss, J. (2002). Role of the anterodorsal and anteroventral nuclei of the thalamus in spatial memory in the rat. *Behav. Brain Res.* 132, 19–28. doi: 10.1016/s0166-4328(01)00390-4

Vann, S. D. (2005). Transient spatial deficit associated with bilateral lesions of the lateral mammillary nuclei. *Eur. J. Neurosci.* 21, 820–824. doi: 10.1111/j.1460-9568.2005.03896.x

Vann, S. D. (2011). A role for the head-direction system in geometric learning. *Behav. Brain Res.* 224, 201–206. doi: 10.1016/j.bbr.2011.05.033

Vann, S. D. (2013). Dismantling the Papez circuit for memory in rats. *Elife* 2:e00736. doi: 10.7554/elife.00736

Vann, S. D. (2018). Lesions within the head direction system reduce retrosplenial c-fos expression but do not impair performance on a radial-arm maze task. *Behav. Brain Res* 338, 153–158. doi: 10.1016/j.bbr.2017.10.026

Weiss, S., and Derdikman, D. (2018). Role of the head-direction signal in spatial tasks: when and how does it guide behavior? *J. Neurophysiol.* 120, 78–87. doi: 10.1152/jn.00560.2017

Wiener, S. I. (1993). Spatial and behavioral correlates of striatal neurons in rats performing a self-initiated navigation task. *J. Neurosci.* 13, 3802–3817. doi: 10.1523/JNEUROSCI.13-09-03802.1993

Wills, T. J., Cacucci, F., Burgess, N., and O'Keefe, J. (2010). Development of the hippocampal cognitive map in preweanling rats. *Science* 328, 1573–1576. doi: 10.1126/science.1188224

Winter, S. S., Clark, B. J., and Taube, J. S. (2015). Spatial navigation. Disruption of the head direction cell network impairs the parahippocampal grid cell signal. *Science* 347, 870–874. doi: 10.1126/science.1259591

Yoder, R. M., Peck, J. R., and Taube, J. S. (2015). Visual landmark information gains control of the head direction signal at the lateral mammillary nuclei. *J. Neurosci.* 35, 1354–1367. doi: 10.1523/JNEUROSCI.1418-14.2015

Yoder, R. M., Valerio, S., Crego, A. C. G., Clark, B. J., and Taube, J. S. (2019). Bilateral postsubiculum lesions impair visual and nonvisual homing performance in rats. *Behav. Neurosci.* doi: 10.1037/bne0000321 [Epub ahead of print].

Conflict of Interest Statement: The authors declare that the research was conducted in the absence of any commercial or financial relationships that could be construed as a potential conflict of interest.

frontiers in Neural Circuits

ORIGINAL RESEARCH
published: 27 September 2019
doi: 10.3389/fncir.2019.00059

Neural Dynamics Indicate Parallel Integration of Environmental and Self-Motion Information by Place and Grid Cells

Dmitri Laptev[1,2]* *and Neil Burgess*[1]

[1] UCL Institute of Cognitive Neuroscience, University College London, London, United Kingdom, [2] UCL Centre for Computation, Mathematics and Physics in the Life Sciences and Experimental Biology, Department of Computer Science, University College London, London, United Kingdom

Place cells and grid cells in the hippocampal formation are thought to integrate sensory and self-motion information into a representation of estimated spatial location, but the precise mechanism is unknown. We simulated a parallel attractor system in which place cells form an attractor network driven by environmental inputs and grid cells form an attractor network performing path integration driven by self-motion, with inter-connections between them allowing both types of input to influence firing in both ensembles. We show that such a system is needed to explain the spatial patterns and temporal dynamics of place cell firing when rats run on a linear track in which the familiar correspondence between environmental and self-motion inputs is changed. In contrast, the alternative architecture of a single recurrent network of place cells (performing path integration and receiving environmental inputs) cannot reproduce the place cell firing dynamics. These results support the hypothesis that grid and place cells provide two different but complementary attractor representations (based on self-motion and environmental sensory inputs, respectively). Our results also indicate the specific neural mechanism and main predictors of hippocampal map realignment and make predictions for future studies.

Keywords: continuous attractor, neural network, place cells, grid cells, hippocampus, spatial navigation, path integration

OPEN ACCESS

Edited by:
Desdemona Fricker,
UMR8119 Centre de Neurophysique, Physiologie, Pathologie, France

Reviewed by:
Matthew Nolan,
University of Edinburgh, United Kingdom
Federico Stella,
Institute of Science and Technology Austria (IST Austria), Austria

***Correspondence:**
Dmitri Laptev
dlaptev@workmail.com

Received: *20 May 2019*
Accepted: *21 August 2019*
Published: *27 September 2019*

Citation:
Laptev D and Burgess N (2019) Neural Dynamics Indicate Parallel Integration of Environmental and Self-Motion Information by Place and Grid Cells. Front. Neural Circuits 13:59. doi: 10.3389/fncir.2019.00059

INTRODUCTION

The place cells in the rat hippocampus show strong behavioral correlates by firing only when the animal visits a particular localised region of the surrounding environment (O'Keefe and Dostrovsky, 1971; O'Keefe, 1976). Collectively these place cells provide a population code for spatial position. A neural representation ("cognitive map") of a particular environment is formed in such a way (O'Keefe and Nadel, 1978). As the animal moves around a particular environment, the firing pattern of place cells is continuously updated, reflecting the current position of the animal. This continuous shifting of neural representation could be driven by at least two types of information—perceptual from the environment and internally generated concerning the rat's own movements, and takes place even in total darkness (O'Keefe, 2007).

Another type of spatially selective cells was found in the subiculum by Lever et al. (2009), and is referred to as Boundary Vector Cells (BVCs), due to the fact that a particular BVC fires maximally

when a boundary is encountered at the BVC's preferred distance and allocentric direction from the rat. "Border cells," fulfilling the criteria for BVCs, have also been found in the mEC and adjacent parasubiculum by Solstad et al. (2008), and may represent a subset of BVCs. Initially, the model that incorporated putative BVCs as providing sensory inputs to place cells was developed by Hartley et al. (2000), based on the findings from earlier studies of O'Keefe and Burgess (1996). Barry et al. (2006) then further demonstrated experimentally that impediments to movement, whether walls, a free standing barrier or a sheer drop, play a key role in defining place cell firing, and predicted existence of cells in the subiculum that fit important elements of the BVCs in the Hartley et al. (2000) model. Recently, Grieves et al. (2018) used a similar BVC model of place cell firing to replicate place field repetition seen in various experiments with multicompartment environments.

Updating of place cells' activity according to the rat's internally generated motion signals could be achieved via grid cells, another type of spatially selective cell, that fire whenever a rat enters one of an array of locations arranged in a hexagonal grid across the environment (Hafting et al., 2005) and provide anatomical inputs to areas CA3 and CA1 of the hippocampus. Since grid cells preserve the shape and size of their grid-like firing patterns despite removal of visual cues, it is possible that a path integration mechanism is responsible for maintenance of the grid structure. The fact that neighbouring grid cells have the same field size and spacing, as well as slightly offset grid phasing (Hafting et al., 2005), and that recurrent connections are present in the mEC (Germroth et al., 1991; Lingenhöhl and Finch, 1991; Dhillon and Jones, 2000) suggest that grid cells may perform path integration via a continuous attractor based mechanism (McNaughton et al., 2006). At the same time, a number of experiments have shown an influence of environmental boundaries also on grid cell firing. For example, in the experiments by Barry et al. (2007) and Stensola et al. (2012), the environment deformation caused partial rescaling of grid cell firing patterns, while the experiments by Krupic et al. (2015) and Stensola et al. (2015) showed effects of alignment between grid patterns and boundaries. Recently, Krupic et al. (2018) also found that local changes to the enclosure configuration lead to localised changes in the grid structure (together with local changes in place and boundary cells' responses).

In this study we investigate whether the integration of environmental and self-motion information into a representation of an estimated position could result from a reciprocal interaction between recurrent networks of place cells (receiving inputs from BVCs) and grid cells (implementing path integration) (O'Keefe and Burgess, 2005; Laptev, 2008). We test our hypothesised model against experimental data on place cell firing in situations where sensory and self-motion information are put into conflict (Gothard et al., 1996b; Redish et al., 2000). The Gothard et al. experiment was previously simulated by Sheynikhovich et al. (2009) using a model that integrates visual and self-motion information in its grid cell population, and recently by Keinath et al. (2018) using a model in which path integrating grid cells receive direct input from border cells. Importantly, however, these single-layer attractor models could not capture the neural dynamics observed in the experiment, as we discuss below.

Together with testing the hypothesis about the specific neural implementation of self-motion and sensory information integration, we also address the questions (initially raised by Redish et al., 2000) regarding the specific mechanisms and the main predictors of the hippocampal map realignment process. Finally, we compare the model to an alternative, single-layer continuous attractor model, and discuss its relationship to other related models in terms of their ability to explain the temporal dynamics of place cell firing in these experiments.

THE MODEL

In our firing rate model, integration of self-motion occurs between grid cells and projections from grid cells to place cells provide the self-motion contribution to place cell firing. The sensory contribution to place cell firing comes through BVCs, and the projections from place cells to grid cells maintain the stability of grid cell firing relative to the environment. The animal's location is hypothesised to be determined on the basis of these interactions.

Place Cells With Boundary Vector Cell (BVC) Environmental Inputs

Place cells in area CA3 of the rat hippocampus receive inputs from the mEC, which contains grid cells, BVC-like border cells and itself receives inputs from the BVC-containing subiculum. CA3 in turn projects to CA1, another hippocampal area with a large place cell population. We assume that the place cells in CA1 represent direct feed-forward readout of CA3 place cells' activity, and thus could be omitted from our model without significantly affecting its overall dynamics.

A characteristic anatomical feature of the CA3 region of the hippocampus is the extensive recurrent connections between its pyramidal cells (Amaral and Witter, 1989). The presence of recurrent connections suggests that the network may be subject to stable attractor dynamics, which means that place cell activity patterns correspond to the stable equilibria states of a potential CA3 attractor network. A number of researchers to date have taken an attractor dynamics approach to modelling the behaviour of recurrent networks (Zhang, 1996; Samsonovich and McNaughton, 1997; Redish and Touretzky, 1998; Stringer et al., 2002; Conklin and Eliasmith, 2005), referred to as "continuous attractor" networks, since they can stably maintain patterns of firing of their neurons corresponding to any location in a continuous physical space, forming a whole Cartesian plane of stable fixed points (a "plane attractor").

In our model, we use a 2-D sheet of recurrently connected place cells, arranged so that each one's location in the sheet (covering the simulated full track environment) corresponds to its preferred firing location in the environment, so that the firing pattern over the neural ensemble forms an "activity bump." The connection strength between any two neurons is inversely related to the distance between their locations, which, together with a

global feedback inhibition, produces a plane attractor (see the **Appendix** for details).

Every place cell in the model is assumed to receive inputs from four orthogonally tuned BVCs, each of which has directional tuning perpendicular to one of the four surrounding boundaries. Our estimated BVC tuning curves (see "*BVC inputs to place cells*" in the **Appendix** for details) differ from the Gaussian tuning curves used by O'Keefe and Burgess (1996) to model inputs to individual place cells in that the standard deviation of a particular (otherwise Gaussian) curve is not constant, but instead is a linear function of the distance from the peak of the curve (see **Figure 1**). This makes our curves skewed, so that the side oriented toward the boundary of interest is steeper than the one oriented away. Such a shape seems to be physiologically plausible, since shorter distances are easier to estimate.

Grid Cells and Path Integration

Each grid cell fires in multiple locations, arranged as the nodes of an equilateral triangular grid spanning the whole environment (Hafting et al., 2005). The field sizes and spacing of the grid cells located more dorsally/ventrally in the mEC differ, increasing with depth from the post-rhinal border in a stepwise manner indicating the presence of discrete modules (Barry et al., 2007; Stensola et al., 2012). Neighbouring grid cells have the same field size, orientation and period of grids, but their grids are offset in phase. This indicates that conjunctions of active neurons are repeated periodically as the rat moves over a surface, so that the whole environment is covered by the nodes of a local cell module with a common grid spacing and orientation. This, together with the presence of recurrent connections in the mEC (Germroth et al., 1991; Lingenhöhl and Finch, 1991; Dhillon and Jones, 2000), suggests that modules of cyclically organised grid cells may perform path integration via a continuous attractor based mechanism (McNaughton et al., 2006; Guanella et al., 2007; Burak and Fiete, 2009; Couey et al., 2013).

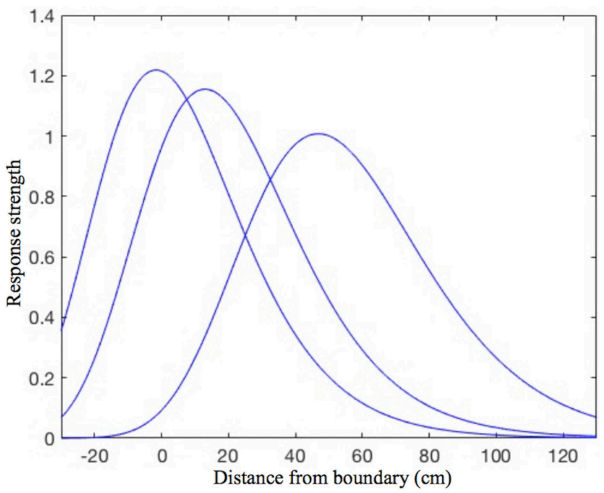

FIGURE 1 | The shape of the BVC tuning curves in our model. Note the slight asymmetry, as the curves standard deviation is not constant, but increases linearly with increasing distance of the rat from the boundary. The distance tuning is narrower for cells which have a peak response near to boundaries and gradually widens with the distance of peak response. This is consistent with the rat being able to judge shorter distances more accurately, which also implies that the BVCs tuned to shorter distances exert more influence on place cell firing (which is reflected in the curves height).

In order for a continuous attractor neural network in our model to perform path integration requires the presence of asymmetric synaptic pathways between grid cells with firing patterns offset in six directions (defined by the axes of the cells hexagonal firing pattern). These pathways need to transmit activity determined by the agent's movement direction and speed, as suggested for place cells (for which four directions were used, e.g., Zhang, 1996; Samsonovich and McNaughton, 1997; Conklin and Eliasmith, 2005). We assume the pathways are mediated by the conjunctive grid by head-direction cells that have been found in the mEC by Sargolini et al. (2006) [see Equations (A.9) and (A.10)], whose output we assume to also be modulated by running speed.

Grid cells from superficial mEC layers project to place cells (Witter and Amaral, 2004), which can provide the means of combining inputs from grid cell modules with different scales into a unified path integration–based estimate of position. In our model, a particular place cell receives connections from all the grid cells, with various grid spacing, that have firing fields overlapping with its place field in a particular environment. The connections strength is inversely related to the distance between the centres of the place and grid cell firing fields, similarly to the recurrent connections among the place or grid cells. The combined input from all the grid cells connected to a particular place cell will be maximal at the centre of the place field and will decay with increasing distance from it, since the inputs from cells with different grid scales will no longer converge. Combining the output of grid cells from multiple modules also allows a significantly larger representational capacity than a single network with the same overall number of cells would allow (Fiete et al., 2008).

Continuous attractor models of grid cell networks have been shown to be capable of accurate path integration over distance and time lengths comparable to those probed in behavioural assays (Burak and Fiete, 2009), and are preferable to single cell models due to their greater robustness to the presence of noise (Navratilova et al., 2011). Yet even noise-free, large networks have only finite integration accuracy (Burak and Fiete, 2009), and potential errors in their velocity input would also contribute to an increasingly incorrect position estimate over time. Thus, perceptual environmental information is required to maintain the grid cell-based representation of location in register with the environment. In the absence of such information, behavioural measures of path integration demonstrate rapid increase in error with movement (Etienne et al., 1996).

In order to anchor the grid cell firing patterns to the environment, place cells are presumed to project to grid cells, with the connections strength being inversely related to the distance between their preferred firing locations. This anchoring cannot be achieved so easily by providing sensory inputs, e.g., from the BVCs, directly to grid cells, since their responses are not constrained to one specific location in the environment. The

same place cell–grid cell connections also serve the purpose of registering together different modules of grid cells. This is needed in order to maintain a stable relationship between them, and cannot be achieved by connecting these modules directly since the firing of two grid cells from different modules might only overlap at a single location in an environment. CA1 place cells have been shown to project to neurons in layer 5b of the mEC (Sürmeli et al., 2015), which then relay the signal to grid cells in the superficial mEC layers. It may require a certain strength of the place cell signal to activate the layer 5b neurons, so that they could then relay the signal to the superficial mEC layers. Although we don't explicitly implement the layer 5b synaptic connections in the model, they are represented there by a threshold that needs to be exceeded by place cell activity in order for it to be transmitted to the superficial layer grid cells (see "*The place cell–grid cell model*" part in the **Appendix**).

The Place Cell–Grid Cell Model

In order to model the behavior of the navigation system based on the reciprocal interactions between place cells and grid cells, we assume (for simplicity) that inputs to the layer of place cells are provided by three modules of grid and grid by head-direction cells, each with different grid scaling. Each module includes 441 grid cells which grid-like firing patterns have the same spatial scale but an offset phase relative to each other, in accordance with experimental findings. All grid cells within a module are recurrently connected in a manner that could result via Hebbian learning from the hexagonal topology of multiple firing fields of individual cells. The grid scale of each successive module is a factor 0.72 smaller (or 1.39 larger) than the next, which is similar to the ratio found by Stensola et al. (2012). The standard deviations of the individual firing fields scale accordingly, consistent with physiological data, as follows: 5, 7, and 9.65 cm. The standard deviation of the place cell firing fields is 7 cm. The strength of synaptic connections from both the grid cells to place cells, and the place cells to grid cells, is defined by a Gaussian function of the distance between the grid and place cell preferred locations, with the variance of the Gaussian given by the average of the variances of the place and grid cell firing fields. The outlined system is represented by the set of Equations (A.11) in the **Appendix**.

MATERIALS AND METHODS

Neural Population Dynamics, Gothard et al. (1996b) and Redish et al. (2000)

Gothard et al. (1996b) recorded populations of hippocampal neurons in rats shuttling on a linear track between a movable reward site, mounted in a sliding start box, at one end and a fixed reward site at the opposite end. The rats were pretrained on the full-length track with a constant box position. On each subsequent trial, the box was randomly moved to one of five equally spaced locations, thereby creating mismatches with the originally learned relationships of the box to other cues in the environment (**Figure 2**). The movement of the box took place while the rat ran "outbound" toward the fixed reward site, with the rat then returning "inbound" to the box in its new position. Along a journey, the same cells were active, in the same order, regardless of the box location, although parts of the place fields sequence present on the full track were sometimes skipped.

The rat's internal spatial representation, defined by place cell population activity, was quantified in terms of population vectors. Then the similarity of the population activity on the full-length journey to the population activity on each of the four types of shortened journeys was tested by correlating point by point the population vectors computed for each spatial location. The results of these correlation procedures for a single rat are represented graphically in **Figure 3**, adapted from Gothard et al. (1996b).

The principal finding was that when a mismatch existed between the rat's internal spatial representation and the rat's coordinates in the external reference frame centered on the reward site the rat was running to, a dynamic correction process took place. The correction always took place after some initial delay, which was longer for the longer outbound journeys and shorter for the shorter ones. On longer tracks with moderate mismatches the activity realignment usually occurred already past the midpoint, in the second half of the journey. On some outbound journeys the internal representation remained more aligned with the distance from the box for about 1 meter, even though the start box was right behind the rat, outside its field of view. For moderate mismatches, the internal representation, after some initial delay, was shifted continuously through intervening states, faster than the actual speed of rat, until it was closely aligned with the landmarks corresponding to the end of the track the rat was approaching. The shorter the track, the more rapid the correcting shifting of the activity. In case of large mismatches, however, the internal representation jumped abruptly to the new position, skipping the intervening states, which occurred in the first half of journey, before the midpoint between the front of the start box and the end boundary.

Based on the results of this work and also of their earlier study (Gothard et al., 1996a), in which rats shuttled between a box and a pair of landmarks placed variably in a large arena, Gothard et al. proposed that the firing of place cells is controlled by a competitive interaction between path integration and external sensory inputs, primarily vision.

In Gothard et al.'s (1996b) experiment, there is a considerable difference between the outbound and inbound journeys. In case of the outbound journey, a change in the box location results in a change of the rat's starting position relative to the entire room. In case of the inbound journey, on the contrary, the rat's position in the room frame does not change, only one of the track boundaries changes its location. And this difference between the two journey types manifests in Gothard et al.'s data, with the population activity realignment on the inbound journeys occurring much later than on the outbound, just before the rat enters the box.

According to the difference in the realignment dynamics of the population activity on the outbound vs. inbound journeys, the room features have a strong influence on the place cell activity. This could be primarily due to the room walls, since the track was placed across the corner of the room. Thus, on the inbound journey, for a large part of the journey (e.g., till the vicinity of the box) the sensory inputs from ahead of the rat may

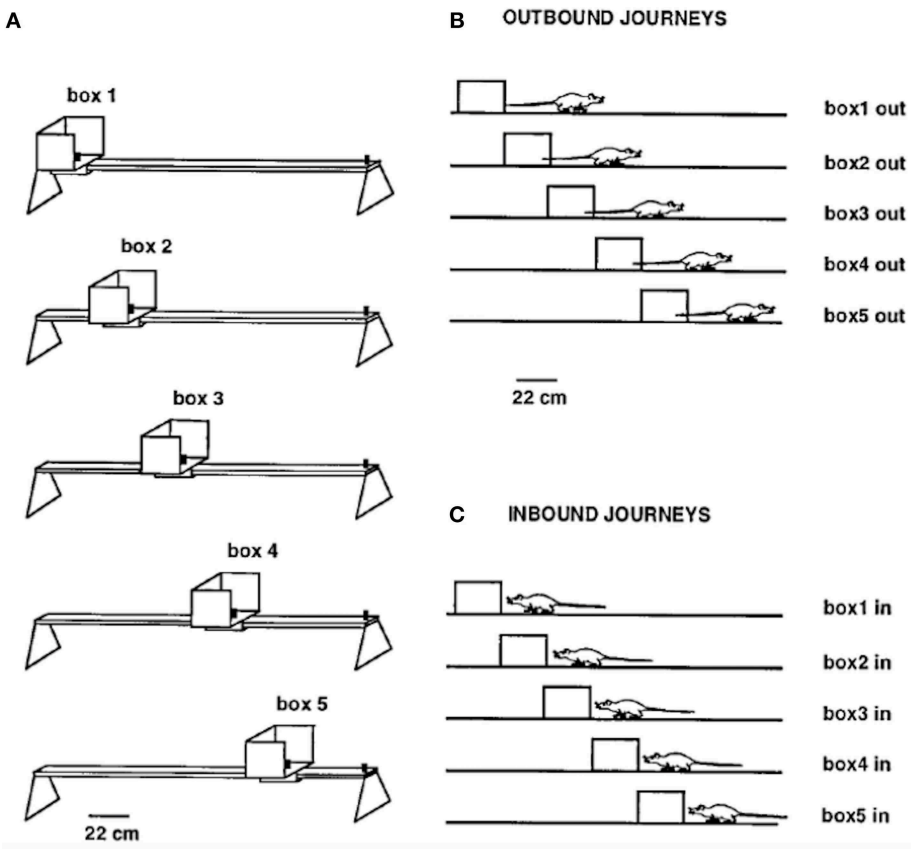

FIGURE 2 | (A) Linear track (161 cm long outside the movable box) with the five equally spaced box locations used as the start or end point of each journey. **(B)** Shows the five types of outbound journeys, labeled box1 out, box2 out, etc. **(C)** Shows the five types of inbound journeys. Adapted from Gothard et al. (1996b).

be coming predominantly from the room wall, rather than the mismatched box that is much smaller, which may explain the observed dynamics (i.e., the realignment to the reference frame of the box occurring just before it on all the track lengths). Because of this ambiguity, we focus on the outbound journeys, in which path integration from the start box mis-matches with constant environmental sensory inputs from all around the rat, excepting only the small start box directly behind it. Any sensory input from the box is likely cancelled out by the conflicting sensory input from the wall behind the rat in the overall sensory input from behind the rat. Therefore, in our outbound runs simulations we assume that there is no sensory influence on the rat from the movable box.

In a subsequent study, Redish et al. (2000) randomly varied the shortened track lengths (by varying a movable box position) between 150 and 90 cm (as measured from the front of the box to the end barrier) across different trials, thus sampling different track lengths from within the range during a 30 min experiment. The full track length was similar to that used by Gothard et al., and each trial also consisted of outbound (toward the end barrier) and inbound (back to the box) journeys.

The study replicated and extended that of Gothard et al. (1996b) through studying the realignment dynamics by measuring properties of the place cell ensemble activity and observing the realignment at frequent intervals throughout individual journeys. The major conclusion of the study was that the realignment of the ensemble activity takes place after a temporal delay, suggesting that there is a stochastic switch happening somewhere in the system. We provide more details of the study in the "*Detailed analysis of Redish et al.'s (2000) data*" part of "*Results*," where we analyse Redish et al.'s data using our simulation results.

Simulation Methods

We simulate the situation of competitive interaction between path integration and external sensory inputs, corresponding to outbound runs in Gothard et al. (1996b) and Redish et al. (2000), using the place cell–grid cell model, represented by Equations (A.11). We vary the maximum strength of synaptic connections from grid cells to place cells, given by G in the model, in the range between 1 and 3, in order to investigate its influence on the model. The strength of synaptic connections from place cells to grid cells (P) we keep constant and equal to 10, to make the place cell input strength comparable to the strength of the combined input of the three grid cell modules, since the synaptic transmission threshold is higher for place cells (see the **Appendix**).

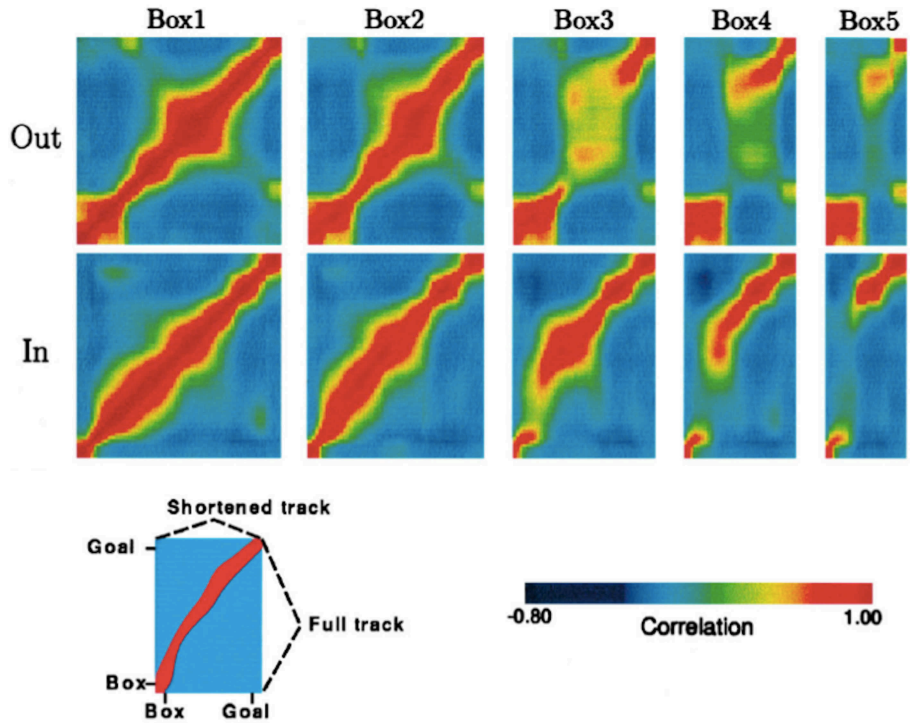

FIGURE 3 | Population vector correlations between the pattern of firing on the full track and on the shortened tracks for one rat, whose pattern is representative of all other rats except one. Correlation plots are shown for the outbound (top row) and inbound (bottom row) journeys. For each plot, the vertical axis represents the full track (including the box), whereas the horizontal axis represents the length of the track (including the box) covered by the rat during one of the five trial types, i.e., box1, box2, etc. (see Key at the bottom). Highly correlated firing patterns between two locations, one on the full track and another on one of the shortened tracks, are shown in red. In both rows, the first plot is a spatial autocorrelation of the population vectors on the full track, with values of 1.0 along the diagonal. For the journey types 4 and 5, when the track was greatly shortened, the discontinuity of the ridges can be seen, which is due to the "jumping" of the activity packet over the intermediate stages.

As explained in the "*Neural Population Dynamics*" part, we assign a weighting factor of zero to the inputs from the BVCs tuned to the start box on outbound runs. Therefore, the total external input h_i to the place cell *i,* given by (A.8) in our model (A.11), is comprised of an input from the BVC tuned to the boundaries ahead of the rat and inputs from two BVCs tuned to the boundaries in the lateral directions. The sum of the three BVC inputs is thresholded using a fixed threshold T that we set equal to the sum of the two laterally tuned BVCs inputs, which remain constant along the track since the rat runs parallel to the track side borders. Each individual BVC i input b_i is given by (A.7), with the following parameters: $A_0 = 4.5$, $\sigma_0 = 21.5$, $\alpha = 0.109$, $\beta = 0.016$, $\gamma = 0.101$.

During simulations the starting position of the rat was changed in such a way as to represent the ranges of track lengths in both Gothard et al.'s (1996b) and Redish et al.'s (2000) experiments. Similar to those experiments, the full (familiar to the rat) track length was 160 cm (outside the moveable starting box), and its four equally spaced shortened versions were 140, 120, 100, and 80 cm in length. The direction of the rat's movement was $\theta = 0$ (i.e., from the box front along the track to its end) and the speed $V = 15$ cm/s across all trials.

For comparison, using the same settings, we also simulate a "place cell only" model in which there are no grid cells and only a single continuous attractor network. As for the place cell–grid cell model simulation, we use a similar 2-D sheet of recurrently connected place cells (a plane attractor) that covers the full length of the familiar 160 cm track. Path integration is performed via asymmetric connections between the place cells, which strength is modulated by the rat's direction and velocity signals. At the same time sensory inputs to the place cells are provided by BVCs, in the same way as in the main model (A.11). Further details of the place cell only model (A.12) implementation are given in the **Appendix**.

RESULTS

Realignment Dynamics Favour the Place Cell–Grid Cell Model

The behaviour of the place cell–grid cell model (A.11), with $G = 2.1$ (i.e., the grid cell–place cell connection strength that we varied between 1 and 3), provides a good qualitative fit to the behaviour of place cells on outbound journeys in Gothard et al.'s (1996b) study, across all simulated track lengths.

During moderate self-motion and sensory information mismatches (as on the longer two of the shortened tracks), after a pronounced initial delay, the place cell activity bump was continuously shifted through intervening positions until its

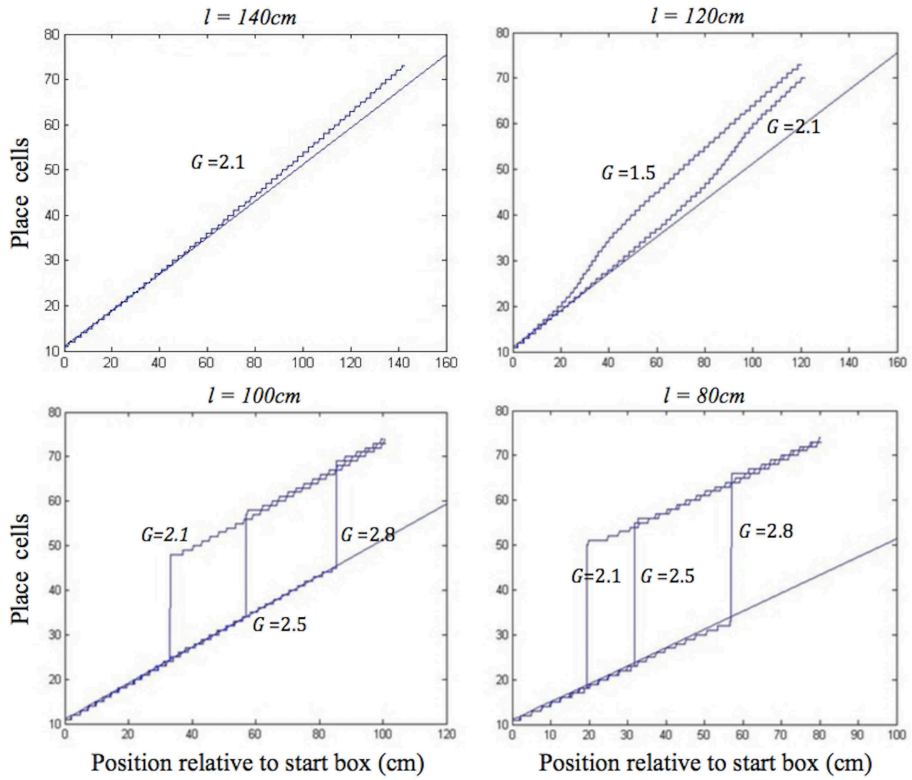

FIGURE 4 | Realignment of the simulated place cell representation of location as track length varies in the place cell-grid cell model. Plots show position on the track on the *x* axis and the relevant place cells ordered by their location of peak firing on the full length track (160 cm) on the *y* axis. The place cells in rows 11–75 have firing peaks evenly distributed along the full length track from the front of the box. The straight blue line in each plot shows where these place cells (labelled by their row number) have their peak firing location on the full track. Each blue graph represents a particular simulation and shows where each cell has its peak firing location in that simulation. The plots show how the behaviour of the model changes when the track length (*l*), and the strength of grid cell—place cell connections (*G*), are varied.

location was in agreement with the sensory inputs provided by the BVCs tuned to the approaching end of the track. The speed of transition depended on the mismatch size, with a larger mismatch resulting in a more rapid transition, following an initial delay (**Figure 4**, top). When the mismatch was large (as on the two shortest tracks), the activity bump dissolved in its initial location and instead emerged in a "correct" one, in line with Gothard et al.'s findings (**Figure 4**, bottom). Such jump realignments occurred quicker, in the first half of the journey (from the front of the box to the track end), whereas the continuous shift realignments occurred much farther from the start, in the second half. The shorter the track, and thus the nearer the start box to its end, the sooner the realignment occurred across all the track lengths.

In the place cell only model (A.12), in contrast, on the two longest of the shortened tracks the shift realignment begins practically straight from the start, even though BVC inputs there are quite weak, and completes in the first half of the journey (**Figure 5**, top). This is in clear contradiction with Gothard et al.'s (1996b) experiment, where on the tracks of similar lengths the realignment only began with the rat approaching the midpoint and completed with it already far into the second half of the journey. On the two shortest tracks the activity bump realigns via jumping also much earlier than jump realignments occurred in Gothard et al.'s (1996b) experiment (**Figure 5**, bottom).

We first consider the mechanism behind the dynamics of the place cell only model, and then how the dynamics of the place cell–grid cell model differ from this simpler model. In the place cell only model, the symmetrical connections between place cells (PCs) act to maintain a single activity bump on the PC sheet, whereas asymmetric connectivity, mediated by place by direction cells (Equation A.12), acts to shift the bump, performing path integration (Zhang, 1996; Samsonovich and McNaughton, 1997).

For moderate mismatches (i.e., on the two least shortened tracks) the BVC input to the PC sheet overlaps the activity bump sufficiently to make it shift (with more activity to the leading edge of bump than falling edge), and there are no grid cell projections to stop the bump shifting to align with the BVC input immediately (**Figure 5**, top). In addition, shifts of the PC bump immediately affect the PI input to PCs (as it comes from asymmetric connectivity from the bump itself). For big mismatches (i.e., on the two shortest tracks) the BVC input does not overlap the PC bump, and can cause the bump to jump from the original location to the new location, once the BVC input overcomes the self-support of the initial bump (via the

symmetrical and asymmetrical recurrent connections). As the new bump grows it gets the same recurrent support as the original bump, proportional to its size.

For the place cell–grid cell model, the PC activity bump is supported by symmetrical recurrent connections, and receives inputs from BVCs, but, unlike the place cell only model, the path integrative input to place cells comes from the grid cell (GC) layers, rather than asymmetric connectivity between PCs. In this case, mismatches between BVC inputs and the PC bump have to affect place cell firing before this change can spread to the GC sheets and change their firing before finally affecting the path integrative input to the PC sheet.

For moderate mismatches (i.e., on the two least shortened tracks) when the BVC input overlaps the PC bump sufficiently to make it shift, the PC bump is still receiving a location-specific PI input from the GC layers, preventing any shift faster than that indicated by the rat's speed. It takes some time for the BVC input to push some of the receiving place cells firing rates above the threshold necessary for synaptic transmission to the GC layers, which initially produces elongation of the PC bump. When the place cells exceed the firing threshold, they start providing inputs to the GC layers, producing shifting of the GC bumps. Feedback from the additionally shifting GC bumps finally allows the PC bump to start to shift faster than the rat's speed to eventually realign with the frame of reference of the approaching end of the track.

The larger the mismatch between the path integration and BVC inputs (i.e., on the second least shortened track vs. the least shortened one), the more elongated between the two misaligned inputs the PC activity bump initially becomes, before inducing the realignment of GC bumps by which it is being held back. Therefore, the larger the mismatch, the larger the shifting input to grid cells from place cells, the faster the subsequent activity transition (**Figure 4**, top). During the realignment process, the delay in the feed from the PC to GC layers, the inertia of the GC bumps, and the delay in feedback from the GC to PC layers, all contribute to the pronounced delay before the place cell bump starts shifting, as well as acting as a drag on the speed of its subsequent progress. This produces the shift realignment dynamics as in Gothard et al. (1996b).

For big mismatches (i.e., on the two shortest tracks) the BVC input does not overlap the PC bump and can cause it to jump from its original location to the new one, if the BVC input is sufficiently strong to overcome the self-support of the initial bump and the input from the grid cell modules that holds it in its original location. The BVC input strength, in addition to determining the possibility of realignment, also determines

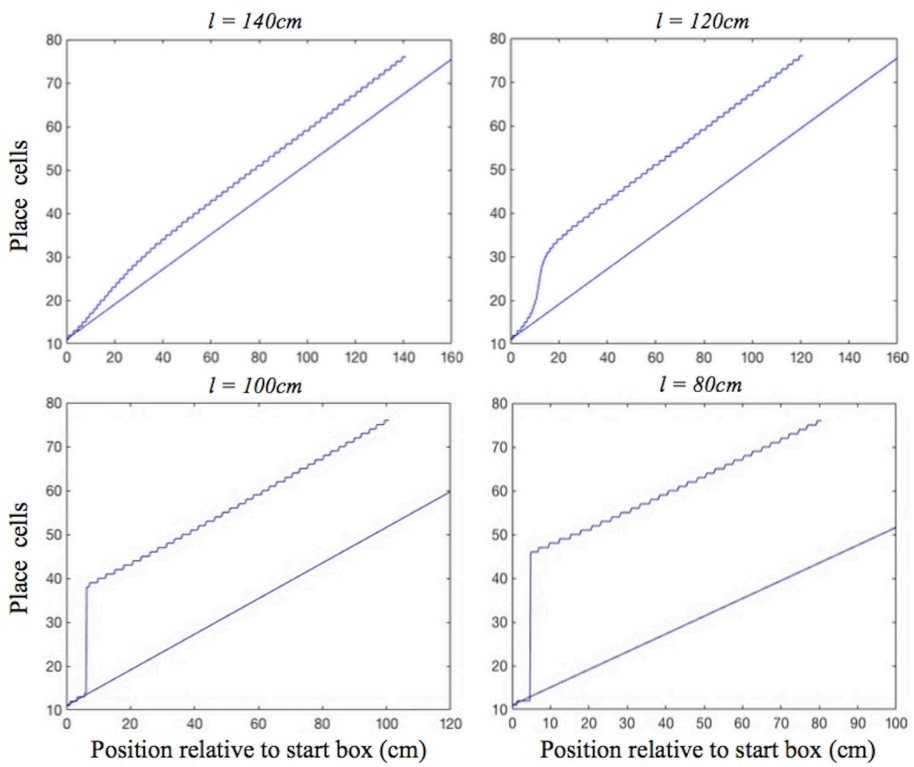

FIGURE 5 | Realignment of the simulated place cell representation of location as track length varies in the place cell only model. Plots show position on the track on the *x* axis and the relevant place cells ordered by their location of peak firing on the full length track (160 cm) on the *y* axis. The place cells in rows 11–75 have firing peaks evenly distributed along the full length track from the front of the box. The straight blue line in each plot shows where these place cells (labelled by their row number) have their peak firing location on the full track. Each blue graph represents a particular track length (*l*) simulation and shows where each cell has its peak firing location in that simulation.

its rapidity, with stronger inputs producing faster place cell activity buildup. Thus, with all values of G (2.1, 2.5, 2.8), the bump jumps sooner on the 80 cm track than on the 100 cm track (**Figure 4**, bottom), since the shorter distance to the end boundary results in stronger BVC inputs. The delay before jump realignments in the place cell–grid cell model (with $G = 2.1$) is much longer than in the place cell only model (as in Gothard et al., 1996b), since, due to the grid cell inputs, greater BVC input buildup is needed for the PC bump to jump. When the bump jumps, it causes the GC bumps to follow, with a slight delay after the place cells realignment. The delay is required for the activities of the grid cells driven by inputs from the realigned PC bump to become strong enough to overcome the initial GC bumps.

In both shift and jump realignments, the dynamics are influenced by the strength of grid cell–place cell connections (G). Larger values of G increase the influence of grid cell activity on the PC bump, therefore requiring greater BVC input buildup to start the place cell activity transition, leading to a longer initial delay (see **Figure 4**). The strength of place cell–grid cell connections (P) also affects the dynamics of the PC and GC bumps. The value of P was set sufficiently high so that changes to the place cell activity affect the GC bumps without significant delay. In shift realignments, this avoids slowing of the rate of shifting of the GC and PC bumps which occurs for low values of P. In jump realignments, reducing P increases the delay required for the GC bumps to jump, but this delay is relatively short, since, in contrast to the PC bump, only the self-support of the original GC bumps resists their realignment (as for the PC bump in the PC only model jump realignments).

The delays before both shift and jump realignments are significantly longer in the place cell–grid cell model than in the place cell only model. Although the rate of realignment in the place cell only model could be altered by varying parameters, such as the relative strength of BVC inputs vs. recurrent connectivity, this model cannot show the initial delay before the activity bump starts shifting, as seen in the continuous realignment data. The realignment behavior of the place cell only model is similar to that of the place cell–grid cell model with $G = 0$. In addition, the place cell–grid cell model jumps occurred much earlier on the track than shift realignments (in the middle of the first half of the track vs. the second half, see **Figure 4** for $G = 2.1$), as seen in the data (Gothard et al., 1996b; Figures 7, 8). This is because in jump realignments the model place cells initially realign alone, via their activity bump jumping, with grid cell bumps jumping after. In shift realignments, on the contrary, place cells have to continuously pull along resisting grid cell inputs, which slows the realignment. In the place cell only model, both types of realignment occurred on the first half of the track, soon after the start, as the place cells always realign alone. The inability of the place cell only model to show the observed large difference between jump and shift realignment locations provides further support for a parallel place cell–grid cell architecture.

Detailed Analysis of Redish et al.'s (2000) Data

Redish et al. (2000) investigated which of the following four hypotheses provides the best explanation for the dynamics of hippocampal activity realignment:

(1) Rats rely on path integration for a certain distance from their starting location, predicting that realignment locations should be distributed as a Gaussian in the box-aligned coordinate frame; (2) Rats use path integration until the room-cues, like the barrier at the end of the track, are perceived, predicting that realignment locations should be distributed as a Gaussian in the room-aligned coordinate frame; (3) Specific landmarks have influence over their own local space, predicting that realignments should occur around the halfway point of the journey. (4) Place cells are part of a dynamic system in a semi-stable state that needs to overcome an energy barrier in order to transit into another semi-stable state, predicting that realignment should at least partially depend on the time passed since the mismatch between the sensory and self-motion information occurred.

For 20 time windows throughout the journey, the first window where place cell activity became more coherent with the room-aligned than box-aligned coordinate frame was determined. This was considered to be the transition point at which the realignment occurred. The consistency of the distribution of the transitions was measured with respect to: (1) the box-aligned coordinate frame; (2) the room-aligned coordinate frame; (3) the midpoint between the box and the end barrier; (4) the time since the rat started the journey. The mutual information between each of the four domains and the transition occurrence was measured, to see which of the four would be a more consistent predictor of the realignment occurrence.

The time passed since leaving the box was found to be a more consistent predictor than any of the three spatial parameters examined, indicating that the shift between coordinate frames is at least partially controlled by a time-dependent process. Redish et al. explained the temporal delay before realignment as a stochastic switch happening somewhere in the system, the stochasticity reflecting noise in the neural network. They concluded that the time preceding the transition reflected the accumulation of sufficient energy for the switch to occur, i.e., for an energy barrier to be surpassed. It was noted that some combination of the four hypotheses could possibly predict the data more completely. The nature of the switch and the specific mechanism and time course of the activity transition itself were left for future research. Below, we address these questions by interpreting the Redish et al. data in terms of the jump and shift mechanisms in our simulations.

Figure 6 shows the distribution of realignment points over all outbound journeys (on different track lengths within the 90–150 cm range) of a single animal in the Redish et al. study. Different histograms show distributions of the same realignment points as functions of the four different hypothesised variables. The points of realignment occurrence on the four shortened track lengths from our simulations (with $G = 2.1$) are also shown for comparison in all four different coordinate frames.

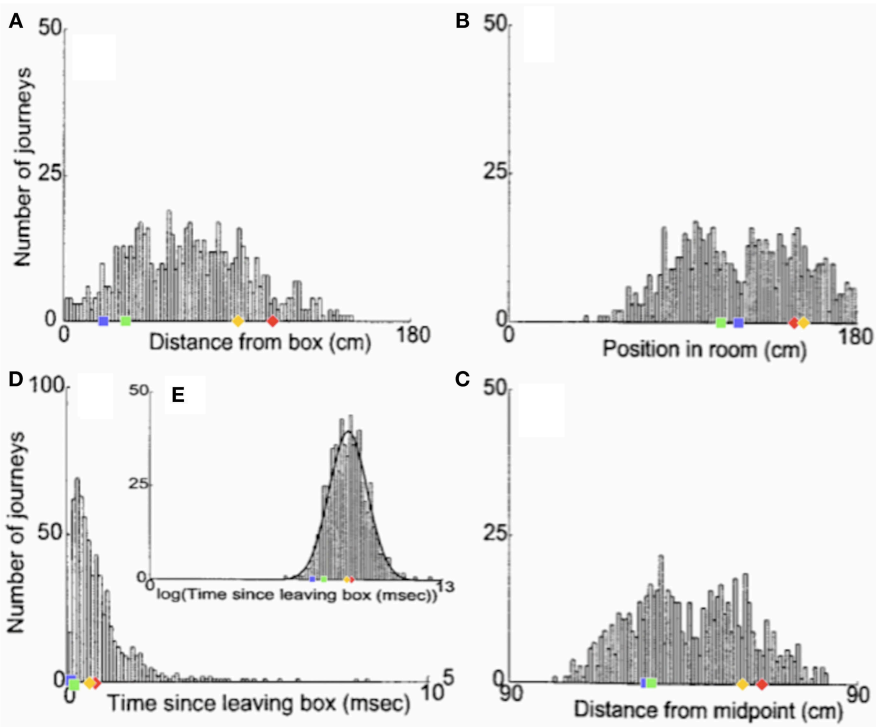

FIGURE 6 | The distribution of realignment points across all outbound journeys from a single rat. **(A)** Distribution of realignments as a function of distance from the box. **(B)** Distribution of realignments as a function of position within the room. **(C)** Distribution of realignments as a function of midpoint between the box and the barrier. **(D,E)** Distribution of realignments as a function of time since the rat started its journey: **(D)** Time plotted on linear scale. **(E)** Time plotted on logarithmic scale. A Gaussian function had been fit to the distribution of realignment times with time plotted on a log axis (**E**, solid line). Adapted from Redish et al. (2000). Overlayed over the histograms are shown the activity realignment points from our simulations on different track lengths: 140 cm in Red; 120 cm in Yellow; 100 cm in Green; 80 cm in Blue. Diamonds indicate continuous (shift) realignments, whereas discontinuous (jump) realignments are represented by squares.

Histogram **6A**, with a coordinate system aligned to the movable box, appears to consist of two main overlapping groups of journeys, a narrower group closer to the box (comprising around 40% of journeys), and a much broader group farther from the box. The first group likely comprises jump realignments, since the group spans the range of distances from the box where jumps occur in Gothard et al.'s study and in our simulations. These journeys likely occurred mostly on tracks in the 90–110 cm range, since these lengths give the large mismatches that cause jump realignments according to Gothard et al.'s data and our simulations (with $G = 2.1$, blue and green dots in **Figure 6A**). In our simulations, jump realignments occur at ∼20 cm from the box on the 80 cm track, and at 32 cm on the 100 cm track. Thus, the observed realignment points forming the peak between 25 and 40 cm (from the box) are consistent with jump realignments in the model, given the differences between the path lengths used and simulated. Earlier realignments (<25 cm) likely occurred on the journeys where the rat initially moved very slowly. The second group in **Figure 6A** consists of journeys where realignment occurred farther away from the box, and thus likely via a shift. The wider realignment points spread in this group is due to a wider range of track lengths with shift realignments (∼110–150 cm), resulting in a wider range of BVC input strengths experienced across different journeys, and to a range of mismatch distances to be covered by shifting activity on different journeys.

In the time histogram **6D**, the mode and adjacent slices likely represent jump realignments, which have shorter delays, and the wider-spread shift realignment points compose the right slope and the tail of histogram **6D**. The histogram peaks at shorter delay times because of lower delay time variability in jump than in shift realignments. Slightly greater variability of the distance passed (in **6A**) than the delay times (in **6D**) before the jump realignment occurrences could be explained by varying speed and trajectory of the rat. Also, at the beginning of longer tracks the strength of BVC input may be insufficient to enable realignment, which, if the rat on these tracks sometimes progressed very slowly in the beginning, could account for the long tail of **6D**.

Histogram **6B**, with a coordinate system aligned to the end barrier and the room, also shows two distinct groups. The left group should primarily be due to jump realignment cases, since shift realignments mostly occur past the midpoint (which is 75 cm from the end for the longest track), according to Gothard et al.'s data and our simulations. The second group, on the contrary, starts around the point where typical jump realignments are expected to stop (see **6B**, green and blue dots) and covers the distance range where shift realignments should typically occur (see red and yellow dots in **6B**), thus likely

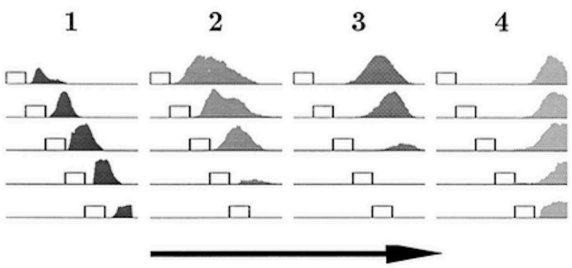

FIGURE 7 | Firing profiles of four outbound-selective cells (1, 2, 3, 4) shown for all five lengths of outbound journey (running direction is indicated by the arrow). The horizontal lines represent the track, and the small rectangles represent the box. The last 27 cm segment of the track, containing the fixed reward cup, is omitted. Cell 1 fired immediately after the rat exited the box, cell 2 fired farther away from the box, cell 3 fired approximately halfway between the box and the end of the track and cell 4 fired close to the end of the track. Adapted from Gothard et al. (1996b).

representing these. The realignment location variability in both groups is caused, apart from various noise, by the variation in track length across the journeys (e.g., BVC input buildup starts farther from the end on longer tracks).

Consistently with histograms **6A** and **6B**, histogram **6C** is also composed of two salient groups. The sharp right edge of the left group is next to the tracks midpoint, so the group likely consists mostly of jump realignments. Some shift realignments may also contribute to it (e.g., due to rat speed variability), but the bulk of these should compose the right group located after the midpoint. The data shown visibly matches our results (see **6C**), as well as Gothard et al.'s data. The presence of both jump and shift realignments is one of the main factors responsible for the wide spread and seeming inconsistency of realignment locations in all three spatial histograms.

Thus the delay in place cell activity realignment, attributed to a stochastic switch by Redish et al. (2000), may result from a parallel place cell–grid cell architecture, as discussed above. Specifically, the variation in the delay across the 90–150 cm range of shortened tracks in Redish et al. (2000) is consistent with the delay variation across a similar 80–140 cm range of track lengths in our place cell–grid cell model simulations. On the contrary, a single recurrent network of place cells appears to be insufficient to produce similar delay variation across the range of track lengths, in particular the large difference in delays before jump and shift realignments.

Redish et al. (2000) suggested that the variability of the delay prior to realignment reflects noise in the system, using a log-normal distribution to fit the delays across all track lengths (see **Figure 6E**), although they noted that a hybrid hypothesis may predict the data more fully. Instead, the variation in delay may reflect variations in track lengths and mismatch magnitudes across trials, which are the main predictors of realignment dynamics in our simulations. The further the rat from the end barrier, the weaker the BVC inputs from it, and thus the rate of place cell activity buildup, which leads to longer delays on longer tracks (**Figures 6A,D**). Also, at the beginning of longer tracks the strength of BVC inputs may be insufficient to override the competing grid cell input to place cells. Additionally, the realignment happens much faster in jump realignments, caused by large mismatches on much shortened tracks, than in continuous (shift) realignments caused by smaller mismatches on moderately shortened tracks (**Figures 6A,D**).

Individual Neural Responses During Realignment: Place Cells

The place cell–grid cell model (A.11) can also account for the changes in firing fields of individual place cells on different outbound journeys, as seen in Gothard et al.'s (1996b) study. In the experiment, outbound-selective place cells 2 and 3 showed reduction in size of their firing fields as the track was progressively shortened, and did not fire on the shortest track (**Figure 7**). The place cells that were active near the box and the track end did not show such changes in firing fields and maintained their position relative to the nearest end of the track across the different track lengths.

Figure 8 shows the plots of simulated place cell firing fields on the different track lengths, which qualitatively resemble those of Gothard et al. (1996b). The firing fields centred toward the start and end of the track (**Figure 8A**, cells 1 and 4) maintain their location relative to the nearest end of the track across the different track lengths. On the shortest track, the firing field near the start of the track (**Figure 8A**, cell 1) overlaps the location of discontinuous realignment of population activity (see **Figure 4**)—resulting in curtailment of the right hand side of the firing field. The firing field of Gothard et al.'s cell 1 is also reduced on the shortest track compared to longer tracks.

The firing field centred at ∼1/3 of the full length track (**Figure 8A**, cell 2) shows large changes as the track shrinks. The field of cell 2 narrows on the third shortest track (120 cm) and the cell does not fire on the two shortest tracks, since the activity bump jumps over it when realigning there. Gothard et al.'s cells 2 and 3 show a similar behaviour.

The field centred at ∼2/3 of the full length track (**Figure 8B**, cell 3) largely decreases on the 120 cm track, this corresponds to the location of the rapid continuous realignment of population activity (see **Figure 4**). Our cell 3 firing then recovers on the 100 cm track, since the cell fires closer to the end than is the jump realignment location on the track. The cell 3 firing is partially affected by the jump realignment on the shortest track (80 cm)—its firing field on the track has a sharp cut off at the left side. The cell 3 behaviour through the progressive track shortening provides a prediction for the pattern of behaviour of the cells that in the Gothard et al.-like experimental conditions on the full length track fire around the firing location of our cell 3 (between Gothard et al.'s cells 3 and 4).

Individual Neural Responses During Realignment: Grid Cells

What happens to grid cells during the place cell realignment? This experiment (recording grid cells in the situation of Gothard et al., 1996b) has not yet been performed, to our

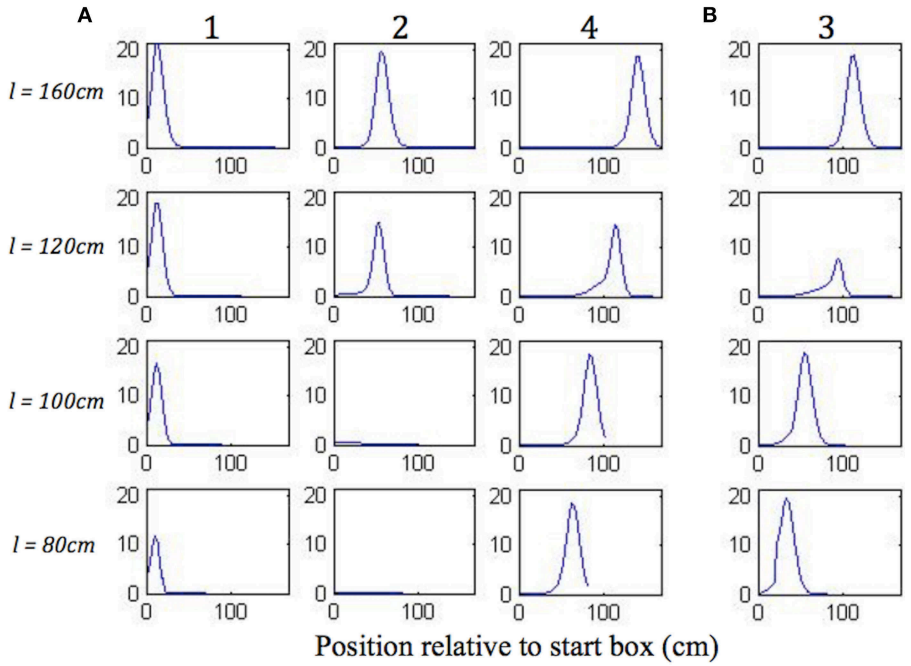

FIGURE 8 | (A,B) Firing profiles of four illustrative simulated place cells (1, 2, 3, 4) shown for four out of five lengths of outbound journey (the full 160 cm track, 120, 100, 80 cm). The distance from the box is shown on the *x* axis in all the plots. Cell 1 fired right after the journey start, cell 4 fired close to the end of the track, and the firing locations of cells 2 and 3 are approximately equally spaced between them on the full length track.

knowledge. However, the model presented here makes a clear prediction: because we assume that place cell firing is used to reset the otherwise path-integration driven firing of grid cells. Thus, there should be a smooth compression of the grid in the region of the smooth realignment of place cell firing on the slightly shortened tracks, and a significant disruption or discontinuity in firing of grid cells around the location of the abrupt jump realignment of place cell firing on the shortest tracks.

Figure 9 shows single run simulations of three grid cells, one from each module with a different grid scale in the model, on the full length track and four shortened track lengths. Since in the simulations the rat's head direction $\theta = 0$ in (A.9), this makes the corresponding axis of the grid cells' hexagonal firing patterns (in 2D environments) aligned with the track. On the 140 cm track, a gradual realignment takes place on the second half of the track, with the realignment close to completion by the end of the track. The distance between two neighbouring peaks gets shorter and individual fields get narrower. On the 120 cm track, a rapid shift realignment takes place in the second half. During the rapid realignment, when there is a strong decrease in place cell firing rates, there is a simultaneous increase in corresponding grid cell firing rates. This indicates an increasing input from place cells (due to elongation of the PC activity bump), which results in a more rapid shift of the grid cell activity bumps. On the two shortest tracks, the grid cell activities jump to a new location soon after the place cell activity jump. As can be seen from the figure, the jumping in all three modules of grid cells happens at the same location, i.e., around the time of the place cell activity jump.

Yoon et al. (2016) earlier showed that grid cell responses on 1D tracks are linear slices through 2D hexagonal firing patterns and provided evidence of a common computation in both 1D and 2D environments. Thus, our results provide a clear experimental prediction of the model, although the problems of averaging experimental data trial-by-trial, when the location of place cell realignment may vary from trial to trial will need to be borne in mind.

DISCUSSION

We have presented a detailed description of the mechanisms hypothesised to underline the integration of self-motion and sensory information into a representation of an estimated position. Our navigational model consists of two coupled complementary subsystems working in competition, with the grid cell subsystem specialising in continuous attractor-based path integration and the place cell subsystem in sensory-driven navigation (via Boundary Vector Cells). The model reproduces well the place cell firing rate data from the experiments with conflicting sensory and self-motion inputs, which supports the plausibility of the hypothesised architecture.

Our simulations of the place cell–grid cell model provide explanations for the experimental results of Gothard et al. (1996b) and Redish et al. (2000), and grid cell firing predictions that can be tested in future studies.

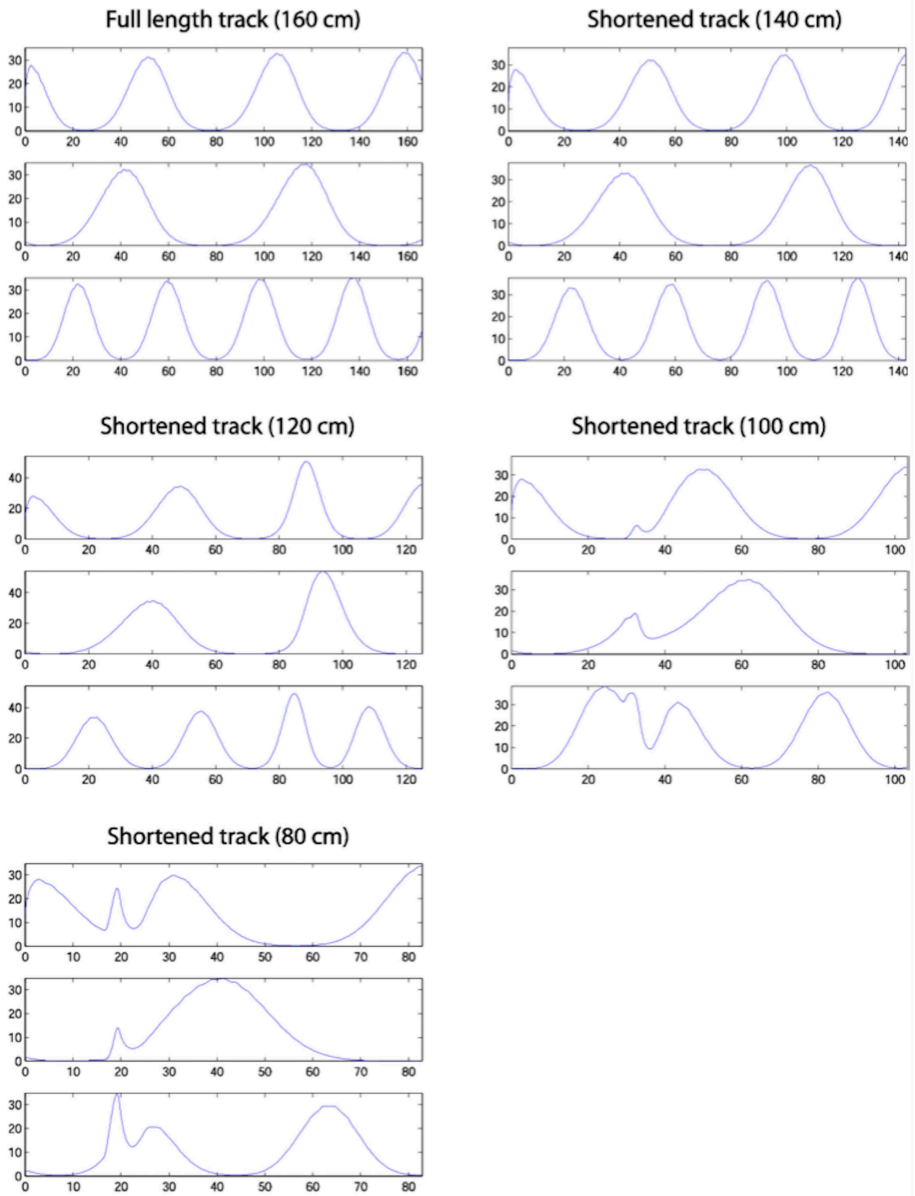

FIGURE 9 | Firing profiles of three simulated grid cells from the three modules with different scales (the ratio between successive grid scales is 0.72). Each plot represents a simulation on the track length shown above the plot, with the same cells shown in the same rows in each plot. Smooth compression of grid cells' fields is seen on the 140 cm track. The same effect is seen on the 120 cm track, but also with considerable changes in peak firing rate. The two shortest tracks, on which the place cell representation shows discontinuous realignment (see **Figure 4**), show clear discontinuities in grid cell firing around the location of place cell realignment—indicating a clear effect on the grid cells of the place cell realignment.

The Place Cell–Grid Cell System Plausibility and Potential Advantages

The hypothesised model architecture is supported by comparison to the simulations of our place cell only model, which is unable to reproduce Gothard et al. (1996b) and Redish et al. (2000) realignment dynamics.

Sheynikhovich et al. (2009) also simulated Gothard et al.'s (1996b) experiment with conflicting sensory and motion inputs, using their model that, like the place cell only model, does not contain competing semi-autonomous place cell and grid cell subsystems. Instead, modules of recurrently connected grid cells perform path integration as well as receive sensory (visual) inputs directly (like place cells in the place cell only model), and place cells are simply used for read-out. The model shows some of the observed realignment effects (e.g., abrupt activity jumping), but does not fully replicate the Gothard et al. (1996b) and Redish et al. (2000) realignment dynamics. For example, in Sheynikhovich et al.'s model continuous realignments occur before the midpoint

even on the longest of shortened tracks. We think that single-layer attractor models cannot show the correct dynamics, as in our place cell only model.

Byrne et al. (2007) also simulated the effects of environment manipulation on place cell firing with their model, which also did not fully reproduce the Gothard et al. (1996b) and Redish et al. (2000) realignment dynamics. As in the place cell only and Sheynikhovich et al. (2009) models, there is one common attractor base, formed by recurrently connected place cells, which receive inputs from BVCs as well as provide location information to a path integration circuit for spatial updating. Thus, the path integration circuit does not have its own independent influence on dynamics that would capture the dynamics observed after environmental manipulations.

In contrast to the single-attractor models, the coupled place cell–grid cell system captures the dynamics caused by mis-matching path integration and sensory inputs due to a competitive interaction between two subsystems with semi-independent dynamics. Recent findings suggest that path integration and sensory information influence the behaviour of CA3 place cells with comparable strengths (Posani et al., 2018), which provides a further support for the type of neural architecture that allows an equal competition between the two types of information.

It is also physiologically plausible for environmental sensory inputs (e.g., provided through boundary related firing: Solstad et al., 2008; Lever et al., 2009) to preferentially control place cell firing, while grid cell firing patterns predominantly reflect self-motion. Recordings in mice running in virtual environments while changing the gain between physical motion and visual motion reveals strong sensory influence on place cell firing patterns compared to much greater influence of self-motion on grid cell firing patterns (Chen et al., 2019). This, together with the evidence for place and grid cells interconnectivity (Brun et al., 2008) and the evidence for excitatory drive from the hippocampus to grid cells (Bonnevie et al., 2013), support the outlined architecture of our model. For grid cells to receive sensory inputs via place cells (rather than directly) also has an advantage of keeping activity patterns in different grid cell modules aligned when visual inputs are not available, otherwise they may quickly lose coherence due to errors accumulating in different modules, leading to place cell activity degradation.

Hardcastle et al. (2015) suggested, based on the results of their experiment, that path integrating grid cells get reset near borders by direct inputs from border cells. The suggested mechanism was recently implemented in the model of Keinath et al. (2018). However, it seems unable to replicate the Gothard et al. (1996b) data as realignment occurs only near the end on all track lengths in their model. In contrast, in our model, grid cells can be reset in any place where adequate boundary-related information is available, via inputs from place cells driven by BVCs, rather than border cells that fire only near borders.

In the recent experiment by Campbell et al. (2018), a mismatch in gain between physical and visual motion was created in mice navigating a virtual linear track (see also Chen et al., 2019). The grid cell behavior was found to depend on the amount of mismatch between self-motion and visual motion. Thus, weaker disagreements caused grid cell firing patterns to shift relative to baseline, as if grid cells constantly tried to align with visual inputs. Larger disagreements, in contrast, led to grid cells breaking free from the influence of landmarks, changing scale relative to them. These findings show a certain similarity to our simulations, where grid cell behavior was also found to depend on the amount of mismatch between self-motion and sensory information, with smaller mismatches resulting in continuous corrective shifting of grid cell activity pattern, while larger mismatches produced discontinuous changes in the activity pattern. In the latter case, our grid cells also for a brief time become free from an influence of environmental sensory inputs, in similarity to Campbell et al. (2018), since the PC activity bump jumps first and therefore the link between the PC and GC activities gets temporarily broken.

The model consisting of two coupled specialist subsystems has certain advantages over models where sensory inputs go directly to a single continuous attractor network that also does path integration, such as place cell-based (e.g., Samsonovich and McNaughton, 1997) or grid cell-based (e.g., Sheynikhovich et al., 2009; Ocko et al., 2018) models. In our model different subsystems serve different purposes and complement each other. The mediation of path integration by recurrent connections between grid cells leaves the recurrent connections between place cells in area CA3 free for other purposes, such as the formation of different continuous attractors for different environments. Thus, the place cells can remap between different environments, and perform pattern completion within these remapped representations to accommodate minor sensory changes or cue removal (Nakazawa et al., 2002; Wills et al., 2005) on the basis of the CA3 recurrent connections, independent of the recurrent connections between grid cells. Given that the grid cell representation does not remap, which facilitates development of appropriate recurrent connections for path integration, it is useful to have a separate place cell representation to associate to salient locations. Place cells tend to code for single locations, enabling unambiguous representation of a single goal location, and the place cell representations remap, which allows different goal locations to be represented in different environments.

Mechanism and Time-Course Predictors of Hippocampal Map Realignment

According to Redish et al. (2000), a temporal delay preceding the realignment of place cell population activity in their variable track length experiment could at least partially be explained by a stochastic switch between two semi-stable states. It assumes that place cell population firing patterns form a dynamic system that can only transit into a new state after accumulating enough energy to surpass an energy barrier.

According to our model, the switch effect can be explained by grid cell projections to place cells, which must be overpowered by contradicting sensory inputs in order for the realignment to occur. The sensory stimulus required for inducing the

switch is provided by boundaries ahead of the rat via BVC inputs to place cells, which take time to build up sufficiently for the place cells to overcome the path integration influence from grid cells. This causes an initial temporal delay before the population activity transition starts. The complete switch process includes grid cell resetting by place cells (through place cell–grid cell projections), either via grid cell activity packets shifting (concurrently with place cell activity shifting), or via grid cell activity jumping (following place cell activity jumping).

The realignment dynamics are determined by the length of the shortened track on a particular journey. The shortened track length defines the rat's starting distance to the boundaries ahead (and thus forward-tuned BVC inputs' strength) and the mismatch magnitude (equal to the amount of track shortening), which determine the initial delay (increasing with the track length) and the time-course of the population activity transition. The larger the mismatch magnitude, as the track length is progressively shortened, the more rapid the continuous activity shifts, which turn into jump transitions when the mismatch magnitude increases above a certain value. Jumps typically occur much earlier on the track than shift realignments, because, according to our model, in jump realignments place cells initially realign alone, with grid cell activities following slightly later. In shift realignments, on the contrary, place cell activity continuously pulls along grid cell activity, which slows the realignment.

Modelling Implications and Predictions for Future Research

The results of our simulations show that an architecture of interconnected recurrent networks of place cells (driven by environmental BVC inputs) and grid cells (implementing path integration) can explain the spatial firing patterns and temporal dynamics seen in place cell firing rate data from experiments where the familiar correspondence between environmental and self-motion inputs is manipulated (Gothard et al., 1996b; Redish et al., 2000). In contrast, the alternative architecture of a single recurrent network of place cells (implementing path integration as well as receiving BVC inputs) cannot reproduce these dynamics. Both results support the hypothesis that grid cells and place cells are organised in such a way as to allow two different representations (self-motion and sensory based) to interact with each other. The simulations provide insights into the specific neural mechanisms enabling integration of these two types of information to estimate location.

The simulated place cell–grid cell model makes neuron firing predictions that could be tested in future animal studies. For example, it would be interesting to conduct experiments in rats, similar to those of Gothard et al. and Redish et al., but recording from grid cells as well as place cells. It should be possible to verify that the realignment is driven by a conflict in which sensory input from ahead of the rat eventually resets the path integrative mechanism implemented by grid cells. If so, the model predicts that initially the realignment should start amongst place cells, with the activity realignment dynamics predicted by the track length and amount of shortening (as described above). And the grid cell activity should either realign concurrently with the place cell activity shifting or soon after the abrupt place cell activity jump, depending on the amount of track shortening. The realignment should occur simultaneously across all the grid cell modules with different spatial scales (due to the inputs from the same group of place cells), as well as coherently among the grid cells within each module (due to their recurrent connectivity).

DATA AVAILABILITY STATEMENT

All datasets generated for this study are included in the manuscript/supplementary files.

AUTHOR CONTRIBUTIONS

DL and NB conceptualised the model and the study. DL designed and implemented the computational model, performed the simulations, and data analysis. DL and NB wrote the manuscript.

ACKNOWLEDGMENTS

Some of the work presented in the article was done as a part of DL's Ph.D. project (cited in the References), which was funded by the UK Medical Research Council. The work was also supported by a Wellcome Principal Research Fellowship and the ERC Advanced grant NEUROMEM. We thank Alexander Mozeika and Christian Doeller for graphical assistance.

REFERENCES

Amaral, D. G., and Witter, M. P. (1989). The three-dimensional organization of the hippocampal formation: a review of anatomical data. *Neuroscience* 31, 571–591. doi: 10.1016/0306-4522(89)90424-7

Barry, C., Hayman, R., Burgess, N., and Jeffery, K. J. (2007). Experience-dependent rescaling of entorhinal grids. *Nat. Neurosci.* 10, 682–684. doi: 10.1038/nn1905

Barry, C., Lever, C., Hayman, R., Hartley, T., Burton, S., O'Keefe, J., et al. (2006). The boundary vector cell model of place cell firing and spatial memory. *Rev. Neurosci.* 17, 71–79. doi: 10.1515/REVNEURO.2006.17.1-2.71

Bonnevie, T., Dunn, B., Fyhn, M., Hafting, T., Derdikman, D., Kubie, J. L., et al. (2013). Grid cells require excitatory drive from the hippocampus. *Nat. Neurosci.* 16, 309–317. doi: 10.1038/nn.3311

Brun, V. H., Leutgeb, S., Wu, H. Q., Schwarcz, R., Witter, M. P., Moser, E. I., et al. (2008). Impaired spatial representation in CA1 after lesion of direct input from entorhinal cortex. *Neuron* 57, 290–302. doi: 10.1016/j.neuron.2007.11.034

Burak, Y., and Fiete, I. R. (2009). Accurate path integration in continuous attractor network models of grid cells. *PLoS Comput. Biol.* 5:e1000291. doi: 10.1371/journal.pcbi.1000291

Byrne, P., Becker, S., and Burgess, N. (2007). Remembering the past and imagining the future: a neural model of spatial memory and imagery. *Psychol. Rev.* 114, 340–375. doi: 10.1037/0033-295X.114.2.340

Campbell, M. G., Ocko, S. A., Mallory, C. S., Low, I. I. C., Ganguli, S., and Giocomo, L. M. (2018). Principles governing the integration of landmark and self-motion cues in entorhinal cortical codes for navigation. *Nat. Neurosci.* 21, 1096–1106. doi: 10.1038/s41593-018-0189-y

Chen, G., Lu, Y., King, J. A., Cacucci, F., and Burgess, N. (2019). Differential influences of environment and self-motion on place and grid cell firing. *Nat. Commun. 10*:630. doi: 10.1038/s41467-019-08550-1

Conklin, J., and Eliasmith, C. (2005). A controlled attractor network model of path integration in the rat. *J. Comput. Neurosci.* 18, 183–203. doi: 10.1007/s10827-005-6558-z

Couey, J. J., Witoelar, A., Zhang, S. J., Zheng, K., Ye, J., Dunn, B., et al. (2013). Recurrent inhibitory circuitry as a mechanism for grid formation. *Nat. Neurosci.* 16, 318–324. doi: 10.1038/nn.3310

Dhillon, A., and Jones, R. S. (2000). Laminar differences in recurrent excitatory transmission in the rat entorhinal cortex *in vitro*. *Neuroscience* 99, 413–422. doi: 10.1016/S0306-4522(00)00225-6

Doiron, B., Longtin, A., Berman, N., and Maler, L. (2000). Subtractive and divisive inhibition: effect of voltage-dependent inhibitory conductances and noise. *Neural Comput.* 12, 1–22. doi: 10.1162/089976601300014691

Etienne, A. S., Maurer, R., and Séguinot, V. (1996). Path integration in mammals and its interaction with visual landmarks. *J. Exp. Biol.* 199, 201–209.

Fiete, I. R., Burak, Y., and Brookings, T. (2008). What grid cells convey about rat location. *J. Neurosci.* 28, 6858–6871. doi: 10.1523/JNEUROSCI.5684-07.2008

Germroth, P., Schwerdtfeger, W. K., and Buhl, E. H. (1991). Ultrastructure and aspects of functional organization of pyramidal and nonpyramidal entorhinal projection neurons contributing to the perforant path. *J. Comp. Neurol.* 305, 215–231. doi: 10.1002/cne.903050205

Gothard, K. M., Skaggs, W. E., and McNaughton, B. L. (1996b). Dynamics of mismatch correction in the hippocampal ensemble code for space: interaction between path integration and environmental cues. *J. Neurosci.* 16, 8027–8040. doi: 10.1523/JNEUROSCI.16-24-08027.1996

Gothard, K. M., Skaggs, W. E., Moore, K. M., and McNaughton, B. L. (1996a). Binding of hippocampal CA1 neural activity to multiple reference frames in a landmark-based navigation task. *J. Neurosci.* 16, 823–835.

Grieves, R. M., Duvelle, É., and Dudchenko, P. A. (2018). A boundary vector cell model of place field repetition. *Spat. Cogn.* Comput. 18, 217–256. doi: 10.1080/13875868.2018.1437621

Guanella, A., Kiper, D., and Verschure, P. (2007). A model of grid cells based on a twisted torus topology. *Int. J. Neural Syst.* 17, 231–240. doi: 10.1142/S0129065707001093

Hafting, T., Fyhn, M., Molden, S., Moser, M.-B., and Moser, E. I. (2005). Microstructure of a spatial map in the entorhinal cortex. *Nature* 436, 801–806. doi: 10.1038/nature03721

Hardcastle, K., Ganguli, S., and Giocomo, L. M. (2015). Environmental boundaries as an error correction mechanism for grid cells. *Neuron* 86, 827–839. doi: 10.1016/j.neuron.2015.03.039

Hartley, T., Burgess, N., Lever, C., Cacucci, F., and O'Keefe, J. (2000). Modeling place fields in terms of the cortical inputs to the hippocampus. *Hippocampus* 10, 369–379. doi: 10.1002/1098-1063(2000)10:4<369::AID-HIPO3>3.0.CO;2-0

Keinath, A. T., Epstein, R. A., and Balasubramanian, V. (2018). Environmental deformations dynamically shift the spatial metric. *Elife* 7:e38169. doi: 10.7554/eLife.38169

Krupic, J., Bauza, M., Burton, S., Barry, C., and O'Keefe, J. (2015). Grid cell symmetry is shaped by environmental geometry. *Nature* 518, 232–235. doi: 10.1038/nature14153

Krupic, J., Bauza, M., Burton, S., and O'Keefe, J. (2018). Local transformations of the hippocampal cognitive map. *Science* 359, 1143–1146. doi: 10.1126/science.aao4960

Laptev, D. (2008). *Interaction of Motion and Perception in Continuous Attractor Representations of Position* (dissertation). London: University College London.

Lever, C., Burton, S., Jeewajee, A., O'Keefe, J., and Burgess, N. (2009). Boundary vector cells in the subiculum of the hippocampal formation. *J. Neurosci.* 29, 9771–9777. doi: 10.1523/JNEUROSCI.1319-09.2009

Lingenhöhl, K., and Finch, D. M. (1991). Morphological characterization of rat entorhinal neurons *in vivo*: soma-dendritic structure and axonal domains. *Exp. Brain Res.* 84, 57–74. doi: 10.1007/BF00231762

Lisman, J. E. (1997). Bursts as a unit of neural information: making unreliable synapses reliable. Trends. *Neuroscience* 20, 38–43. doi: 10.1016/S0166-2236(96)10070-9

McNaughton, B. L., Battaglia, F. P., Jensen, O., Moser, E. I., and Moser, M. B. (2006). Path integration and the neural basis of the 'cognitive map'. *Nat. Rev. Neurosci.* 7, 663–678. doi: 10.1038/nrn1932

Nakazawa, K., Quirk, M. C., Chitwood, R. A., Watanabe, M., Yeckel, M. F., Sun, L. D., et al. (2002). Requirement for hippocampal CA3 NMDA receptors in associative memory recall. *Science* 297, 211–218. doi: 10.1126/science.1071795

Navratilova, Z., Giocomo, L. M., Fellous, J.-M., Hasselmo, M. E., and McNaughton, B. L. (2011). Phase precession and variable spatial scaling in a periodic attractor map model of medial entorhinal grid cells with realistic after-spike dynamics. *Hippocampus* 22, 772–789. doi: 10.1002/hipo.20939

Ocko, S. A., Hardcastle, K., Giocomo, L. M., and Ganguli, S. (2018). Emergent elasticity in the neural code for space. *Proc. Natl. Acad. Sci. U.S.A.* 115, E11798–E11806. doi: 10.1073/pnas.1805959115

O'Keefe, J. (1976). Place units in the hippocampus of the freely moving rat. *Exp. Neurol.* 51, 78–109. doi: 10.1016/0014-4886(76)90055-8

O'Keefe, J. (2007). "Hippocampal neurophysiology in the behaving animal," in *The Hippocampus Book (Chapter 11)*, eds P. Andersen, R. Morris, D. Amaral, T. Bliss, and J. O'Keefe (New York, NY: Oxford University Press), 475–540.

O'Keefe, J., and Burgess, N. (1996). Geometric determinants of the place fields of hippocampal neurons. *Nature* 381, 425–428. doi: 10.1038/381425a0

O'Keefe, J., and Burgess, N. (2005). Dual phase and rate coding in hippocampal place cells: theoretical significance and relationship to entorhinal grid cells. *Hippocampus* 7, 853–866. doi: 10.1002/hipo.20115

O'Keefe, J., and Dostrovsky, J. (1971). The hippocampus as a spatial map. Preliminary evidence from unit activity in the freely-moving rat. *Brain Res.* 34, 171–175. doi: 10.1016/0006-8993(71)90358-1

O'Keefe, J., and Nadel, L. (1978). *The Hippocampus as a Cognitive Map*. Oxford: Oxford University Press.

Posani, L., Cocco, S., and Monasson, R. (2018). Integration and multiplexing of positional and contextual information by the hippocampal network. *PLoS Comput. Biol.* 14:e1006320. doi: 10.1371/journal.pcbi.1006320

Redish, A. D., Rosenzweig, E. S., Bohanick, J. D., McNaughton, B. L., and Barnes, C. A. (2000). Dynamics of hippocampal ensemble activity realignment: time versus space. *J. Neurosc.* 20, 9298–9309. doi: 10.1523/JNEUROSCI.20-24-09298.2000

Redish, A. D., and Touretzky, D. S. (1998). The role of the hippocampus in solving the Morris water maze. *Neural Comput.* 10, 73–112. doi: 10.1162/089976698300017908

Samsonovich, A., and McNaughton, B. L. (1997). Path integration and cognitive mapping in a continuous attractor neural network model. *J. Neurosci.* 17, 5900–5920. doi: 10.1523/JNEUROSCI.17-15-05900.1997

Sargolini, F., Fyhn, M., Hafting, T., McNaughton, B. L., Witter, M. P., Moser, M. B., et al. (2006). Conjunctive representation of position, direction, and velocity in entorhinal cortex. *Science* 312, 758–762. doi: 10.1126/science.1125572

Sheynikhovich, D., Chavarriaga, R., Strösslin, T., Arleo, A., and Gerstner, W. (2009). Is there a geometric module for spatial orientation? Insights from a rodent navigation model. *Psychol. Rev.* 116, 540–66. doi: 10.1037/a0016170

Solstad, T., Boccara, C. N., Kropff, E., Moser, M. B., and Moser, E. I. (2008). Representation of geometric borders in the entorhinal cortex. *Science* 322, 1865–1868. doi: 10.1126/science.1166466

Stensola, H., Stensola, T., Solstad, T., Frøland, K., Moser, M.-B., and Moser, E. I. (2012). The entorhinal grid map is discretized. *Nature* 492, 72–78. doi: 10.1038/nature11649

Stensola, T., Stensola, H., Moser, M.-B., and Moser, E. I. (2015). Shearing-induced asymmetry in entorhinal grid cells. *Nature* 518, 207–212. doi: 10.1038/nature14151

Stringer, S. M., Rolls, E. T., Trappenberg, T. P., and de Araujo, I. E. (2002). Self-organizing continuous attractor networks and path integration: two-dimensional models of place cells. *Netw. Comput. Neural Syst.* 13, 429–446. doi: 10.1088/0954-898X/13/4/301

Sürmeli, G., Marcu, D. C., McClure, C., Garden, D. L. F., Pastoll, H., and Nolan, M. F. (2015). Molecularly defined circuitry reveals input-output segregation in deep layers of the medial entorhinal cortex. *Neuron* 88, 1040–1053. doi: 10.1016/j.neuron.2015.10.041

Wills, T. J., Lever, C., Cacucci, F., Burgess, N., and O'Keefe, J. (2005). Attractor dynamics in the hippocampal representation of the local environment. *Science* 308, 873–876. doi: 10.1126/science.1108905

Wilson, H. R. (1999). *Spikes, Decisions and Actions. The Dynamical Foundations of Neuroscience*. Oxford: Oxford University Press. p. 126.

Witter, M. P., and Amaral, D. (2004). "Hippocampal formation," in *The Rat Nervous System*, ed G. Paxinos (Amsterdam: Elsevier Inc.), 635–704. doi: 10.1016/B978-012547638-6/50022-5

Yoon, K., Lewallen, S., Kinkhabwala, A. A., Tank, D. W., and Fiete, I. R. (2016). Grid cell responses in 1D environments assessed as slices through a 2D lattice. *Neuron* 89, 1086–1099. doi: 10.1016/j.neuron.2016.01.039

Zhang, K. (1996). Representation of spatial orientation by the intrinsic dynamics of the head-direction cell ensemble: a theory. *J. Neurosci.* 16, 2112–2126. doi: 10.1523/JNEUROSCI.16-06-02112.1996

Conflict of Interest: The authors declare that the research was conducted in the absence of any commercial or financial relationships that could be construed as a potential conflict of interest.

APPENDIX

Implementation of the Place Cell—Grid Cell Model

Place Cell Network Dynamics

The dynamics of recurrently connected place cells with global feedback inhibition, resulting in a continuous attractor network, can be described by the following equation:

$$\tau \frac{dr_i}{dt} = -r_i + F\left(\left(\sum_j W_{i-j} r_j + h_i\right) \Big/ J\gamma \sum_j r_j\right) \quad (A.1)$$

Here r_i is the firing rate of the place cell i, τ is the place cell time constant, W_{i-j} is the weight of the recurrent connection from the place cell j to the place cell i, h_i is an external input and F is the response function of the place cells. γ represents the strength of the synapse from any place cell onto the global inhibitory neuron and J is the synaptic strength of the negative feedback from it (the inhibitory neuron time constant is assumed to be much smaller than that of place cells and is approximated by zero).

We assume the inhibition to be shunting, consistent with the action of shunting GABA synapses (Wilson, 1999). Doiron et al. (2000) have shown that the shunting inhibition has a divisive, rather than subtractive, effect on firing rates of pyramidal cells when they operate at frequencies below 40 Hz. Since place cells fire at lower frequencies, we implement a divisive inhibition in our model. The inhibition is performed through the action of a single, global inhibitory neuron that receives equally strong synapses from all the place cells in the network and provides equal negative feedbacks to all as well, broadly consistent with the very large dendritic and axonal spread of basket cells.

Stringer et al. (2002) developed a model of Hebbian associative learning of recurrent connections in CA3 during novel environment exploration, which generated a recurrent connections profile with a shape very close to a Gaussian function of the distance between favorite locations of presynaptic and postsynaptic place cells. Therefore, we adopt the following function to represent the profile in our model:

$$W\left(x_i - x_j, y_i - y_j\right) = A_w \exp[-(s_{i-j})^2 / 2{\sigma_w}^2\ ] \quad (A.2)$$

where $s_{i-j} = \sqrt{(x_i - x_j)^2 + (y_i - y_j)^2}$ is the distance between the preferred locations of the cells i (x_i, y_i) and j (x_j, y_j), ${\sigma_w}^2$ represents the broadness of the profile and A_w is the maximum weight strength.

We also use the same function to represent recurrent connections between grid cells in the three grid cell modules in our model (A.11), which are also continuous attractor–based. In addition, the function is used to determine the connections between place cells and grid cells in Equation (A.11) (with their profile broadness defined by the average of the variances of the place and grid cell firing fields), since these are assumed to be learnt in a similar Hebbian way.

Since place cell tuning to location often has a shape close to a Gaussian (Hartley et al., 2000), we use the following formula for the place cell tuning curve:

$$f(x - x_i, y - y_i) = A_p \exp[-(s_i)^2 / 2{\sigma_p}^2\ ] \quad (A.3)$$

where $s_i = \sqrt{(x - x_i)^2 + (y - y_i)^2}$ is the distance between the current location of the agent (x, y) and the preferred location of cell i (x_i, y_i), at which it fires maximally. ${\sigma_p}^2$ is the variance of the place field and A_p is the peak firing rate of the place cell (both assumed to be the same for all place cells in the model for simplicity).

The activation pattern over the population of place cells, virtually arranged so that each one's location on the Cartesian grid corresponds to its preferred location, is basically equivalent to the place cell tuning curve (Zhang, 1996). We refer to the implicit 2D space represented by the set of activities of so arranged neurons as the "state space" of the system.

If we have a sufficient density of coverage of the represented space by the place cells, in case of a stable activity pattern we can approximate the sum $\sum_j W_{i-j} r_j$ in Equation (A.1) by the 2D-convolution:

$$f\left(x, y\right) * W(x, y) = \int_{-\infty}^{\infty} \int_{-\infty}^{\infty} w\left(x - X, y - Y\right) f\left(X, Y\right) dXdY \quad (A.4)$$

where $f\ (x, y)$ is the stable firing rate of the place cells given by Equation (A.3).

Since both W and f are Gaussian, the result of their convolution is another 2D-Gaussian, with the variance $\sigma^2 = {\sigma_w}^2 + {\sigma_p}^2$. In order for Equation (A.1) to be true, our response function F has to be a power function of the form:

$$F\left(x\right) = (x)^n, \text{where } n = \frac{{\sigma_p}^2 + {\sigma_w}^2}{{\sigma_p}^2} \quad (A.5)$$

In the case when ${\sigma_p}^2 = {\sigma_w}^2$, F is simply a square function ($n = 2$). We can think of this function as a non-saturating region of the Naka-Rushton function, which is considered to provide a reasonably good description of neuronal responses. Thus, with ${\sigma_p}^2 = {\sigma_w}^2$, Equation (A.1) becomes:

$$\tau \frac{dr_i}{dt} = -r_i + \left(\left(\sum_j W_{i-j} r_j + h_i\right) \Big/ J\gamma \sum_j r_j\right)^2 \quad (A.6)$$

This equation is used as a basis for the description of place cell network dynamics, as well as grid cell network dynamics, since both cell types are assumed to form continuous attractor networks.

Boundary Vector Cell (BVC) Inputs to Place Cells

In our model every place cell is assumed to receive inputs from four orthogonally tuned BVCs, each of which has directional tuning perpendicular to one of the four surrounding boundaries. The position of the bump-shaped population activity pattern in the state space, representing the environment, is thus controlled by four sets of BVC inputs, each associated with a boundary in a

specific direction. Each set of these inputs, or an "input profile," is composed of the individual inputs from all the BVCs tuned to that boundary.

In our modelling we assume these input profiles to have a Gaussian crossection in the plane orthogonal to their associated boundary, with the mean of the Gaussian occurring at the current distance of the rat from that boundary. We use a Gaussian shape for the input profiles in line with the Gaussian shape of the place cell activity bump, and the point where the peaks of all four profiles overlap corresponds to the activity bump centre. We assume that the amplitude and variance of these Gaussian profiles vary linearly with the distance from their associated boundaries, with the amplitude decreasing and variance increasing, corresponding to the decreasing influence of more distant boundaries.

We then translate a set, consisting of all the input profiles associated with a particular boundary and distributed through 160 cm [the original track length in Gothard et al. (1996b)] starting from the boundary, into a set of tuning curves for individual BVCs distributed through that distance. Equation (A.7) has been found to provide the description for the firing response b_i of each individual BVC i with its preferred distance d_i as a function of distance to the boundary x:

$$b_i(x) = A(d_i)\exp\left(\frac{-(x-d_i)^2}{2(\sigma(d_i)+\alpha(x-d_i))^2}\right) \quad (A.7)$$

Both A and σ here vary linearly with variation of the preferred distance across BVCs, i.e., $\sigma(d_i) = \sigma_0 + \gamma d_i$ and $A(d_i) = A_0 - \beta d_i$, where γ and β are constants determining, respectively, rates of σ increase and A decrease with the preferred distance increase. α gives the rate with which σ of a particular BVC varies linearly with the difference between its preferred and current distance from the boundary.

On the contrary, if we assumed a Gaussian shape for the tuning curves of individual BVCs, rather than for the overall input profile from a boundary, the resulting overall input profiles would not be Gaussian but skewed, and consequently their combined input (i.e., their sum) to the place cell activity bump would not be well-focused. Although in the case of single place cells a Gaussian BVC curve may give a reasonable fit, as in O'Keefe and Burgess (1996), it does not work so well for a whole group of place cells.

The total external input h_i to the place cell i we model as proportional to the thresholded linear sum of all BVC inputs b_j (see Equation A.7) it receives:

$$h_i = A\Phi\left(\sum_{j=1}^{n} b_j - T\right) \quad (A.8)$$

where the weighting parameter A is constant, T is a threshold, and Φ is the Heaviside function (i.e., $\Phi(x) = x$ if $x > 0$, $\Phi(x) = 0$ otherwise).

Conjunctive Grid by Head-Direction Cell Responses

In order for each grid cell to have asymmetric connections to the six grid cells with firing patterns offset in six directions, mediated by conjunctive cells with the corresponding directional preferences, there need to be six distinct groups of grid by head-direction cells, each composed of cells tuned to one of the six directions. The number of cells in each group is equal to the total number of grid cells, so that each grid cell has a corresponding (i.e., with the same grid node locations) grid by head-direction cell in each of the six groups. We define the firing response g_{jD} of the grid by head-direction cell j_D from the group D, consisting of cells with the preferred head direction θ^D, as follows:

$$g_{jD} = g_j\Phi(|\theta - \theta^D|) \quad (A.9)$$

where g_j is the firing response of the corresponding grid cell j (which may potentially be providing a feed-forward input to the grid by head-direction cell j_D). The function Φ (of rat's head direction θ) describes the directional modulation of the grid by head-direction cell responses in the following way:

$$\Phi\left(\left|\theta-\theta^D\right|\right) = \begin{cases} \frac{2\cos(|\theta-\theta^D|+30^\circ)}{\sqrt{3}}, & \left|\theta-\theta^D\right| \le 60^\circ \\ 0 \qquad otherwise \end{cases} \quad (A.10)$$

Equation (A.10) provides the form of modulation of conjunctive cell inputs to a grid cell that is necessary for correct path integration, i.e., so that the sum of different translation vectors (produced by different conjunctive cell inputs to a grid cell) was always equal to the actual rat's translation [In the case of 6 directions, conjunctive cell firing modulation by Equation (A.10) has the same overall effect as the modulation by a cosine function has in a Cartesian coordinate system (four directions)].

The Place Cell—Grid Cell Model

The proposed place cell—grid cell system is represented by the following set of equations (based on Equation A.6):

$$\tau\frac{dg_i^1}{dt} = -g_i^1 + \left(\left(\sum_j W_{i-j}g_j^1 + Va^1g_1^1 + Va^1g_2^1 + Va^1g_3^1 + Va^1g_4^1 + Va^1g_5^1 + Va^1g_6^1 + \sum_j P_{i-j}^1 p_j\right)\Big/ J\gamma\sum_j g_j^1\right)^2;$$

$$\tau\frac{dg_i^2}{dt} = -g_i^2 + \left(\left(\sum_j W_{i-j}g_j^2 + Va^2g_1^2 + Va^2g_2^2 + Va^2g_3^2 + Va^2g_4^2 + Va^2g_5^2 + Va^2g_6^2 + \sum_j P_{i-j}^2 p_j\right)\Big/ J\gamma\sum_j g_j^2\right)^2;$$

$$\tau\frac{dg_i^3}{dt} = -g_i^3 + \left(\left(\sum_j W_{i-j}g_j^3 + Va^3g_1^3 + Va^3g_2^3 + Va^3g_3^3 + Va^3g_4^3 + Va^3g_5^3 + Va^3g_6^3 + \sum_j P_{i-j}^3 p_j\right)\Big/ J\gamma\sum_j g_j^3\right)^2;$$

$$\tau \frac{dp_i}{dt} = -p_i + \left(\left(\sum_j W_{i-j} p_j + \sum_j g^1_{i-j} g^1_j + \sum_j g^2_{i-j} g^2_j + \sum_j g^3_{i-j} g^3_j + h_i \right) \Big/ J\gamma \sum_j p_j \right)^2 . \quad \text{(A.11)}$$

Here g^1_i, g^2_i, and g^3_i are the firing rates of the grid cells i from the first, second and third module of cells correspondingly, whereas p_i is the firing rate of the place cell i. W_{i-j} is the weight of the recurrent connection from the grid/place cell j to the grid/place cell i, given by Equation (A.2). P_{i-j} is the connection weight from the place cell j to the grid cell i and G_{i-j} is the connection weight from the grid cell j to the place cell i, both determined according to Equation (A.2). g^1_D, g^2_D, and g^3_D are the firing rates of the grid by head-direction cells from the first, second and third module correspondingly, given by Equation (A.9) with $D = 1, 2, 3, 4, 5, 6$ and $\theta^D = 0^\circ, 60^\circ, 120^\circ, 180^\circ, 240^\circ, 300^\circ$, which corresponding grid cells are located (in the state space) next to and in the direction θ^D+180° from the grid cells i (in the three modules). a^1, a^2, a^3 are the weights of the input to the grid cell i from each of the six grid by head-direction cells in the first, second and third module correspondingly. γ represents the strength of a synapse from any grid/place cell onto the global inhibitory neuron for its module of grid/place cells, and J is the synaptic strength of the negative feedback from it. V is the speed of rat's movement. h_i is the external input to the place cell i, given by Equation (A.8). The synaptic strengths γ and J are, respectively, set to 0.04 and 0.123 for each grid cell module and place cells, and the model time constant τ is set to 0.05.

An assumption is made regarding synaptic transmission from the place to grid cell layers: that only firing rates exceeding a threshold r (due to the layer 5b synaptic connections) propagate from the place to grid cells, with $r = r_{max} - 4$, where r_{max} is the highest place cell firing rate at a particular time. A lower threshold is also set for synaptic transmission from the grid to place cell layers: only firing rates exceeding $r = r_{max} - 6$ propagate through the grid cell—place cell connections. This is done to ensure the input to the place cell layer is spatially specific, i.e., only firing from the middle of the grid cell activity bumps influences the place cell representation. There is some physiological evidence that only spikes fired during periods of high-firing rate ("bursts" of spikes) are reliably transmitted by synapses in the hippocampal region (see Lisman, 1997, for a review).

Implementation of the Place Cell Only Model

The following Equation (A.12) describes the place cell only model for spatial navigation. The model does not have grid cells, instead path integration is performed by recurrently connected place cells with place by direction neurons:

$$\tau \frac{dr_i}{dt} = -r_i + \left(\left(\sum_j W_{i-j} r_j + Var^1 + Var^2 + Var^3 + Var^4 + Var^5 + Var^6 + h_i \right) \Big/ J\gamma \sum_j r_j \right)^2 \quad \text{(A.12)}$$

Here r_i is the firing rate of the place cell i. $r^D = r\Phi(|\theta - \theta^D|)$, with $D = 1, 2, 3, 4, 5, 6$ and $\theta^D = 0^\circ, 60^\circ, 120^\circ, 180^\circ, 240^\circ, 300^\circ$ correspondingly, is the firing rate of the place by direction neuron from the group D (with Φ given by Equation A.10), which corresponding place cell (with firing rate r) is located (in the state space) next to and in the direction θ^D+180° from the place cell i. W_{i-j} is the weight of the recurrent connection from the place cell j to the place cell i given by Equation (A.2) and a is the weight of the input to the place cell i from each of the six place by direction neurons. γ represents the strength of a synapse from any place cell onto the global inhibitory neuron for place cells, and J is the synaptic strength of the negative feedback from it. V is the speed and θ is the direction of rat's movement. h_i is the external input to the place cell i given by Equations (A.8) and (A.7) as for the place cell—grid cell model. The synaptic strengths γ and J are, respectively, set to 0.04 and 0.123, and the model time constant τ is set to 0.05, all as in the other model.

frontiers in Neural Circuits

REVIEW
published: 18 October 2019
doi: 10.3389/fncir.2019.00066

The Growing Evidence for the Importance of the Otoliths in Spatial Memory

Paul F. Smith[1,2,3]*

[1] Department of Pharmacology and Toxicology, Brain Health Research Centre, School of Biomedical Sciences, University of Otago Medical School, Dunedin, New Zealand, [2] Brain Research New Zealand, Auckland, New Zealand, [3] Eisdell Moore Centre for Hearing and Balance Research, University of Auckland, Auckland, New Zealand

Many studies have demonstrated that vestibular sensory input is important for spatial learning and memory. However, it has been unclear what contributions the different parts of the vestibular system – the semi-circular canals and otoliths – make to these processes. The advent of mutant otolith-deficient mice has made it possible to isolate the relative contributions of the otoliths, the utricle and saccule. A number of studies have now indicated that the loss of otolithic function impairs normal spatial memory and also impairs the normal function of head direction cells in the thalamus and place cells in the hippocampus. Epidemiological studies have also provided evidence that spatial memory impairment with aging, may be linked to saccular function. The otoliths may be important in spatial cognition because of their evolutionary age as a sensory detector of orientation and the fact that velocity storage is important to the way that the brain encodes its place in space.

Keywords: otoliths, vestibular, spatial learning and memory, hippocampus, head direction cells, place cells

OPEN ACCESS

Edited by:
Mathieu Beraneck,
Université Paris Descartes, France

Reviewed by:
Jerome Carriot,
McGill University, Canada
Philip A. Blankenship,
Lewis University, United States

***Correspondence:**
Paul F. Smith
paul.smith@otago.ac.nz;
paul.smith@stonebow.otago.ac.nz

Received: *09 August 2019*
Accepted: *30 September 2019*
Published: *18 October 2019*

Citation:
Smith PF (2019) The Growing Evidence for the Importance of the Otoliths in Spatial Memory. Front. Neural Circuits 13:66. doi: 10.3389/fncir.2019.00066

INTRODUCTION

The otolith organs in the vestibular inner ear, which comprise the utricle and saccule, represent the most ancient part of the vestibular system in evolutionary terms. Estimated to have evolved more than 500 million years ago, a primitive otolithic system ("statoliths") even exists in invertebrates such as jellyfish (see Fritzsch, 1998; Spoor et al., 2002; Jeffery and Spoor, 2004; Schulz-Mirbach et al., 2019, for reviews). In mammals, the vestibular system develops early in embryogenesis and provides the fetus with the ability to detect gravitational vertical and self-motion before birth (Baker, 1998; Ronca, 2003; Jeffery and Spoor, 2004; Ronca et al., 2008; Lim and Brichta, 2016). Unlike the visual system, the vestibular system is almost fully functional at birth (see Lim and Brichta, 2016 for a review) and provides the brain and body with an immediate sense of direction in the spatial environment (Jamon, 2014). While the three semi-circular canals detect angular acceleration of the head in different planes, the otoliths, the utricle and saccule, sense linear acceleration, including linear acceleration by gravity. The maculae of the utricle and saccule are oriented at right angles to one another, and in the usual supine position of the head for humans, the saccule responds to changes in acceleration by gravity as the head is tilted relative to gravitational vertical (see **Figure 1**). In both the utricle and saccule, the hair cells, which are oriented in different directions, are activated by the inertial force exerted upon them by otoconia (calcium carbonate crystals) which sit above, on an epithelial layer (see Lim and Brichta, 2016 for a review; **Figure 1**). The specific role of the

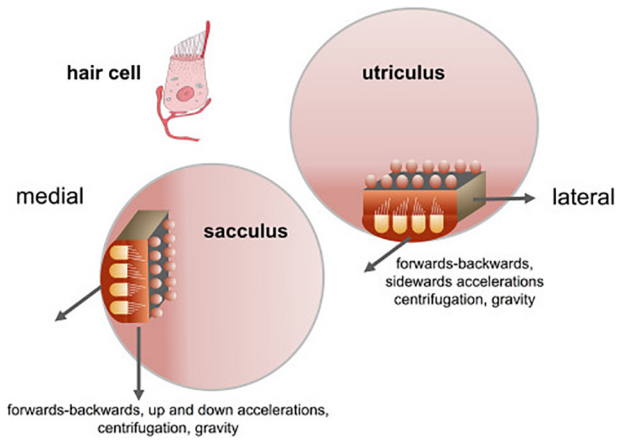

FIGURE 1 | Orientation of the sacculus and utriculus in the labyrinth. From Kingma and Van De Berg (2016) with permission.

otoliths is to provide a gravitational frame of reference with which to interpret other sensory signals, including those generated by the semi-circular canals, and to contribute to the perception of linear motion within that framework (Andreescu et al., 2005; Cullen, 2012; Jamon, 2014; Curthoys et al., 2017). This, in turn, is critical for the vestibular contribution to cognitive processes such as spatial memory (see Besnard et al., 2016; Smith, 2017 for reviews), the body representation of the self (see Mast et al., 2014; Lopez et al., 2015 for reviews), and even social cognition (see Deroualle and Lopez, 2014 for a review). Any role that the otoliths have in these processes is especially important since: aging is associated with reduced otolith function (e.g., Agrawal et al., 2012; Zu Eulenburg et al., 2017); impaired vestibular function and specifically otolithic function, has been recently associated with an increased risk of cognitive impairment and dementia (Aranda-Moreno and Jáuregui-Renaud, 2016; Harun et al., 2016; Wei et al., 2017, 2019; Xie et al., 2017; Kamil et al., 2018, in press; see Agrawal et al., 2019, in press, for a review); and otolithic lesions can occur in humans independently of lesions of the semi-circular canals (e.g., Manzari et al., 2014). In addition to other forms of dysfunction that can occur in the vestibular system (e.g., benign paroxysmal positional vertigo, vestibular migraine, Meniere's disease, vestibular vertigo, vestibular neuritis, vestibular schwannomas, etc.), there is evidence that high intensity noise exposure can damage the otoliths as well as the cochlea (e.g., Stewart et al., 2016; Xu et al., 2016).

While evidence has continued to accumulate for a significant role of the vestibular system as a whole, in the development of spatial learning and memory, the importance of the otoliths themselves has remained relatively obscure, due to the difficulty in accessing them surgically in order to lesion or electrically stimulate them selectively and independently of the semi-circular canals, in experimental studies (e.g., Hitier et al., 2016). Hence, while there is a wealth of evidence that global lesions of the peripheral vestibular system impair spatial memory in animals and humans in a variety of tasks (e.g., Zheng et al., 2006, 2009; Baek et al., 2010; see Besnard et al., 2016; Smith, 2017, for reviews), there are relatively few data relating specifically to the otoliths. Studies in extraterrestrial microgravity and in parabolic flight are possible avenues to investigate their significance; however, in each case there are confounding factors (e.g., Zheng et al., 2017). In microgravity the otoliths are no longer stimulated by gravity, but they respond to other forms of linear acceleration (Ronca, 2003). In parabolic flight, subjects experience microgravity but they are also subjected to hypergravity, which may cancel out the effects of the microgravity (Zheng et al., 2017). One development that has provided a new path to investigate the specific contributions of the otoliths, is the production of mutant mouse strains which are devoid of otoconia and therefore, of otolithic function. The aim of this review is to summarize and critically evaluate what is currently known of the importance of the otoliths for spatial memory and its neural substrates.

EVIDENCE FOR OTOLITHIC INVOLVEMENT IN SPATIAL MEMORY IN MICE

There are relatively few studies to date, but one model of otolith loss is the B6Ei.GL-Nox3het/J mouse ("*tilted Het*" mouse), which presents a mutation on chromosome 17 which inhibits the expression of the NADPH oxidase 3 gene (Paffenholz, 2004). *Het–/–* mice exhibit a complete and specific loss of utricular and saccular otoconia (Bergstrom et al., 1998). Another model is the –/–; B6.Cg-*Otop1tlt/j tilted* mouse (Jackson Laboratories, Bar Harbor, ME; Jones et al., 2008; Kim et al., 2010), which exhibits a similar deletion of the otoliths (de Caprona et al., 2004; Blankenship et al., 2017; Khan et al., 2019a,b).

The importance of the otoliths for spatial memory has been demonstrated in a number of studies published between 2012 and 2019, which have tested otolith-deficient mice in behavioral tests that assess cognitive performance. Most of these have involved testing spatial memory (e.g., the Y maze test, place recognition test, radial arm maze test, Barnes test, T maze alternation test, homing test, home retrieval test) but others have assessed other aspects of memory such as memory for objects (object recognition memory test).

In order to investigate the effects of selective otolith loss on cognitive and emotional function, Machado et al. (2012) investigated the performance of B6Ei.GL-Nox3het/J mice ("*tilted Het*" mice) in a series of behavioral tests: the Y maze, place recognition, elevated plus maze tests, as well as the rotarod test as a measure of motor control. The mice were 6–8 months of age. In the object recognition test, only the wild-type controls exhibited an exploration time that was significantly greater than chance; however, the discrimination index was not significantly different between the two groups. In the spontaneous alternation test in the Y maze, again, only the wild-type controls but not the *Het* mice showed performance significantly greater than chance (**Figure 2**). In the place recognition test, wild-type mice spent significantly more time in the new arm compared to *Het* mice (**Figure 2**). However, the *Het* mice could execute neither the rotarod test nor the elevated plus maze test. The authors noted

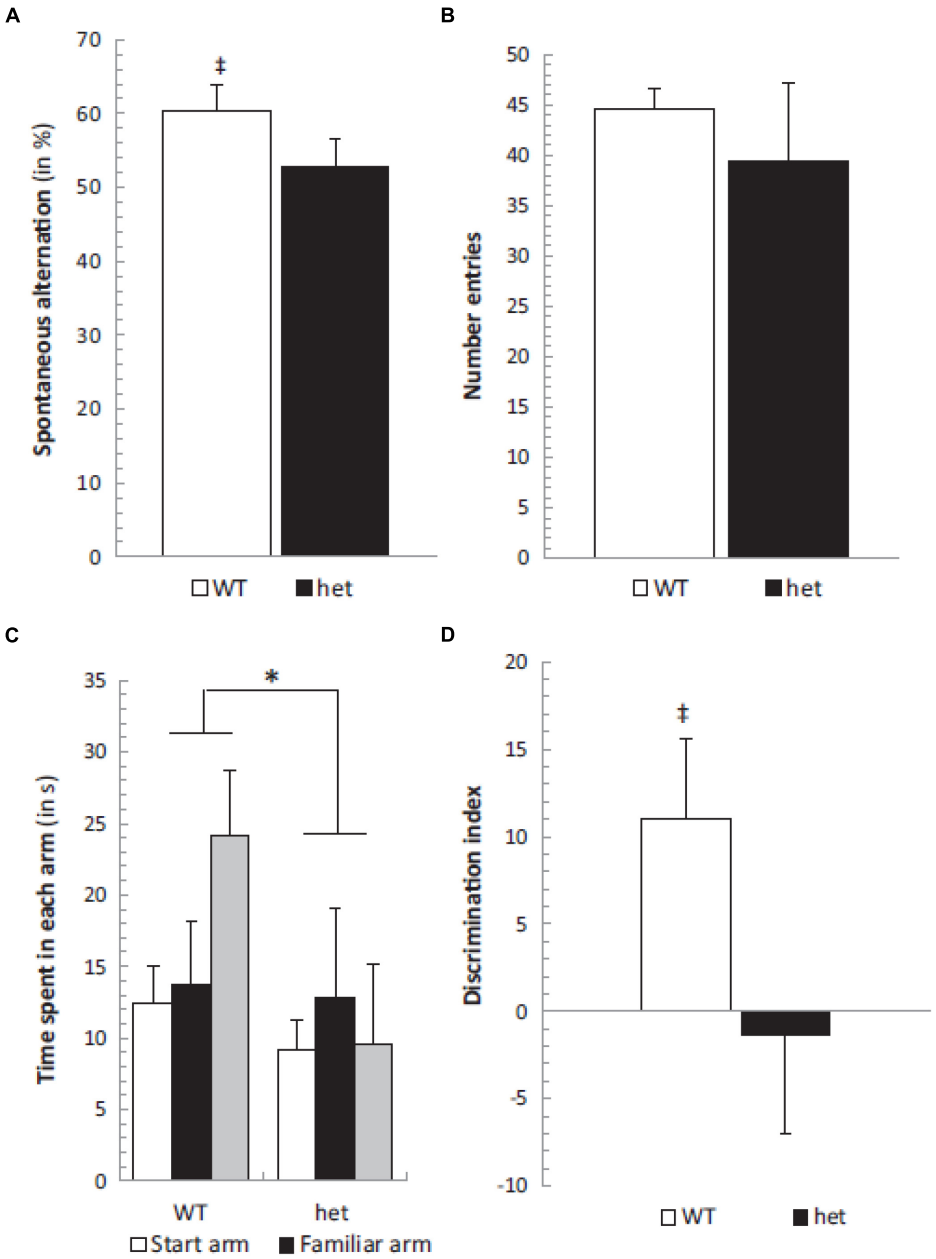

FIGURE 2 | Spontaneous alternation was significantly different from chance level (50%) in the WT group (‡, $p < 0.05$) **(A)** while the number of entries remained similar in both *het/het* and WT groups **(B)**. The place recognition test showed a significant group effect between WT and *het/het* mice without any specific arm effect or group × arm interaction, but the time spent in the new arm was significantly different in WT and *het/het* groups **(C)**. Additionally, the discrimination index was different between groups (* and ‡, $p < 0.05$), and not different from zero in the *het/het* group **(D)**. Reproduced from Machado et al. (2012) with permission.

that the *Het* mice were impaired in spatial memory performance (the spontaneous alternation and place recognition tests) but not non-spatial memory performance (object recognition test).

In order to explore the effects of otolith loss on spatial cognition specifically, Yoder and Kirby (2014) investigated spatial memory in mice lacking otolithic function using the B6.Cg-*Otop1*$^{tlt/J}$ model, evaluating their performance in both a radial arm maze and a Barnes task in light, compared to heterozygous controls. In this case the status of the mice as –/– or ± was determined using a swim test, since –/– mice are unable to swim at 12 weeks of age. *Tilted* mice were able to learn to navigate to a visible goal in the radial arm maze; however, they exhibited a significantly lower percentage of correct choices and their improvement in performance over trials was significantly worse than the controls (**Figure 3**). The authors analyzed the specific types of memory errors that were being made. *Tilted* mice made more reference memory (RM) errors (the mouse did not enter an arm that was a correct choice) than controls, and also a slower

rate of decrease in these errors over trials (**Figure 3**). *Tilted* mice also made more working memory (WM) errors than controls (i.e., either they re-entered an arm that was previously baited (WM-C) or an arm that had never been baited (WM-I)). The number of WM-C errors was higher for the *tilted* mice; however, this did not change across trials. For WM-I errors, *tilted* mice exhibited a greater number of them and this was maintained across trial blocks (**Figure 3**). The *tilted* mice showed a longer latency to complete the radial arm maze task, although the latency decreased across trials and was not significantly different compared to the control group.

In the case of the Barnes maze, the control and *tilted* mice were similar in terms of RM, with both groups employing a serial strategy during the first 2 days of the experiment. By the final day, the control mice were using either a spatial or serial strategy, whereas the *tilted* mice were still using a serial

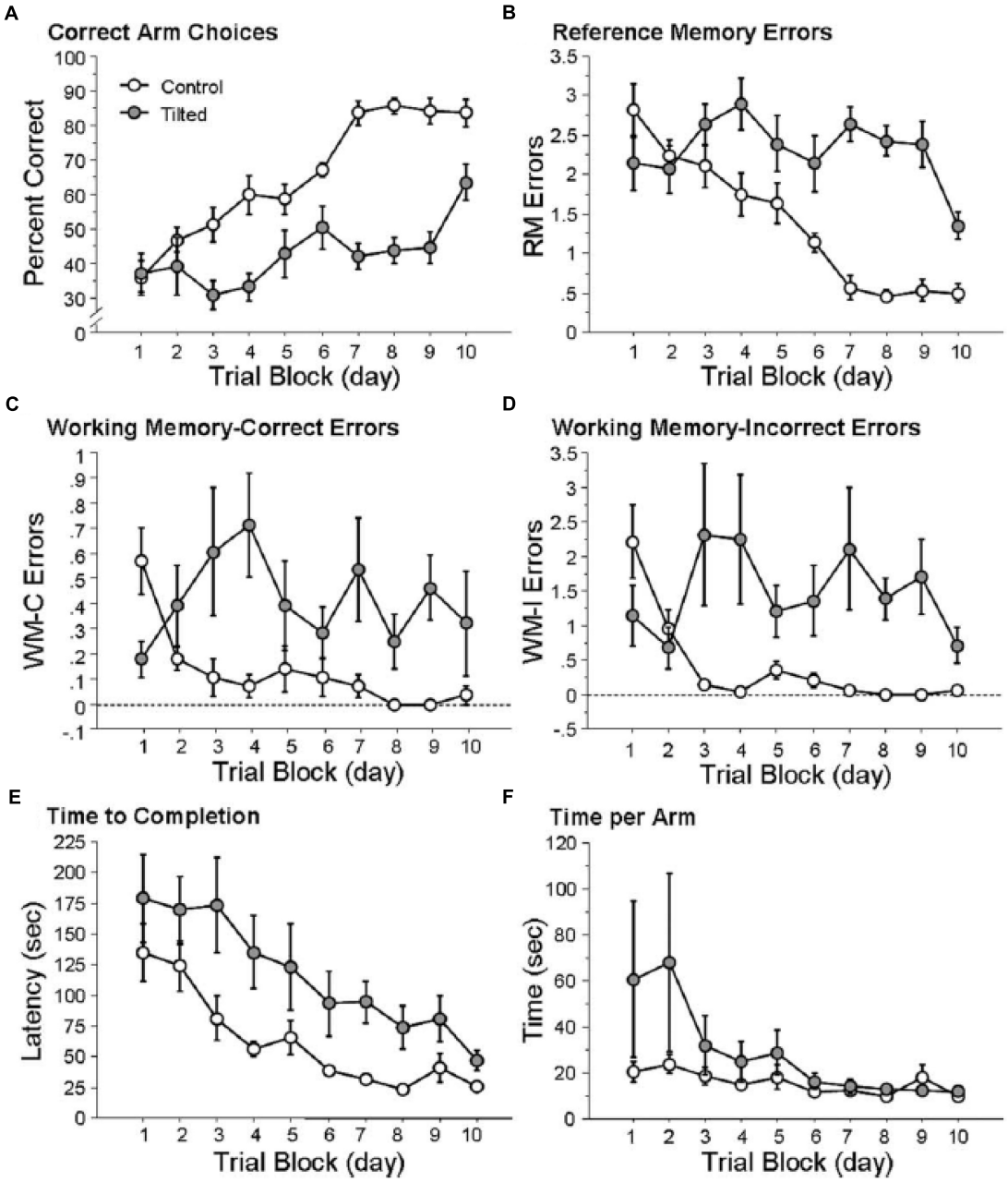

FIGURE 3 | *Tilted* mice were impaired at place learning on the radial arm maze. **(A)** Percentage of correct arm choices increased more rapidly across trial blocks for control mice than for *tilted* mice. **(B–D)** RM, WM-C, and WM-I errors decreased across trial blocks for control mice but not for *tilted* mice. **(E)** Latency to complete the task decreased across trial blocks for both groups. **(F)** Time per arm did not differ between control and *tilted* mice. Mean ± SEM. Reproduced from Yoder and Kirby (2014) with permission.

strategy. There were no significant differences in latency, error rates or distance traveled. The fact that the *tilted* mice were impaired in the radial arm maze but not the Barnes maze is very interesting. Impairment in the radial arm maze has been observed previously with complete bilateral vestibular lesions (e.g., Ossenkopp and Hargreaves, 1993; Russell et al., 2003a; Besnard et al., 2012); therefore, these results suggest that similar impairment in this task can be caused by otolith dysfunction alone. Yoder and Kirby (2014) suggested that the impaired performance of the *tilted* mice was a result of them not being able to discriminate between the arms of the radial arm maze, rather than any general memory deficit. The authors point out that rats with complete bilateral vestibular lesions have been reported to be unimpaired in an open field homing task when distal cues were available (Wallace et al., 2002; see also Stackman and Herbert, 2002), indicating that vestibular information is not necessary for the development of spatial memory. They suggest that in tasks such as these as well as the Barnes maze, animals are only required to navigate to a single goal which is defined by its position in relation to landmarks, whereas in the radial arm maze they are required to learn to navigate between multiple goals.

In a further study of the effects of otolith loss on spatial cognitive function, Yoder et al. (2015) studied the homing ability in the B6.Cg-*Otop1*$^{tlt/J}$ model, in both darkness and light, compared to heterozygous controls. The mice were classified as –/– or ± based on the same swim test, used by Yoder and Kirby (2014) and were 3–8 months of age at the beginning of testing. They found that in darkness, in the absence of visual information, the *tilted mice* made more short duration stops while they were on the outward journey to find food, and, once they had found it, their route home was more circuitous than for heterozygous control mice (see **Figure 4**). When this was quantified, the *tilted mice* exhibited greater heading error and journey duration than the controls. When they were tested in light, while the *tilted* mice still exhibited a more circuitous journey than the controls, their heading error and journey duration were similar. Blankenship et al. (2017) have also reported that B6.Cg-*Otop1*$^{tlt/J}$ mice, at 12 weeks of age, exhibit significantly greater circuitous exploratory movements in darkness, with greater changes in heading direction, compared to controls. The *tilted* mice also exhibited greater heading changes in light, and the authors concluded that they were using visual cues to compensate for the lack of otolithic information about self-motion.

As part of a larger study of the effects of otolith loss on sensorimotor development, Le Gall et al. (2019) evaluated *tilted Het* mice in a home retrieval test on post-natal day 9, in order to test their spatial memory. Their phenotype was confirmed by PCR and they were compared to heterozygous controls. The home retrieval test is based on the natural tendency of blind pups to find their way back to the safety of their nest, using olfactory information. Le Gall et al. (2019) found that the *Het* mice exhibited a significantly longer latency to reach the nest area, they spent significantly less time in that area and were significantly less successful in reaching it, compared to the controls (**Figure 5**). Although this task involved an element of spatial memory in the form of spatial olfactory guidance, the *Het* mice were found to exhibit significant delays in sensorimotor reflex development and ultrasonic communication; maternal care was, however, normal.

In the most recent study of the effects of otolith loss on cognitive and emotional function, Manes et al. (2019) used the *mergulhador (mlh)* otoconia-deficient mouse model, to investigate the effects of otolith deficiency on open field activity, performance in the novel object recognition test, the T maze alternation test, the elevated plus maze test as well as neurochemical activity in various brain regions. The *mlh* mutation was confirmed by genetic analysis and the mice were 8 weeks of age at the beginning of testing. Compared to *BALB/c* mice, the mutant mice exhibited reduced locomotor behavior and rearing, with increased grooming in the open field maze. Motor coordination on the wooden beam test was reduced, and immobility time increased in the tail suspension test. In addition, the mutant mice displayed reduced auricular reflexes and responsiveness to touch. Although the T maze performance was significantly reduced for the mutant mice, there were no significant differences for the novel object recognition test or the elevated plus maze test.

In order to explore the neurochemical basis of the effects of otolith loss, the authors conducted a neurochemical investigation of the cerebellum, anterior part of the cortex, striatum and hippocampus, following decapitation, and analyzed the levels of dopamine (DA), noradrenaline (NA) and their metabolites [4,4-dihydrophenylacetic acid (DOPAC) and homovanillic acid (HVA)], in addition to serotonin and its metabolite, 5-hydroindole, 3-acetic acid (5HIAA). The results were complex (see Table 2 in Manes et al., 2019), but suggested an increase in DA turnover in the hippocampus with a concomitant decreased turnover of DA and reduced NA activity in the frontal cortex. The authors suggested that these neurochemical alterations could be responsible for the impaired response of the *mlh* mice in the T maze task.

Taken together, although there is still a small number of studies, most of this evidence suggests that the loss of otolith function results in an impairment of spatial memory.

EVIDENCE FOR OTOLITHIC INVOLVEMENT IN SPATIAL MEMORY IN HUMANS

The studies described in the previous section provide evidence that the absence of otolith function from birth in mice, appears to cause spatial memory deficits. Is there also a relationship between otolithic dysfunction and spatial memory in humans and can this develop later in life? Over the last several years, a number of epidemiological studies have been published on the relationship between vestibular function, aging and spatial memory (see Agrawal et al., 2019 for a review). Many of these studies have related spatial memory specifically to cervical vestibular-evoked myogenic potentials (cVEMPs), a vestibulo-spinal reflex that originates in the saccular part of the otoliths (see Curthoys et al., 2017 for a review; see **Figure 1**). Some studies have also assessed ocular VEMPs (oVEMPs), which are generated by the utricle (see **Figure 1**).

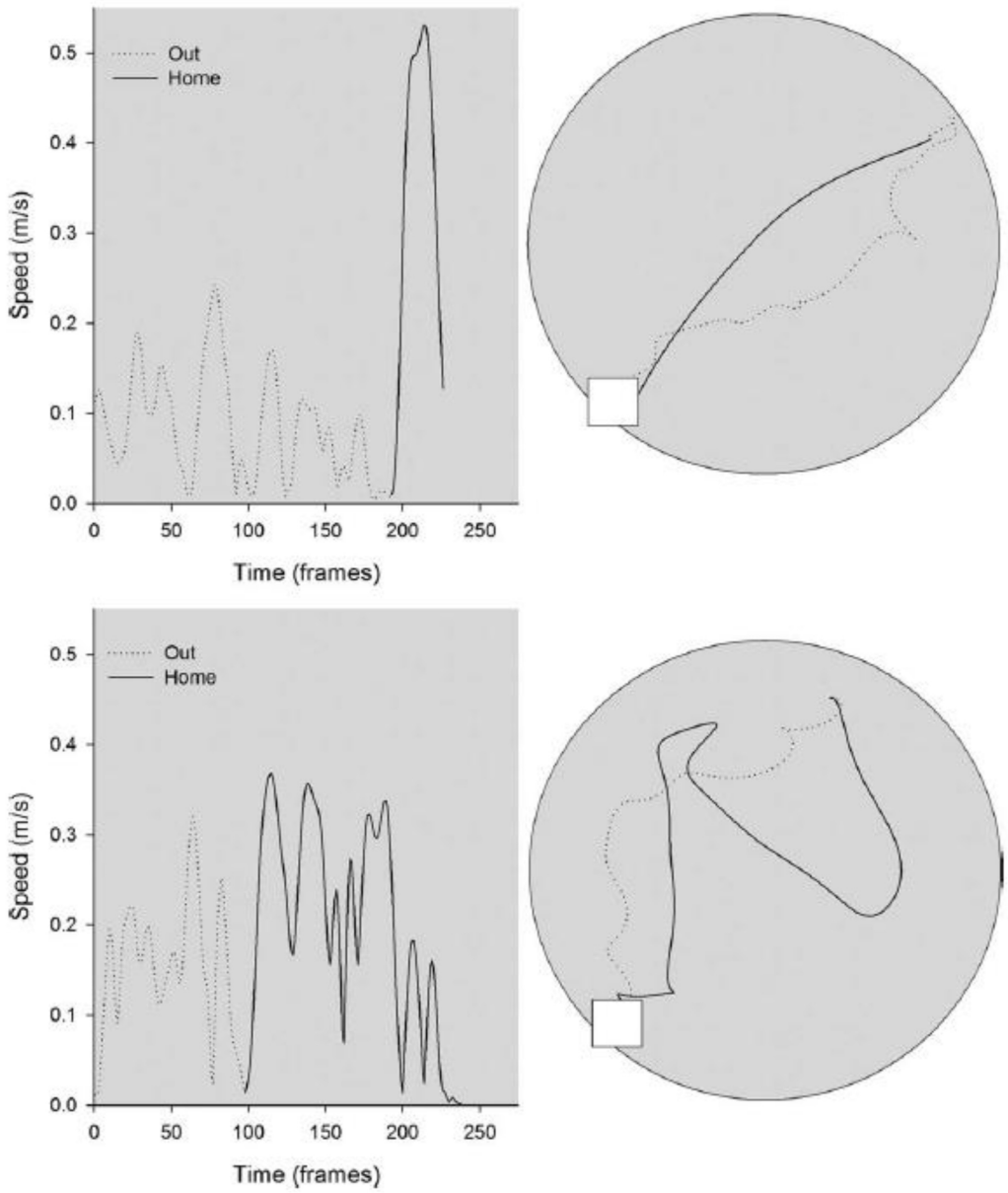

FIGURE 4 | Kinematic **(left)** and topographic **(right)** characteristics are plotted for a representative control **(top)** and *tilted* mouse **(bottom)** on the homing task in darkness. The outward path (gray dashed line) is circuitous for both mice; the homeward segment (black line) is relatively direct for the control mouse, but is more circuitous for the *tilted* mouse. Reproduced from Yoder et al. (2015) with permission.

Harun et al. (2016) studied older subjects with mild cognitive impairment (MCI, n = 15) or Alzheimer's Disease (AD, n = 32) and measured their cVEMPs and oVEMPs, comparing them with age-, sex-, and education-matched controls (n = 94) from the Baltimore Longitudinal Study of Aging (BLSA). Surprisingly, the authors found that bilaterally absent cVEMPs were associated with a more than 3-fold increased odds of AD (OR 3.42, 95% CI 1.33–8.91). However, there were no significant differences in vestibulo-ocular reflex (VOR) gain between the groups. The same group have reported that patients with MCI (n = 22) or AD (n = 28) and saccular dysfunction, measured using cVEMPs, made significantly more errors on the Money Road Map Test (MRMT) of spatial cognition compared to patients without vestibular impairment. AD patients who were spatially impaired exhibited a significantly greater prevalence of vestibular loss (Wei et al., 2018). Wei et al. (2017) examined driving ability in 21 patients with MCI and 39 with AD and related these data to saccular function. Using multiple regression, they found that patients with MCI or AD, who also had bilateral saccular impairment, had a significant increase in the odds of experiencing driving difficulty (OR 12.1; 95% CI 1.2, 117.7), compared to MCI or AD patients with normal saccular function.

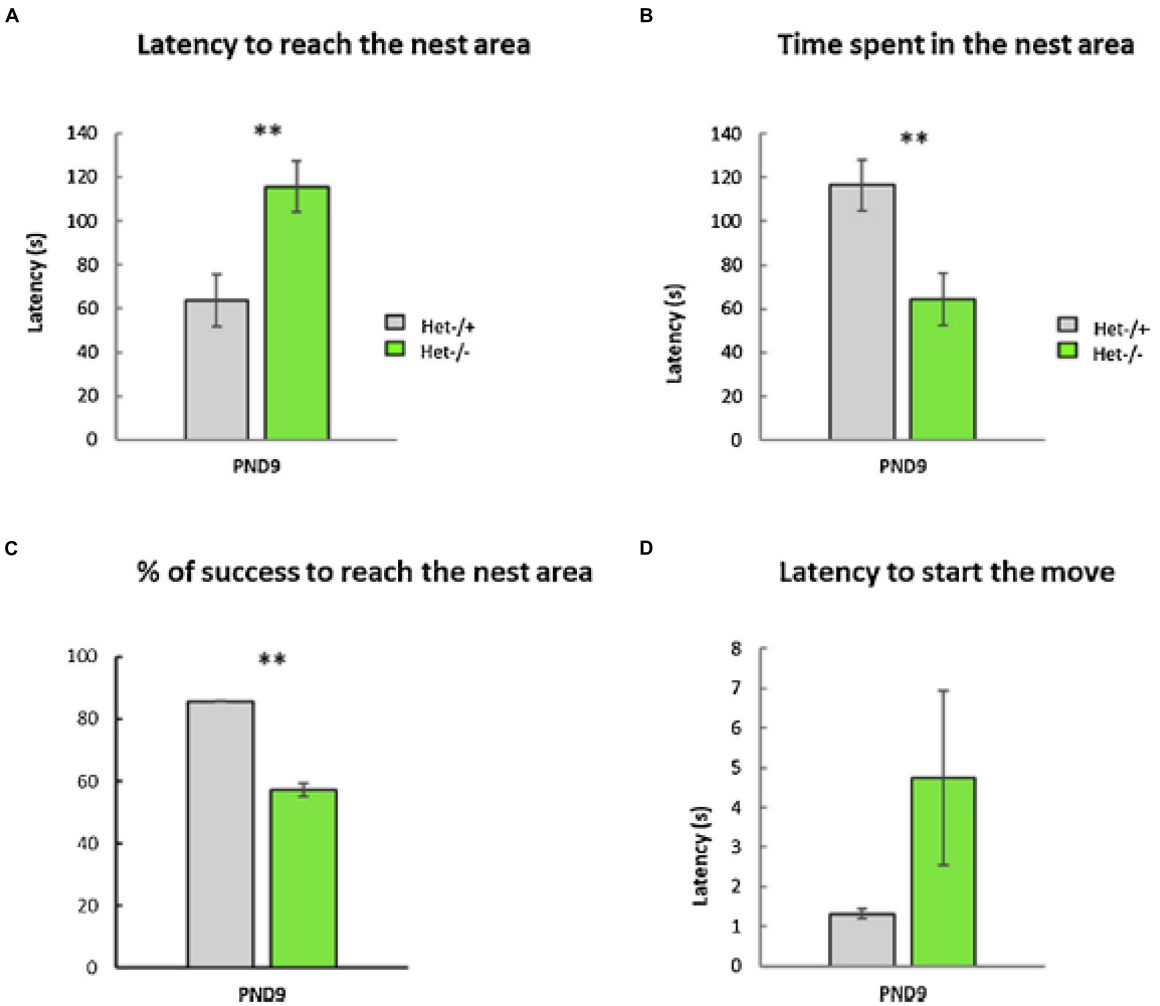

FIGURE 5 | The Home Retrieval test performed at PND9. No differences were detected between males and females; therefore, data were collapsed across sex (p-value > 0.05, $n = 25$ *Het–/–* versus 36 *Het–/+*). Two aberrant values were excluded in this test. **(A)** The *Het–/–* group needed significantly more time to reach the nest area compared to the *Het–/+* control group ("Latency to reach the nest," Mann–Whitney test, $p \leq 0.01$, **, data ± sem). **(B)** The time spent in the nest area was significantly lower in the *Het–/–* group compared to the *Het–/+* control group (Mann–Whitney test, $p \leq 0.01$, **, data ± sem). **(C)** The otolith-deficient *Het–/–* pups showed a lower percentage of success reaching the nest area compared to *Het–/+* mice (Chi^2-tests for equality of proportions, $p \leq 0.01$, **, data ± sem). **(D)** Conversely, the latency before the first movement reaction of pups (Mann–Whitney test, $p > 0.05$, ns, data ± sem) was similar in both groups (*Het–/–, Het–/+*). Reproduced from Le Gall et al. (2019) with permission.

The patients' performance on the MRMT suggested that the driving difficulty might be attributable to spatial memory deficits [see also Anson et al. (2019) and Pineault et al. (2019) for the most recent evidence].

Xie et al. (2017) studied the performance of young (<55 years) and older (≥55 years) subjects in the Triangle Completion Task (TCT), which tests spatial navigation ability, and related it to vestibular function. They found that loss of otolith function, as measured using the cVEMP, as well as loss of function of the semi-circular canals, was related to poor performance in the TCT in older subjects. Kamil et al. (2018) studied 103 subjects from the BLSA, measuring cVEMP function and relating it to MRI analysis of the hippocampus. They found that decreased saccular function, defined as a lower cVEMP amplitude, was significantly related to a lower average hippocampal volume. This result suggests the possibility that age-related impairment of spatial memory, as well as impairment of saccular function, may be related to a decrease in hippocampal volume. In their most recent study, Wei et al. (2019), studied 26 patients with MCI, 51 with AD and 295 matched control subjects and evaluated their cVEMPs, oVEMPs and VOR gain. They found that with increased cognitive impairment, there was a significant decrease in cVEMP and oVEMP responses. The VOR gain was lowest in MCI patients, followed by AD patients and then control subjects. Using logistic regression, they found that abnormal cVEMPs were associated with a 3-fold increased odds of MCI and a 5-fold increased odds of AD, and that abnormal oVEMPs were associated with an almost 4-fold increased odds of MCI and an over 4-fold increased odds of AD. However, VOR gain was not significantly related to the probability of having AD. See

Addendum for further references published while this paper was in press.

Vestibular loss has often been associated with depersonalization/derealization (DD) symptoms in humans (see Besnard et al., 2016 for a review). These symptoms include feelings of déjà vu, of time passing slowly, being "spaced out," difficulty concentrating, thoughts seeming blurred, one's body feeling strange and not feeling in control of one's self. In an experimental study, Aranda-Moreno and Jáuregui-Renaud (2016) used unilateral centrifugation in order to stimulate the utricle of 100 healthy subjects, who then completed a depersonalization/derealization (DD) questionnaire. The subjects reported symptoms such as "Body feels strange or different in some way" (56%) and "Time seems to pass very slowly" (55%). The authors concluded that utricular stimulation induces DD symptoms in healthy subjects.

EFFECTS OF OTOLITH LOSS ON NEURAL ACTIVITY

Given the evidence that loss of the otoliths in mice or otolith dysfunction in humans is associated with spatial memory deficits, it was logical to consider what effect the loss of otolithic information might have on the neural pathways subserving spatial memory. An obvious place to look was head direction cells in the thalamus and elsewhere, and place cells in the hippocampus, since they are known to be critical for spatial memory. Although it is clear that vestibular information is transmitted to the thalamus and hippocampus via polysynaptic pathways (see Hitier et al., 2014 for a review), the pathways through which specifically otolithic information might be communicated, are unclear.

Few studies have electrically stimulated the otoliths selectively in rodents, in order to determine where otolithic information might be represented in structures such as the hippocampus. Cuthbert et al. (2000) reported inducing field potentials in CA1 by selective electrical stimulation of the utricle in guinea pig, and furthermore they found that they could still induce field potentials when the stimulus amplitude was too low to evoke the VOR. Hitier et al. (2019) have also reported that they could induce local field potentials in many areas of the hippocampus by selective electrical stimulation of the utricle and saccule in anesthetized rats.

Thalamic Studies

Apart from selective otolithic stimulation, another way of studying the effect of the otoliths on brain regions which are spatially responsive, is to employ the same otolith-deficient mouse models that were described in the behavioral studies. The effects of otolith deficiency on the neural substrates of spatial navigation and memory were first studied by Taube (2011) and Yoder and Taube (2014) (for reviews). Stackman and Taube (1997) had demonstrated that the normal firing properties of head direction (HD) cells in the anterior thalamus of the rat, required vestibular input in general. Yoder and Taube (2009) used *Otop1*^{tlt} mice to investigate the effects of otolith deficiency on HD neurons in the anterodorsal thalamus. The firing properties of cells in the *tilted* mice were not as robust as those in wild-type *C57BL/6J* mice (see **Figure 6**) and exhibited significant degradation across trials. In similar experiments, Calton and Taube (2005) demonstrated that when rats performed inverted locomotion, 47% of HD cells in the anterodorsal thalamus showed no directional firing selectivity, even though they had demonstrated this on the walls before they were inverted. During the process of inverted locomotion, the action of gravity on the saccule should have been the opposite of what it is normally.

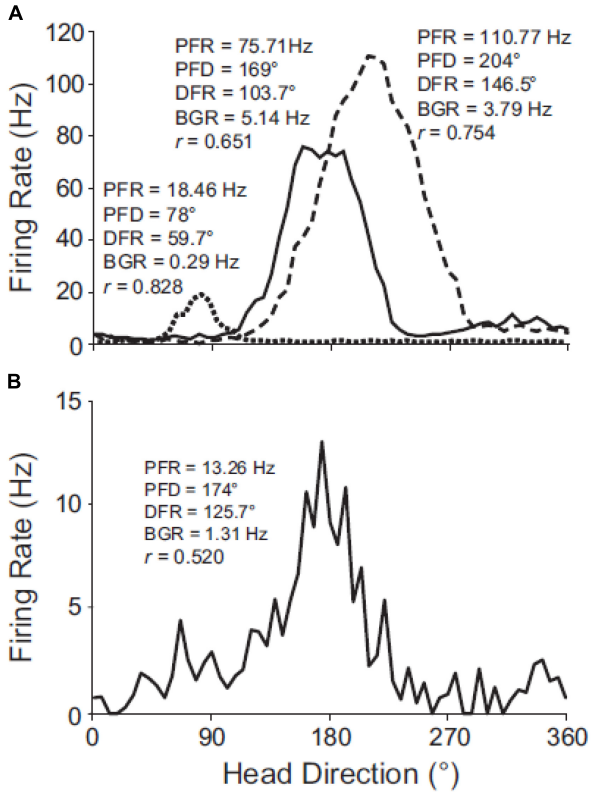

FIGURE 6 | Directional tuning curves of HD cells in C57BL/6J and *tilted* mice. **(A)** Robust directional tuning of three classic HD cells recorded simultaneously on different electrodes from the same C57BL/6J mouse. Peak firing rate (PFR), preferred direction (PFD), directional firing range (DFR), and background firing rate (BFR) are unique to each HD cell. **(B)** Tuning curve of representative HD cell recorded from a *tilted* mouse. Note the variable background firing rate (outside of the directional firing range) for the *tilted* HD cell, which contrasts with the relatively uniform background firing rates of C57BL/6J HD cells. Rayleigh's *r* is noted for each cell. Reproduced from Yoder and Taube (2009) with permission.

Some studies of HD cells have been conducted in microgravity, where the normal stimulation of the otoliths by gravitational acceleration is absent. Taube et al. (2004) studied anterodorsal thalamic HD cells during the zero gravity phase of parabolic flight. They found that HD cells maintained their directional tuning during both the zero gravity and hypergravity phases of the flight when the rat was positioned on the floor, but that when the rat climbed the wall or moved upside down on the ceiling in zero gravity, they lost their directional firing and exhibited

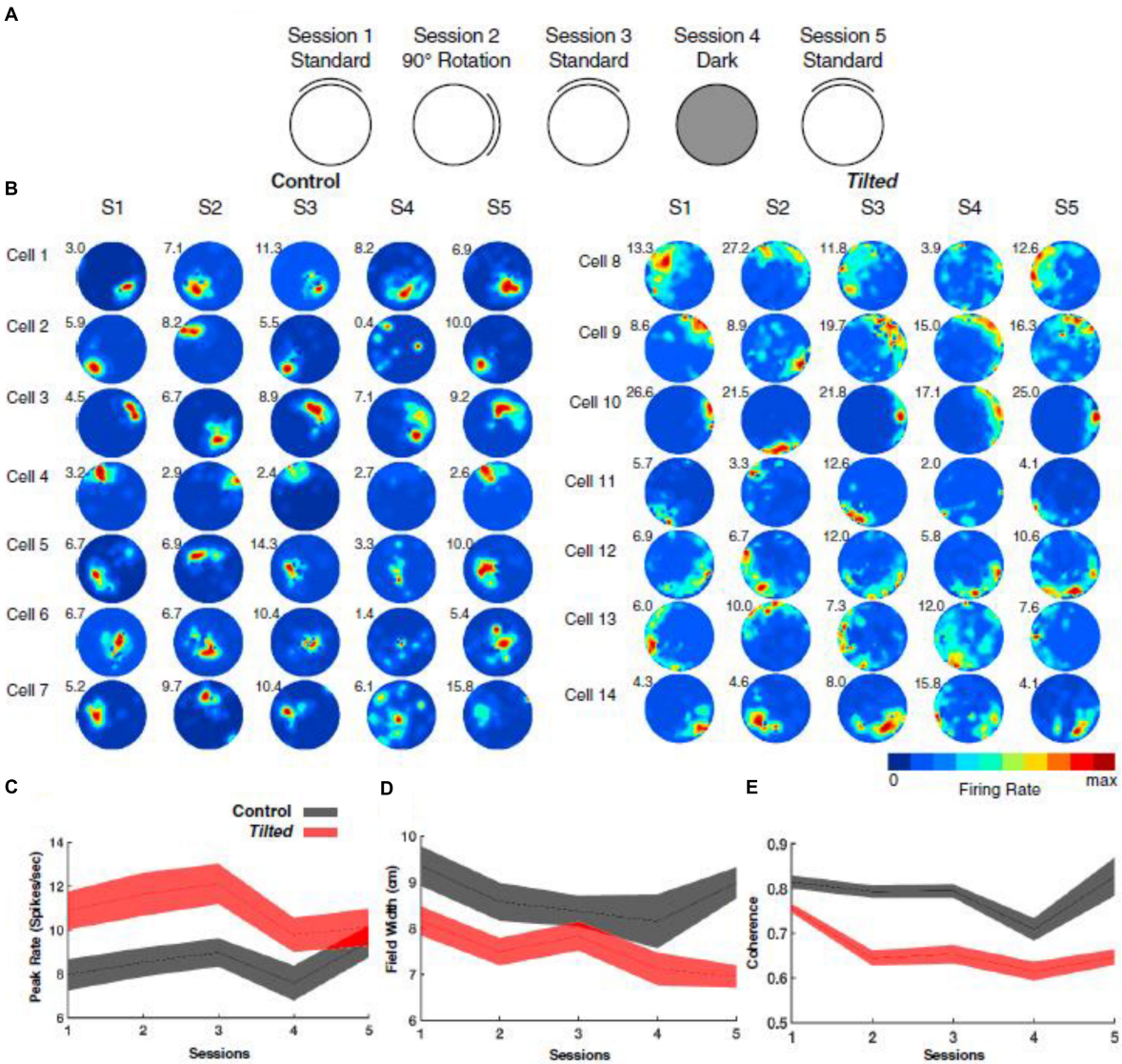

FIGURE 7 | Overview of experimental design, place-cell examples, and basic firing characteristics. **(A)** Depiction of recording procedure across five recording sessions: Session 1, cue card was positioned in the standard north position; Session 2, cue card was rotated 90° clockwise or counterclockwise from the standard location; Session 3, cue card was returned to the standard location; Session 4, cue card was removed, and overhead lights were extinguished; and Session 5, white cue card was replaced at the standard location, and lights were turned on. **(B)** Representative place cells from control (cells 1–7) and *tilted* (cells 8–14) mice over five sessions. Numbers at the top left of each rate map represent peak firing rate (Hz). **(C)** Plot showing the peak firing rate (spikes/second) for each place cell recorded in *tilted* and control mice with values from all sessions included. **(D)** Plot showing the field width (cm) for each place cell recorded in *tilted* and control mice with values from all sessions included. **(E)** Plot showing coherence measures for each place cell recorded in *tilted* and control mice with values from all sessions included. **(C–E)** Shaded error bars represent SEM. Reproduced from Harvey et al. (2018) with permission.

an increase in spontaneous firing rate. There was no significant difference for the peak firing rate and baseline firing rate for 1-G and 0-G on the floor, but significant decreases for the signal-to-noise ratio and information content of the HD firing. The cells exhibited a significantly reduced directionality score in 0-G, on average, by 25.8%, although they still exhibited directional tuning. While on the wall in 0-G, the HD cells that were recorded exhibited little directional preference. Compared to 0-G on the floor, all 7 HD cells that were recorded were found to lose their directional tuning when on the ceiling in 0-G: there were significant decreases in the signal-to-noise ratio, information content and the directionality score, with a significant increase in baseline firing rate. The authors speculated that during 0-G, the rats may have been experiencing visual reorientation illusions (VRIs).

The fact that both HD cell function and spatial memory are degraded by the loss of otolithic information, does not prove that there is a causal connection between the two. The data presented by Taube et al. (2004) would suggest that rats might have difficulty learning and remembering a spatial memory task

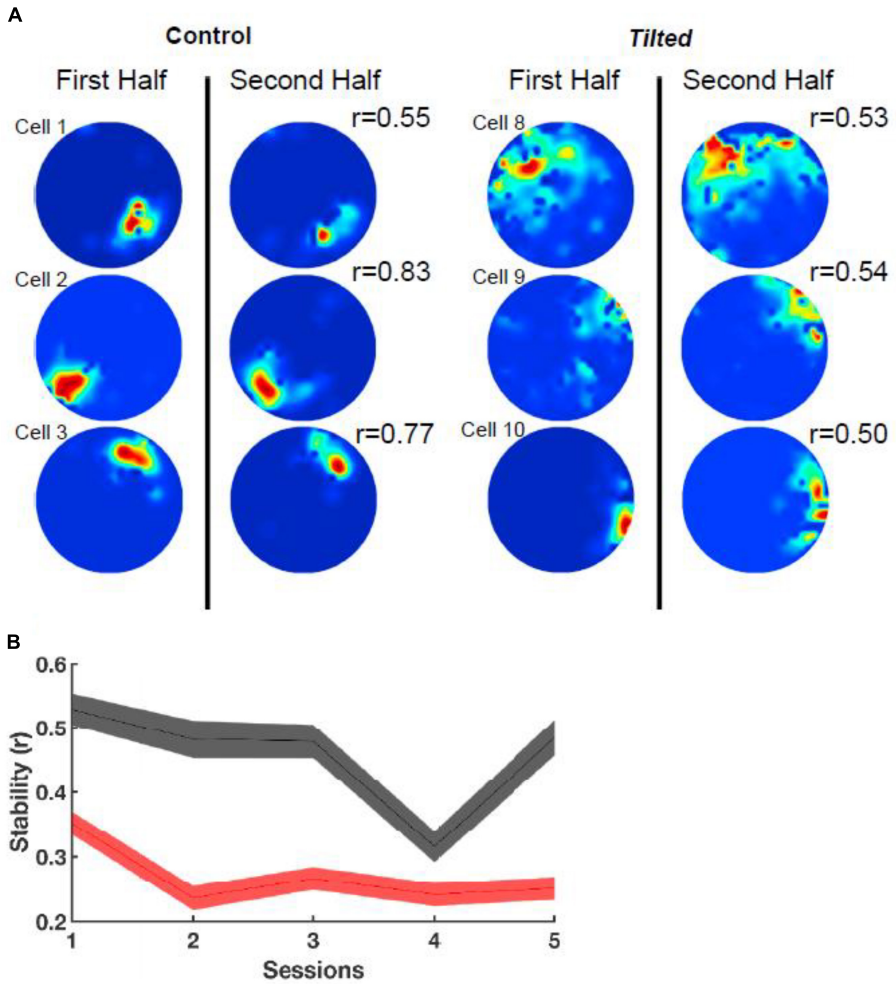

FIGURE 8 | Intra-session stability. **(A)** Rate maps depict the stability (r) between the first and second half of the first session using six example cells from **Figure 1**. Note that *tilted* cells appear to be less stable than control cells. **(B)** Stability between groups over all sessions. Note that *tilted* mice have much lower stability compared to control mice for all sessions. Red, *tilted*; black: control; shaded lines represent SEM. Reproduced from Harvey et al. (2018) with permission.

while upside down. Valerio et al. (2010) investigated whether rats that were inverted on a circular platform suspended from the ceiling, could learn to navigate to an escape hole from a start point. They found that none of the animals trained from 4 start points were able to reach the criterion, even following 29 training sessions; by contrast, all of the rats trained from one start point reached the criterion after a mean of 5.9 training sessions. Further experiments suggested that rats used distal visual landmarks when navigating from 1 or 2 start points, but that their performance was degraded when they needed to navigate to the escape hole from a novel start point. The authors suggested that in the upside down situation, the rats do not learn to reach a certain place, but rather learn a series of separate trajectories to reach the target.

One of the optimal ways of studying the effects of the loss of the otolithic response to gravitational acceleration, without using lesions or a mutant mouse model, is to investigate the behavior of mice in space. Ronca et al. (2019) have recently reported a study of mice aboard the International Space Station (ISS). Following a 4 day transit from Earth to the ISS, they analyzed the behavior of 16- and 32-week old female mice. They found that the young flight mice engaged in more physical activity than controls on Earth, but that 7–10 days following the launch, the younger, but not older mice, exhibited a form of "race-tracking behavior" which was expressed as circling. The significance of this result is unclear. Interestingly, however, circling and hyperactivity are common symptoms of bilateral vestibular loss in rats and mice (see Stiles and Smith, 2015, for a review).

Hippocampal Studies

In addition to thalamic HD cells, it is also of interest to determine the effects of the lack of graviception by the otoliths, on place cells in the hippocampus. Place cells in the hippocampus have been demonstrated to rely on input from the vestibular system (e.g., Stackman et al., 2002; Russell et al., 2003b); however, once again, the extent to which the otoliths are specifically implicated has been unclear. Knierim et al. (2000) had recorded hippocampal place cells on the Neurolab Spacelab Mission and reported, in

a brief letter, that normal place fields could be obtained by day 9 of the space flight. However, the more comprehensive NASA report did indicate that abnormal place fields were observed earlier in the flight, for example, day 4 (Knierim et al., 2003). The only study to address this question using otolith-deficient mice is by Harvey et al. (2018), who recorded hippocampal place cells in B6.Cg-*Otop1tlt/j tilted* mice (Jackson Laboratories, Bar Harbor, ME). They investigated place cells across five sessions (standard, cue rotation, standard, dark, standard) and found that those in *tilted* mice exhibited higher peak firing rates, with lower spatial coherence and smaller fields, compared to controls (see **Figure 7**); on the other hand, the average firing rates and spatial information content, were similar between the groups. The place fields from *tilted* mice were also less smooth than for controls and were concentrated near boundaries. Although hippocampal place cells are modulated by theta rhythm and theta has been reported to be degraded following complete bilateral vestibular loss (e.g., Russell et al., 2006), place cell activity was still modulated by theta in *tilted* mice. The place fields from *tilted* mice exhibited lower intra-trial stability than controls (**Figure 8**). It had been suggested in previous studies that otolithic information might be especially important for accurate spatial navigation performance in darkness in homing tasks and radial arm mazes (Yoder and Kirby, 2014; Yoder et al., 2015).

One of the most recent studies linking hippocampal and otolithic function in mice is by Kompotis et al. (2019). They observed that rocking mice at 1 Hz increased the amount of time spent in non-rapid eye movement sleep by accelerating the onset of sleep and shortening waking episodes, and that during active wakefulness, the theta EEG (6–10 Hz) moved toward slower frequencies. They used *Otop1*$^{tlt/tlt}$ *tilted* mice to test whether the otoliths were involved in this phenomenon and found that they were insensitive to rocking at 1 Hz and did not exhibit the same changes in theta EEG.

Although some would consider that galvanic vestibular stimulation (GVS) might be useful to probe the effects of otolith stimulation on the brain (e.g., Cohen et al., 2012), the evidence that it affects "mainly" the otoliths, is divided, and there is evidence that it also affects the semi-circular canals (see Curthoys and MacDougall, 2012, for a review). Therefore, GVS studies will not be discussed here.

CONCLUSION

These studies suggest that the otolithic part of the peripheral vestibular system, the utricle and saccule, make some contribution to spatial learning and memory in tests such as the radial arm maze, Y maze and homing tasks, but not the Barnes task or non-spatial memory tests such as the object recognition test or elevated plus maze task. The link between otolithic function and spatial memory is reinforced by human epidemiological studies in which it has been shown that saccular function, as measured using cVEMPs, is a predictor of the odds of having poor spatial memory, AD, and a smaller hippocampal volume. A link between hippocampal volume and vestibular function was first reported by Brandt et al. (2005), in a study in which patients with bilateral vestibular loss were found to have a bilateral atrophy of the hippocampus of approximately 17%. However, it was not clear from this study whether the otoliths were important in this relationship. The neurophysiological studies in otolith-deficient mice indicate that otolithic function is important for the normal function of both thalamic HD cells and hippocampal place cells, although HD cells can maintain directional tuning as long as they are on the floor in microgravity (Taube et al., 2004) and place cells can still develop place fields in microgravity (Knierim et al., 2000, 2003). Taube et al. (2004) suggested that the loss of directional firing of HD cells when they are on the walls or ceiling in 0-G may be a correlate of Type II/III spatial disorientation in humans, in which the subject is consciously aware of their disorientation and tries to correct it (Type II) or is so disoriented that they are incapacitated (Type III), respectively. Clearly, the loss of HD cell tuning is due to more than the loss of a gravitational signal (Taube et al., 2004).

In the case of the otolith-deficient mice, which is the easiest form of otolith manipulation to interpret, an interesting question is whether the sensation of linear acceleration by gravity is more important for spatial memory than the sensation of other kinds of linear acceleration, such as translation in the anterio-caudal or medio-lateral planes? In fact, the "tilt-translation illusion" demonstrates that the otoliths cannot distinguish between tilting of the head with respect to gravitational vertical and any other kind of linear acceleration that would induce the same stimulation of the otoliths ("Einstein's Equivalence Principle," Merfeld et al., 1999; **Figure 9**). Therefore, the brain must use information from the semi-circular canals and other sensory information to disambiguate tilt from translation (Merfeld et al., 1999; Straka et al., 2016). Since every form of sensory stimulation on Earth must be interpreted in terms of the framework of gravitational acceleration, it may be that otolithic stimulation is essential for normal spatial learning and memory. This is consistent with the evolutionary age of the otoliths. Although

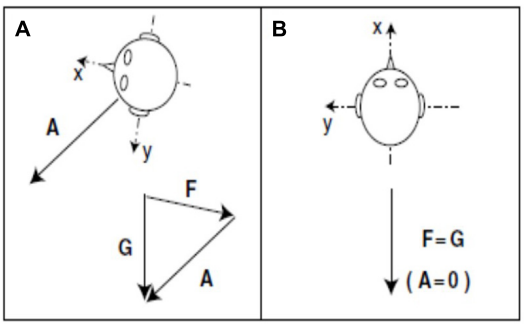

FIGURE 9 | During acceleration on Earth, gravity (G) minus linear acceleration (A) yields specific gravito-inertial force (GIF, F). Different combinations of gravity and linear acceleration can yield the same measured GIF. **(A)** GIF equals gravity minus linear acceleration (F = G – A or F + A = G). **(B)** GIF equals gravity alone. Since the measurement of GIF relative to the head is identical for these two situations, additional information is required for the nervous system to determine how much of the measured GIF is due to gravity and how much is due to linear acceleration.

a number of studies have attempted to neutralize the influence of the vestibular system by fixing the heads of rats or mice and recording from HD, place or grid cells (e.g., Harvey et al., 2009; Ravassard et al., 2013; Aghajan et al., 2015; Acharya et al., 2016), it is debatable whether these studies have done any more than "minimize" vestibular stimulation, because the head will still be subject to linear acceleration by gravity.

Yoder and Taube (2009) speculated that part of the explanation for the broader tuning curves of HD cells in *tilted* mice in light, might be degraded visual perception of visual cues due to an impaired VOR ("oscillopsia"). This certainly seems possible in light, however, the greater reductions in HD cell directional preference in darkness indicates that oscillopsia is not necessary for their impaired function. The authors suggested that loss of otolithic function may impair velocity storage, which provides a prolonged representation of the angular velocity signal in the brain and may be necessary for accurate spatial navigation. Although the otoliths do not encode angular acceleration themselves, they are known to be important in velocity storage (e.g., Angelaki et al., 1992; Koizuka et al., 1996; Mittelstaedt and Mittelstaedt, 1996; Wearne et al., 1999). Recent studies using *Otop1* mice show that although the otoliths do not appear to contribute to the baseline angular velocity of the VOR in mice, they are necessary for its adaptation to changes in gravitational stimulation (Khan et al., 2019a,b). As Shinder and Taube (2014) noted, the fact that the otoliths are known to be important for HD cell firing, suggests that linear acceleration information from the otoliths and rotational acceleration information from the semi-circular canals, must converge by the time they reach the thalamus. Indeed, Curthoys and Markham (1971) demonstrated the convergence of otolith and semi-canal signals at the level of the medial vestibular nucleus.

Taken together, the evidence to date suggests that the otolithic organs of the vestibular system are important for normal spatial learning and memory. Although the mechanisms by which they contribute to these processes are yet to be fully elucidated, the saccule and utricle appear to contribute to the development and maintenance of normal HD and place cell signals. This may be due to the evolutionary age of this part of the vestibular system and the fact that velocity storage has become an important part of the way that the brain encodes its place in space (Yoder and Taube, 2009).

AUTHOR CONTRIBUTIONS

PS conceived the study and wrote the manuscript.

REFERENCES

Acharya, L., Aghajan, Z. M., Vuong, C., Moore, J. J., and Mehta, M. R. (2016). Causal influence of visual cues on hippocampal directional selectivity. *Cell* 164, 197–207. doi: 10.1016/j.cell.2015.12.015

Aghajan, Z. M., Acharya, L., Moore, J. J., Cushman, J. D., Vuong, C., and Mehta, M. R. (2015). Impaired spatial selectivity and intact phase precession in two-dimensional virtual reality. *Nat. Neurosci.* 18, 121–128. doi: 10.1038/nn.3884

Agrawal, Y., Smith, P. F., and Rosenberg, P. B. (2019). Vestibular impairment, cognitive decline and Alzheimer's disease: balancing the evidence. *Aging Mental Health* 29, 1–4. doi: 10.1080/13607863.2019.1566813

Agrawal, Y., Zuniga, M. G., Davalos-Bichara, M., Schubert, M. C., Walston, J. D., Hughes, J., et al. (2012). Decline in semicircular canal and otolith function with age. *Otol. Neurotol.* 33, 832–839. doi: 10.1097/MAO.0b013e3182545061

Andreescu, C. E., De Ruiter, M. M., De Zeeuw, C. I., and De Jeu, M. T. (2005). Otolith deprivation induces optokinetic compensation. *J. Neurophysiol.* 94, 3487–3496. doi: 10.1152/jn.00147.2005

Angelaki, D. E., Perachio, A. A., Mustari, M. J., and Strunk, C. L. (1992). Role of irregular otolith afferents in the steady-state nystagmus during off-vertical axis rotation. *J. Neurophysiol.* 68, 1895–1900. doi: 10.1152/jn.1992.68.5.1895

Anson, E. R., Ehrenburg, M. R., Wei, E. X., Bakar, D., Simonsick, E., and Agrawal, Y. (2019). Saccular function is associated with both angular and distance errors on the triangle completion test. *Clin. Neurophysiol.* 130, 2137–2143. doi: 10.1016/j.clinph.2019.08.027 [Epub ahead of print].

Aranda-Moreno, C., and Jáuregui-Renaud, K. (2016). Derealization during utricular stimulation. *J. Vestib. Res.* 26, 425–431. doi: 10.3233/VES-160597

Baek, J.-H., Zheng, Y., Darlington, C. L., and Smith, P. F. (2010). Evidence that spatial memory deficits in rats following bilateral vestibular loss are probably permanent. *Neurobiol. Learn. Mem.* 94, 402–413. doi: 10.1016/j.nlm.2010.08.007

Baker, R. (1998). From genes to behavior in the vestibular system. *Otolaryngol. Head Neck Surg.* 119, 263–275. doi: 10.1016/s0194-5998(98)70061-0

Bergstrom, R. A., You, Y., Erway, L. C., Lyon, M. F., and Schimenti, J. C. (1998). Deletion mapping of the head tilt (het) gene in mice: a vestibular mutation causing specific absence of otoliths. *Genetics* 150, 815–822.

Besnard, S., Lopez, C., Brandt, T., Denise, P., and Smith, P. F. (eds) (2016). "The vestibular system in cognitive and memory processes in mammals," in *Frontiers in Integrative Neuroscience*, (Lausanne: Frontiers Media), 246.

Besnard, S., Machado, M. L., Vignaux, G., Boulouard, M., Coquerel, A., Bouet, V., et al. (2012). Influence of vestibular input on spatial and nonspatial memory and on hippocampal NMDA receptors. *Hippocampus.* 22, 814–826. doi: 10.1002/hipo.20942

Blankenship, P. A., Cherep, L. A., Donaldson, T. N., Brockman, S. N., Trainer, A. D., Yoder, R. M., et al. (2017). Otolith dysfunction alters exploratory movement in mice. *Behav. Brain Res.* 325, 1–11. doi: 10.1016/j.bbr.2017.02.031

Brandt, T., Schautzer, F., Hamilton, D. A., Bruning, R., Markowitsch, H., Kalla, R., et al. (2005). Vestibular loss causes hippocampal atrophy and impaired spatial memory in humans. *Brain* 128, 2732–2741. doi: 10.1093/brain/awh617

Calton, J. L., and Taube, J. S. (2005). Degradation of head direction cell activity during inverted locomotion. *J. Neurosci.* 25, 2420–2428. doi: 10.1523/jneurosci.3511-04.2005

Cohen, B., Yakushin, S. B., and Holstein, G. R. (2012). What does galvanic vestibular stimulation actually activate? *Front. Neurol.* 2:90. doi: 10.3389/fneur.2011.00090

Cullen, K. E. (2012). The vestibular system: multimodal integration and encoding of self-motion for motor control. *Trends Neurosci.* 35, 185–196. doi: 10.1016/j.tins.2011.12.001

Curthoys, I. S., and MacDougall, H. G. (2012). What galvanic vestibular stimulation actually activates. *Front. Neurol.* 3:117. doi: 10.3389/fneur.2012.00117

Curthoys, I. S., MacDougall, H. G., Vidal, P. P., and de Waele, C. (2017). Sustained and transient vestibular systems: a physiological basis for interpreting vestibular function. *Front. Neurol.* 8:117. doi: 10.3389/fneur.2017.00117

Curthoys, I. S., and Markham, C. H. (1971). Convergence of labyrinthine influences on units in the vestibular nuclei of the cat. I. Natural stimulation. *Brain Res.* 35, 469–490. doi: 10.1016/0006-8993(71)90489-6

Cuthbert, P. C., Gilchrist, D. P., Hicks, S. L., MacDougall, H. G., and Curthoys, I. S. (2000). Electrophysiological evidence for vestibular activation of the guinea pig hippocampus. *Neuroreport* 11, 1443–1447. doi: 10.1097/00001756-200005150-00018

de Caprona, M. D., Beisel, K. W., Nichols, D. H., and Fritzsch, B. (2004). Partial behavioral compensation is revealed in balance tasked mutant mice lacking otoconia. *Brain Res. Bull.* 64, 289–301. doi: 10.1016/j.brainresbull.2004.08.004

Deroualle, D., and Lopez, C. (2014). Toward a vestibular contribution to social cognition. *Front. Integr. Neurosci.* 8:16. doi: 10.3389/fnint.2014.00016

Fritzsch, B. (1998). Evolution of the vestibulo-ocular system. *Otolaryngol. Head Neck Surg.* 119, 182–192. doi: 10.1016/s0194-5998(98)70053-1

Harun, A., Oh, E. S., Bigelow, R. T., Studenski, S., and Agrawal, Y. (2016). Vestibular impairment in dementia. *Otol. Neurotol.* 37, 1137–1142. doi: 10.1097/mao.0000000000001157

Harvey, C. D., Collman, F., Dombeck, D. A., and Tank, D. W. (2009). Intracellular dynamics of hippocampal place cells during virtual navigation. *Nature* 461, 941–946. doi: 10.1038/nature08499

Harvey, R. E., Rutan, S. A., Willey, G. R., Siegel, J. J., Clark, B. J., and Yoder, R. M. (2018). Linear self-motion cues support the spatial distribution and stability of hippocampal place cells. *Curr. Biol.* 28:1803-1810.e5. doi: 10.1016/j.cub.2018.04.034

Hitier, M., Besnard, S., and Smith, P. F. (2014). Vestibular pathways involved in cognition. *Front. Integr. Neurosci.* 8:59. doi: 10.3389/fnint.2014.00059

Hitier, M., Sato, G., Zhang, Y., Zheng, Y., Besnard, S., Smith, P. F., et al. (2016). Anatomy and surgical approach to rat's vestibular sensors and nerves. *J. Neurosci. Meth.* 270, 1–8. doi: 10.1016/j.jneumeth.2016.05.013

Hitier, M., Zhang, Y., Sato, G., Besnard, S., Zheng, Y., and Smith, P. F. (2019). *Stratification of Hippocampal Electrophysiological Activation Evoked by Electrical Stimulation of Different Parts of the Rat Peripheral Vestibular System*. L Taormina: Spring Hippocampal Research Conference.

Jamon, M. (2014). The development of vestibular system and related functions in mammals: impact of gravity. *Front. Integr. Neurosci.* 8:11. doi: 10.3389/fnint.2014.00011

Jeffery, N., and Spoor, F. (2004). Prenatal growth and development of the modern human labyrinth. *J. Anat.* 20, 471–492.

Jones, T. A., Jones, S. M., and Hoffman, L. F. (2008). Resting discharge patterns of macular primary afferents in otoconia-deficient mice. *J. Assoc. Res. Otolaryngol.* 9, 490–505. doi: 10.1007/s10162-008-0132-0

Kamil, R. J., Jacob, A., Ratnanather, J. T., Resnick, S. M., and Agrawal, Y. (2018). Vestibular function and hippocampal volume in the Baltimore Longitudinal Study of Aging (BLSA). *Otol. Neurotol.* 39, 765–771. doi: 10.1097/MAO.0000000000001838

Khan, S. I., Della Santina, C. C., and Migliaccio, A. A. (2019a). Angular vestibuloocular reflex responses in Otop1 mice. I. Otolith sensor input is essential for gravity context-specific adaptation. *J. Neurophysiol.* 121, 2291–2299. doi: 10.1152/jn.00811.2018

Khan, S. I., Della Santina, C. C., and Migliaccio, A. A. (2019b). Angular vestibuloocular reflex responses in Otop1 mice. II. Otolith sensor input improves compensation after unilateral labyrinthectomy. *J. Neurophysiol.* 121, 2300–2307. doi: 10.1152/jn.00812.2018

Kim, E., Hyrc, K. L., Speck, J., Lundberg, Y. W., Salles, F. T., Kachar, B., et al. (2010). Regulation of cellular calcium in vestibular supporting cells by otopetrin 1. *J. Neurophysiol.* 104, 3439–3450. doi: 10.1152/jn.00525.2010

Kingma, H., and Van De Berg, R. (2016). "Anatomy, physiology and physics of the peripheral vestibular system," in *Handbook of Clinical Neurology*, Vol. 137, Chapter 1, eds J. M. Furman and T. Lempert (New York, NY: Elsevier), 1–16.x.

Knierim, J. J., McNaughton, B. L., and Poe, G. R. (2000). Three-dimensional spatial selectivity of hippocampal neurons during space flight. *Nat. Neurosci.* 3, 209–210. doi: 10.1038/72910

Knierim, J. J., Poe, G. R., and McNaughton, B. L. (2003). "Ensemble neural coding of place in zero-G," in *The Neurolab Spacelab Mission: Neuroscience Research in Space: Results from the STS-90, Neurolab Spacelab Mission. NASA SP-2003-535*, eds J. C. Buckey, and J. L. Homick (Houston, TX: Johnson Space Center), 63–68.

Koizuka, I., Schor, R. H., and Furman, J. M. (1996). Influence of otolith organs, semicircular canals, and neck afferents on post-rotatory nystagmus. *J. Vestib. Res.* 6, 319–329.

Kompotis, K., Hubbard, J., Emmenegger, Y., Perrault, A., Mühlethaler, M., Schwartz, S., et al. (2019). Rocking promotes sleep in mice through rhythmic stimulation of the vestibular system. *Curr. Biol.* 29, 392–401. doi: 10.1016/j.cub.2018.12.007

Le Gall, A., Hilber, P., Chesneau, C., Bulla, J., Toulouse, J., Machado, M. L., et al. (2019). The critical role of vestibular graviception during cognitive-motor development. *Behav. Brain Res.* 372:112040. doi: 10.1016/j.bbr.2019.112040

Lim, R., and Brichta, A. M. (2016). Anatomical and physiological development of the human inner ear. *Hear. Res.* 338, 9–21. doi: 10.1016/j.heares.2016.02.004

Lopez, C., Falconer, C. J., Deroualle, D., and Mast, F. W. (2015). In the presence of others: self-location, balance control and vestibular processing. *Neurophysiol. Clin.* 45, 241–254. doi: 10.1016/j.neucli.2015.09.001

Machado, M. L., Kroichvili, N., Freret, T., Philoxène, B., Lelong-Boulouard, V., Denise, P., et al. (2012). Spatial and non-spatial performance in mutant mice devoid of otoliths. *Neurosci. Letts.* 522, 57–61. doi: 10.1016/j.neulet.2012.06.016

Manes, M., de, S. A., Garcia-Gomes, M., Sandini, T. M., Zaccarelli-Magalhães, J., Florio, J. C., et al. (2019). Behavioural and neurochemical characterization of the mlh mutant mice lacking otoconia. *Behav. Brain Res.* 359, 958–966. doi: 10.1016/j.bbr.2018.06.012

Manzari, L., MacDougall, H. G., Burgess, A. M., and Curthoys, I. S. (2014). Selective otolith dysfunction objectively verified. *J. Vestib. Res.* 24, 365–373. doi: 10.3233/VES-140537

Mast, F. W., Preuss, N., Hartmann, M., and Grabherr, L. (2014). Spatial cognition, body representation and affective processes: the role of vestibular information beyond ocular reflexes and control of posture. *Front. Integr. Neurosci.* 8:44. doi: 10.3389/fnint.2014.00044

Merfeld, D. M., Zupan, L., and Peterka, R. J. (1999). Humans use internal models to estimate gravity and linear acceleration. *Nature* 398, 615–618. doi: 10.1038/19303

Mittelstaedt, M. L., and Mittelstaedt, H. (1996). The influence of otoliths and somatic graviceptors on angular velocity estimation. *J. Vestib. Res.* 6, 355–366.

Ossenkopp, K. P., and Hargreaves, E. L. (1993). Spatial learning in an enclosed eight-arm radial maze in rats with sodium arsanilate-induced labyrinthectomies. *Behav. Neural Biol.* 59, 253–257. doi: 10.1016/0163-1047(93)91034-k

Paffenholz, R. (2004). Vestibular defects in head-tilt mice result from mutations in Nox3, encoding an NADPH oxidase. *Genes Dev.* 18, 486–491. doi: 10.1101/gad.1172504

Pineault, K., Pearson, D., Wei, E., Kamil, R., Klatt, B., and Agrawal, Y. (2019). Association between saccule and semicircular canal impairments and cognitive performance among vestibular patients. *Ear Hear.* doi: 10.1097/AUD.0000000000000795 [Epub ahead of print].

Ravassard, P., Kees, A., Willers, B., Ho, D., Aharoni, D. A., Cushman, J., et al. (2013). Multisensory control of hippocampal spatiotemporal selectivity. *Science* 340, 1342–1346. doi: 10.1126/science.1232655

Ronca, A. E. (2003). Mammalian development in space. *Adv. Space Biol. Med.* 9, 217–251. doi: 10.1016/s1569-2574(03)09009-9

Ronca, A. E., Fritzsch, B., Bruce, L. L., and Alberts, J. R. (2008). Orbital spaceflight during pregnancy shapes function of mammalian vestibular system. *Behav. Neurosci.* 122, 224–232. doi: 10.1037/0735-7044.122.1.224

Ronca, A. E., Moyer, E. L., Talyansky, Y., Lowe, M., Padmanabhan, S., Choi, S., et al. (2019). Behavior of mice aboard the international space station. *Sci. Rep.* 9:4717.

Russell, N., Horii, A., Smith, P. F., Darlington, C. L., and Bilkey, D. (2003a). Effects of bilateral vestibular deafferentation on radial arm maze performance. *J. Vest. Res.* 13, 9–16.

Russell, N., Horii, A., Smith, P. F., Darlington, C. L., and Bilkey, D. (2003b). The long-term effects of permanent vestibular lesions on hippocampal spatial firing. *J. Neurosci.* 23, 6490–6498. doi: 10.1523/jneurosci.23-16-06490.2003

Russell, N., Horii, A., Smith, P. F., Darlington, C. L., and Bilkey, D. (2006). Lesions of the vestibular system disrupt hippocampal theta rhythm in the rat. *J. Neurophysiol.* 96, 4–14. doi: 10.1152/jn.00953.2005

Schulz-Mirbach, T., Ladich, F., Plath, M., and Heß, M. (2019). Enigmatic ear stones: what we know about the functional role and evolution of fish otoliths. *Biol. Rev. Camb. Philos. Soc.* 94, 457–482. doi: 10.1111/brv.12463

Shinder, M. E., and Taube, J. S. (2014). Resolving the active versus passive conundrum for head direction cells. *Neuroscience* 270, 123–138. doi: 10.1016/j.neuroscience.2014.03.053

Smith, P. F. (2017). The vestibular system and cognition. *Curr. Opin. Neurol.* 30, 84–89. doi: 10.1097/wco.0000000000000403

Spoor, F., Bajpai, S., Hussain, S. T., Kumar, K., and Thewissen, J. G. (2002). Vestibular evidence for the evolution of aquatic behaviour in early cetaceans. *Nature* 417, 163–166. doi: 10.1038/417163a

Stackman, R. W., Clark, A. S., and Taube, J. S. (2002). Hippocampal spatial representations require vestibular input. *Hippocampus* 12, 291–303. doi: 10.1002/hipo.1112

Stackman, R. W., and Herbert, A. M. (2002). Rats with lesions of the vestibular system require a visual landmark for spatial navigation. *Behav. Brain Res.* 128, 27–40. doi: 10.1016/s0166-4328(01)00270-4

Stackman, R. W., and Taube, J. S. (1997). Firing properties of head direction cells in the rat anterior thalamic nucleus: dependence on vestibular input. *J. Neurosci.* 17, 4349–4358. doi: 10.1523/jneurosci.17-11-04349.1997

Stewart, C., Yu, Y., Huang, J., Maklad, A., Tang, X., Allison, J., et al. (2016). Effects of high intensity noise on the vestibular system in rats. *Hear. Res.* 335, 118–127. doi: 10.1016/j.heares.2016.03.002

Stiles, L., and Smith, P. F. (2015). The vestibular-basal ganglia connection: balancing motor control. *Brain Res.* 1597, 180–188. doi: 10.1016/j.brainres.2014.11.063

Straka, H., Zwergal, A., and Cullen, K. E. (2016). Vestibular animal models: contributions to understanding physiology and disease. *J. Neurol.* 263, S10–S23. doi: 10.1007/s00415-015-7909-y

Taube, J. S. (2011). Head direction cell firing properties and behavioural performance in 3-D space. *J. Physiol.* 589(Pt 4), 835–841. doi: 10.1113/jphysiol.2010.194266

Taube, J. S., Stackman, R. W., Calton, J. L., and Oman, C. M. (2004). Rat head direction cell responses in zero-gravity parabolic flight. *J. Neurophysiol.* 92, 2887–2997. doi: 10.1152/jn.00887.2003

Valerio, S., Clark, B. J., Chan, J. H., Frost, C. P., Harris, M. J., and Taube, J. S. (2010). Directional learning, but no spatial mapping by rats performing a navigational task in an inverted orientation. *Neurobiol. Learn. Mem.* 93, 495–505. doi: 10.1016/j.nlm.2010.01.007

Wallace, D. G., Hines, D. J., Pellis, S. M., and Whishaw, I. Q. (2002). Vestibular information is required for dead reckoning in the rat. *J. Neurosci.* 22, 10009–10017. doi: 10.1523/jneurosci.22-22-10009.2002

Wearne, S., Raphan, T., and Cohen, B. (1999). Effects of tilt of the gravito-inertial acceleration vector on the angular vestibuloocular reflex during centrifugation. *J. Neurophysiol.* 81, 2175–2190. doi: 10.1152/jn.1999.81.5.2175

Wei, E. X., Oh, E. S., Harun, A., Ehrenburg, M., and Agrawal, Y. (2017). Saccular impairment in Alzheimer's disease is associated with driving difficulty. *Dement. Geriatr. Cogn. Disord.* 44, 294–302. doi: 10.1159/000485123

Wei, E. X., Oh, E. S., Harun, A., Ehrenburg, M., and Agrawal, Y. (2018). Vestibular loss predicts poorer spatial cognition in patients with Alzheimer's disease. *J. Alzheimers. Dis.* 61, 995–1003. doi: 10.3233/JAD-170751

Wei, E. X., Oh, E. S., Harun, A., Ehrenburg, M., Xue, Q. L., Simonsick, E., et al. (2019). Increased prevalence of vestibular loss in mild cognitive impairment and Alzheimer's disease. *Curr. Alzheimer Res.* doi: 10.2174/1567205016666190816114838 [Epub ahead of print].

Xie, Y., Bigelow, R. T., Frankenthaler, S. F., Studenski, S. A., Moffat, S. D., and Agrawal, Y. (2017). Vestibular loss in older adults is associated with impaired spatial navigation: data from the triangle completion task. *Front. Neurol.* 8:173. doi: 10.3389/fneur.2017.00173

Xu, X. D., Ding, C. R., Yu, J., Han, Z., Gu, J., Gao, N., et al. (2016). The hidden dysfunction of otolithic organs in patients with profound sensorineural hearing loss. *Hear. Res.* 331, 41–46. doi: 10.1016/j.heares.2015.10.006

Yoder, R. M., Goebel, E. A., Köppen, J. R., Blankenship, P. A., Blackwell, A. A., and Wallace, D. G. (2015). Otolithic information is required for homing in the mouse. *Hippocampus* 25, 890–899. doi: 10.1002/hipo.22410

Yoder, R. M., and Kirby, S. L. (2014). Otoconia-deficient mice show selective spatial deficits: impaired spatial performance in otoconia-deficient mice. *Hippocampus* 24, 1169–1177. doi: 10.1002/hipo.22300

Yoder, R. M., and Taube, J. S. (2009). Head direction cell activity in mice: robust directional signal depends on intact otolith organs. *J. Neurosci.* 29, 1061–1076. doi: 10.1523/JNEUROSCI.1679-08.2009

Yoder, R. M., and Taube, J. S. (2014). The vestibular contribution to the head direction signal and navigation. *Front. Integr. Neurosci.* 8:32. doi: 10.3389/fnint.2014.00032

Zheng, Y., Darlington, C. L., and Smith, P. F. (2006). Impairment and recovery on a food foraging task following unilateral vestibular deafferentation in rat. *Hippocampus* 16, 368–378. doi: 10.1002/hipo.20149

Zheng, Y., Gliddon, C. M., Aitken, P., Stiles, L., Machado, M. L., Philoxene, B., et al. (2017). Effects of acute altered gravity during parabolic flight and/or vestibular loss on cell proliferation in the rat dentate gyrus. *Neurosci. Lett.* 654, 120–124. doi: 10.1016/j.neulet.2017.06.033

Zheng, Y., Goddard, M., Darlington, C. L., and Smith, P. F. (2009). Long-term deficits on a foraging task after bilateral vestibular deafferentation in rats. *Hippocampus* 19, 480–486. doi: 10.1002/hipo.20533

Zu Eulenburg, P., Ruehl, R. M., Runge, P., and Dieterich, M. (2017). Ageing-related changes in the cortical processing of otolith information in humans. *Eur. J. Neurosci.* 46, 2817–2825. doi: 10.1111/ejn.13755

Conflict of Interest: The author declares that the research was conducted in the absence of any commercial or financial relationships that could be construed as a potential conflict of interest.

frontiers in Neural Circuits

ORIGINAL RESEARCH
published: 29 October 2019
doi: 10.3389/fncir.2019.00069

Age-Related Differences in Functional and Structural Connectivity in the Spatial Navigation Brain Network

Stephen Ramanoël[1]*, *Elizabeth York*[1,2], *Marine Le Petit*[1,3], *Karine Lagrené*[1], *Christophe Habas*[4] *and Angelo Arleo*[1]

[1]Sorbonne Universités, INSERM, CNRS, Institut de la Vision, Paris, France, [2]Centre for Clinical Brain Sciences, University of Edinburgh, Edinburgh, United Kingdom, [3]Normandie Université, UNICAEN, PSL Université Paris, EPHE, INSERM, U1077, CHU de Caen, Neuropsychologie et Imagerie de la Mémoire Humaine, Caen, France, [4]CHNO des Quinze-Vingts, INSERM-DHOS CIC 1423, Paris, France

Spatial navigation involves multiple cognitive processes including multisensory integration, visuospatial coding, memory, and decision-making. These functions are mediated by the interplay of cerebral structures that can be broadly separated into a posterior network (subserving visual and spatial processing) and an anterior network (dedicated to memory and navigation planning). Within these networks, areas such as the hippocampus (HC) are known to be affected by aging and to be associated with cognitive decline and navigation impairments. However, age-related changes in brain connectivity within the spatial navigation network remain to be investigated. For this purpose, we performed a neuroimaging study combining functional and structural connectivity analyses between cerebral regions involved in spatial navigation. Nineteen young (μ = 27 years, σ = 4.3; 10 F) and 22 older (μ = 73 years, σ = 4.1; 10 F) participants were examined in this study. Our analyses focused on the parahippocampal place area (PPA), the retrosplenial cortex (RSC), the occipital place area (OPA), and the projections into the visual cortex of central and peripheral visual fields, delineated from independent functional localizers. In addition, we segmented the HC and the medial prefrontal cortex (mPFC) from anatomical images. Our results show an age-related decrease in functional connectivity between low-visual areas and the HC, associated with an increase in functional connectivity between OPA and PPA in older participants compared to young subjects. Concerning the structural connectivity, we found age-related differences in white matter integrity within the navigation brain network, with the exception of the OPA. The OPA is known to be involved in egocentric navigation, as opposed to allocentric strategies which are more related to the hippocampal region. The increase in functional connectivity between the OPA and PPA may thus reflect a compensatory mechanism for the age-related alterations around the HC, favoring the use of the preserved structural network mediating egocentric navigation. Overall, these findings on age-related differences of functional and structural connectivity may help to elucidate the cerebral bases of spatial navigation deficits in healthy and pathological aging.

Keywords: healthy aging, MRI, resting-state, diffusion, connectivity, spatial navigation, vision

OPEN ACCESS

Edited by:
Desdemona Fricker, UMR8119 Centre de Neurophysique, Physiologie, Pathologie, France

Reviewed by:
Seralynne Vann, Cardiff University, United Kingdom
Gillian Theresa Coughlan, University of East Anglia, United Kingdom

***Correspondence:**
Stephen Ramanoël
stephen.ramanoel@inserm.fr

Received: *29 May 2019*
Accepted: *09 October 2019*
Published: *29 October 2019*

Citation:
Ramanoël S, York E, Le Petit M, Lagrené K, Habas C and Arleo A (2019) Age-Related Differences in Functional and Structural Connectivity in the Spatial Navigation Brain Network. Front. Neural Circuits 13:69. doi: 10.3389/fncir.2019.00069

INTRODUCTION

Spatial navigation represents one of the most fundamental activities of daily life and it requires the integration of multiple processes. These processes include the perception of spatial information from a variety of sensory cues, the creation and maintenance of spatial representations in memory, and the manipulation of these representations to guide navigational behavior (Wolbers and Hegarty, 2010; Julian et al., 2018). These spatial navigation abilities are mediated by numerous cerebral regions across the brain (Burgess, 2008; Spiers and Barry, 2015). These cerebral regions encompass interconnected structures of the medial temporal lobe such as the hippocampus (HC) and parahippocampal cortices, along with distal areas including the retrosplenial, posterior-parietal and prefrontal cortices. These brain structures relevant to spatial navigation are involved in diverse ways depending on the spatial representation strategy used. The medial temporal lobes, including the HC and entorhinal cortex, are predominantly activated for allocentric (world-centered) representations, whereas the posterior parietal regions tend to support egocentric (self-centered) strategies (Burgess et al., 2002; Herweg and Kahana, 2018). The medial prefrontal cortex (mPFC) plays a key role in maintaining useful information in working memory and in selecting the most appropriate navigational strategy for the complexity of the task at hand (Wolbers et al., 2007; Spiers and Gilbert, 2015; Chrastil et al., 2017; Ito, 2018).

Given the advanced nature of the human visual system, successful human spatial navigation requires the careful integration of complex high-resolution visual information (Ekstrom, 2015). A growing body of work has shed light on the importance of three high-level visual regions for the integration of relevant visual information for navigation—namely, the parahippocampal place area (PPA), the retrosplenial cortex (RSC), and the occipital place area (OPA; Vann et al., 2009; Julian et al., 2018). The PPA, located close to the parahippocampal and the lingual gyri, plays a role in landmark processing (Janzen and van Turennout, 2004; Epstein, 2008), such as 3D geometric structures (Henderson et al., 2008) and spatial boundaries (Park et al., 2011). The PPA appears to be involved in contextual association (Marchette et al., 2015) and place recognition (Epstein and Vass, 2014) during navigation tasks. Lesions to the RSC, located posteriorly to the corpus callosum, produce topographical disorientation but they may also transiently impair visual memory (Maguire, 2001). The RSC is thought to play a role in general scene processing, stability of landmarks (Auger et al., 2012; Auger and Maguire, 2018) and viewpoint integration—particularly with regards to translation of information between egocentric and allocentric representations (Vann et al., 2009; Mitchell et al., 2018). Finally, the function of the OPA, located near the intraparietal sulcus, remains unclear but its hypothesized roles include the representation of environmental boundaries (Julian et al., 2016) and the integration of discrete views in a 360° environment (Robertson et al., 2016). Furthermore, two recent studies have demonstrated the capacity of the OPA to encode potential future pathways during spatial navigation (Bonner and Epstein, 2017; Patai and Spiers, 2017). Although the PPA, RSC and OPA appear to be crucial for high-level visual processing related to spatial navigation, these scene-selective regions are also sensitive to low-visual features in scenes including dominant cardinal orientations (Nasr and Tootell, 2012), spatial frequencies, and contrast (Kauffmann et al., 2015).

All these cerebral areas, which process visual information and encode spatial representations, form the spatial navigation network. Healthy aging has a deleterious impact on this neural network, which manifests itself as navigational impairments, reducing the autonomy of older adults (Moffat, 2009; Lithfous et al., 2013; Lester et al., 2017). Several studies have reported a specific decline in the use of allocentric strategies in navigation tasks (for a review, see Klencklen et al., 2012). This is linked to the age-related atrophy and dysfunction of hippocampal regions, as well as to age-dependent changes occurring in the parahippocampal gyrus, the RSC, and the frontal regions (Moffat et al., 2006; Zhong and Moffat, 2018). On the other hand, egocentric strategies, which are supported by parietal and striatal regions, appear to be relatively well preserved in older adults (Harris and Wolbers, 2012; Harris et al., 2012). In addition, recent neuroimaging studies have highlighted age-related changes within low-visual regions dedicated to central visual field processing (Brewer and Barton, 2012; Ramanoël et al., 2015). A decline in low-level visual processing is expected to negatively influence spatial navigation.

To date, the majority of work investigating the age-related neurocognitive decline in navigation abilities has focused on brain regions engaged during spatial navigation separately. Less consideration has been given to the navigation network as a whole. Magnetic resonance imaging (MRI) is a useful tool for non-invasively studying the age-related differences in functional and structural connectivity between regions within the navigation network. Functional connectivity can be probed using resting-state functional MRI, which measures the correlation between low-frequency spontaneous fluctuations in the blood oxygen level dependent (BOLD) signal across brain regions in the absence of an explicit stimulus (Damoiseaux, 2017). The absence of a specific task in resting-state paradigms is advantageous in the study of healthy aging as it reduces confounding variables related to skill level, experience and fatigue. Structural connectivity can be evaluated using diffusion-weighted MRI. This technique is sensitive to the Brownian motion of water molecules within a given voxel of the brain, and, in particular, within the constraints of white matter tracts, hence allowing tract alterations to be studied. More precisely, this technique measures the general diffusion of water molecules related to barriers and obstacles imposed by the arrangement of fibers and cell membranes in brain tissue (for a detailed description of diffusion-weighted imaging methods, see Jones et al., 2013; Wandell, 2016; Jeurissen et al., 2017). Different parameters of interest can be extracted from which the white matter fiber organization can be inferred (Soares et al., 2013). The fractional anisotropy quantifies the diffusion direction preference, and it is particularly sensitive to microstructure changes like axonal density (Mori and Zhang, 2006; Lerner et al., 2014). The axial and radial diffusivity enable

the characterization of diffusivity in the principal diffusion axis and in both secondary axes, respectively. Both axial and radial diffusivities are sensitive to changes in myelin and axonal integrity in healthy subjects (Kumar et al., 2013; Winklewski et al., 2018).

Aging induces a reorganization of the functional and structural connectivity of the brain. A decrease in connectivity within several cerebral networks, including the default-mode network and the executive network, is a common finding of whole brain functional studies and it is associated with age-related cognitive decline (for a review, see Ferreira and Busatto, 2013). With respect to structural connectivity, recent studies using diffusion imaging have reported a decrease in fractional anisotropy associated with an increase in mean and radial diffusivities in normal aging (Bennett and Madden, 2014). While there is evidence for functional and structural connectivity changes in normal aging, such effects in the spatial navigation brain network remain poorly studied. To our knowledge, only Korthauer et al. (2016) have investigated age-related structural connectivity changes within the spatial navigation network. In this study, participants performed a computerized version of the hidden-platform Morris water-maze task. Results from this study showed a fractional anisotropy decrease in the uncinate fasciculus (a white matter tract connecting the HC with the mPFC) amongst older adults, which was associated with an increased time delay when solving the task. However, only whole brain analysis was performed as opposed to network analysis of structural connectivity between those brain structures that are specifically dedicated to spatial navigation. Furthermore, with the exception of the RSC, brain structures involved in high-level visual information processing during human spatial navigation were not considered.

The present study evaluated the effect of normal aging on the spatial navigation brain network. To accomplish this aim, we focused on how functional and structural connectivity differ between young and older groups within key structures involved in navigation: the mPFC, the HC, and the scene-selective regions (PPA, RSC, and OPA). In addition, considering the crucial role of vision for human spatial navigation, we additionally included the projection into the visual cortex of central and peripheral visual fields in our navigation network analysis. We anticipated age-related differences in the spatial navigation network in functional and structural connectivity. We hypothesized that there would be heterogeneous connectivity changes between key regions of interest within our spatial navigation network, and that such changes would be associated with spatial cognition, in particular regarding navigational strategies.

MATERIALS AND METHODS

Participants

Among the 41 healthy participants initially enrolled in the study, two older participants were excluded due to anatomical abnormalities, which resulted in failure of the normalization procedure. The participants were part of the French cohort population SilverSight (∼350 subjects) established and followed-up ever since 2015 at the Vision Institute—Quinze-Vingts National Ophthalmology Hospital, Paris. All participants were native French speakers, and they gave their written informed consent to participate in the study. All screening and experimental procedures were in accordance with the tenets of the Declaration of Helsinki and they were approved by the Ethical Committee "CPP Ile de France V" (ID_RCB 2015-A01094-45, CPP N°: 16122). All participants had normal or corrected-to-normal vision, and they had no history of neurological or psychiatric disorders, or sensorimotor dysfunctions. Older participants had a score of 26 or higher on the Mini Mental State Examination (MMSE; Folstein et al., 1975). The ensemble of clinical and functional examinations used to enroll the participants included: an ophthalmological and functional visual screening, a neuropsychological evaluation, an oculomotor screening, an audio-vestibular assessment as well as a static/dynamic balance examination. The neuropsychological assessment included a computerized version of the 3D mental rotation test (3D-Rotation, Vandenberg and Kuse, 1978), the perspective-taking test (PTT, Kozhevnikov and Hegarty, 2001), the Corsi block-tapping task (Corsi, 1972), and the figural memory test (FGT, short and long) implemented in the Vienna test system software (Schuhfried, 2012).

MRI Acquisition

Images were acquired using a 3T Siemens Magnetom Skyra whole-body MRI system (Siemens Medical Solutions, Erlangen, Germany) with a 64-channel head coil at the Quinze-Vingts National Ophthalmology Hospital in Paris, France. Resting-state functional magnetic resonance imaging (fMRI), diffusion-weighted imaging and an anatomical image were acquired for all participants, followed by two additional functional localizer runs. The anatomical volume consisted of a T1-weighted, high-resolution, three-dimensional MPRAGE sequence (TR/TE/IT/flip angle = 2,300 ms/2.9 ms/900 ms/9°; matrix size = 256 × 240 × 176; voxel size = 1 × 1 × 1.2 mm). For the resting-state functional scan, 304 volumes of 60 slices were acquired using a T2*-weighted simultaneous multi-slice echo planar sequence (SMS-EPI; TR/TE/flip angle = 1,000 ms/30 ms/90°; matrix size = 96 × 96; SMS = 2; GRAPPA = 2; voxel size = 2.5 mm isotropic). Diffusion-weighted images were acquired along 128 gradient directions (TR/TE/flip angle = 1,600 ms/84 ms/90°; 14 volumes $b = 0$ and 128 volumes $b = 1{,}500$ s/mm^2, SMS = 2; GRAPPA = 4; voxel size = 2.5 mm isotropic). For the functional localizer scans of scene-selective regions and low-visual areas, 364 and 304 volumes respectively of 64 slices were acquired using a T2*-weighted SMS-EPI sequence (TR/TE/flip angle = 1,000 ms/30 ms/90°; matrix size = 100 × 100; SMS = 2; GRAPPA = 2; voxel size = 2.5 × 2.5 × 2.4 mm).

Stimuli and Procedure

Two independent functional localizers were used to map individually scene-selective regions (PPA, RSC, OPA) and the projection into visual cortex of central and peripheral visual fields (CVF, PVF). A block fMRI paradigm, adapted from Ramanoël et al. (2015) was then employed to locate scene-selective areas. Participants were presented with blocks of gray scale photographs (256 gray scales), all sized 900 × 900 pixels

(or 18 × 18 degrees of visual angle) for scenes, faces, everyday objects, scrambled scenes and scrambled objects. The functional run lasted 6 min and it was composed of 14, 20 s task blocks (four blocks of scenes, four blocks of scrambled scenes, two blocks of faces, two blocks of objects and two blocks of scrambled objects), including 20 different images of the same category, and interspersed with four block of 20 s each, with a fixation dot in the center of the screen displayed against a gray background. Each stimulus was presented for 400 ms followed by a 600 ms inter-stimulus interval with a fixation dot in the center of the screen. Participants performed a "one-back" repetition detection task.

To define ROIs for CVF and PVF regions, we used a blocked eccentricity mapping experiment adapted from Chang et al. (2015). Two rings composed of a black and white checkboard flickering at 4 Hz were sequentially presented at the center (2° eccentricity) for 15 s and at the periphery (8° eccentricity) for 15 s of the visual field. All participants completed one 5 min functional run. To ensure that participants remained focused on the central point, they were asked to respond with a button press when they saw a red or a green cross on the fixation dot. During the resting-state fMRI acquisition, participants were asked to close their eyes, to not think about anything in particular and to remain awake.

MRI Data Pre-processing and Statistical Analyses

Definition of the Navigation Network (ROIs)

Processing of localizer data was performed using SPM12 release 7,487 (Wellcome Department of Imaging Neuroscience, London, UK[1]) implemented in MATLAB 2018a (Mathworks Inc., Natick, MA, USA). For each participant, the first four functional localizer volumes were discarded to allow for equilibration effects and the remaining images were realigned to correct for head movements and co-registered to the T1-weighted anatomical image. The images were analyzed using a single participant general linear model. Slice-timing correction was not applied in line with the recommendations of the Human Connectome Project functional pre-processing pipeline for multi-slice sequences (Glasser et al., 2013). Similarly to Ramanoël et al. (2018), a study-specific template in MNI space was created using Diffeomorphic Anatomical Registration Exponentiated Lie algebra (DARTEL) to improve inter-subject alignment during normalization (Ashburner and Friston, 2005; Ashburner, 2007). Finally, functional scans were smoothed with a 6 mm full-width half maximum (FWHM) Gaussian kernel.

Statistical analysis was performed using general linear model (Friston et al., 1995) at single participant level. For each participant, eight conditions of interest (scenes, faces, objects, scrambled scenes, scrambled objects, fixation, center ring and peripheral ring) were modeled as eight regressors, constructed as box-car functions and convolved with a canonical hemodynamic response function. Movement parameters obtained from realignment corrections were also considered in the model as an additional factor of no interest. Time-series for each voxel were high-pass-filtered (1/128 Hz cut-off) to remove low-frequency noise and signal drift.

PPA, RSC and OPA regions were located independently for each participant as ROIs using the fMRI contrast [Scenes > (Faces + Objects)]. CVF and PVF areas were mapped using the contrasts (Center > Periphery) and (Periphery > Center), respectively. Significant voxel clusters on individual t-maps were identified using false discovery rate correction (FDR) for multiple comparisons (alpha = 0.05) to control for the overall false-positive rate. Sphere ROIs (5 mm radius) were created at individual peaks of activation in each scene-selective and low-visual region and in each cerebral hemisphere (individual peak coordinates for PPA, RSC, OPA, CVF and PVF are available in the **Supplementary Table S1**).

For the hippocampal region, participant-specific ROI masks for the left and right HC were created using the VolBrain online brain volumetry software (Manjón and Coupé, 2015[2]). Furthermore, ROI masks for the mPFC in the right and left hemispheres were obtained from the automated anatomic labeling atlas (AAL; Tzourio-Mazoyer et al., 2002).

Pre-processing and Statistical Analysis of Functional Connectivity Data

Resting-state pre-processing steps were similar to those for localizer paradigms described above. In addition, the Artifact Detection Toolbox, included within the CONN functional connectivity toolbox[3] (Whitfield-Gabrieli and Nieto-Castanon, 2012), was used to detect scans with excessive movement. The resulting scrubbing parameters were added as a first-level covariate, along with realignment parameters (six parameters obtained by rigid body correction of head motion). Physiological and other spurious sources of noise were estimated using CompCor (Behzadi et al., 2007), and they were regressed out together with white matter, cerebrospinal fluid, motion parameters, age and gender covariates. Linear detrending and band-pass filtering (0.008–0.09 Hz) were carried out during regression. Correlation analyses were performed by extracting the mean BOLD signal time series from ROIs and computing Pearson's correlation coefficients between subject-specific ROIs including the PPA, RSC, OPA, CVF, PVF, HC, and the mPFC for each hemisphere and each group. We applied Fisher's r-to-z transformation to improve the normality of the bivariate correlation matrix for each participant (14 × 14). To investigate the age-related difference in functional connectivity, two-sided two-sample *t*-tests were then performed to compare ROI-to-ROI connectivity between the young and the older group. The results were considered significant at $p < 0.05$ FDR corrected for multiple comparisons and effect sizes were evaluated with Hedges' g score.

Pre-processing and Statistical Analysis of Diffusion Data

All diffusion processing steps were performed using functions implemented in FSL (FMRIB Software Library[4]). Diffusion MRI

[1]www.fil.ion.ucl.ac.uk/spm/

[2]http://volbrain.upv.es/

[3]https://web.conn-toolbox.org/

[4]http://www.fmrib.ox.ac.uk

data were first pre-processed to remove eddy-current-induced distortions and motion artifacts. Brain tissues, were extracted using the Brain Extraction Tool. Diffusion images were visually inspected after each processing step to control for obvious artifacts. Maps of diffusion parameters (including fractional anisotropy, FA, mean diffusivity, MD, axial diffusivity, AD, and radial diffusivity, RD) were calculated using DTIfit. A tract-based ROI-to-ROI approach was taken for diffusion analyses. The diffusion tensors were fitted using the Bayesian Estimation of Diffusion Parameters Obtained using Sampling Techniques (BEDPOSTX), which models fibers crossing in each voxel.

The resulting parameters were used to reconstruct the distribution probability of tract locations using probabilistic tractography (PROBTRACKX). This approach considers crossing-fiber pathways and it provides maps of the probability of the presence of a fiber in a voxel (Jbabdi and Johansen-Berg, 2011; Soares et al., 2013). This probabilistic technique includes a parameter which accounts for the number of tracts between the seed ROI (i.e., the starting point) and the target ROI (i.e., the destination) divided by the total number of tracts from the seed ROI. The connection between the seed and the target depends on other tracts than those included in the seed-target pathway. The probability of connection from the seed to the target can differ from the probability of connection from the target to the seed (Wandell, 2016). Therefore, each navigational ROI, after being registered to the diffusion space, was used consecutively as a seed and as a target. This enabled the creation of a map for each combination of anatomical connectivity between two ROIs. Five thousand samples per voxel were generated, a curvative threshold of 0.2 was used and a correction for the distance across seed and target regions was applied. Each tracking image was normalized to MNI space using linear and nonlinear registration tools (FLIRT and FNIRT) and divided by the total number of samples generated creating a proportion image. Those maps were also divided by the total number of tracts in order to account for cross-subject "tractability" differences. Participants' proportion maps were merged to create a mean group image with a threshold fixed at $p < 5.10E\text{-}6$ to generate a mean mask of tracts that were not rejected by the selection criteria. Group masks were then restricted to voxels for which FA value was superior to 0.2. Mean masks of each tract were used as restriction masks on individual proportion maps to extract mean diffusion parameters (FA, MD, AD, RD) for each pair of ROIs and each hemisphere (14×14).

Despite the correction, the probability of connectivity between two ROIs decreases as a function of distance (Morris et al., 2008). In cases where the mPFC was used as a seed, the signal was lost after thresholds were applied. Hence, the anatomical connectivity of this region was not considered here.

Differences in mean diffusion parameters between young and older groups in the new matrix (12×12) were assessed using a two-sided two-sample *t*-test and they were considered significant for $p < 0.05$ corrected for multiple comparisons [$p = 0.05/(12 \times 12 \times 4 \times 2)$]. Similarly to the functional connectivity analysis, gender was included as a covariate and effect sizes were evaluated with Hedges' g score. Mean diffusion parameters were not averaged across tracts however using two regions as seed and target (Wandell, 2016). This allowed more accurate results to be obtained and it provided confirmation that tracts in these two sides showed the same diffusion parameter direction differences between groups.

RESULTS

MRI data were analyzed from 39 participants divided into two age groups: a young group ($N = 19$; 10 females; mean age $\pm$ SD: 27 $\pm$ 4.3 years; age range: 21–37 years) and an older group ($N = 20$; 10 females; mean age $\pm$ SD: 73 $\pm$ 4.1 years; age range: 66–80 years). All subjects had visual, oculomotor, and audio-vestibular faculties in between or above normative age-dependent limits. In **Table 1**, we present the behavioral performances obtained in the cognitive tests for the older group only. Cognitive data for the young participants were not included here for the partial dataset of neuropsychological assessment for young participants (12 of 19 young participants completed the entire neuropsychological evaluation).

Age-Related Differences in Functional Connectivity in the Spatial Navigation Network

We performed a ROI-to-ROI functional connectivity analysis on the resting-state fMRI data by computing the strength of correlation between all possible pairs of ROIs within the navigation network. We sought age-related differences by directly comparing ROI-to-ROI correlation values between young and older groups (**Figure 1**). We found a significant age-related decrease in the functional connectivity between visual cortical fields and the HC ($p < 0.05$, FDR correction for multiple comparisons; see **Supplementary Table S2** for full details on statistical correlations). More precisely, older adults exhibited a decrease in the functional connectivity between the left peripheral visual field region and the right and left HC as compared to the young group (**Figures 1A,B**). Associated with these changes between visual and hippocampal regions, we found a significant increase in the functional connectivity between OPA and PPA regions in the left hemisphere of older adults (**Figures 1A,C**; see **Supplementary Table S2** for detailed statistics). Finally, we did not find any significant age-related differences in functional connectivity for the RSC and the mPFC regions.

TABLE 1 | Mean and standard deviation (SD) of scores obtained on cognitive tests in the old group; 3D mental rotation test (3D-Rotation), perspective-taking test (PPT), short and long-term figural memory test (FGT-short and FGT-long), short and long Corsi block-tapping task (Corsi-short and Corsi-long).

Gender (M/F)	Old group	
	10/10	
	Mean	SD
3D-Rotation	11.2	2.9
PTT	45.5	26.4
FGT-short	5.8	1.8
FGT-long	6.2	1.9
Corsi-short	4.4	0.8
Corsi-long	4.4	0.8

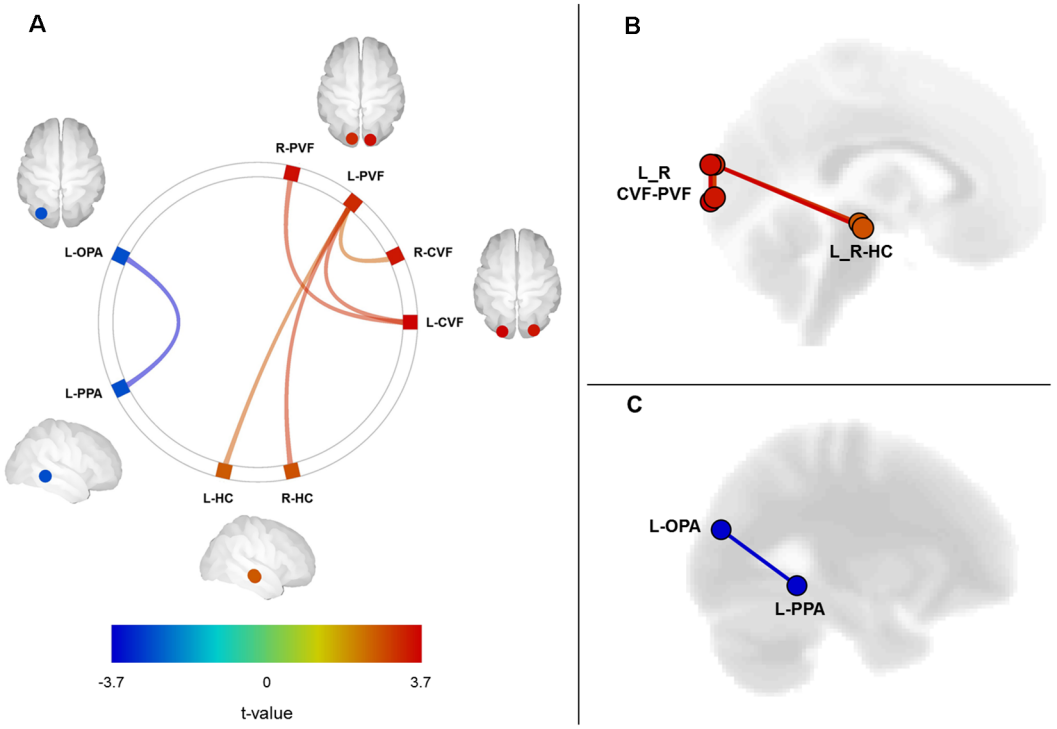

FIGURE 1 | Cerebral regions (ROI-to-ROI analysis) showing a significant difference between groups (Young Group vs. Older Group) in functional connectivity. **(A)** Connectome ring with navigational brain regions showing a decrease (in red) and an increase of functional connectivity for older adults compared to young ones. **(B)** Sagittal view of the brain with regions showing a significant decrease of functional connectivity in older adults. **(C)** Sagittal view of the brain with regions showing a significant increase in functional connectivity in older subjects. The statistical significance threshold was set at $p < 0.05$ FDR-corrected for two-sided analysis. L, left; R, right; CVF, central visual field; PVF, peripheral visual field; OPA, occipital place area; PPA, parahippocampal place area; HC, hippocampus.

Hedges'g scores for the effect size of significant differences between young and older participants ranged from 0.8 to 1.1. As proposed by Cohen (1988), the magnitude of the effects reported here was considered large (effect size > 0.8).

Age-Related Differences in Structural Connectivity in the Spatial Navigation Network

We conducted a probabilistic tract-based ROI-to-ROI analysis on diffusion data to assess the structural connectivity within the navigation network. We evaluated age-related differences by comparing ROI-to-ROI diffusion values for each diffusion parameter (fractional anisotropy, mean diffusivity, axial diffusivity, and radial diffusivity) between groups (**Figure 2**). We found age group differences with a significant decrease in fractional anisotropy and an increase in mean and radial diffusivity for older adults as compared to young participants across all ROIs (see **Supplementary Table S3** for full statistical details and **Supplementary Figure S1**). More precisely, we reported significant age-related structural connectivity differences between all ROIs for at least one diffusion parameter. Interestingly, we also found that the anatomical connectivity around the OPA region was more preserved in older adults with respect to other navigational ROIs (with the exception of the connectivity between the OPA and RSC). The ROI-to-ROI tracts showing age-related differences in our spatial navigation network matched with three main tracts from the JHU-white matter tractography atlas: the posterior part of the inferior longitudinal fasciculus (ILF), the posterior part of the inferior fronto-occipital fasciculus (IFOF) and the forceps major.

We then examined the co-variation of fractional anisotropy, the mean and radial diffusivities between age groups. Results revealed differences in structural connectivity only between both hemispheres in the navigation network (**Figure 3A**). We found age-related differences between the left low-visual areas and the right HC (red lines), as well as between the right low-visual areas and the left HC (blue lines). We also found structural age-related connectivity differences between the right and the left HC and between HC and PPA for both hemispheres (green line). Interestingly, the ROI-to-ROI tracts from our analysis showing a covariation of fractional anisotropy, mean and radial diffusivities for young adults compared to older subjects (**Figure 3B**), which appeared to be very similar to the forceps major tract from the JHU white-matter tractography atlas (**Figure 3C**; Hua et al., 2008). As expected, the connectivity matrices were asymmetric (see **Supplementary Figure S1**). We found similar age-related

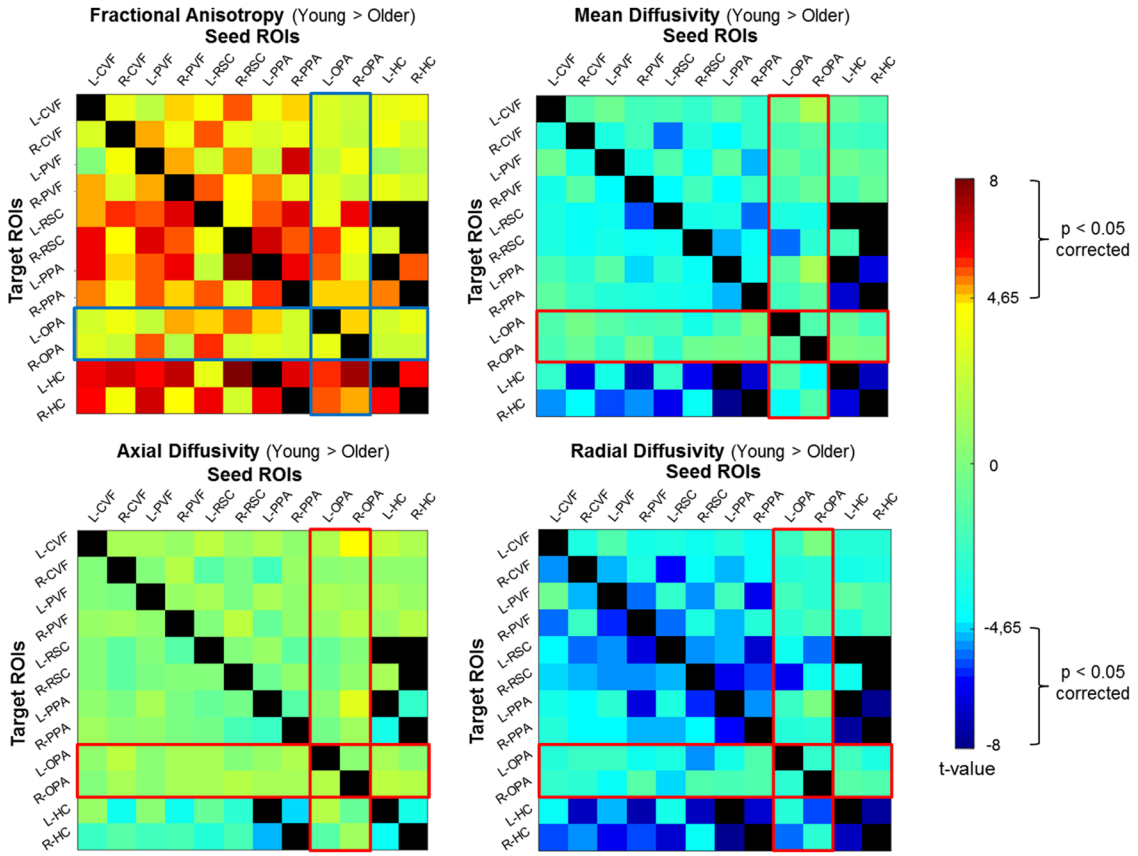

FIGURE 2 | Correlation matrices representing differences between groups (Young Group vs. Old Group) for diffusion parameters. The statistical significance threshold was set at $p < 0.05$ corrected for multiple comparisons for two-sided analysis. FA, fractional anisotropy; MD, mean diffusivity; AD, axial diffusivity; RD, radial diffusivity.

diffusion parameter differences when ROIs were considered as seed and target, with the exception of the HC. Indeed, differences were only seen for the HC as a target ROI, but not as a seed. This result could be explained by the correction applied during the normalization of maps related to the size of the seed ROI.

The magnitude of the effects for structural results reported here was between 1.1 and 2.2 (> 0.8 considered large).

Association Between Neuropsychological Assessment and Connectivity Measures

We conducted correlational analyses between cognitive scores obtained from the neuropsychological evaluation (3D-Rotation, PPT, FGT short and long, Corsi short and long) and connectivity measures (functional and structural) for the older group only. We found no significant association between functional connectivity and cognitive scores. By contrast, for structural connectivity, we showed a significant correlation between fractional anisotropy values and two pairs of ROIs within our navigational network. More precisely, we found a negative correlation ($r = -0.87$) for the 3D-Rotation test between the R-CVF and the R-OPA; and a positive correlation ($r = 0.80$) for the FGT (long) between the R-OPA and the R-RSC [p-values were Bonferroni-corrected for multiple comparisons: $p = 0.05/(12 \times 12 \times 6)$].

Finally, we conducted a correlation analysis between functional and structural brain connectivity measures for all participants. Results showed no significant correlations.

DISCUSSION

The present neuroimaging study assessed age-related brain connectivity differences within the spatial navigation network. Our results indicate that both functional and structural connectivity of brain areas involved in spatial coding and navigation are altered in healthy aging. Our functional results show decreased connectivity between low-visual areas and the HC, associated with an increase in connectivity between OPA and PPA in older participants compared to young subjects. Concerning anatomical connectivity, we observed a general decline in white matter integrity of the spatial navigation network in older adults. We found altered anatomical connectivity in several ROIs including low-visual areas, scene-selective regions and the HC, characterized by a modification of fractional anisotropy, as well as mean and radial diffusivities.

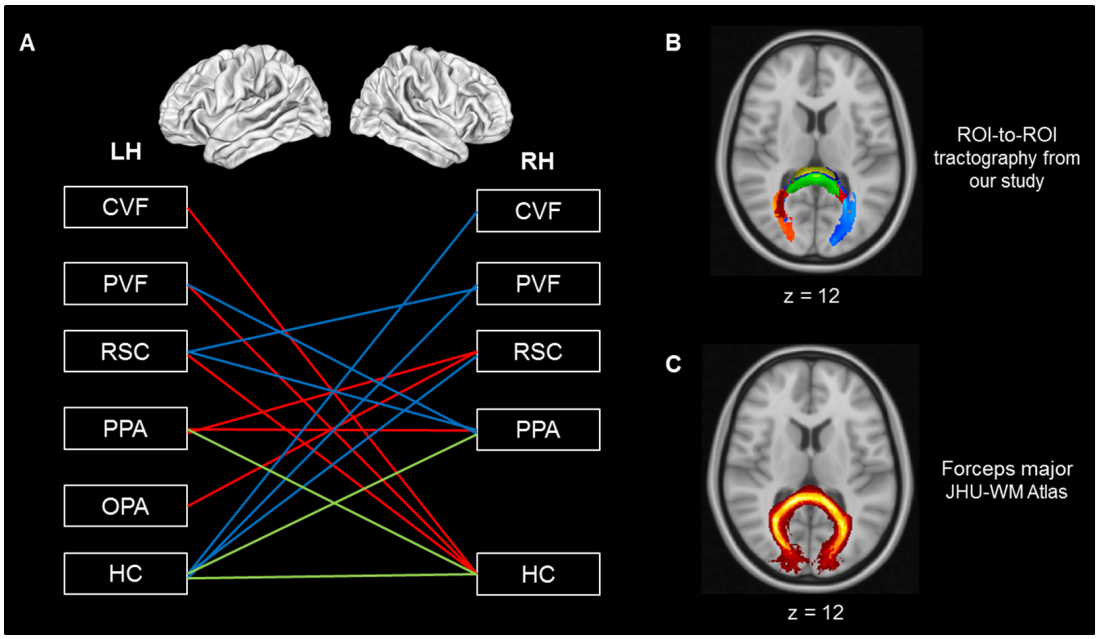

FIGURE 3 | (A) Cerebral regions showing covariation of diffusion parameters between hemispheres. **(B)** Tractography from our analysis showing a covariation of FA, MD and RD parameters for young compared to older adults. **(C)** Forceps major tract from the JHU white-matter tractography atlas (Hua et al., 2008). Red line: connection from LH to RH, blue line: connection from RH to LH, green line: both hemispheres, LH, left hemisphere; RH, right hemisphere; CVF, central visual field; PVF, peripheral visual field; OPA, occipital place area; PPA, parahippocampal place area; RSC, retrosplenial cortex; HC, hippocampus. FA, fractional anisotropy; MD, mean diffusivity; RD, radial diffusivity; YG, young group; OG, old group.

In addition, the relative lack of differences in OPA connectivity suggests that the structural connectivity of this region is less disrupted than that of other regions within the spatial navigation network.

Functional Connectivity

From a functional perspective, we found age-related differences in the connectivity between low-level visual areas and high-level spatial areas. First, we showed a decrease in functional connectivity within the posterior part of our network, encompassing CVF and PVF between both hemispheres and dedicated to processing low-visual information in older adults. Age-related functional connectivity changes between low-visual regions could be interpreted in light of subtle visual deficits (e.g., decreases in visual acuity and contrast sensitivity) typically seen in normal aging (Owsley, 2011, 2016) and related brain changes. Healthy older adults, for example, show a reduced surface area and increased population receptive field sizes in the foveal representations of V1, V2 and hV4 compared to young adults (Brewer and Barton, 2012, 2014). In addition, previous studies highlighted specific visual deficits in normal aging related to low-visual activation within early visual areas and scene-selective regions (Ramanoël et al., 2015). Second, our results showed an age-related decrease in functional connectivity between low-visual areas and the HC, a key structure within the navigation network. Several studies on healthy subjects (Chadwick et al., 2013; Zeidman et al., 2015) and on patients with hippocampal lesions (Lee et al., 2005) have demonstrated the role of the HC in visual perception. For example, Chadwick et al. (2013) reported a top-down influence of the HC on early visual areas. Our results, showing a decreased functional connectivity associated with aging, do not allow us to determine the direction of effect between top-down modulation (i.e., reactivation of sensory representations) and bottom-up modulation (i.e., visuospatial input leading to representations of visual environment).

Conversely, the functional connectivity was higher for older compared to young participants in the anterior part of the spatial navigation network, between the left OPA and left PPA. The role of PPA in spatial navigation has previously been described in relation to the representation of landmark-based navigation (Epstein and Vass, 2014). The HC, on the other hand, is considered to provide the neural basis for the encoding of spatial information and long-term memory (see Maguire and Mullally, 2013 for a review). The PPA is able to sufficiently support the recognition of scenes and landmarks, however, without the need for engagement of the HC (Köhler et al., 2002; Epstein, 2008). Furthermore, the parahippocampal regions are less affected by normal aging than the HC itself (Zhong and Moffat, 2018). The increased functional connectivity between the OPA and the PPA in normal aging may, therefore, represent a putative compensatory mechanism in spatial navigation as these regions assume greater navigational roles in order to counter the reduced connectivity of the HC. Previous work has suggested that the PPA may be functionally divided into two distinct scene-processing networks (Baldassano et al., 2016). Of note is the posterior PPA

association with the OPA as a visual network. The increased connectivity between the OPA and PPA in the present study may hence represent visual components in aging. Alternatively, the anterior-posterior distinction of the PPA may disappear with age, as the anterior PPA assumes a role similar to the HC.

Contrary to previous research, we did not observe an age-related difference in functional connectivity of the RSC. Moffat et al. (2006), for example, demonstrated that older participants exhibited reduced fMRI activation in the posterior HC, posterior parahippocampal gyrus and RSC compared to younger participants when encoding a virtual environment. Again, our focus on functional connectivity at rest rather than task-related activity may be the source of such discrepancies.

Structural Connectivity

Concerning anatomical connectivity, our results showed a general decline in white matter integrity of the spatial navigation network in older adults, in line with previous studies using a whole-brain MRI diffusion approach (Fjell et al., 2009; Bennett and Madden, 2014; Coupé et al., 2017). These results, in conjunction with the absence of change for the axial diffusivity parameter, suggest an age-related loss of white matter integrity within the spatial navigation network, which is likely to reflect demyelination rather than axonal loss (Madden et al., 2009; Bennett et al., 2010). Interestingly, we found a relative lack of differences in OPA connectivity suggesting that the structural connectivity of this region is less disrupted than that of other regions within the spatial navigation network.

The consideration of the covariation of diffusion parameters in our structural connectivity analyses permits further interpretation of our results. The covariation of multiple diffusion metrics within a given tract, compared to single-factor variation, aids the biological interpretation of white matter structural changes (Soares et al., 2013). As such, when solely ROIs presenting fractional anisotropy, mean and radial diffusivities co-varying connectivity differences between older and young groups are considered, the apparent inter-hemispheric nature of these differences is noteworthy. Moreover, these connectivity differences between hemispheres involve a unique white matter tract, namely the forceps major located on the splenium of the corpus callosum. The forceps major connects the occipital lobes and it plays an important role in processing visual cues (Goldstein and Mesfin, 2017). Since axial diffusivity remains unmodified, white matter modifications of this tract during aging appear to be related to demyelination. This result is consistent with previous studies showing a decrease in the structural integrity of the forceps major during aging (Bennett and Madden, 2014). Furthermore, this tract seems to be largely involved in spatial navigation. For example, Tamura et al. (2007) reported the case of a patient who developed similar symptoms to pure topographical disorientation after experiencing a lesion within the right forceps major. More specifically, this patient presented with visuospatial deficits and difficulty using information derived from landmarks. Diffusion modifications observed in the forceps major during aging in our study are consistent with the interhemispheric disconnection model proposed by O'Sullivan et al. (2001), thus suggesting that disconnection plays a role in cognitive deficits with aging.

Behavioral Relevance of Age-Related Connectivity Differences

Altogether, our structural and functional findings suggest an age-related decline in the connectivity of the pathway from low-visual areas to the HC, combined with a maintained connectivity around the OPA. These results may be interpreted as a compensatory mechanism for age-related alterations around the HC, favoring the use of the preserved structural network in the region of the OPA mediating egocentric navigation. This pattern agrees with the current literature regarding spatial navigational strategies in aging. The HC, and in particular the hippocampal body, is known to be vulnerable to normal aging (Malykhin et al., 2017). Volume reductions of the HC have been associated with allocentric spatial navigation deficits (Guderian et al., 2015; Colombo et al., 2017), and there is a tendency for greater reliance on egocentric as opposed to allocentric spatial navigation strategies with increasing age (Harris et al., 2012; Rodgers et al., 2012; Gazova et al., 2013). The OPA, on the other hand, plays a key role in egocentric spatial navigation strategy, related to visual information (Bonner and Epstein, 2017). For example, this high-level visual region appears to be sensitive to egocentric distance and to first-person perspective motion (Kamps et al., 2016; Persichetti and Dilks, 2016).

Moreover, the age-related differences reported here are also involved in the visual cortex. Visual information is crucial for successful navigation (Ekstrom, 2015). Several studies have emphasized a key interaction between the HC and areas involved in visual perception during the internal representation of spatially coherent scenes (Zeidman et al., 2015; Zeidman and Maguire, 2016). In the past, age-related changes in spatial cognition have generally been attributed to poor strategic choice and memory loss due to frontal and hippocampal atrophy. The impact of a decline in visuo-perceptual ability with age has tended to be neglected and future studies should consider the impact of such a decline. This is particularly relevant in light of the distinct visual scene-processing network, composed of the OPA and PPA, described by Baldassano et al. (2016). The age-related changes in the posterior regions of the spatial navigation network in the present study adhere to the classic posterior-to-anterior shift theory of healthy aging (Davis et al., 2008). However, Cabeza et al. (2018) recently proposed greater clarification of the terminology surrounding compensation mechanisms in healthy aging. In particular, Cabeza et al. (2018) differentiated between compensation by selection, by upregulation and by reorganization. As the current study focused on functional connectivity at rest and structural connectivity only, it is not possible to know precisely which compensation mechanism is engaged. Contrary to our expectations, one of our findings showed a negative correlation between fractional anisotropy values between the CVF and OPA and 3D-Mental Rotation scores for older participants. In other words, greater fractional anisotropy in normal aging was associated with a decrease in mental visual rotation abilities. Future work could clarify this last result and the nature of the compensation

mechanism, perhaps by using task-based functional MRI to measure BOLD response within the spatial navigation network during a task aimed at testing allocentric and egocentric navigation strategies.

Concerning the involvement of the RSC in the spatial navigation network, our results show an age-related loss of structural white matter integrity around the RSC, but no changes in functional connectivity of this high-level visual brain region. Several studies have highlighted the key function of the RSC in spatial navigation (for a review, see Mitchell et al., 2018) such as its role in translating from egocentric into allocentric reference frames. Neuroimaging studies have reported that the RSC activity was related to recollection processing of permanent visual landmark during a navigation task using a first-person perspective (Auger et al., 2012; Auger and Maguire, 2018). This point was partially assessed by our results showing that older participants with fractional anisotropy values close to young participants between the OPA and RSC exhibited better performance on the figural memory test. Concerning RSC-PPA connectivity, a recent study showed that functional and anatomical changes in a patient suffering from developmental topographic disorientation were associated with spatial navigation impairments (Kim et al., 2015). However, in the present study of healthy aging, we did not observe functional connectivity differences within the RSC-PPA pathway. The preservation of functional connectivity here in healthy older adults may account for their relatively spared navigational abilities compared to patients with topographic disorientation. Indeed, several studies have suggested that a loss of white matter integrity leads to functional connectivity changes (Ferreira and Busatto, 2013).

Surprisingly, regarding the anterior component of the spatial navigation network, there were no specific age-related changes in functional and structural connectivity between the mPFC and other ROIs in the spatial navigation network. Previous work has nonetheless shown white matter damage to be more pronounced in anterior compared to posterior regions (Gunning-Dixon et al., 2009; Madden et al., 2009), as well as between the HC and the mPFC (Korthauer et al., 2016). The divergence of our results from current literature could be partially explained by methodological differences. In the majority of MRI studies, diffusion data is acquired in each phase-encoding direction in order to correct image distortions, which mainly appear in frontal regions. In our work, with the aim of minimizing the MRI examination duration for older participants, diffusion data were acquired in solely one direction. Moreover, in our probabilistic tractography analysis, a conservative threshold was applied. These two factors are associated with a bias related to the longer distance between mPFC and all other ROIs, which could explain the absence of results from the mPFC in the spatial navigation brain network. As such, caution is advised regarding the results from the frontal regions of the spatial navigation brain network.

Limitations

The findings of the present study should be considered in light of several limitations. Here, we focused solely on certain key visual structures within the spatial navigation network. Previous studies have, however, considered additional cerebral areas such as prefrontal, motor and cerebellar regions or the entorhinal cortex (Doeller et al., 2008; Rodriguez, 2010;Iglói et al., 2014; Hao et al., 2016; Stangl et al., 2018). Further research using task-based fMRI involving different navigation strategies, combined with a complete neuropsychological assessment of navigation skills, would permit the validation of the inclusion and/or exclusion of key structures within the spatial navigation network as well as the investigation of brain connectivity related to visual information processing for navigation. Notably, a recent computational modeling study (Bicanski and Burgess, 2019) highlighted the importance of considering entorhinal cortex connectivity with frontal and parietal regions to investigate age-related changes in visuospatial abilities. Furthermore, this would address difficulties regarding the interpretation of functional connectivity changes. For example, increases in functional connectivity could represent a disruption rather than an improvement related to behavior. An additional limitation of the present study is the lack of information regarding the dynamic nature of connectivity changes in normal aging. Longitudinal studies of normal aging would provide a means to evaluate this issue. Finally, future studies should consider investigating the hippocampal subfields as proposed by Hrybouski et al. (2019, see also Dalton et al., 2019) to further elucidate age-related changes in the spatial navigation network.

CONCLUSION

To conclude, the present study sheds light on specific age-related differences in connectivity between key cerebral structures involved in spatial navigation. The older adults enrolled in this study exhibited a decrease in functional connectivity between low-visual areas and the HC, associated with greater functional connectivity between OPA and PPA regions. Interestingly, structural connectivity results showed differences in white matter integrity within the navigation brain network, although less pronounced around the OPA. This pattern of brain connectivity differences can be interpreted as a compensatory mechanism for the age-related alterations concerning the HC, thus favoring the use of the preserved structural network mediating egocentric navigation. These findings emphasize the importance of considering the link between the decline of visual and navigation abilities in future studies on the effects of normal or pathological aging in spatial cognition.

DATA AVAILABILITY STATEMENT

The datasets generated for this study are available on reasonable request to the corresponding author.

ETHICS STATEMENT

The studies involving human participants were reviewed and approved by Ethical Committee "CPP Ile de France V" (ID_RCB 2015-A01094-45, CPP N°: 16122). The patients/participants

provided their written informed consent to participate in this study.

AUTHOR CONTRIBUTIONS

SR, CH and AA: conceived the study. SR, EY, MP and KL: data acquisition. SR, EY and MP: data processing. SR, EY, MP and AA: manuscript writing.

FUNDING

This research was supported by Agence Nationale de la Recherche (ANR)—Essilor SilverSight Chair ANR-14-CHIN-0001.

ACKNOWLEDGMENTS

We thank the participants of this study for their valuable contributions. We thank the CHNO des Quinze-Vingts for enabling us to perform the MRI acquisitions. We thank Felix Renard for helpful discussion on data analysis.

SUPPLEMENTARY MATERIAL

The Supplementary Material for this article can be found online at: https://www.frontiersin.org/articles/10.3389/fncir.2019.00069/full#supplementary-material.

REFERENCES

Ashburner, J. (2007). A fast diffeomorphic image registration algorithm. *Neuroimage* 38, 95–113. doi: 10.1016/j.neuroimage.2007.07.007

Ashburner, J., and Friston, K. J. (2005). Unified segmentation. *Neuroimage* 26, 839–851. doi: 10.1016/j.neuroimage.2005.02.018

Auger, S. D., and Maguire, E. A. (2018). Retrosplenial cortex indexes stability beyond the spatial domain. *J. Neurosci.* 38, 1472–1481. doi: 10.1523/JNEUROSCI.2602-17.2017

Auger, S. D., Mullally, S. L., and Maguire, E. A. (2012). Retrosplenial cortex codes for permanent landmarks. *PLoS One* 7:e43620. doi: 10.1371/journal.pone.0043620

Baldassano, C., Esteva, A., Fei-Fei, L., and Beck, D. M. (2016). Two distinct scene-processing networks connecting vision and memory. *eNeuro* 3:ENEURO.0178-16.2016. doi: 10.1523/ENEURO.0178-16.2016

Behzadi, Y., Restom, K., Liau, J., and Liu, T. T. (2007). A component based noise correction method (CompCor) for BOLD and perfusion based fMRI. *Neuroimage* 37, 90–101. doi: 10.1016/j.neuroimage.2007.04.042

Bennett, I. J., and Madden, D. J. (2014). Disconnected aging: cerebral white matter integrity and age-related differences in cognition. *Neuroscience* 276, 187–205. doi: 10.1016/j.neuroscience.2013.11.026

Bennett, I. J., Madden, D. J., Vaidya, C. J., Howard, D. V., and Howard, J. H. Jr. (2010). Age-related differences in multiple measures of white matter integrity: a diffusion tensor imaging study of healthy aging. *Hum. Brain Mapp.* 31, 378–390. doi: 10.1002/hbm.20872

Bicanski, A., and Burgess, N. (2019). A computational model of visual recognition memory via grid cells. *Curr. Biol.* 29, 979.e4–990.e4. doi: 10.1016/j.cub.2019.01.077

Bonner, M. F., and Epstein, R. A. (2017). Coding of navigational affordances in the human visual system. *Proc. Natl. Acad. Sci. U S A* 114, 4793–4798. doi: 10.1073/pnas.1618228114

Brewer, A. A., and Barton, B. (2012). Effects of healthy aging on human primary visual cortex. *Health* 4, 695–702. doi: 10.4236/health.2012.429109

Brewer, A. A., and Barton, B. (2014). Visual cortex in aging and Alzheimer's disease: changes in visual field maps and population receptive fields. *Front. Psychol.* 5:74. doi: 10.3389/fpsyg.2014.00074

Burgess, N. (2008). Spatial cognition and the brain. *Ann. N. Y. Acad. Sci.* 1124, 77–97. doi: 10.1196/annals.1440.002

Burgess, N., Maguire, E. A., and O'Keefe, J. (2002). The human hippocampus and spatial and episodic memory 1. *Neuron* 35, 625–641. doi: 10.1016/s0896-6273(02)00830-9

Cabeza, R., Albert, M., Belleville, S., Craik, F. I. M., Duarte, A., Grady, C. L., et al. (2018). Maintenance, reserve and compensation: the cognitive neuroscience of healthy ageing. *Nat. Rev. Neurosci.* 19, 701–710. doi: 10.1038/s41583-018-0068-2

Chadwick, M. J., Mullally, S. L., and Maguire, E. A. (2013). The hippocampus extrapolates beyond the view in scenes: an fMRI study of boundary extension. *Cortex* 49, 2067–2079. doi: 10.1016/j.cortex.2012.11.010

Chang, L. H., Yotsumoto, Y., Salat, D. H., Andersen, G. J., Watanabe, T., and Sasaki, Y. (2015). Reduction in the retinotopic early visual cortex with normal aging and magnitude of perceptual learning. *Neurobiol. Aging* 36, 315–322. doi: 10.1016/j.neurobiolaging.2014.08.025

Chrastil, E. R., Sherrill, K. R., Aselcioglu, I., Hasselmo, M. E., and Stern, C. E. (2017). Individual differences in human path integration abilities correlate with gray matter volume in retrosplenial cortex, hippocampus and medial prefrontal cortex. *eNeuro* 4:ENEURO.0346-16.2017. doi: 10.1523/ENEURO.0346-16.2017

Cohen, J. (1988). *Statistical Power Analysis for the Behavioral Sciences.* Hillsdale, MI: Lawrence Eribaum Associates.

Colombo, D., Serino, S., Tuena, C., Pedroli, E., Dakanalis, A., Cipresso, P., et al. (2017). Egocentric and allocentric spatial reference frames in aging: a systematic review. *Neurosci. Biobehav. Rev.* 80, 605–621. doi: 10.1016/j.neubiorev.2017.07.012

Corsi, P. M. (1972). *Human Memory and the Medial Temporal Region of the Brain (Doctoral Dissertation, McGill University, 1972)*, Dissertation Abstracts International, 34:819-B.

Coupé, P., Catheline, G., Lanuza, E., and Manjon, J. V. (2017). Towards a unified analysis of brain maturation and aging across the entire lifespan: a MRI analysis. *Hum. Brain Mapp.* 38, 5501–5518. doi: 10.1002/hbm.23743

Dalton, M. A., McCormick, C., and Maguire, E. A. (2019). Differences in functional connectivity along the anterior-posterior axis of human hippocampal subfields. *Neuroimage* 192, 38–51. doi: 10.1016/j.neuroimage.2019.02.066

Damoiseaux, J. S. (2017). Effects of aging on functional and structural brain connectivity. *Neuroimage* 160, 32–40. doi: 10.1016/j.neuroimage.2017.01.077

Davis, S. W., Dennis, N. A., Daselaar, S. M., Fleck, M. S., and Cabeza, R. (2008). Que PASA? The posterior-anterior shift in aging. *Cereb. Cortex* 18, 1201–1209. doi: 10.1093/cercor/bhm155

Doeller, C. F., King, J. A., and Burgess, N. (2008). Parallel striatal and hippocampal systems for landmarks and boundaries in spatial memory. *Proc. Natl. Acad. Sci. U S A* 105, 5915–5920. doi: 10.1073/pnas.0801489105

Ekstrom, A. D. (2015). Why vision is important to how we navigate. *Hippocampus* 25, 731–735. doi: 10.1002/hipo.22449

Epstein, R. A. (2008). Parahippocampal and retrosplenial contributions to human spatial navigation. *Trends Cogn. Sci.* 12, 388–396. doi: 10.1016/j.tics.2008.07.004

Epstein, R. A, and Vass, L. K. (2014). Neural systems for landmark-based wayfinding in humans. *Philos. Trans. R. Soc. Lond. B. Biol. Sci.* 369:20120533. doi: 10.1098/rstb.2012.0533

Ferreira, L. K., and Busatto, G. F. (2013). Resting-state functional connectivity in normal brain aging. *Neurosci. Biobehav. Rev.* 37, 384–400. doi: 10.1016/j.neubiorev.2013.01.017

Fjell, A. M., Walhovd, K. B., Fennema-Notestine, C., McEvoy, L. K., Hagler, D. J., Holland, D., et al. (2009). One-year brain atrophy evident in healthy aging. *J. Neurosci.* 29, 15223–15231. doi: 10.1523/JNEUROSCI.3252-09.2009

Folstein, M. F., Folstein, S. E., and McHugh, P. R. (1975). "Mini-mental state". A practical method for grading the cognitive state of patients for the clinician. *J. Psychiatr. Res.* 12, 189–198. doi: 10.1016/0022-3956(75)90026-6

Friston, K. J., Holmes, A. P., Worsley, K. J., Poline, J. P., Frith, C. D., and Frackowiak, R. S. J. (1995). Statistical parametric maps in functional imaging:

a general linear approach. *Hum. Brain Mapp.* 2, 189–210. doi: 10.1002/hbm.460020402

Gazova, I., Laczó, J., Rubinova, E., Mokrisova, I., Hyncicova, E., Andel, R., et al. (2013). Spatial navigation in young versus older adults. *Front. Aging Neurosci.* 5, 1–8. doi: 10.3389/fnagi.2013.00094

Glasser, M. F., Sotiropoulos, S. N., Wilson, J. A., Coalson, T. S., Fischl, B., Andersson, J. L., et al. (2013). The minimal preprocessing pipelines for the human connectome project. *Neuroimage* 80, 105–124. doi: 10.1016/j.neuroimage.2013.04.127

Goldstein, A., and Mesfin, F. B. (2017). "Neuroanatomy, Corpus Callosum," in *StatPearls* (Treasure Island, FL: StatPearls).

Guderian, S., Dzieciol, A. M., Gadian, D. G., Jentschke, S., Doeller, C. F., Burgess, N., et al. (2015). Hippocampal volume reduction in humans predicts impaired allocentric spatial memory in virtual-reality navigation. *J. Neurosci.* 35, 14123–14131. doi: 10.1523/jneurosci.0801-15.2015

Gunning-Dixon, F. M., Brickman, A. M., Cheng, J. C., and Alexopoulos, G. S. (2009). Aging of cerebral white matter: a review of MRI findings. *Int. J. Geriatr. Psychiatry* 24, 109–117. doi: 10.1002/gps.2087

Hao, X., Huang, Y., Li, X., Song, Y., Kong, X., Wang, X., et al. (2016). Structural and functional neural correlates of spatial navigation: a combined voxel-based morphometry and functional connectivity study. *Brain Behav.* 6:e00572. doi: 10.1002/brb3.572

Harris, M. A., and Wolbers, T. (2012). Ageing effects on path integration and landmark navigation. *Hippocampus* 22, 1770–1780. doi: 10.1002/hipo.22011

Harris, M. A., Wiener, J. M., and Wolbers, T. (2012). Aging specifically impairs switching to an allocentric navigational strategy. *Front. Aging Neurosci.* 4:9. doi: 10.3389/fnagi.2012.00029

Henderson, J. M., Larson, C. L., and Zhu, D. C. (2008). Full scenes produce more activation than close-up scenes and scene-diagnostic objects in parahippocampal and retrosplenial cortex: an fMRI study. *Brain Cogn.* 66, 40–49. doi: 10.1016/j.bandc.2007.05.001

Herweg, N. A., and Kahana, M. J. (2018). Spatial representations in the human brain. *Front. Hum. Neurosci.* 12:297. doi: 10.3389/fnhum.2018.00297

Hrybouski, S., MacGillivray, M., Huang, Y., Madan, C. R., Carter, R., Seres, P., et al. (2019). Involvement of hippocampal subfields and anterior-posterior subregions in encoding and retrieval of item, spatial and associative memories: longitudinal versus transverse axis. *Neuroimage* 191, 568–586. doi: 10.1016/j.neuroimage.2019.01.061

Hua, K., Zhang, J., Wakana, S., Jiang, H., Li, X., Reich, D. S., et al. (2008). Tract probability maps in stereotaxic spaces: analyses of white matter anatomy and tract-specific quantification. *Neuroimage* 39, 336–347. doi: 10.1016/j.neuroimage.2007.07.053

Iglói, K., Doeller, C. F., Paradis, A.-L., Benchenane, K., Berthoz, A., Burgess, N., et al. (2014). Interaction between hippocampus and cerebellum crus I in sequence-based but not place-based navigation. *Cereb. Cortex* 25, 4146–4154. doi: 10.1093/cercor/bhu132

Ito, H. T. (2018). Prefrontal-hippocampal interactions for spatial navigation. *Neurosci. Res.* 129, 2–7. doi: 10.1016/j.neures.2017.04.016

Janzen, G., and van Turennout, M. (2004). Selective neural representation of objects relevant for navigation. *Nat. Neurosci.* 7, 673–677. doi: 10.1038/nn1257

Jbabdi, S., and Johansen-Berg, H. (2011). Tractography: where do we go from here? *Brain Connect.* 1, 169–183. doi: 10.1089/brain.2011.0033

Jeurissen, B., Descoteaux, M., Mori, S., and Leemans, A. (2017). Diffusion MRI fiber tractography of the brain. *NMR Biomed.* 32:e3785. doi: 10.1002/nbm.3785

Jones, D. K., Knösche, T. R., and Turner, R. (2013). White matter integrity, fiber count and other fallacies: the do's and don'ts of diffusion MRI. *Neuroimage* 73, 239–254. doi: 10.1016/j.neuroimage.2012.06.081

Julian, J. B., Keinath, A. T., Marchette, S. A., and Epstein, R. A. (2018). The neurocognitive basis of spatial reorientation. *Curr. Biol.* 28, R1059–R1073. doi: 10.1016/j.cub.2018.04.057

Julian, J. B., Ryan, J., Hamilton, R. H., Epstein, R. A., Julian, J. B., Ryan, J., et al. (2016). The occipital place area is causally involved in representing environmental boundaries during navigation. *Curr. Biol.* 26, 1104–1109. doi: 10.1167/15.12.512

Kamps, F. S., Lall, V., and Dilks, D. D. (2016). The occipital place area represents first-person perspective motion information through scenes. *Cortex* 83, 17–26. doi: 10.1016/j.cortex.2016.06.022

Kauffmann, L., Ramanoël, S., Guyader, N., Chauvin, A., and Peyrin, C. (2015). Spatial frequency processing in scene-selective cortical regions. *Neuroimage* 112, 86–95. doi: 10.1016/j.neuroimage.2015.02.058

Kim, J. G., Aminoff, E. M., Kastner, S., and Behrmann, M. (2015). A neural basis for developmental topographic disorientation. *J. Neurosci.* 35, 12954–12969. doi: 10.1523/jneurosci.0640-15.2015

Klencklen, G., Després, O., and Dufour, A. (2012). What do we know about aging and spatial cognition? Reviews and perspectives. *Ageing Res. Rev.* 11, 123–135. doi: 10.1016/j.arr.2011.10.001

Köhler, S., Crane, J., and Milner, B. (2002). Differential contributions of the parahippocampal place area and the anterior hippocampus to human memory for scenes. *Hippocampus* 12, 718–723. doi: 10.1002/hipo.10077

Korthauer, L. E., Nowak, N. T., Moffat, S. D., An, Y., Rowland, L. M., Barker, P. B., et al. (2016). Correlates of virtual navigation performance in older adults. *Neurobiol. Aging* 39, 118–127. doi: 10.1016/j.neurobiolaging.2015.12.003

Kozhevnikov, M., and Hegarty, M. (2001). A dissociation between object-manipulation spatial ability and spatial orientation ability. *Mem. Cognit.* 29, 745–756. doi: 10.3758/bf03200477

Kumar, R., Chavez, A. S., Macey, P. M., Woo, M. A., and Harper, R. M. (2013). Brain axial and radial diffusivity changes with age and gender in healthy adults. *Brain Res.* 1512, 22–36. doi: 10.1016/j.brainres.2013.03.028

Lee, A. C. H., Bussey, T. J., Murray, E. A., Saksida, L. M., Epstein, R. A., Kapur, N., et al. (2005). Perceptual deficits in amnesia: challenging the medial temporal lobe "mnemonic" view. *Neuropsychologia* 43, 1–11. doi: 10.1016/j.neuropsychologia.2004.07.017

Lerner, A., Mogensen, M. A., Kim, P. E., Shiroishi, M. S., Hwang, D. H., and Law, M. (2014). Clinical applications of diffusion tensor imaging. *World Neurosurg.* 82, 96–109. doi: 10.1016/j.wneu.2013.07.083

Lester, A. W., Moffat, S. D., Wiener, J. M., Barnes, C. A., and Wolbers, T. (2017). The aging navigational system. *Neuron* 95, 1019–1035. doi: 10.1016/j.neuron.2017.06.037

Lithfous, S., Dufour, A., and Després, O. (2013). Spatial navigation in normal aging and the prodromal stage of Alzheimer's disease: insights from imaging and behavioral studies. *Ageing Res. Rev.* 12, 201–213. doi: 10.1016/j.arr.2012.04.007

Madden, D. J., Bennett, I. J., and Song, A. W. (2009). Cerebral white matter integrity and cognitive aging: contributions from diffusion tensor imaging. *Neuropsychol. Rev.* 19, 415–435. doi: 10.1007/s11065-009-9113-2

Maguire, E. A. (2001). The retrosplenial contribution to human navigation: a review of lesion and neuroimaging findings. *Scand. J. Psychol.* 42, 225–238. doi: 10.1111/1467-9450.00233

Maguire, E. A., and Mullally, S. L. (2013). The hippocampus: a manifesto for change. *J. Exp. Psychol. Gen.* 142, 1180–1189. doi: 10.1037/a0033650

Malykhin, N. V., Huang, Y., Hrybouski, S., and Olsen, F. (2017). Differential vulnerability of hippocampal subfields and anteroposterior hippocampal subregions in healthy cognitive aging. *Neurobiol. Aging* 59, 121–134. doi: 10.1016/j.neurobiolaging.2017.08.001

Manjón, J. V., and Coupé, P. (2015). volBrain: an online MRI brain volumetry system. *Front. Neuroinform.* 10:30. doi: 10.3389/fninf.2016.00030

Marchette, S. A., Vass, L. K., Ryan, J., and Epstein, R. A. (2015). Outside looking in: landmark generalization in the human navigational system. *J. Neurosci.* 35, 14896–14908. doi: 10.1523/jneurosci.2270-15.2015

Mitchell, A. S., Czajkowski, R., Zhang, N., Jeffery, K., and Nelson, A. J. D. (2018). Retrosplenial cortex and its role in spatial cognition. *Brain Neurosci. Adv.* 2:2398212818757098. doi: 10.1177/2398212818757098

Moffat, S. D. (2009). Aging and spatial navigation: what do we know and where do we go? *Neuropsychol. Rev.* 19, 478–489. doi: 10.1007/s11065-009-9120-3

Moffat, S. D., Elkins, W., and Resnick, S. M. (2006). Age differences in the neural systems supporting human allocentric spatial navigation. *Neurobiol. Aging* 27, 965–972. doi: 10.1016/j.neurobiolaging.2005.05.011

Mori, S., and Zhang, J. (2006). Principles of diffusion tensor imaging and its applications to basic neuroscience research. *Neuron* 51, 527–539. doi: 10.1016/j.neuron.2006.08.012

Morris, D. M., Embleton, K. V., and Parker, G. J. M. (2008). Probabilistic fibre tracking: differentiation of connections from chance events. *Neuroimage* 42, 1329–1339. doi: 10.1016/j.neuroimage.2008.06.012

Nasr, S., and Tootell, R. B. H. (2012). A cardinal orientation bias in scene-selective visual cortex. *J. Neurosci.* 32, 14921–14926. doi: 10.1523/jneurosci.2036-12.2012

O'Sullivan, M., Jones, D. K., Summers, P. E., Morris, R. G., Williams, S. C., and Markus, H. S. (2001). Evidence for cortical "disconnection" as a mechanism of age-related cognitive decline. *Neurology* 57, 632–638. doi: 10.1212/wnl.57.4.632

Owsley, C. (2011). Aging and vision. *Vision Res.* 51, 1610–1622. doi: 10.1016/j.visres.2010.10.020

Owsley, C. (2016). Vision and aging. *Annu. Rev. Vis. Sci.* 2, 255–271. doi: 10.1146/annurev-vision-111815-114550

Park, S., Brady, T. F., Greene, M. R., and Oliva, A. (2011). Disentangling scene content from spatial boundary: complementary roles for the parahippocampal place area and lateral occipital complex in representing real-world scenes. *J. Neurosci.* 31, 1333–1340. doi: 10.1523/jneurosci.3885-10.2011

Patai, E. Z., and Spiers, H. J. (2017). Human navigation: occipital place area detects potential paths in a scene. *Curr. Biol.* 27, R599–R600. doi: 10.1016/j.cub.2017.05.012

Persichetti, A. S., and Dilks, D. D. (2016). Perceived egocentric distance sensitivity and invariance across scene-selective cortex. *Cortex* 77, 155–163. doi: 10.1016/j.cortex.2016.02.006

Ramanoël, S., Hoyau, E., Kauffmann, L., Renard, F., Pichat, C., Boudiaf, N., et al. (2018). Gray matter volume and cognitive performance during normal aging. A voxel-based morphometry study. *Front. Aging Neurosci.* 10:235. doi: 10.3389/fnagi.2018.00235

Ramanoël, S., Kauffmann, L., Cousin, E., Dojat, M., and Peyrin, C. (2015). Age-related differences in spatial frequency processing during scene categorization. *PLoS One* 10:e0134554. doi: 10.1371/journal.pone.0134554

Robertson, C. E., Hermann, K. L., Mynick, A., Kravitz, D. J., and Kanwisher, N. (2016). Neural representations integrate the current field of view with the remembered 360 degrees panorama in scene-selective cortex. *Curr. Biol.* 26, 2463–2468. doi: 10.1016/j.cub.2016.07.002

Rodgers, M. K., Sindone, J. A.III, and Moffat, S. D. (2012). Effects of age on navigation strategy. *Neurobiol. Aging* 33, 202.e15–202.e22. doi: 10.1016/j.neurobiolaging.2010.07.021

Rodriguez, P. F. (2010). Neural decoding of goal locations in spatial navigation in humans with fMRI. *Hum. Brain Mapp.* 31, 391–397. doi: 10.1002/hbm.20873

Schuhfried, G. (2012). *Vienna Test System (VTS) [Computer software]*. Moedling, Austria: Schuhfried GmbH.

Soares, J. M., Marques, P., Alves, V., and Sousa, N. (2013). A hitchhiker's guide to diffusion tensor imaging. *Front. Neurosci.* 7:31. doi: 10.3389/fnins.2013.00031

Spiers, H. J., and Barry, C. (2015). Neural systems supporting navigation. *Curr. Opin. Behav. Sci.* 1, 47–55. doi: 10.1016/j.cobeha.2014.08.005

Spiers, H. J., and Gilbert, S. J. (2015). Solving the detour problem in navigation: a model of prefrontal and hippocampal interactions. *Front. Hum. Neurosci.* 9:125. doi: 10.3389/fnhum.2015.00125

Stangl, M., Achtzehn, J., Huber, K., Dietrich, C., Tempelmann, C., and Wolbers, T. (2018). Compromised grid-cell-like representations in old age as a key mechanism to explain age-related navigational deficits. *Curr. Biol.* 28, 1108.e6–1115.e6. doi: 10.1016/j.cub.2018.02.038

Tamura, I., Kitagawa, M., Otsuki, M., Kikuchi, S., Tashiro, K., and Dubois, B. (2007). Pure topographical disorientation following a right forceps major of the splenium lesion: a case study. *Neurocase* 13, 178–184. doi: 10.1080/13554790701448812

Tzourio-Mazoyer, N., Landeau, B., Papathanassiou, D., Crivello, F., Etard, O., Delcroix, N., et al. (2002). Automated anatomical labeling of activations in SPM using a macroscopic anatomical parcellation of the MNI MRI single-subject brain. *Neuroimage* 15, 273–289. doi: 10.1006/nimg.2001.0978

Vandenberg, S. G., and Kuse, A. R. (1978). Mental rotations, a group test of three dimensional space visualization. *Percpetual and Motor Skills.* 10, 792–802. doi: 10.2466/pms.1978.47.2.599

Vann, S. D., Aggleton, J. P., and Maguire, E. A. (2009). What does the retrosplenial cortex do? *Nat. Rev. Neurosci.* 10, 792–802. doi: 10.1038/nrn2733

Wandell, B. A. (2016). Clarifying human white matter. *Annu. Rev. Neurosci.* 39, 103–128. doi: 10.1146/annurev-neuro-070815-013815

Whitfield-Gabrieli, S., and Nieto-Castanon, A. (2012). Conn: a functional connectivity toolbox for correlated and anticorrelated brain networks. *Brain Connect.* 2, 125–141. doi: 10.1089/brain.2012.0073

Winklewski, P. J., Sabisz, A., Naumczyk, P., Jodzio, K., Szurowska, E., and Szarmach, A. (2018). Understanding the physiopathology behind axial and radial diffusivity changes-what do we know? *Front. Neurol.* 9:92. doi: 10.3389/fneur.2018.00092

Wolbers, T., and Hegarty, M. (2010). What determines our navigational abilities? *Trends Cogn. Sci.* 14, 138–146. doi: 10.1016/j.tics.2010.01.001

Wolbers, T., Wiener, J. M., Mallot, H. A., and Büchel, C. (2007). Differential recruitment of the hippocampus, medial prefrontal cortex and the human motion complex during path integration in humans. *J. Neurosci.* 27, 9408–9416. doi: 10.1523/jneurosci.2146-07.2007

Zeidman, P., and Maguire, E. A. (2016). Anterior hippocampus: the anatomy of perception, imagination and episodic memory. *Nat. Rev. Neurosci.* 17, 173–182. doi: 10.1038/nrn.2015.24

Zeidman, P., Mullally, S. L., and Maguire, E. A. (2015). Constructing, perceiving and maintaining scenes: hippocampal activity and connectivity. *Cereb. Cortex (New York, N.Y. 1991)* 25, 3836–3855. doi: 10.1093/cercor/bhu266

Zhong, J. Y., and Moffat, S. D. (2018). Extrahippocampal contributions to age-related changes in spatial navigation ability. *Front. Hum. Neurosci.* 12:272. doi: 10.3389/fnhum.2018.00272

Conflict of Interest: The authors declare that the research was conducted in the absence of any commercial or financial relationships that could be construed as a potential conflict of interest.

frontiers in Neural Circuits

ORIGINAL RESEARCH
published: 30 October 2019
doi: 10.3389/fncir.2019.00070

Two Neural Circuits to Point Towards Home Position After Passive Body Displacements

Jean Blouin[1], Anahid H. Saradjian[1], Jean-Philippe Pialasse[2], Gerome A. Manson[1,3], Laurence Mouchnino[1] and Martin Simoneau[2,4]*

[1]Aix-Marseille Univ, CNRS, Laboratoire de Neurosciences Cognitives, Marseille, France, [2]Faculté de Médecine, Département de Kinésiologie, Université Laval, Québec, QC, Canada, [3]Centre for Motor Control, University of Toronto, Toronto, ON, Canada, [4]Centre Interdisciplinaire de Recherche en Réadaptation et Intégration Sociale (CIRRIS), Québec, QC, Canada

A challenge in motor control research is to understand the mechanisms underlying the transformation of sensory information into arm motor commands. Here, we investigated these transformation mechanisms for movements whose targets were defined by information issued from body rotations in the dark (i.e., idiothetic information). Immediately after being rotated, participants reproduced the amplitude of their perceived rotation using their arm (Experiment 1). The cortical activation during movement planning was analyzed using electroencephalography and source analyses. Task-related activities were found in regions of interest (ROIs) located in the prefrontal cortex (PFC), dorsal premotor cortex, dorsal region of the anterior cingulate cortex (ACC) and the sensorimotor cortex. Importantly, critical regions for the cognitive encoding of space did not show significant task-related activities. These results suggest that arm movements were planned using a sensorimotor-type of spatial representation. However, when a 8 s delay was introduced between body rotation and the arm movement (Experiment 2), we found that areas involved in the cognitive encoding of space [e.g., ventral premotor cortex (vPM), rostral ACC, inferior and superior posterior parietal cortex (PPC)] showed task-related activities. Overall, our results suggest that the use of a cognitive-type of representation for planning arm movement after body motion is necessary when relevant spatial information must be stored before triggering the movement.

Keywords: idiothetic, vestibular, movement planning, frontal lobe, posterior lobe, space updating, body motion, human

OPEN ACCESS

Edited by:
Michele Tagliabue, Université Paris Descartes, France

Reviewed by:
Luc Selen, Radboud University, Netherlands
Scott S. Bolkan, Princeton University, United States

****Correspondence:***
Jean Blouin
jean.blouin@univ-amu.fr

Received: *29 May 2019*
Accepted: *15 October 2019*
Published: *30 October 2019*

Citation:
Blouin J, Saradjian AH, Pialasse J-P, Manson GA, Mouchnino L and Simoneau M (2019) Two Neural Circuits to Point Towards Home Position After Passive Body Displacements. Front. Neural Circuits 13:70. doi: 10.3389/fncir.2019.00070

INTRODUCTION

After exposure to passive rotation with the eyes closed, we have a fair idea of our new position relative to the surrounding objects. It would then be possible to move the arm to point towards these objects even without visual feedback. These perceptual and motor outcomes are thought to reflect the brain's capacity to process idiothetic information generated during self-motion (e.g., from vestibular receptors) to update the spatial representation of the environment and to plan the arm motor commands.

Much progress has been made on the neural processes underlying spatial updating through idiothetic information since the seminal discovery of hippocampal place cells by O'Keefe and Dostrovsky (1971; for recent advances, see Cullen and Taube, 2017;

Moser et al., 2017; Laurens and Angelaki, 2018). In contrast, the neural mechanisms underlying the control of movements through idiothetic information remain largely unknown. To help elucidate these mechanisms, we recorded human cortical activities associated with the planning of arm movements defined through self-motion sensory cues. We adapted an established protocol for investigating space updating processes in human and non-human primates by asking seated participants to move their arm with the same amplitude, but in the opposite direction, of the passive body rotation they just experienced (Bloomberg et al., 1988; Israël et al., 1993; Ivanenko et al., 1997; Blouin et al., 1998; Medendorp et al., 2002; Baker et al., 2003; Bresciani et al., 2005; Wei et al., 2006; Ventre-Dominey and Vallee, 2007; Simoneau et al., 2009). Relevant body rotation information for planning such movements are deemed to be largely mediated by vestibular inputs, as perception of passive motion in the dark is largely impaired in patients suffering total bilateral vestibular loss (Valko et al., 2012).

According to research on space perception, the parameters of the arm movement produced after body motion would be defined using a cognitive representation of the body-in-space position which is updated while being rotated (Loomis et al., 1996; Klier and Angelaki, 2008; Medendorp, 2011). As an important hub structure for processing visuospatial information (Andersen et al., 1997; Medendorp et al., 2003; Gutteling and Medendorp, 2016), the occipito-parietal cortex could then provide relevant information for planning the arm movement. This hypothesis is consistent with the observation made by Ventre-Dominey and Vallee (2007) that patients with an occipito-parietal lesion show large errors when pointing towards memorized targets after passive body motion.

The cingulate and prefrontal cortices, which both respond to vestibular inputs (Dieterich et al., 2003; Stephan et al., 2005; Smith et al., 2012), could also contribute to movement planning processes. The cingulate cortex indeed contains hand motor areas that connect to spinal motor neurons (Amiez and Petrides, 2014) and to the arm area of the motor cortex (Dum and Strick, 1991). The contribution of the prefrontal cortex (PFC) to vestibular-based motor processes is supported by the large errors observed in individuals with PFC lesions when producing vestibular memory-contingent ocular movements (Israël et al., 1992; Pierrot-Deseilligny et al., 1993; Pierrot-Deseilligny et al., 1995).

In the present study, we used the electroencephalographic (EEG) source localization to determine if the pattern of activation in the fronto-parietal areas would be consistent with the hypothesis that arm motor commands are built according to a cognitive representation of visual space that is updated during body rotations.

MATERIALS AND METHODS

Participants

Nine healthy adults participated in this study (three women, mean age: 26.6 ± 2.7 years). All participants were right-handed with normal or corrected-to-normal vision. The experiment was conducted in accordance with the Declaration of Helsinki. A written informed consent was obtained from the participants before the study and the experiment was approved by the Laval University Biomedical Ethics Committee.

Experimental Set-Up

We used the same experimental set-up that has been employed in other investigations of the vestibular functions (Simoneau et al., 2009; Mackrous and Simoneau, 2011, 2014, 2015). The participants sat on a chair in a completely dark room. They were secured to the chair using a four-point belt and the use of a chin rest limited movements of the head relative to the trunk during the chair rotations. The chair could be manually rotated around the vertical axis by an experimenter using a handle attached behind the chair. Rotating the chair manually minimized the risk of contaminating EEG recordings by electric noise that could be generated by motorized revolving chairs (for a discussion on this issue, see Nolan et al., 2009). An array of four LEDs placed on the floor behind the chair indicated to the experimenter the initial chair position and the angular targets of the rotations (i.e., 20°, 30° and 40° in the counter-clockwise direction). A laser fixed on the handle behind the chair and directed toward the array of LEDs helped the experimenter to produce the required chair displacements. The experimenter produced discrete chair motion without making corrections when the LEDs of the chair and of the angular target did not match. Note that the variability in the manually-produced rotations observed for each angular target, which was expected to be small according to previous studies from different laboratories using similar set-ups (e.g., Hanson and Goebel, 1998; Blouin et al., 2010; Mackrous et al., 2019), was not detrimental in the present experimental context. In fact, it introduced, together with the use of three different rotation amplitudes, uncertainty into movement planning and minimized the risk of participants implementing stereotyped arm motor responses. Chair angular position was recorded with an optical encoder

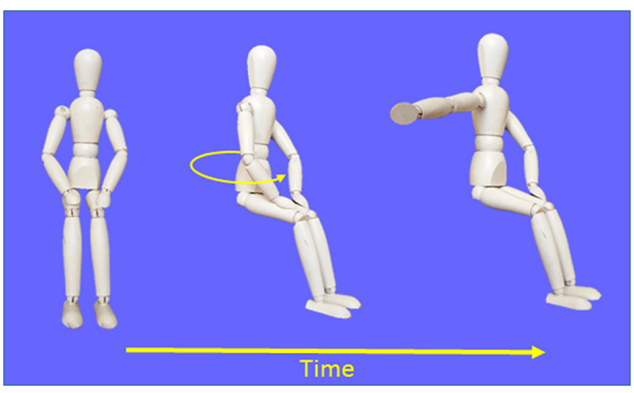

FIGURE 1 | Schematic representation of the procedures used in the Movement condition.

(1 kHz, US digital, model H5S, Vancouver, WA, USA) fixed at the center of rotation of the chair (see below for chair kinematics analyses).

Design of the Experiment

Diagrams depicting the experimental task are provided in **Figure 1**. Throughout the trials, participants had to gaze at a chair-fixed LED located 1 m straight-ahead at eye level. This prevented participants from determining body displacements through sensorimotor signals linked to eye position and motion. Before each trial, the verbal instruction "ready" was given to the participants while their right hand was resting on their right thigh. Then, 2–3 s later, one of the three angular targets behind the chair turned on, indicating to the experimenter the rotation amplitude that had to be produced in the counter-clockwise direction. One-hundred milliseconds after rotation offset (i.e., after the chair angular velocity dropped below 2.5° s^{-1}), a buzzer emitted a 50 ms tone. For the participants, this auditory cue served as an imperative (go) signal to reproduce the amplitude of perceived body rotations with a rapid horizontal movement of the right arm in the clockwise direction (i.e., opposite to the rotation direction). The movement consisted of external and upper rotations of the shoulder. Note that because the buzzer was fixed 1.5 m above the participants' head, the tone could not be used as a spatial reference to determine body orientation after rotation. After the arm movement, the participants were rotated back to the starting position and got ready for the next trial which started only after a minimum delay of 15 s.

The EEG recordings after body rotations (i.e., during the planning of the arm movement) could contain noise and task-irrelevant activities induced for instance by the imperative auditory stimulus, residual rotation-induced ocular movements or artifacts arising from motion of the electrode cables. To identify the cortical activities related to arm movement planning, we compared the EEG recordings with those obtained in a control condition (referred to as no-movement condition) wherein no instruction other than keeping quiet during the rotation and after the tone (i.e., after rotation offset) were given to the participants. Our reasoning was that any differential activities after the tone between conditions with and without arm movement would reflect cognitive or sensorimotor processes relevant to movement planning. Participants performed 75 trials in both the movement and no-movement conditions (25 trials for each pseudo-randomly selected angular target) for a total of 150 trials. Five participants started the experimental session with the movement condition.

Figure 2 shows the mean amplitudes (left column) and velocities (right column) of the chair angular displacement (with and without arm movements). The figure illustrates that, in both conditions, the body rotations had amplitudes close to the angular targets of the rotation (i.e., 20°, 30°, 40°) and had similar bell-shaped velocity profiles. Chair kinematics similarity between conditions was confirmed by the results of

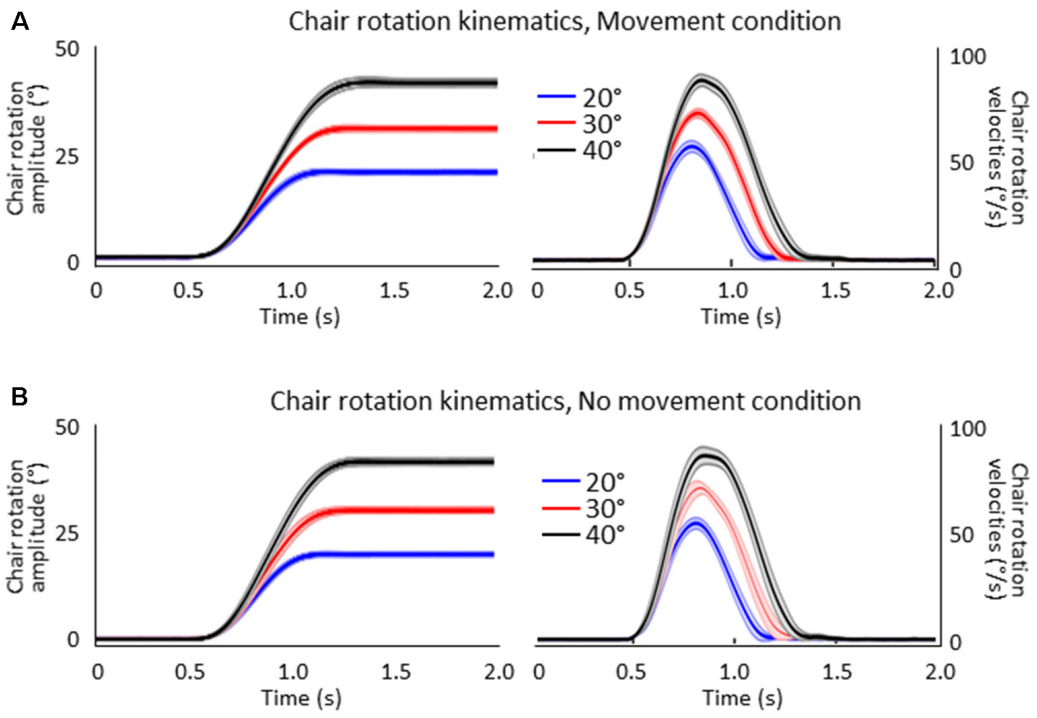

FIGURE 2 | Mean amplitudes (left column) and velocities (right column) of the chair rotations for the 20°, 30° and 40° chair rotation conditions. Shaded areas represent the between-participant standard deviation of the means. **(A)** Movement condition. **(B)** No-movement condition.

the ANOVAs 2 (Condition) × 3 (Angular rotation) which did not show significant effect ($p > 0.05$) of Condition on rotation amplitudes ($F_{(1,16)} = 0.23$, $p = 0.64$) or on peaks angular velocity ($F_{(1,16)} = 0.85$, $p = 0.37$) and neither an interaction of Condition × Angular rotation ($F_{(2,32)} = 0.75$, $p = 0.48$ and $F_{(2,32)} = 1.96$, $p = 0.16$, respectively). Overall, these results suggest that participants experienced similar idiothetic information when they produced or did not produce arm movements after the rotations.

EEG Activity

EEG activity was recorded continuously at 1,000 Hz with a Geodesic 64-channel EEG sensor net (Electrical Geodesics Inc., Eugene, OR, USA). Data pre-processing was performed with BrainVision Analyzer 2 (Brain Products, Germany). The raw recordings were referenced to the averaged activity of the 64 electrodes before being synchronized with respect to the time of the auditory cue (i.e., the imperative signal in the movement conditions). Then, ocular artifacts (e.g., blinks, saccades) were subtracted from the EEG recordings by removing the corresponding component as revealed by the independent component analyses (ICA). In both conditions, we averaged the data for each participant and electrode. The EEG activities associated with the planning of the arm movement were therefore analyzed without considering the amplitude of the rotations that preceded the arm movements.

We estimated the neural sources of the late SEPs using the dynamical Statistical Parametric Mapping (dSPM, Dale et al., 2000) implemented in the Brainstorm software (Tadel et al., 2011, freely available at: http://neuroimage.usc.edu/brainstorm). We used the data from all processed sensors and averaged for each participant, condition, and electrode. The forward model was computed using a three-shell sphere boundary element model (BEM) on the anatomical MRI brain MNI Colin27 template (15,000 vertices), a predominant volume conductor model (Mosher et al., 1999; Huang et al., 2016). The baseline used to compute the co-variance matrices was set between −1.5 s and −1 s prior to the auditory cue, i.e., before the rotations as the longest recorded rotation duration was 1,490 ms.

Based on classical topographical maps of the cortex, we manually defined several region of interests (ROIs) in the frontal, parietal and occipital lobes. The location of these ROIs allowed us to assess the activation of regions that are deemed to be important for spatial representation and motor processes (see **Figure 3**). The number of vertices was similar for corresponding ROIs of the right and left hemispheres. In the movement condition, the mean absolute current amplitude (which reflects brain activation Tadel et al., 2011, 2019) was computed for each ROI between the auditory tone and the arm electromyography (EMG) onset (see below for EMG recordings). We operationally defined this time window as corresponding to the movement planning phase. Note however that processes related to motor planning might have occurred before the tone, for instance during body rotation, and that the activity recorded close to the movement onset could also be related to the commands triggering the arm movements.

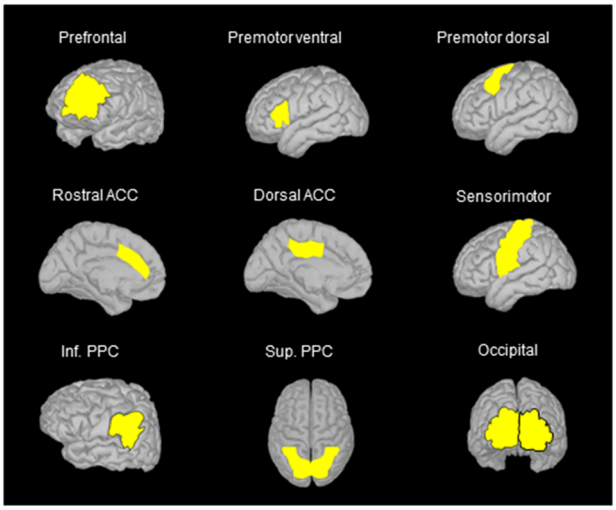

FIGURE 3 | Location of the regions of interest (ROIs) on the anatomical MRI Colin 27 brain template that was used to compute cortical activations. The names of the ROIs were selected on the basis of the areas identified in classical cortical topographical maps that better represent the location of the ROIs used in the present study. Note that similar ROIs were defined for the left and right hemispheres, but only ROIs in the left hemisphere are illustrated when using side views. ACC, anterior cingulate cortex; Inf. PPC, inferior posterior parietal cortex; Sup. PPC, superior posterior parietal cortex.

The dynamics of the ongoing EEG activities was investigated by computing the mean absolute current amplitude during the planning phase for each ROI, for each quintile (see below "Muscle activity" section for quintile computation). The analysis of the ongoing cortical activity was made possible by the EEG's excellent temporal resolution (Nunez and Srinivasan, 2006). It enabled us to determine if the activities computed in the different ROIs were more related to the generation of the motor commands (e.g., in case of a late increase of current amplitude) or rather to non-motoric processes (e.g., spatial or working memory processes, in case of an early or more sustained current flow).

Behavioral Recordings

Hand movements were recorded at 100 Hz using a small (2.0 mm × 9.9 mm) 6-degree-of-freedom electromagnetic sensor (trackSTAR model 180, Ascension Technology Corporation, Shelburne, VT, USA) attached to the right fingertip. The norm of the vector between the initial and final hand position was respectively 32.55 ± 6.85 cm, 39.83 ± 6.92 cm and 48.19 ± 8.32 cm for the 20°, 30° and 40° body rotations. These observations indicate that participants scaled the amplitude of their movements according to the magnitude of their passive rotations as specified in the instructions.

Muscle Activity

We recorded the EMG activity of the right posterior deltoid and of the triceps brachial muscles, which were the prime mover muscles for the required arm movements. After cleaning the skin with alcohol, we affixed self-adhesive bipolar Ag-AgCl electrodes (2 cm center-to-center inter-electrodes spacing) near the middle third of these muscles, along a line parallel to their

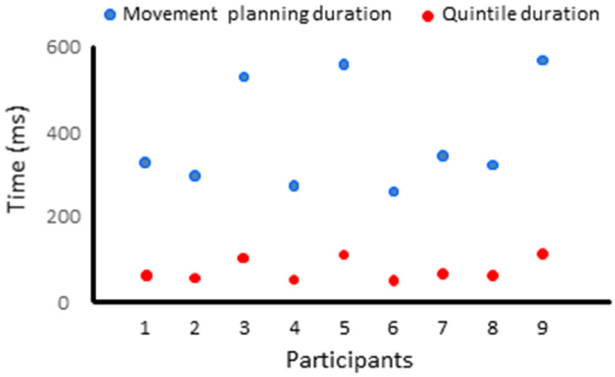

FIGURE 4 | Duration of the movement planning phase and of the quintiles for each participant.

fiber orientation (Brindle et al., 2006; Cram and Kasman, 2011). The EMG signals were pre-amplified (1,000×) at the skin site and then digitally sampled at 1 kHz using a Bortec AMT-8 system (Bortec Biomedical, Calgary, AB, Canada). The time elapsed between the imperative signal and the EMG onset was operationally defined as the planning phase. EMG onset was determined visually after summing the rectified EMG signals from both agonist muscles and squaring the results.

The movement planning phase was divided in quintiles, for each participant (i.e., the EMG reaction times were divided in five bins of equal duration). The duration of the quintiles depended on each participant's average EMG reaction time (average EMG reaction times = 391 ± 127 ms, average quintile duration = 78 ms, see **Figure 4**). Quintiles of the same durations served to analyze the dynamics of the cortical activation for the Movement and No-movement conditions.

Statistical Analyses

ANOVAs were used to contrast the mean current computed for each ROI between conditions with and without arm movements. All analyses employed a 2 (Condition: movement, no-movement) × 5 (Quintile: 1–5) design with repeated measures on both factors. As noted above, in all conditions, the EEG recording after the auditory signal (i.e., imperative signal in the movement condition) could contain noise or task-irrelevant activities that could decline with post-rotation duration. We thus reasoned that any differential activity between the movement and no-movement conditions would be specifically associated with task-relevant cognitive or sensorimotor processes. In this light, we will only consider here the significant main effects of Condition and the significant Condition × Quintile interactions as they were deemed to strictly reflect task-related processes. Significant Condition × Quintile interactions were further analyzed using Newman–Keul's tests. Note that when main effects could be solely explained by a higher-order interaction, only the break-down of the interaction will be reported. Alpha level was set to 0.05 for all analyses. **Table 1** reports all statistical results of the ANOVAs. **Figure 5** depicts the results of the *post hoc* tests and the differences in activity between the Movement and No-movement conditions for all participants for ROIs showing significant effects.

RESULTS AND DISCUSSION

The ROIs showing significant movement-related activations were mainly circumscribed in the frontal lobe (**Figure 5**). The PFC contralateral to the reaching arm showed greater activation in the movement condition in all quintiles. The PFC is an important cortical region for stocking egocentric spatial information in working memory (Ma et al., 2012). The fact

TABLE 1 | Results of the statistical analyses of Experiment 1 (No delay) and of Experiment 2 (Delay).

ROIs	No delay (Experiment 1)		Delay (Experiment 2)	
	Condition	Condition × Quintile	Task	Task × Quintile
Left PFC	$F_{(1,8)} = 6.29$; $p = 0.03$*	$F_{(4,32)} = 0.67$; $p = 0.61$	$F_{(1,8)} = 12.56$; $p = 0.008$**	$F_{(4,32)} = 2.25$; $p = 0.08$
Right PFC	$F_{(1,8)} = 4.30$; $p = 0.07$	$F_{(4,32)} = 1.42$; $p = 0.25$	$F_{(1,8)} = 9.45$; $p = 0.01$*	$F_{(4,32)} = 0.87$; $p = 0.48$
Left SMC	$F_{(1,8)} = 2.65$; $p = 0.14$	$F_{(4,32)} = 3.95$; 0.01*	$F_{(1,8)} = 7.34$; $p = 0.02$*	$F_{(4,32)} = 3.23$; $p = 0.02$*
Right SMC	$F_{(1,8)} = 0.002$; $p = 0.96$	$F_{(4,32)} = 1.88$; $p = 0.14$	$F_{(1,8)} = 3.68$; $p = 0.09$	$F_{(4,32)} = 3.26$; $p = 0.02$*
Left vPM	$F_{(1,8)} = 0.09$; $p = 0.67$	$F_{4,32} = 0.59$; $p = 0.67$	$F_{(1,8)} = 5.36$; $p = 0.04$*	$F_{(4,32)} = 2.68$; $p = 0.04$*
Right vPM	$F_{(1,8)} = 0.01$; $p = 0.92$	$F_{(4,32)} = 0.24$; $p = 0.91$	$F_{(1,8)} = 0.21$; $p = 0.61$	$F_{(4,32)} = 0.30$; $p = 0.87$
Left dPM	$F_{(1,8)} = 0.001$; $p = 0.97$	$F_{(4,32)} = 4.77$; $p = 0.004$**	$F_{(1,8)} = 13.06$; $p = 0.007$**	$F_{(4,32)} = 6.44$; $p = 0.001$**
Right dPM	$F_{(1,8)} = 0.10$; $p = 0.755$	$F_{(4,32)} = 0.31$; 0.87	$F_{(1,8)} = 8.22$; $p = 0.02$*	$F_{(4,32)} = 2.63$; $p = 0.05$
Left rACC	$F_{(1,8)} = 3.44$; $p = 0.10$	$F_{(4,32)} = 1.62$; $p = 0.93$	$F_{(1,8)} = 18.26$; $p = 0.003$**	$F_{(4,32)} = 2.84$; $p = 0.04$*
Right rACC	$F_{(1,8)} = 1.90$; $p = 0.21$	$F_{(4,32)} = 1.28$; $p = 0.30$	$F_{(1,8)} = 17.13$; $p = 0.003$**	$F_{(4,32)} = 2.20$; $p = 0.09$
Left dACC	$F_{(1,8)} = 3.55$; $p = 0.09$	$F_{(4,32)} = 5.16$; $p = 0.003$**	$F_{(1,8)} = 11.58$; $p = 0.009$**	$F_{(4,32)} = 3.62$; $p = 0.01$*
Right dACC	$F_{(1,8)} = 2.11$; $p = 0.18$	$F_{(4,32)} = 4.04$; $p = 0.009$**	$F_{(1,8)} = 9.99$; $p = 0.01$*	$F_{(4,32)} = 2.76$; $p = 0.04$*
Left iPPC	$F_{(1,8)} = 1.47$; $p = 0.26$	$F_{(4,32)} = 1.98$; $p = 0.12$	$F_{(1,8)} = 13.7$; $p = 0.004$**	$F_{(4,32)} = 2.39$; $p = 0.07$
Right iPPC	$F_{(1,8)} = 0.15$; $p = 0.71$	$F_{(4,32)} = 1.02$; $p = 0.41$	$F_{(1,8)} = 0.23$; $p = 0.64$	$F_{(4,32)} = 7.77$; $p = 0.0001$***
Left sPPC	$F_{(1,8)} = 2.28$; $p = 0.16$	$F_{(4,32)} = 0.49$; $p = 0.74$	$F_{(1,8)} = 5.44$; $p = 0.04$*	$F_{(4,32)} = 3.96$; $p = 0.01$*
Right sPPC	$F_{(1,8)} = 0.51$; $p = 0.49$	$F_{(4,32)} = 2.06$; $p = 0.11$	$F_{(1,8)} = 3.90$; $p = 0.08$	$F_{(4,32)} = 4.69$; $p = 0.004$**
Left Occip.	$F_{(1,8)} = 0.0003$; $p = 0.98$	$F_{(4,32)} = 1.77$; $p = 0.16$	$F_{(1,8)} = 3.46$; $p = 0.10$	$F_{(4,32)} = 3.49$; $p = 0.01$*
Right Occip.	$F_{(1,8)} = 2.08$; $p = 0.19$	$F_{(4,32)} = 2.04$; $p = 0.11$	$F_{(1,8)} = 1.38$; $p = 0.27$	$F_{(4,32)} = 0.75$; $p = 0.56$

*$p < 0.05$; **$p < 0.01$; ***$p < 0.001$.

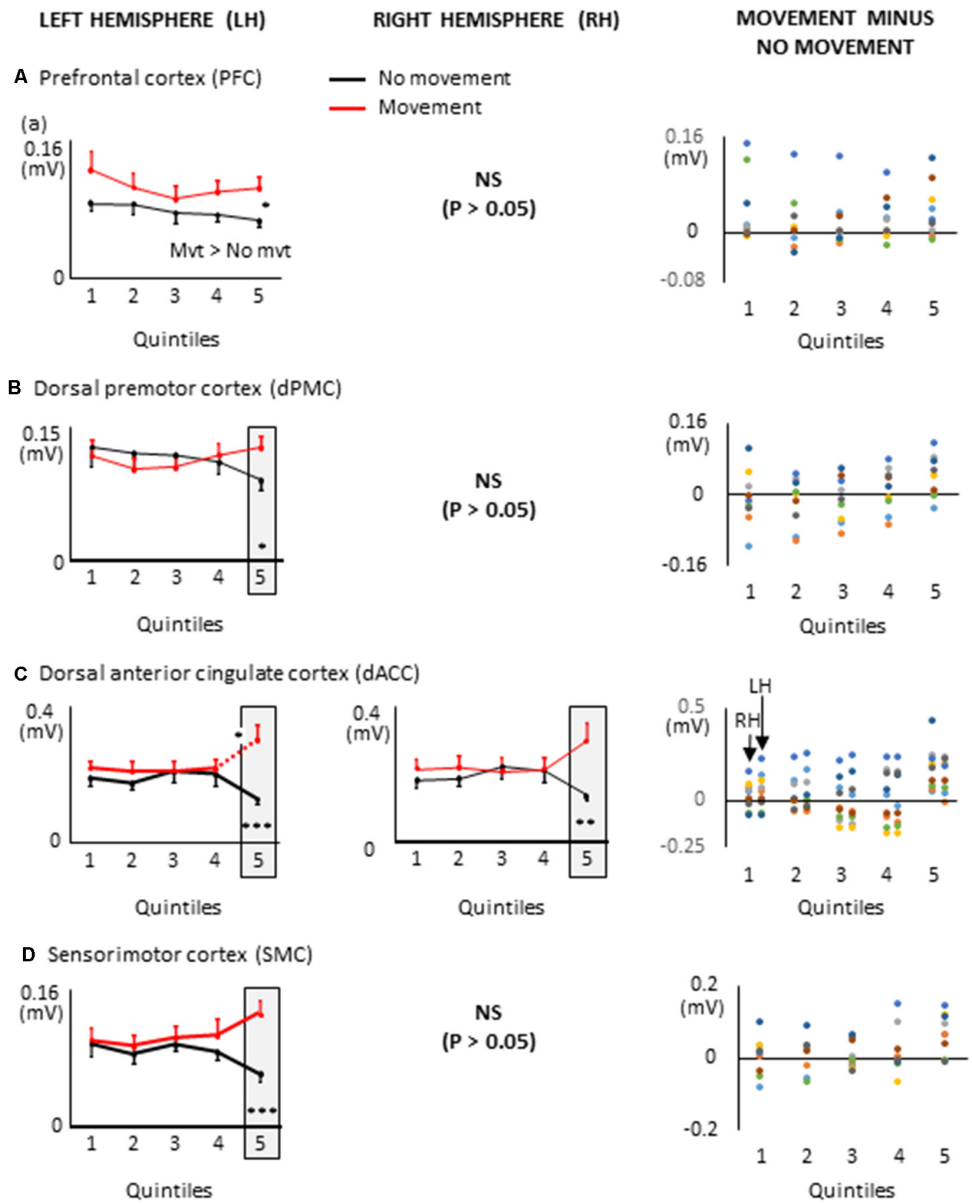

FIGURE 5 | Mean activities recorded in the ROIs of the left and right hemispheres (left and middle columns, respectively) showing significant main effects of movement and significant interactions between Movement × Quintile in Experiment 1 [i.e., prefrontal cortex, **(A)**; dorsal premotor cortex, **(B)**; dorsal anterior cingulate cortex, **(C)** and sensorimotor cortex, **(D)**]. Error bars represent standard error of the mean. Dotted lines link consecutive quintiles showing significantly different activities (*$p < 0.05$, **$p < 0.01$, ***$p < 0.001$). Graphs of the right column depict the differences in activity between the Movement and No-movement conditions for all participants. Dots of the same color represent data from the same participant. Values greater than 0 (i.e., above the X-axis) indicate that the activity in the Movement condition was greater than the activity in the No-movement conditions. LH and RH indicate left and right hemispheres, respectively.

that the activity of the PFC was greater in movement condition from quintile 1 might suggest that information storage started during body rotations. The sustained activation found in the left PFC thus provides an electrophysiological support for the hypothesis issued from lesion studies that the PFC is involved in the storage of task-relevant vestibular signals (Berthoz et al., 1987; Pierrot-Deseilligny et al., 1993, 1995). On the other hand, the left dorsal premotor (dPMC) and sensorimotor (SMC) cortices, and the dorsal anterior cingulate cortices (dACC) of both hemispheres showed significantly greater activation in the movement condition only in the last quintile. The dPMC is known to contribute to the selection of motor responses that are based on spatial cues irrespective of the sensory modality of the cues (Weinrich and Wise, 1982; Wise, 1985). Thus, the increased activation of the dPMC during movement planning could be linked to the sensorimotor processes associated with the processing of vestibular spatial cues. Furthermore, the increased activation of both the dACC and SMC were expected near

the end of movement planning, as these regions are important sources of descending motor commands. The bilateral increased activation of the dACC is also consistent with the existence of direct bilateral connections of this motor area of the medial wall with the spinal cord and the primary motor cortex (He et al., 1995; Dum et al., 2016). The motor commands issued from the dACC may have benefited from relevant spatial information stored in the PFC which has dense interconnections with the dACC (Yeterian et al., 2012). Note that the activations of the SMC and dACC could also be linked to the anticipatory postural adjustments observed before rapid arm movements (e.g., Massion, 1994; Kurtzer et al., 2005).

Remarkably, critical regions for the cognitive encoding of space, such as the ventral premotor cortex (vPM) or the posterior parietal cortex (PPC), did not show significantly different activities between conditions with and without arm movements. This result is not consistent with the scheme that movement planning was based on a cognitive representation of space updated during body rotations. Rather, the observation that task-related activities were exclusively found in PFC, dPM, dACC and SMC points to a dominant role of sensorimotor-type of spatial representations for converting self-motion sensory cues into arm motor commands. The short time elapsed between the end of the rotation and the onset of the arm muscular activity (i.e., 391 ms, see "Materials and Methods" section) is in line with the use of such sensorimotor representations wherein encoded information is short-lived.

Indeed, the motor representations of space rapidly decay when sensory stimuli relevant for triggering motor action becomes unavailable (Bridgeman, 1991; Goodale et al., 1994; Rossetti, 1998; Burgess, 2008; Ball et al., 2010). Therefore, the contribution of cortical regions involved in the cognitive encoding of space, including those tightly linked to spatio-motor integration, could increase for planning movements when there is a delay between body motion and the goal-directed arm movement. We tested this hypothesis in Experiment 2.

EXPERIMENT 2

Nine new participants participated in Experiment 2 (three women, mean age: 25.5 ± 3.4). A written informed consent was obtained from the participants before the study and the experiment was approved by the Laval University Biomedical Ethics Committee.

Design of the Experiment

This experiment reproduced the movement condition of Experiment 1 with the only exception being that the imperative signal prompting the participants to produce the arm movement occurred 8 s after the end of the chair rotation. This delay was chosen based on previous studies showing that most motor actions rely on a cognitive representation after a 8 s delay (Bridgeman, 1991; Gentilucci et al., 1996). As in Experiment 1, participants performed 25 trials for each of the three pseudo-randomly presented angular rotations (i.e., 20°, 30° and 40°, total of 75 trials). The kinematics of the chair rotations were like those of Experiment 1. On average, the rotation amplitudes were 20.16 ± 0.46°, 29.96 ± 0.34° and 40.43 ± 0.35° and their respective peak angular velocities were 58.10 ± 6.34°/s, 75.31 ± 7.49°/s and 92.59 ± 5.98°/s. Similarities of the chair rotation kinematics between both experiments were confirmed by the results of the mixed-design ANOVAs [3 (Condition: movement Experiment 1, no-movement Experiment 2) × 3 (Amplitude: 20°, 30°, 40°)] that did not reveal significant effect of Condition on the amplitude of the rotations ($F_{(2,24)} = 1.79$, $p = 0.19$) or on the chair peak angular velocities ($F_{(2,24)} = 0.48$, $p = 0.62$).

The norms of the vectors between the initial and final hand positions were also scaled in Experiment 2 to the amplitude of the chair rotations (i.e., 31.26 ± 6.56 cm, 37.42 ± 6.83 cm and 45.23 ± 5.88 cm, for the 20°, 30° and 40° body rotations, respectively). Moreover, the results of a 2 (Experiment) × 3 (Angular amplitude) mixed-design ANOVA showed that the norms of the movement vectors were not significantly different between both experiments (no significant main effect of Experiment ($F_{(1,14)} = 0.43$, $p = 0.52$).

The fact that participants remained motionless while waiting for the imperative signal which occurred 8 s after rotation offsets, minimized the possibility of contamination of the EEG recordings from residual eye movements or cable motion as in Experiment 1. However, the response to the auditory stimulation and the non-motoric activity related to anticipation (Simons et al., 1979) and expectancy (Ruchkin et al., 1986) of this stimulation could affect the post imperative signal cortical activity. To control for this possibility, we contrasted the recorded EEG activity with the EEG activity recorded after the second of two tones interspaced by 3 s that were presented in a control condition without body rotation and arm movement. Note that the first tone in this control condition and the end of the rotation in the delayed movement condition both served as a preparatory pre-cue signal as they were both followed by a tone that occurred after a fixed interval. In this control condition, each participant also performed 75 trials. Five participants started the experimental session with the delayed movement condition.

EEG processing was performed as in Experiment 1. The baseline used to compute the co-variance matrices in the delayed arm movement condition was set between −9.5 s to −10 s with

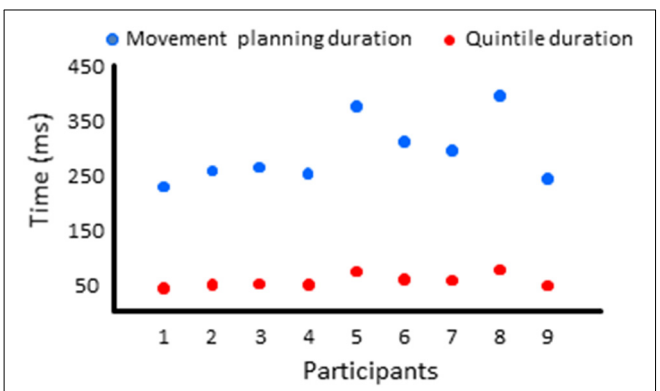

FIGURE 6 | Duration of the movement planning phase and of the quintiles for each participant in Experiment 2.

respect to the auditory cue (i.e., before body rotation for all trials of all participants). In the control condition, the baseline was set −1.5 s to −2 s prior to the first of the two tones. Albeit spatial and sensorimotor processes most likely took place before the imperative signal, for each ROI, we compared the mean current amplitude computed in each quintile of movement reaction time with the mean current amplitude computed during similar five time-windows in the control condition. EMG reaction time and quintile durations are provided for all participants in **Figure 6**. On average, the EMG reaction times and quintile duration were 294 ± 59 ms and 59 ms, respectively. Statistical results of the 2 (Condition: delayed movement, control) × 5 (Quintile: 1–5) repeated measures ANOVAs and of the *post hoc* tests are presented in **Figures 7–9** and **Table 1**, respectively.

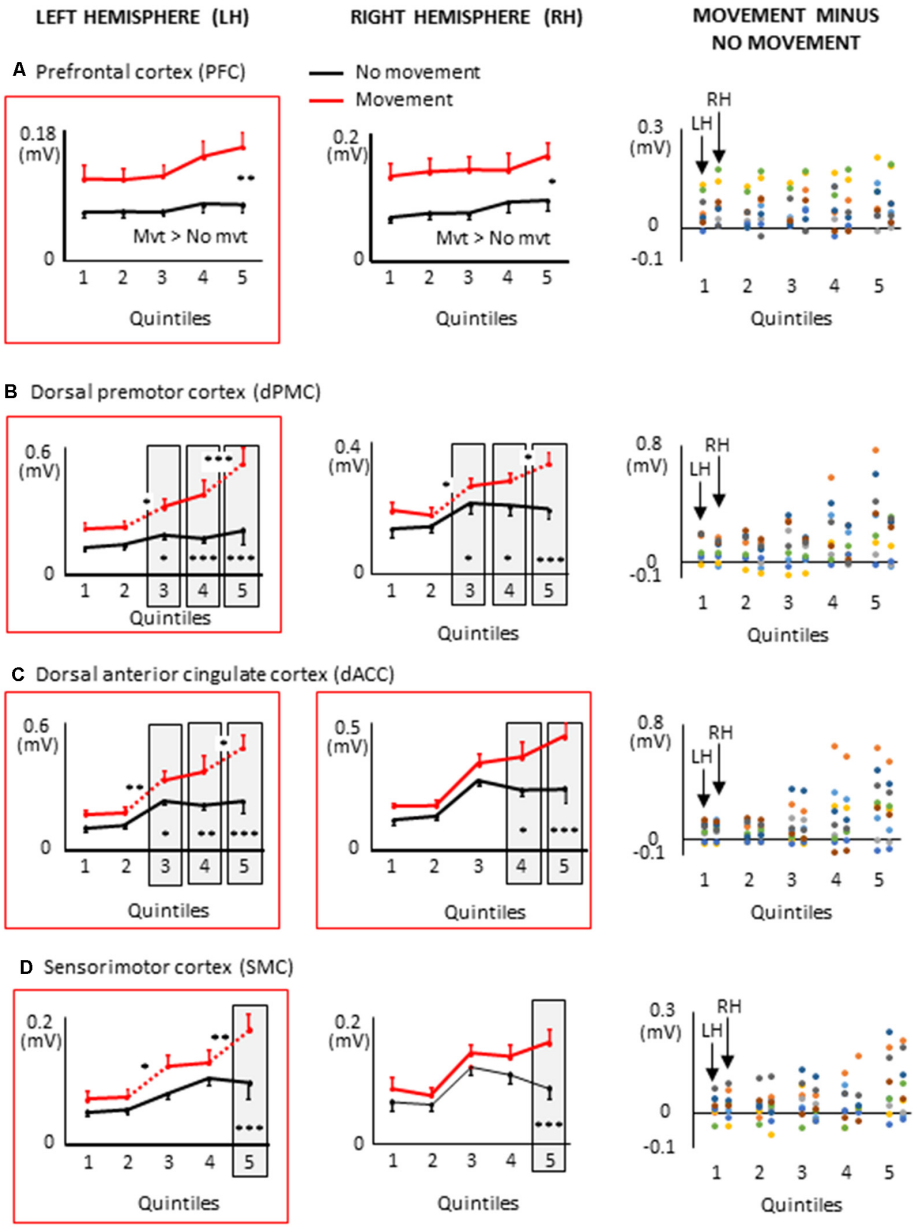

FIGURE 7 | Mean activities recorded in the ROIs of the left and right frontal lobes (left and middle columns, respectively) showing a significant main effect of movement and a significant interaction between movement × quintile in Experiment 2 (delayed movements): i.e., prefrontal cortex, **(A)**; dorsal premotor cortex, **(B)**; Dorsal anterior cingulate cortex, **(C)**; sensorimotor cortex, **(D)**. The figure depicts only the results of the cortical regions that also showed significant effects in Experiment 1 (no delay) in either hemisphere (identified by red boxes). Error bars represent standard error of the mean. Dotted lines link consecutive quintiles showing significantly different activities (*$p < 0.05$, **$p < 0.01$, ***$p < 0.001$). Graphs of the right column depict the differences in activity between the Movement and No-movement conditions for all participants. Dots of the same color represent data from the same participant. Values greater than 0 (i.e., above X-axis) indicate that the participants showed greater activity in the Movement condition than in the No-movement conditions.

RESULTS AND DISCUSSION

Extended Task-Related Activities in the Frontal Lobe With Delayed Arm Movements

All frontal ROIs that showed greater activation during movement planning in Experiment 1 also showed additional activation during movement planning in the delayed movement condition (i.e., PFC, dPMC, SMC, dACC; see **Figure 7**). However, in contrast to Experiment 1, the increased activations of the PFC, dPMC and SMC in the arm movement condition were bilateral rather than being restricted to the hemisphere contralateral to the moving arm (i.e., left hemisphere). In the light of the temporal constraints imposed in the delayed movement condition, the sustained task-related activation of the right PFC might have been associated with both the maintenance of body rotation and spatial information in working memory (Courtney et al., 1998; Romo et al., 1999; Katsuki et al., 2014), and the shift from cue monitoring (i.e., self-motion cues) to cued arm response (Howe et al., 2013). The greater activation of the right dPMC observed throughout movement planning could have also contributed to the storage of spatial information during the imposed delay (Smith and Jonides, 1999). Supplementary activation was also found in the right SMC in the last quintile of the movement condition. This ipsilateral activity could reflect motor processes related to postural adjustments associated to the execution of the rapid upper limb movement (Massion, 1994; Kurtzer et al., 2005).

Other ROIs from the frontal lobe showed significant task-related activations during the delayed arm movement that were not observed in Experiment 1 (i.e., without an imposed delay; see **Figure 8**). This was the case of the rostral ACC (rACC) where current amplitude was found to be bilaterally greater throughout movement planning. This observation could be linked to visuo-spatial attention and exploratory processes that have been identified in the rACC (Corbetta et al., 1993; Kim et al., 1999; Amiez et al., 2012). Besides, the current amplitude of the rACC contralateral to the reaching hand progressively increased during movement planning, reaching its maximum value in the last quintile. This increased activation is consistent with studies demonstrating that the rACC plays an important role in the control of arm movements (Picard and Strick, 1996; Paus, 2001), notably those relying on working memory (Paus et al., 1998).

Task-related activations were also found in the left ventral premotor cortex (vPMC) when arm movements

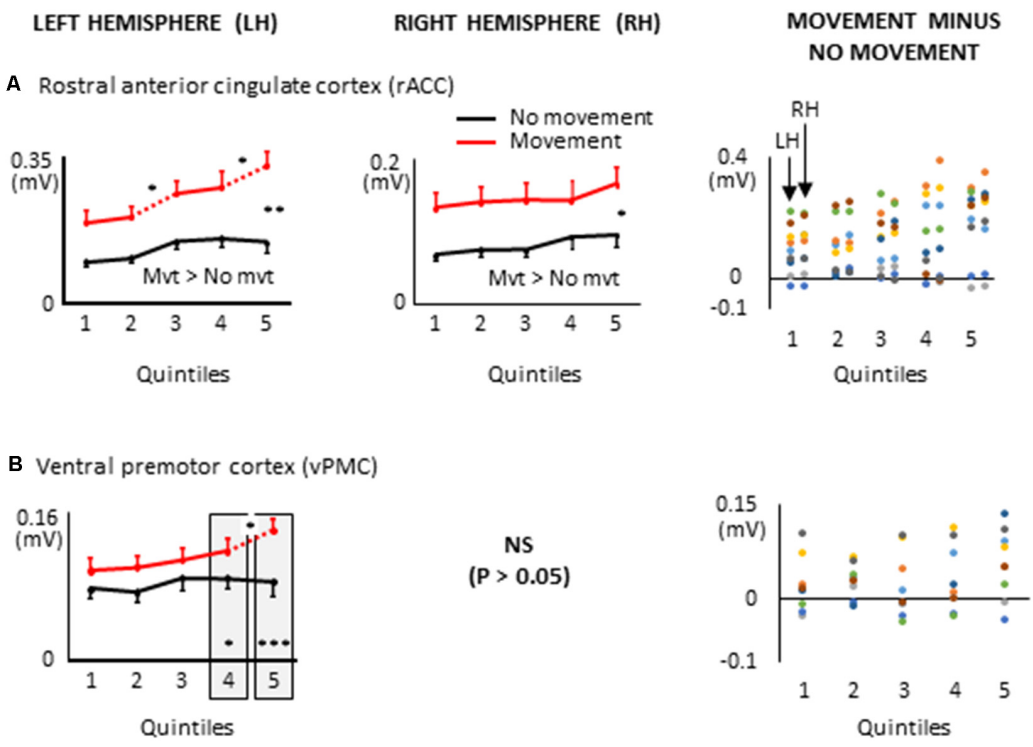

FIGURE 8 | ROIs of the frontal lobe showing significant effects only when a 8 s delay was imposed between body motion and the arm movement: i.e., rostral anterior cingulate cortex, **(A)**; ventral premotor cortex, **(B)**. More specifically, the graphs show the mean activities recorded in the ROIs of the left and right hemispheres (left and middle columns, respectively) showing a significant main effect of movement and a significant interaction between movement × quintile in Experiment 2 (delayed movements). Error bars represent standard error of the mean. Dotted lines link consecutive quintiles showing significantly different activities (*$p < 0.05$, **$p < 0.01$, ***$p < 0.001$). Graphs of the right column depict the differences in activity between the Movement and No-movement conditions for all participants. Dots of the same color represent data from the same participant. Values greater than 0 (i.e., above the X-axis) indicate that the participants showed greater activity in the Movement condition than in the No-movement conditions. LH and RH indicate left and right hemispheres, respectively.

were delayed. More specifically, the vPMC showed greater activation in the movement condition than in the no-movement condition in the last two quintiles. The vPMC is an important area for space perception and activity in this area has been associated with the encoding of hand movements in extrinsic coordinates (Kakei et al., 2001; Rizzolatti et al., 2002). Thus, the increased vPMC activation observed towards the end of movement planning could reflect processes related to the transformation of the extrinsically encoded spatial goal of the movement into arm motor commands.

Large Task-Related Activations in the Posterior Cortex During Delayed Arm Movements

Several ROIs from the posterior cortex showed larger activation during movement planning when arm movements were delayed after body rotations (see **Figure 9**). This was the case of the left occipital cortex which showed greater activation in the movement condition in the last three quintiles (i.e., last 60% of the movement planning). This observation is important when considering the frame of reference used for motor planning. Indeed, it suggests that despite the absence of visual information, a visual-type of spatial representation might have been used to plan the arm movement. This finding is consistent with studies showing that even in the absence of visual feedback, the occipital cortex can provide relevant information to the motor system (Singhal et al., 2013; Manson et al., 2019).

Both superior PPC showed greater current amplitudes in the last two quintiles of movement planning. Previous studies have found that in this area of the parietal lobe, movement planning is based on visual space representations (e.g., Andersen et al., 1997). Specifically, it has been shown that

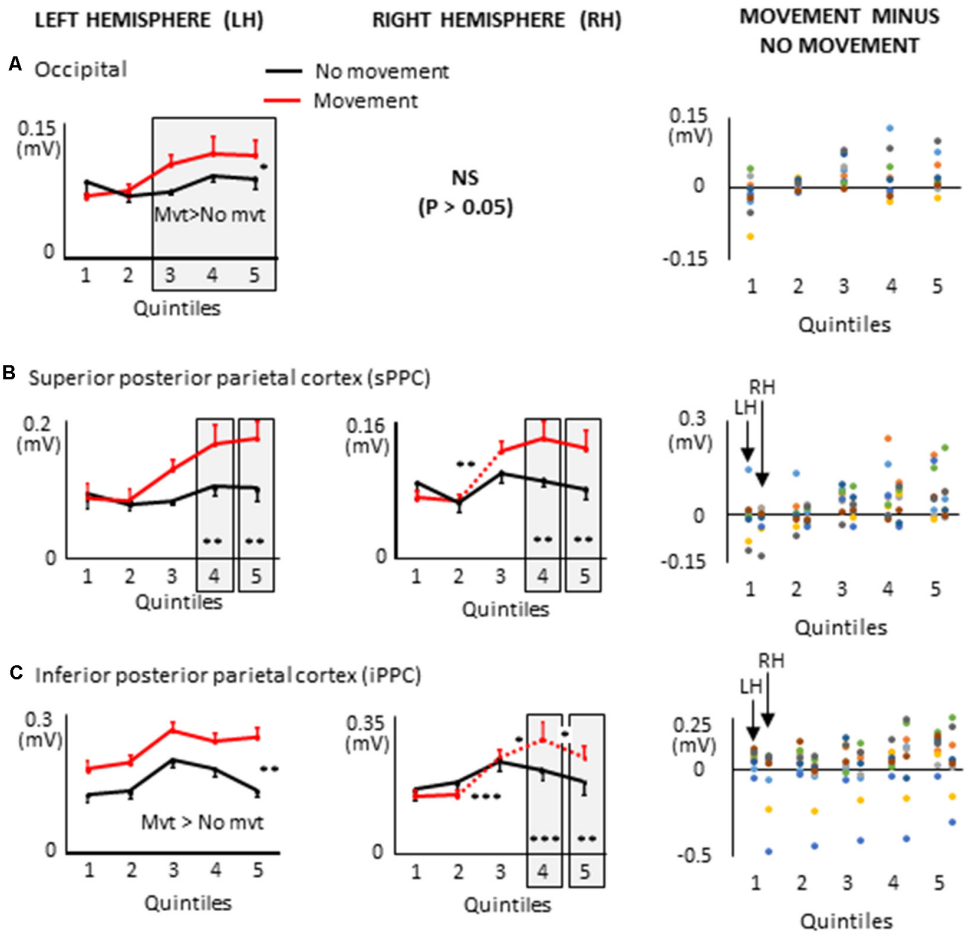

FIGURE 9 | Mean activities recorded in the ROIs of the left and right hemispheres (left and middle columns, respectively) of the posterior cortex showing a significant main effect of movement and a significant interaction between movement × quintile in Experiment 2 (delayed movements): i.e., occipital cortex, **(A)**; superior posterior parietal cortex, **(B)**; inferior posterior parietal cortex, **(C)**. Error bars represent standard error of the mean. Dotted lines link consecutive quintiles showing significantly different activities (*$p < 0.05$, **$p < 0.01$, ***$p < 0.001$). Graphs of the right column depict the differences in activity between the Movement and No-movement conditions for all participants. Dots of the same color represent data from the same participant. Values greater than 0 (i.e., above the X-axis) indicate that the participants showed greater activity in the Movement condition than in the No-movement conditions. LH and RH indicate left and right hemispheres, respectively.

activity in superior PPC is associated with the computation of motor errors in extrinsic coordinates, even for movements produced in darkness (Darling et al., 2007; Medendorp et al., 2008; Filimon et al., 2009). Note that because the activation of the superior PPC did not significantly differ between the movement and no-movement conditions in the first three quintiles, the results obtained with the present protocol cannot provide support for the hypothesis that this region contributes to hold motor plans during delayed actions (e.g., Gnadt and Andersen, 1988).

The left and right inferior PPC showed greater activation throughout movement planning and in the last two quintiles, respectively. These activities could be associated to space encoding which is known to be performed relative to the arm and hand in the inferior PPC (Rozzi et al., 2008). The additional activation found in this area during movement planning could, therefore, be relevant for computing the motor vector in the superior PPC.

GENERAL DISCUSSION AND CONCLUSION

The pattern of cortical activations found in the present study when the arm movements were triggered 8 s after the passive body rotations (Experiment 2) is consistent with the scheme that goal-directed arm movements produced after body motion was derived from a visually-based updated internal representation of the environment. These results are therefore coherent with the most widely adopted view that cognitive maps intervene in the organization of spatially-oriented behavior based on body motion information (Loomis et al., 1996; Klier and Angelaki, 2008; Mackrous and Simoneau, 2011, 2014; Medendorp, 2011). These cognitive representations would be particularly suited for storing relevant spatial information when the motor response is postponed after body motion (Bridgeman, 1991; Burgess, 2008). To our knowledge, these observations provide the first human electrophysiological evidence for the contribution of such cognitive processes for planning motor actions based on idiothetic information. These results, therefore, build on recent studies describing cortical activities evoked by body rotations (e.g., Gale et al., 2016) or activities strictly linked to spatial, non-motor updating processes (Gutteling and Medendorp, 2016; Gutteling et al., 2017; de Winkel et al., 2017).

Importantly, however, the spatio-temporal patterns of cortical activation revealed in the present study confer greater contribution of higher-order cognitive processes in movement planning when a delay is introduced between body motion and the arm motor response. Indeed, the results of Experiment 1 suggest that a more sensorimotor type of representation is responsible for organizing arm movements that are promptly triggered after body motion. Observations made in Experiment 1 are therefore consistent with studies suggesting that, despite being context-dependent (Keyser et al., 2017; Smith and Reynolds, 2017), the control of arm movements based on vestibular input can be largely independent of cognitive processes (Bresciani et al., 2005; Blouin et al., 2010; Guillaud et al., 2011; for review, see Blouin et al., 2015). Nonetheless, our observation that task-related activities were found in similar frontal areas in conditions with and without delay (e.g., dACC and dPM) suggests that the cognitive processes occurring in occipito-parietal regions did not supersede the frontal sensorimotor processes. Rather, our findings provide evidence that cognitive and sensorimotor processes contribute together for triggering delayed arm motor actions based on idiothetic information.

DATA AVAILABILITY STATEMENT

The datasets generated for this study are available on request to the corresponding author.

ETHICS STATEMENT

The studies involving human participants were reviewed and approved by Laval University Biomedical Ethics Committee. The patients/participants provided their written informed consent to participate in this study.

AUTHOR CONTRIBUTIONS

JB, MS and LM designed the experiments, interpreted the data and wrote the manuscript. JB and MS performed the experiments. AS and GM analyzed the data. GM revised the manuscript. J-PP programmed the experiment.

FUNDING

This research was undertaken thanks to funding of the French Agence Nationale de la Recherche (ANR) to JB and LM (ANR-14-CE30-007-02) and Natural Sciences and Engineering Research Council of Canada (NSERC) discovery grants program (RGPIN-2015-04068) to MS.

ACKNOWLEDGMENTS

We thank Shannon Cyr-Kirk for his help with processing the chair and arm kinematics and EMG data. We thank to Marcel Kaszap for computing expertise.

REFERENCES

Amiez, C., Hadj-Bouziane, F., and Petrides, M. (2012). Response selection versus feedback analysis in conditional visuo-motor learning. *Neuroimage* 59, 3723–3735. doi: 10.1016/j.neuroimage.2011.10.058

Amiez, C., and Petrides, M. (2014). Neuroimaging evidence of the anatomo-functional organization of the human cingulate motor areas. *Cereb. Cortex* 24, 563–578. doi: 10.1093/cercor/bhs329

Andersen, R. A., Snyder, L. H., Bradley, D. C., and Xing, J. (1997). Multimodal representation of space in the posterior parietal cortex and its use in planning

movements. *Annu. Rev. Neurosci.* 20, 303–330. doi: 10.1146/annurev.neuro.20.1.303

Baker, J. T., Harper, T. M., and Snyder, L. H. (2003). Spatial memory following shifts of gaze. I. Saccades to memorized world-fixed and gaze-fixed targets. *J. Neurophysiol.* 89, 2564–2576. doi: 10.1152/jn.00610.2002

Ball, K., Smith, D., Ellison, A., and Schenk, T. (2010). A body-centred frame of reference drives spatial priming in visual search. *Exp. Brain Res.* 204, 585–594. doi: 10.1007/s00221-010-2327-y

Berthoz, A., Israël, I., Viéville, T., and Zee, D. (1987). Linear head displacement measured by the otoliths can be reproduced through the saccadic system. *Neurosci. Lett.* 82, 285–290. doi: 10.1016/0304-3940(87)90270-9

Bloomberg, J., Jones, G. M., Segal, B., Mcfarlane, S., and Soul, J. (1988). Vestibular-contingent voluntary saccades based on cognitive estimates of remembered vestibular information. *Adv. Otorhinolaryngol.* 41, 71–75. doi: 10.1159/000416034

Blouin, J., Bresciani, J. P., Guillaud, E., and Simoneau, M. (2015). Prediction in the vestibular control of arm movements. *Multisens. Res.* 28, 487–505. doi: 10.1163/22134808-00002501

Blouin, J., Guillaud, E., Bresciani, J. P., Guerraz, M., and Simoneau, M. (2010). Insights into the control of arm movement during body motion as revealed by EMG analyses. *Brain Res.* 1309, 40–52. doi: 10.1016/j.brainres.2009.10.063

Blouin, J., Labrousse, L., Simoneau, M., Vercher, J. L., and Gauthier, G. M. (1998). Updating visual space during passive and voluntary head-in-space movements. *Exp. Brain Res.* 122, 93–100. doi: 10.1007/s002210050495

Bresciani, J. P., Gauthier, G. M., Vercher, J. L., and Blouin, J. (2005). On the nature of the vestibular control of arm-reaching movements during whole-body rotations. *Exp. Brain Res.* 164, 431–441. doi: 10.1007/s00221-005-2263-4

Bridgeman, B. (1991). "Complementary cognitive and motor image processing," in *Presbyopia Research, From Molecular Biology to Visual Adaptation*, eds G. Obrecht and L. W. Stark (New York, NY: Plemun), 189–198.

Brindle, T. J., Nitz, A. J., Uhl, T. L., Kifer, E., and Shapiro, R. (2006). Kinematic and EMG characteristics of simple shoulder movements with proprioception and visual feedback. *J. Electromyogr. Kinesiol.* 16, 236–249. doi: 10.1016/j.jelekin.2005.06.012

Burgess, N. (2008). Spatial cognition and the brain. *Ann. N Y Acad. Sci.* 1124, 77–97. doi: 10.1196/annals.1440.002

Corbetta, M., Miezin, F. M., Shulman, G. L., and Petersen, S. E. (1993). A PET study of visuospatial attention. *J. Neurosci.* 13, 1202–1226. doi: 10.1523/jneurosci.13-03-01202.1993

Courtney, S. M., Petit, L., Maisog, J. M., Ungerleider, L. G., and Haxby, J. V. (1998). An area specialized for spatial working memory in human frontal cortex. *Science* 279, 1347–1351. doi: 10.1126/science.279.5355.1347

Cram, J. R., and Kasman, G. S. (2011). *Cram's Introductin to Surface Electromyography—Second Edition.* Boston, MA: Jones and Bartlett publishers.

Cullen, K. E., and Taube, J. S. (2017). Our sense of direction: progress, controversies and challenges. *Nat. Neurosci.* 20, 1465–1473. doi: 10.1038/nn.4658

Dale, A. M., Liu, A. K., Fischl, B. R., Buckner, R. L., Belliveau, J. W., Lewine, J. D., et al. (2000). Dynamic statistical parametric mapping: combining fMRI and MEG for high-resolution imaging of cortical activity. *Neuron* 26, 55–67. doi: 10.1016/s0896-6273(00)81138-1

Darling, W. G., Seitz, R. J., Peltier, S., Tellmann, L., and Butler, A. J. (2007). Visual cortex activation in kinesthetic guidance of reaching. *Exp. Brain Res.* 179, 607–619. doi: 10.1007/s00221-006-0815-x

de Winkel, K. N., Nesti, A., Ayaz, H., and Bulthoff, H. H. (2017). Neural correlates of decision making on whole body yaw rotation: an fNIRS study. *Neurosci. Lett.* 654, 56–62. doi: 10.1016/j.neulet.2017.04.053

Dieterich, M., Bense, S., Lutz, S., Drzezga, A., Stephan, T., Bartenstein, P., et al. (2003). Dominance for vestibular cortical function in the non-dominant hemisphere. *Cereb. Cortex* 13, 994–1007. doi: 10.1093/cercor/13.9.994

Dum, R. P., Levinthal, D. J., and Strick, P. L. (2016). Motor, cognitive, and affective areas of the cerebral cortex influence the adrenal medulla. *Proc. Natl. Acad. Sci. U S A* 113, 9922–9927. doi: 10.1073/pnas.1605044113

Dum, R. P., and Strick, P. L. (1991). The origin of corticospinal projections from the premotor areas in the frontal lobe. *J. Neurosci.* 11, 667–689. doi: 10.1523/jneurosci.11-03-00667.1991

Filimon, F., Nelson, J. D., Huang, R. S., and Sereno, M. I. (2009). Multiple parietal reach regions in humans: cortical representations for visual and proprioceptive feedback during on-line reaching. *J. Neurosci.* 29, 2961–2971. doi: 10.1523/jneurosci.3211-08.2009

Gale, S., Prsa, M., Schurger, A., Gay, A., Paillard, A., Herbelin, B., et al. (2016). Oscillatory neural responses evoked by natural vestibular stimuli in humans. *J. Neurophysiol.* 115, 1228–1242. doi: 10.1152/jn.00153.2015

Gentilucci, M., Chieffi, S., Deprati, E., Saetti, M. C., and Toni, I. (1996). Visual illusion and action. *Neuropsychologia* 34, 369–376. doi: 10.1016/0028-3932(95)00128-x

Gnadt, J. W., and Andersen, R. A. (1988). Memory related motor planning activity in posterior parietal cortex of macaque. *Exp. Brain Res.* 70, 216–220. doi: 10.1007/bf00271862

Goodale, M. A., Jakobson, L. S., and Keillor, J. M. (1994). Differences in the visual control of pantomimed and natural grasping movements. *Neuropsychologia* 32, 1159–1178. doi: 10.1016/0028-3932(94)90100-7

Guillaud, E., Simoneau, M., and Blouin, J. (2011). Prediction of the body rotation-induced torques on the arm during reaching movements: evidence from a proprioceptively deafferented subject. *Neuropsychologia* 49, 2055–2059. doi: 10.1016/j.neuropsychologia.2011.03.035

Gutteling, T. P., and Medendorp, W. P. (2016). Role of alpha-band oscillations in spatial updating across whole body motion. *Front. Psychol.* 7:671. doi: 10.3389/fpsyg.2016.00671

Gutteling, T. P., Schutter, D., and Medendorp, W. P. (2017). Alpha-band transcranial alternating current stimulation modulates precision, but not gain during whole-body spatial updating. *Neuropsychologia* 106, 52–59. doi: 10.1016/j.neuropsychologia.2017.09.005

Hanson, J. M., and Goebel, J. A. (1998). Comparison of manual whole-body and passive and active head-on-body rotational testing with conventional rotary chair testing. *J. Vestib. Res.* 8, 273–282. doi: 10.1016/S0957-4271(97)00071-2

He, S. Q., Dum, R. P., and Strick, P. L. (1995). Topographic organization of corticospinal projections from the frontal lobe: motor areas on the medial surface of the hemisphere. *J. Neurosci.* 15, 3284–3306. doi: 10.1523/jneurosci.15-05-03284.1995

Howe, W. M., Berry, A. S., Francois, J., Gilmour, G., Carp, J. M., Tricklebank, M., et al. (2013). Prefrontal cholinergic mechanisms instigating shifts from monitoring for cues to cue-guided performance: converging electrochemical and fMRI evidence from rats and humans. *J. Neurosci.* 33, 8742–8752. doi: 10.1523/jneurosci.5809-12.2013

Huang, Y., Parra, L. C., and Haufe, S. (2016). The NewYork head-a precise standardized volume conductormodel for EEG source localization and tES targeting. *Neuroimage* 140, 150–162. doi: 10.1016/j.neuroimage.2015.12.019

Israël, I., Fetter, M., and Koenig, E. (1993). Vestibular perception of passive whole-body rotation about horizontal and vertical axes in humans: goal-directed vestibulo-ocular reflex and vestibular memory-contingent saccades. *Exp. Brain Res.* 96, 335–346. doi: 10.1007/bf00227113

Israël, I., Rivaud, S., Berthoz, A., and Pierrot-Deseilligny, C. (1992). Cortical control of vestibular memory-guided saccades. *Ann. N Y Acad. Sci.* 656, 472–484. doi: 10.1111/j.1749-6632.1992.tb25229.x

Ivanenko, Y. P., Grasso, R., Israel, I., and Berthoz, A. (1997). The contribution of otoliths and semicircular canals to the perception of two-dimensional passive whole-body motion in humans. *J. Physiol.* 502, 223–233. doi: 10.1111/j.1469-7793.1997.223bl.x

Kakei, S., Hoffman, D. S., and Strick, P. L. (2001). Direction of action is represented in the ventral premotor cortex. *Nat. Neurosci.* 4, 1020–1025. doi: 10.1038/nn726

Katsuki, F., Qi, X. L., Meyer, T., Kostelic, P. M., Salinas, E., and Constantinidis, C. (2014). Differences in intrinsic functional organization between dorsolateral prefrontal and posterior parietal cortex. *Cereb. Cortex* 24, 2334–2349. doi: 10.1093/cercor/bht087

Keyser, J., Medendorp, W. P., and Selen, L. P. J. (2017). Task-dependent vestibular feedback responses in reaching. *J. Neurophysiol.* 118, 84–92. doi: 10.1152/jn.00112.2017

Kim, Y. H., Gitelman, D. R., Nobre, A. C., Parrish, T. B., Labar, K. S., and Mesulam, M. M. (1999). The large-scale neural network for spatial attention displays multifunctional overlap but differential asymmetry. *Neuroimage* 9, 269–277. doi: 10.1006/nimg.1999.0408

Klier, E. M., and Angelaki, D. E. (2008). Spatial updating and the maintenance of visual constancy. *Neuroscience* 156, 801–818. doi: 10.1016/j.neuroscience.2008.07.079

Kurtzer, I., Herter, T. M., and Scott, S. H. (2005). Random change in cortical load representation suggests distinct control of posture and movement. *Nat. Neurosci.* 8, 498–504. doi: 10.1038/nn1420

Laurens, J., and Angelaki, D. E. (2018). The brain compass: a perspective on how self-motion updates the head direction cell attractor. *Neuron* 97, 275–289. doi: 10.1016/j.neuron.2017.12.020

Loomis, J. M., Da Silva, J. A., Philbeck, J. W., and Fukusima, S. S. (1996). Visual perception of location and distance. *Curr. Dir. Psychol. Sci.* 5, 72–77. doi: 10.1111/1467-8721.ep10772783

Ma, Y., Hu, X., and Wilson, F. A. (2012). The egocentric spatial reference frame used in dorsal-lateral prefrontal working memory in primates. *Neurosci. Biobehav. Rev.* 36, 26–33. doi: 10.1016/j.neubiorev.2011.03.011

Mackrous, I., Carriot, J., and Simoneau, M. (2019). Learning to use vestibular sense for spatial updating is context dependent. *Sci. Rep.* 9:11154. doi: 10.1038/s41598-019-47675-7

Mackrous, I., and Simoneau, M. (2011). Visuo-vestibular interaction: predicting the position of a visual target during passive body rotation. *Neuroscience* 195, 45–53. doi: 10.1016/j.neuroscience.2011.07.032

Mackrous, I., and Simoneau, M. (2014). Generalization of vestibular learning to earth-fixed targets is possible but limited when the polarity of afferent vestibular information is changed. *Neuroscience* 260, 12–22. doi: 10.1016/j.neuroscience.2013.12.002

Mackrous, I., and Simoneau, M. (2015). Improving spatial updating accuracy in absence of external feedback. *Neuroscience* 300, 155–162. doi: 10.1016/j.neuroscience.2015.05.024

Manson, G. A., Tremblay, L., Lebar, N., De Grosbois, J., Mouchnino, L., and Blouin, J. (2019). Auditory cues for somatosensory targets invoke visuomotor transformations: behavioral and electrophysiological evidence. *PLoS One* 14:e0215518. doi: 10.1371/journal.pone.0215518

Massion, J. (1994). Postural control system. *Curr. Opin. Neurobiol.* 4, 877–887. doi: 10.1016/0959-4388(94)90137-6

Medendorp, W. P. (2011). Spatial constancy mechanisms in motor control. *Philos. Trans. R. Soc. Lond. B Biol. Sci.* 366, 476–491. doi: 10.1098/rstb.2010.0089

Medendorp, W. P., Beurze, S. M., Van Pelt, S., and Van Der Werf, J. (2008). Behavioral and cortical mechanisms for spatial coding and action planning. *Cortex* 44, 587–597. doi: 10.1016/j.cortex.2007.06.001

Medendorp, W. P., Goltz, H. C., Vilis, T., and Crawford, J. D. (2003). Gaze-centered updating of visual space in human parietal cortex. *J. Neurosci.* 23, 6209–6214. doi: 10.1523/jneurosci.23-15-06209.2003

Medendorp, W. P., Smith, M. A., Tweed, D. B., and Crawford, J. D. (2002). Rotational remapping in human spatial memory during eye and head motion. *J. Neurosci.* 22:RC196. doi: 10.1523/jneurosci.22-01-j0006.2002

Moser, E. I., Moser, M. B., and Mcnaughton, B. L. (2017). Spatial representation in the hippocampal formation: a history. *Nat. Neurosci.* 20, 1448–1464. doi: 10.1038/nn.4653

Mosher, J. C., Leahy, R. M., and Lewis, P. S. (1999). EEG and MEG: forward solutions for inverse methods. *IEEE Trans. Biomed. Eng.* 46, 245–259. doi: 10.1109/10.748978

Nolan, H., Whelan, R., Reilly, R., Bulthoff, H. H., and Butler, J. S. (2009). "Acquisition of human EEG data during linear self motion on a Stewart platform," in *IEEE EMBS Conference Neural Engineering*, (Antalya: IEEE), 1–4.

Nunez, P. L., and Srinivasan, R. (2006). *Electric Fields of the Brain: The Neurophysics of EEG, 2nd Edition*. New York, NY: Oxford University Press, Inc.

O'Keefe, J., and Dostrovsky, J. (1971). The hippocampus as a spatial map. Preliminary evidence from unit activity in the freely-moving rat. *Brain Res.* 34, 171–175. doi: 10.1016/0006-8993(71)90358-1

Paus, T. (2001). Primate anterior cingulate cortex: where motor control, drive and cognition interface. *Nat. Rev. Neurosci.* 2, 417–424. doi: 10.1038/35077500

Paus, T., Koski, L., Caramanos, Z., and Westbury, C. (1998). Regional differences in the effects of task difficulty and motor output on blood flow response in the human anterior cingulate cortex: a review of 107 PET activation studies. *Neuroreport* 9, R37–R47. doi: 10.1097/00001756-199806220-00001

Picard, N., and Strick, P. L. (1996). Motor areas of the medial wall: a review of their location and functional activation. *Cereb. Cortex* 6, 342–353. doi: 10.1093/cercor/6.3.342

Pierrot-Deseilligny, C., Israël, I., Berthoz, A., Rivaud, S., and Gaymard, B. (1993). Role of the different frontal lobe areas in the control of the horizontal component of memory-guided saccades in man. *Exp. Brain Res.* 95, 166–171. doi: 10.1007/bf00229665

Pierrot-Deseilligny, C., Rivaud, S., Gaymard, B., Muri, R., and Vermersch, A. I. (1995). Cortical control of saccades. *Ann. Neurol.* 37, 557–567. doi: 10.1002/ana.410370504

Rizzolatti, G., Fogassi, L., and Gallese, V. (2002). Motor and cognitive functions of the ventral premotor cortex. *Curr. Opin. Neurobiol.* 12, 149–154. doi: 10.1016/s0959-4388(02)00308-2

Romo, R., Brody, C. D., Hernandez, A., and Lemus, L. (1999). Neuronal correlates of parametric working memory in the prefrontal cortex. *Nature* 399, 470–473. doi: 10.1038/20939

Rossetti, Y. (1998). Implicit short-lived motor representations of space in brain damaged and healthy subjects. *Conscious. Cogn.* 7, 520–558. doi: 10.1006/ccog.1998.0370

Rozzi, S., Ferrari, P. F., Bonini, L., Rizzolatti, G., and Fogassi, L. (2008). Functional organization of inferior parietal lobule convexity in the macaque monkey: electrophysiological characterization of motor, sensory and mirror responses and their correlation with cytoarchitectonic areas. *Eur. J. Neurosci.* 28, 1569–1588. doi: 10.1111/j.1460-9568.2008.06395.x

Ruchkin, D. S., Sutton, S., Mahaffey, D., and Glaser, J. (1986). Terminal CNV in the absence of motor response. *Electroencephalogr. Clin. Neurophysiol.* 63, 445–463. doi: 10.1016/0013-4694(86)90127-6

Simoneau, M., Lamothe, V., Hutin, E., Mercier, P., Teasdale, N., and Blouin, J. (2009). Evidence for cognitive vestibular integration impairment in idiopathic scoliosis patients. *BMC Neurosci.* 10:102. doi: 10.1186/1471-2202-10-102

Simons, R. F., Ohman, A., and Lang, P. J. (1979). Anticipation and response set: cortical, cardiac and electrodermal correlates. *Psychophysiology* 16, 222–233. doi: 10.1111/j.1469-8986.1979.tb02982.x

Singhal, A., Monaco, S., Kaufman, L. D., and Culham, J. C. (2013). Human fMRI reveals that delayed action re-recruits visual perception. *PLoS One* 8:e73629. doi: 10.1371/journal.pone.0073629

Smith, E. E., and Jonides, J. (1999). Storage and executive processes in the frontal lobes. *Science* 283, 1657–1661. doi: 10.1126/science.283.5408.1657

Smith, C. P., and Reynolds, R. F. (2017). Vestibular feedback maintains reaching accuracy during body movement. *J. Physiol.* 595, 1339–1349. doi: 10.1113/jp273125

Smith, A. T., Wall, M. B., and Thilo, K. V. (2012). Vestibular inputs to human motion-sensitive visual cortex. *Cereb. Cortex* 22, 1068–1077. doi: 10.1093/cercor/bhr179

Stephan, T., Deutschlander, A., Nolte, A., Schneider, E., Wiesmann, M., Brandt, T., et al. (2005). Functional MRI of galvanic vestibular stimulation with alternating currents at different frequencies. *Neuroimage* 26, 721–732. doi: 10.1016/j.neuroimage.2005.02.049

Tadel, F., Baillet, S., Mosher, J. C., Pantazis, D., and Leahy, R. M. (2011). Brainstorm: a user-friendly application for MEG/EEG analysis. *Comput. Intell. Neurosci.* 2011:879716. doi: 10.1155/2011/879716

Tadel, F., Bock, E., Niso, G., Mosher, J. C., Cousineau, M., Pantazis, D., et al. (2019). MEG/EEG group analysis with brainstorm. *Front. Neurosci.* 13:76. doi: 10.3389/fnins.2019.00076

Valko, Y., Lewis, R. F., Priesol, A. J., and Merfeld, D. M. (2012). Vestibular labyrinth contributions to human whole-body motion discrimination. *J. Neurosci.* 32, 13537–13542. doi: 10.1523/jneurosci.2157-12.2012

Ventre-Dominey, J., and Vallee, B. (2007). Vestibular integration in human cerebral cortex contributes to spatial remapping. *Neuropsychologia* 45, 435–439. doi: 10.1016/j.neuropsychologia.2006.06.031

Wei, M., Li, N., Newlands, S. D., Dickman, J. D., and Angelaki, D. E. (2006). Deficits and recovery in visuospatial memory during head motion after

bilateral labyrinthine lesion. *J. Neurophysiol.* 96, 1676–1682. doi: 10.1152/jn.00012.2006

Weinrich, M., and Wise, S. P. (1982). The premotor cortex of the monkey. *J. Neurosci.* 2, 1329–1345. doi: 10.1523/JNEUROSCI.02-09-01329.1982

Wise, S. P. (1985). The primate premotor cortex: past, present, and preparatory. *Annu. Rev. Neurosci.* 8, 1–19. doi: 10.1146/annurev.ne.08.030185.000245

Yeterian, E. H., Pandya, D. N., Tomaiuolo, F., and Petrides, M. (2012). The cortical connectivity of the prefrontal cortex in the monkey brain. *Cortex* 48, 58–81. doi: 10.1016/j.cortex.2011.03.004

Conflict of Interest: The authors declare that the research was conducted in the absence of any commercial or financial relationships that could be construed as a potential conflict of interest.

frontiers in Neural Circuits

ORIGINAL RESEARCH
published: 30 October 2019
doi: 10.3389/fncir.2019.00068

A Biologically-Inspired Model to Predict Perceived Visual Speed as a Function of the Stimulated Portion of the Visual Field

Fabio Solari[1*†], *Martina Caramenti*[2,3†], *Manuela Chessa*[1], *Paolo Pretto*[4], *Heinrich H. Bülthoff*[5] *and Jean-Pierre Bresciani*[2,6*]

[1] Department of Informatics, Bioengineering, Robotics, and Systems Engineering, University of Genova, Genoa, Italy, [2] Department of Neuroscience and Movement Science, University of Fribourg, Fribourg, Switzerland, [3] Istituto di Bioimmagini e Fisiologia Molecolare, Consiglio Nazionale delle Ricerche, Segrate, Italy, [4] Virtual Vehicle Research Center, Graz, Austria, [5] Department of Cognitive and Computational Psychophysics, Max Planck Institute for Biological Cybernetics, Tubingen, Germany, [6] University Grenoble Alpes, LPNC, Grenoble, France

Spatial orientation relies on a representation of the position and orientation of the body relative to the surrounding environment. When navigating in the environment, this representation must be constantly updated taking into account the direction, speed, and amplitude of body motion. Visual information plays an important role in this updating process, notably via optical flow. Here, we systematically investigated how the size and the simulated portion of the field of view (FoV) affect perceived visual speed of human observers. We propose a computational model to account for the patterns of human data. This model is composed of hierarchical cells' layers that model the neural processing stages of the dorsal visual pathway. Specifically, we consider that the activity of the MT area is processed by populations of modeled MST cells that are sensitive to the differential components of the optical flow, thus producing selectivity for specific patterns of optical flow. Our results indicate that the proposed computational model is able to describe the experimental evidence and it could be used to predict expected biases of speed perception for conditions in which only some portions of the visual field are visible.

Keywords: vision, optical flow, motion perception, field of view, computational model, MST area

OPEN ACCESS

Edited by:
K. J. Jeffery,
University College London,
United Kingdom

Reviewed by:
Aman B. Saleem,
University College London,
United Kingdom
Paul Graham,
University of Sussex, United Kingdom

***Correspondence:**
Fabio Solari
fabio.solari@unige.it
Jean-Pierre Bresciani
jean-pierre.bresciani@unifr.ch

†These authors have contributed equally to this work

Received: *31 May 2019*
Accepted: *07 October 2019*
Published: *30 October 2019*

Citation:
Solari F, Caramenti M, Chessa M, Pretto P, Bülthoff HH and Bresciani J-P (2019) A Biologically-Inspired Model to Predict Perceived Visual Speed as a Function of the Stimulated Portion of the Visual Field. Front. Neural Circuits 13:68. doi: 10.3389/fncir.2019.00068

1. INTRODUCTION

Spatial orientation is a cognitive function based on the ability to understand, manipulate, visually interpret, and reorganize spatial relationships (Tartre, 1990). It relies on a representation of the position and orientation of the body relative to the surrounding environment and requires a mental readjustment of one's perspective to become consistent with the representation of a visually presented object (McGee, 1979; Tartre, 1990). When navigating in the environment, this representation must be constantly updated taking into account different aspects of body motion, such as its direction, speed and amplitude. Spatial navigation is a complex process that requires the integration of sensory information provided by different sensory channels such as vision, proprioception and the vestibular system. Visual information plays a particularly important role in this updating process, notably via the integration of optical flow information. Optical flow may

be defined as the array of optical velocities that surround the moving subject (Kirschen et al., 2000), and it refers to the visual apparent motion between the body and the environment. Its characteristics are related not only to the speed and direction of motion, but also to the properties of the environment, such as for instance texture gradients. Optical flow information is particularly important for human locomotion, where it is integrated by the central nervous system, along with visual, vestibular, motor, kinesthetic and auditory signals, to give rise to motion perception (Mergner and Rosemeier, 1998). The alteration or manipulation of one of these signals may lead to an altered perception. In fact, studies that investigated how visual and non-visual/kinesthetic signals are integrated for speed perception with walking (Thurrell et al., 1998; Banton et al., 2005; Durgin et al., 2005; Kassler et al., 2010; Powell et al., 2011) and running participants (Caramenti et al., 2018, 2019) consistently reported an altered perception of visual speed.

One factor that has repeatedly been shown to affect perceived visual speed is the size of the field of view (FoV). Specifically, several studies demonstrated that peripheral vision is fundamental for motion perception. Indeed, the size of the FoV affects navigation abilities (Alfano and Michel, 1990; Cornelissen and van den Dobbelsteen, 1999; Turano et al., 2005), postural control (Dickinson and Leonard, 1967; Amblard and Carblanc, 1980; Stoffregen, 1986; Wade and Jones, 1997), speed perception (Osaka, 1988; Pretto et al., 2009) as well as vection, i.e., the self-motion perception induced by moving visual stimuli (Brandt et al., 1973; Berthoz et al., 1975; Held et al., 1975). Regarding speed perception in particular, smaller FoVs have been shown to induce a larger underestimation of visual speed, and this with walking (Thurrell et al., 1998; Thurrell and Pelah, 2002; Banton et al., 2005; Nilsson et al., 2014), cycling (Van Veen et al., 1998) and sitting still individuals (Pretto et al., 2009). Such reduction of the FoV can occur not only with simulated optical flows, due to the restrictions of the visualization device (e.g., screen, head-mounted displays), but also in medical conditions such as scotoma, in which there is a localized defect (i.e., blind spot) in the visual field that is surrounded by an area of normal vision.

Here we present a study in which we systematically investigated how the size and the simulated portion of the FoV affect perceived visual speed with human observers. In contrast to previous studies that only focused on the effect of the size of the FoV on visual speed perception, we also investigated the perceptual differences associated to the visible portion of the FoV. We propose a biologically-inspired computational model to account for the observed perceptual patterns. Different computational models have been suggested to qualitatively explain human visual speed perception. These models commonly assume that the perception of visual motion is optimal either within a deterministic framework with a regularization constraint that causes the solution to bias toward zero motion (Yuille and Grzywacz, 1988; Stocker, 2001), or within a probabilistic framework of Bayesian estimation with a prior that favors slow velocities (Simoncelli, 1993; Weiss et al., 2002). Stocker and Simoncelli (2005) presented a refined probabilistic model that can account for trial-to-trial variabilities that are typically observed in psychophysical speed perception problems. It is worth noting that these models take into account neural mechanisms that can be related to V1 and MT neural areas. However, to model the speed perception of motion patterns that are common in self-motion, we have to consider also the dorsal MST area, which encodes visual cues to self-motion (e.g., expansion and contraction) (Duffy and Wurtz, 1991; Pitzalis et al., 2013; Cottereau et al., 2017). Thus, we propose a computational model that takes into account the dorsal neural pathway (Goodale and Westwood, 2004), specifically V1, MT and MST areas, and the spatial non-linearity of log-polar mapping (Schwartz, 1977) in order to mimic the patterns of the perceived visual speed of human observers.

2. MATERIALS AND METHODS

2.1. Perceived Visual Speed of Human Observers

2.1.1. Participants

Eight participants aged 19–31 (mean=24.5 $\pm$ 3.82) participated in the experiment. All participants had normal or corrected-to-normal vision, and they were naive as to the purpose of the research. Written informed consent was obtained from all participants before their inclusion in the study. The experiment was performed in accordance with the ethical standards laid down in the 1964 Declaration of Helsinki, and approved by the ethical committee of the University of Tuebingen. The participants were paid, and they had the option to withdraw from the study at any time without penalty and without having to give a reason.

2.1.2. Experimental Setup

The participants seated at the center of a panoramic screen (quarter of sphere) surrounding them in order to cover almost their entire visual field (see **Figure 1**). Specifically, the screen was cylindrical with a curved extension onto the floor, which provided a projection surface of 230° horizontally and 125° vertically. The screen surface was entirely covered by four LCD projectors with a resolution of 1,400 $\times$ 1,050 pixels each, and OpenWARP technology (Eyevis, Reutlingen, Germany) was used to blend overlapping regions. The height of the seat was adjusted so that eye height was 1.7 m for each participant. The geometry of the visual scene was adjusted for this eye height and a distance of 3 m of the vertical portion of the screen, i.e., the portion that is perpendicular to the floor and to the line of sight when looking straight ahead. These adjustments were made to avoid geometrical distortions induced by the curved display. The visual scene was generated using the Virtools software (Dassault Systemes SE) version 4.1.

2.1.3. Visual Stimuli

The visual stimuli consisted of random patterns of either:

1. White dots generated as point sprites, which subtended a visual angle of a fifth of a degree, i.e., 12 arcminutes. The visual angle subtended by the dots (i.e., retinal size) did not change with distance from the viewer (Dots condition).

FIGURE 1 | Panoramic screen, 230 × 125° of field of view, including floor.

2. White 3D spheres, the "physical" size of which was 10 cm. The visual angle subtended by the spheres depended on the distance from the viewer (3D spheres condition).

Dots and 3D spheres were randomly located within a large virtual cube. The movement of a virtual camera through the dots induced a radial visual flow corresponding to a self-translation along the antero-posterior axis of the subject. Note that the eccentricity of the dots/spheres with respect to the fixation point varied from 0 to 115°, i.e., the half of the horizontal visual field of the panoramic screen used for the experiment. Accordingly, the speed profile of each dot/sphere varied from 0 m per second at a 0° eccentricity to the speed of the generated flow at a 180° eccentricity. The near clipping plane of the camera was set at 0.5 m, and the far clipping plane at 500 m. In the Dots condition, because the retinal size of the dots was distance-independent, the optical flow did not provide visual expansion cues. On the other hand, the 3D spheres provided visual expansion cues because the retinal size of the spheres increased as they moved closer to the viewer. A central fixation cross subtending 1.5° of visual angle and located in front of the participant at eye level was visible for the whole duration of the trials. The fixation cross corresponded to the focus of expansion of the optical flow.

2.1.4. FoV Conditions

Soft-edge disc-shaped transparent masks were implemented in the visual scene in order to manipulate the extent of the visible area on the screen. In the Full field of view (FoV) condition, the optical flow, whether consisting of Dots or 3D spheres, was visible on the whole screen (see **Figures 2A1,B1**). In the other FoV conditions, the masks were combined in order to generate four different types of optical flow. In the 10, 40, and 70C FoV conditions, only the central 10, 40, and 70° of the visual scene, respectively, displayed the optical flow (see **Figures 2A2,B2**). The 10, 40, and 70P FoV conditions corresponded to the exact opposite, and the central 10, 40, and 70° of the visual scene, respectively, were masked, so that the optical flow was visible only in the periphery of the mask (see **Figures 2A3,B3**). In the 10P40C, 10P70C, and 40P70C FoV conditions, the central and peripheral part of the visual scene were masked, and the optical flow was visible only in a ring-shaped of 10–to–40°, 10–to–70°, and 40–to–70°, respectively (see **Figures 2A4,B4**). Finally, in the 10C40P, 10C70P, and 40C70P FoV conditions, both the central and the peripheral part of the visual scene were visible, while a ring-shaped area of 10–to–40°, 10–to–70°, and 40–to–70°, respectively, was masked, so that no optical flow was displayed in the masked area (see **Figures 2A5,B5**). In all FoV conditions, the disc-shaped masks and rings were centered on the fixation cross, i.e., on the focus of expansion of the optical flow.

2.1.5. Procedure

The stimuli were presented using a two-interval forced-choice (2-IFC) method. For each trial, two stimuli, namely a standard and a comparison stimulus, were successively presented to the participant. Both stimuli were moving at constant speed. At the end of the trial, the participant had to indicate in which interval (i.e., first or second) the stimulus was moving faster. For all FoV conditions, the standard stimulus was with Full FoV and it always moved at 5 m/s, i.e., 18 km/h. On the other hand, the speed of the comparison stimulus varied from trial to trial. Specifically, the speed of the comparison stimulus was determined for each trial by a Bayesian adaptive staircase (Kontsevich and Tyler, 1999), which took into account the speed of the previous visual stimuli as well as the corresponding responses of the participants. This method is based on an algorithm that optimizes the information gained with the previous trials. The Fov of the comparison stimulus was defined by the FoV condition (see FoV conditions).

At the beginning of each interval, the fixation cross appeared on a dark background. Participants were instructed to gaze at the cross and maintain the fixation until the end of the trial. 500 ms later, the first moving stimulus was presented for 700 ms, which included a 100 ms fade-in phase at the beginning and a 100 ms fade-out phase at the end. The second moving stimulus was presented 500 ms after the end of the first stimulus and had the same temporal structure as the first one. The fixation cross disappeared at the end of the second stimulus. The participant could then give its response by pressing on one of the two buttons of a joystick (i.e., first stimulus vs. second stimulus was faster). The time course of trials is presented in **Figure 2C**.

For each combination of visual stimulus (i.e., Dots vs. 3D spheres) and FoV condition (13 in total, see above), the adaptive staircase of the 2IFC method consisted of 80 trials. In total, the experiment consisted of 26 staircases of 80 trials each. The 26 staircases were split over two sessions that were run on two different days. The 13 staircases with Dots were all run on 1 day (Dots session), and the 13 staircases with 3D spheres (3D spheres session) were run on another day. Half of the subjects started with the Dots session, and the other half started with the 3D spheres session. For each type of visual stimulus/session, the 1040 trials (i.e., 13 staircases × 80 trials) were randomly interleaved, and presented in 8 blocks of 130 trials each. Each block lasted about 10 min with a 5 to 10 min break in between two consecutive blocks, so that in total, a session lasted about 2 h. During the breaks, the lights of the experimental room were switched on and subjects could walk and relax.

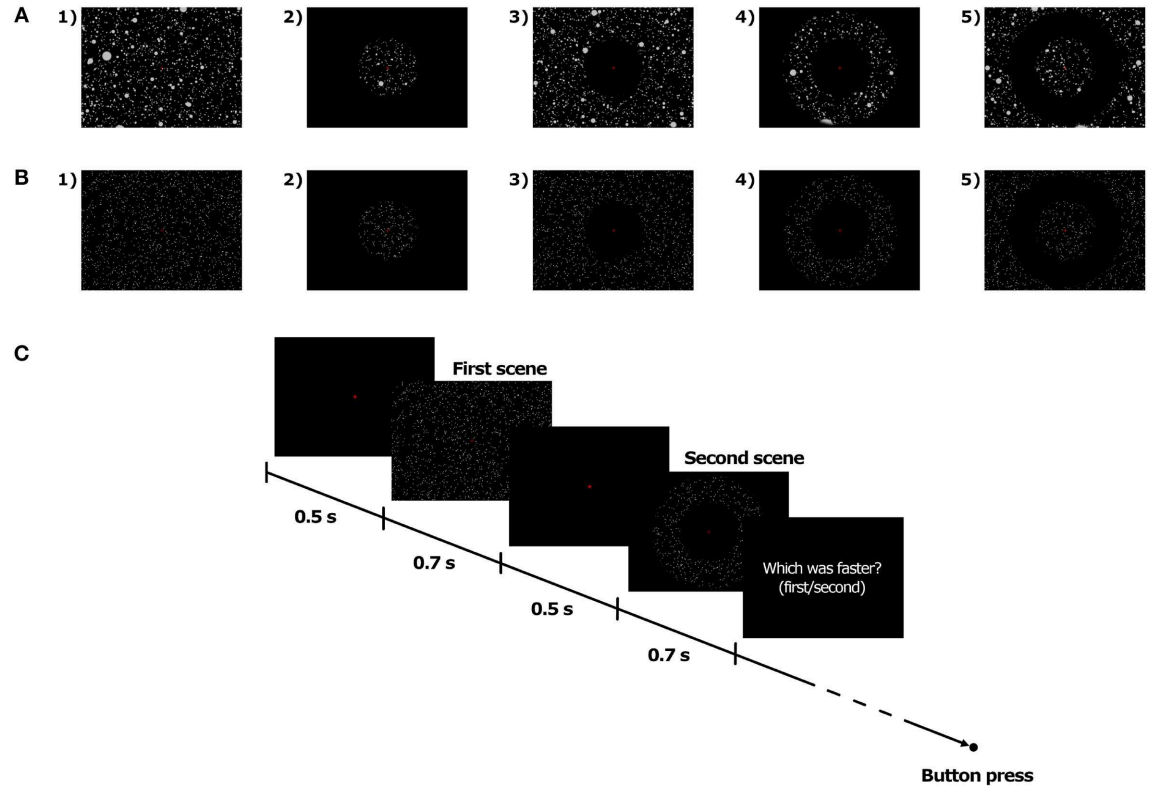

FIGURE 2 | Illustration of the FoV condition with 3D spheres **(A)** and dots **(B)**, and time course of trials **(C)**.

2.1.6. Statistical Analyses

For each condition, the perceived speed was measured as the Point of Subjective Equality (PSE), i.e., the speed at which the comparison stimulus was perceived to move as fast as the standard stimulus. Note that when the PSE is higher than the actual speed of the standard stimulus, it indicates that the comparison stimulus was perceived as moving slower than the standard stimulus. Conversely, when the PSE is lower than the actual speed of the standard stimulus, it indicates that the comparison stimulus was perceived as moving faster than the standard stimulus. Both for the Dots condition (i.e., optical flow only) and for the 3D spheres condition (i.e., optical flow + expansion cues), mean PSEs were compared using either a one-way repeated measures analysis of variance (ANOVA) when data was parametric, or a Friedman rank sum test when data was not parametric. *Post-hoc* paired-comparisons were then performed using either Bonferroni correction for multiple comparisons (parametric data) or Friedman multiple comparisons test (non-parametric data). Additionally, a linear mixed model was used to directly compare the dots condition with the spheres condition. For all tests (except for the linear mixed model), in order to determine whether to use parametric (i.e., ANOVA) or non-parametric (i.e., Friedman test) methods of mean comparison, the normality of the residuals was assessed using the Shapiro-Wilk test, and p-values were Huynh-Feldt-corrected when the sphericity assumption was violated (as assessed with the Mauchly's test). All statistical tests were performed using the R statistical software.

2.2. Computational Model of Motion Processing

The proposed model, based on bio-inspired paradigms, describes a neural architecture that mimics the psychophysical outcomes of the previously described experiment that assess the influence of the size of the field of view on motion perception.

The neural architecture is composed of hierarchical cell layers that model the processing stages of the dorsal visual pathway (Goodale and Westwood, 2004; Orban, 2008). The activity of the MT area can be modeled by a V1-MT feed forward architecture. In particular, we can model V1 cells by using the motion energy model, based on spatio-temporal filtering, and MT pattern cells by pooling V1 cell responses (Adelson and Bergen, 1985; Simoncelli and Heeger, 1998; Solari et al., 2015; Chessa et al., 2016b). Then, the neural activity of the MT area is processed by populations of MST cells that have selectivity for specific patterns of optical flow: in particular, they can be sensitive to the differential components of the optical flow (Grossberg et al., 1999; Beardsley and Vaina, 2001; Chessa et al., 2013). The selectivity of the MST cells can be related to the relative motion between an observer and the scene, in particular to the speed of forward translation during self-motion through the environment (Chessa et al., 2013, 2016a).

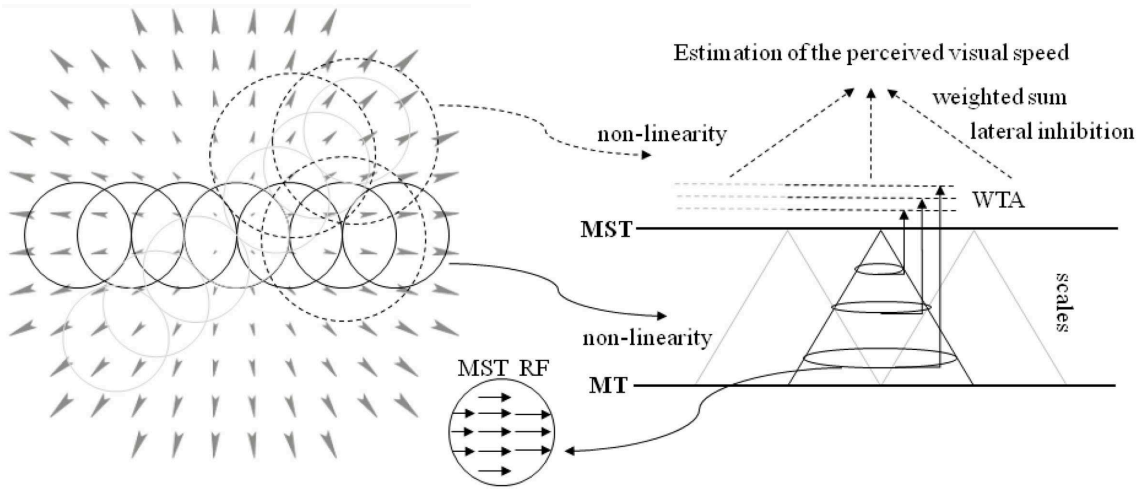

FIGURE 3 | A sketch of the proposed model. **(Left)** The circular RFs of the model are superimposed on the visual stimulus (optical flow, expansion). The RFs tile all the visual field: the solid line circles denote the MST RFs, and the dotted circles denote the area, where the MST activity is processed. **(Right)** The neural architecture to estimate the speed of forward translation during self-motion (see text for details). The activity of MT visual area is processed by the MST RFs that perform an adaptive template matching (in the middle inset a template is shown) to detect variation of velocity. A multi-scale approach is adopted. The population of each MST scale is processed through a WTA, and such outputs are used in a weighted sum to estimate the forward translation motion, i.e., the perceived visual speed.

Here, we propose a novel neural model that processes the output of the aforementioned layers (see Solari et al., 2015; Chessa et al., 2016a,b for details) for the estimation of the perceived visual speed. The proposed computational neural model can be summarized as follows (see **Figure 3** for a sketch of the proposed model):

- The population of MST cells at different scales performs an adaptive template matching (e.g., see the example of a MST RF in **Figure 3**) on the MT motion patterns that take into account a non-linearity to describe the space-variant resolution of retinas (Solari et al., 2012, 2014).
- An approach is adopted, in order to take into account both the evidence that MST RFs have different sizes and the fact that the visual signal contains information at different spatial scales.
- The activity of the MST cells is locally processed by a Winner-Take-All (WTA) approach: specifically, the WTA is locally applied on the sub-populations of each scale. Moreover, a compressive non-linearity is applied on the WTA outputs.
- In order to estimate the perception of speed of forward translation during self-motion, the most active scale is selected and its spatial neural activity is pooled through a weighted sum: in particular, we consider both positive and negative weights (i.e., there is an inhibition due to the activity in the periphery of the visual field).

2.2.1. Modeled MST Area

The dorsal MST area is associated with the specialized function of encoding visual cues to self-motion: in particular, there are neurons that are selectively sensitive to specific components (i.e., elementary components of optical flow patterns, as expansion, contraction, rotation, and translation) of the optical flow that occurs during self-motion (Tanaka et al., 1989; Duffy and Wurtz, 1991; Pitzalis et al., 2013; Cottereau et al., 2017), but (Wall and Smith, 2008) identified also two other areas sensitive to egomotion in humans. Several biologically plausible models of the MST functionality have been proposed (Perrone and Stone, 1994; Grossberg et al., 1999; Yu et al., 2010; Mineault et al., 2012). Specifically, we consider the approach presented in Chessa et al. (2013) and extend it to model the experimental data we present in our current work.

Cortical representation We consider the representation of optical flow as provided by a bio-inspired model (Chessa et al., 2016b) and we model the space-variant resolution of retinas by using the blind spot approach, i.e., log-polar mapping (Solari et al., 2012).

The log polar mapping modifies the Cartesian polar coordinates by applying a non-linearity on the radius ρ, as $\xi = \log_a(\rho/\rho_0)$, and a normalization on the angle coordinate θ (Schwartz, 1977; Traver and Pla, 2008; Solari et al., 2012, 2014). The transformation of a vector field from the Cartesian domain to the cortical domain can be expressed in terms of a general coordinates transformation (Chan Man Fong et al., 1997; Solari et al., 2014):

$$\begin{bmatrix} v_x \\ v_y \end{bmatrix} = \frac{1}{\rho_0 a^{\xi} \ln(a)} \begin{bmatrix} \cos\theta & \sin\theta \\ -\sin\theta & \cos\theta \end{bmatrix} \begin{bmatrix} v_{xCart} \\ v_{yCart} \end{bmatrix}, \qquad (1)$$

where a parameterizes the non-linearity of the mapping, and ρ_0 is the radius of the central blind spot. v_{xCart} and v_{yCart} denote the components along x and y axes of the Cartesian optic flow, and the v_x and v_y components describe the transformed cortical optic flow. The scalar coefficient of Equation (1) represents the scale factor of the log-polar vector, and the matrix describes the rotation due to the mapping. It is worth noting that Cartesian annular regions of expansion optical flow that are centered

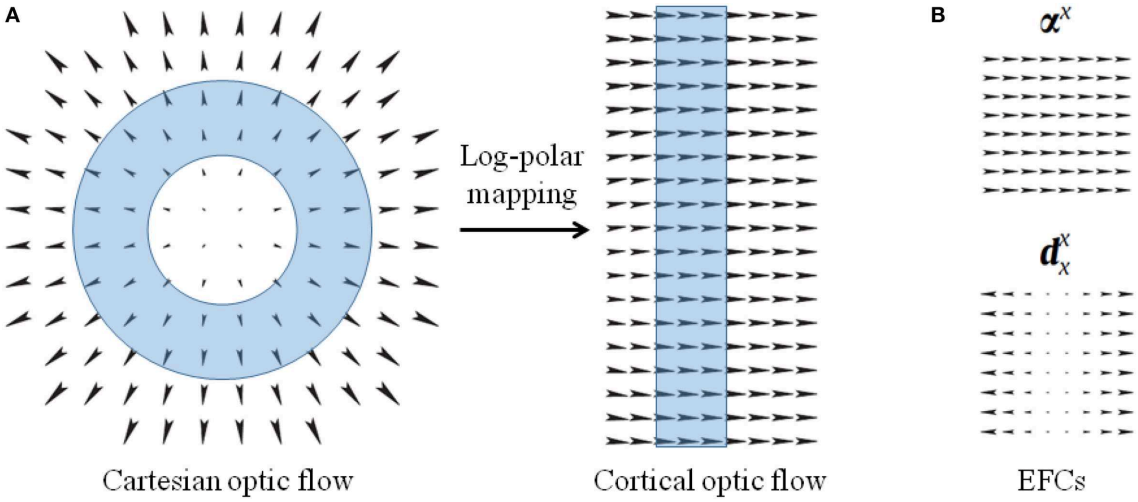

FIGURE 4 | (A) Optical flows representing expansion in the Cartesian domain and the corresponding cortical optical flow. The log-polar mapping transforms Cartesian annular regions (cyan ring-shaped area) into cortical vertical stripes. **(B)** Example of elementary flow components representing cardinal deformations of the optical flow.

around the fixation point, i.e., the fovea, are mapped into vertical stripes of horizontal optical flow in the uniform cortical representation (see **Figure 4A**). In **Appendix** some relevant optic flow patterns and their log-polar mappings are reported.

Elementary flow components The MST neurons are sensitive to elementary flow components (EFCs), such as expansion, shear, and rotation, or their combination with translation components (Koenderink, 1986; Orban et al., 1992). Since such EFCs can be described in terms of affine descriptions (Chessa et al., 2013), we describe the optical flow $\boldsymbol{v}(x, y)$ as linear deformations by a first-order Taylor decomposition, around each point: $\boldsymbol{v} = \bar{\boldsymbol{v}} + \overline{\mathbf{T}}\boldsymbol{x}$, where $\overline{\mathbf{T}}$ is the tensor composed of the partial derivatives of the optical flow.

By describing the tensor through its dyadic components, the optical flow can be locally described through two-dimensional maps ($\boldsymbol{m} : \mathrm{R}^2 \mapsto \mathrm{R}^2$) representing elementary flow components:

$$\begin{aligned}\boldsymbol{v} = {} & \boldsymbol{\alpha}^x \bar{v}_x + \boldsymbol{\alpha}^y \bar{v}_y + \boldsymbol{d}_x^x \left.\frac{\partial v_x}{\partial x}\right|_{\boldsymbol{x}_0} + \boldsymbol{d}_y^x \left.\frac{\partial v_x}{\partial y}\right|_{\boldsymbol{x}_0} \\ & + \boldsymbol{d}_x^y \left.\frac{\partial v_y}{\partial x}\right|_{\boldsymbol{x}_0} + \boldsymbol{d}_y^y \left.\frac{\partial v_y}{\partial y}\right|_{\boldsymbol{x}_0},\end{aligned} \tag{2}$$

where, the first two terms are pure translations and the other ones are cardinal deformations, basis of a linear deformation space: for instance, $\boldsymbol{\alpha}^x : (x, y) \mapsto (1, 0)$ and $\boldsymbol{d}_x^x : (x, y) \mapsto (x, 0)$ (see **Figure 4B**).

We can model the sensitivity to such deformations through a population of MST cells whose response is obtained by an adaptive template matching on the cortical optical flow. From the responses of such a population we compute the first-order (affine) description of the cortical optical flow (Koenderink, 1986; Orban et al., 1992).

Affine flow model and motion interpretation The affine description of optical flow is related to the interpretation of visual motion (Chessa et al., 2013): specifically, the affine coefficients can be combined in order to compute quantities related to the relative motion between an observer and the scene, such as the estimation of the 3-D orientation of the surfaces, of the time to collision, of the focus of expansion, and of the translational speed that is of interest for the current work.

To clarify the relationships, we can consider the following affine description of the optical flow:

$$\begin{bmatrix} v_x \\ v_y \end{bmatrix} = \begin{bmatrix} c_1 \\ c_4 \end{bmatrix} + \begin{bmatrix} c_2 & c_3 \\ c_5 & c_6 \end{bmatrix} \cdot \begin{bmatrix} x \\ y \end{bmatrix}. \tag{3}$$

The relative motion between an observer and the scene can be described as a rigid-body motion: a 3D point $\mathbf{X} = (X, Y, Z)^T$ has a motion given by $\dot{\mathbf{X}} = -(\mathbf{T} + \boldsymbol{\Omega} \wedge \mathbf{X})$, where $\mathbf{T} = (T_X, T_Y, T_Z)^T$ denotes the translational velocity and $\boldsymbol{\Omega} = (\Omega_X, \Omega_Y, \Omega_Z)^T$ the angular velocity (Longuet-Higgins and Prazdny, 1980). By considering a pinhole camera model with focal length f, we obtain the perspective projection of the motion:

$$\begin{aligned}\begin{bmatrix} v_x \\ v_y \end{bmatrix} = {} & f \begin{bmatrix} -T_X/Z - \Omega_Y \\ -T_Y/Z + \Omega_X \end{bmatrix} + \begin{bmatrix} T_Z/Z & \Omega_Z \\ -\Omega_Z & T_Z/Z \end{bmatrix} \cdot \begin{bmatrix} x \\ y \end{bmatrix} \\ & + \frac{1}{f} \begin{bmatrix} xy\Omega_X - x^2\Omega_Y \\ y^2\Omega_X - xy\Omega_Y \end{bmatrix}.\end{aligned} \tag{4}$$

By considering a smooth surface structure, specifically we locally approximate the surface through a planar surface, we can describe the affine coefficients in terms of the motion quantities of Equation (4) (Chessa et al., 2013). In particular, the affine coefficient c_2 (in the condition of the experiment considered in this work) is proportional to T_Z, i.e., the forward translation speed in an ego-motion scenario.

The coefficient c_2 can be estimated through a template matching by using the map $\boldsymbol{d}_x^x$ that describes the MST RFs of a population of cells. Thus, the output of such a template matching can be considered as the MST neural activity $E(p)$, where $p = (x, y)$ denotes the domain, i.e., the coordinate reference system.

2.2.2. Modeled Perceived Visual Speed

To take into account the experimental data about the range of the RF size (Raiguel et al., 1997), we consider four scales (s) in the range $10 - 50^\circ$, thus the MST neural activity is described as $E(p, s)$. Moreover, we implemented a multi-scale approach also to consider the fact that the visual signal contains information at different spatial scales.

With the aim of obtaining an estimate of perceived forward translation speed, the distributed neural MST activity $E(p, s)$ is processed through a Winner-Take-All approach. Specifically, we locally apply a WTA on the neural sub-population of each scale: the WTA processes the MST activity on an area W of 70° with 75% overlap. Moreover, a compressive non-linearity β is applied on the WTA output:

$$E_{WTA}(p, s) = \left(\max_{p \in W} * \; E(p, s) \right)^{\beta}, \tag{5}$$

where $*$ denotes that the WTA is applied by using a moving window W.

To exploit the information gathered by the multi-scale approach, we model a WTA layer that selects the most active neural sub-population among the ones of the considered scales:

$$E_{WTA}(p) = \max_{s} E(p, s). \tag{6}$$

We propose a spatial pooling of the MST activity to obtain a scalar value Pz as an estimate of the perceived forward translation speed. In particular, the activity in the visual periphery (area W_p) has an inhibitory role with respect to the central area W_c (see section 2.2.3 also), if there is an activity in a small area W_f around the fovea:

$$Pz = \sum_{p \in W_c} E_{WTA}(p) + g(\underset{p \in W_f}{E_{WTA}(p)}) \sum_{p \in W_p} E_{WTA}(p), \tag{7}$$

where $g(\cdot)$ denotes a gating function that has a negative value when there is an activity in the area W_f around the fovea (otherwise it assumes a positive value). In the current implementation, we have $W_f = 5^\circ$, $W_c = 85^\circ$ (i.e., a central 85° area) and $W_p = 25^\circ$ (i.e., peripheral 25°).

Comparison with human data The model estimate Pz of the perceived forward translation speed (see Equation 7) can be directly compared with the human estimates of the described experiment: **Figure 9** shows the model estimates Pz for the 13 visual stimulus conditions with respect to the corresponding human data. To provide a measure of the difference between human and model data (i.e., the simulation error), we compute the Pz for the $N = 13$ visual conditions and we evaluate the relative error e_{mh} as follows:

$$e_{mh} = (1/N) \sum_{i=1}^{N} |HD_i - Pz_i| / HD_i, \tag{8}$$

where $|\cdot|$ denotes the absolute value, HD_i denotes the average human perception of speed for the i-th condition and Pz_i the model estimate for the same condition. All simulations were performed using the Matlab software.

TABLE 1 | Average relative errors (Equation 8) of the proposed model with their standard deviations as a function of the processing stages.

Removal of the processing stage	e_{mh} ± its std
Full model	**0.036 ± 0.034**
Log-polar mapping	0.186 ± 0.135
A single scale with the smallest RF size	0.068 ± 0.059
A single scale with the largest RF size	0.107 ± 0.065
Both WTA, Equations (5) and (6) (by using an averaging)	0.229 ± 0.066
WTA, Equation (5) (by using an averaging)	0.179 ± 0.043
WTA, Equation (6) (by using an averaging)	0.090 ± 0.052
Gating function, Equation (7)	0.148 ± 0.251

2.2.3. Systematic Analysis of the Influence of Processing Stages on the Model Performance

In order to understand how the different processing stages affect the model performance in modeling human estimates, we selectively remove specific processing stages of the proposed neural model and analyze the resulting outputs with respect to human data.

Table 1 shows the average relative error e_{mh} (see Equation 8) of the model in replicating the human data by removing specific processing stages. In **Figure 5** the distribution of the relative errors on the 13 stimulus conditions is shown, for the same model changes as in **Table 1**.

The removal of the log-polar mapping affects the performances of the model in mimicking the human data: indeed, the average relative error is $e_{mh} = 0.186$ with respect the full model that has $e_{mh} = 0.036$ (see **Table 1**). By looking at **Figure 5A** we can see that the conditions 10P and 40P (also 10P70C and 40P70C) are hugely affected, indeed they are the areas between fovea and periphery, where the log-polar mapping mainly acts.

Conversely, to use a single scale instead of four scales has a smaller impact on the model performances and the effect on the different visual conditions is uniform, **Figures 5B,C**. By using a single scale with the smallest RF size (i.e., 10°) produces an average relative error $e_{mh} = 0.068$. The error is $e_{mh} = 0.107$ with the largest RF (i.e., 50°).

To change the WTA approach with an averaging affects hugely the model performances by causing an average relative error $e_{mh} = 0.229$, however the effect on the visual conditions is uniform (see **Figures 5D–F**). By removing the WTA that acts within each scale (Equation 5) has the most effect ($e_{mh} = 0.179$) with respect the WTA that acts among scales (Equation 6, $e_{mh} = 0.090$).

The removal of the gating function (see Equation 7) has a medium impact on the model performances, i.e., $e_{mh} = 0.148$. Nevertheless, it affects in an asymmetric way the relative errors on the visual conditions (see **Figure 5G**): the visual conditions 10C40P, 10C70P, and 40C70P are the most affected. For such conditions both the central and the peripheral part of the visual scene are visible: this suggests that might be present an (inhibitory) interaction between the foveal and peripheral areas.

FIGURE 5 | Relative errors (Equation 8) of the proposed model with respect to human data as a function of the 13 visual stimulus conditions by varying the processing stages, as in **Table 1**. In particular, the average relative errors by removing specific processing stages are as follows: about 4% (i.e., 0.036 by using Equation 8) for the full model; 19% without log-polar mapping **(A)**; 7 and 11% with a single scale, the smallest **(B)** and largest **(C)** RF size, respectively; 23% by changing both WTA with an averaging **(D)**; 18 and 9% by changing only one WTA **(E,F)**; 15% without gating function **(G)**.

3. RESULTS

3.1. Influence on the FoV on Perceived Visual Speed With Dots (Optical Flow Only)

When the optical flow consisted of dots, the Shapiro-Wilks test performed on the residuals indicated that data was not normally distributed. The Friedman rank sum test indicated a main effect of the FoV condition (i.e., the type of field of view) on perceived visual speed [$\chi^2_{(12)} = 56.60$, $p < 0.001$]. *Post-hoc* tests performed with the Friedman multiple comparisons function indicated that in the 10C condition, the PSE was significantly higher than in the 10P, 40P, 10P70C, and 40P70C conditions.

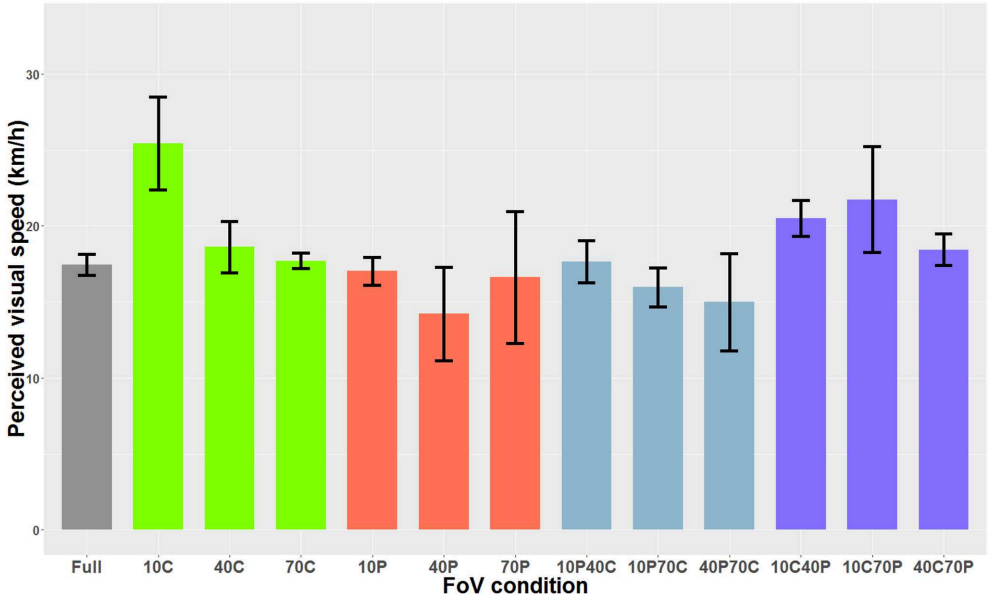

FIGURE 6 | PSE mean values as a function of the FoV when the optical flow consisted of dots (i.e., optical flow only). The error bars represent the standard error of the mean.

In other words, the optical flow was perceived as significantly slower in the 10C condition than in the 10P, 40P, 10P70C, and 40P70C conditions. In addition, the optical flow was perceived as significantly slower (i.e., higher PSE) in the 10C40P than in the 40P and 10P70C condition. Finally, the optical flow was perceived as significantly slower in the 10C70P condition than in the 40P, 10P70C, and 40P70C conditions. **Figure 6** shows the PSEs for all 13 FoV conditions.

3.2. Influence on the FoV on Perceived Visual Speed With 3D Spheres (Optical Flow + Expansion Cues)

When the optical flow consisted of 3D spheres and included optical expansion cues, the Shapiro-Wilk analysis indicated that the residuals were normally distributed. The one-way ANOVA indicated a main effect of the FoV condition on perceived visual speed [$F_{(12,84)}$=47.37, $p < 0.001$]. Bonferroni-corrected paired-comparisons indicated that in the 10C condition, the optical flow was perceived as significantly slower (i.e., higher PSE) than in all other FoV conditions. Also, the optical flow was perceived as significantly faster in the 40P and 70P FoV conditions than in the 40C, 70C, 10C40P, 10C70P, 40C70P, and 10P40C conditions. **Figure 7** shows the PSEs for all 13 FoV conditions.

3.3. Direct Comparison of Perceived Visual Speed With Dots and 3D Spheres

We then compared "directly" the Dots condition with the 3D spheres condition. Because data was non-parametric and we had a repeated measures design, we used a linear mixed model. The analysis revealed that the type of visual stimulus used for the optical flow (i.e., dots vs. 3D spheres) did not have any effect on perceived speed ($\chi^2_{(1)}$=0.0004, $p = 0.98$). On the other hand, there was a main effect of the type of FoV ($\chi^2_{(12)}$=226.06, $p < 0.0001$) as well as a significant interaction between the two main factors ($\chi^2_{(12)}$=58.12, $p < 0.0001$). Therefore, for each FoV condition, we directly compared the PSE measured with dots and the PSE measured with 3D spheres. These tests were performed using paired *t*-tests or Wilcoxon signed-rank test (when data was non-parametric). These tests were Bonferroni-corrected for multiple comparisons. None of the 13 tests indicated a significant difference between the PSE measured with dots and the PSE measured with 3D spheres. The only FoV condition for which the test was close to reaching significance ($p = 0.063$) was the 10C condition. Note that using a two-way repeated measures ANOVA instead of the linear mixed model gave the exact same pattern of result, namely no effect whatsoever of the type of stimulus (i.e., dots vs. 3D spheres) on perceived speed ($p = 0.99$), a main effect of the type of FoV ($p < 0.001$) and an interaction between the two main factors ($p < 0.001$). **Figure 8** shows perceived speed for all FoV conditions and with the two types of visual stimuli.

3.4. A Computational Model of Motion Processing Accounts for the Patterns of Human Data

Figure 9 shows the estimates of perceived visual speeds of the proposed model (i.e., *Pz*, see section 2.2 for details), assessed by using the same stimuli and procedure as the human observers. The underestimation and overestimation of speed exhibited by the model are very similar to the ones of human observers: in particular, the model is able to replicate the human behavior for 10C, 10C70P, 10P40C, 40C, and 40C70P, but 10C40P shows a larger error, though acceptable. In general, the proposed

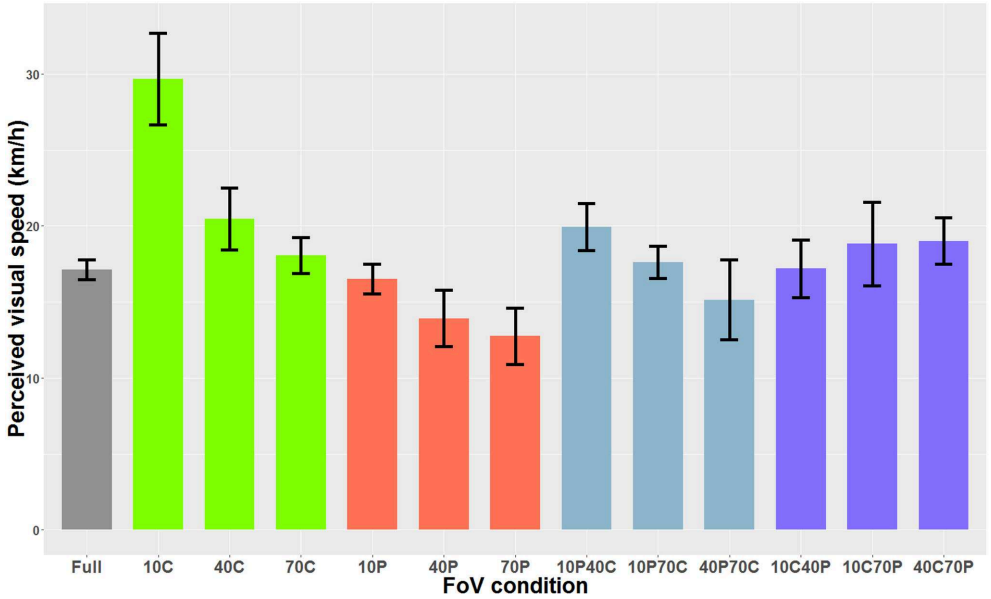

FIGURE 7 | PSE mean values as a function of the FoV when the optical flow consisted of 3D sphere (i.e., optical flow + expansion cues). The error bars represent the standard error of the mean.

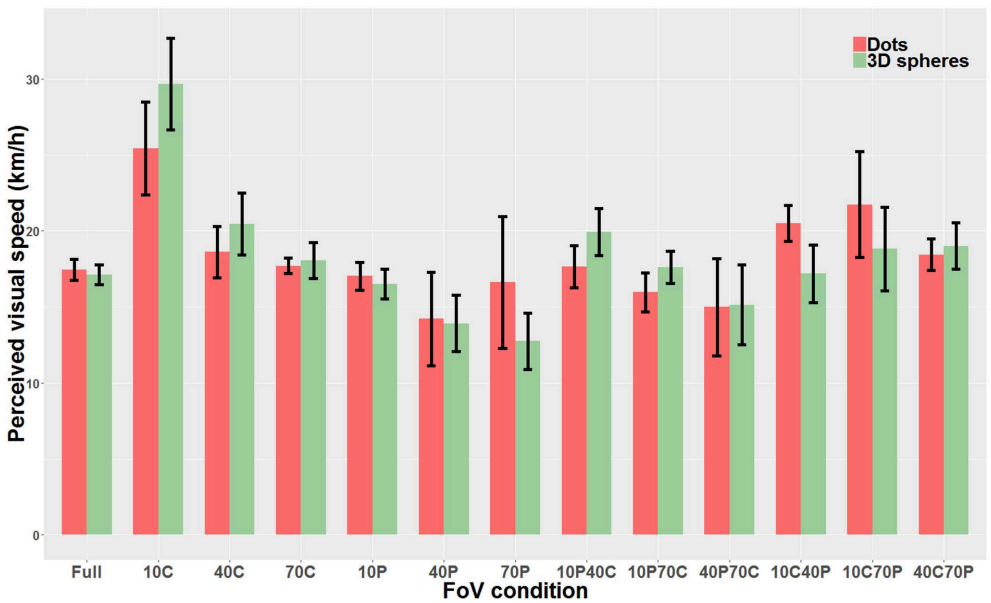

FIGURE 8 | Direct comparison of PSE mean values measured with dots (red) and 3D spheres (green). The error bars represent the standard error of the mean.

computational model shows a high level of agreement with the human data: the average relative error e_{mh} is about 4% (i.e., 0.04 by using Equation 8).

4. DISCUSSION

Participants were presented with an optical flow constituted of limited-life-time random dots or 3D spheres moving in their direction along the antero-posterior axis. The size and portion of the moving FoV was systematically manipulated. For all FoV conditions, we did not observe any significant difference between the two types of visual stimuli, namely dots and 3D spheres. In other words, irrespective of the size and portion of the displayed FoV, visual speed perception was similar whether only optical flow information was available (i.e., Dots condition), or additional expansion/looming cues

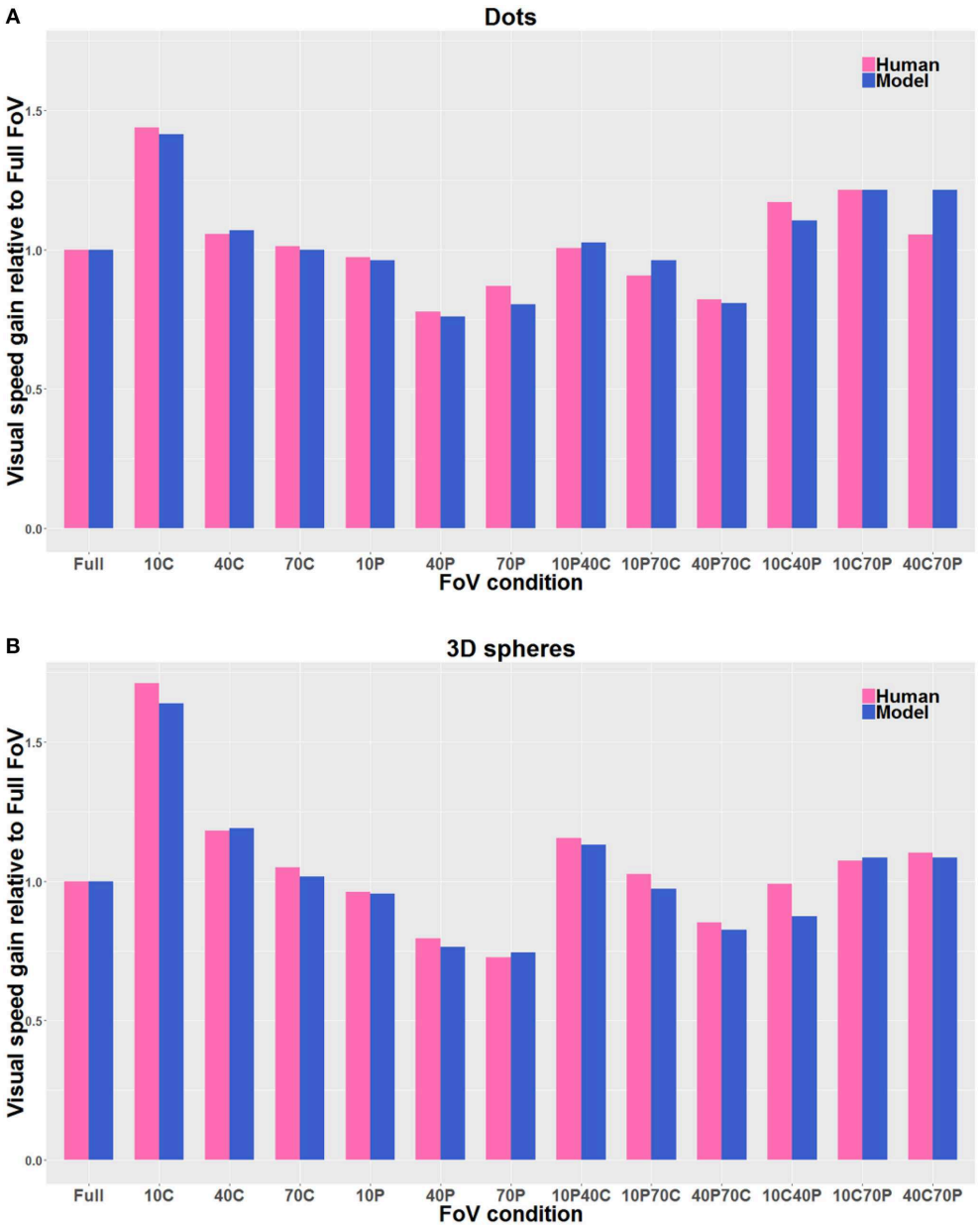

FIGURE 9 | Direct comparison of the visual gains measured with the participants (Human) with the visual gains given by the model (Model), both when the visual stimulus consisted of Dots **(A)** and of 3D spheres **(B)**. The pink bars correspond to the human data, and the blue bars correspond to the model estimates. The gain values are directly derived from the PSE values, so that gain values smaller than 1 indicate an overestimation of visual speed (relative to Full FoV), and gain values larger than 1 indicate an underestimation of visual speed. The visual stimulus conditions are reported in the text. The average relative error is about 4% by using Equation 8.

were present (i.e., 3D spheres conditions). On the other hand, both the size and portion of the moving visual field affected visual speed perception. In particular, patterns in which only the central part of the visual field was moving resulted in a larger underestimation of flow speed. Importantly, a bio-inspired computational model of the neural processing stages of the dorsal pathway allowed us to predict perceived speed based on the visible portion of the moving optical flow, and this with a 96 percent reliability.

Our results show that the size and the portion of visible FoV significantly affect perceived visual speed. In particular, as already described by Pretto and colleagues (Pretto et al., 2009), the wider peripheral-only conditions (namely 40P and 70P) resulted in an overestimation of the speed of the optical flow. However, and contrary to what was described by Pretto et al., this overestimation was significant only when the visual stimulus consisted of 3D spheres (i.e., when expansion cues were provided), and not when the visual stimulus consisted of

dots. When only the central 10° of FoV were displayed (i.e., FoV condition 10C), we also found an effect on perceived visual speed, that was significantly underestimated as compared to most other FoV conditions, depending on the type of visual stimulus. With 3D spheres, the underestimation (in the 10C condition) was significant as compared to all other FoV conditions. With dots however, the underestimation was significant as compared to the FoV conditions in which a small portion of the central FoV was covered (i.e., 10P, 40P, 10P70C, 40P40C), but not as compared to the Full FoV condition. This result is at odds with the 2009 study by Pretto and colleagues who using dots, found that all FoVs smaller than 60° gave rise to a significant underestimation of visual speed as compared to the Full FoV condition. Overall, our results indicate that visual speed tend to be underestimated when only a small central portion of the FoV is visible. Several studies have highlighted the importance of peripheral vision for motion perception, with a direct influence on speed perception (Pretto et al., 2009, 2012), but also on navigation abilities (Czerwinski et al., 2002; Turano et al., 2005) and on vection, i.e., the sensation of self-motion that derives from a moving stimulus (Brandt et al., 1973; Berthoz et al., 1975; Mohler et al., 2005). In line with this, the underestimation of visual speed that we observed when the peripheral part of the FoV was occluded likely results from the fact that in this situation, only the low angular velocities of the visible central portion can be used for speed estimation, thereby "biasing" perception.

Importantly, using a biologically-inspired model, we were able to predict the influence of the size and portion of the moving visual field on speed perception. Specifically, by providing the appropriate parameters of the neural processing stages, our model allowed us to predict with 96% of reliability the perceived speed based on the visible portion of the moving optical flow. In the past, different computational models have been proposed to "explain/describe" the processes underlying human perception of visual speed, mainly by focusing on local computation of motion. Commonly, these models assumed that the perception of visual motion is optimal in one of two conditions: (i) in a deterministic framework with a regularization constraint induces the solution to bias toward zero motion (Yuille and Grzywacz, 1988; Stocker, 2001); (ii) in a probabilistic framework of Bayesian estimations, which a prior that favors slow velocities (Simoncelli, 1993; Weiss et al., 2002). Other studies have shown that it is possible to capture basic qualitative features of translational motion perception with an ideal Bayesian observer model based on Gaussian forms for likelihood and prior (Weiss et al., 2002). Because the previous model deviates from human perceptual data regarding trial-to-trial variability and the form of interaction between perceived speed and contrast, Stocker and Simoncelli (2005) proposed a refined probabilistic model that could account for trial-to-trial variabilities. These authors derived the prior distribution and the likelihood function of speed perception from a set of psychophysical measurements of speed discrimination and matching.

Nevertheless, in order to perceive motion patterns that are related to visual navigation, one should consider a hierarchical processing and a spatial integration of the local motion, as described by previous models. Indeed, several models take into account the MST functionality and its larger receptive fields (Perrone and Stone, 1994; Grossberg et al., 1999; Yu et al., 2010; Mineault et al., 2012). In their seminal work, Perrone and Stone (1994) introduced a template-based model of self-motion that showed similar responses properties to MST neurons. In Grossberg et al. (1999), the model considers also log-polar mapping, though by using a formulation that does not allow a signal processing description as in our model. In Yu et al. (2010) and Mineault et al. (2012), the authors analyzed different types of neural combinations of local motion processing in order to account for the observed stimulus selectivity of MST neurons. It is worth noting that our model allows the prediction of perceived visual speed considering also the size and portion of the visual field. To obtain such a result, we have introduced several neural mechanisms by combining them in a novel computational model. In particular, we model a population of MST cells that perform an adaptive template matching by considering the spatial non-linearity produced by the log-polar mapping and multi-scale layers. Such a template matching allows a decomposition of motion patterns into an affine description that can be directly related to forward speed of the observer: the results show that the model estimates are similar to the perceived visual speed of human observers (i.e., the average relative error is about 4%).

Though there were some slight differences, the two types of visual stimuli, namely dots and 3D spheres, resulted in similar patterns of perceived visual speed. Specifically, providing expansion cues (3D spheres condition) in addition to the optical flow information did not alter perceived visual speed, and no significant difference could be observed between the Dots and the 3D spheres conditions. The only FoV condition for which a difference coming close to significance could be observed was the 10C condition, i.e., the FoV condition in which only the central 10° of FoV were visible. Note that this "tendency" could simply be due to the fact that in the 3D spheres condition, optical flow information might have been reduced because of the rapid expansion of the sprites which tended to cover the "small" visible area. This absence of significant difference between the Dots and the 3D spheres suggests that to estimate visual speed, at least in the conditions of the experiment, i.e., with simple visual stimuli, the optical flow provides sufficient motion information, and expansion cues do not provide much additional "benefit."

DATA AVAILABILITY STATEMENT

The datasets generated for this study are available on request to the corresponding author.

ETHICS STATEMENT

The studies involving human participants were reviewed and approved by Max Planck Institute for Biological Cybernetics and University of Tuebingen. The patients/participants

provided their written informed consent to participate in this study.

AUTHOR CONTRIBUTIONS

PP, J-PB, MCh, and FS conceived and designed the study. J-PB and PP collected the human participants data. MCa, PP, and J-PB analyzed the data. MCh and FS developed the neural computational model. All authors contributed to the drafting of the manuscript.

ACKNOWLEDGMENTS

The authors would like to thank Heike Bischoff (Eberhard Karls University, Tübingen, Germany) for her help with data collection.

REFERENCES

Adelson, E. H., and Bergen, J. R. (1985). Spatiotemporal energy models for the perception of motion. *Josa A* 2, 284–299.

Alfano, P. L., and Michel, G. F. (1990). Restricting the field of view: perceptual and performance effects. *Perceptual Motor Skills* 70, 35–45.

Amblard, B., and Carblanc, A. (1980). Role of foveal and peripheral visual information in maintenance of postural equilibrium in man. *Perceptual Motor Skills* 51, 903–912.

Banton, T., Stefanucci, J., Durgin, F., Fass, A., and Proffitt, D. R. (2005). The perception of walking speed in a virtual environment. *Presence* 14, 394–406. doi: 10.1162/105474605774785262

Beardsley, S. A., and Vaina, L. M. (2001). A laterally interconnected neural architecture in MST accounts for psychophysical discrimination of complex motion patterns. *J. Comput. Neurosci.* 10, 255–280. doi: 10.1023/A:1011264014799

Berthoz, A., Pavard, B., and Young, L. (1975). Perception of linear horizontal self-motion induced by peripheral vision (linearvection) basic characteristics and visual-vestibular interactions. *Exp. Brain Res.* 23, 471–489.

Brandt, T., Dichgans, J., and Koenig, E. (1973). Differential effects of central versus peripheral vision on egocentric and exocentric motion perception. *Exp. Brain Res.* 16, 476–491.

Caramenti, M., Lafortuna, C. L., Mugellini, E., Abou Khaled, O., Bresciani, J.-P., and Dubois, A. (2018). Matching optical flow to motor speed in virtual reality while running on a treadmill. *PLoS ONE* 13:e0195781. doi: 10.1371/journal.pone.0195781

Caramenti, M., Lafortuna, C. L., Mugellini, E., Abou Khaled, O., Bresciani, J.-P., and Dubois, A. (2019). Regular physical activity modulates perceived visual speed when running in treadmill-mediated virtual environments. *PLoS ONE* 14:e0219017. doi: 10.1371/journal.pone.0219017

Chan Man Fong, C., Kee, D., and Kaloni, P. (1997). *Advanced Mathematics For Applied And Pure Sciences*. Amsterdam: CRC Press.

Chessa, M., Maiello, G., Bex, P. J., and Solari, F. (2016a). A space-variant model for motion interpretation across the visual field. *J. Vision* 16:12. doi: 10.1167/16.2.12

Chessa, M., Sabatini, S. P., and Solari, F. (2016b). A systematic analysis of a V1–MT neural model for motion estimation. *Neurocomputing* 173, 1811–1823. doi: 10.1016/j.neucom.2015.08.091

Chessa, M., Solari, F., and Sabatini, S. P. (2013). Adjustable linear models for optic flow based obstacle avoidance. *Comput. Vision Image Understand.* 117, 603–619. doi: 10.1016/j.cviu.2013.01.012

Cornelissen, F. W., and van den Dobbelsteen, J. J. (1999). Heading detection with simulated visual field defects. *Visual Impairm. Res.* 1, 71–84.

Cottereau, B. R., Smith, A. T., Rima, S., Fize, D., Héjja-Brichard, Y., Renaud, L., et al. (2017). Processing of egomotion-consistent optic flow in the rhesus macaque cortex. *Cereb. Cortex* 27, 330–343. doi: 10.1093/cercor/bhw412

Czerwinski, M., Tan, D. S., and Robertson, G. G. (2002). "Women take a wider view," in *Proceedings of the SIGCHI Conference on Human Factors in Computing Systems* (Minneapolis, MN: ACM), 195–202.

Dickinson, J., and Leonard, J. (1967). The role of peripheral vision in static balancing. *Ergonomics* 10, 421–429.

Duffy, C. J., and Wurtz, R. H. (1991). Sensitivity of MST neurons to optic flow stimuli. i. a continuum of response selectivity to large-field stimuli. *J. Neurophysiol.* 65, 1329–1345.

Durgin, F. H., Fox, L. F., Schaffer, E., and Whitaker, R. (2005). "The perception of linear self-motion," in *Electronic Imaging 2005,* eds B. E. Rogowitz, T. N. Pappas, and S. J. Daly (San Jose, CA: International Society for Optics and Photonics), 503–514.

Goodale, M. A., and Westwood, D. A. (2004). An evolving view of duplex vision: separate but interacting cortical pathways for perception and action. *Curr. Opin. Neurobiol.* 14, 203–211. doi: 10.1016/j.conb.2004.03.002

Grossberg, S., Mingolla, E., and Pack, C. (1999). A neural model of motion processing and visual navigation by cortical area MST. *Cereb. Cortex* 9, 878–895.

Held, R., Dichgans, J., and Bauer, J. (1975). Characteristics of moving visual scenes influencing spatial orientation. *Vision Res.* 15, 357–65.

Kassler, L., Feasel, J., Lewek, M. D., Brooks, F. P. Jr., and Whitton, M. C. (2010). "Matching actual treadmill walking speed and visually perceived walking speed in a projection virtual environment," in *Proceedings of the 7th Symposium on Applied Perception in Graphics and Visualization* (Los Angeles, CA: ACM), 161–161.

Kirschen, M. P., Kahana, M. J., Sekuler, R., and Burack, B. (2000). Optic flow helps humans learn to navigate through synthetic environments. *Perception* 29, 801–818. doi: 10.1068/p3096

Koenderink, J. (1986). Optic flow. *Vision Res.* 26, 161–179.

Kontsevich, L. L., and Tyler, C. W. (1999). Bayesian adaptive estimation of psychometric slope and threshold. *Vision Res.* 39, 2729–2737.

Longuet-Higgins, H., and Prazdny, K. (1980). The interpretation of a moving retinal image. *Phil. Trans. R. Soc. Lond. B* 208, 385–397.

McGee, M. G. (1979). Human spatial abilities: psychometric studies and environmental, genetic, hormonal, and neurological influences. *Psychol. Bull.* 86:889.

Mergner, T., and Rosemeier, T. (1998). Interaction of vestibular, somatosensory and visual signals for postural control and motion perception under terrestrial and microgravity conditions—a conceptual model. *Brain Res. Rev.* 28, 118–135.

Mineault, P. J., Khawaja, F. A., Butts, D. A., and Pack, C. C. (2012). Hierarchical processing of complex motion along the primate dorsal visual pathway. *Proc. Natl. Acad. Sci. U.S.A.* 109, E972–E980. doi: 10.1073/pnas.1115685109

Mohler, B. J., Thompson, W. B., Riecke, B., and Bülthoff, H. H. (2005). "Measuring vection in a large screen virtual environment," in *Proceedings of the 2nd Symposium on Applied Perception in Graphics and Visualization* (New York, NY: ACM), 103–109.

Nilsson, N. C., Serafin, S., and Nordahl, R. (2014). Establishing the range of perceptually natural visual walking speeds for virtual walking-in-place locomotion. *IEEE Trans. Visual. Comput. Graph.* 20, 569–578. doi: 10.1109/TVCG.2014.21

Orban, G. A. (2008). Higher order visual processing in macaque extrastriate cortex. *Physiol. Rev.* 88, 59–89. doi: 10.1152/physrev.00008.2007

Orban, G. A., Lagae, L., Verri, A., Raiguel, S., Xiao, D., Maes, H., et al. (1992). First-order analysis of optical flow in monkey brain. *Proc. Natl. Acad. Sci. U.S.A.* 89, 2595–2599.

Osaka, N. (1988). "Speed estimation through restricted visual field during driving in day and night: naso-temporal hemifield differences," in *Vision in Vehicles II. Second International Conference on Vision in Vehicles* (Burlington, MA).

Perrone, J. A., and Stone, L. S. (1994). A model of self-motion estimation within primate extrastriate visual cortex. *Vision Res.* 34, 2917–2938.

Pitzalis, S., Sdoia, S., Bultrini, A., Committeri, G., Di Russo, F., Fattori, P., et al. (2013). Selectivity to translational egomotion in human brain motion areas. *PLoS ONE* 8:e60241. doi: 10.1371/journal.pone.0060241

Powell, W., Stevens, B., Hand, S., and Simmonds, M. (2011). "Blurring the boundaries: the perception of visual gain in treadmill-mediated virtual environments," in *3rd IEEE VR 2011 Workshop on Perceptual Illusions in Virtual Environments* (Singapore).

Pretto, P., Bresciani, J.-P., Rainer, G., and Bülthoff, H. H. (2012). Foggy perception slows us down. *eLife* 1:e00031. doi: 10.7554/eLife.00031

Pretto, P., Ogier, M., Bülthoff, H. H., and Bresciani, J.-P. (2009). Influence of the size of the field of view on motion perception. *Comput. Graph.* 33, 139–146. doi: 10.1016/j.cag.2009.01.003

Raiguel, S., Van Hulle, M. M., Xiao, D. K., Marcar, V. L., Lagae, L., and Orban, G. A. (1997). Size and shape of receptive fields in the medial superior temporal area (MST) of the macaque. *Neuroreport* 8, 2803–2808.

Schwartz, E. L. (1977). Spatial mapping in the primate sensory projection: analytic structure and relevance to perception. *Biol. Cybernet.* 25, 181–194.

Simoncelli, E. P. (1993). *Distributed analysis and representation of visual motion* (unpublished doctoral dissertation). MIT.

Simoncelli, E. P., and Heeger, D. J. (1998). A model of neuronal responses in visual area MT. *Vision Res.* 38, 743–761.

Solari, F., Chessa, M., Medathati, N. K., and Kornprobst, P. (2015). What can we expect from a V1-MT feedforward architecture for optical flow estimation? *Signal Proc. Image Commun.* 39, 342–354. doi: 10.1016/j.image.2015.04.006

Solari, F., Chessa, M., and Sabatini, S. P. (2012). Design strategies for direct multi-scale and multi-orientation feature extraction in the log-polar domain. *Pattern Recogn. Lett.* 33, 41–51. doi: 10.1016/j.patrec.2011.09.021

Solari, F., Chessa, M., and Sabatini, S. P. (2014). An integrated neuromimetic architecture for direct motion interpretation in the log-polar domain. *Comput. Vision Image Understand.* 125, 37–54. doi: 10.1016/j.cviu.2014.02.012

Stocker, A. A. (2001). *Constraint optimization networks for visual motion perception: analysis and synthesis*. Ph.D thesis, ETH Zurich.

Stocker, A. A., and Simoncelli, E. P. (2005). "Constraining a bayesian model of human visual speed perception," in *Advances in neural information processing systems* (Vancouver, BC), 1361–1368.

Stoffregen, T. A. (1986). The role of optical velocity in the control of stance. *Percept. Psychophys.* 39, 355–360.

Tanaka, K., Fukada, Y., and Saito, H. (1989). Underlying mechanisms of the response specificity of expansion/contraction and rotation cells in the dorsal part of the medial superior temporal area of the macaque monkey. *J. Neurophysiol.* 62, 642–656.

Tartre, L. A. (1990). Spatial orientation skill and mathematical problem solving. *J. Res. Math. Educ.* 21, 216–229.

Thurrell, A., Pelah, A., and Distler, H. (1998). The influence of non-visual signals of walking on the perceived speed of optic flow. *Perception* 27, 147–148.

Thurrell, A. E., and Pelah, A. (2002). Reduction of perceived visual speed during walking: Effect dependent upon stimulus similarity to the visual consequences of locomotion. *J. Vision* 2, 628–628. doi: 10.1167/2.7.628

Traver, V. J., and Pla, F. (2008). Log-polar mapping template design: From task-level requirements to geometry parameters. *Image Vision Comput.* 26, 1354–1370. doi: 10.1016/j.imavis.2007.11.009

Turano, K. A., Yu, D., Hao, L., and Hicks, J. C. (2005). Optic-flow and egocentric-direction strategies in walking: central vs peripheral visual field. *Vision Res.* 45, 3117–3132. doi: 10.1016/j.visres.2005.06.017

Van Veen, H. A., Distler, H. K., Braun, S. J., and Bülthoff, H. H. (1998). Navigating through a virtual city: using virtual reality technology to study human action and perception. *Fut. Gen. Comput. Syst.* 14, 231–242.

Wade, M. G., and Jones, G. (1997). The role of vision and spatial orientation in the maintenance of posture. *Phys. Therapy* 77, 619–628.

Wall, M. B., and Smith, A. T. (2008). The representation of egomotion in the human brain. *Curr. Biol.* 18, 191–194. doi: 10.1016/j.cub.2007.12.053

Weiss, Y., Simoncelli, E. P., and Adelson, E. H. (2002). Motion illusions as optimal percepts. *Nat. Neurosci.* 5:598. doi: 10.1038/nn0602-858

Yu, C.-P., Page, W. K., Gaborski, R., and Duffy, C. J. (2010). Receptive field dynamics underlying MST neuronal optic flow selectivity. *J. Neurophysiol.* 103, 2794–2807. doi: 10.1152/jn.01085.2009

Yuille, A. L., and Grzywacz, N. M. (1988). A computational theory for the perception of coherent visual motion. *Nature* 333:71.

Conflict of Interest: PP was employed by Virtual Vehicle Research Center, Graz, Austria.

The remaining authors declare that the research was conducted in the absence of any commercial or financial relationships that could be construed as a potential conflict of interest.

APPENDIX

Figure A1 shows how the Cartesian optic flow patterns are transformed into the cortical domain. In particular, **Figure A1A** shows that constant optic flows in the Cartesian domain map to non-linear flows in cortical domain. Whereas, expansion (see **Figure 4**) and rotation (**Figure A1B**) flow patterns are mapped to constant flows along the horizontal and the vertical cortical axes, respectively. In general, a Cartesian optic flow is warped in the cortical domain, e.g., in **Figure A1C** the transformation of a Cartesian shear pattern is shown.

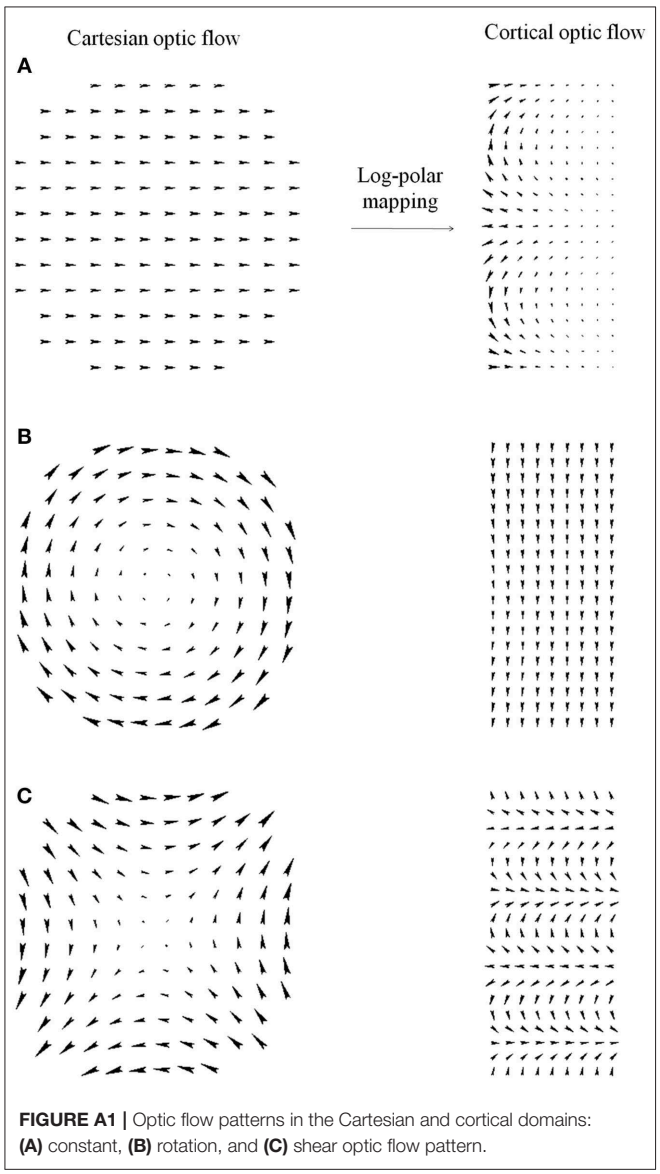

FIGURE A1 | Optic flow patterns in the Cartesian and cortical domains: **(A)** constant, **(B)** rotation, and **(C)** shear optic flow pattern.

frontiers in Neural Circuits

ORIGINAL RESEARCH
published: 10 December 2019
doi: 10.3389/fncir.2019.00075

A Comparison of Neural Decoding Methods and Population Coding Across Thalamo-Cortical Head Direction Cells

Zishen Xu[1]†, Wei Wu[1]*†, Shawn S. Winter[2], Max L. Mehlman[2], William N. Butler[2], Christine M. Simmons[3], Ryan E. Harvey[4], Laura E. Berkowitz[4], Yang Chen[1], Jeffrey S. Taube[2], Aaron A. Wilber[3]*† and Benjamin J. Clark[4]*†*

[1] Department of Statistics, Florida State University, Tallahassee, FL, United States, [2] Department of Psychological and Brain Sciences, Center for Cognitive Neuroscience, Dartmouth College, Hanover, NH, United States, [3] Department of Psychology, Program in Neuroscience, Florida State University, Tallahassee, FL, United States, [4] Department of Psychology, University of New Mexico, Albuquerque, NM, United States

OPEN ACCESS

Edited by:
Desdemona Fricker,
UMR 8119 Centre de Neurophysique, Physiologie, Pathologie, France

Reviewed by:
Adrien Peyrache,
McGill University, Canada
Federico Stella,
Radboud University, Netherlands

***Correspondence:**
Zishen Xu
zx16@my.fsu.edu
Wei Wu
wwu@stat.fsu.edu
Aaron A. Wilber
awilber@fsu.edu
Benjamin J. Clark
bnjclark@unm.edu

† These authors have contributed equally to this work

Received: 13 June 2019
Accepted: 12 November 2019
Published: 10 December 2019

Citation:
Xu Z, Wu W, Winter SS, Mehlman ML, Butler WN, Simmons CM, Harvey RE, Berkowitz LE, Chen Y, Taube JS, Wilber AA and Clark BJ (2019) A Comparison of Neural Decoding Methods and Population Coding Across Thalamo-Cortical Head Direction Cells. Front. Neural Circuits 13:75. doi: 10.3389/fncir.2019.00075

Head direction (HD) cells, which fire action potentials whenever an animal points its head in a particular direction, are thought to subserve the animal's sense of spatial orientation. HD cells are found prominently in several thalamo-cortical regions including anterior thalamic nuclei, postsubiculum, medial entorhinal cortex, parasubiculum, and the parietal cortex. While a number of methods in neural decoding have been developed to assess the dynamics of spatial signals within thalamo-cortical regions, studies conducting a quantitative comparison of machine learning and statistical model-based decoding methods on HD cell activity are currently lacking. Here, we compare statistical model-based and machine learning approaches by assessing decoding accuracy and evaluate variables that contribute to population coding across thalamo-cortical HD cells.

Keywords: spatial behavior, navigation, memory, anterior thalamus, parahippocampal, parietal

INTRODUCTION

Animals can navigate by monitoring an online record of their spatial orientation in an environment and using this information to produce direct trajectories to hidden goals (Cullen and Taube, 2017; Epstein et al., 2017; Moser et al., 2017). Head direction (HD) cells, which fire action potentials whenever an animal points its head in a particular direction, are thought to subserve the animal's sense of spatial orientation (Taube et al., 1990a,b; Taube, 1995, 2007). The direction of maximum response, or the preferred firing direction, varies between cells, such that a small population of HD cells can encode the full range of possible HDs. HD cells are found prominently in anterior thalamic nuclei (ATN), including the anterodorsal, anteroventral, and anteromedial thalamic nuclei (Taube, 1995; Tsanov et al., 2011; Jankowski et al., 2015; for review see Clark and Harvey, 2016); in parahippocampal regions such as the postsubiculum (PoS) (Taube et al., 1990a), medial entorhinal cortex (MEC), and parasubiculum (PaS)

(Sargolini et al., 2006; Boccara et al., 2010); and in dorsal cortical regions such as the parietal cortex (PC) (Chen et al., 1994a,b; Wilber et al., 2014; reviewed in Clark et al., 2018).

Several studies have reported that simultaneously recorded populations of HD cells tend to maintain coherence across their preferred firing directions (Taube et al., 1990b; Taube, 1995; Johnson et al., 2005; Peyrache et al., 2015; Bassett et al., 2018). For example, Taube et al. (1990b) recorded pairs of HD cells in the PoS simultaneously and found that cells responded similarly, with the same angular relationship with one another, across a broad range of environmental manipulations and testing procedures. Coherence between HD cells has also been reported across the ATN and PoS (Peyrache et al., 2015) and between HD cells in the ATN and place signals within the hippocampal formation (Knierim et al., 1998; Hargreaves et al., 2007). However, a recent study suggests that the coherence of HD cell populations recorded from the mouse MEC and PaS may become uncoupled during some environmental cue manipulations (Kornienko et al., 2018). Another previous study subjectively noted that decoding accuracy by ATN HD cell populations is superior to PoS HD cell ensembles (see Supplementary Figure S1 in Viejo et al., 2018). We are unaware of other studies that have quantified the accuracy of HD cell population coding across thalamo-cortical circuitry.

Although a number of methods have been developed to assess the dynamics of thalamo-cortical HD signals (e.g., Rybakken et al., 2018; Viejo et al., 2018; Fresno et al., 2019), few studies have conducted a quantitative comparison of neural decoding. Statistical model-based approaches have generally been favored with respect to studying population activity of the HD cell system, however recent advances have stimulated new interest in using machine learning approaches for neural decoding. Model-based methods directly characterize a probabilistic relationship between neural firing and HD, while machine-learning approaches assume a "black-box" neural network to describe the relationship. Although machine learning methods can in general deal with complex relationships in datasets, they depend on a multi-layered structure and come with a significant time cost.

A central aim of the present study was to provide a comparison of the various methods used to assess the neural dynamics of spatial behavior. Specifically, we compare linear methods such as Kalman Filter, Vector Reconstruction, Optimal Linear Estimator, and Wiener Filter and non-linear methods such as Generalized Linear Models and Wiener Cascade. We compare these statistical model-based methods with several machine learning methods. In addition, we present a quantitative assessment of population coding by HD cells within the ATN, PoS, PaS, MEC, and PC and explore contributing variables to decoding accuracy such as the number of classified HD cells per dataset as well as the firing rate and tuning strength of HD cell populations.

MATERIALS AND METHODS

Datasets

Neuronal recordings analyzed in the present report were presented in previous work (Wilber et al., 2014, 2017; Winter et al., 2015a,b; Butler and Taube, 2017). Briefly, for data collected in ATN, PoS, PaS and MEC, 4 female Long-Evans rats (3–6 months of age) were used (5 recording sessions or datasets/region; 1–2 rats/region). Rats were either surgically implanted with moveable microdrives containing four tetrodes targeting the PoS, PaS, or MEC (Winter et al., 2015a,b), or eight individually moveable stereotrodes targeting the ATN (Butler and Taube, 2017). Neural activity in PoS, PaS, or MEC was recorded while animals foraged for scattered food in a large square enclosure (120 × 120 cm; 50 cm in height; session duration: 10–20 min) and in the ATN while rats foraged in a small cylindrical environment (71 × 50 cm; session duration: 8 min).

For data collected in PC, 4 male Fisher-Brown Norway hybrid rats were used. Rats were 5–10 months of age at initial surgery and were implanted with an 18-tetrode electrode array targeting the PC (for details see Wilber et al., 2014). Recordings were conducted while rats performed a "random lights" task in which the animal visited one of 32 light/reward zone located along the perimeter of a large circular open field (4 ft in dia). Each zone was rewarded with medial forebrain stimulation. Animals made up to 900 light/reward zones visits in a single recording session (session duration: ∼45 min). Each visit to the light/reward zone consisted of the animal making a trajectory from one end of the open field to the other. Because the light/reward zones were presented in a random order, the animal's cumulative path for each session resulted in wide spatial and HD coverage in the environment. These experiments were carried out in accordance with protocols approved by the University of Lethbridge Animal Welfare Committee or Dartmouth College's Institutional Animal Care and Use Committee and conformed to the National Institutes of Health *Guide for the Care and Use of Laboratory Animals*.

For all datasets, electrical signals were pre-amplified on a headstage (HS18 or HS27) and were recorded using a Digital Lynx Data Acquisition System (Neuralynx, Bozeman, MT), and thresholded (adjusted prior to each session) spike waveforms (filtered 0.6–6 kHz, digitized at 32 kHz) and timestamps were collected for each session. Rat position and HD were tracked by either using red and green LEDs attached to the animal's headstage (secured ∼8 cm apart) or by using colored domes of reflective tape which were created by covering 1/2 Styrofoam balls in reflective tape. A video tracking system provided x-y coordinates of each LED or Styrofoam ball position at a sampling rate of 30–60 Hz as interleaved video. However, for one animal included in the PC datasets, data was collected at 30 Hz (rat 4) and co-registered with spikes and stimuli.

For PoS, PaS, MEC, and ATN datasets, spike sorting was conducted using SpikeSort3D (Neuralynx, Bozeman, MT). First, waveform characteristics from each tetrode/stereotrode were plotted as scatterplots from one of the four tetrode wires and signal waveform characteristics (amplitude, peak and valley) were used for cell isolation. Individual units formed clusters of points in these plots and the boundaries were identified and manually "cut." For PC datasets, spike data were automatically overclustered using KlustaKwik[1] then manually adjusted using a modified version of MClust (A.D. Redish).

[1] http://klustakwik.sourceforge.net

HD Cell Categorization

ATN, PoS, PaS, and MEC Recordings

The HD of the animal was determined by the relative position of the red and green LEDs. The amount of time and number of spikes in each HD was sorted into sixty 6° bins. The firing rate for each 6° bin was determined by dividing the number of spikes by the amount of time. A firing rate by HD plot was constructed for each cell in the dataset and the directionality of each cell was quantified using a number of measures. First, we computed the mean vector length (Rayleigh r) for each cell. The mean vector length ranges between 0 and 1, with higher values indicating that spike occurrence is clustered around a particular direction. Second, we computed a stability score for each cell. Stability was calculated by dividing the recording session into four equal time bins and cross-correlating the 60 directional firing bins across each time bin and averaging these values (Directional Stability = (Q1:Q2 + Q1:Q3 + Q1:Q4 + Q2:Q3 + Q2:Q4 + Q3:Q4)/6). Because the mean vector length is susceptible to reporting high values when cells display low firing rates, we used a dual criterion for classifying neural activity as an HD cell. Cells were classified as an HD cell if the resulting mean vector length and directional stability scores exceeded the 95th percentile chance level generated by shuffling the neural data (see Boccara et al., 2010; Winter et al., 2015a). Briefly, each cell had its sequence of spikes time-shifted relative to the animal's tracked location and HD (400 iterations for each cell) and the mean vector length and stability was calculated for each iteration. The 95th percentile value for each region was taken as the cut-off criteria for cell inclusion. In addition, cells with criteria values below the mean cutoff across brains regions, without clear directionality and repeat recordings were removed from further analysis. A sample of 5 recording sessions or datasets per brain region was selected. Each dataset contained at least 5 simultaneously recorded HD cells that met the criteria outlined above (n = 20 datasets from 4 rats).

PC

Cells not sufficiently active during maze sessions (< 250 spikes/session; session = ∼50 min) were excluded from all analyses (39 cells excluded so 339 putative pyramidal cells remained). Data from video frames in which HD tracking was lost or segments in which the rat was still for relatively long (60 s) periods (calculated from smoothed positioning data) were excluded. Occupancy data were binned per 6° of HD and converted to firing rate (spikes/s). Rayleigh statistics were calculated using a combination of custom Matlab scripts and the circular statistics toolbox (Berens, 2009). Because directionally modulated PC cells typically expressed low firing rates across behavioral testing, we adjusted the HD cell classification criteria to assess stability across a longer recording duration. Thus, neurons were classified as HD cells if (1) they had a significant Rayleigh test for unimodal deviation from a uniform distribution corrected for binned data on the collapsed-across-behavioral-sessions firing rate data ($p \leq 0.05$) and (2) they were stable (change in peak vector direction of < 7 bins) across behavioral sessions (or split 1/2 sessions when data were not available for two consecutively recorded sessions). All datasets for which at least 3 HD cells met these criteria were included in the present paper (n = 7 sessions from 3 rats; 2 session from rat #1; 2 sessions from rat #3; 3 sessions from rat #4).

Neural Decoding Methods

Twelve decoding methods were applied. Six are statistical model-based methods: Kalman Filter, Generalized Linear Model, Vector Reconstruction, Optimal Linear Estimator, Wiener Filter and Wiener Cascade. The remaining six are machine learning methods: Support Vector Regression, XGBoost, Feedforward Neural Network, Recurrent Neural Network, Gated Recurrent Unit, and Long Short-Term Memory. The python code for Wiener Filter, Wiener Cascade and the machine learning methods is from the freely available Neural Decoding package from Glaser et al. (2017)[2]. Head direction data were transformed using directional cosines, then fed into the decoding algorithm, then transformed back to polar coordinates (Gumiaux et al., 2003; Wilber et al., 2014, 2017). For better explanatory power, a four-fold cross-validation is applied in this paper. Since the data have a time series structure and so do the models, it was not appropriate to use a middle portion as testing where the training data is not continuous. Thus, we only included two cases: upper 3/4 of the dataset to be training (UT) and lower 3/4 of the dataset to be training (LT).

Statistical Model-Based Methods

Kalman Filter

The Kalman Filter model (Kalman, 1960) is a hidden Markov chain model that uses HD (trigonometric) as the states and spike counts as the observations.

The relationship between these variables is shown in **Figure 1**.

The model assumes that the HD follows a first-order auto-regression structure with additive Gaussian noise. The model is given as:

$$\begin{cases} \vec{X}_{t+1} = A\vec{X}_t + \vec{w}_t \\ \vec{Y}_t = H\vec{X}_t + \vec{q}_t \end{cases}$$

where $\vec{X}_t$ is the centralized trigonometric HD vector (centralized [cos, sin] vector) at time t; $\vec{Y}_t$ is the centralized spike counts vector for all observed brain cells at time t; $\vec{w}_t, \vec{q}_t$ are the random noises where $\vec{w}_t \sim N(0, W)$, $\vec{q}_t \sim N(0, Q)$, and $\vec{w}_t, \vec{q}_t$ are

[2]https://github.com/KordingLab/Neural_Decoding

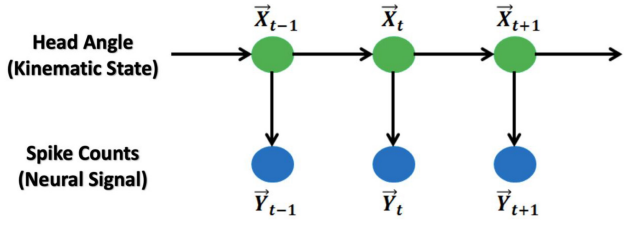

FIGURE 1 | Graphic representation of the Kalman Filter and Generalized Linear Model: The main model is a hidden Markov chain structure. HDs follow a Markov chain and spike counts at the current time bin are independent from the counts from previous time bins.

independent. The Kalman Filter method assumes a mean of zero for the noise model, so, the mean spike count must be subtracted from the neural data, i.e., we "centralized the spike counts." Note that since $\vec{X}_t$ and $\vec{Y}_t$ are centralized, no intercept term is included in the model.

For parameter fitting, the classical approach, maximum likelihood method (MLE) is used to obtain the values of A, W, H, Q (see **Supplementary Material S1**). For decoding, the Kalman Filter algorithm (Wu et al., 2006) is applied to predict $\vec{X}_t$ given $\vec{Y}_t$ after the estimation of model parameter (see the algorithm in **Supplementary Material S2**).

Generalized linear model

Similar to the Kalman Filter model, the generalized linear model is also a hidden Markov Chain model with HD (trigonometric) as the states and spike counts as the observations (**Figure 1**). The model assumptions are: (1) the HD itself is a first-order autoregression model with additive Gaussian noise; (2) the HD and spike counts at the same time point follow a Poisson log-linear model; and (3) the spike counts from each observed brain cell are conditional independent given the HD at the same time point. The model is:

$$\begin{cases} \vec{X}_{t+1} = A\vec{X}_t + \vec{w}_t \\ Y_{t,c}|\vec{X}_t \sim Poisson(\lambda_{t,c}) \end{cases}$$

Where $\vec{X}_t$ is the centralized trigonometric HD vector at time t; $Y_{t,c}$ is the spike counts for brain cell c at time t and $\{Y_{t,c}\}_{c=1}^{C}$ is independent given $\vec{X}_t$; $\vec{w}_t$ is random noise with $\vec{w}_t \sim N(0, W)$, $\lambda_{t,c} = e^{\mu_c + \vec{a}_c^T \vec{X}_t}$. Similarly, there is no intercept term in the autoregression model because $\vec{X}_t$ has been centralized.

To fit the model parameters A, W, μ_c, $\vec{a}_c$, we again use the maximum likelihood method (Lawhern et al., 2010; see **Supplementary Material S3**). For decoding, the Point Process Filter method (Eden et al., 2004) is applied to predict the HD given the spike counts (see the algorithm in **Supplementary Material S4**). Based on the model, the mean of $Y_{t,c}$ given $\vec{X}_t$ can be numerically approximated by $\hat{\lambda}_{t,c} = e^{\hat{\mu}_c + \hat{\vec{a}}_c^T \vec{X}_t}$ after parameter estimation, so the mean curve of spike counts among different HDs can be obtained.

Vector reconstruction

Since the training dataset contains the HD and spike counts at each observed time bin, we can make an estimation of the preferred direction for each cell (Georgopoulos et al., 1983). The estimation is done by fitting a cosine curve to the plot of firing rate and HD from the training data. The angle at the peak of the curve, which is the phase of the cosine function, is treated as the angle of the fitted preferred direction for the cell. In other words, $\hat{\vec{L}}_c = \left[cos\hat{\theta},\ sin\hat{\theta}\right]^T$ will be the fitted unit direction vector for cell c. The prediction of the HD given firing rates can then be obtained by computing the average of the direction vectors, weighted by the corresponding cell's firing rate, as in Johnson et al. (2005).

$$\phi_{est}(t) = angle\left[\sum_{c=1}^{C} f_c(t) * \hat{\vec{L}}_c\right]$$

Where $f_c(t)$ is the given firing rate of cell c at time t; $\hat{\vec{L}}_c$ is the fitted preferred direction vector for cell c; $\phi_{est}(t)$ is the predicted HD at time t; *angle* (•) returns the angle of the input vector (see the computation in **Supplementary Material S5**).

To achieve an accurate reconstruction with this method, there are several critical criteria for the training dataset. First, the data should have a sufficiently strong unimodal peak for a specific HD and firing rate, or else the estimation of preferred directions will be poor. Second, the preferred direction vectors must cover the full range of directions from 0° to 360°. Without input data covering some HDs, some predicted HDs may never be achieved (see **Figure 2**).

Optimal linear estimator

The Optimal Linear Estimator (OLE) method (Salinas and Abbott, 1994) is similar to the vector reconstruction method that estimates a direction vector for each cell and uses the weighted average over those vectors with firing rates as the weights to make a prediction of the HD. Since Vector Reconstruction and Optimal Linear Estimator both depend on the preferred direction vector (unlike other decoding methods), these methods are especially susceptible to inhomogeneity of preferred directions as illustrated in **Figure 2**. The vector, $\hat{\vec{D}}_c$ for cell c, unlike the preferred direction vector, is obtained by finding the optimal solution that minimizes the squared error between the estimated and true HD vector, averaged over firing rates and true direction vectors, i.e.

$$\hat{D} = \underset{D}{argmin} \int \left(\vec{V} - \vec{V}_{est}\right)^2 * P\left(\vec{r} \mid \vec{V}\right) d\vec{r} d\vec{V}$$

Where $\vec{V}$ is the true HD vector; $\vec{V}_{est} = \sum_{c=1}^{C} r_c * \vec{D}_c$ is the estimated HD vector; $\vec{r} = [r_1,\ r_2,\ \ldots\ r_C]^T$ is the firing rate for each brain cell; $D = \left[\vec{D}_1,\ \vec{D}_2,\ \ldots\ \vec{D}_C\right]$ is the matrix of all the vectors to find.

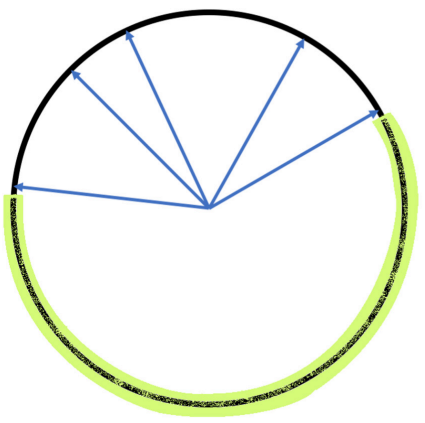

FIGURE 2 | Illustration of the coverage of the full range of HDs: If all the preferred direction vectors cover only half of the possible HDs, then the vectors in the other half circle cannot be achieved by a non-negative weighted linear combination of these vectors, so the predicted angles will not cover all values between 0° and 360°.

The solution for $\hat{D}$ can be computed by taking the derivative of the formula above, which results in:

$$\hat{\tilde{D}}_c = \sum_{i=1}^{C} \left(\hat{Q}^{-1}\right)_{ci} * \hat{\tilde{L}}_c$$

Where $\hat{\tilde{L}}_c$ is the numerical approximation of the center of mass vector for the tuning curve function of cell c; $\hat{Q}$ is the numerical approximation of the correlation matrix of firing rates for all cells (see details in **Supplementary Material S6**).

With fitted $\hat{D}$, the prediction of the HD at time t, as stated above, is

$$\phi_{est}(t) = angle\left[\sum_{c=1}^{C} r_c(t) * \hat{\tilde{D}}_c\right]$$

The OLE method also has the prerequisite on the training dataset like the vector reconstruction method that the non-negative linear combination of $\hat{\tilde{D}}_c$ should cover all directions from 0° to 360°, or else the prediction can never achieve some angles (see **Figure 2**).

Wiener Filter

The Wiener Filter model (Wiener, 1949) is a classical regression method that builds a multiple linear regression relation between the HD and the firing rate from every observed cell at the corresponding time bins. This model is the basis of all the statistical filtering methods. Computational details are given in **Supplementary Material S7**.

Wiener cascade

The Wiener Cascade model (Hunter and Korenberg, 1986) is a direct extension of the Wiener Filter model that first applies a multiple linear regression model on the HD vs. the firing rate from each cell, and then builds a non-linear model on the fitted values from the linear model vs. the true firing rate values. In the present paper, the order of the polynomial in the non-linear component was searched by Bayesian Optimization (see section Machine Learning Methods below). Computational details are also given in **Supplementary Material S7**.

Machine Learning Methods

To conduct HD decoding, we also used the following 6 machine learning methods. The selection on input-output is consistent for each method. In these methods, together with Wiener Cascade, there exists some free parameters that are not tuned during training. Instead they are set before the optimization process. These values are called "hyper-parameters." In this paper, hyper-parameter selection was based on Bayesian Optimization (Snoek et al., 2012, freely available python package[3]). It searched over a range of values for the hyper-parameters and chose the optimal one. Further detail is provided in **Supplementary Material S8**.

Support vector regression

The support vector regression (Drucker et al., 1996) is a machine learning tool that uses a non-linear kernel to project the input to another space and then builds a linear model on the projected input and the output. In this manuscript, a radial basis function kernel was applied. The penalty parameter of the error term and the maximum number of iterations were searched by Bayesian Optimization.

XGBoost

XGBoost (Chen and Guestrin, 2016) is a machine learning algorithm that implements the idea of gradient boosted trees. It builds a sequence of regression trees. The first tree is for predicting the HDs using the firing rates, while each subsequent

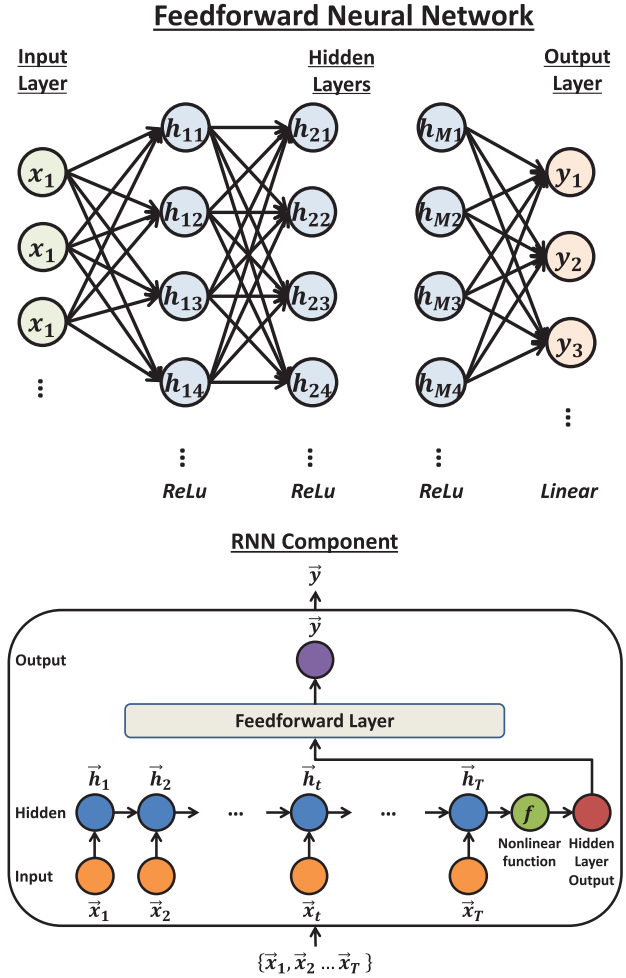

FIGURE 3 | The structure of feedforward neural network and Recurrent Neural Network (RNN): **Top:** The typical structure of a feedforward neural network. Each unit will calculate a weighted sum of the units in the previous layer that connect to it by an arrow. Then by adding an intercept term and transforming the value by an activation function, the unit obtains the value it sends out. **Bottom:** the structure of a Recurrent Neural Network component. The input vectors are connected by a chain hidden layer. Each hidden unit is the transformed value of the linear combination of the corresponding input unit and previous hidden unit. The last hidden unit value (vector) will be transformed by another non-linear function and sent to the dense layer to compute the output.

[3]https://github.com/fmfn/BayesianOptimization

tree is built on the firing rate vs. the residual of the previous fit. In this manuscript, the total number of trees, maximum depth of each tree and the learning rate were all searched by Bayesian Optimization.

Feedforward neural network

The feedforward neural network (Haykin, 1994), also called dense neural network or multi-layer perceptron, is the basic structure in deep learning. In this method, each two consecutive layers are fully connected, which means that every unit in the subsequent layer will be computed by a linear function on the values from all the units in the previous layer, followed by an activation function (**Figure 3** *Top*). In the present paper, 3 hidden layers were used. The activation functions were rectified linear unit, abbreviated as ReLU (Glorot et al., 2011), for all the hidden layers and linear for the output layer. To avoid overfitting, we applied the dropout method (Srivastava et al., 2014). The optimization algorithm was *Adam* (Kingma and Ba, 2014). The number of units in the layers, the dropout rate and the number of epochs were all searched by Bayesian Optimization.

Recurrent Neural Network

The Recurrent Neural Network is the basic neural network structure designed for time series data (Haykin, 1994). A Recurrent Neural Network component includes one hidden layer, where each unit is a linear combination of the values from the corresponding input unit and the previous hidden unit. The last hidden unit value is then transformed by a non-linear function and finally fully connected to the output layer (**Figure 3** *Bottom*). In this paper, a series of Recurrent Neural Network components were applied so that each component predicts the HD in one time bin, given the firing rates. The non-linear function was set to ReLU. Similar to feedforward neural network, the dropout method was applied. The optimization algorithm was chosen to be RMSprop (Tieleman and Hinton, 2012). The dimension of the hidden unit, the dropout proportion and the number of epochs were searched by Bayesian Optimization.

Gated recurrent unit

The gated recurrent unit (Cho et al., 2014) is a complex recurrent neural network unit. Its structure (shown in **Figure 4** *Left*) is similar to the Recurrent Neural Networks but includes gated units which can better memorize the long-term history.

In this paper, the use of Gated Recurrent Unit (GRU) was the same as the hidden units in the Recurrent Neural Network (RNN) component. The GRU component was a chain structure of several gated units and it was applied to predict HD in one time bin. The model also applied the dropout method to avoid overfitting and used RMSprop to be the optimization algorithm. Same as the RNN methods, the dimension of gated units, the dropout proportion and the number of epochs were searched by Bayesian Optimization. An implementation difference was that the activation function between the output from the recurrent part and input to the feedforward layer was hyperbolic tangent (tanh) instead of ReLU since the former is the standard choice for Gated Recurrent Unit.

Long short-term memory

The Gated Recurrent Unit and Long Short-Term Memory (Hochreiter and Schmidhuber, 1997) were developed from Recurrent Neural Network and can better handle the long-term dependencies (the structure is shown in **Figure 4** *Right*).

Compared to the Gated Recurrent Unit, the Long Short-Term Memory unit has a more complex structure which includes more parameters. In the present paper, the use of Long Short-Term Memory was just a replacement of the Gated Recurrent Unit with the same settings: optimization algorithm = RMSprop; activation non-linear function = tanh; dimension of LSTM components, dropout proportion and number of epochs were searched by Bayesian Optimization.

Statistical Analyses

Data were analyzed using two-way repeated measures ANOVAs (e.g., Decoding Method or Brain Region). In order to avoid large numbers of pairwise post-tests, we determined which factors were contributing to significant ANOVA results by removing factors one at a time. We started with the factor that was furthest from the mean, removed it, and reran the ANOVA. We repeated this process until the ANOVA was no longer significant. We also explored factors that may contribute to variability in decoding accuracy including the number of classified HD cells per dataset, cell firing rate, HD tuning strength, and angular head velocity (described in section Factors Influencing Variability Across Decoding Method, Brain Region, and Datasets). Linear regression was used to compare decoding accuracy to each of these factors. For all statistical analyses, $p < 0.05$ was considered significant and Matlab statistics toolbox was used for statistical analyses (Mathworks). Rayleigh statistics were calculated using a combination of custom Labview and Matlab scripts using the circular statistics toolbox (Berens, 2009).

RESULTS

As described in section Neural Decoding Methods, cross-validation has been applied. There are two cross validation approaches: UT and LT. After running the code for all datasets, the results of the two cases is consistent. For brevity, only the results for UT are displayed. The output for LT can be seen in **Supplementary Material S13.1–S13.12**.

Neural Decoding

Modeling Tuning Properties

Some decoding approaches use a likelihood model (i.e., firing rate given HD) in a Bayesian framework to represent individual single units. Two of the twelve methods we used, the Kalman filter and Generalized Linear Model, use likelihood representations. An examination of the likelihood representations is useful for understanding successful (and unsuccessful) decoding of HD. Thus, to compare the approaches, we first produced tuning curve plots (i.e., polar plots) showing the relationship between the cells firing rate and the animal's HD (**Figure 5**; black curves). The modeling result is overlaid on the firing rate polar plots (blue curves: Generalized Linear Model estimation,

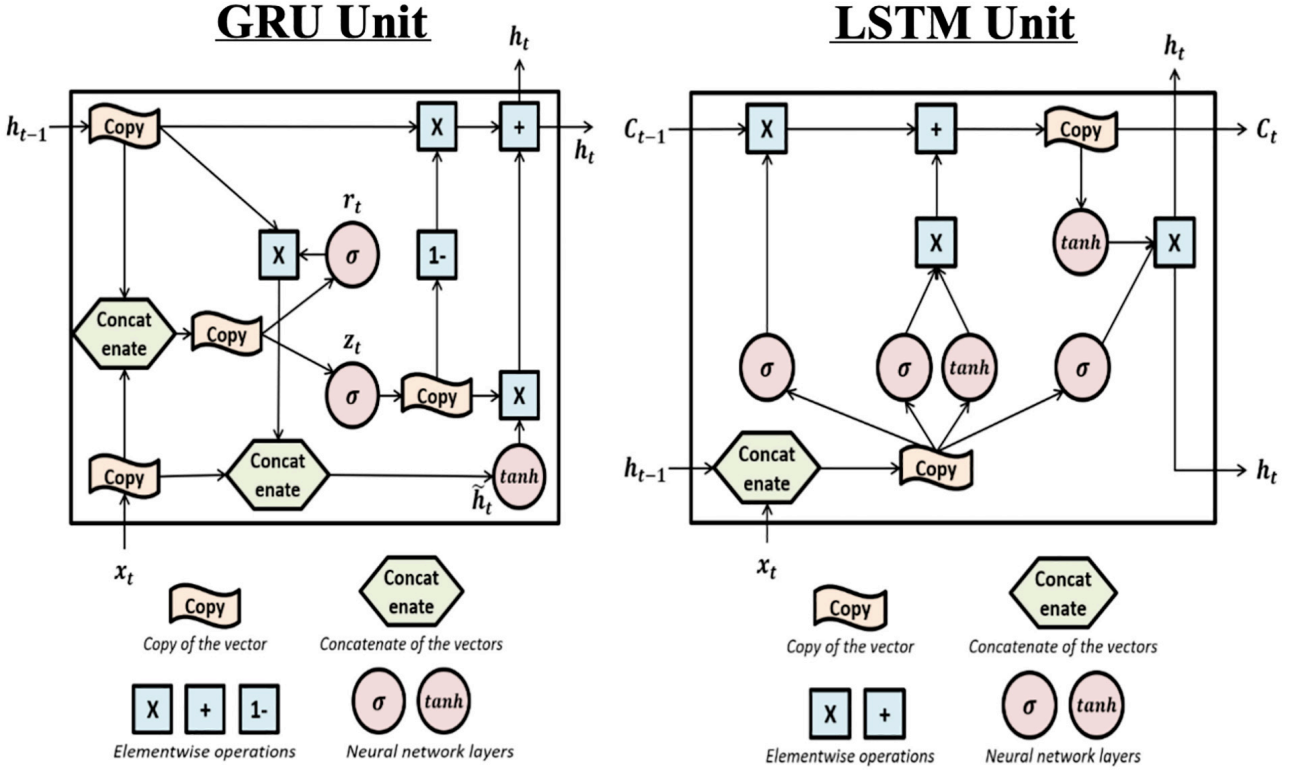

FIGURE 4 | The structure of Gated Recurrent Unit and Long Short-Term Memory units: **Left:** this is the structure of the Gated Recurrent Unit (GRU). The "update gate" z_t is used to determine if the update $\tilde{h}_t$ will be applied to h_t. r_t is the "reset gate" and is used to determine if the previous hidden value (also the output value) h_{t-1} will be kept in the memory. The effects of the two gates are achieved by sigmoid activation functions which can be learned during training. **Right:** The structure of the Long Short-Term Memory (LSTM) unit. LSTM is complex and includes one more hidden value C_t and more gates compared to GRU. Each gate can be seen in the plot where the **σ** sign appears (i.e., sigmoid activation function). The first **σ** is the "forget gate" which controls whether previous hidden value, C_{t-v} will be used to calculate current output and kept in the memory. The second **σ** is the "input gate" which controls whether the new input will be used to calculate current output. The third **σ** is the "output gate" which filters the output, i.e., controls what part of the output values to send out as h_t.

red curves: Kalman Filter estimation). One can roughly assess the model fitness for these two methods by visually comparing the similarity between the estimated tuning curve and the true tuning curve. By comparing the black (true), blue (Generalized Linear Model) and red (Kalman Filter) curves, it is apparent that Generalized Linear Model estimations are more similar to the true curves compared to the Kalman Filter estimations. The poorer performance of the Kalman Filter is likely a consequence of the model assumption. Specifically, the Generalized Linear Model proposes a Poisson distribution on the discrete spike count, which is more appropriate than the Gaussian distribution assumed by the Kalman Filter model.

Decoding Output

After training the model, we decoded the HD for the validating data and contrasted the decoding result with the true values. As a first-step, we visually compared the true and reconstructed HD as a function of time (**Figure 6**). This revealed that while some approaches are more accurate than others, all approaches were capable of producing at least moderately accurate decoding.

Next, we quantified decoding accuracy by calculating the median absolute error (*MAE*) and comparing this measure across datasets and brain regions. The median absolute error is computed by taking the circular difference between the predicted and true angle, rescaling the angle difference to be within [−180°, 180°], taking the absolute value of this angle, and then calculating the median value. For instance, if the true angle is 10° and the predicted angle is 350°, then the absolute difference after rescaling is 20°. The median absolute error, *MAE*, is:

$$MAE = \underset{t=1,\,2\,\ldots\,T}{median} \left| rescale\left[\phi\left(t\right) - \phi_{est}\left(t\right)\right]\right|$$

where $\phi(t)$ is the true valid HD at time t, $\phi_{est}(t)$ is the predicted HD at time t, *rescale* (θ) is the function that changes the angle θ to be within [−180°, 180°].

For comparison, we also computed the average absolute error (*AAE*). Compared to the median, the average is much more sensitive to outliers and extreme values, so the *AAE* values turn out to be larger and not as stable as the *MAE*. As a result, we used the *MAE* as the measure of decoding performance for the main text in this paper. The result associated with *AAE* can be seen in **Supplementary Material S14.1–S14.16**.

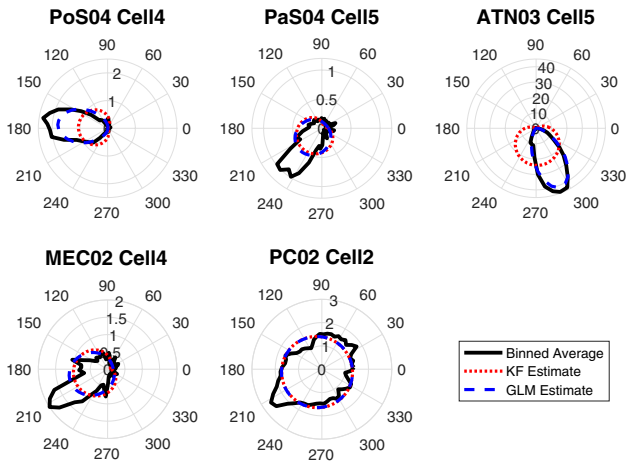

FIGURE 5 | The true-vs.-estimated tuning plots in 6-degree bins for one HD cell in each brain region: The polar plots show firing rates vs. HD. The black curves are the true tuning functions, smoothed by a Gaussian kernel function. The red curves are the estimated functions using the Kalman Filter (KF) method and the blue curves are the estimated functions using the Generalized Linear Model (GLM) method.

MAE is negatively related to prediction accuracy such that a smaller *MAE* indicates better prediction accuracy. Twenty-seven datasets from 5 brain regions were decoded using each of the 12 methods. The *MAE* was calculated for each dataset and method. All values and dataset details are shown in the **Supplementary Material S9.1**.

Figure 7 shows the *MAE* for each method, brain region, and dataset. Notably, the Vector Reconstruction method and Optimal Linear Estimator methods produced larger *MAE* compared to other methods. The LSTM method had the smallest average *MAE* value (34°). Regardless of the decoding method, *MAE* varied dramatically across datasets and brain regions. The average decoding accuracy was greatest in ATN, with datasets from this region expressing the lowest measures of *MAE*. For parahippocampal cortex and PC, *MAE* was greater relative to ATN, and progressively increased in a topographical manner from POS < PaS < MEC < PC. Finally, within each brain region, *MAE* values varied substantially for different datasets. For example, PC datasets PC_02 and PC_03 have much larger *MAE* values than the other PC datasets. This suggests that other factors in addition to regional differences may contribute to variability in decoding accuracy.

Decoding Accuracy as a Function of Computational Method and Brain Region

Decoding Accuracy Across Computational Methods

Next, we aimed to quantify the variance observed across decoding methods. The Optimal Linear Estimator method and Vector Reconstruction method appear to have large error relative to the other 10 methods (see **Figure 7**). Therefore, we compared *MAE* values collapsed across datasets and brain regions. As expected, we found that decoding accuracy varied significantly across computational methods [$F_{(11,\ 312)} = 7.27$, $p < 0.001$; **Figure 8**]. Next, to determine which methods were contributing to this variance, we removed data from one method at a time starting with the method furthest from the mean (Vector Reconstruction) and repeated the ANOVA until a non-significant result was obtained (see section Materials and methods). It was necessary to remove both Vector Reconstruction and Optimal Linear Estimator methods before decoding accuracy no longer varied significantly across method [$F_{(9,\ 260)} = 1.00$, $p = 0.44$], suggesting that decoding accuracy is similar for the remaining 10 methods. Potential causes of the poor performance for the Vector Reconstruction and Optimal Linear Estimator methods are explored in the section Factors Influencing Variability Across Decoding Method, Brain Region, and Datasets.

Decoding Accuracy Varied Across Brain Regions

In addition to variability across decoding methods, we observed variance in *MAE* across the 5 brain regions (see **Figure 7**). It is visually apparent that *MAE* is topographically organized such that the measure progressively decreases from PC > MEC > PaS > PoS > ATN, however, there is considerable overlap between the decoding accuracy across these brain regions (**Figure 9**). We therefore quantified the effect of brain region for each decoding method and collapsed across datasets. We found that for most methods (11/12), accuracy significantly varied across brain region [**Figure 9** and **Supplementary Material S10**; $F_{(4,\ 22)} > 2.82$, $p < 0.05$], with the exception of Vector Reconstruction [$F_{(4,\ 22)} = 1.27$, $p = 0.31$]. Further, for the 11 methods with significant variance across brain region, ATN accuracy was highest and furthest from the mean. For 9 of the methods, removing ATN resulted in a non-significant ANOVA [$F_{(3,\ 18)} < 3.16$, $p > 0.05$]. The only exceptions were Support Vector Regression and Long Short-Term Memory. For these methods, it was necessary to also remove the brain region that was the second furthest from the mean, PC [$F_{(2,12)} < 3.89$, $p > 0.05$].

We also investigated whether our findings above could be influenced by variability in the animal's movement characteristics. We first measured whether there were significant biases in the animal's trajectory by determining the dwell time in each HD. Plotting the data in this way demonstrates that good coverage of the full range of HDs occurred for all datasets from each brain region (**Supplementary Material S11**). We next measured the animals angular head velocity (absolute angular velocity calculated across 0.2 s time bins). The ANOVA determined that the absolute angular head velocity varied significantly across brain region [$F_{(4,\ 22)} > 6.814$, $p < 0.001$]. When PC was removed, the ANOVA was no longer significant [$F_{(3,\ 16)} < 2.462$, $p > 0.1$; consistent for both UT and LT datasets]. On average, fewer high velocity head movements were performed by rats in the PC datasets (mean: 41°/s). This observation is not entirely surprising given that animals in the PC datasets performed a task involving direct trajectories to a goal location (Wilber et al., 2014), which contrasts with the varied head movements made during random foraging in the other datasets (see section Datasets). Finally, a linear regression found that the relationship between the absolute angular head

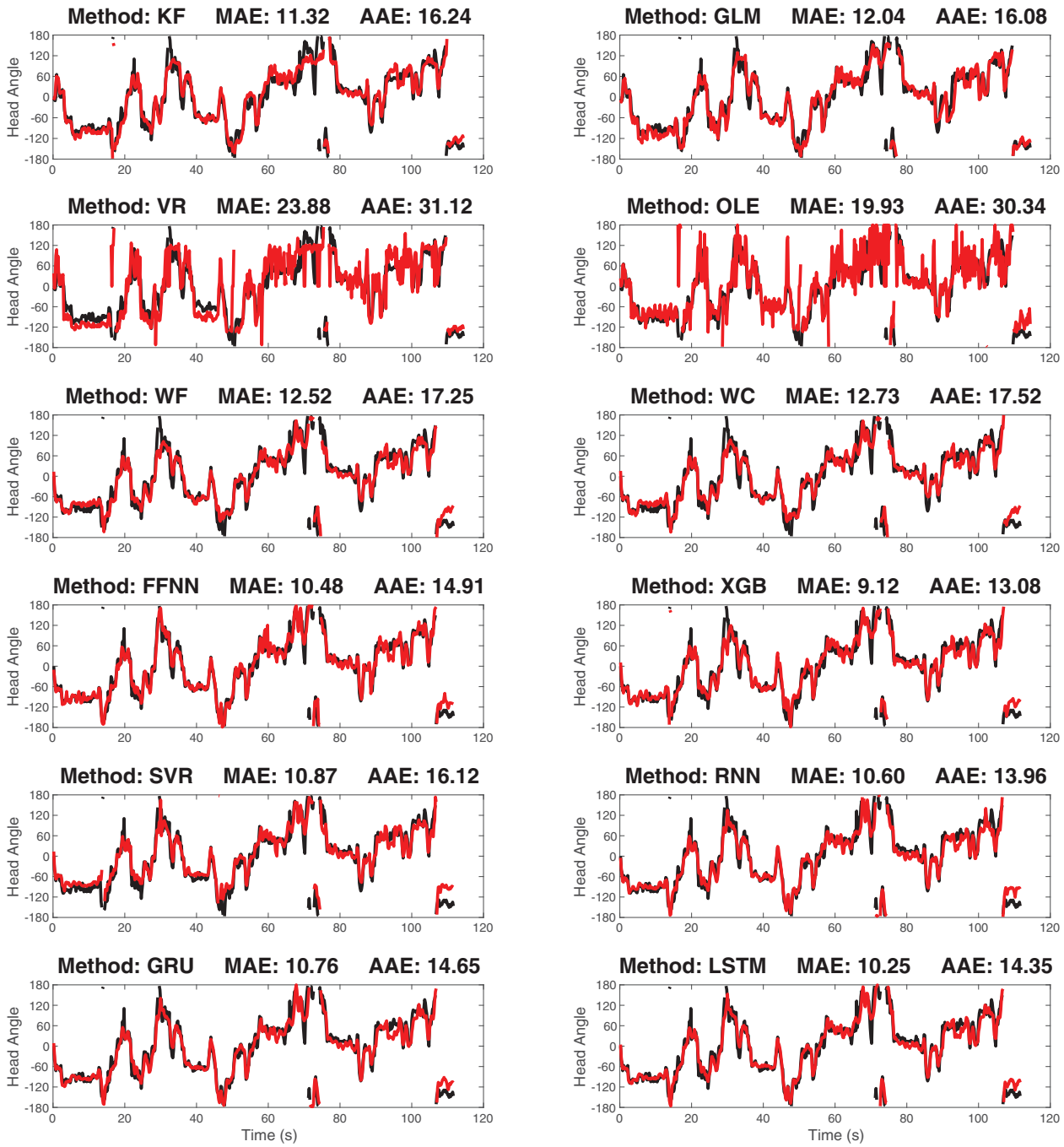

FIGURE 6 | The true-vs.-predicted head angle plotted as a function of time for a representative ATN dataset for each of the 12 decoding methods: The black curves are the true curves and the red curves are the predicted curves. Test data is shown. Predicted curves are constructed using a model generated from a separate training segment of the data. The method name and decoding accuracy measured as median absolute error (MAE) are shown on the title of each plot (average absolute error, AAE, is also shown). KF, Kalman Filter; GLM, Generalized Linear Model; VR, Vector Reconstruction; OLE, Optimal Linear Estimator; WF, Wiener Filte, and WC, Wiener Cascade. The remaining six are machine learning methods: SVR, Support Vector Regression; XGB, XGBoost; FFNN, Feedforward Neural Network; RNN, Recurrent Neural Network; GRU, Gated Recurrent Unit; LSTM, Long Short-Term Memory.

velocity and *MAE* was not significant for Kallman Filter, General Linear Model, and Optimal Linear Estimator methods (absolute value of the $rs \leq 0.27$, $ps \geq 0.08$), but was for all other methods (absolute value of the $rs \geq 0.34$, $ps < 0.05$).

It should be noted that there are at least three additional variables that could influence our findings above. First, the density of HD cells varies considerably across brain regions (reviewed in Taube and Bassett, 2003; Taube, 2007). So, it is

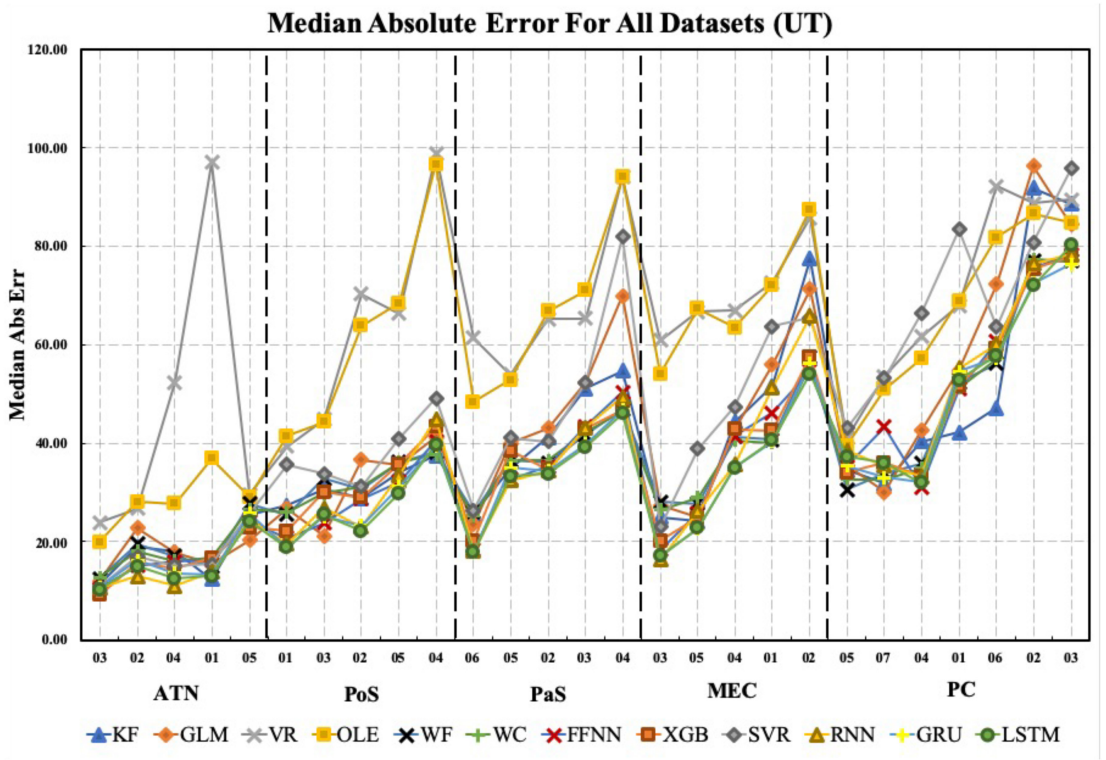

FIGURE 7 | The median absolute error is shown for each brain region, each dataset, and each decoding method. Datasets for each brain region are sorted from lowest to highest median absolute error (i.e., from best to worst decoding accuracy). Note that median absolute error varies considerably within regions and on average increases from ATN to parahippocampal and PC regions. KF, Kalman Filter; GLM, Generalized Linear Model; VR, Vector Reconstruction; OLE, Optimal Linear Estimator; WF, Wiener Filter; WC, Wiener Cascade; SVR, Support Vector Regression; XGB, XGBoost; FFNN, Feedforward Neural Network; RNN, Recurrent Neural Network; GRU, Gated Recurrent Unit; LSTM, Long Short-Term Memory.

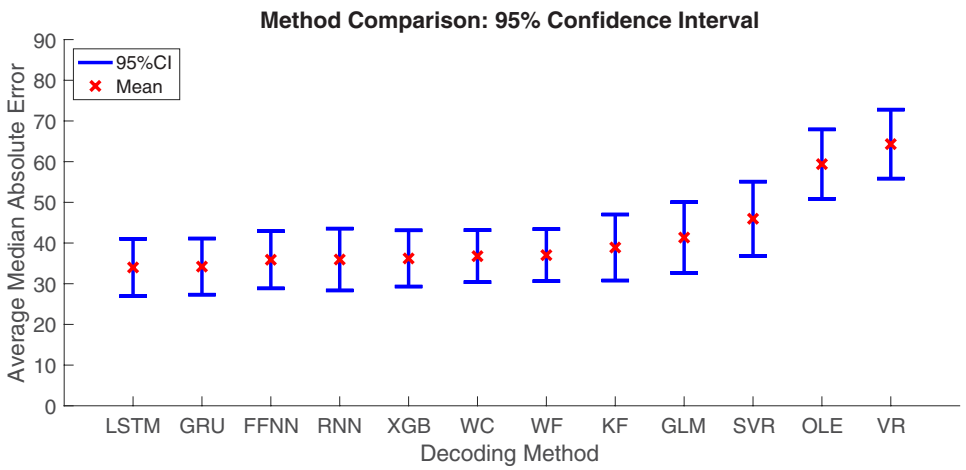

FIGURE 8 | Mean ± 95% Confidence-Interval (CI) Median Absolute Error (MAE) for each decoding method. Data from different brain regions and datasets were pooled. KF, Kalman Filter; GLM, Generalized Linear Model; VR, Vector Reconstruction; OLE, Optimal Linear Estimator; WF, Wiener Filter; WC, Wiener Cascade; SVR, Support Vector Regression; XGB, XGBoost; FFNN, Feedforward Neural Network; RNN, Recurrent Neural Network; GRU, Gated Recurrent Unit; LSTM, Long Short-Term Memory.

possible that some of the variability in decoding accuracy across brain regions may be an indirect result of HD cell density. We directly assess the potential influence of the number of cells on decoding accuracy below (Factors Influencing Variability Across Decoding Method, Brain Region, and Datasets). Second, a number of studies have observed that HD cells can vary in

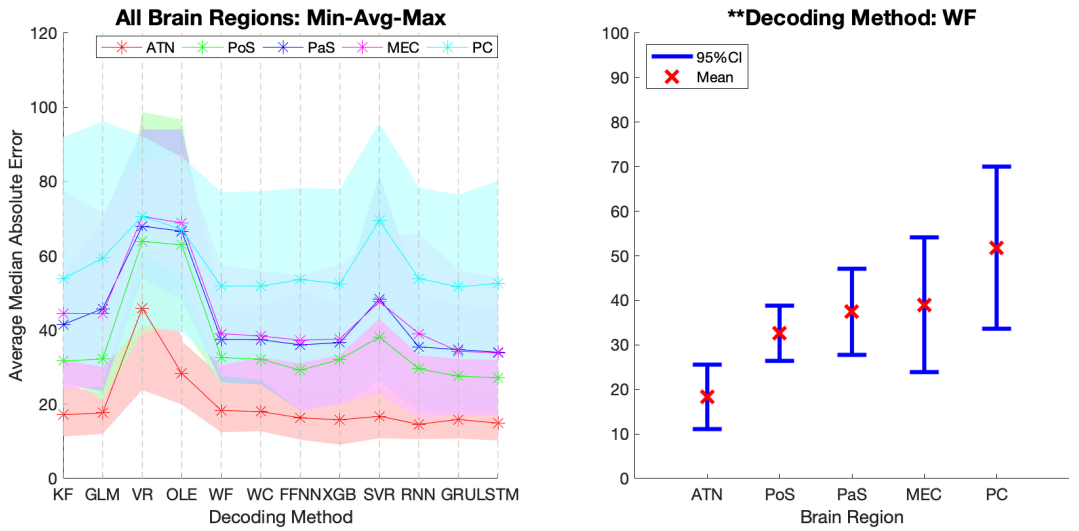

FIGURE 9 | Decoding accuracy varies across brain regions. The average Median Absolute Error (MAE) for each area and each decoding method. The shading in the **left panel** represents the range of the MAE values while the error bars in the **right panel** represents the 95% Confidence-intervals of the average MAE values for a representative decoding method. 95% Confidence-interval plots for the remaining 11 methods are shown in **Supplementary Material S10**. KF, Kalman Filter; GLM, Generalized Linear Model; VR, Vector Reconstruction; OLE, Optimal Linear Estimator; WF, Wiener Filter; WC, Wiener Cascade; SVR, Support Vector Regression; XGB, XGBoost; FFNN, Feedforward Neural Network; RNN, Recurrent Neural Network; GRU, Gated Recurrent Unit; LSTM, Long Short-Term Memory; ATN, Anterior Thalamic Nuclei; PoS, Postsubiculum; PaS, Parasubiculum; MEC, Medial Entorhinal Cortex; PC, Parietal Cortex. $^{**}p < 0.01$.

their peak firing rate and other firing characteristics that can influence the cells signal-to-noise ratio. Again, we evaluate these variables in the section below (Factors Influencing Variability Across Decoding Method, Brain Region, and Datasets). Last, it is important to note that different recording procedures, numbers of HD cells, behavior testing, and a distinct set of criteria were used for classification of HD cells for PC datasets. So, the slightly weaker decoding accuracy in PC could be attributed to one or all of these variables. Finally, the inclusion criteria for HD cells do not exclude cell firing which may correlate with HD but additionally fire relative to other spatial features such as egocentric bearing (Wilber et al., 2014; Peyrache et al., 2017).

Factors Influencing Variability Across Decoding Method, Brain Region, and Datasets

Next, we set out to explore factors that could underlie the variability we observed across brain regions and datasets (**Figure 7**). We identified three factors that could influence the decoding accuracy: the number of observed cells, the HD tuning strength, and the response rate of the cells.

Number of observed cells

As noted above, the percentage of cells classified as HD cells varies among the different brain regions (Taube and Bassett, 2003; Taube, 2007). For instance, previous studies report that HD cells are most abundant in the ATN (∼60%; Taube, 1995) and slightly more sparse within PoS (∼25%; Taube et al., 1990a; Sharp, 1996) and in other cortical regions such as PC (∼12%; Wilber et al., 2014). Boccara et al. (2010) found large proportions of directionally modulated cell types in PoS, PaS, and MEC (53.7, 58.5, and 55.1%, respectively). In the present study, the density of HD cells varied from 3 to 9, which is within the range of cell densities reported in other studies using neural decoding methods (e.g., minimum of 3 cells/session in Johnson et al., 2005; a minimum of 9 cells/session in Bassett et al., 2018; a minimum of 6 cells/session in Peyrache et al., 2015). We used linear regression to assess the relationship between the number of identified HD cells and the accuracy of decoding (**Figure 10**). For 11 of the 12 computational methods, there was a significant negative correlation with *MAE* (absolute value of the $r > 0.32$, $p < 0.05$). The correlation between the number of HD cells and *MAE* for Vector Reconstruction failed to reach significance ($r = -0.28$, $p = 0.08$). It is possible the lack of significance for Vector Reconstruction is a consequence of generally poor decoding by this method. However, for all of the other decoding methods, the results suggest that as the number of classified HD cells increases, decoding accuracy improves (i.e., there is less error). The correlations (r-values) between *MAE* and head angular velocity were smaller than the correlations between *MAE* and the number of cells [$t_{(22)} = 4.77$, $p < 0.001$].

Given that the number of cells influences decoding accuracy, we next investigated whether the regional differences reported in the previous section can be explained by the number of cells per datasets. To address this question, we repeated our decoding analyses on datasets composed of a random subsample of at least 3 cells. For datasets with 6 or more cells, we split the datasets in half, each composed of 3 randomly selected cells (without repeats). Due to the higher computational demands of machine learning approaches, and the similarity in results between model-based and machine learning methods (see **Figure 7**), we only used model-based methods to investigate this question. In short, the results of this analysis again indicate superior

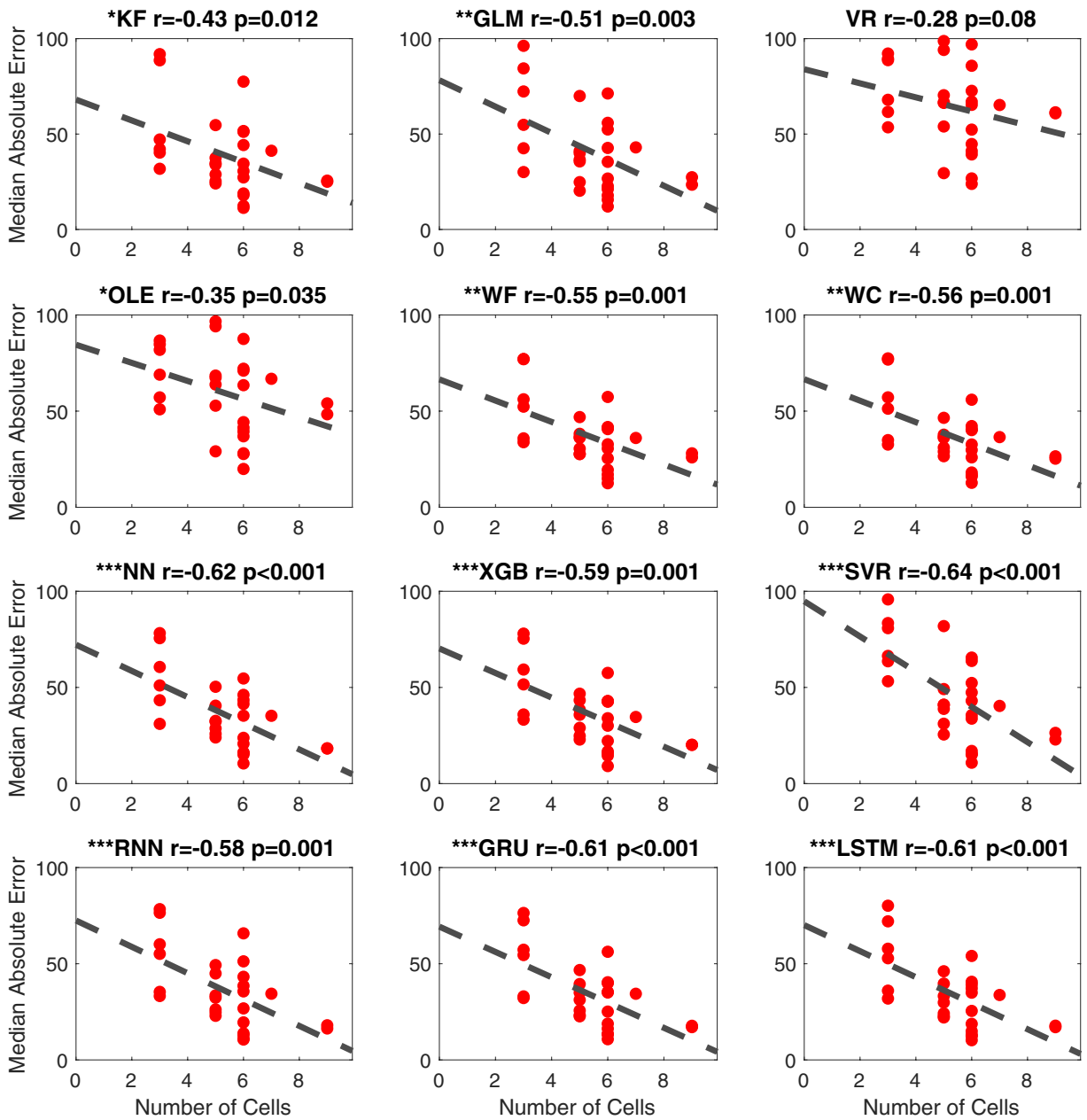

FIGURE 10 | Scatterplots of median absolute error vs. number of cells for all 12 methods. The dashed line is the fitted linear regression. The correlation coefficient (r) and the corresponding *p*-value are shown on the top-right corner of each panel. The significance levels are shown with symbols on the top-left corner ***$p < 0.001$; **$p < 0.01$; *$p < 0.05$. KF, Kalman Filter; GLM, Generalized Linear Model; VR, Vector Reconstruction; OLE, Optimal Linear Estimator; WF, Wiener Filter; WC, Wiener Cascade; SVR, Support Vector Regression; XGB, XGBoost; FFNN, Feedforward Neural Network; RNN, Recurrent Neural Network; GRU, Gated Recurrent Unit; LSTM, Long Short-Term Memory.

decoding by ATN units relative to other regions, and similar decoding across parahippocampal and cortical cell populations (see **Supplementary Material S15.1–S15.6**). However, for some methods, MEC produced weaker decoding relative to other regions. For all methods, accuracy significantly varied across brain region [**Supplementary Material S15.3**; $F_{(4,46)} > 2.57$, $p < 0.05$]. For all model-based methods, ATN accuracy was greatest and furthest from the mean. For 3 of the methods, removing ATN resulted in a non-significant ANOVA [$F_{(3, 37)} < 2.86$, $p > 0.05$]. For Generalized Linear Model, it was necessary to also remove the brain region that was second furthest from the mean, PoS [$F_{(2, 28)} < 3.34$, $p > 0.05$], indicating that for this method, both PoS and ATN had significantly better decoding. Finally, for Vector Reconstruction and Optimal

Linear Estimator, MEC was second furthest from the mean and removing MEC resulted in a non-significant ANOVA [$F_{(2,\ 27)} < 3.34$, $p > 0.05$], indicating that for these methods ATN had significantly better decoding and MEC had significantly worse decoding. To summarize, subsampling the number of cells produced a similar outcome: while decoding is on average most accurate for ATN cell populations, accurate decoding is also possible for parahippocampal and cortical regions and is generally similar across PoS, PaS, MEC, and PC.

Tuning strength

We additionally examined the contribution of the directional specificity of HD cell tuning to decoding accuracy. We first removed the influence of the cell's firing rate by normalizing each cell's tuning curve relative to the directional bin with the peak firing rate. We then calculated the standard deviation of the standardized firing rate by HD tuning function as a proxy for tuning strength (**Figure 11** *Top*). Thus, a low standard deviation would reflect a flat tuning curve, and a high standard deviation would reflect a large peak in the preferred direction of the HD cell. Because this measure is independent of firing rate it is comparable to a measure of signal-to-noise. Finally, we performed linear regressions for each decoding method and a set of randomly selected cells from each dataset (**Figure 11** *Bottom 4 rows*). This analysis indicated that each decoding method was significantly negatively correlated with *MAE* (absolute value of the $rs > 0.4451$, $ps < 0.01$). Thus, poorer tuning, independent of firing rate, is associated with lower decoding accuracy. Finally, the correlations (r-values) significantly varied across head angular velocity, tuning strength, and the number of cells [$F_{(2,\ 33)} = 36.83$, $p < 0.001$]. Next head angular velocity was removed (furthest from the mean, see Statistical Methods) and tuning strength r-values were lower than the number of cells r-values [$F_{(1,\ 22)} = 10.74$, $p < 0.01$]. Thus, the contribution of the number of HD cells had a larger impact than the tuning of individual cells which had a larger impact than the head angular velocity on decoding accuracy.

Firing rate

HD cell firing rates can vary between different HD cells (Taube, 2007) and on average the peak firing rate can differ between recording locations within cortical-limbic regions, approximately ranging from 2 spikes/s to 120 spikes/s (Blair and Sharp, 1995; Taube and Muller, 1998; Peyrache et al., 2015; Lozano et al., 2017). Notably, ATN HD cells on average express higher firing rates compared to those recorded in PoS (Blair and Sharp, 1995; Taube and Muller, 1998; Peyrache et al., 2015) and some preliminary work indicates that the firing rates of PaS and MEC HD cells are on average lower than ATN cells (Winter et al., 2015b). In addition, parahippocampal and cortical HD cells are often multi-dimensional or conjunctive for other spatial variables which can influence cell firing rates (Sargolini et al., 2006; Boccara et al., 2010; Wilber et al., 2014). Thus, because PoS HD cell populations are more sparsely active in a given recording session compared to ATN, it would be expected that decoding accuracy would be relatively low due to the limited spike information predicting the animals HD.

Thus, to evaluate the relationship between decoding accuracy and firing rate, we created a measure that we refer to as the cell's response rate, which is the proportion of video frames in which there was HD cell activity (i.e., cell spikes). As noted above, the number of cells per dataset can influence measures of *MAE*. We therefore subsampled one cell from each dataset, because some datasets had as few as 3 HD cells. We limited our analysis to the HD cell that expressed the greatest spike counts for each dataset. This allowed us to examine the response rate independent of the contribution of the number of cells. We next generated a histogram of the spike counts for the selected HD cell in each dataset and calculated the proportion of video frames in which spikes occurred (**Figure 12**). Thus, we hypothesized that a lower response rate, which is equivalent to a larger proportion of video frames with no spikes, should predict poorer decoding. The histograms suggest that, apart from ATN, parahippocampal and PC regions have very low response rates (less than half the ATN response rate). Importantly, as expected, *MAE* was negatively correlated with the response rate of the cells and was significant for every decoding method (absolute value of the $rs > 0.3233$, $ps < 0.05$; **Figure 12** *Bottom Right and* **Supplementary Material S12**). Interestingly, the response rate seems to be the weakest contributor to decoding accuracy compared to number of cells and tuning. However, response rate was stronger than the absolute angular velocity [Omnibus ANOVA: $F_{(3,\ 44)} = 30.93$, $p < 0.001$; Even after removing head angular velocity and tuning the *F*-test remained significant: $F_{(1,\ 22)} = 7.73$, $p \leq 0.01$]. Thus the strongest predictor of decoding accuracy was tuning strength which was significantly more predictive than the number of cells which was significantly more predictive than the response rate, which was significantly more predictive than the head angular velocity (i.e., Tuning > Number of Cells > Response Rate > Head Angular Velocity).

Time Cost for Each Decoding Method

Time cost is an important indicator of the decoding method's performance. **Table 1** shows the mean elapsed time for training and testing for each decoding method.

The full table can be seen in **Supplementary Material S9.2**. The testing time varies within a few seconds and is largely similar across the decoding methods. As for training, the time cost of using machine learning methods (mean: 3473.33 s or 57.88 min) was considerably greater than statistical model-based methods [mean: 34.87 s or 0.58 min; $t_{(5)} = 3.13$, $p = 0.013$].

DISCUSSION

The general aim of the present study was to compare statistical model-based and machine learning approaches for decoding an animal's directional orientation from populations of HD cells. Overall, 12 computational models were evaluated using HD cell recordings from 27 datasets and from across 5

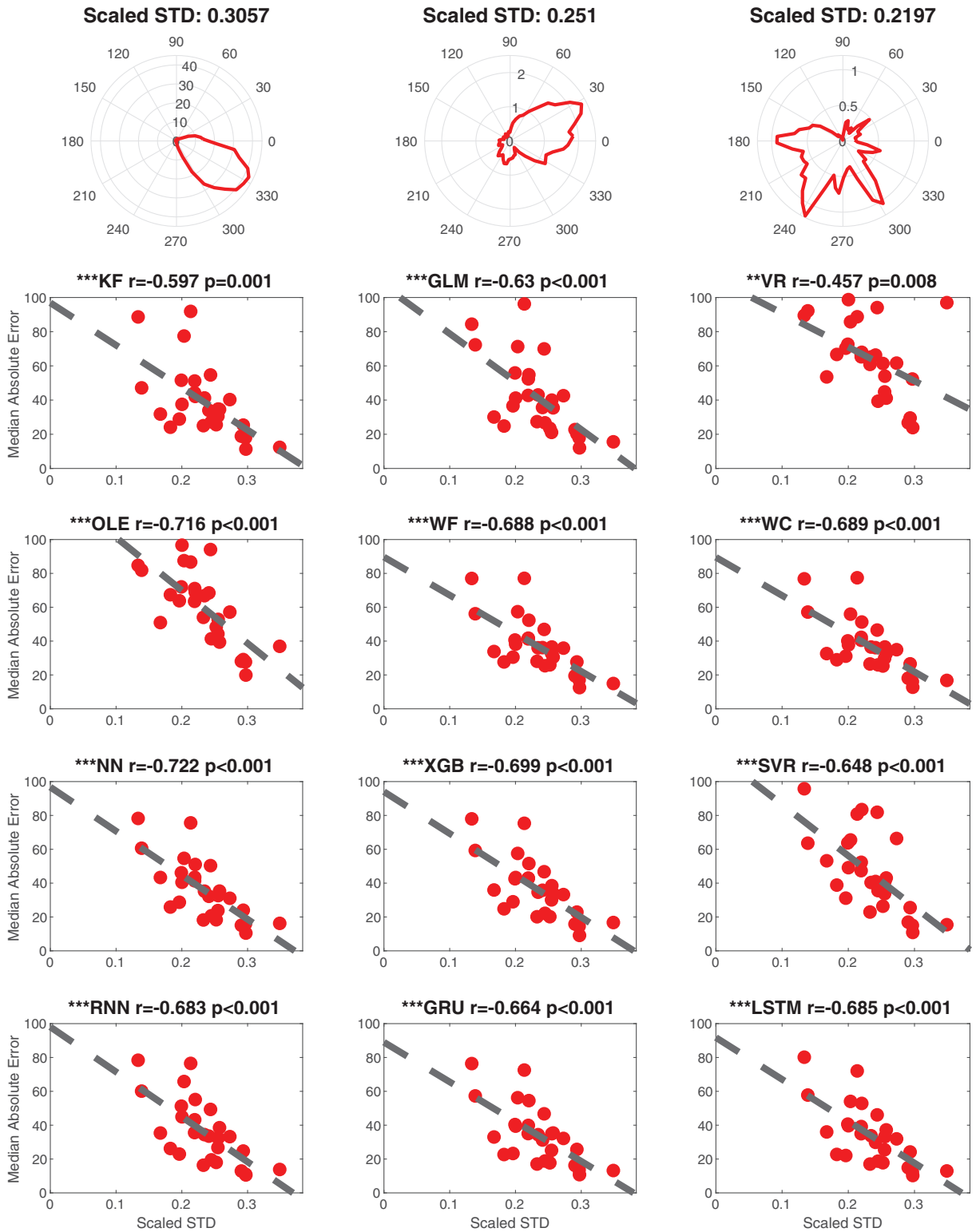

FIGURE 11 | Tuning influences decoding accuracy. Top Row. Examples illustrating the relationship between scaled standard deviation (scaled STD) and tuning for single cells from ATN **(left)**, PoS **(middle),** and MEC **(right)**. The plots of tuning curves were smoothed by a Gaussian kernel function. The scaled STD is computed by taking standard deviation of the scaled (divided by maximum) firing rate. Bottom 4 Rows. Linear regression data is shown for each decoding method as a function of scaled STD (i.e., indicator of tuning strength). One cell was randomly selected from each dataset to avoid repeatedly sampling the same decoding score. $^{***}p < 0.001$; $^{**}p < 0.01$.

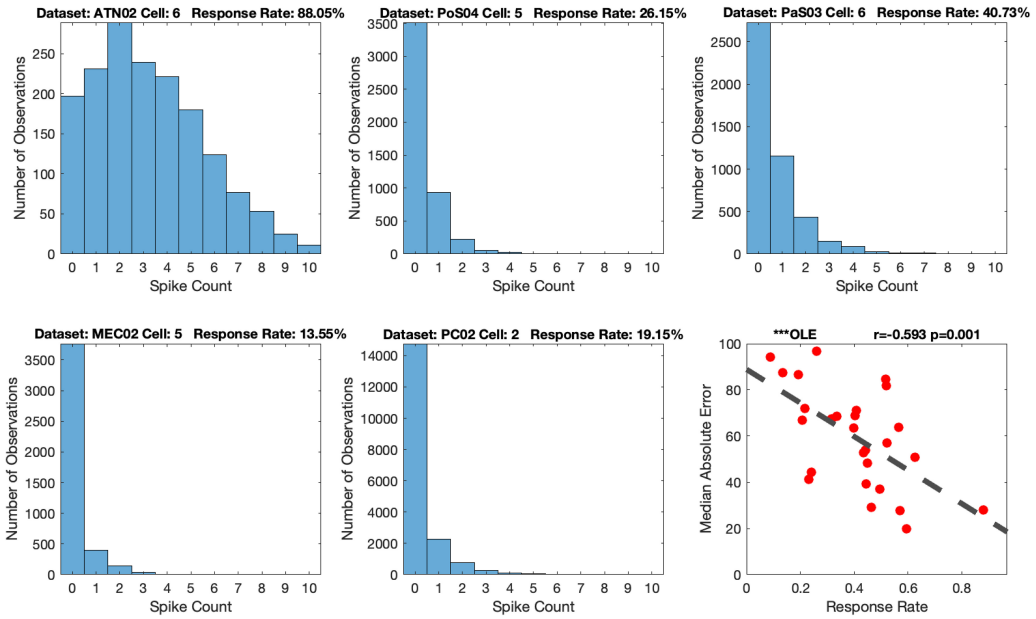

FIGURE 12 | Example histograms of spike counts **(top three, bottom left and bottom middle)**, and an example Median Absolute Error (MAE) vs. response rate scatterplot **(bottom right)**: The dataset's label and response rate are listed in the title. The example scatterplot illustrates the modest relationship between response rate and decoding accuracy. Scatterplots for all the 12 methods are shown in **Supplementary Material S12**. The dashed line in the scatterplot is the fitted linear regression. Optimal Linear Estimator (OLE).

brain regions (PC, MEC, PaS, PoS, and ATN). Performance was similar for most methods (10 of the 12), but with significantly poorer performance by Vector Reconstruction and Optimal Linear Estimator methods. The generality of this result is supported by the fact that the findings were consistent across datasets from different laboratories (i.e., PC vs. other datasets), across different HD cell criteria (i.e., PC vs. other datasets), and across different behavioral testing procedures and recording environments (i.e., PC vs. ATN vs. all other datasets). For the Wiener Filter, Wiener Cascade and the machine learning methods, the prediction performance was highly accurate. One interesting result is that the Recurrent Neural Network model has a much simpler structure than the Gated Recurrent Unit model and Long Short-Term Memory model. In other words, the Recurrent Neural Network model has fewer parameters. The decoding result, however, indicates that these three methods do not have much performance difference. This result suggests that the more complex models may be overfitting the data, while the simpler, Recurrent Neural Network model may capture the critical parameters.

TABLE 1 | The average training time and testing time is shown for each decoding method grouped by category, model-based methods (above) and machine learning methods (below).

	Method	Average training time (seconds)	Average testing time (seconds)
Statistical model-based methods	VR	0.00	2.65
	OLE	0.00	2.70
	KF	0.12	2.65
	WF	0.29	0.00
	GLM	2.88	2.63
	WC	31.58	0.00
Machine learning methods	SVR	126.88	0.46
	XGB	339.90	0.02
	FFNN	3213.17	1.94
	RNN	5274.18	2.23
	GRU	5548.07	4.15
	LSTM	6337.79	4.50

Both Kalman Filter and Generalized Linear Models are based on the hidden Markov chain framework. They make use of a Bayesian framework, assuming that firing rate is distributed according to HD. These two approaches model the activity of single cells as a function of HD. As a result, we can obtain the function curve generated by the model for spike count with HD as the input, which can be used as an estimation of the count-angle curve and the tuning curve. As shown in **Figure 5**, the Generalized Linear Model provides a more accurate model of the single cell tuning curves. Surprisingly, as shown in **Figure 7**, the more biologically accurate model of firing rate as a function of HD does not make the Generalized Linear Model more accurate than the Kalman Filter model. Instead, the latter has slightly lower error on average than the former. The decoding method in Generalized Linear Model, the point process filter, may account for this behavior. It uses Gaussian distribution for approximation, which greatly reduces the computation cost on

the non-linear model prediction, but on the other hand may introduce more errors.

We found significantly poorer performance by Vector Reconstruction and Optimal Linear Estimator methods. There are several possible reasons for this inferior performance. For these methods, there are two critical criteria for the training dataset. First, the data should have a sufficiently strong unimodal peak for a specific HD between HD and firing rate, or else the estimation of preferred directions will be poor. This limitation may further explain poor decoding performance, particularly for cortical datasets, as classification of HD cells could include cells that are stable yet have low mean vector length. Second, the preferred direction vectors must cover the full range of directions from 0° to 360°. Without input data covering some HDs, some predicted HDs may never be achieved (see **Figure 2**). Both Vector Reconstruction and Optimal Linear Estimator methods are more sensitive than other approaches to violations of these criteria.

In general, the machine-learning methods displayed similar decoding accuracy to 4 of the model-based methods (Kalman Filter, Generalized Linear Models, Wiener Filter, Wiener Cascade). This indicates that the relationship between neural firing and HD is well captured by the 4 methods and do not differ from more complicated networks, which may have the problem of over-fitting the data. While it is possible that machine-learning methods would provide a benefit when dealing with larger scale recordings and high dimensional inputs, a large advantage of the model-based methods is their efficiency and robustness. All parameters can be efficiently estimated, and the linear methods can even have closed-form estimation. Related to these points, we also compared decoding accuracy with the elapsed time of training and testing decoding methods (time cost). All methods, with the exception of Vector Reconstruction and Optimal Linear Estimator, did not significantly differ with respect to *MAE*. However, the time cost was much greater for machine learning methods. This finding is not entirely surprising given the fact that machine learning methods include several parameters to be optimized and require Bayesian Optimization to tune the hyper-parameters. Thus, these features likely multiply the time cost of machine learning approaches. In sum, when considering the trade-off between accuracy and time, Kalman Filter, Generalized Linear Models, Wiener Filter and Wiener Cascade would be preferred methods for neural decoding of HD. Thus, for the datasets in the present study, machine-learning methods do not result in a better decoding and cost more with greater computation time.

We also contrasted the accuracy of HD cell decoding between 5 brain regions, including ATN, PoS, PaS, MEC, and PC. From these comparisons, we found that decoding performance varied considerably across datasets and brain regions (see **Figure 9** and **Supplementary Material S15.3**). Specifically, decoding accuracy was greater for ATN when compared to parahippocampal cortex (PoS, MEC, PaS). Our initial analyses indicated that decoding accuracy was weakest for PC units. However, after controlling for the numbers of cells, our analyses indicated that decoding accuracy was similar across parahippocampal regions and PC, and for some decoding methods, was weaker for MEC populations. Our observations are consistent with a previous report suggesting greater decoding accuracy by ATN HD cell populations compared to PoS HD ensembles (see Supplementary Figure S1 in Viejo et al., 2018).

Greater decoding accuracy by ATN populations support the hypothesis that the ATN has a pivotal role in processing the HD cell signal (Cullen and Taube, 2017). Notably, damage to the ATN is known to disrupt HD signals in the parahippocampal cortex (Goodridge and Taube, 1997; Winter et al., 2015a); thus, a high precision readout of ATN HD signals may be critical for "downstream" networks (Wilber et al., 2014, 2015; Peyrache et al., 2015). HD cells in the ATN express some unique firing characteristics that may provide an advantage for neural decoding. For instance, previous studies have reported that HD cells in the ATN have higher peak firing rates compared to the PoS (Blair and Sharp, 1995; Taube and Muller, 1998; Peyrache et al., 2015) which, as described in the present study, has a significant impact on decoding accuracy. In addition, HD cells in the ATN can exhibit anticipatory firing characteristics, which can also influence the accuracy of HD decoding. Specifically, during a given head movement, ATN HD cells tend to fire maximally ∼25 ms before the animal's head reaches the cell's preferred firing direction (Blair and Sharp, 1995; Taube and Muller, 1998). A recent study by Zirkelbach et al. (2019) determined that anticipatory firing can improve decoding of the animals current HD by compensating for sensory or motion-induced decoding errors. In contrast to the ATN, experimental work has found that anticipatory firing is limited in the PoS (Taube and Muller, 1998). In PC, anticipatory firing has been reported by HD cells for action anticipation but not HD anticipation and the timescale of this anticipatory firing varies (Wilber et al., 2014). Anticipatory firing by HD cells in other regions of the parahippocampal cortex has not been well characterized (Winter et al., 2015b). Thus, it is possible that anticipatory firing by HD cells may have a critical influence over decoding accuracy across the entire HD cell circuit. Future studies should provide a quantitative comparison of these features of HD cell firing across thalamo-parahippocampal and cortical regions.

We considered several variables that may have contributed to the observed regional differences in decoding accuracy. These included the population firing rate (response rate), tuning strength, and cell density. Our analyses found that measures of tuning strength and cell density were significantly related to *MAE*. Notably, differences in the tuning strength of individual cells was the strongest predictor. The number of HD cells was the next strongest predictor and the overall response rate was comparatively the weakest predictor of decoding accuracy. However, all three methods were still significantly predictive of decoding accuracy. Thus, variance in *MAE* may be a consequence of differences in recording location, spike counts, tuning strength and HD cell density.

In summary, the present study suggests three general conclusions regarding the use of statistical model-based and machine learning approaches for neural decoding of HD: first, our comparison of different computational models suggests limitations in decoding accuracy by Vector Reconstruction and Optimal Linear Estimator methods. Second, we found that decoding accuracy is variable across the HD cell system, with superior decoding in ATN compared to parahippocampal and cortical regions. Last, we found that decoding accuracy can be influenced by variables such as tuning strength, the response rate, and the recording density of HD cells. Thus, the present study provides a framework for the use of these computational approaches for future investigation of the neural basis of spatial orientation.

DATA AVAILABILITY STATEMENT

The datasets generated for this study are available on request to the corresponding authors.

ETHICS STATEMENT

The animal study was reviewed and approved by Dartmouth College IACUC and University of Lethbridge Animal Welfare Committee.

AUTHOR CONTRIBUTIONS

All authors contributed to the preparation of the manuscript.

FUNDING

BC was supported through an Alzheimer's Association grant AARG-17-531572 and the National Institute of Health grant AA024983. AW was supported through the National Institute of Health grant AG049090. JT was supported through the National Institute of Health grant NS053907.

ACKNOWLEDGMENTS

We thank Dr. Bruce L. McNaughton for assistance with the parietal cortex data and acknowledge funding to Dr. McNaughton that made this possible: NSERC Grant RGPIN-2017-03857 and NSERC Grant RGPIN-2017-03857.

SUPPLEMENTARY MATERIAL

The Supplementary Material for this article can be found online at: https://www.frontiersin.org/articles/10.3389/fncir.2019.00075/full#supplementary-material

REFERENCES

Bassett, J. P., Wills, T. J., and Cacucci, F. (2018). Self-organized attractor dynamics in the developing head direction circuit. *Curr. Biol.* 28, 609–615. doi: 10.1016/j.cub.2018.01.010

Berens, P. (2009). CircStat: a MATLAB toolbox for circular statistics. *J. Stat. Softw.* 31, 1–21.

Blair, H. T., and Sharp, P. E. (1995). Anticipatory head direction signals in anterior thalamus: evidence for a thalamocortical circuit that integrates angular head motion to compute head direction. *J. Neurosci.* 15, 6260–6270. doi: 10.1523/jneurosci.15-09-06260.1995

Boccara, C. N., Sargolini, F., Thoresen, V. H., Solstad, T., Witter, M. P., and Moser, E. I. (2010). Grid cells in pre- and parasubiculum. *Nat. Neurosci.* 13, 987–994. doi: 10.1038/nn.2602

Butler, W. N., and Taube, J. S. (2017). Oscillatory synchrony between head direction cells recorded bilaterally in the anterodorsal thalamic nuclei. *J. Neurophysiol.* 117, 1847–1852. doi: 10.1152/jn.00881.2016

Chen, L. L., Lin, L.-H., Green, E. J., Barne, C. A., and Mcnaughton, B. L. (1994a). Head-direction cells in the rat posterior cortex I. anatomical distribution and behavioral modulation. *Exp. Brain Res.* 101, 8–23. doi: 10.1007/bf00243212

Chen, L. L., Lin, L.-H., Green, E. J., Barne, C. A., and Mcnaughton, B. L. (1994b). Head-direction cells in the rat posterior cortex II. anatomical distribution and behavioral modulation. *Exp. Brain Res.* 101, 24–34. doi: 10.1007/bf00243213

Chen, T., and Guestrin, C. (2016). "Xgboost: a scalable tree boosting system," in *Proceedings of the 22nd ACM SIGKDD International Conference on Knowledge Discovery and Data Mining; 2016 Aug 13 – Aug 7*, (San Francisco, CA: ACM).

Cho, K., Bahdanau, D., Bengio, Y., Bougares, F., Gulcehre, C., Schwnk, H., et al. (2014). Learning phrase representations using RNN encoder-decoder for statistical machine translation. *arXiv* Available at: https://arxiv.org/abs/1406.1078 (accessed September 3, 2014).

Clark, B. J., and Harvey, R. E. (2016). Do the anterior and lateral thalamic nuclei make distinct contribution to spatial representation and memory? *Neurobiol. Learn. Mem.* 133, 69–78. doi: 10.1016/j.nlm.2016.06.00

Clark, B. J., Simmons, C. M., Berkowitz, L. E., and Wilber, A. A. (2018). The retrosplenial-parietal network and reference frame coordination for spatial navigation. *Behav. Neurosci.* 132, 416–429. doi: 10.1037/bne0000260

Cullen, K. E., and Taube, J. S. (2017). Our sense of direction: progress, controversies and challenges. *Nat. Neurosci.* 20, 1465–1473. doi: 10.1038/nn.4658

Drucker, H., Burges, C., Kaufman, L., Smola, A., and Vapnik, V. (1996). "Support vector regression machines," in *Proceedings of the 9th International Conference on Neural Information Processing Systems, 1996 Dec 3 – Dec 5*, (Cambridge: MIT Press), 155–161.

Eden, U. T., Frank, L. M., Barbieri, R., Solo, V., and Brown, E. N. (2004). Dynamic analysis of neural encoding by point process adaptive filtering. *Neural Comput.* 16, 971–998. doi: 10.1162/089976604773135069

Epstein, R. A., Patai, E. Z., Julian, J. B., and Spiers, H. J. (2017). The cognitive map in humans: spatial navigation and beyond. *Nat. Neurosci.* 20, 1504–1513. doi: 10.1038/nn.4656

Fresno, V., Parkes, S. L., Faugère, A., Coutureau, E., and Wolff, M. (2019). A thalamocortical circuit for updating action-outcome associations. *eLife* 8:e46187. doi: 10.7554/eLife.46187

Georgopoulos, A. P., Caminiti, R., Kalaska, J. F., and Massey, J. T. (1983). Spatial coding of movement: a hypothesis concerning the coding of movement direction by motor cortical populations. *Exp. Brain Res.* 49(Supp. 7), 327–336. doi: 10.1007/978-3-642-68915-4_34

Glaser, J. I., Chowdhury, R. H., Perich, M. G., Miller, L. E., and Kording, K. P. (2017). Machine learning for neural decoding. arXiv:1708.00909. Available at: https://arxiv.org/abs/1708.00909

Glorot, X., Bordes, A., and Bengio, Y. (2011). "Deep sparse rectifier neural networks," in *Proceedings of the Fourteenth International Conference on Artificial Intelligence and Statistics; 2011 April 11 – April 13*, Vol. 15, (Ft. Lauderdale, FL: PMLR), 315–323.

Goodridge, J. P., and Taube, J. S. (1997). Interaction between postsubiculum and anterior thalamus in the generation of head direction cell activity. *J. Neurosci.* 17, 9315–9330. doi: 10.1523/jneurosci.17-23-09315.1997

Gumiaux, C., Gapais, D., and Brun, J. P. (2003). Geostatistics applied to best-fit interpolation of orientation data. *Tectonophysics* 376, 241–259. doi: 10.1016/j.tecto.2003.08.008

Hargreaves, E. L., Yoganarasimha, D., and Knierim, J. J. (2007). Cohesiveness of spatial and directional representations recorded from neural ensembles in the anterior thalamus, parasubiculum, medial entorhinal cortex, and hippocampus. *Hippocampus* 17, 826–841. doi: 10.1002/hipo.20316

Haykin, S. (1994). *Neural Networks: A Comprehensive Foundation*. Upper Saddle River, NJ: Prentice Hall.

Hochreiter, S., and Schmidhuber, J. (1997). Long short-term memory. *Neural Comput.* 9, 1735–1780.

Hunter, I. W., and Korenberg, M. (1986). The identification of nonlinear biological systems: Wiener and Hammerstein cascade models. *Biol. Cybern.* 55, 135–144.

Jankowski, M. M., Passecker, J., Islam, M. N., Vann, S., Erichsen, J. T., Aggleton, J. P., et al. (2015). Evidence for spatially-responsive neurons in the rostral thalamus. *Front. Behav. Neurosci.* 9:256. doi: 10.3389/fnbeh.2015.00256

Johnson, A., Seeland, K., and Redish, A. D. (2005). Reconstruction of the postsubiculum head direction signal from neural ensembles. *Hippocampus* 15, 86–96. doi: 10.1002/hipo.20033

Kalman, R. E. (1960). A new approach to linear filtering and prediction problems. *J. Basic Eng.* 82, 35–45. doi: 10.1103/PhysRevE.98.022137

Kingma, D. P., and Ba, J. (2014). "Adam: a method for stochastic optimization," in *International Conference on Learning Representations (ICLR), 2015*. Available at: https://arxiv.org/abs/1412.6980

Knierim, J. J., Kudrimoti, H. S., and McNaughton, B. L. (1998). Interactions between idiothetic cues and external landmarks in the control of place cells and head direction cells. *J. Neurophysiol.* 80, 425–446. doi: 10.1152/jn.1998.80.1.425

Kornienko, O., Latuske, P., Bassler, M., Kohler, L., and Allen, K. (2018). Non-rhythmic head-direction cells in the parahippocampal region are not constrained by attractor network dynamics. *eLife* 7:e35949. doi: 10.7554/eLife.35949

Lawhern, V., Wu, W., Hatsopoulos, N., and Paninski, L. (2010). Population decoding of motor cortical activity using a generalized linear model with hidden states. *J. Neurosci. Methods* 189, 267–280. doi: 10.1016/j.jneumeth.2010.03.024

Lozano, Y. R., Page, H., Jacob, P. Y., Lomi, E., Street, J., and Jeffery, K. (2017). Retrosplenial and postsubicular head direction cells compared during visual landmark discrimination. *Brain Neurosci. Adv.* 1:2398212817721859. doi: 10.1177/2398212817721859

Moser, E. I., Moser, M., and McNaughton, B. L. (2017). Spatial representation in the hippocampal formation: a history. *Nat. Neurosci.* 20, 1448–1464. doi: 10.1038/nn.4653

Peyrache, A., Lacroix, M. M., Petersen, P. C., and Buzsáki, G. (2015). Internally organized mechnaisms of the head direction sense. *Nat. Neurosci.* 18, 569–575. doi: 10.1038/nn.3968

Peyrache, A., Schieferstein, N., and Buzsáki, G. (2017). Transformation of the head-direction signal into a spatial code. *Nat. Commun.* 8:1752. doi: 10.1038/s41467-017-01908-3

Rybakken, E., Baas, N., and Dunn, B. (2018). Decoding of neural data using cohomological feature extraction. *BioRxiv* doi: 10.1101/222331

Salinas, E., and Abbott, L. F. (1994). Vector reconstruction from firing rates. *J. Comput. Neurosci.* 1, 89–107. doi: 10.1007/bf00962720

Sargolini, F., Fyhn, M., Hafting, T., McNaughton, B. L., Witter, M. P., Moser, M.-B., et al. (2006). Conjunctive representation of position, direction, and velocity in entorhinal cortex. *Science* 312, 758–762. doi: 10.1126/science.1125572

Sharp, P. E. (1996). Multiple spatial/behavioral correlates for cells in the rat postsubiculum: multiple regression analysis and comparison to other hippocampal areas. *Cereb. Cortex* 6, 238–259. doi: 10.1093/cercor/6.2.238

Snoek, J., Larochelle, H., and Adams, R. P. (2012). "Practical bayesian optimization of machine learning algorithms," in *Proceedings of the 26th Annual Conference on Advances in neural information processing systems*, Lake Tahoe, NV, 2951–2959.

Srivastava, N., Hinton, G., Krizhevsky, A., Sutskever, I., and Salakhutdinov, R. (2014). Dropout: a simple way to prevent neural networks from overfitting. *J. Mach. Learn. Res.* 15, 1929–1958.

Taube, J. S. (1995). Head direction cells recorded in the anterior thalamic nuclei of freely moving rats. *J. Neurosci.* 15, 70–86. doi: 10.1523/JNEUROSCI.15-01-00070.1995

Taube, J. S. (2007). The head direction signal: origins and sensory-motor integration. *Annu. Rev. Neurosci.* 30, 181–207. doi: 10.1146/annurev.neuro.29.051605.112854

Taube, J. S., and Bassett, J. P. (2003). Persistent neural activity in head direction cells. *Cereb. Cortex* 13, 1162–1172. doi: 10.1093/cercor/bhg102

Taube, J. S., and Muller, R. U. (1998). Comparisons of head direction cell activity in the postsubiculum and anterior thalamus of freely moving rats. *Hippocampus* 8, 87–108. doi: 10.1002/(sici)1098-1063(1998)8:2<87::aid-hipo1>3.3.co;2-l

Taube, J. S., Muller, R. U., and Ranck, J. B. Jr. (1990a). Head-direction cells recorded from the postsubiculum in freely moving rats. I. Description and quantitative analysis. *J. Neurosci.* 10, 420–435. doi: 10.1523/jneurosci.10-02-00420.1990

Taube, J. S., Muller, R. U., and Ranck, J. B. Jr. (1990b). Head-direction cells recorded from the postsubiculum in freely moving rats. II. Effects of environmental manipulations. *J. Neurosci.* 10, 436–447. doi: 10.1523/jneurosci.10-02-00436.1990

Tieleman, T., and Hinton, G. (2012). Lecture 6.5-rmsprop: divide the gradient by a running average of its recent magnitude. *COURSERA Neural Netw. Mach. Learn.* 4, 26–31.

Tsanov, M., Chah, E., Vann, S. D., Reilly, R., Erichsen, J. T., and Aggleton, J. P. (2011). Theta-modulated head-direction cells in the rat anterior thalamus. *J. Neurosci.* 31, 9489–9502. doi: 10.1523/JNEUROSCI.0353-1511.2011

Viejo, C. G., Cortier, T., and Peyrache, A. (2018). Brain-state invariant thalamo-cortical coordination revealed by non-linear encoders. *PLoS Comput. Biol.* 14:e1006041. doi: 10.1371/journal.pcbi.1006041

Wiener, N. (1949). *Extrapolation, Interpolation and Smoothing of Stationary Time Series: With Engineering Applications*. Cambridge, MA: MIT Press.

Wilber, A. A., Clark, B. J., Demecha, A. J., Mesina, L., Vos, J. M., and McNaughton, B. L. (2015). Cortical connectivity maps reveal anatomically distinct areas in the parietal cortex of the rat. *Front. Neural Circ.* 8:146. doi: 10.3389/fncir.2014.00146

Wilber, A. A., Clark, B. J., Forster, T. C., Tatsuno, M., and McNaughton, B. L. (2014). Interaction of egocentric and world centered reference frames in the rat posterior parietal cortex. *J. Neurosci.* 34, 5431–5446. doi: 10.1523/JNEUROSCI.0511-14.2014

Wilber, A. A., Skelin, I., Wu, W., and McNaughton, B. L. (2017). Laminar organization of encoding and memory reactivation in the parietal cortex. *Neuron* 95, 1406–1419. doi: 10.1016/j.neuron.2017.08.033

Winter, S. S., Clark, B. J., and Taube, J. S. (2015a). Disruption of the head direction cell network impairs the parahippocampal grid cell signal. *Science* 347, 870–874. doi: 10.1126/science.1259591

Winter, S. S., Mehlman, M. L., Clark, B. J., and Taube, J. S. (2015b). *Comparison of Head Direction Cell Tuning in Entorhinal Cortex, Postsubiculum and Parasubiculum. Program No. 444.09. Neuroscience Meeting Planner*. Chicago, IL: Society for Neuroscience.

Wu, W., Gao, Y., Bienenstock, E., Donoghue, J. P., and Black, M. J. (2006). Bayesian population decoding of motor cortical activity using a Kalman filter. *Neural Comput.* 18, 80–118. doi: 10.1162/089976606774841585

Zirkelbach, J., Stemmler, M., and Herz, A. V. M. (2019). Anticipatory neural activity improves the decoding accuracy for dynamic head-direction signals. *J. Neurosci.* 39, 2847–2859. doi: 10.1523/JNEUROSCI.2605-18.2019

Conflict of Interest: The authors declare that the research was conducted in the absence of any commercial or financial relationships that could be construed as a potential conflict of interest.

frontiers in Neural Circuits

REVIEW
published: 06 March 2020
doi: 10.3389/fncir.2020.00006

Testing Navigation in Real Space: Contributions to Understanding the Physiology and Pathology of Human Navigation Control

Florian Schöberl[1,2], *Andreas Zwergal*[1,2*†] *and Thomas Brandt*[2,3†]

[1]*Department of Neurology, University Hospital, Ludwig Maximilian University (LMU) of Munich, Munich, Germany,* [2]*German Center for Vertigo and Balance Disorders, DSGZ, LMU Munich, Munich, Germany,* [3]*Clinical Neurosciences, LMU Munich, Munich, Germany*

Successful navigation relies on the flexible and appropriate use of metric representations of space or topological knowledge of the environment. Spatial dimensions (2D vs. 3D), spatial scales (vista-scale vs. large-scale environments) and the abundance of visual landmarks critically affect navigation performance and behavior in healthy human subjects. Virtual reality (VR)-based navigation paradigms in stationary position have given insight into the major navigational strategies, namely egocentric (body-centered) and allocentric (world-centered), and the cerebral control of navigation. However, VR approaches are biased towards optic flow and visual landmark processing. This major limitation can be overcome to some extent by increasingly immersive and realistic VR set-ups (including large-screen projections, eye tracking and use of head-mounted camera systems). However, the highly immersive VR settings are difficult to apply particularly to older subjects and patients with neurological disorders because of cybersickness and difficulties with learning and conducting the tasks. Therefore, a need for the development of novel spatial tasks in real space exists, which allows a synchronous analysis of navigational behavior, strategy, visual explorations and navigation-induced brain activation patterns. This review summarizes recent findings from real space navigation studies in healthy subjects and patients with different cognitive and sensory neurological disorders. Advantages and limitations of real space navigation testing and different VR-based navigation paradigms are discussed in view of potential future applications in clinical neurology.

Keywords: visual exploration, landmarks, navigation, egocentric and allocentric navigation, brain imaging, spatial disorientation, hippocampus

OPEN ACCESS

Edited by:
Desdemona Fricker, UMR8002 Centre de neuroscience et de cognition intégrative, France

Reviewed by:
Zita Patai, University College London, United Kingdom
Hugo Spiers, University College London, United Kingdom

***Correspondence:**
Andreas Zwergal
andreas.zwergal@med.uni-muenchen.de

†These authors have contributed equally to this work

Received: *04 June 2019*
Accepted: *14 February 2020*
Published: *06 March 2020*

Citation:
Schöberl F, Zwergal A and Brandt T (2020) Testing Navigation in Real Space: Contributions to Understanding the Physiology and Pathology of Human Navigation Control. Front. Neural Circuits 14:6. doi: 10.3389/fncir.2020.00006

INTRODUCTION

In the last decades, we have gained fundamental insight into human navigation control from case studies in patients with circumscribed cerebral lesions and functional MRI (fMRI) studies using navigation tasks in well-controlled and distinct virtual reality (VR) settings (Maguire et al., 1998, 2000, 2003, 2006; Astur et al., 2002; Boccia et al., 2014; McCormick et al., 2017, 2018).

However, performing navigation tasks in VR has obvious methodological limitations. The need for a stationary body position (e.g., in the MRI scanner) may result in a bias towards optic flow and visual landmark processing. In contrast, real space navigation relies on simultaneous processing of visual, vestibular, proprioceptive and motor-efference signals, as well as on their integration and weighting for online spatial updating of one's position in space (Loomis et al., 1993; Waller et al., 2003; Ruddle and Lessels, 2006; Waller and Lippa, 2007; Ruddle et al., 2011; Chrastil and Warren, 2012, 2013; Bates and Wolbers, 2014; Ekstrom and Isham, 2017; Diersch and Wolbers, 2019). Input from the otoliths contributes only to 2-dimensional (2D) egocentric navigation in stationary subjects, while input from otoliths and semicircular canals is used to guide 3-dimensional (3D) allocentric navigation in mobile subjects (Brandt and Dieterich, 2016). Recent technological developments have improved the capability to include multisensory input in VR. Examples are the highly immersive VR settings displayed in head-mounted goggles and hybrid approaches using treadmill locomotion in immersive VR (Diersch and Wolbers, 2019; Huffman and Ekstrom, 2019; Starrett et al., 2019) or *post hoc* imagination and simulation of real space environments (Hirshhorn et al., 2012; Howard et al., 2014; Brunec et al., 2018; Patai et al., 2019). Under these conditions, however, simultaneous measurements of brain activation (by fMRI) are a particular challenge. Furthermore, the application of such highly immersive and hybrid VR approaches may be limited by cybersickness and deficits in handling due to decreased embodiment, particularly in elderly subjects and patients with neurological disorders (Costello and Bloesch, 2017; Diersch and Wolbers, 2019). Consequently, novel navigation paradigms in real space have been developed, which allow for synchronous analysis of navigation performance, visual explorations and brain activation in different natural environments. The aim of this review article is: (1) to summarize recent experiences with the application of real space navigation tasks in healthy subjects and patients with cognitive and sensory deficits; and (2) to discuss the advantages, limitations and potential future clinical applications of real space navigation tests compared to currently available VR based set-ups.

NAVIGATION TESTING IN HEALTHY SUBJECTS

2D Navigation: Behavior, Cerebral Networks and Current Concepts

Human navigational behavior critically depends on the surrounding environment, specifically the spatial dimension, scale and the abundance of visual cues suitable as landmarks. Most of the human real-life navigation takes place in 2D environments within four major vectors of movement (i.e., forward/backward, right/left). Spatial scale can vary greatly from vista-space (e.g., navigation within a room) to large-scale environments (e.g., navigation in a city or landscape).

In the late 1990s, first studies combined fMRI techniques with stationary desktop VR settings to study human 2D spatial navigation control. These studies revealed a distributed cerebral navigation network in humans consisting of frontal lobe regions, mesiotemporal regions (hippocampus and parahippocampal cortex), parietal lobe regions [posterior parietal cortex (PPC) and retrosplenial cortex (RSC)], as well as subcortical regions (basal ganglia and thalamus; Ghaem et al., 1997; Epstein and Kanwisher, 1998; Maguire et al., 1998; Epstein et al., 1999, 2017; Grön et al., 2000; Burgess et al., 2002; Hartley et al., 2003; Spiers and Maguire, 2006; Ekstrom et al., 2014; Epstein and Vass, 2014; Ekstrom, 2015; Ekstrom and Isham, 2017). fMRI approaches in more complex VR environments pointed towards a particular and navigation-specific role of the hippocampal formation, the RSC and PPC (Berthoz, 1997; Hartley et al., 2003; Ohnishi et al., 2006; Spiers and Maguire, 2006; Wolbers et al., 2007, 2008; Brown and Stern, 2014; Howard et al., 2014; Marchette et al., 2014, 2017; Spiers and Gilbert, 2015; Ekstrom and Isham, 2017; Epstein et al., 2017; Vass and Epstein, 2017; Huffman and Ekstrom, 2019; Patai et al., 2019). VR set-ups presenting cityscapes and landscapes, as well as visual scenarios, induced strong activation in the parahippocampus, RSC and PPC thus confirming their particular role in visual cue and scene processing (Epstein and Kanwisher, 1998; Spiers and Maguire, 2006). More advanced task designs in VR and progress of fMRI techniques allowed further differentiation of visual scene and cue processing within the human brain. The parahippocampal place area (PPA) located directly posterior to the parahippocampus is important for the recognition of visual scenes and particularly the identification and selection of visual landmarks within a visual scenario (Epstein et al., 2005). The occipital place area (OPA) located in the dorsal occipital lobe next to the transverse occipital sulcus is mandatory for the recognition of the spatial geometry and particularly boundaries of a presented visual scene, as well as the local elements (Dilks et al., 2013; Kamps et al., 2016). The RSC located dorsally to the splenium of the corpus callosum within the medial parietal cortex uses the selected landmarks to determine the current location in space, as well as heading/facing direction in space (Epstein and Vass, 2014; Vass and Epstein, 2017). Thus, VR-based scene processing and navigation tasks are well suited to study the brain networks and principles of human visual cue and scene processing when combined with advanced fMRI techniques.

Complementary to VR experiments, real space navigation paradigms have been developed, which combine synchronous measurements of navigation behavior, visual exploration and navigation-induced brain activation (using [^{18}F]fluorodeoxyglucose ([^{18}F]FDG)-PET; Zwergal et al., 2016; Irving et al., 2018b; **Figure 1**). Real space navigation paradigms are prone to study natural visual exploration behavior (visual fixations, saccadic eye movements) by eye-tracking (Irving et al., 2018b). Furthermore, navigation-induced brain activations can be captured by [^{18}F]FDG-PET, because more than 90% of [^{18}F]FDG accumulates in neurons activated by real navigation within 10 min. Recent studies have shown that 2D real space navigation activated a cerebral network consisting of the

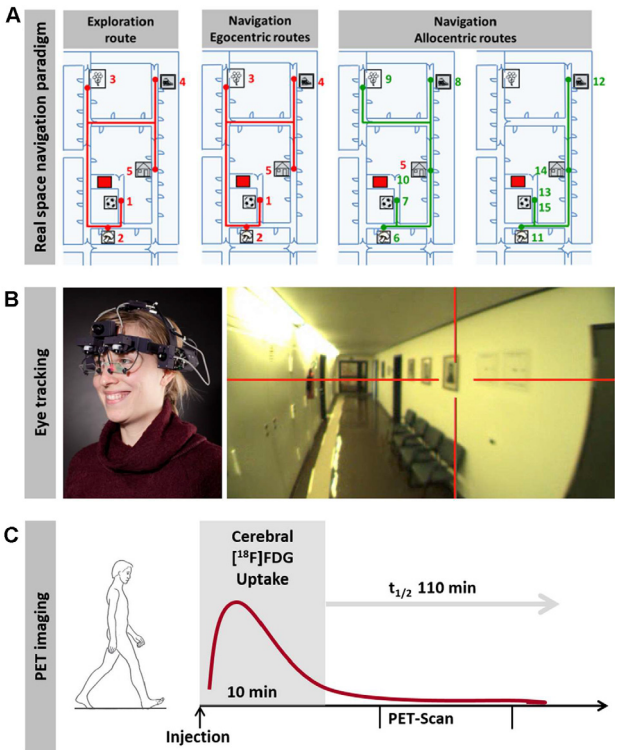

FIGURE 1 | Horizontal real space navigation paradigm. **(A)** real space navigation is tested in a complex and unfamiliar spatial environment, where items are placed as target points. These items are shown to the subjects first on an investigator-guided walk (exploration). Afterward, subjects have to find the items in a pseudo-randomized order over the next 10 min (navigation). In the first part of the navigation paradigm, routes, which are identical to the previous exploration route (so-called egocentric routes, red lines), are tested; in the second part, the order of target items is changed in a way that requires the planning of new routes (so-called allocentric routes, green lines). **(B)** Subjects wear a gaze-monitoring head camera throughout the experiment to allow *post hoc* analysis of their visual exploration. **(C)** [^{18}F]FDG is injected at the start of the 10-min navigation phase. After the end of navigation testing subjects rest in a supine position for 20 min and image acquisition starts 30 min after tracer administration. This paradigm can be used to depict navigation-induced brain activations because the cerebral glucose utilization is weighted to the 10 min following [^{18}F]FDG injection and is integrative due to intracellular trapping of the tracer (adapted from Irving et al., 2018b; permission from the journal obtained).

hippocampus, posterior temporal, RSC, parieto-occipital and frontal cortex, as well as the pontine brainstem centers for horizontal eye movement control (Zwergal et al., 2016). Cerebral control of real space navigation shows considerable overlap with regions reported in VR experiments. However, there are also differences in navigation strategies and brain activations in VR and real space:

(1) Brain regions important for processing of novel visual scenes such as the PPA and OPA are not active during real space navigation experiments. The most likely explanation is that transient brain activations during a confrontation with a novel spatial environment are not reflected by PET due to low temporal resolution (Zwergal et al., 2016). Furthermore, most real space navigation experiments are preceded by an exploration of the environment. Consequently, the space during navigation is not novel anymore.

(2) Visual cue-based and location-based strategies are used to a different extent in VR and real space environments (Bohbot et al., 2012; Chersi and Burgess, 2015; Ekstrom et al., 2017; Starrett and Ekstrom, 2018). Continuous integration of vestibular and proprioceptive afferent inputs during self-motion enables online updating of our current position in space—a way to navigate successfully even in the absence of landmark processing. The technical term for this navigational strategy is path integration and the underlying computations mainly take place in the PPC and to some extent also in the basal ganglia (Packard and McGaugh, 1992; Packard and Knowlton, 2002; Iaria et al., 2003; Yin and Knowlton, 2006; Hwang and Andersen, 2009; Pennartz et al., 2011; Hwang et al., 2014). The PPC seems to be a hub region for the estimation of distances and heading/body directions (Guariglia et al., 2005; Weniger et al., 2009, 2011; Ciaramelli et al., 2010), while the basal ganglia are indispensable for stimulus-response learning, i.e., connecting a distinct sensory cue to a specific action (Packard and Knowlton, 2002; Iaria et al., 2003). Location-based strategies tend to be underrepresented in VR based tasks due to the lack of idiothetic, i.e., vestibular and proprioceptive input. We know from research in rodents, that passive movement in VR induces other vestibular signals than active movement in real environments, which in consequence has also effects on upstream cell systems important for spatial navigation (i.e., head direction cells, grid cells and place cells; Stackman and Taube, 1997; Stackman et al., 2002; Russell et al., 2003a,b; Taube et al., 2013; Yoder and Taube, 2014). Accordingly, in humans head movements in the horizontal plane are mandatory for regular processing of the head direction system and upstream cell systems for spatial navigation (Frissen et al., 2011). In fact, numerous behavioral studies suggest that body-based cues enhance spatial representations in humans by aiding encoding and retrieval of spatial information (Waller et al., 2003; Ruddle and Lessels, 2006; Ruddle et al., 2011; Chrastil and Warren, 2013). Novel VR technologies such as head-mounted VR systems try to allow for linear and rotational movements by high immersion to the virtual environment. However, this approach excludes the simultaneous capturing of brain activations by fMRI (Diersch and Wolbers, 2019). Furthermore, despite ongoing improvements of VR technology, vestibular and visual inputs are often still not matching perfectly in these VR designs thus leading to manifest cybersickness or at least vestibular discomfort and dizziness particularly in the older participants (Diersch and Wolbers, 2019). Real space navigation paradigms are still the gold standard for the exact assessment of the role of vestibular and proprioceptive processing in humans, at least when using a multimodal approach with eye tracking for *post hoc* analysis of eye and head movements and simultaneous measurement of brain activations by [^{18}F]FDG-PET (Zwergal et al., 2016; Irving et al., 2018b). Indeed, during real space navigation, there is significantly higher recruitment of vestibular brain regions

in the brainstem and cerebellum, as well as cortical regions important for vestibular and multisensory processing such as the cingulate and insular cortex (Zwergal et al., 2016; Irving et al., 2018b). During the last years, the novel "hybrid-approaches" has come up, which have the potential to further overcome existing limitations of dedicated VR technologies. One strategy combines the simultaneous application of immersive head-mounted VR systems, which allows for free head movements, with continuous walking on a treadmill to simulate locomotion within the VR (Huffman and Ekstrom, 2019; Starrett et al., 2019). Despite the multisensory nature of these approaches, they still differ significantly from the navigational situations in everyday life, because there is no one by one translation of step size to the VR. The training sessions before the trial sessions are very extensive, which is definitely not the case in most real space navigation situations. Application in older people and particularly patient groups with cognitive decline or sensory deficits is still difficult due to technical challenges and the high risk of cybersickness. Previous studies have found no differences in spatial learning of novel environments with addicting treadmill walking to immersive head-mounted VR, which suggests a modality-independent network for retrieval of spatial layout information in humans and questions the relevance of hybrid-approaches (Wolbers et al., 2011). As imaging of brain activation is concerned, fMRI can be applied only *post hoc* by memorizing or simulating navigational situations within the VR. An alternative approach for studying spatial orientation in fMRI is the *post hoc* imagination of navigation through recently learned real space layouts (e.g., London Soho's streets; Howard et al., 2014; Javadi et al., 2017; Brunec et al., 2018; Patai et al., 2019). The imagination of real tasks in fMRI has been successfully established for the investigation of body movements, standing and locomotion under various conditions (Jahn and Zwergal, 2010; Zwergal et al., 2012). A direct PET/fMRI comparison of real space and imagined locomotion has shown similarity in activated brain networks (e.g., cerebellar activations), but also differences as a function of the task (e.g., primary motor cortex activation in real locomotion vs. prefrontal-basal ganglia activation in imagined locomotion; la Fougère et al., 2010). In navigation research, fMRI imagination paradigms gave valuable insights into the differential contributions of the anterior hippocampus and entorhinal cortex (i.e., gist-like, scheme-like global spatial representations and Euclidean distance), the posterior parts of the hippocampus (i.e., detail-rich spatial representations) and the medial prefrontal cortex (PFC; i.e., decision making, detours). These paradigms helped to support the Multiple Trace Theory (MTT) respectively the Trace Transformation Theory (TTT) as a concept of memory generation and consolidation because they allowed comparing brain activations in familiar environments (e.g., RSC) to those in novel environments (e.g., posterior hippocampus; Nadel and Moscovitch, 1997; Nadel et al., 2000; Patai et al., 2019). The task-inherent need for decision-making at way crossings and the reliably high success rates in correct wayfinding underline that imagination protocols are in principle valid and reliable. However, these approaches are not real space navigation in a narrower sense, as the trial sessions are done while lying supine in an fMRI-scanner and mentalizing the before learned real space environments. An additional problem may be the ability for imagination, which varies greatly between subjects and can be bearly controlled.

(3) The flexible interplay of landmark-based and location-based navigation is fundamental for the creation of metric map-like representations of space. Such a cognitive map seems to be the scaffolding for navigating most efficiently and accurately by using short cuts and being able to react flexibly to unforeseen obstacles and changes in routinely used routes (Epstein et al., 2017). It has been shown that a larger hippocampal volume is associated with superior performance in learning allocentric spatial relationships between buildings on a college campus and allocentric topography of an artificial landscape (Hartley and Harlow, 2012; Schinazi et al., 2013). fMRI techniques such as fMRI adaptation in the last years brought evidence that a spatial map like code exists in the human hippocampus (Hassabis et al., 2009; Doeller et al., 2010; Morgan et al., 2011; Nielson et al., 2015). However, in many VR based fMRI studies, hippocampal activations were not found. It is still a matter of debate, whether the hippocampus or rather the RSC is the main hub for human spatial navigation due to controversial findings from previous fMRI studies (Epstein and Vass, 2014; Ekstrom and Isham, 2017). PET-based measurement of cerebral glucose metabolism while absolving a real space navigation task confirmed the prominent role of simultaneous hippocampal as well as RSC activations for human navigation, thus indicating that these two brain regions are the critical hubs for human navigation in naturalistic and novel environments (Zwergal et al., 2016; Irving et al., 2018b). Furthermore, the results from real space navigation studies favor the view that there indeed is no hierarchical order between these two hubs.

(4) In real space navigation experiments the frontal lobe is regularly activated, which is not the case in many VR tasks. Only a few fMRI studies in VR have shown frontal lobe activations, mostly in the PFC. These studies used tasks that explicitly examined decision making at way crossings with multiple-choice or during detour planning (Kaplan et al., 2017). Real space navigation in novel environments always requires planning processes for routes and decision making at way crossings, which leads to continuous frontal lobe activations. Therefore, it has to be seen as bias and weakness of several VR settings that frontal lobe activations are underrepresented.

3D Navigation: Behavior, Cerebral Networks and Current Concepts

Everyday life navigation mostly takes place in the horizontal plane. However, in some situations, such as finding the correct way in multi-floor buildings, humans also need to deal with an additional third dimension of space (3D) and to orient

themselves correctly in the vertical plane (Thibault et al., 2013; Brandt et al., 2017). Previous studies in different animal species over the last decades revealed an anisotropy of performance and cellular activations in favor of the prevailing plane in ground-based species, such as dogs and rats, as well as flying species, such as bats and hummingbirds (Burt de Perera and Holbrook, 2012; Burt de Perera et al., 2013; Jeffery et al., 2013; Brandt and Dieterich, 2013; Flores-Abreu et al., 2014).

Recently, a study in humans for the first time investigated performance, visual exploration, and brain activation during real space navigation in either the earth-horizontal or earth-vertical plane (Zwergal et al., 2016; **Figure 2**). Similar to other ground-based species, an anisotropy of performance in favor of navigation in the horizontal plane was observed in humans (Jeffery et al., 2013; Zwergal et al., 2016). Detailed analysis of behavioral parameters revealed a more prominent role of visual cue processing during horizontal navigation, whereas vertical navigation seemed to rely more on non-visual sensory input such as the vestibular sense (Zwergal et al., 2016). The annotation of visual fixation targets to the spatial environment indicated a weighted distribution to strategic waypoints in the horizontal navigation task compared to a more even distribution in the vertical navigation task (**Figure 2**). In terms of brain activation, the hippocampus and RSC were activated in both conditions (**Figure 2**). During horizontal navigation, there was a clear right-sided dominance of the hippocampal activations, whereas during vertical navigation hippocampal activations were bilateral and of similar extent (Zwergal et al., 2016). The higher reliance on visual cues during horizontal navigation was reflected by increased activations of secondary visual cortical areas. During vertical navigation vestibular cortical processing within the insular cortex and anterior cingulate cortex was detected (Zwergal et al., 2016).

In contrast to the results of 3D real space navigation, a recent fMRI study in a virtual 3D lattice structure revealed no difference in performance for the horizontal and vertical plane. Activations of the right hippocampus and RSC were similar for movements along the horizontal and vertical axis (Kim M. et al., 2017; Kim and Maguire, 2019a,b). Differences in results between real space and VR 3D navigation testing are explained mostly by the applied task design. Participants moved in the virtual 3D lattice structure by a keyboard using mainly visual cue processing, while sitting. Given the lack of vestibular and proprioceptive input, missing activations of vestibular and somatosensory brain regions seem plausible. The poorer performance in vertical real space navigation could be due to differences in scale and texture of the environment. The 2D horizontal environment was rich in visual cues and on the border from vista- to large-scale, whereas the 3D vertical environment had less potential landmarks and was definitely large-scale (Zwergal et al., 2016). Another important factor might be that during naturalistic vertical navigation in a staircase, subjects always have conflicting reference frames for visual input (earth-horizontal) and vestibular input (earth-vertical). In contrast, during horizontal 2D navigation, the visual and vestibular reference frames match in the earth-horizontal plane. Given the importance of vestibular inputs for path integration in the vertical plane, a largely visually guided VR-task (like a 3D lattice structure) may not be optimal to depict the subtle difference in 3D navigation performance and cerebral navigation control.

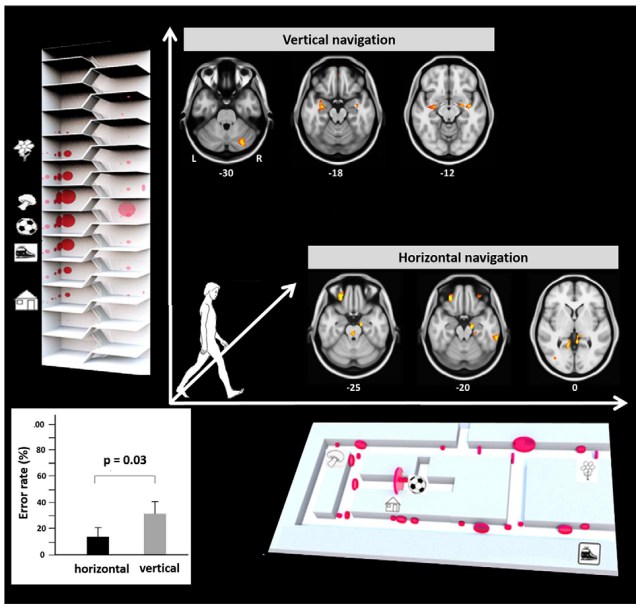

FIGURE 2 | Earth-horizontal vs. earth-vertical real space navigation in healthy subjects. The individual error rate in finding the right items was significantly higher in the vertical than in the horizontal navigation paradigm (bottom left). In the horizontal navigation paradigm selection and recall of landmarks were orientated to strategic waypoints along the path like crossings and prominent items (bottom right). This strategy reflects the importance of landmark-guided navigation in the horizontal plane. In contrast, during vertical navigation landmark fixations were distributed more evenly along the path (top left). This strategy may indicate that vertical navigation is less reliant on visual landmarks. The most frequent fixation targets are indicated as red circles with the diameter being proportional to the mean number of fixations. During horizontal navigation, regional cerebral glucose metabolism was relatively increased in the right anterior hippocampus, bilateral retrosplenial cortex (RSC), and the pontine brainstem tegmentum. The glucose uptake in the eye muscles was higher in horizontal navigation, indicating increased exploration. During vertical navigation regional cerebral glucose metabolism was relatively increased in the anterior hippocampus, insula, and cerebellum bilaterally. Significance level $p < 0.005$, L, left; R, right side, level of the section are marked by MNI-z-coordinates (adapted from Zwergal et al., 2016; permission from the journal obtained).

NAVIGATION DISORDERS IN HUMANS

Given the complex control of human navigation, it seems self-evident that sensory deficits and dysfunctions of critical hubs of the cerebral navigation network (e.g., the hippocampus, RSC, PPC) lead to spatial navigation deficits in humans. However, no established tests are available in clinical routine to detect spatial orientation deficits in an easy and reliable way. Consequently, there is a pressing need to transfer knowledge from the laboratory setting to the bedside of affected patients. Neurological navigation disorders can be classified based on the underlying pathology in patients with: (1) sensory

deficits; (2) acute strategic cerebral lesions; and (3) chronic dysfunction of cerebral navigation networks (mostly due to neurodegeneration).

Sensory Deficits: Bilateral Vestibular Failure

Research in rodents disclosed how vestibular inputs reach the hippocampal formation *via* different brainstem and thalamic pathways (Smith, 1997; Shinder and Taube, 2010). Accordingly, complete bilateral vestibular deafferentation results in hippocampal cell loss as well as pronounced and permanent deficits in spatial learning tasks in rodents (Smith et al., 2005, 2015; Zheng et al., 2009; Baek et al., 2010). The neurophysiological correlate of this behavioral finding is a pronounced impairment of the head direction cell system as a direct consequence of a missing vestibular input (Yoder and Taube, 2014). Additionally, there is also a dysfunction of the place cells and grid cells in rodents with vestibular deficits (Stackman et al., 2002). Brandt and colleagues were the first to show that complete bilateral vestibular deafferentation in humans resulted in hippocampal volume loss and concomitant deficits of spatial learning in a virtual version of the Morris water maze task, while other cognitive functions, such as memory, executive or visuoconstructive functions, remained unaffected (Brandt et al., 2005). Desktop VR based spatial learning tasks in vista space revealed mild deficits of allocentric place learning and an atrophy of the middle and posterior parts of the hippocampal formation in patients with bilateral vestibular failure (BVF; Schautzer et al., 2003; Kremmyda et al., 2016). A fMRI study in a large-scale virtual environment showed that impaired place learning in patients with incomplete BVF may be compensated by cerebellar-driven sequence-based spatial navigation (Jandl et al., 2015).

All previous VR based studies in vestibular pathologies have the major limitation that they cannot fully account for the role of different sensory inputs for spatial updating as patients sit or lie during the task (Taube et al., 2013). Consequently, spatial navigation testing in patients with sensory deficits should be preferably applied in real space settings, where vestibular signals from the otoliths (linear motion) and semicircular canals (rotatory motion), as well as proprioceptive signals, contribute to the head direction and grid cell function (Taube et al., 2013; Yoder and Taube, 2014; Cullen and Taube, 2017). In a real space navigation paradigm, mild deficits in allocentric route learning were found in patients with BVF compared to healthy and age-matched controls. The allocentric navigational performance was better in patients with residual vestibular function. In contrast, egocentric navigation was well preserved in the BVF patients. When analyzing the navigational behavior, patients with BVF showed characteristic repetitive stops along the way, which allowed for updating of the position in space by landmark fixations. Patients with BVF had less right-sided hippocampal activations and more activation in the bilateral PPAs during navigation (Zwergal et al., 2011). This pattern likely reflects a more landmark-based strategy to compensate for deficient allocentric map-like coding.

Acute Strategic Cerebral Lesions: Stroke and Transient Global Amnesia

It has been well documented by single case reports and small case series that acute or subacute lesions in critical brain regions can affect spatial navigation abilities dramatically, leading to severe topographical disorientation (Aguirre et al., 1996; Aguirre and D'Esposito, 1999; Nyffeler et al., 2005; Ritchie et al., 2018). However, a valid and structured classification system and generally accepted taxonomy of spatial navigation deficits are still missing. Recently, Claessen and van der Ham (2017) tried to classify the different clinical forms of topographagnosia based on a retrospective analysis of published lesion cases. Deficits in visual landmark encoding, location, and path processing were rated for this purpose (Claessen and van der Ham, 2017). The major limitation of this retrospective approach was the great heterogeneity in lesion size and localization, as well as time points and methods of spatial navigation testing. For the future, it seems reasonable to tests patients with strategic lesions of the hippocampal formation, RSC and parietal cortex for deficits of ego- and allocentric navigation in a standardized way. Furthermore, it is important to characterize the functional outcomes of patients with distinct lesions affecting the cerebral navigation network. Several case reports showed the great potential for functional compensation in the human spatial navigation network, when only a circumscribed part is affected (**Figure 3**; Irving et al., 2018a). Although not known exactly, it might be possible that intact subfields of the affected hub or other critical hubs within the cerebral navigation contribute to the compensation of the spatial navigation performance and strategy.

Besides well-selected lesion patients due to stroke or brain trauma, TGA seems to be a selective hippocampal lesion model in humans. TGA is a disorder of as far unknown etiology manifesting with sudden onset of anterograde and retrograde amnesia lasting for 1–24 h (Bartsch and Deuschl, 2010; Bartsch and Butler, 2013). MRI regularly depicts focal lesions in the lateral CA1 regions of the hippocampus on one or both sides during the acute stage of disease (Bartsch et al., 2006). As a model of intermittent hippocampal dysfunction, it is of particular interest, whether and to what extent spatial learning and navigation are affected in these patients. Bartsch and colleagues have shown that hippocampus-based place learning is critically impaired in patients with TGA in the very acute stage when they still suffer from anterograde amnesia (Bartsch et al., 2010). A recent study in real space confirmed an allocentric navigation deficit in TGA patients in the post-acute stage (3 days after symptom onset), when verbal and figural memory functions had already normalized (Schöberl et al., 2019). Navigation deficits were accompanied by altered visual explorations reflecting a higher reliance on visual landmarks (Schöberl et al., 2019; **Figure 4A**). PET measurements in the post-acute stage showed increased brain activations of the right hippocampus and bilateral RSC, posterior parietal and mesiofrontal cortex (Schöberl et al., 2019; **Figure 4B**). These findings can be interpreted as a compensatory upregulation of the human cerebral navigation network including the regions

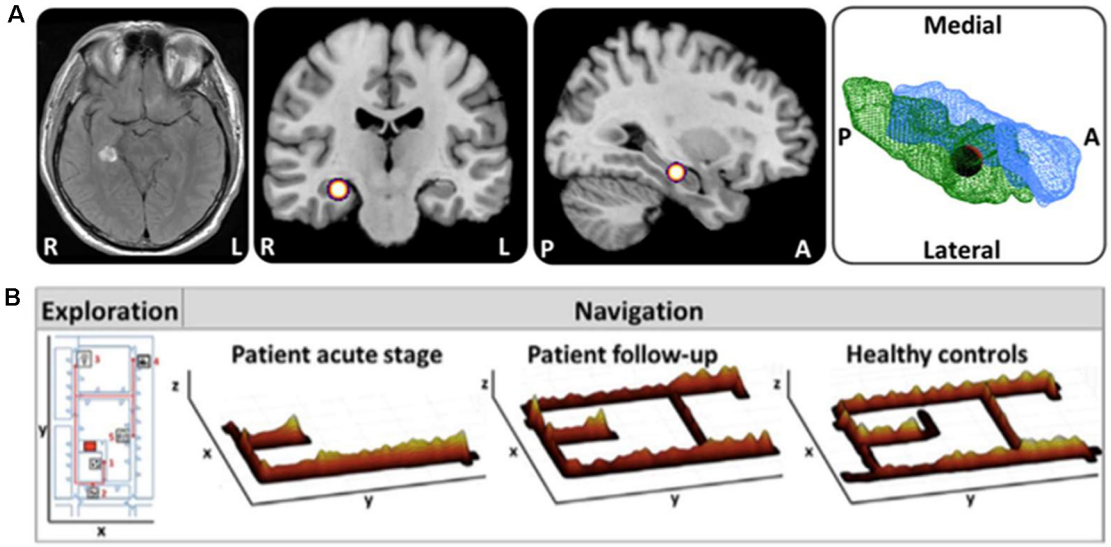

FIGURE 3 | Horizontal navigation in a patient after acute hemorrhage of the right posterior hippocampus. **(A)** Schematic drawing of the exact lesion localization in the right posterior hippocampus and adjacent parahippocampal cortex. **(B)** In the acute stage the patient exhibited severe topographical disorientation with a completely missing cognitive map of the environment. In a follow-up investigation after 4 months, the patient's navigation performance was completely normalized with an intact cognitive map of the environment. Search paths during navigation are color-coded on a ground map (x, y) as the cumulative time at the location (z). The most frequent fixation targets are indicated as green circles on the ground map with diameter proportional to the cumulative time of fixation (adapted from Irving et al., 2018a; permission from the journal obtained). L, left; R, right.

for allocentric spatial representations (i.e., hippocampus and RSC), egocentric spatial representations (i.e., PPC) and for the planning of the applied spatial strategy (i.e., mesiofrontal cortex). Contrary to previous reports, allocentric navigation deficits in real space persisted up to 4 months after symptom onset. Egocentric wayfinding was not affected in the patients at any time point. These real space findings show that strategic bilateral lesions in hippocampal subfields in TGA can induce severe spatial disorientation, even in the presence of a functional extrahippocampal navigation network. Compensation may be less effective than in unilateral hippocampal lesions.

Neurodegenerative Disorders: Mild Cognitive Impairment and Alzheimer's Disease

In the clinical setting, spatial disorientation often is the leading symptom in patients with Alzheimer's disease (AD; Tu and Pai, 2006). This clinical observation could be confirmed by several studies, which tested spatial learning abilities either by VR or in real space in patients with early AD (Pai and Jacobs, 2004; Cushman et al., 2008; Allison et al., 2016). From a neuropathological viewpoint, it is not surprising that spatial navigation is affected early in the course of AD and progresses dramatically over time. Neuropathological changes, such as tau-deposits, synaptic dysfunction, and neuronal loss, manifest very early in critical hubs of the human spatial navigation network such as the mesiotemporal lobe (i.e., hippocampus and entorhinal cortex) and RSC (Braak et al., 1993; Braak and Braak, 1995, 1998; Vlček and Laczó, 2014). Research in the last decades revealed that navigation deficits can be already found in patients with amnestic mild cognitive impairment (aMCI), which is thought to be a pre-stage of impeding dementia (Hort et al., 2007; Laczó et al., 2009, 2010; Lithfous et al., 2013; Vlček and Laczó, 2014; Rusconi et al., 2015; Kim J. W. et al., 2017). Spatial navigation testing, therefore, has great potential for the early diagnosis of aMCI/AD in pre-symptomatic stages (Coughlan et al., 2018). Multiple-domain aMCI patients, i.e., patients with deficits in more than one cognitive subdomain, exhibit deficits in virtual allocentric and egocentric spatial navigation tasks, whereas single-domain aMCI patients still seem to have intact egocentric spatial navigation abilities (Hort et al., 2007). In previous aMCI/AD navigation research, different VR-based or small-scale real space tasks were applied, which at least might bias the transfer to everyday life navigational situations. Only a few studies investigated visual exploration patterns during spatial navigation. Only advanced analysis of eye movements allows for differentiation of deficits in higher-order visual functions, such as the selection of appropriate visual cues, from deficits in visual scene processing or deficits in estimating directions and distances. More advanced VR technologies with a higher immersion of real space navigation testing are mandatory to solve open questions around visual processing in aMCI/AD.

A recent study demonstrated that path integration performance in an immersive VR can differentiate amyloid positive from amyloid negative aMCI with high sensitivity and specificity (Howett et al., 2019). The cumulative distance error during path integration was significantly higher in amyloid positive as compared to amyloid negative aMCI patients and age-matched healthy controls. Furthermore, this behavioral

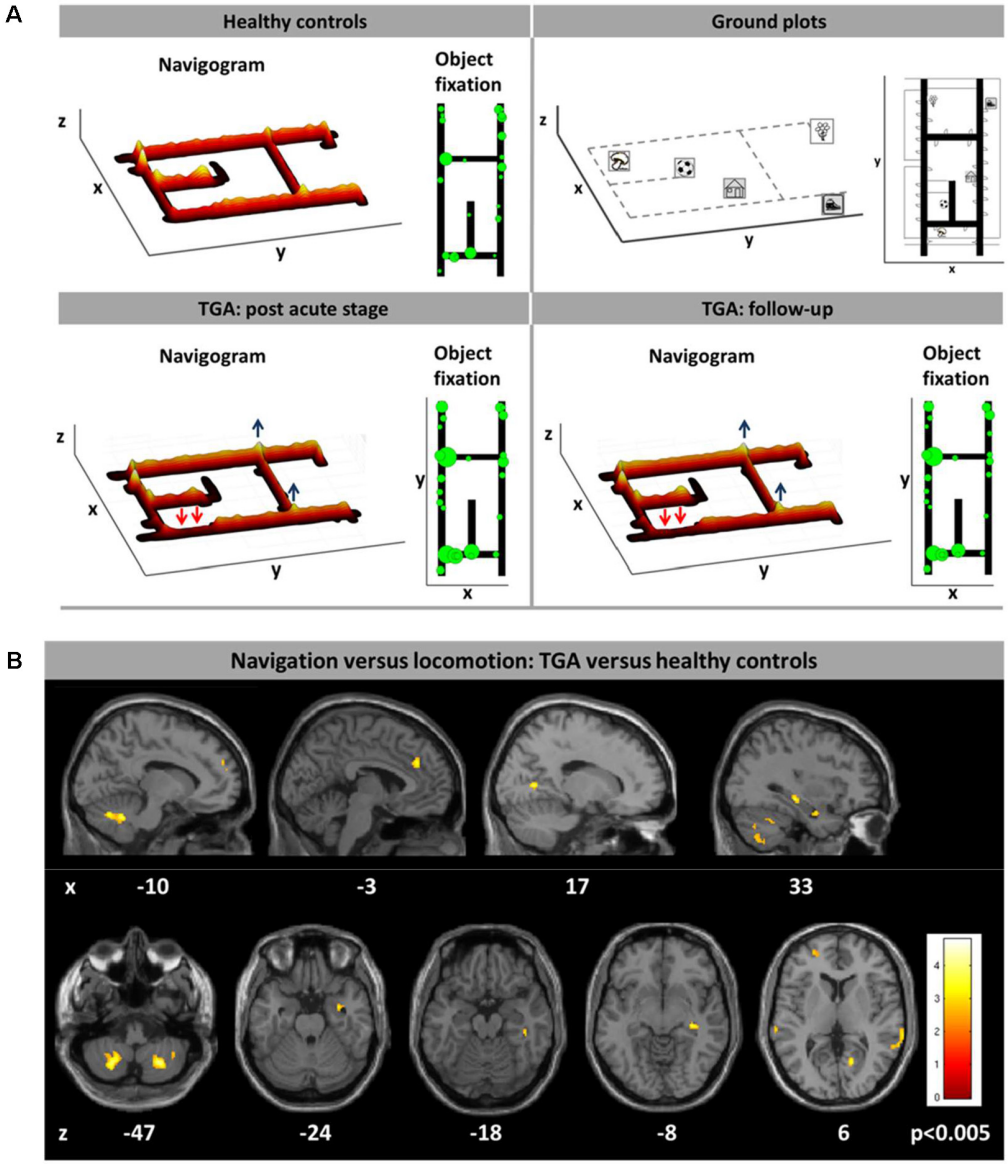

FIGURE 4 | Horizontal real space navigation in patients with transient global amnesia (TGA). **(A)** TGA-patients, as compared to healthy controls, had a different navigation strategy in the post-acute stage (day 3 after symptom onset) with less usage of short cuts (red arrows), a longer duration at strategic way crossings (blue arrows) and more visual fixations along the path, particularly at strategic way crossings. This pattern persisted until follow-up after 3–4 months. Search paths during navigation are color-coded on a ground map (x, y) as the cumulative time at the location (z). The most frequent fixation targets are indicated as green circles on the ground map with diameter proportional to the cumulative time of fixation. **(B)** During navigation in the post-acute stage the regional cerebral glucose metabolism in TGA-patients was increased in the right hippocampus, bilateral posterior parietal, retrosplenial, mesiofrontal cortex, and the cerebellar dentate nucleus, indicating compensatory recruitment of the hippocampal and extrahippocampal navigation network. Significance level $p < 0.005$; the level of sections is given in MNI-coordinates (adapted from Schöberl et al., 2019; permission from the journal obtained).

effect showed a statistical correlation with entorhinal cortex volume. The entorhinal cortex is essential for path integration due to self-motion tracking by grid cell signaling (Moser et al., 2008) and known to be one of the first brain regions to be affected by tau deposition in Alzheimer's pathology (Coughlan et al., 2018). In the aforementioned study, direct measurement of entorhinal activations during the immersive VR path integration task could not be performed due to technical limitations.

A recent real space navigation study in aMCI patients could also differentiate amyloid positive from amyloid negative aMCI patients with high diagnostic accuracy (Schöberl et al., 2020). The main difference between these two groups was an inferior performance for allocentric and egocentric route learning in amyloid positive aMCI patients as compared to amyloid negative patients, who had impaired navigation abilities only on allocentric routes (Schöberl et al., 2020). aMCI patients had decreased activations in the hippocampus, RSC, PPC,

TABLE 1 | Comparison of different virtual reality (VR) and real space-based navigation paradigms.

	Advantages	Limitations	Future applications
2D desktop	High level of control and standardization, combination with fMRI experiments possible	Overly dependency on visual processing, no vestibular or proprioceptive feedback or motor-efference signals, low degree of immersion to VR	Investigation of specific aspects of navigation control (in fMRI), quantification of spatial orientation deficits in patients with cognitive disorders or mobility restrictions
Large-screen	Analysis of eye movements and visual exploration patterns in more naturalistic and ecologically valid environments	High visual dependency, no multisensory feedback or motor-efference signals, the potential for cybersickness, hardly adaptable to online fMRI	Analysis of visual exploration strategies in environments of different scales, textures, and abundance of landmarks
Hybrid	Allows some degree of multisensory feedback and motor-efference control	Increasing risk of cybersickness by sensory mismatch, moderate immersion to VR, restricted degree of interaction, combined with online fMRI not possible	Training of spatial navigation abilities for patients with cognitive disorders or acute/subacute cerebral lesions (e.g., during in-patient rehabilitation)
Head-mounted	Highly interactive allows for multisensory inputs and motor-efference signals, multiple options to track behavior, possibility to go beyond reality	Higher risk of cybersickness, problems with embodiment (in older subjects), the dependence of performance on previous VR experience, combined with online fMRI restricted	Investigation of behavioral responses to controlled environmental changes, the potential for combination with advanced fMRI techniques or PET-based approaches
Real space navigation	Investigation of multisensory contribution to navigation control, analysis of visual exploration patterns in natural environments, navigation in 3D environments, combination with PET imaging to depict navigation-induced brain activations, no cybersickness	Problems with standardization of the navigation task, limitations in experimental manipulation of the task, problems if mobility restrictions exist, potential ceiling effects for repetitive testing	Application as an easy screening test for patients with navigation disorders in clinical routine, analysis of eye movements as a potential biomarker for navigation control, transfer to everyday life situations (by combination with mobile tracking technologies like GPS)

and the PFC, as the underlying correlate of a decreased spatial navigation performance. Differences in performance between both aMCI subgroups were reflected by reduced activations in the hippocampus and PPC in amyloid positive aMCI patients. aMCI patients used more horizontal search saccades and fixations compared to controls (Schöberl et al., 2020), which implies either an increased reliance on visual cues, a disturbed strategy to select relevant visual cues and incorporate them correctly into a spatial cognitive map, or a combination of both (Uiga et al., 2015). Detailed analyses of visual explorations revealed that amyloid positive aMCI patients used fewer landmarks than amyloid negative aMCI patients did. Taken together, the results from VR and real space studies suggest great potential for navigation testing for early and specific detection of aMCI.

NAVIGATION TESTING IN VR AND REAL SPACE—A CRITICAL DISCUSSION

Previous spatial navigation literature in humans shows a predominance of VR based on real space navigation studies (**Table 1**). VR set-ups combined with fMRI has given important insights into cerebral networks underlying navigation control (Maguire et al., 1998; Grön et al., 2000). The current concepts on navigation strategies like stimulus-response, egocentric or location-based, landmark-based, allocentric or spatial map based resulted mostly from studies using VR settings (Ekstrom et al., 2014; Epstein and Vass, 2014; Ekstrom and Isham, 2017; Epstein et al., 2017; Lester et al., 2017). At the beginning of VR development, VR environments were applied in a reductionistic way to study specific aspects of human navigation (i.e., processing of optic flow, perception of visual scenes, identification, selection and use of landmarks). The traditional VR set-ups (like the human variant of the Morris water maze task) were displayed on 2D screens combined with joystick navigation in a sitting position (**Figures 5A,B**). Novel VR technologies allow for more realistic presentations like large-scale projection with eye-tracking, and combination with physical movement on treadmill or by direct immersion of walking, eye and head movements using head-mounted VR systems (Diersch and Wolbers, 2019; **Figures 5C,D**). However, the currently available VR set-ups do have considerable limitations, especially if it comes to application in older subjects and patients with sensory or cognitive disorders: (1) desktop VR has a strong bias towards optic flow and visual processing and therefore does not resemble the multisensory inputs during naturalistic real space navigation; (2) treadmill walking in large-scale VR and highly immersive head-mounted VR systems allow for some degree of optic flow, vestibular and proprioceptive input. However, the dominance of optic flow and visual processing persists. Both approaches may induce subtle sensory temporal mismatch and thus lead to cybersickness (Taube et al., 2013; Diersch and Wolbers, 2019); (3) previous studies have shown that gaming experience and the degree of immersion have an impact on performance in VR tasks (Richardson and Collaer, 2011; Ruddle et al., 2011). Application of immersive VR set-ups may be especially challenging in older subjects, because of missing gaming experience and problems in immersion due to susceptibility to cybersickness. More training sessions, simpler set-ups, reduced optic flow

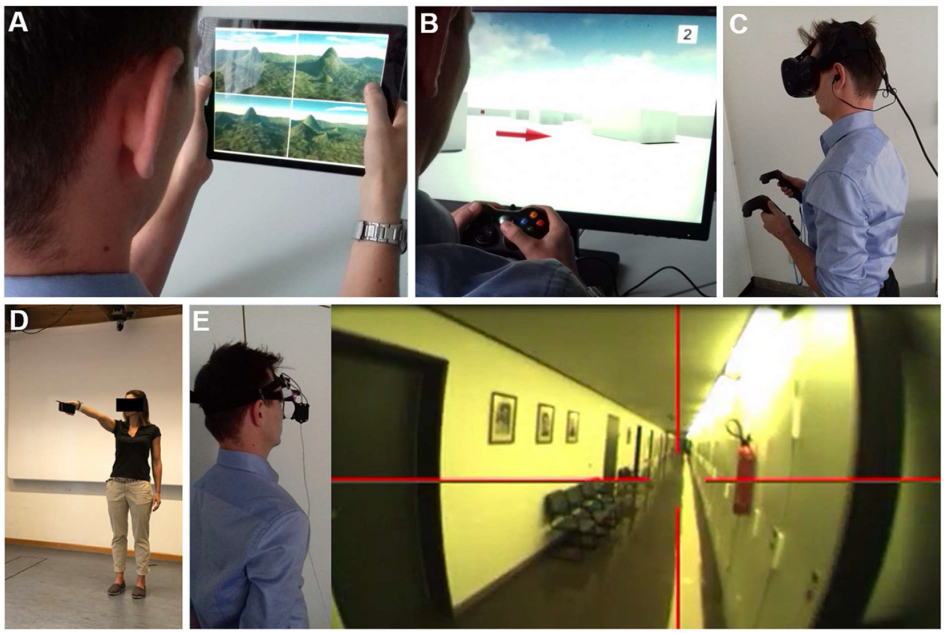

FIGURE 5 | Navigation testing in virtual reality (VR) and real space. Examples of VR set-ups to study spatial navigation using **(A)** a 2D tablet touch screen paradigm (4 Mountains Test, which assesses allocentric spatial memory by altering the viewpoint, colors, and textures of the topographical layout of four mountains within a computer-generated landscape). **(B)** A 2D desktop screen paradigm with joystick navigation. **(C)** A VR paradigm displayed with a head-mounted device and motion recording. The degree of immersion increased from **(A–C)**. Functional MRI (fMRI) based studies are mostly possible in 2D paradigms and hard to achieve in immersive VR set-ups. Examples of real space spatial orientation and navigation testing by **(D)** pointing experiments to a known position in vista space (Flanagin et al., 2019) and **(E)** navigation in large-scale environments. Navigation strategy and visual exploration patterns are recorded by a head-mounted eye-tracking system and are analyzed *post hoc* in navigograms. Brain activations during real space navigation can be captured by an [^{18}F]FDG-PET based approach.

and movement speed can improve comfort of subjects in VR (Diersch and Wolbers, 2019); and (4) immersive head-mounted VR systems cannot easily be combined with synchronous fMRI to depict navigation-induced brain activations (Diersch and Wolbers, 2019; Howett et al., 2019). Alternative approaches like *post hoc* imagination and memorization in fMRI or fMRI adaptation may be used to overcome this problem partially (Hassabis et al., 2009; Doeller et al., 2010; Morgan et al., 2011; Schinazi et al., 2013; Epstein et al., 2017). Imagination techniques in fMRI may also be used after learning spatial layouts of real environments (Howard et al., 2014; Javadi et al., 2017; Brunec et al., 2018; Patai et al., 2019). Indeed, these approaches increased our understanding of the different roles of the hippocampus, entorhinal, retrosplenial and PFC for human spatial navigation. Nevertheless, certain limitations exist, especially the lack of vestibular and somatosensory inputs during the fMRI-trial sessions. The very extensive and strict training program, which is necessary for a successful *post hoc* trial period, is somehow artificial, as the spatial layout of our surrounding environments is not learned as systematically in everyday life. While the task design can be applied successfully to young and healthy students, older subjects and patients with neurological disorders (i.e., cognitive decline, acute brain lesions) might have more problems in learning these paradigms, which might cause high dropout rates.

Despite considerable advances in the development of VR technologies and novel "hybrid-approaches" (i.e., immersive VR plus treadmill-locomotion, *post hoc* mental navigation of previously learned real space environments), human real space navigation still remains the benchmark to study the processing and integration of multiple sensory inputs during navigation in an everyday life scenario. This does not only include optic flow, vestibular and proprioceptive inputs but potentially also auditory and olfactory stimuli. All these sensory modalities have to be continuously weighted in a natural environment to extract the ones important for spatial navigation. Thus, not only the integration but also intentional suppression of rather disturbing or conflicting sensory inputs might be of high relevance during real space navigation. Real space orientation can be implemented in paradigms like pointing to known landmarks or navigating in large-scale environments (**Figure 5E**). Older subjects or patients with neurological disorders tend to accept and tolerate real space navigation better because they are used to it. A disadvantage of real space paradigms is the more difficult standardization and experimental manipulation. Repetitive testing in the known spatial environment may lead to a ceiling effect of navigation performance.

CONCLUSIONS

VR and real space navigation paradigms have contributed to the understanding of human spatial navigation control and thus seem to be complementary. VR settings may have advantages

for the investigation of specific aspects of navigation control, because they can be ecologically applied, excellently controlled and manipulated. Immersive VR tasks, for example, have helped to disentangle the role of the hippocampus for coding spatial and temporal metrics in a concrete manner (Hassabis et al., 2009; Morgan et al., 2011; Schinazi et al., 2013). However, VR based approaches may be limited by the over-reliance on visual input while neglecting vestibular, somatosensory and motor-efference signal processing. More recent "hybrid-approaches" such as combining head-mounted VR techniques with treadmill-locomotion or fMRI with mentalization of recently learned real environments significantly increased our understanding of the exact contribution of core components of the human spatial navigation network and the cue-dependence of spatial memory retrieval (Howard et al., 2014; Javadi et al., 2017; Huffman and Ekstrom, 2019; Patai et al., 2019). Nevertheless, real space navigation experiments with a dedicated analysis of eye movement data and navigation strategies may help to study the sensory contribution to navigation in more detail. Recent studies have clearly shown that this approach is feasible to investigate the physiological control of navigation in healthy subjects, as well as the pathology of spatial navigation disorders in patients with sensory disorders, acute cerebral lesions and chronic brain dysfunction due to neurodegeneration. It thereby can help to identify patients at risk for impending dementia. Real space navigation paradigms are potentially easier to apply to neurological patients because problems like cybersickness due to sensory mismatch can be avoided. Future strategies of navigation testing should aim to bridge the gap between laboratory and bedside conditions. Navigation testing in clinical routine needs to be time-economical and reliable in the detection of deficits of cerebral navigation control.

AUTHOR CONTRIBUTIONS

FS: drafting and revising the manuscript, review of literature, concept and design of article. AZ: drafting and revising the manuscript, review of literature, concept and design of article. TB: drafting and revising the manuscript, concept and design of article.

FUNDING

We acknowledge funding from the German Federal Ministry of Education and Research (Bundesministerium für Bildung und Forschung, BMBF) in the context of the foundation of the German Center for Vertigo and Balance Disorders (DSGZ; grant number 01 EO 0901) and from the Hertie Foundation (Gemeinnützige Hertie-Stiftung).

ACKNOWLEDGMENTS

We thank Katie Göttlinger for copyediting the article.

REFERENCES

Aguirre, G. K., and D'Esposito, M. (1999). Topographical disorientation: a synthesis and taxonomy. *Brain* 122, 1613–1628. doi: 10.1093/brain/122.9.1613

Aguirre, G. K., Detre, J. A., Alsop, D. C., and D'Esposito, M. (1996). The parahippocampus subserves topographical learning in man. *Cereb. Cortex* 6, 823–829. doi: 10.1093/cercor/6.6.823

Allison, S. L., Fagan, A. M., Morris, J. C., and Head, D. (2016). Spatial navigation in preclinical Alzheimer's disease. *J. Alzheimers Dis.* 52, 77–90. doi: 10.3233/JAD-150855

Astur, R. S., Taylor, L. B., Mamelak, A. N., Philpott, L., and Sutherland, R. J. (2002). Humans with hippocampus damage display severe spatial memory impairments in a virtual Morris water task. *Behav. Brain Res.* 132, 77–84. doi: 10.1016/s0166-4328(01)00399-0

Baek, J. H., Zheng, Y., Darlington, C. L., and Smith, P. F. (2010). Evidence that spatial memory deficits following bilateral vestibular deafferentation in rats are probably permanent. *Neurobiol. Learn. Mem.* 94, 402–413. doi: 10.1016/j.nlm.2010.08.007

Bartsch, T., Alfke, K., Stingele, R., Rohr, A., Freitag-Wolf, S., Jansen, O., et al. (2006). Selective affection of hippocampal CA-1 neurons in patients with transient global amnesia without long-term sequelae. *Brain* 129, 2874–2884. doi: 10.1093/brain/awl248

Bartsch, T., and Butler, C. (2013). Transient amnesic syndromes. *Nat. Rev. Neurol.* 9, 86–97. doi: 10.1038/nrneurol.2012.264

Bartsch, T., and Deuschl, G. (2010). Transient global amnesia: functional anatomy and clinical implications. *Lancet Neurol.* 9, 205–214. doi: 10.1016/s1474-4422(09)70344-8

Bartsch, T., Schönfeld, R., Müller, F. J., Alfke, K., Leplow, B., Aldenhoff, J., et al. (2010). Focal lesions of human hippocampal CA1 neurons in transient global amnesia impair place memory. *Science* 328, 1412–1415. doi: 10.1126/science.1188160

Bates, S. L., and Wolbers, T. (2014). How cognitive aging affects multisensory integration of navigational cues. *Neurobiol. Aging* 35, 2761–2769. doi: 10.1016/j.neurobiolaging.2014.04.003

Berthoz, A. (1997). Parietal and hippocampal contribution to topokinetic and topographic memory. *Philos. Trans. R. Soc. Lond. B Biol. Sci.* 352, 1437–1448. doi: 10.1098/rstb.1997.0130

Boccia, M., Nemmi, F., and Guariglia, C. (2014). Neuropsychology of environmental navigation in humans: review and meta-analysis of FMRI studies in healthy participants. *Neuropsychol. Rev.* 24, 236–251. doi: 10.1007/s11065-014-9247-8

Bohbot, V. D., McKenzie, S., Konishi, K., Fouquet, C., Kurdi, V., Schachar, R., et al. (2012). Virtual navigation strategies from childhood to senescence: evidence for changes across the life span. *Front. Aging Neurosci.* 4:28. doi: 10.3389/fnagi.2012.00028

Braak, H., and Braak, E. (1995). Staging of Alzheimer's disease-related neurofibrillary changes. *Neurobiol. Aging* 16, 271–284. doi: 10.1016/0197-4580(95)00021-6

Braak, H., and Braak, E. (1998). Evolution of neuronal changes in the course of Alzheimer's disease. *J. Neural Transm. Suppl.* 53, 127–140. doi: 10.1007/978-3-7091-6467-9_11

Braak, H., Braak, E., and Bohl, J. (1993). Staging of Alzheimer-related cortical destruction. *Eur. Neurol.* 33, 403–408. doi: 10.1159/000116984

Brandt, T., and Dieterich, M. (2013). "Right door," wrong floor: a canine deficiency in navigation. *Hippocampus* 23, 245–246. doi: 10.1002/hipo.22091

Brandt, T., and Dieterich, M. (2016). Vestibular contribution to three-dimensional dynamic (allocentric) and two-dimensional static (egocentric) spatial memory. *J. Neurol.* 263, 1015–1016. doi: 10.1007/s00415-016-8067-6

Brandt, T., Schautzer, F., Hamilton, D. A., Brüning, R., Markowitsch, H. J., Kalla, R., et al. (2005). Vestibular loss causes hippocampal atrophy and impaired spatial memory in humans. *Brain* 128, 2732–2741. doi: 10.1093/brain/awh617

Brandt, T., Zwergal, A., and Glasauer, S. (2017). 3-D spatial memory and navigation: functions and disorders. *Curr. Opin. Neurol.* 30, 90–97. doi: 10.1097/WCO.0000000000000415

Brown, T. I., and Stern, C. E. (2014). Contributions of medial temporal lobe and striatal memory systems to learning and retrieving overlapping

spatial memories. *Cereb. Cortex* 24, 1906–1922. doi: 10.1093/cercor/bht041

Brunec, I. K., Bellana, B., Ozubko, J. D., Man, V., Robin, J., Liu, Z.-X., et al. (2018). Multiple scales of representation along the hippocampal anteroposterior axis in humans. *Curr. Biol.* 28, 2129.e6–2135.e6. doi: 10.1016/j.cub.2018.05.016

Burgess, N., Maguire, E. A., and O'Keefe, J. (2002). The human hippocampus and spatial and episodic memory. *Neuron* 35, 625–641. doi: 10.1016/s0896-6273(02)00830-9

Burt de Perera, T., and Holbrook, R. I. (2012). Three-dimensional spatial representation in freely swimming fish. *Cogn. Process.* 13, S107–S111. doi: 10.1007/s10339-012-0473-9

Burt de Perera, T., Holbrook, R., Davis, V., Kacelnik, A., and Guilford, T. (2013). Navigating in a volumetric world: metric encoding in the vertical axis of space. *Behav. Brain Sci.* 36, 546–547. doi: 10.1017/s0140525x13000344

Chersi, F., and Burgess, N. (2015). The cognitive architecture of spatial navigation: hippocampal and striatal contributions. *Neuron* 88, 64–77. doi: 10.1016/j.neuron.2015.09.021

Chrastil, E. R., and Warren, W. H. (2012). Active and passive contributions to spatial learning. *Psychon. Bull. Rev.* 19, 1–23. doi: 10.3758/s13423-011-0182-x

Chrastil, E. R., and Warren, W. H. (2013). Active and passive spatial learning in human navigation: acquisition of survey knowledge. *J. Exp. Psychol. Learn. Mem. Cogn.* 39, 1520–1537. doi: 10.1037/a0032382

Ciaramelli, E., Grady, C., Levine, B., Ween, J., and Moscovitch, M. (2010). Top-down and bottom-up attention to memory are dissociated in posterior parietal cortex: neuroimagingand and neuropsychological evidence. *J. Neurosci.* 30, 4943–4956. doi: 10.1523/jneurosci.1209-09.2010

Claessen, M. H. G., and van der Ham, I. J. M. (2017). Classification of navigation impairment: a systematic review of neuropsychological case studies. *Neurosci. Biobehav. Rev.* 73, 81–97. doi: 10.1016/j.neubiorev.2016.12.015

Costello, M. C., and Bloesch, E. K. (2017). Are older adults less embodied? A review of age effects through the lens of embodied cognition. *Front. Psychol.* 8:267. doi: 10.3389/fpsyg.2017.00267

Coughlan, G., Laczó, J., Hort, J., Minihane, A. M., and Hornberger, M. (2018). Spatial navigation deficits—overlooked cognitive marker for preclinical Alzheimer disease? *Nat. Rev. Neurol.* 14, 496–506. doi: 10.1038/s41582-018-0031-x

Cullen, K. E., and Taube, J. S. (2017). Our sense of direction: progress, controversies and challenges. *Nat. Neurosci.* 20, 1465–1473. doi: 10.1038/nn.4658

Cushman, L. A., Stein, K., and Duffy, C. J. (2008). Detecting navigational deficits in cognitive aging and Alzheimer disease using virtual reality. *Neurology* 71, 888–895. doi: 10.1212/01.wnl.0000326262.67613.fe

Diersch, N., and Wolbers, T. (2019). The potential of virtual reality for spatial navigation research across the adult lifespan. *J. Exp. Biol.* 222:jeb187252. doi: 10.1242/jeb.187252

Dilks, D. D., Julian, J. B., Paunov, A. M., and Kanwisher, N. (2013). The occipital place area is causally and selectively involved in scene perception. *J. Neurosci.* 33, 1331a–1336a. doi: 10.1523/jneurosci.4081-12.2013

Doeller, C. F., Barry, C., and Burgess, N. (2010). Evidence for grid cells in a human memory network. *Nature* 463, 657–661. doi: 10.1038/nature08704

Ekstrom, A. D. (2015). Why vision is important to how we navigate. *Hippocampus* 25, 731–735. doi: 10.1002/hipo.22449

Ekstrom, A. D., Arnold, A. E. G. F., and Iaria, G. (2014). A critical review of the allocentric spatial representation and its neural underpinnings: toward a network-based perspective. *Front. Hum. Neurosci.* 8:803. doi: 10.3389/fnhum.2014.00803

Ekstrom, A. D., Huffman, D. J., and Starrett, M. (2017). Interacting networks of brain regions underlie human spatial navigation: a review and novel synthesis of the literature. *J. Neurophysiol.* 118, 3328–3344. doi: 10.1152/jn.00531.2017

Ekstrom, A. D., and Isham, E. A. (2017). Human spatial navigation: representations across dimensions and scales. *Curr. Opin. Behav. Sci.* 17, 84–89. doi: 10.1016/j.cobeha.2017.06.005

Epstein, R., Harris, A., Stanley, D., and Kanwisher, N. (1999). The parahippocampal place area: recognition, navigation, or encoding? *Neuron* 23, 115–125. doi: 10.1016/s0896-6273(00)80758-8

Epstein, R. A., Higgins, J. S., and Thompson-Schill, S. L. (2005). Learning places from views: variation in scene processing as a function of experience and navigational ability. *J. Cogn. Neurosci.* 17, 73–83. doi: 10.1162/0898929052879987

Epstein, R., and Kanwisher, N. (1998). A cortical representation of the local visual environment. *Nature* 392, 598–601. doi: 10.1038/33402

Epstein, R. A., Patai, E. Z., Julian, J. B., and Spiers, H. J. (2017). The cognitive map in humans: spatial navigation and beyond. *Nat Neurosci.* 20, 1504–1513. doi: 10.1038/nn.4656

Epstein, R. A., and Vass, L. K. (2014). Neural systems for landmark-based wayfinding in humans. *Philos. Trans. R. Soc. Lond. B Biol. Sci.* 369:20120533. doi: 10.1098/rstb.2012.0533

Flanagin, V. L., Fisher, P., Olcay, B., Kohlbecher, S., and Brandt, T. (2019). A bedside application-based assessment of spatial orientation and memory: approaches and lessons learned. *J. Neurol.* 266, 126–138. doi: 10.1007/s00415-019-09409-7

Flores-Abreu, I. N., Hurly, T. A., Ainge, J. A., and Healy, S. D. (2014). Three-dimensional space: locomotory style explains memory differences in rats and hummingbirds. *Proc. Biol. Sci.* 281:20140301. doi: 10.1098/rspb.2014.0301

Frissen, I., Campos, J. L., Souman, J. L., and Ernst, M. O. (2011). Integration of vestibular and proprioceptive signals for spatial updating. *Exp. Brain Res.* 212, 163–176. doi: 10.1007/s00221-011-2717-9

Ghaem, O., Mellet, E., Crivello, F., Tzourio, N., Mazoyer, B., Berthoz, A., et al. (1997). Mental navigation along memorized routes activates the hippocampus, precuneus, and insula. *Neuroreport* 8, 739–744. doi: 10.1097/00001756-199702100-00032

Grön, G., Wunderlich, A. P., Spitzer, M., Tomczak, R., and Riepe, M. W. (2000). Brain activation during human navigation: gender-different neural networks as substrate of performance. *Nat. Neurosci.* 3, 404–408. doi: 10.1038/73980

Guariglia, C., Piccardi, L., Iaria, G., Nico, D., and Pizzamiglio, L. (2005). Representational neglect and navigation in real space. *Neuropsychologia* 43, 1138–1143. doi: 10.1016/j.neuropsychologia.2004.11.021

Hartley, T., and Harlow, R. (2012). An association between human hippocampal volume and topographical memory in healthy young adults. *Front. Hum. Neurosci.* 6:338. doi: 10.3389/fnhum.2012.00338

Hartley, T., Maguire, E. A., Spiers, H. J., and Burgess, N. (2003). The well-worn route and the path less traveled: distinct neural bases of route following and wayfinding in humans. *Neuron* 37, 877–888. doi: 10.1016/s0896-6273(03)00095-3

Hassabis, D., Chu, C., Rees, G., Weiskopf, N., Molyneux, P. D., and Maguire, E. A. (2009). Decoding neuronal ensembles in the human hippocampus. *Curr. Biol.* 19, 546–554. doi: 10.1016/j.cub.2009.02.033

Hirshhorn, M., Grady, C., Rosenbaum, R. S., Winocur, G., and Moscovitch, M. (2012). The hippocampus is involved in mental navigation for a recently learned, but not a highly familiar environment: a longitudinal fMRI study. *Hippocampus* 22, 842–852. doi: 10.1002/hipo.20944

Hort, J., Laczó, J., Vyhnálek, M., Bojar, M., Bures, J., and Vlcek, K. (2007). Spatial navigation deficit in amnestic mild cognitive impairment. *Proc. Natl. Acad. Sci. U S A* 104, 4042–4047. doi: 10.1073/pnas.0611314104

Howard, L. R., Javadi, A. H., Yu, Y., Mill, R. D., Morrison, L. C., Knight, R., et al. (2014). The hippocampus and entorhinal cortex encode the path and Euclidean distances to goals during navigation. *Curr. Biol.* 24, 1331–1340. doi: 10.1016/j.cub.2014.05.001

Howett, D., Castegnaro, A., Krzywicka, K., Hagman, J., Marchment, D., Henson, R., et al. (2019). Differentiation of mild cognitive impairment using an entorhinal cortex-based test of virtual reality navigation. *Brain* 142, 1751–1766. doi: 10.1093/brain/awz116

Huffman, D. J., and Ekstrom, A. D. (2019). A modality-independent network underlies the retrieval of large-scale spatial environments in the human brain. *Neuron* 104, 611.e7–622.e7. doi: 10.1016/j.neuron.2019.08.012

Hwang, E. J., and Andersen, R. A. (2009). Brain control of movement execution onset using local field potentials in posterior parietal cortex. *J. Neurosci.* 29, 14363–14370. doi: 10.1523/jneurosci.2081-09.2009

Hwang, E. J., Hauschild, M., Wilke, M., and Andersen, R. A. (2014). Spatial and temporal eye-hand coordination relies on the parietal reach region. *J. Neurosci.* 34, 12884–12892. doi: 10.1523/jneurosci.3719-13.2014

Iaria, G., Petrides, M., Dagher, A., Pike, B., and Bohbot, V. D. (2003). Cognitive strategies dependent on the hippocampus and caudate nucleus in human navigation: variability and change with practice. *J. Neurosci.* 23, 5945–5952. doi: 10.1523/jneurosci.23-13-05945.2003

Irving, S., Pradhan, C., Dieterich, M., Brandt, T., Zwergal, A., and Schöberl, F. (2018a). Transient topographical disorientation due to right-sided hippocampal hemorrhage. *Brain Behav.* 8:e01078. doi: 10.1002/brb3.1078

Irving, S., Schöberl, F., Pradhan, C., Brendel, M., Bartenstein, P., Dieterich, M., et al. (2018b). A novel real-space navigation paradigm reveals age- and gender-dependent changes of navigational strategies and hippocampal activation. *J. Neurol.* 265, 113–126. doi: 10.1007/s00415-018-8987-4

Jahn, K., and Zwergal, A. (2010). Imaging supraspinal locomotor control in balance disorders. *Restor. Neurol. Neurosci.* 28, 105–114. doi: 10.3233/rnn-2010-0506

Jandl, N. M., Sprenger, A., Wojak, J. F., Göttlich, M., Münte, T. F., Krämer, U. M., et al. (2015). Dissociable cerebellar activity during spatial navigation and visual memory in bilateral vestibular failure. *Neuroscience* 305, 257–267. doi: 10.1016/j.neuroscience.2015.07.089

Javadi, A.-H., Emo, B., Howard, L. R., Zisch, F. E., Yu, Y., Knight, R., et al. (2017). Hippocampal and prefrontal processing of network topology to simulate the future. *Nat. Commun.* 8:14652. doi: 10.1038/ncomms14652

Jeffery, K. J., Jovalekic, A., Verriotis, M., and Hayman, R. (2013). Navigating in a three-dimensional world. *Behav. Brain Sci.* 36, 523–543. doi: 10.1017/S0140525X12002476

Kamps, F. S., Julian, J. B., Kubilius, J., Kanwisher, N., and Dilks, D. D. (2016). The occipital place area represents the local elements of scenes. *NeuroImage* 132, 417–424. doi: 10.1016/j.neuroimage.2016.02.062

Kaplan, R., King, J., Koster, R., Penny, W. D., Burgess, N., and Friston, K. J. (2017). The neural representation of prospective choice during spatial planning and decisions. *PLoS Biol.* 15:e1002588. doi: 10.1371/journal.pbio.1002588

Kim, J. W., Byun, M. S., Sohn, B. K., Yi, D., Seo, E. H., Choe, Y. M., et al. (2017). Clinical dementia rating orientation score as an excellent predictor of the progression to Alzheimer's disease in mild cognitive impairment. *Psychiatry Investig.* 14, 420–426. doi: 10.4306/pi.2017.14.4.420

Kim, M., Jeffery, K. J., and Maguire, E. A. (2017). Multivoxel pattern analysis reveals 3D place information in the human hippocampus. *J. Neurosci.* 37, 4270–4279. doi: 10.1523/jneurosci.2703-16.2017

Kim, M., and Maguire, E. A. (2019a). Can we study 3D grid codes non-invasively in the human brain? Methodological considerations and fMRI findings. *NeuroImage* 186, 667–678. doi: 10.1016/j.neuroimage.2018.11.041

Kim, M., and Maguire, E. A. (2019b). Encoding of 3D head direction information in the human brain. *Hippocampus* 29, 619–629. doi: 10.1002/hipo.23060

Kremmyda, O., Hüfner, K., Flanagin, V. L., Hamilton, D. A., Linn, J., Strupp, M., et al. (2016). Beyond dizziness: virtual navigation, spatial anxiety and hippocampal volume in bilateral vestibulopathy. *Front. Hum. Neurosci.* 10:139. doi: 10.3389/fnhum.2016.00139

Laczó, J., Andel, R., Vyhnalek, M., Vlcek, K., Magerova, H., Varjassyova, A., et al. (2010). Human analogue of the morris water maze for testing subjects at risk of Alzheimer's disease. *Neurodegener. Dis.* 7, 148–152. doi: 10.1159/000289226

Laczó, J., Vlcek, K., Vyhnálek, M., Vajnerová, O., Ort, M., Holmerová, I., et al. (2009). Spatial navigation testing discriminates two types of amnestic mild cognitive impairment. *Behav. Brain Res.* 202, 252–259. doi: 10.1016/j.bbr.2009.03.041

la Fougère, C., Zwergal, A., Rominger, A., Förster, S., Fesl, G., Dieterich, M., et al. (2010). Real versus imagined locomotion: a [18F]-FDG PET-fMRI comparison. *NeuroImage* 50, 1589–1598. doi: 10.1016/j.neuroimage.2009.12.060

Lester, A. W., Moffat, S. D., Wiener, J. M., Barnes, C. A., and Wolbers, T. (2017). The aging navigational system. *Neuron* 95, 1019–1035. doi: 10.1016/j.neuron.2017.06.037

Lithfous, S., Dufour, A., and Després, O. (2013). Spatial navigation in normal aging and the prodromal stage of Alzheimer's disease: insights from imaging and behavioral studies. *Ageing Res. Rev.* 12, 201–213. doi: 10.1016/j.arr.2012.04.007

Loomis, J. M., Klatzky, R. L., Golledge, R. G., Cicinelli, J. G., Pellegrino, J. W., and Fry, P. A. (1993). Nonvisual navigation by blind and sighted: assessment of path integration ability. *J. Exp. Psychol. Gen.* 122, 73–91. doi: 10.1037/0096-3445.122.1.73

Maguire, E. A., Burgess, N., Donnett, J. G., Frackowiak, R. S., Frith, C. D., and O'Keefe, J. (1998). Knowing where and getting there: a human navigation network. *Science* 280, 921–924. doi: 10.1126/science.280.5365.921

Maguire, E. A., Gadian, D. G., Johnsrude, I. S., Good, C. D., Ashburner, J., Frackowiak, R. S., et al. (2000). Navigation-related structural change in the hippocampi of taxi drivers. *Proc. Natl. Acad. Sci. U S A* 97, 4398–4403. doi: 10.1073/pnas.070039597

Maguire, E. A., Nannery, R., and Spiers, H. J. (2006). Navigation around London by a taxi driver with bilateral hippocampal lesions. *Brain* 129, 2894–2907. doi: 10.1093/brain/awl286

Maguire, E. A., Spiers, H. J., Good, C. D., Hartley, T., Frackowiak, R. S. J., and Burgess, N. (2003). Navigation expertise and the human hippocampus: a structural brain imaging analysis. *Hippocampus* 13, 250–259. doi: 10.1002/hipo.10087

Marchette, S. A., Ryan, J., and Epstein, R. A. (2017). Schematic representations of local environmental space guide goal-directed navigation. *Cognition* 158, 68–80. doi: 10.1016/j.cognition.2016.10.005

Marchette, S. A., Vass, L. K., Ryan, J., and Epstein, R. A. (2014). Anchoring the neural compass: coding of local spatial reference frames in human medial parietal lobe. *Nat. Neurosci.* 17, 1598–1606. doi: 10.1038/nn.3834

McCormick, C., Ciaramelli, E., De Luca, F., and Maguire, E. A. (2018). Comparing and contrasting the cognitive effects of hippocampal and ventromedial prefrontal cortex damage: a review of human lesion studies. *Neuroscience* 374, 295–318. doi: 10.1016/j.neuroscience.2017.07.066

McCormick, C., Rosenthal, C. R., Miller, T. D., and Maguire, E. A. (2017). Deciding what is possible and impossible following hippocampal damage in humans. *Hippocampus* 27, 303–314. doi: 10.1002/hipo.22694

Morgan, L. K., Macevoy, S. P., Aguirre, G. K., and Epstein, R. A. (2011). Distances between real-world locations are represented in the human hippocampus. *J. Neurosci.* 31, 1238–1245. doi: 10.1523/JNEUROSCI.4667-10.2011

Moser, E. I., Kropff, E., and Moser, M. B. (2008). Place cells, grid cells, and the brain's spatial representation system. *Annu. Rev. Neurosci.* 31, 69–89. doi: 10.1146/annurev.neuro.31.061307.090723

Nadel, L., and Moscovitch, M. (1997). Memory consolidation, retrograde amnesia and the hippocampal complex. *Curr. Opin. Neurobiol.* 7, 217–227. doi: 10.1016/s0959-4388(97)80010-4

Nadel, L., Samsonovich, A., Ryan, L., and Moscovitch, M. (2000). Multiple trace theory of human memory: computational, neuroimaging and neuropsychological results. *Hippocampus* 10, 352–368. doi: 10.1002/1098-1063(2000)10:4<352::aid-hipo2>3.0.co;2-d

Nielson, D. M., Smith, T. A., Sreekumar, V., Dennis, S., and Sederberg, P. B. (2015). Human hippocampus represents space and time during retrieval of real-world memories. *Proc. Natl. Acad. Sci. U S A* 112, 11078–11083. doi: 10.1073/pnas.1507104112

Nyffeler, T., Gutbrod, K., Pflugshaupt, T., von Wartburg, R., Hess, C. W., and Müri, R. M. (2005). Allocentric and egocentric spatial impairments in a case of topographical disorientation. *Cortex* 41, 133–143. doi: 10.1016/s0010-9452(08)70888-8

Ohnishi, T., Matsuda, H., Hirakata, M., and Ugawa, Y. (2006). Navigation ability dependent neural activation in the human brain: an fMRI study. *Neurosci. Res.* 55, 361–369. doi: 10.1016/j.neures.2006.04.009

Packard, M. G., and Knowlton, B. J. (2002). Learning and memory functions of the Basal Ganglia. *Annu. Rev. Neurosci.* 25, 563–593. doi: 10.1146/annurev.neuro.25.112701.142937

Packard, M. G., and McGaugh, J. L. (1992). Double dissociation of fornix and caudate nucleus lesions on acquisition of two water maze tasks: further evidence for multiple memory systems. *Behav. Neurosci.* 106, 439–446. doi: 10.1037/0735-7044.106.3.439

Pai, M.-C., and Jacobs, W. J. (2004). Topographical disorientation in community-residing patients with Alzheimer's disease. *Int. J. Geriatr. Psychiatry* 19, 250–255. doi: 10.1002/gps.1081

Patai, E. Z., Javadi, A.-H., Ozubko, J. D., O'Callaghan, A., Ji, S., Robin, J., et al. (2019). Hippocampal and retrosplenial goal distance coding after long-term consolidation of a real-world environment. *Cereb. Cortex* 29, 2748–2758. doi: 10.1093/cercor/bhz044

Pennartz, C. M. A., Ito, R., Verschure, P. F. M. J., Battaglia, F. P., and Robbins, T. W. (2011). The hippocampal-striatal axis in learning, prediction and goal-directed behavior. *Trends Neurosci.* 34, 548–559. doi: 10.1016/j.tins.2011.08.001

Richardson, A. E., and Collaer, M. L. (2011). Virtual navigation performance: the relationship to field of view and prior video gaming experience. *Percept. Mot. Skills* 112, 477–498. doi: 10.2466/22.24.pms.112.2.477-498

Ritchie, K., Carrière, I., Howett, D., Su, L., Hornberger, M., O'Brien, J. T., et al. (2018). Allocentric and egocentric spatial processing in middle-aged adults at high risk of late-onset Alzheimer's disease: the PREVENT dementia study. *J. Alzheimers Dis.* 65, 885–896. doi: 10.3233/jad-180432

Ruddle, R. A., and Lessels, S. (2006). For efficient navigational search, humans require full physical movement, but not a rich visual scene. *Psychol. Sci.* 17, 460–465. doi: 10.1111/j.1467-9280.2006.01728.x

Ruddle, R. A., Volkova, E., Mohler, B., and Bülthoff, H. H. (2011). The effect of landmark and body-based sensory information on route knowledge. *Mem. Cognit.* 39, 686–699. doi: 10.3758/s13421-010-0054-z

Rusconi, M. L., Suardi, A., Zanetti, M., and Rozzini, L. (2015). Spatial navigation in elderly healthy subjects, amnestic and non amnestic MCI patients. *J. Neurol. Sci.* 359, 430–437. doi: 10.1016/j.jns.2015.10.010

Russell, N. A., Horii, A., Smith, P. F., Darlington, C. L., and Bilkey, D. K. (2003a). Long-term effects of permanent vestibular lesions on hippocampal spatial firing. *J. Neurosci.* 23, 6490–6498. doi: 10.1523/jneurosci.23-16-06490.2003

Russell, N. A., Horii, A., Smith, P. F., Darlington, C. L., and Bilkey, D. K. (2003b). Bilateral peripheral vestibular lesions produce long-term changes in spatial learning in the rat. *J. Vestib. Res.* 13, 9–16.

Schautzer, F., Hamilton, D., Kalla, R., Strupp, M., and Brandt, T. (2003). Spatial memory deficits in patients with chronic bilateral vestibular failure. *Ann. N Y Acad. Sci.* 1004, 316–324. doi: 10.1196/annals.1303.029

Schinazi, V. R., Nardi, D., Newcombe, N. S., Shipley, T. F., and Epstein, R. A. (2013). Hippocampal size predicts rapid learning of a cognitive map in humans. *Hippocampus* 23, 515–528. doi: 10.1002/hipo.22111

Schöberl, F., Irving, S., Pradhan, C., Bardins, S., Trapp, C., Schneider, E., et al. (2019). Prolonged allocentric navigation deficits indicate hippocampal damage in TGA. *Neurology* 92, e234–e243. doi: 10.1212/wnl.0000000000006779

Schöberl, F., Pradhan, C., Irving, S., Buerger, K., Xiong, G., Kugler, G., et al. (2020). Real space navigation testing differentiates between amyloid-positive and -negative aMCI. *Neurology* doi: 10.1212/wnl.0000000000008758 [Epub ahead of print].

Shinder, M. E., and Taube, J. S. (2010). Differentiating ascending vestibular pathways to the cortex involved in spatial cognition. *J. Vestib. Res.* 20, 3–23. doi: 10.3233/ves-2010-0344

Smith, P. F. (1997). Vestibular-hippocampal interactions. *Hippocampus* 7, 465–471. doi: 10.1002/(sici)1098-1063(1997)7:5<465::aid-hipo3>3.0.co;2-g

Smith, P. F., Darlington, C. L., and Zhen, Y. (2015). The effects of complete vestibular deafferentation on spatial memory and the hippocampus in the rat: the Dunedin experience. *Multisens. Res.* 28, 461–485. doi: 10.1163/22134808-00002469

Smith, P. F., Horii, A., Russell, N., Bilkey, D. K., Zheng, Y., Liu, P., et al. (2005). The effects of vestibular lesions on hippocampal function in rats. *Prog. Neurobiol.* 75, 391–405. doi: 10.1016/j.pneurobio.2005.04.004

Spiers, H. J., and Gilbert, S. J. (2015). Solving the detour problem in navigation: a model of prefrontal and hippocampal interactions. *Front. Hum. Neurosci.* 9:125. doi: 10.3389/fnhum.2015.00125

Spiers, H. J., and Maguire, E. A. (2006). Thoughts, behaviour, and brain dynamics during navigation in the real world. *NeuroImage* 31, 1826–1840. doi: 10.1016/j.neuroimage.2006.01.037

Stackman, R. W., Clark, A. S., and Taube, J. S. (2002). Hippocampal spatial representations require vestibular input. *Hippocampus* 12, 291–303. doi: 10.1002/hipo.1112

Stackman, R. W., and Taube, J. S. (1997). Firing properties of head direction cells in the rat anterior thalamic nucleus: dependence on vestibular input. *J. Neurosci.* 17, 4349–4358. doi: 10.1523/jneurosci.17-11-04349.1997

Starrett, M. J., and Ekstrom, A. D. (2018). Perspective: assessing the flexible acquisition, integration and deployment of human spatial representations and information. *Front. Hum. Neurosci.* 12:281. doi: 10.3389/fnhum.2018.00281

Starrett, M. J., Stokes, J. D., Huffman, D. J., Ferrer, E., and Ekstrom, A. D. (2019). Learning-dependent evolution of spatial representations in large-scale virtual environments. *J. Exp. Psychol. Learn. Mem. Cogn.* 45, 497–514. doi: 10.1037/xlm0000597

Taube, J. S., Valerio, S., and Yoder, R. M. (2013). Is navigation in virtual reality with FMRI really navigation? *J. Cogn. Neurosci.* 25, 1008–1019. doi: 10.1162/jocn_a_00386

Thibault, G., Pasqualotto, A., Vidal, M., Droulez, J., and Berthoz, A. (2013). How does horizontal and vertical navigation influence spatial memory of multifloored environments? *Atten Percept. Psychophys.* 75, 10–15. doi: 10.3758/s13414-012-0405-x

Tu, M.-C., and Pai, M.-C. (2006). Getting lost for the first time in patients with Alzheimer's disease. *Int. Psychogeriatr.* 18, 567–570. doi: 10.1017/s1041610206224025

Uiga, L., Cheng, K. C., Wilson, M. R., Masters, R. S. W., and Capio, C. M. (2015). Acquiring visual information for locomotion by older adults: a systematic review. *Ageing Res. Rev.* 20, 24–34. doi: 10.1016/j.arr.2014.12.005

Vass, L. K., and Epstein, R. A. (2017). Common neural representations for visually guided reorientation and spatial imagery. *Cereb. Cortex* 27, 1457–1471. doi: 10.1093/cercor/bhv343

Vlček, K., and Laczó, J. (2014). Neural correlates of spatial navigation changes in mild cognitive impairment and Alzheimer's disease. *Front. Behav. Neurosci.* 8:89. doi: 10.3389/fnbeh.2014.00089

Waller, D., and Lippa, Y. (2007). Landmarks as beacons and associative cues: their role in route learning. *Mem. Cognit.* 35, 910–924. doi: 10.3758/bf03193465

Waller, D., Loomis, J. M., and Steck, S. D. (2003). Inertial cues do not enhance knowledge of environmental layout. *Psychon. Bull. Rev.* 10, 987–993. doi: 10.3758/bf03196563

Weniger, G., Ruhleder, M., Lange, C., Wolf, S., and Irle, E. (2011). Egocentric and allocentric memory as assessed by virtual reality in individuals with amnestic mild cognitive impairment. *Neuropsychologia* 49, 518–527. doi: 10.1016/j.neuropsychologia.2010.12.031

Weniger, G., Ruhleder, M., Wolf, S., Lange, C., and Irle, E. (2009). Egocentric memory impaired and allocentric memory intact as assessed by virtual reality in subjects with unilateral parietal cortex lesions. *Neuropsychologia* 47, 59–69. doi: 10.1016/j.neuropsychologia.2008.08.018

Wolbers, T., Hegarty, M., Büchel, C., and Loomis, J. M. (2008). Spatial updating: how the brain keeps track of changing object locations during observer motion. *Nat. Neurosci.* 11, 1223–1230. doi: 10.1038/nn.2189

Wolbers, T., Klatzky, R. L., Loomis, J. M., Wutte, M. G., and Giudice, N. A. (2011). Modality-independent coding of spatial layout in the human brain. *Curr. Biol.* 21, 984–989. doi: 10.1016/j.cub.2011.04.038

Wolbers, T., Wiener, J. M., Mallot, H. A., and Büchel, C. (2007). Differential recruitment of the hippocampus, medial prefrontal cortex, and the human motion complex during path integration in humans. *J. Neurosci.* 27, 9408–9416. doi: 10.1523/jneurosci.2146-07.2007

Yin, H. H., and Knowlton, B. J. (2006). The role of the basal ganglia in habit formation. *Nat. Rev. Neurosci.* 7, 464–476. doi: 10.1038/nrn1919

Yoder, R. M., and Taube, J. S. (2014). The vestibular contribution to the head direction signal and navigation. *Front. Integr. Neurosci.* 8:32. doi: 10.3389/fnint.2014.00032

Zheng, Y., Goddard, M., Darlington, C. L., and Smith, P. F. (2009). Long-term deficits on a foraging task after bilateral vestibular deafferentation in rats. *Hippocampus* 19, 480–486. doi: 10.1002/hipo.20533

Zwergal, A., la Fougère, C., Xiong, G., Kugler, G., Schlichtiger, J., Brandt, T., et al. (2011). When the brain misses the vestibular compass-complete vestibular loss alters navigational behaviour and brain activation during real navigation. *J. Neurol.* 258:S39.

Zwergal, A., Linn, J., Xiong, G., Brandt, T., Strupp, M., and Jahn, K. (2012). Aging of human supraspinal locomotor and postural control in fMRI. *Neurobiol. Aging* 33, 1073–1084. doi: 10.1016/j.neurobiolaging.2010.09.022

Zwergal, A., Schöberl, F., Xiong, G., Pradhan, C., Covic, A., Werner, P., et al. (2016). Anisotropy of human horizontal and vertical navigation in real space: behavioral and PET correlates. *Cereb. Cortex* 26, 4392–4404. doi: 10.1093/cercor/bhv213

Conflict of Interest: The authors declare that the research was conducted in the absence of any commercial or financial relationships that could be construed as a potential conflict of interest.

frontiers in Neural Circuits

ORIGINAL RESEARCH
published: 05 June 2020
doi: 10.3389/fncir.2020.00020

Spatial Updating Depends on Gravity

Alexander Christoph Stahn[1,2†], Martin Riemer[3†], Thomas Wolbers[3], Anika Werner[2,4†], Katharina Brauns[2†], Stephane Besnard[4†], Pierre Denise[4†], Simone Kühn[5,6†] and Hanns-Christian Gunga[2†]*

[1]Department of Psychiatry, Perelman School of Medicine at the University of Pennsylvania, Philadelphia, PA, United States, [2]Charité—Universitätsmedizin Berlin, Corporate Member of Freie Universität Berlin, Humboldt-Universität zu Berlin, and Berlin Institute of Health, Institute of Physiology, Berlin, Germany, [3]Aging and Cognition Research Group, German Center for Neurodegenerative Diseases (DZNE), Magdeburg, Germany, [4]Normandie Université, UNICAEN, INSERM, COMETE, Caen, France, [5]Department of Psychiatry and Psychotherapy, University Medical Center Hamburg-Eppendorf, Hamburg, Germany, [6]Lise Meitner Group for Environmental Neuroscience, Max Planck Institute for Human Development, Berlin, Germany

OPEN ACCESS

Edited by:
Mathieu Beraneck,
Université Paris Descartes, France

Reviewed by:
Denise Henriques,
York University, Canada
Michele Tagliabue,
Université Paris Descartes, France

***Correspondence:**
Alexander Christoph Stahn
astahn@pennmedicine.upenn.edu

†ORCID:
Alexander Christoph Stahn
orcid.org/0000-0002-4030-4944
Martin Riemer
orcid.org/0000-0001-6043-4204
Anika Werner
orcid.org/0000-0002-9822-0348
Katharina Brauns
orcid.org/0000-0002-9417-0750
Stephane Besnard
orcid.org/0000-0002-9659-8005
Pierre Denise
orcid.org/0000-0002-9049-7692
Simone Kühn
orcid.org/0000-0001-6823-7969
Hanns-Christian Gunga
orcid.org/0000-0002-0145-179X

Received: 15 July 2019
Accepted: 09 April 2020
Published: 05 June 2020

Citation:
Stahn AC, Riemer M, Wolbers T, Werner A, Brauns K, Besnard S, Denise P, Kühn S and Gunga H-C (2020) Spatial Updating Depends on Gravity.
Front. Neural Circuits 14:20.
doi: 10.3389/fncir.2020.00020

As we move through an environment the positions of surrounding objects relative to our body constantly change. Maintaining orientation requires spatial updating, the continuous monitoring of self-motion cues to update external locations. This ability critically depends on the integration of visual, proprioceptive, kinesthetic, and vestibular information. During weightlessness gravity no longer acts as an essential reference, creating a discrepancy between vestibular, visual and sensorimotor signals. Here, we explore the effects of repeated bouts of microgravity and hypergravity on spatial updating performance during parabolic flight. Ten healthy participants (four women, six men) took part in a parabolic flight campaign that comprised a total of 31 parabolas. Each parabola created about 20–25 s of 0 g, preceded and followed by about 20 s of hypergravity (1.8 g). Participants performed a visual-spatial updating task in seated position during 15 parabolas. The task included two updating conditions simulating virtual forward movements of different lengths (short and long), and a static condition with no movement that served as a control condition. Two trials were performed during each phase of the parabola, i.e., at 1 g before the start of the parabola, at 1.8 g during the acceleration phase of the parabola, and during 0 g. Our data demonstrate that 0 g and 1.8 g impaired pointing performance for long updating trials as indicated by increased variability of pointing errors compared to 1 g. In contrast, we found no support for any changes for short updating and static conditions, suggesting that a certain degree of task complexity is required to affect pointing errors. These findings are important for operational requirements during spaceflight because spatial updating is pivotal for navigation when vision is poor or unreliable and objects go out of sight, for example during extravehicular activities in space or the exploration of unfamiliar environments. Future studies should compare the effects on spatial updating during seated and free-floating conditions, and determine at which g-threshold decrements in spatial updating performance emerge.

Keywords: spatial navigation, spatial updating, precuneus, weightlessness, vestibular system, parabolic flight, spaceflight

INTRODUCTION

Gravity is critical for various physiological functions and goal-directed behavior. The lack of gravity, i.e., weightlessness, leads to cardiovascular deconditioning, negative energy balance, bone and muscle loss, and sensorimotor impairments. The time course of these processes varies considerably between immediate effects upon entry to weightlessness and long-term effects occurring after several weeks to months of space travel (Nicogossian et al., 2016).

One system that is immediately affected by gravity is the vestibular system. The vestibular system senses linear and angular acceleration through signals from the otoliths and semicircular canals, and it drives various reflexes such as keeping gaze and posture when linear accelerations are changing. However, the vestibular system goes beyond maintaining gaze and balance. Interactions between the otoliths and semicircular canals critically contribute to spatial perception including self-motion, orientation, and navigation (Cullen and Taube, 2017). During weightlessness gravity no longer acts as a fundamental reference, and the discrepancy between vestibular (including conflicts between otolith and semicircular canal information), visual, and sensorimotor signals can affect spatial abilities (Clément et al., 1989; McIntyre et al., 2001). So far, microgravity research has concentrated on posture, gaze, functional mobility, and spatial orientation, reporting misperceptions of visual orientation, depth and distance, and difficulties in shape recognition (Reschke and Clément, 2018). Whether the lack of gravity also impairs spatial navigation performance and strategies is not well understood.

Spatial navigation is an essential cognitive process that allows us to perceive our position in the environment and use this information to efficiently move in physical space. A fundamental component of spatial navigation requires to continuously form and update transient sensorimotor representations about self-to-object relations during locomotion. This ability has been termed spatial updating and is closely linked to working memory (Wolbers et al., 2008; Theeuwes et al., 2009; Anderson et al., 2010). It requires special effort when objects are no longer visible (Boon et al., 2018) and is a prerequisite for route learning and wayfinding in large-scale space. Spatial updating is also vital for navigation in small-scale spaces when vision is poor or unreliable and objects go out of sight, for example, during extravehicular activities during spaceflight operations and exploration of unfamiliar planets. Given that the perception of self-motion critically depends on integrating visual information with gravitational cues processed by the vestibular system (Pfeiffer et al., 2014), spatial updating performance could be expected to be impaired when gravity levels change. This prediction is also in line with emerging evidence highlighting the cortical projections of the vestibular system. This includes several brain regions important for spatial navigation, including the hippocampal and parahippocampal formation, cingulate gyrus and retrosplenial cortex, parietal and medial temporal cortices, and the parietoinsular vestibular cortex and temporoparietal junction (Hitier et al., 2014).

Here, we tested the effects of different gravity levels on spatial updating performance using a parabolic flight maneuver. A parabolic flight maneuver starts with a hypergravity phase (1.8 g) of about 20 s, after which the aircraft enters a free-fall state for about 20–25 s that is comparable to 0 g because of the lack of ground reaction forces. The period of weightlessness is followed by another hypergravity phase before reaching 1 g again (**Figure 1**). This maneuver was performed a total of 31 times, with the first parabola being a test parabola, where no data were collected. Subsequently, six blocks of parabolas were performed, separated by 5-min to 8-min breaks. Each parabola within blocks was separated by 2-min to 3-min breaks, yielding a total of about 12 min of weightlessness. Spatial updating performance was assessed at normal Earth gravity (1 g), hypergravity (1.8 g) and zero-g (0 g). The paradigm was specifically designed to meet the requirements of the parabolic flight maneuver and to allow differentiating between changes in spatial working memory performance (static condition) and spatial updating performance (updating condition). During the updating condition participants had to first encode two egocentric object locations, then update these positions during a virtual translational forward movement when the objects were no longer visible and finally point back to the location of one of the original objects after completion of the forward movement. In the static condition, the task was identical except that the participants did not experience the virtual translation, eliciting working memory processes without the need to update egocentric object locations. We hypothesized that compared to 1 g, both 0 g and 1.8 g would selectively impair spatial updating.

MATERIALS AND METHODS

Participants

A total of 10 healthy adults (four women, six men, aged 33–50 years, mean ± SD: 39 ± 4 years) with no previous parabolic flight experience participated in the experiment. All participants had normal or corrected-to-normal vision and underwent a medical aptitude screening to participate in a parabolic flight. Subjects gave informed written consent to participate in the study. The study was approved by the local Ethics Committee of Charité—Universitätsmedizin Berlin, by the European Space Agency (ESA) medical board, and by the French Ethics Committee—Comité de Protection des Personnes (CPP Nord-Ouest III) and authorized by the French Competent Authority (ANSM). All procedures were conducted following the principles of the Declaration of Helsinki.

Procedure

Parabolic Flight

The experiment was conducted as part of the European Space Agency (ESA) 66th parabolic flight campaign in May 2017. The flights were performed by Novespace[1] using a modified Airbus A 310 aircraft, i.e., the Airbus A 310 Zero-G, based at Bordeaux-Merignac International Airport in France. The

[1] www.novespace.fr

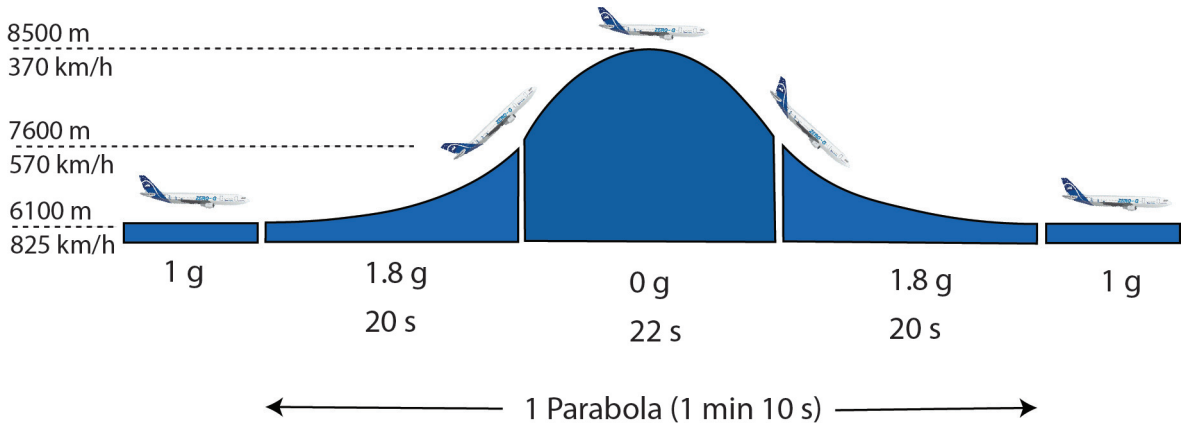

FIGURE 1 | The characteristic profile of a parabolic flight maneuver. At standard cruising altitude (about 12,000 ft) the aircraft is pulled up at a 47° angle, inducing a gravito-inertial acceleration (GIA) of 1.5–1.8 g, after which the engine's thrust is limited to compensate air-drag, entering a phase of free-fall comparable to 0 g, and hence, weightlessness. This phase is completed by another phase of hypergravity before returning to 1 g again. After an initial test parabola, the maneuver is repeated a total of 30 times with 3–5 min breaks between parabolas and a longer (about 8 min) break after the 16th parabola.

campaign consisted of three consecutive flight days. Three participants were flown on the first and second flight day, and four on the third flight day. Each flight consisted of 31 parabolic maneuvers. During each maneuver the aircraft started from a regular horizontal flight at typical flight altitude and pulls up to an angle of 47°, producing a gravito-inertial acceleration (GIA), defined as the sum of gravity's linear acceleration and inertial forces, of 1.5–1.8 g. After about 20 s the engine's thrust was reduced just to compensate air-drag, and the aircraft enters a freefall trajectory for 20–25 s. During this period the aircraft and all materials and passengers in the plane fell at 9.81 m/s^2, achieving a net 0 g-level. We acknowledge that the terms weightlessness is technically not correct to describe this phase. Gravity is still 1 g throughout the entire flight. This is similar to the condition on the International Space Station (ISS), where gravity is still >90% of Earth's gravity, but astronauts experience a constant free fall due to the station's orbit around the Earth. Despite this discrepancy, we follow the typical convention in Space Life Sciences and consider the condition of a net level of 0 g during the free fall as weightlessness. This phase was ended by gradually pulling the aircraft out of the freefall, inducing another hypergravity phase of 1.5–1.8 g before returning to a horizontal flight position again. The aircraft pitch rotation (about 3°/s) is barely detectable by the vestibular system (Karmali and Shelhamer, 2008). Each flight including take-off and landing took about 3.5 h.

Data Acquisition

All participants completed two training sessions on the ground. Both training sessions were performed onsite at Novespace. The first session was performed at the facilities of Novespace, and the second training session was performed in the aircraft using the identical setup that was used during the flight. About 75–90 min before take-off all but one participant received scopolamine subcutaneously to minimize motion-sickness (about 0.125 mg for women and 0.175 mg for men). Inflight testing was performed either between the 2nd and 16th parabola or between the 17th and 31st parabola. Participants were randomly allocated to the order in a balanced fashion. During the remaining parabolas, participants were allowed to free float in a designated area at the end of the aircraft. Before the first, after the 16th and 31st parabola subjects were asked to indicate their current level of motion sickness on a 5-point Likert scale with the two anchors "not at all" (1) and "very sick" (5). During testing, subjects were seated and buckled up in standard aircraft chairs with their feet fixed to the ground floor with foot straps (see **Figure 2**). The laptops were mounted to a plexiglass plate that was strapped to the participants' upper legs that allowed them to maintain the same position throughout testing. During each 1 g phase, hypergravity phase, 0 g phase, and following the completion of the parabolic maneuver participants performed a block of two trials, respectively. Accordingly, a total of 30 trials (15 parabolas x 2 trials) were performed per gravity level. The 30 trials in each phase comprised 6 static trials, 12 spatial updating trials involving a short forward motion, and 12 spatial updating trials involving a long forward motion (see details below). To ensure exact timing during all phases, each block was started by an experimenter who also verbally instructed the participants when each block was started.

Experimental Stimuli and Paradigm

Spatial updating performance was assessed with a paradigm that specifically targets the precuneus (Wolbers et al., 2008). The paradigm was modified to meet the demands of parabolic flight characteristics, programmed in Vizard 5 (WorldViz, Santa Barbara, CA, USA), and presented on a 15-inch laptop (ZBook 15 G5 Mobile Workstation, Hew). Participants saw a virtual three-dimensional (3D) environment from a first-person perspective (eye height: 180 cm). The ground surface consisted of white limited life-time dots randomly fading and appearing (maximal duration: 5 s). Each trial comprised an encoding, a delay, and a retrieval phase. In the encoding phase, participants

FIGURE 2 | Experimental setup in the Airbus A 310 Zero-G. Participants were buckled up in standard aircraft chairs with feet fixed to their ground floor with foot straps. The laptops were mounted to a plexiglass plate that was strapped to the participants' upper legs that allowed them to maintain the same position throughout testing. Testing was performed during 15 parabolas, providing a total of 90 trials (30 trials during 1 g, 1.8 g, and 0 g, respectively). Photo credit: Novespace/ESA.

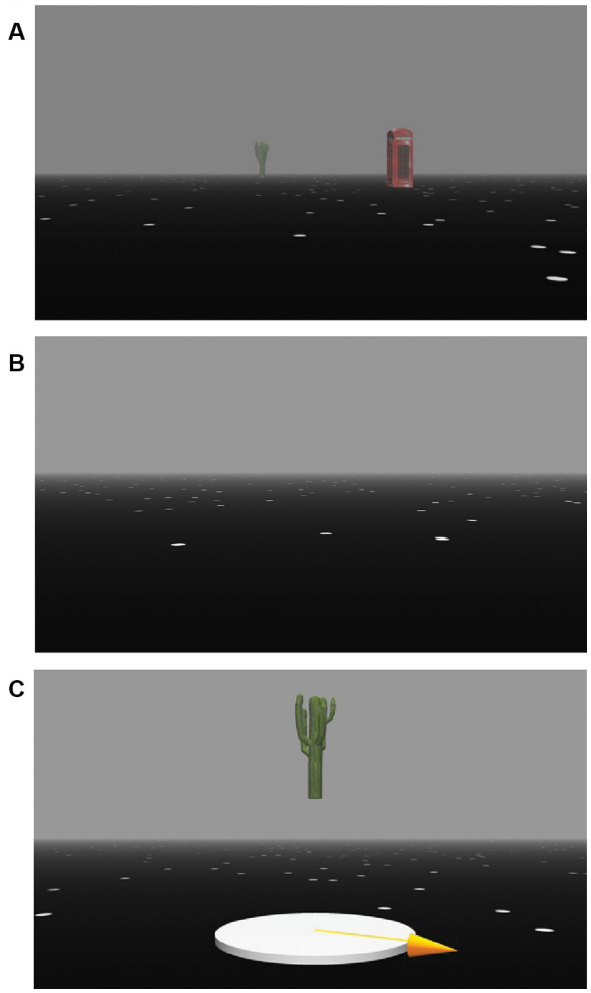

FIGURE 3 | Experimental paradigm. Trials comprise an encoding phase **(A)**, a delay phase **(B)**, and a retrieval phase **(C)**. Each trial started with a static presentation of the virtual environment and two objects located at two different positions during which participants had to memorize the location and identity of the objects. Next, all objects gradually sank into the ground until they completely disappeared. In the delay phase, participants either experienced a forward movement of 25 m or 45 m (updating trials) or remained at their position (static trials). In the subsequent retrieval phase, one of the two objects was presented in the center of the screen, and participants had to turn a 3D-arrow towards the object's original position in the encoding phase.

were presented with two different objects positioned at distances between 15 and 55 m in front of them, one object to the left and one to the right of the participant. The target object locations were the same in all g-levels, but they were presented in randomized order (different randomization for all g-levels). The objects were of similar size typically encountered in everyday life such as a lamppost, a road sign, a phone booth or a statue (**Figure 3**). Participants were instructed to memorize the object locations as precisely as possible. After 1 s of the presentation, the objects sank into the ground. After another second, participants were passively moved forward at a uniform velocity of 8.3 m/s and 15 m/s for short and long updating trials, respectively, or they remained at their original position (static trials). The updating trials consisted of a short or long updating period (forward motion of either 25 or 45 m). For all trials, the duration was kept constant at 3 s to eliminate potential influences of time-keeping mechanisms (Riemer et al., 2014). The delay phase in static trials was also set to 3 s. In the final retrieval phase, an image of one of the two objects shown in the encoding phase was presented at the center of the screen, and participants were asked to turn a 3D-arrow to indicate the direction of the target object's location. The arrow was controlled with the left and right arrow keys of the keyboard and responses were logged with the space bar. The initial orientation of the arrow was always pointing forward for all trials to reduce error variance. No feedback was given, and trials were separated by a black screen with an intertrial interval of 1 s.

Behavioral and Statistical Analysis

We recorded reaction time (RT) and response pointing angle for each trial. Pointing error was defined as our primary outcome and calculated as the difference between the correct angle and response pointing angle. To assess outliers, we first computed the number of signed pointing errors exceeding 1.5 times

the interquartile range (IQR). The number of these potential outliers were then used to perform Rosner's generalized extreme studentized deviate test to confirm outliers that were removed from further analysis. Pointing performance is characterized by perceptual error and noise (Wolbers et al., 2008). The former is associated with the encoding of the object locations in a rather non-immersive virtual environment projected on a 2D screen. However, given that the positions of the target objects were identical across all conditions, any increase in pointing error would reflect increases in noise. To quantify this noise, we computed variable pointing error as the standard deviation of the signed pointing errors across trials for each participant, phase, and condition using circular statistics (Fisher, 1993). High performance is therefore demonstrated by small differences in pointing errors between trials. In contrast, large differences in pointing errors between trials suggest a high uncertainty of pointing performance (Wolbers et al., 2008). Hence, increases in variable pointing errors during 0 g and 1.8 g were expected to reflect impairments in working memory processes associated with the updating of self-to-object relations. We also determined accuracy, i.e., the mean direction of pointing errors calculated as the circular mean of signed pointing errors. Differences between task conditions and g phases were assessed using mixed linear models with g-level and task condition as fixed factors, and subjects as a random factor with random intercepts and random slopes for condition (random slopes were not fitted if the model did not converge). Pre-planned contrasts were used to compare the levels within each factor using Bonferroni-corrected family-wise comparisons (considering each main factor as one family). We first assessed the effect of task condition on pointing performance by comparing static to short and long updating trials and short to long updating trials at each g-level (correction for a total of three comparisons). We then compared 1 g to 0 g, 1 g to 1.8 g, and 0 g to 1.8 g for each task condition (correction for a total of three comparisons). We also assessed the effects of g-levels on RT. No comparisons of RT were performed between task conditions because they were confounded by movement times of the pointing indicator due to the nature of the paradigm. Recall that the pointing indicator displayed in the retrieval phase was always parallel to the direction of the forward translation (see also "Experimental Stimuli and Paradigm" section). Consequently, RTs were necessarily affected by task conditions because the arrow had to be moved a shorter angular distance for static and short updating trials compared to long updating trials. For these reasons, we performed mixed models for RT separately for each task condition using g-level as a fixed factor and subjects as a random factor. Pre-planned contrasts were performed to assess the differences between 1 g and 0 g, 1 g and 1.8 g, and 0 g and 1.8 using Bonferroni-corrected family-wise comparisons (correction for a total of three comparisons). Effect sizes for contrasts were expressed as Cohen's d with Bonferroni-adjusted 95% confidence intervals using bootstrapping (Kirby and Gerlanc, 2013). To assess systematic variations in pointing performance throughout the flight we identified the association between absolute pointing error and trial number for each g-level and condition using repeated measures correlations (r_{rm}; Roy, 2006). All statistical analyses and graphical illustrations were carried out using the software package R (R Core Team, 2016).

RESULTS

None of the participants experienced discomfort and all demonstrated excellent compliance during the task. The level of motion sickness did not change significantly (mean change (95% CI): before 1st vs. after 16th parabola: 0.4 (−1.09, 0.29), $P = 0.22$; before 1st vs. after 31th parabola: 0.45 (−1.32, 0.42), $P = 0.27$). On average only two trials (out of 90) were missed (range: 0 to 6 trials). One hundred and two pointing responses (11.6%) were identified as outliers using boxplot statistics (1.5 × IQR). A Rosner test with a maximum of 102 potential outliers revealed 12 extreme outliers (1.4%) that were excluded from further analysis. Neither condition nor phase was missing more than two responses with a maximum of seven missing responses in total for any participant. The final data set included 864 pointing responses (mean: 86; range: 83 to 90 per participant). All repeated measures correlations between trial number and mean absolute pointing error were minimal and non-significant for all g-levels and task conditions ($r_{rm} = -0.12$, $P = 0.24$ to $r_{rm} = 0.15$, $P = 0.32$), confirming that there were no learning or habituation effects in pointing performance throughout the experiment.

Pointing performance was affected by task condition ($F_{(2,72)} = 10.6$, $P < 0.001$). A trend toward significance was observed for the prediction of g-level on pointing performance ($F_{(2,72)} = 2.5$, $P = 0.089$) and the interaction between g-level and task condition ($F_{(2,72)} = 2.3$, $P = 0.07$). Across all g-levels variable pointing error increased from static to short, and from short to long updating trials (**Figure 4**). Planned contrasts revealed significant differences of pointing performance at 0 g between static and long updating trials [$t_{(72)} = 4.06$, $P < 0.001$; $d = 1.53$ (0.81, 2.88)] and between short and long updating trials [$t_{(72)} = 3.91$, $P < 0.001$; $d = 1.12$ (0.07, 2.33)]. Similarly, we found a significant difference between static and long updating trials [$t_{(72)} = 2.94$, $P = 0.013$, $d = 0.73$ (−0.33, 1.57)] and a nearly significant difference between short and long updating trials [$t_{(72)} = 2.4$, $P = 0.056$; $d = 0.8$ (0.03, 1.58)] in the 1.8 g condition. We also observed a stepwise increase in pointing error from static to short updating to long updating trials. These differences did not reach the level of significance (**Table 1**) because of the somewhat smaller differences in variable pointing error. For instance, we observed a difference between long and static conditions of 26.4° and 19.1° for 0 g and 1.8 g compared to 9.5° for 1 g. We performed a power analysis using the R package pwr and found that a sample size of $N = 36$ would have been needed to detect a significant difference of 9.5° between static and long updating trials during 1 g. Together, these data suggest that long updating trials were particularly more challenging compared to the static or short updating trials, and these effects were most pronounced during 0 g and 1.8 g. Variable pointing error for long updating trials was significantly higher during 0 g compared to 1 g [$t_{(72)} = 3.37$, $P < 0.01$; $d = 0.94$ (0.07,

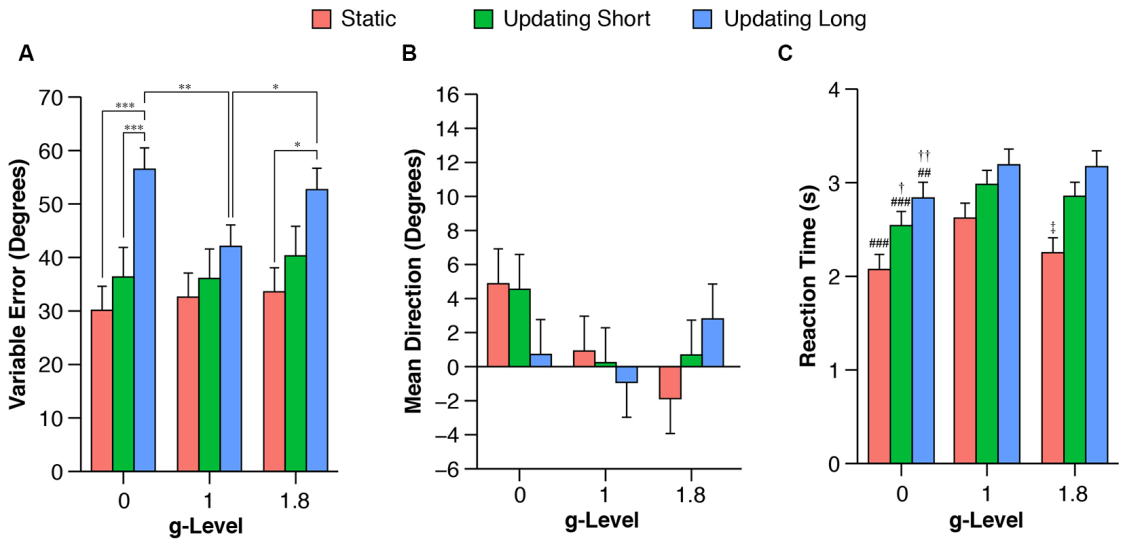

FIGURE 4 | Mean variable **(A)** and signed **(B)** pointing errors, and reaction time (RT; **C**) during 0 g, 1 g, and 1.8 g and different trial conditions (static, updating short, updating long). Variable pointing error was computed as the standard deviation of the signed pointing errors for each participant and each g-level and task condition using circular statistics. Data are estimated means and standard errors. Note that no contrasts were performed between task conditions for RTs because RTs were a logical consequence of task condition, i.e., the 3D arrow had to be moved a shorter angular distance for static and short updating trials compared to long updating trials (for details see "Behavioral and Statistical Analysis" in "Materials and Methods" section). $^{*}P < 0.05$. $^{**}P < 0.01$. $^{***}P < 0.001$. $^{\#\#}P < 0.01$ for 0 g vs. 1 g. $^{\#\#\#}P < 0.01$ for 0 g vs. 1 g. $^{\dagger}P < 0.05$ for 0 g vs. 1.8 g. $^{\dagger\dagger}P < 0.01$ for 0 g vs. 1.8 g. $^{\ddagger}P < 0.05$ for 1 g vs. 1.8 g.

TABLE 1 | Contrasts examining the effects between static (Static), short updating (Short), and long updating (Long) task conditions on variable pointing error (Var PE) and mean direction of signed pointing error (Mean PE) during 0 g, 1 g, and 1.8 g*.

g-level	Contrast	Variable	Estimate	SE	DF	*t*	*P*	Effect Size (95% CI)
0 g	Short vs. Static	Var PE	6.2	7.3	72	0.85	>0.5	0.36 (−0.67, 1.05)
		Mean PE	−0.3	2.6	72	−0.13	>0.5	−0.04 (−1.08, 1.09)
	Long vs. Static	Var PE	26.4	6.5	72	4.06	<0.001	1.53 (0.81, 2.88)
		Mean PE	−4.2	2.6	72	−1.58	0.35	−0.54 (−1.9, 0.49)
	Long vs. Short	Var PE	20.1	5.2	72	3.91	<0.001	1.12 (0.07, 2.33)
		Mean PE	−3.8	2.6	72	−1.46	0.45	−0.34 (−1.67, 0.6)
1 g	Short vs. Static	Var PE	3.5	7.3	72	0.48	>0.5	0.15 (−0.87, 0.94)
		Mean PE	−0.7	2.6	72	−0.26	>0.5	−0.12 (−1.04, 0.84)
	Long vs. Static	Var PE	9.5	6.5	72	1.46	0.45	0.48 (−0.49, 1.68)
		Mean PE	−1.8	2.6	72	−0.70	>0.5	−0.25 (−1.03, 0.67)
	Long vs. Short	Var PE	6.0	5.2	72	1.17	>0.5	0.47 (−0.54, 2.53)
		Mean PE	−1.2	2.6	72	−0.44	>0.5	−0.13 (−0.87, 1.29)
1.8 g	Short vs. Static	Var PE	6.7	7.3	72	0.92	>0.5	0.25 (−0.88, 1.08)
		Mean PE	2.6	2.6	72	0.98	>0.5	0.31 (−0.67, 1.09)
	Long vs. Static	Var PE	19.1	6.5	72	2.94	0.013	0.73 (−0.33, 1.57)
		Mean PE	4.7	2.6	72	1.79	0.24	0.62 (−0.36, 1.2)
	Long vs. Short	Var PE	12.4	5.2	72	2.40	0.056	0.8 (0.03, 1.58)
		Mean PE	2.1	2.6	72	0.81	>0.5	0.22 (−0.76, 1.23)

**SE, standard error; DF, degrees of freedom; t, t-statistic; P, p-value. P values were adjusted for multiple comparisons using a Bonferroni correction. Corrections were applied to each main effect, i.e., for three contrasts. Effect size is Cohen's d with bootstrap 95% confidence intervals (adjusted for three comparisons using Bonferroni correction). Note that no contrasts were performed between task conditions for reactions time because reaction times were a logical consequence of task condition, i.e., the pointing error had to be moved a shorter angular distance for static and short updating trials compared to long updating trials (for details see "Behavioral and Statistical Analysis" in "Materials and Methods" section).*

2.08)], and during 1.8 g compared to 1 g [$t_{(72)} = 2.48$, $P = 0.047$; $d = 0.66$ (−0.21, 1.87)]. Neither static nor short updating trials revealed any significant differences of pointing error between any g-levels (**Table 2**), indicating that gravity affected spatial updating pointing performance in complex (i.e., long) trials and this effect was strongest during 0 g. Mean signed pointing error was larger in both 0 g and 1 g, but neither the main effects (g-level: $F_{(2,72)} = 2.8$, $P = 0.07$; task condition: $F_{(2,72)} = 0.2$, $P = 0.82$) nor their interaction reached statistical significance ($F_{(4,72)} = 1.6$, $P = 0.18$).

TABLE 2 | Contrasts examining the effects of g-level on variable pointing error (Var PE), mean direction of signed pointing error (Mean PE) and reaction time (RT) between 0 g, 1 g and 1.8 g for static (Static), short updating (Short), and long updating (Long) conditions*.

g-level	Contrast	Variable	Estimate	SE	DF	*t*	*P*	Effect Size (95% CI)
Static	0 g vs. 1 g	Var PE	−2.5	4.3	72	−0.58	>0.5	−0.18 (−1.08, 0.84)
		Mean PE	3.9	2.6	72	1.51	0.41	0.67 (−0.21, 1.44)
		RT	−0.6	0.1	162	−3.94	<0.001	−0.46 (−0.76, −0.12)
	0 g vs. 1.8 g	Var PE	−3.5	4.3	72	−0.81	>0.5	−0.25 (−1.43, 0.75)
		Mean PE	6.7	2.6	72	2.57	0.04	1.06 (0.07, 2.07)
		RT	−0.2	0.1	162	−1.28	>0.5	−0.23 (−0.55, 0.07)
	1.8 g vs. 1 g	Var PE	1.0	4.3	72	0.23	>0.5	0.12 (−0.95, 0.94)
		Mean PE	−2.8	2.6	72	−1.07	0.87	−0.47 (−1.16, 0.53)
		RT	−0.4	0.1	162	−2.67	0.025	−0.38 (−0.66, −0.02)
Short	0 g vs. 1 g	Var PE	0.3	4.3	72	0.07	>0.5	0.03 (−0.88, 0.86)
		Mean PE	4.3	2.6	72	1.64	0.31	0.54 (−0.43, 1.78)
		RT	−0.4	0.1	332	−3.82	<0.001	−0.33 (−0.58, −0.06)
	0 g vs. 1.8 g	Var PE	−3.9	4.3	72	−0.92	>0.5	−0.25 (−1.03, 0.67)
		Mean PE	3.9	2.6	72	1.47	0.44	0.45 (−0.57, 1.25)
		RT	−0.3	0.1	332	−2.71	0.021	−0.19 (−0.43, 0.05)
	1.8 g vs. 1 g	Var PE	4.2	4.3	72	0.99	>0.5	0.37 (−0.84, 1.17)
		Mean PE	0.4	2.6	72	0.17	>0.5	0.12 (−1.88, 0.92)
		RT	−0.1	0.1	332	−1.11	>0.5	−0.08 (−0.29, 0.14)
Long	0 g vs. 1 g	Var PE	14.4	4.3	72	3.37	<0.01	0.94 (0.07, 2.08)
		Mean PE	1.6	2.6	72	0.62	>0.5	0.13 (−1.04, 1.01)
		RT	−0.4	0.1	334	−3.31	<0.01	−0.25 (−0.47, −0.02)
	0 g vs. 1.8 g	Var PE	3.8	4.3	72	0.89	>0.5	0.24 (−0.79, 1.64)
		Mean PE	−2.1	2.6	72	−0.80	>0.5	−0.16 (−1.22, 0.9)
		RT	−0.3	0.1	334	−3.12	<0.01	−0.28 (−0.51, −0.04)
	1.8 g vs. 1 g	Var PE	10.6	4.3	72	2.48	0.047	0.66 (−0.21, 1.87)
		Mean PE	3.7	2.6	72	1.42	0.48	0.66 (−0.17, 1.96)
		RT	0.0	0.1	334	−0.18	>0.5	−0.05 (−0.27, 0.17)

*SE, standard error; DF, degrees of freedom; t, t-statistic; P, p-value. P values were adjusted for multiple comparisons using a Bonferroni correction. Corrections were applied to each main effect, i.e., for three contrasts. Effect size is Cohen's d with bootstrap 95% confidence intervals (adjusted for three comparisons using Bonferroni correction).

RT was significantly affected by g-level in each task condition (static: $F_{(2,162)} = 8.1$, $P < 0.001$; short updating: $F_{(2,332)} = 7.7$, $P < 0.001$; long updating: $F_{(2,334)} = 6.9$, $P < 0.01$). Contrasts showed that subjects responded significantly faster during 0 g compared to 1 g across all task conditions (static: $t_{(162)} = -3.9$, $P < 0.001$; $d = -0.46$ (−0.76, −0.12); short updating: $t_{(332)} = -3.8$, $P < 0.001$; $d = -0.33$ (−0.58, −0.06); long updating: $t_{(334)} = -3.3$, $P < 0.01$; $d = -0.25$ (−0.47, −0.02). RTs were also significantly shorter during 1.8 g compared to 1 g for static trials [$t_{(162)} = -2.7$, $P = 0.03$; $d = -0.38$ (−0.66, −0.02)], but neither for short updating [$t_{(332)} = -1.1$, $P > 0.5$; $d = -0.08$ (−0.29, 0.14)] nor for long updating trials [$t_{(334)} = -0.2$, $P > 0.5$; $d = -0.05$ (−0.27, 0.17)]. Comparisons and effects of RT between 0 g and 1.8 g are provided in **Table 2**. Variable pointing error was negatively correlated with average RT (Pearson's r) across all conditions at 1 g (static: $r = -0.16$; short updating: $r = -0.18$; long updating: $r = -0.1$), in static trials at 1.8 g ($r = -0.09$), and in short and long updating trials at 0 g ($r = -0.26$ and $r = -0.33$, respectively). To assess whether the effects on pointing performance in 0 g were confounded by RTs, i.e., that lower pointing performance was caused by shorter response times, we reanalyzed the effect of g-level on pointing performance by adjusting for RT. We fitted a mixed model to predict variable pointing error in 0 g that included g-level and mean RT as fixed factors and subject as a random factor (random intercept and slopes for g-level). This model confirmed the evidence of an effect of g-level after controlling for RT ($F_{(2,17)} = 3.92$, $P = 0.04$), which was qualified by a nearly significant difference between 0 g and 1 g ($t_{(17)} = 2.62$, $P = 0.054$). Note that this analysis is limited to the level of subjects and does not account for any relationship between RT and pointing error at the trial level, i.e., within subjects. This is due to the nature of the definition of variable pointing error reflecting the precision across trials in each condition. To verify the robustness of these results we also fitted a model on absolute pointing error, where we estimated the within- and between-subject effects of RT on pointing performance. As suggested by van de Pol and Wright (2009), we first determined the mean values of RT for each individual, condition and g-level to express the between-subject variation component. Next, we used within-subject centering to characterize within-subject effects by calculating the difference of each observation from the subject's respective mean value. We then estimated the variation in both sources of variance in pointing performance using a mixed linear model with absolute pointing error as a response variable, and between- and within-individual components of RT as fixed effects. These analyses confirmed that pointing performance and RT covaried within individuals much stronger than between subjects. Trial-to-trial changes in RT predicted trial-to-trial changes in absolute pointing error within the same individual ($F_{(1,332)} = 8.89$, $P < 0.01$). In contrast, between-subject variation in reaction did not significantly predict absolute pointing error ($F_{(1,332)} = 1.59$, $P = 0.21$). The effect of g-level remained nearly significant ($F_{(2,332)} = 2.48$, $P = 0.085$) with a significant contrast for absolute pointing error between 0 g and 1 g ($t_{(332)} = 1.97$, $P = 0.049$).

DISCUSSION

This study investigated the acute effects of weightlessness and hypergravity using parabolic flight maneuvers on spatial updating performance in humans. Spatial updating was assessed by a virtual 3D task that required participants to encode the identity and location of objects, memorize and then update the egocentric object coordinates during a forward movement simulated by optic flow. Using different lengths of the translational movement provided a variation in updating complexity. To disentangle the effects between altered gravity conditions and changes in general cognitive performance related to the unique experimental situation, we included a static condition in the paradigm. In this condition, participants did not experience any movement, removing the need to process self-motion cues to update egocentric object positions. Since the target stimuli were presented at identical positions across all three conditions, and given that the virtual environment in the delay and retrieval was identical for all trials, all conditions are directly comparable. The delay phase, i.e., the time between encoding and retrieval of the memorized object locations, introduces noise due to working memory decay and the updating process. Given that the noise further decreases the ability to correctly memorize the target locations, we quantified the noise by calculating the standard deviation of the pointing errors for each condition and subject. Because the target locations were identical across all conditions, any pointing error would be indicative of an effect of gravity conditions.

We found that pointing error variability was increased in updating compared to static trials across all gravity conditions. The difference between task conditions was particularly prominent for long updating trials in 0 g and 1.8, where the effect reached statistical significance, suggesting an increased complexity of keeping track of object locations. Spatial updating requires to memorize egocentric object representations. This process requires to direct visual attention to the target locations, which is closely linked to working memory (Wolbers et al., 2008; Theeuwes et al., 2009; Anderson et al., 2010) and particularly demanding when objects are no longer visible and body position changes (Boon et al., 2018). Accordingly, increased errors in the long updating trials suggest the need for higher working memory and processing demands to update changing object coordinates. These findings are well in line with data reported by Wolbers et al. (2008) and Müller et al. (2018), confirming the validity of the paradigm to assess spatial updating performance.

The primary objective was to investigate the effects of weightlessness and hypergravity on spatial updating performance. We found that 0 g and 1.8 g significantly impaired performance for long spatial updating trials compared to 1g as indicated by higher variable pointing errors. This difference could not be explained by a tradeoff between pointing error and RT. Neither short updating nor static trials, which required only little or no spatial updating and therefore served as control conditions, revealed any impairments. These findings confirm our hypothesis that general cognitive performance is not impaired *per se* during weightlessness, but gravity affects distinctive cognitive domains.

Grabherr et al. (2007) compared object-based and egocentric spatial transformation tasks during parabolic flight and observed poorer performance for egocentric spatial transformation during 0 g, but no changes for object-based transformations. The authors concluded that spatial rotations of external objects can be solved by visual cues, whereas spatially updating the egocentric representation of one's own body relies on the integration of visual information to a gravitational reference frame (Grabherr et al., 2007; Grabherr and Mast, 2010). This assumption is related to the notion that gravity provides distinct cues for sensorimotor integration and transformations of retinotopic, gravitational, and proprioceptive reference frames (Tagliabue and McIntyre, 2011, 2013, 2014). Note that the visibility of objects in the encoding phase was identical across all conditions (all objects were displayed for 1 s in each condition). The difference between static and updating conditions, and particularly long updating conditions, could be related to a change in the point of view during the encoding phase. In the static condition, the point of view and egocentric object locations remain constant. Hence, despite the disappearance of the objects, participants can still rely on the same egocentric object locations during the encoding phase. In contrast, in the updating condition the point of view changes as a result of the forward movement. This situation is aggravated in long updating trials because the object locations lie outside the visual scene most of the time due to the extended forward translation. Encoding retinotopic representations of egocentric object representations are particularly demanding when objects are no longer visible and body position changes (Boon et al., 2018). Objects that are outside the field of view (FOV) increasingly rely on input from nonretinotopic (e.g., motion-based and proprioceptive) cues. In the 0 g condition, this situation may be particularly challenging because gravity is critical for sensory transformations when visual information is lacking (Tagliabue and McIntyre, 2011, 2013, 2014).

To verify this hypothesis, we analyzed the interaction between the g-level and the visibility of the object locations. In other words, we did not assess the effect of the visibility of the objects themselves—they disappeared after 1 s in all trials—but whether their original locations remained in the FOV during the encoding phase. We ran a mixed model on variable pointing error and entered g-level and FOV as fixed factors. The factor FOV was characterized by three levels as follows. The first level comprised trials, in which both object locations remained within the FOV. The second level included trials, in which only one of the object locations remained within FOV. The third level characterized trials, in which none of the two object locations remained visible in the FOV. The interaction between g-level and the FOV on variable pointing error was nearly significant ($F_{(4,72)} = 2.15$, $P = 0.084$). A contrast analysis revealed that the interaction was driven by trials, in which none of the two objects remained constantly within the FOV. We observed a significant difference of variable pointing error between 0 g and 1 g (0 g vs. 1 g: $t_{(72)} = 2.53$, $P = 0.041$) and between 0 g and 1.8 g ($t_{(72)} = 2.80$, $P = 0.02$), but not between 1 g and 1.8 g ($t_{(72)} = 0.26$, $P > 0.5$). These data suggest that lack of gravity may have impaired the ability to update

egocentric object locations when these locations are no longer in the FOV.

A methodological explanation that may have contributed to higher variable pointing error during long updating trials could be related to potential geometrical artifacts associated with the anterior-posterior distance between the target and subject's position. Longer anterior-posterior distances would be expected to result in smaller angular errors. In static trials the average displacement was 35 m vs. 10 m for short and −10 m for long updating trials, predicting that the same positional error has a smaller effect in static compared to updating trials. Our findings, however, argue against such a confounding effect. Note that the absolute distance between short and long updating trials is identical (10 m). Accordingly, assuming that the subject responses are driven by geometrical effects the short and long updating condition should be characterized by similar errors. Second, if geometrical artifacts had confounded pointing errors, we would most certainly expect a difference between static and short updating trials. Neither of these two conditions was confirmed by our data. We did not observe any difference between static and short updating trials, and long updating trials were characterized by substantially larger errors than short updating trials. We are therefore confident that our findings are not confounded by geometrical effects associated with the anterior-posterior distance between targets and the virtual subject position.

In summary, our data show support for the notion that the absence of gravity affected the ability to encode egocentric object representations when their locations are outside the FOV. However, this may not fully account for the increased variability of pointing error during 0 g, and particularly 1.8 g. A broader alternative explanation for the vulnerability of spatial perception upon entry into microgravity and hypergravity observed in the present study and other experiments could be related to a mismatch between semicircular canals vs. otolith signals (Glasauer and Mittelstaedt, 1998). Our task was designed to require participants to integrate visual flow and egocentric object vectors in working memory, which was shown to be attributed to the precuneus (Wolbers et al., 2008). The precuneus receives input from various vestibular and multi-sensory cortical areas, such as the intraparietal sulcus, the inferior parietal lobe, and the parietal operculum (Leichnetz, 2001). A recent study showed that a single galvanic vestibular stimulation resulted in a positive blood-oxygen-level-dependent (BOLD) response in the precuneus (Della-Justina et al., 2015), suggesting a direct relationship between the vestibular system and the precuneus. It is possible that the impaired spatial updating performance during 0 g was caused by the unloading of the otoliths, lacking a critical reference cue (Glasauer and Mittelstaedt, 1998) for integrating visual information to efficiently update egocentric object locations during the presence of motion. Given the strong projections of the vestibular system to the precuneus, possibly, the reduced gravity affected the precuneus and its ability to perceive self-motion cues to update the stored egocentric object representations. This is also in line with clinical findings in patients with vestibular lesions, showing that vestibular signals are necessary for other sensory cues to be properly integrated and play a critical role in the representation of extrapersonal space (Borel et al., 2008). Support for this assumption comes from previous behavioral and neurophysiological data obtained during and after the parabolic flight. Klein et al. (2019) reported that cortical current density in the parietal area was decreased in 0 g compared to 1 g, and these reductions were not related to hemodynamic changes (Klein et al., 2019). Van Ombergen et al. (2017) performed resting-state functional magnetic resonance imaging (MRI) before and after the parabolic flight and found a lower intrinsic connectivity in the right temporoparietal junction after the flight exposure. Clément et al. (2016) recently investigated the effects of weightlessness during parabolic flight on egocentric distance perception (Clément et al., 2016). They found that egocentric distance using self-motion is overestimated during weightlessness for distances less than 4 m, and underestimated for distances over 4 m. Although these findings remain inconclusive regarding the direction or interaction of the relationship between gravity and distance perception, they suggested that altered gravity levels can change the perceived representation of distance. Data from spaceflight have also revealed that depth perception is altered during microgravity (Clément and Demel, 2012). The current experimental setup cannot verify whether poorer performance in spatial updating was mediated *via* impairments in spatial perception and orientation or other mechanisms. Long-duration studies on the ISS and future exploratory space missions could help to better understand the role of such mechanisms using specific tasks assessing spatial orientation (e.g., line orientation test) and more complex and integrative tasks of spatial cognition such as spatial updating, path integration, and spatial navigation.

Notably, our data should be interpreted in light of some confounders associated with the parabolic flight maneuver. Clément et al. (1989) showed that the gaze position can shift downwards in 0 g and shift up in 1.8 g, potentially affecting visual perception. Given that the stimuli were presented at a distance of about 50 cm at a viewing angle of approximately 15° (normal line of sight), we do not expect that the gaze position affected our data. Moreover, the target stimuli were presented at identical positions across all three conditions and the virtual environment in the delay and retrieval was identical for all trials. Hence, the selective impairment in spatial updating but not control conditions in microgravity argues against a mere conflict between head posture and gravitational acceleration, which is essential for encoding the spatial orientation of the human body in space (Cullen and Taube, 2017). Degradations in visual acuity associated with altered optokinetic responses during changing gravity conditions may also account for changes in neuro-vestibular performance. Experiments on the Mir station have shown that vertical pursuit movements are strongly affected. André-Deshays et al. (1993) showed that upward visual pursuit was largely suppressed in weightlessness, whereas less dramatic effects were reported for downward visual pursuit (André-Deshays et al., 1993). It has been suggested that this degradation of performance relates to the altered otolith input in weightless conditions (Lackner and DiZio, 2000). These results are also supported by parabolic flights, showing a tendency for upward

slow phase velocity to be attenuated and downward optokinetic responses to be augmented (Clément et al., 1992a,b). Since otolith signaling drives not only vertical but also torsional eye movements, it may not be surprising that parabolic flight has also been shown to induce torsional misalignments during 0 g and 1.8 g (Markham et al., 2000; Beaton et al., 2015). To better understand the effects of changing g-levels on task performance, future studies should consider tracking eye movements during neurobehavioral testing. Other research has also shown that gravity affects visual processing. Cheron et al. (2014) recorded visual evoked EEG potentials (VEP) during a virtual spatial navigation task in astronauts on ISS. They showed that VEP potentials were preserved in weightlessness for the control condition (2D checkerboard), but not the 3D stimuli. They also reported changes in EEG spectral power for the 3D stimuli, indicative of a modulation of primary visual signals. Given the nature of the virtual 3D paradigm used in the present study, it is, therefore, possible that the effects on pointing performance observed in 0 g and 1.8 g are at least somewhat explained by a suppression of feedback or top-down mechanisms acting on the primary visual cortex. We acknowledge that scopolamine, a muscarinic acetylcholine antagonist, can dampen arousal and impair sensorimotor function, working memory, and spatial cognition (Blokland et al., 2016; Svoboda et al., 2017). However, all inflight testing was performed after the administration of scopolamine. Given that the task conditions were randomized across parabolas it is very unlikely that pharmacokinetic effects can account for the present findings. For the same reasons, it is rather unlikely that affective changes, previously suggested to be related to changes in electrocortical activity during microgravity (Schneider et al., 2008; Brümmer et al., 2011), account for the impaired spatial updating performance observed in 0 g.

It is important to acknowledge some limitations regarding our experimental design. First, to avoid potential effects associated with time-keeping mechanisms (Riemer et al., 2014), the duration of all trials was kept constant at 3 s. As a result, movement speed was correlated with the length of the traversed distance in updating trials. Given that the time between encoding and retrieval was identical across task conditions, longer moving distances were necessarily combined with a higher speed, which represents a potential confound. It is therefore also possible that the g-related variation in velocity-to-position integration could be the mechanism of the observed increases in variable pointing error. Second, the pointing indicator shown in the retrieval phase was always aligned with the direction of the virtual forward movement to reduce error variance. Consequently, RTs were correlated with movement times because the pointer had to be moved larger angular distances for updating trials. To compare conditions, future studies may consider using a joystick to log responses by pointing to the target object. With longer exposures to weightlessness, i.e., suborbital flights of experiments on the ISS, it is also feasible to use a range of pointer orientations during the start of the retrieval phase and elucidate the effect of movement speed on spatial updating performance. Finally, the task was presented on a 2D screen, creating a limited immersive virtual experience that can increase errors associated with the initial encoding phase of the objects and the perception of locomotion. However, these inaccuracies were constant across all conditions because the target objects and their locations were identical across all gravity conditions. We only included straight forward translations. This was necessary to prevent nausea in the subjects, which could be caused by passive virtual movements along curved paths. Furthermore, movements along curved paths would also introduce a potential source of ambiguity for the task, as individuals have different preferences for the frame of reference against which to make their judgments (Gramann et al., 2006). Irrespective of the degree of immersion, passive or virtual information on locomotion can be interpreted differently with respect to actual movements (Cullen and Taube, 2017). For instance, the perception of self-motion can be underestimated when no actual movements are performed (Frissen et al., 2011). The present experimental paradigm used a visual flow to simulate a forward movement, potentially lacking proprioceptive or vestibular information about locomotion. However, these cues were absent across all conditions and general differences in spatial updating performance between self-propelled, passive or no locomotion may not necessarily question our findings. Nevertheless, the present data should be interpreted cautiously concerning natural movements that provide both visual and body-based self-motion cues.

Taken together, our data show that performance for long spatial updating trials is impaired during weightlessness and hypergravity. We also demonstrated that general cognitive performance is not affected *per se* as indicated by the lack of any effects in the static control task condition, suggesting that gravity levels affect those areas of the brain that have strong projections to the vestibular system. We suggest that the discrepancy between canal and otolith signaling associated with altered gravity conditions may have played a critical role in the impaired pointing performance observed in the present study because of the various afferents between the precuneus and other parietal brain areas associated with spatial abilities and the vestibular system. The adverse effects of g-levels on performance for long spatial updating trials observed in the present study could be relevant for spaceflight because spatial updating is a critical skill for navigation, particularly when visibility is poor or objects go out of sight such as during extravehicular activities. Moreover, the effect could be exacerbated because our data were collected in a seated position. Future studies should compare the effects of seated vs. free-floating conditions on pointing error and determine at which g-threshold decrements in spatial updating performance emerge.

DATA AVAILABILITY STATEMENT

The data that support the findings of this study are available from the corresponding author (AS), upon reasonable request.

ETHICS STATEMENT

The studies involving human participants were reviewed and approved by the Ethics Committee of Charité—Universitätsmedizin Berlin, the European Space Agency (ESA) medical board, and the French Ethics

Committee—Comité de Protection des Personnes (CPP Nord-Ouest III) and authorized by the French Competent Authority (ANSM). The participants provided their written informed consent to participate in this study.

AUTHOR CONTRIBUTIONS

AS designed and directed the project, analyzed all data and wrote the manuscript. AW and KB helped supervise the project and performed data collections. PD and SB provided technical and scientific expertise in designing parabolic flight experiments. PD also allowed performing a feasibility study as part of the 62nd CNES parabolic flight campaign that provided the basis for the design and implementation of the present experiment. PD also obtained Ethical approval from the French Ethics Committee—Comité de Protection des Personnes (CPP Nord-Ouest III). SB served as the flight surgeon. He performed a final medical check and administered the scopolamine. TW designed the original paradigm, MR and AS adapted it for spaceflight. H-CG and SK provided critical feedback and contributed to the interpretation of the results. All authors discussed the results and contributed to the final manuscript.

FUNDING

The study was supported by the European Space Agency (ESA) and the German Aerospace Center (Deutsches Zentrum für Luft- und Raumfahrt; DLR) through grant 50WB1525 and 50WB1915.

ACKNOWLEDGMENTS

We thank the European Space Agency (ESA) for the opportunity to participate in the ESA 66th parabolic flight campaign. We also thank Frédéric Gai and Yannick Bailhé from Novespace and Jennifer Ngo-Anh and Neil Melville from ESA for their operational, technical, and logistic support. We also thank all participants for their participation in the experiment. We acknowledge the support from the German Research Foundation (DFG) and the Open Access Publication Fund of Charité—Universitätsmedizin Berlin.

REFERENCES

Anderson, E. J., Mannan, S. K., Rees, G., Sumner, P., and Kennard, C. (2010). Overlapping functional anatomy for working memory and visual search. *Exp. Brain Res.* 200, 91–107. doi: 10.1007/s00221-009-2000-5

André-Deshays, C., Israël, I., Charade, O., Berthoz, A., Popov, K., and Lipshits, M. (1993). Gaze control in microgravity. 1. Saccades, pursuit, eye-head coordination. *J. Vestib. Res.* 3, 331–343.

Beaton, K. H., Huffman, W. C., and Schubert, M. C. (2015). Binocular misalignments elicited by altered gravity provide evidence for nonlinear central compensation. *Front. Syst. Neurosci.* 9:81. doi: 10.3389/fnsys.2015.00081

Blokland, A., Sambeth, A., Prickaerts, J., and Riedel, W. J. (2016). Why an m1 antagonist could be a more selective model for memory impairment than scopolamine. *Front. Neurol.* 7:167. doi: 10.3389/fneur.2016.00167

Boon, P. J., Zeni, S., Theeuwes, J., and Belopolsky, A. V. (2018). Rapid updating of spatial working memory across saccades. *Sci. Rep.* 8:1072. doi: 10.1038/s41598-017-18779-9

Borel, L., Lopez, C., Péruch, P., and Lacour, M. (2008). Vestibular syndrome: a change in internal spatial representation. *Neurophysiol. Clin.* 38, 375–389. doi: 10.1016/j.neucli.2008.09.002

Brümmer, V., Schneider, S., Vogt, T., Strüder, H., Carnahan, H., Askew, C. D., et al. (2011). Coherence between brain cortical function and neurocognitive performance during changed gravity conditions. *J. Vis. Exp.* 51:2670. doi: 10.3791/2670

Cheron, G., Leroy, A., Palmero-Soler, E., De Saedeleer, C., Bengoetxea, A., Cebolla, A. M., et al. (2014). Gravity influences top-down signals in visual processing. *PLoS One* 9:e82371. doi: 10.1371/journal.pone.0082371

Clément, G., André-Deshays, C., and Lathan, C. E. (1989). Effects of gravitoinertial force variations on vertical gaze direction during oculomotor reflexes and visual fixation. *Aviat Space Environ Med.* 60, 1194–1198.

Clément, G., and Demel, M. (2012). Perceptual reversal of bi-stable figures in microgravity and hypergravity during parabolic flight. *Neurosci. Lett.* 507, 143–146. doi: 10.1016/j.neulet.2011.12.006

Clément, G., Loureiro, N., Sousa, D., and Zandvliet, A. (2016). Perception of egocentric distance during gravitational changes in parabolic flight. *PLoS One* 11:e0159422. doi: 10.1371/journal.pone.0159422

Clément, G., Reschke, M. F., Verrett, C. M., and Wood, S. J. (1992a). Effects of gravitoinertial force variations on optokinetic nystagmus and on perception of visual stimulus orientation. *Aviat. Space Environ. Med.* 63, 771–777.

Clément, G., Wood, S. J., and Reschke, M. F. (1992b). Effects of microgravity on the interaction of vestibular and optokinetic nystagmus in the vertical plane. *Aviat. Space Environ. Med.* 63, 778–784.

Cullen, K. E., and Taube, J. S. (2017). Our sense of direction: progress, controversies and challenges. *Nat. Neurosci.* 20, 1465–1473. doi: 10.1038/nn.4658

Della-Justina, H. M., Gamba, H. R., Lukasova, K., Nucci-da-Silva, M. P., Winkler, A. M., and Amaro, E. (2015). Interaction of brain areas of visual and vestibular simultaneous activity with fmri. *Exp. Brain Res.* 233, 237–252. doi: 10.1007/s00221-014-4107-6

Fisher, N. I. (1993). *Statistical Analysis of Circular Data.* Cambridge; New York, NY: Cambridge University Press.

Frissen, I., Campos, J. L., Souman, J. L., and Ernst, M. O. (2011). Integration of vestibular and proprioceptive signals for spatial updating. *Exp. Brain Res.* 212, 163–176. doi: 10.1007/s00221-011-2717-9

Glasauer, S., and Mittelstaedt, H. (1998). Perception of spatial orientation in microgravity. *Brain Res. Rev.* 28, 185–193. doi: 10.1016/s0165-0173(98)00038-1

Grabherr, L., and Mast, F. W. (2010). Effects of microgravity on cognition: the case of mental imagery. *J. Vestib. Res.* 20, 53–60. doi: 10.3233/ves-2010-0364

Grabherr, L., Karmali, F., Bach, S., Indermaur, K., Metzler, S., and Mast, F. W. (2007). Mental own-body and body-part transformations in microgravity. *J. Vestib. Res.* 17, 279–287.

Gramann, K., Müller, H. J., Schönebeck, B., and Debus, G. (2006). The neural basis of ego-and allocentric reference frames in spatial navigation: evidence from spatio-temporal coupled current density reconstruction. *Brain Res.* 1118, 116–129. doi: 10.1016/j.brainres.2006.08.005

Hitier, M., Besnard, S., and Smith, P. F. (2014). Vestibular pathways involved in cognition. *Front. Integr. Neurosci.* 8:59. doi: 10.3389/fnint.2014.00059

Karmali, F., and Shelhamer, M. (2008). The dynamics of parabolic flight: flight characteristics and passenger percepts. *Acta Astronaut.* 63, 594–602. doi: 10.1016/j.actaastro.2008.04.009

Kirby, K. N., and Gerlanc, D. (2013). BootES: an R package for bootstrap confidence intervals on effect sizes. *Behav. Res. Methods* 45, 905–927. doi: 10.3758/s13428-013-0330-5

Klein, T., Wollseiffen, P., Sanders, M., Claassen, J., Carnahan, H., Abeln, V., et al. (2019). The influence of microgravity on cerebral blood flow and electrocortical activity. *Exp. Brain Res.* 237, 1057–1062. doi: 10.1007/s00221-019-05490-6

Lackner, J. R., and DiZio, P. (2000). Human orientation and movement control in weightless and artificial gravity environments. *Exp. Brain Res.* 130, 2–26. doi: 10.1007/s002210050002

Leichnetz, G. R. (2001). Connections of the medial posterior parietal cortex (area 7m) in the monkey. *Anat. Rec.* 263, 215–236. doi: 10.1002/ar.1082

Markham, C. H., Diamond, S. G., and Stoller, D. F. (2000). Parabolic flight reveals independent binocular control of otolith-induced eye torsion. *Arch. Ital. Biol.* 138, 73–86.

McIntyre, J., Zago, M., Berthoz, A., and Lacquaniti, F. (2001). Does the brain model newton's laws? *Nat. Neurosci.* 4, 693–694. doi: 10.1038/89477

Müller, N. G., Riemer, M., Brandt, L., and Wolbers, T. (2018). Repetitive transcranial magnetic stimulation reveals a causal role of the human precuneus in spatial updating. *Sci. Rep.* 8:10171. doi: 10.1038/s41598-018-28487-7

Nicogossian, A. E., Williams, R. S., Huntoon, C. L., Doarn, C., Polk, J. D., and Schneider, V. S. (2016). *Space Physiology and Medicine: From Evidence to Practice.* New York, NY: Springer.

Pfeiffer, C., Serino, A., and Blanke, O. (2014). The vestibular system: a spatial reference for bodily self-consciousness. *Front. Integr. Neurosci.* 8:31. doi: 10.3389/fnint.2014.00031

R Core Team. (2016). *R: A Language and Environment for Statistical Computing.* Vienna, Austria: R Foundation for Statistical Computing. Available online at: https://www.R-project.org/. Accessed March 27, 2020

Reschke, M. F., and Clément, G. (2018). Vestibular and sensorimotor dysfunction during space flight. *Curr. Pathobiol. Rep.* 6, 177–183. doi: 10.1007/s40139-018-0173-y

Riemer, M., Hölzl, R., and Kleinböhl, D. (2014). Interrelations between the perception of time and space in large-scale environments. *Exp. Brain Res.* 232, 1317–1325. doi: 10.1007/s00221-014-3848-6

Roy, A. (2006). Estimating correlation coefficient between two variables with repeated observations using mixed effects model. *Biom. J.* 48, 286–301. doi: 10.1002/bimj.200510192

Schneider, S., Brümmer, V., Carnahan, H., Dubrowski, A., Askew, C. D., and Strüder, H. K. (2008). What happens to the brain in weightlessness? A first approach by eeg tomography. *NeuroImage* 42, 1316–1323. doi: 10.1016/j.neuroimage.2008.06.010

Svoboda, J., Popelikova, A., and Stuchlik, A. (2017). Drugs interfering with muscarinic acetylcholine receptors and their effects on place navigation. *Front. Psychiatry* 8:215. doi: 10.3389/fpsyt.2017.00215

Tagliabue, M., and McIntyre, J. (2011). Necessity is the mother of invention: reconstructing missing sensory information in multiple, concurrent reference frames for eye-hand coordination. *J. Neurosci.* 31, 1397–1409. doi: 10.1523/JNEUROSCI.0623-10.2011

Tagliabue, M., and McIntyre, J. (2013). When kinesthesia becomes visual: a theoretical justification for executing motor tasks in visual space. *PLoS One* 8:e68438. doi: 10.1371/journal.pone.0068438

Tagliabue, M., and McIntyre, J. (2014). A modular theory of multisensory integration for motor control. *Front. Comput. Neurosci.* 8:1. doi: 10.3389/fncom.2014.00001

Theeuwes, J., Belopolsky, A., and Olivers, C. N. (2009). Interactions between working memory, attention and eye movements. *Acta Psychol. Amst.* 132, 106–114. doi: 10.1016/j.actpsy.2009.01.005

van de Pol, M., and Wright, J. (2009). A simple method for distinguishing within- versus between-subject effects using mixed models. *Anim. Behav.* 77, 753–758. doi: 10.1016/j.anbehav.2008.11.006

Van Ombergen, A., Wuyts, F. L., Jeurissen, B., Sijbers, J., Vanhevel, F., Jillings, S., et al. (2017). Intrinsic functional connectivity reduces after first-time exposure to short-term gravitational alterations induced by parabolic flight. *Sci. Rep.* 7:3061. doi: 10.1038/s41598-017-03170-5

Wolbers, T., Hegarty, M., Büchel, C., and Loomis, J. M. (2008). Spatial updating: how the brain keeps track of changing object locations during observer motion. *Nat. Neurosci.* 11, 1223–1230. doi: 10.1038/nn.2189

Conflict of Interest: The authors declare that the research was conducted in the absence of any commercial or financial relationships that could be construed as a potential conflict of interest.

The handling Editor declared a past co-authorship with one of the authors SB.

Advantages of publishing in Frontiers

OPEN ACCESS
Articles are free to read for greatest visibility and readership

FAST PUBLICATION
Around 90 days from submission to decision

HIGH QUALITY PEER-REVIEW
Rigorous, collaborative, and constructive peer-review

TRANSPARENT PEER-REVIEW
Editors and reviewers acknowledged by name on published articles

Frontiers
Avenue du Tribunal-Fédéral 34
1005 Lausanne | Switzerland

Visit us: www.frontiersin.org
Contact us: info@frontiersin.org | +41 21 510 17 00

REPRODUCIBILITY OF RESEARCH
Support open data and methods to enhance research reproducibility

DIGITAL PUBLISHING
Articles designed for optimal readership across devices

FOLLOW US
@frontiersin

IMPACT METRICS
Advanced article metrics track visibility across digital media

EXTENSIVE PROMOTION
Marketing and promotion of impactful research

LOOP RESEARCH NETWORK
Our network increases your article's readership